PROGRAM GUIDE

63RD ELECTRONIC MATERIALS CONFERENCE

June 23-25, 2021

63RD ELECTRONIC MATERIALS CONFERENCE

June 23-25, 2021

WELCOME TO THE CONFERENCE!

It is with great pleasure that we welcome you to the **63rd Electronic Materials Conference (EMC 2021).** Though produced this year in a totally virtual format, the Conference will continue to follow in EMC's long tradition of offering premier research on the preparation and characterization of electronic materials. We have a strong community, and we thank those volunteers who have stepped forward to make this Conference happen. We also thank you for choosing to join us!

Conference Chair
Kris Bertness National Institute of Standards and Technology

Program Chair
Lisa Porter Carnegie Mellon University

CONFERENCE HIGHLIGHTS

The 63rd EMC Program

Scientists from around the world will participate virtually this week to share ideas, present technical information and contribute to the advancement of electronic materials research. Featuring nearly **350 oral/poster presentations,** the 63rd EMC will offer a strong program with **47 technical sessions** focused on electronic materials science and technology; energy storage and conversion materials; nanoscale science and technology; organic materials, thin films and devices; oxide semiconductors and dielectrics; and wide bandgap semiconductors. Poster sessions are slated for Wednesday evening and Thursday morning (EDT).

EMC Awards Ceremony & Plenary Session

The 63rd EMC kicks off Wednesday morning with the Awards Ceremony & Plenary Session. First, the 2020 Best Student Presentation Award recipients will be announced and honored. The Plenary lecture follows, with **David D. Awschalom,** The University of Chicago, presenting ***Abandoning Perfection for Quantum Technologies.*** Learn more on page 4.

Save the Date

64th Electronic Materials Conference
June 22-24, 2022
The Ohio State University
Columbus, Ohio

TABLE OF CONTENTS

SPECIAL THANKS!

RECORDING/PHOTO POLICY

No photographs/recordings of presentations permitted. Any files temporarily downloaded for viewing will be deleted upon completion of the session unless explicit permission is given by the authors.

EMC is being coordinated with the Device Research Conference, held virtually this year, June 20-23

The 63rd EMC has been managed by

MRS CONFERENCE SERVICES
Because the Experience Matters
mrs.org/conference-services

COMMITTEES

Executive Committee

Chair	**Kris Bertness** National Institute of Standards and Technology
Vice-Chair	**Lisa Porter** Carnegie Mellon University
Secretary	**Daniel Wasserman** The University of Texas at Austin
Treasurer	**Becky (R.L.) Peterson** University of Michigan

ELECTRONIC MATERIALS SCIENCE AND TECHNOLOGY

Contacts to Semiconductor Epilayers, Nanostructures and Organic Films

Leonard Brillson, The Ohio State University
Shadi Dayeh, University of California, San Diego
Suzanne Mohney, The Pennsylvania State University
Lisa Porter, Carnegie Mellon University
Tae-Yeon Seong, Korea University
Jerry Woodall, University of California, Davis

Epitaxial Materials and Devices

Seth Bank, The University of Texas at Austin
Kurt Eyink, Air Force Research Laboratory
Archie Holmes, The University of Texas at Austin
Sriram Krishnamoorthy, The University of Utah
Charles Lutz, Lumentum Operations LLC
Nadeemullah Mahadik, U.S. Naval Research Laboratory
Kyle McNicholas, MIT Lincoln Laboratory
Siddharth Rajan, The Ohio State University
Shadi Shahedipour-Sandvik, State University of New York Polytechnic Institute
Stephanie Tomasulo, U.S. Naval Research Laboratory
Christine Wang, Lincoln Laboratory, Massachusetts Institute of Technology
Kin-Man Yu, City University of Hong Kong

Materials Discovery

Anderson Janotti, University of Delaware
Sriram Krishnamoorthy, The University of Utah
Patrick Shea, Northrop Grumman Corporation
Angel Yanguas-Gil, Argonne National Laboratory

Materials for Memory and Computation

Alan Doolittle, Georgia Institute of Technology
Susan Fullerton, University of Pittsburgh
Feng Xiong, University of Pittsburgh
Ke Xu, University of Pittsburgh
Angel Yanguas-Gil, Argonne National Laboratory

Materials Processing and Integration

Daniel Ewing, Department of Energy's Kansas City National Security Campus
Mark Goorsky, University of California, Los Angeles
Doug Hall, University of Notre Dame
Karl Hobart, U.S. Naval Research Laboratory
Becky (R.L.) Peterson, University of Michigan
Nate Quitoriano, McGill University
Steve Ringel, The Ohio State University
Patrick Shea, Northrop Grumman Corporation
Jerry Woodall, University of California, Davis

Metamaterials and Materials for THz, Plasmonics and Polaritons

Joshua Caldwell, Vanderbilt University
Kurt Eyink, Air Force Research Laboratory
Rachel Goldman, University of Michigan
Anthony Hoffman, University of Notre Dame
Stephanie Law, University of Delaware
Thomas Searles, Howard University
Berardi Sensale Rodriguez, The University of Utah
Jason Valentine, Vanderbilt University
Daniel Wasserman, The University of Texas at Austin
Huili Grace Xing, Cornell University

Nanofabrication and Processing

Bruno Azeredo, Arizona State University
Kris Bertness, National Institute of Standards and Technology
Mona Ebrish, U.S. Naval Research Laboratory
Munho Kim, Nanyang Technological University, Singapore
Xiuling Li, University of Illinois at Urbana-Champaign
Parsian Mohseni, Rochester Institute of Technology
Angel Yanguas-Gil, Argonne National Laboratory
Andre Zeumault, The University of Tennessee, Knoxville

Nano-Magnetic, Magnetic Memory and Spintronic Materials

Hemant Dixit, GLOBALFOUNDRIES
Michael Flatté, The University of Iowa
Roland Kawakami, The Ohio State University
Xinyu Liu, University of Notre Dame
Angel Yanguas-Gil, Argonne National Laboratory

Narrow Bandgap Materials and Devices

Ganesh Balakrishnan, The University of New Mexico
Suprem Das, Kansas State University
Sanjay Krishna, The Ohio State University
Andrej Lenert, University of Michigan
Kyle McNicholas, Lincoln Laboratory, Massachusetts Institute of Technology
Kunal Mukherjee, Stanford University
Jamie Phillips, University of Delaware
Gregory Triplett, Virginia Commonwealth University
Christine Wang, Lincoln Laboratory, Massachusetts Institute of Technology
Daniel Wasserman, The University of Texas at Austin
Joshua Zide, University of Delaware

Physical Characterization for Quantum Computing

Ezra Bussman, Sandia National Laboratories
Jay Mody, GLOBALFOUNDRIES
Marvin Warner, Pacific Northwest National Laboratory

Point Defects, Doping and Extended Defects

Andrew Armstrong, Sandia National Laboratories
Ramon Collazo, North Carolina State University
Rachel Goldman, University of Michigan
Lincoln Lauhon, Northwestern University
Kunal Mukherjee, Stanford University
Steve Ringel, The Ohio State University
Shadi Shahedipour-Sandvik, State University of New York Polytechnic Institute
Jun Suda, Nagoya University
Christian Wetzel, Rensselaer Polytechnic Institute
Jerry Woodall, University of California, Davis

Quantum Materials

Matthew Doty, University of Delaware
Rachel Goldman, University of Michigan
Anthony Hoffman, University of Notre Dame
Stephanie Law, University of Delaware
Connie Li, U.S. Naval Research Laboratory
Jeremy Robinson, U.S. Naval Research Laboratory
Chakrakpani Varanasi, U.S. Army Research Office—Materials Science Division

ENERGY STORAGE AND CONVERSION MATERIALS

Electrochemical Energy Storage and Conversion

Susan Fullerton, University of Pittsburgh
David Gundlach, National Institute of Standards and Technology
Jung-Hyun Kim, The Ohio State University
Zetian Mi, University of Michigan
Edward Yu, The University of Texas at Austin

Energy Harvesting

Alan Doolittle, Georgia Institute of Technology
Deidra Hodges, The University of Texas at El Paso
Ken Jones, U.S. Army Research Laboratory
Suzanne Mohney, The Pennsylvania State University
Jamie Phillips, University of Delaware
Shadi Shahedipour-Sandvik, State University of New York Polytechnic Institute

Solar Cell Materials and Devices

Geoffrey Bradshaw, Air Force Research Laboratory
Rachel Goldman, University of Michigan
Mark Goorsky, University of California, Los Angeles
Andrej Lenert, University of Michigan
Steve Ringel, The Ohio State University
Oleg Rubel, McMaster University
Jae-Hyun Ryou, University of Houston
Mike Scarpulla, The University of Utah
Christian Wetzel, Rensselaer Polytechnic Institute
Mark Wistey, Texas State University
Jerry Woodall, University of California, Davis

Thermoelectrics and Thermal Transport

Kris Bertness, National Institute of Standards and Technology
Sukwon Choi, The Pennsylvania State University
Samuel Graham, Georgia Institute of Technology
Ferdinand Poudeu, University of Michigan
Xiaojia Wang, University of Minnesota
Yaguo Wang, The University of Texas at Austin
Andre Zeumault, The University of Tennessee, Knoxville
Joshua Zide, University of Delaware

NANOSCALE SCIENCE AND TECHNOLOGY

Graphene, BN, MoS_2 and Other 2D Materials and Devices

Thomas Beechem, Sandia National Laboratories
Kevin Daniels, University of Maryland
Mona Ebrish, U.S. Naval Research Laboratory
James Edgar, Kansas State University
Randall Feenstra, Carnegie Mellon University
Susan Fullerton, University of Pittsburgh
Jyoti Katoch, Carnegie Mellon University
Roland Kawakami, The Ohio State University
Manos Kioupakis, University of Michigan
Rachel Koltun, Northrop Grumman Corporation
Lincoln Lauhon, Northwestern University
Suzanne Mohney, The Pennsylvania State University
Siddharth Rajan, The Ohio State University
Joan Redwing, The Pennsylvania State University
Joshua Robinson, The Pennsylvania State University
Michael Snure, Air Force Research Laboratory
Michael Spencer, Morgan State University
Christine Wang, Lincoln Laboratory, Massachusetts Institute of Technology
Huili Grace Xing, Cornell University

Low-Dimensional Structures—Quantum Dots, Wires and Wells

Ganesh Balakrishnan, The University of New Mexico
Matthew Doty, University of Delaware
Kurt Eyink, Air Force Research Laboratory
Rachel Goldman, University of Michigan
Lincoln Lauhon, Northwestern University
Minjoo (Larry) Lee, University of Illinois at Urbana-Champaign
Zetian Mi, University of Michigan
Jamie Phillips, University of Delaware
Paul Simmonds, Boise State University
Daniel Wasserman, The University of Texas at Austin

Nanoscale Characterization—Scanning Probes, Electron Microscopy and Other Techniques

Thomas Beechem, Sandia National Laboratories
Rachel Goldman, University of Michigan
Lincoln Lauhon, Northwestern University
James LeBeau, Massachusetts Institute of Technology
Anders Mikkelsen, Lund University
Jay Mody, GLOBALFOUNDRIES
Volker Rose, Argonne National Laboratory
Rainer Timm, Lund University
Heayoung Yoon, The University of Utah
Edward Yu, The University of Texas at Austin

Nanostructured Materials

Kris Bertness, National Institute of Standards and Technology
Matt Brubaker, National Institute of Standards and Technology
Xiuling Li, University of Illinois at Urbana-Champaign
Zetian Mi, University of Michigan
Anders Mikkelsen, Lund University
Parsian Mohseni, Rochester Institute of Technology
Roberto Myers, The Ohio State University
Nate Quitoriano, McGill University
Rainer Timm, Lund University
George Wang, Sandia National Laboratories
William Wong, University of Waterloo

OXIDE SEMICONDUCTORS AND DIELECTRICS

Dielectrics and Multifunctional Oxides

Alan Doolittle, Georgia Institute of Technology
Doug Hall, University of Notre Dame
Anderson Janotti, University of Delaware
David Lederman, University of California, Santa Cruz
Patrick Lenahan, The Pennsylvania State University
Joseph Ngai, The University of Texas at Arlington
Angel Yanguas-Gil, Argonne National Laboratory

Gallium Oxide and Other Ultra-Wide Bandgap Oxides

Elaheh Ahmadi, University of Michigan
Shizuo Fujita, Kyoto University
Masataka Higashiwaki, National Institute of Information and Communications Technology
Sriram Krishnamoorthy, The University of Utah
Shin Mou, Air Force Research Laboratory
Becky (R.L.) Peterson, University of Michigan
Lisa Porter, Carnegie Mellon University
Siddharth Rajan, The Ohio State University
Chintalapalle Ramana, The University of Texas at El Paso
Marko Tadjer, U.S. Naval Research Laboratory
Huili Grace Xing, Cornell University
Hongping Zhao, The Ohio State University

Oxide Semiconductors—Growth, Doping, Defects, Nanostructures and Devices

Leonard Brillson, The Ohio State University
Steve Durbin, Western Michigan University
Thomas Jackson, The Pennsylvania State University
Anderson Janotti, University of Delaware
Mark Losego, Georgia Institute of Technology
Becky (R.L.) Peterson, University of Michigan
Shayla Sawyer, Rensselaer Polytechnic Institute
Sarah Swisher, University of Minnesota

ORGANIC MATERIALS AND THIN FILM TECHNOLOGY

Electronic Materials for Bio

Francesca Cavallo, The University of New Mexico
Buddhadev Paul Chaudhuri, Biolinq Inc.
Tzahi Cohen-Karni, Carnegie Mellon University
Shadi Dayeh, University of California, San Diego
David Estrada, Boise State University
David Gundlach, National Institute of Standards and Technology
Thomas Jackson, The Pennsylvania State University
David Janes, Purdue University

Flexible, Printed and/or Dissolvable Thin Films or Nanomembranes

Suprem Das, Kansas State University
Daniel Ewing, Department of Energy's Kansas City National Security Campus
Gerd Grau, York University
Thomas Jackson, The Pennsylvania State University
Thomas Kuech, University of Wisconsin–Madison
Becky (R.L.) Peterson, University of Michigan
Jae-Hyun Ryou, University of Houston
Sarah Swisher, University of Minnesota
William Wong, University of Waterloo

Organic and Hybrid Optoelectronic Devices

Alexander Ayzner, University of California, Santa Cruz
David Gundlach, National Institute of Standards and Technology
Tina Ng, University of California, San Diego
Oleg Rubel, McMaster University
Adrienne Stiff-Roberts, Duke University
Wei You, University of North Carolina at Chapel Hill

Organic Devices and Molecular Electronics

Gerd Grau, York University
David Gundlach, National Institute of Standards and Technology
Thomas Jackson, The Pennsylvania State University
David Janes, Purdue University
Ioannis Kymissis, Columbia University
Takhee Lee, Seoul National University
Tina Ng, University of California, San Diego
Curt Richter, National Institute of Standards and Technology
Adrienne Stiff-Roberts, Duke University
William Wong, University of Waterloo

WIDE BANDGAP SEMICONDUCTORS

Diamond and Related Materials

Mark Goorsky, University of California, Los Angeles
Andrew Koehler, U.S. Naval Research Laboratory
Jung-Hun Seo, University at Buffalo, The State University of New York
Patrick Shea, Northrop Grumman Corporatio

Group III-Nitrides—Growth, Processing, Characterization, Theory and Devices

Zakaria Y. Al Balushi, University of California, Berkeley
Andrew Allerman, Sandia National Laboratories
Srabanti Chowdhury, Stanford University
Theeradetch Detchprohm, Georgia Institute of Technology
Alan Doolittle, Georgia Institute of Technology
Russell Dupuis, Georgia Institute of Technology
Daniel Ewing, Department of Energy's Kansas City National Security Campus
Qhalid Fareed, Texas Instruments
Daniel Feezell, The University of New Mexico
Hiroshi Fujioka, The University of Tokyo
Jennifer Hite, U.S. Naval Research Laboratory
Andrew Koehler, U.S. Naval Research Laboratory
Xiaohang Li, King Abdullah University of Science and Technology
Michael Manfra, Purdue University
Siddharth Rajan, The Ohio State University
Shadi Shahedipour-Sandvik, State University of New York Polytechnic Institute
Andrei Vescan, RWTH Aachen University
Christian Wetzel, Rensselaer Polytechnic Institute
Jonathan Wierer, Lehigh University
Huili Grace Xing, Cornell University

Silicon Carbide—Growth, Processing, Characterization, Theory and Devices

Joshua Caldwell, Vanderbilt University
MVS Chandrashekhar, University of South Carolina
Sarit Dhar, Auburn University
Michael Dudley, Stony Brook University, The State University of New York
Daniel Ewing, Department of Energy's Kansas City National Security Campus
Nadeemullah Mahadik, U.S. Naval Research Laboratory
Michael Spencer, Morgan State University
Jun Suda, Nagoya University

EMC AWARDS CEREMONY & PLENARY SESSION

Wednesday, 9:00 am – 10:15 am (EDT)
Live Plenary Session

PLENARY SPEAKER

David D. Awschalom
The University of Chicago

Abandoning Perfection for Quantum Technologies

David D. Awschalom is the Liew Family Professor and Deputy Director of the Pritzker School for Molecular Engineering at The University of Chicago. He is also a senior scientist and Quantum Group Leader at Argonne National Laboratory, and director of the Chicago Quantum Exchange. Awschalom is the inaugural Director of Q-NEXT, one of the U.S. Department of Energy Quantum Information Science Research Centers. He was previously the Peter J. Clarke Director of the California NanoSystems Institute and Professor of Physics, Electrical and Computer Engineering at the University of California, Santa Barbara. He served as a research staff member and manager of the Nonequilibrium Physics Department at the IBM Watson Research Center. He works in the emerging fields of spintronics and quantum information engineering, where his students develop new methods to explore and control the quantum states of individual electrons, nuclei and photons in the solid state and in molecules. His research includes implementations of quantum information processing with potential applications in computing, imaging and communication. Awschalom received the American Physical Society Oliver E. Buckley Prize and Julius Edgar Lilienfeld Prize, the European Physical Society Europhysics Prize, the Materials Research Society David Turnbull Award and Outstanding Investigator Prize, the AAAS Newcomb Cleveland Prize, the International Magnetism Prize and the Néel Medal from the International Union of Pure and Applied Physics, and an IBM Outstanding Innovation Award. He is a member of the American Academy of Arts & Sciences, the National Academy of Sciences, the National Academy of Engineering and the European Academy of Sciences.

2020 BEST STUDENT PRESENTATION AWARDS

ORAL PRESENTATIONS

Eamonn Hughes
University of California, Santa Barbara

Compositional Changes at Dislocations and Interfaces in Heteroepitaxial Semiconductors Studied by Atom Probe

Advisor – Kunal Mukherjee

Wenshen Li
Cornell University

Observation of Near-Ideal Reverse Leakage Current in β-Ga_2O_3 Schottky Barrier Diodes and Its Implications for High Electric-Field Operation

Advisor – Huili Grace Xing

Jennifer Selvidge
University of California, Santa Barbara

Displacing Deleterious Misfit Dislocations from the Active Regions of InAs Quantum Dot Lasers on Si

Advisors – Kunal Mukherjee and John Bowers

POSTER PRESENTATION

Evyn Routh
North Carolina State University,

Device Quality $In_xGa_{x-1}N$ Templates ($0.07 < x < 0.10$) for Optoelectronic Applications

Advisors – Nadia El-Masry and Salah Bedair

TMS FOUNDATION
Student participation in this Conference is partially supported by a grant from the TMS Foundation

DAILY SCHEDULE OF EVENTS

All times are EDT

WEDNESDAY	
EMC Awards Ceremony and Plenary Session	9:00 am – 10:15 am
BREAK	10:15 am – 10:45 am
DRC Session 8: Thin Film Devices	10:30 am – 12:10 pm
A: Epitaxial Devices	10:45 am – 12:15 pm
B: Low-Dimensional Structures I	10:45 am – 12:15 pm
C: Plasmonics, Strong-Coupling and Resonant Optical Structures	10:45 am – 12:15 pm
D: Scandium Nitride	10:45 am – 12:15 pm
E: Nanostructured Materials	10:45 am – 12:15 pm
F: Gallium Oxide Devices	10:45 am – 12:15 pm
BREAK	12:15 pm – 1:15 pm
DRC Session 9: Wide Bandgap Devices II	12:50 pm – 2:50 pm
G: Defects and Doping	1:15 pm – 4:15 pm
H: Low-Dimensional Structures II	1:15 pm – 4:15 pm
I: Silicon Carbide—Theory, Characterization and Device Processing	1:15 pm – 4:15 pm
J: Group III-Nitride Growth—MBE	1:15 pm – 2:30 pm
L: Properties of 2D Materials	1:15 pm – 4:15 pm
M: Thermal Transport	1:15 pm – 2:30 pm
BREAK	2:30 pm – 3:00 pm
K: Group III-Nitride MOCVD and Characterization	3:00 pm – 4:15 pm
N: Narrow Bandgap Materials and Devices	3:00 pm – 4:15 pm
DRC Poster Session II	3:00 pm – 5:00 pm
BREAK	4:15 pm – 4:45 pm
PS1: Poster Session I	4:45 pm – 6:15 pm

THURSDAY	
PS2: Poster Session II	9:00 am – 10:30 am
BREAK	10:30 am – 11:00 am
P: Synthesis and Processing of 2D Materials	11:00 am – 1:45 pm
Q: Spin Dynamics in Electronic Materials	11:00 am – 2:00 pm
R: Group III-Nitride Materials and Applications	11:00 am – 12:15 pm
U: Diamond, Gallium Oxide and Related Materials	11:00 am – 2:00 pm
O: Water Splitting, Solar Hydrogen and Batteries	11:15 am – 1:45 pm
T: High Electron Mobility Transistors (HEMT) & Characterization of 2-Dimensional Electron, Hole Gases	11:15 am – 2:00 pm
BREAK	12:15 pm – 12:45 pm
S: Metasurfaces and Epitaxially-Grown Optical Materials and Devices	12:45 pm – 2:00 pm
BREAK	2:00 pm – 3:00 pm
V: Nanoscale Characterization	3:00 pm – 6:00 pm
W: Organic and Hybrid Materials and Devices I	3:00 pm – 5:45 pm
X: 2D Material Devices and Applications	3:00 pm – 6:00 pm
Y: Devices and Materials for Power Electronics	3:00 pm – 6:00 pm
Z: Solar Cell Materials and Devices	3:00 pm – 4:15 pm
BB: Gallium Oxide Processing, Characterization and Defects	3:00 pm – 4:15 pm
BREAK	4:15 pm – 4:45 pm
AA: Heteroepitaxy on Silicon	4:45 pm – 6:00 pm
CC: Gallium Oxide Epitaxy I	4:45 pm – 6:00 pm
BREAK	6:00 pm – 7:30 pm
Panel on Careers and Post-Graduate Studies in Materials Science	7:30 pm – 8:30 pm

FRIDAY	
EE: Organic and Hybrid Materials and Devices II	9:00 am – 11:30 am
FF: Doping and Stoichiometric Effects on Epitaxial Material	9:00 am – 10:15 am
HH: Group III-Nitride LED I	9:00 am – 10:15 am
LL: Materials Processing and Integration	9:00 am – 10:15 am
DD: Materials for Memory and Logic	9:15 am – 12:00 pm
JJ: Printed and Flexible Thin Films	9:15 am – 10:15 am
BREAK	10:15 am – 10:45 am
GG: Oxide Semiconductors—Charge Transport and Optical Properties	10:45 am – 12:00 pm
II: Group III-Nitride Photodetectors	10:45 am – 12:00 pm

FRIDAY	
KK: MBE—Selective Area Growth and Doping	10:45 am – 12:00 pm
MM: Gallium Oxide Epitaxy II	10:45 am – 12:00 pm
BREAK	12:00 pm – 1:00 pm
NN: Group III-Nitride Defects	1:00 pm – 2:15 pm
OO: Novel Materials	1:00 pm – 2:15 pm
PP: Oxide Thin-Film Transistors	1:00 pm – 2:15 pm
QQ: Group III-Nitride LED II	1:00 pm – 2:15 pm
RR: Late News—Novel Properties, Processing, Modeling and Characterization Methods	1:00 pm – 2:15 pm

All times are EDT ▲ Plenary Speaker

EMC Awards Ceremony and Plenary Session			
9:00 am			EMC Awards Ceremony
9:15 am	David D. Awschalom	▲PL01	Abandoning Perfection for Quantum Technologies
10:15 am			Break
A: Epitaxial Devices			
10:45 am	Rasha El-Jaroudi	A01	(Student) Growth of B-III-V Alloys for GaAs-Based Optoelectronic Devices
11:00 am	Andrew Frederick Briggs	A02	(Student) Enhanced Double Heterostructure Infrared LEDs Using Monolithically Integrated Plasmonic Materials
11:15 am	Nayana Remesh	A03	(Student) Impact of Buffer Traps on Temperature-Dependent Dynamic Ron in AlGaN/GaN HEMT
11:30 am	Michael Pedowitz	A05	(Student) Mn+3 Rich Nanofiberous Layered δ-phase MnO_2 on Epitaxial Graphene-Silicon Carbide for Selective Gas Sensing
11:45 pm	Li-Chung Shih	A06	(LATE NEWS, Student) Dual-Function ZTO Phototransistor Memory with Au Nanoparticles Mediated for Photo-Sensing and Multilevel Photo-Memory
B: Low-Dimensional Structures I			
10:45 am	Nicholas Paul Morgan	B01	(Student) Scalable III-V Nanowire Networks for IR Photodetection
11:00 am	Rabin Pokharel	B02	Epitaxial GaAsSbN (Te) NWs for Near-Infrared Region Photodetection Application
11:15 am	Shisir Devakota	B03	(Student) A Te Doped GaAsSb Ensemble Nanowire Photodetector for Near-Infrared Application
11:30 am	Gilbert Daniel Nessim	B04	Towards the Growth of 3D Forests of Carbon Nanotubes—Selective Height Control Using Thin-Film Reservoirs and Overlayers
11:45 pm	Dylan J. McIntyre	B06	(LATE NEWS, Student) Enhancement of Integrated Cu-Ti-CNT Conductors via Joule-Heating Driven CVD
C: Plasmonics, Strong-Coupling and Resonant Optical Structures			
10:45 am	John Tomko	C01	Long-Lived Modulation of Plasmonic Absorption by Ballistic Thermal Injection
11:00 am	Patrick Rufangura	C02	(Student) Enhanced Absorption with Core/Shell Silicon Carbide/Graphene Nanowires for Tunable Mid-Infrared Nanophotonics
11:15 am	Guanyu Lu	C03	(Student) Engineering the Spectral and Spatial Dispersion of Thermal Emission via Strong Coupling
11:30 am	Chan Kyaw	C04	(Student) Polarization-Selective Modulation of Supercavity Resonances Originating from Bound States in the Continuum
11:45 am	Vanessa Breslin	C05	Hyperbolic Phonon Polaritons in Calcite Nanopillar and Nanohole Arrays for Nanoscale Infrared Confinement
12:00 pm	Abhilasha Kamboj	C06	(Student) Long-Wave Infrared Topological Phonon Chain
D: Scandium Nitride			
10:45 am	Matthew Hardy	D01	Stress and Crystal Quality Control in Heteroepitaxial ScAlN Grown on SiC by Molecular Beam Epitaxy
11:00 am	Joseph Casamento	D02	(Student) Physical Properties of $Sc_xAl_{1-x}N$/GaN Heterostructures by Molecular Beam Epitaxy
11:15 am	Micah Haseman	D03	(Student) Cathodoluminescence and X-Ray Photoelectron Spectroscopy of ScN: Dopant, Defects and Band Structure
11:30 am	Morton Greenslit	D04	(Student) Plasma-Assisted Epitaxy of Piezoelectric $Sc_xAl_{1-x}N$ Films for Use in Harsh Environment Microwave Acoustic Sensors
11:45 am	Clarissa Vazquez-Colon	D05	Composition and Electrical Characterization of $Sc_xAl_{1-x}N$ Grown on Si Substrate by DC Sputtering
12:00 pm	Ping Wang	D06	Molecular Beam Epitaxy of N-Polar ScAlN and HEMT Structures
E: Nanostructured Materials			
10:45 am	Matt Brubaker	E01	Gallium Desorption from Selective Epitaxy Growth Mask Surfaces Determined by *In Situ* Reflectance Measurements
11:00 am	Alireza Abrand	E02	(Student) Growth and Characterization of Mixed-Dimensional InAs/MoS_2 Heterostructures
11:15 am	Andrew Nelson	E03	Structural Symmetry Breaking and Fast Chemical Diffusion in the Lead-Cadmium Sulfide Cation Exchange System
11:30 am	Divya Jyoti Prakash	E04	(Student) Self-Assembly of Hybrid Nanomembranes via Reconfiguration of Amorphous Complex Oxides
11:45 am	Wenbo Xin	E05	Graphene-Templated Growth of Surfactant-Free Gold Nanostructures for SERS Applications
12:00 pm	Bryan Melanson	E06	(LATE NEWS, Student) Realization of High-Efficiecy Green InGaN Nanowire Light-Emitting Diodes Using a Novel Dry-Etch Hardmask Removal Process

PROGRAM AT-A-GLANCE

WEDNESDAY

All times are EDT

F: Gallium Oxide Devices			
10:45 am	Andreas Fiedler	F01	Growth and Characterization of Deep Acceptor Mg-Doped/N-Type β-Ga_2O_3 Junctions
11:00 am	Arkka Bhattacharyya	F02	(Student) MOVPE-Grown β-Ga_2O_3 High Current Density (130 mA/mm) MESFET with a Record Metal/Ga_2O_3 Specific Contact Resistance of 8.3×10^{-7} Ω.cm^2
11:15 am	Dawei Wang	F03	(Student) Modulation-Doped β-$(Al_xGa_{1-x})_2O_3/Ga_2O_3$ HEMTs: Design Principles and Performance Optimization via TCAD
11:30 am	Dinusha Herath Mudiyanselage	F04	(Student) Vertical Wide Bandgap β-Ga_2O_3/GaN p-n Heterojunction with Mesa Based Edge Termination
11:45 am	Rujun Sun	F05	Temperature Dependent Current Stress of β-Ga_2O_3 Schottky Devices
12:00 pm	Zhe Ashley Jian	F06	(LATE NEWS, Student) Electrical Properties of MOCVD-Grown AlSiO Gate Dielectric on (001) β-Ga_2O_3
DRC Session 8: Thin Film Devices			
10:30 am	Mengwei Si	8A	High-Performance Atomic-Layer-Deposited In_2O_3 Transistors with EOT Scaling Down to 0.86 nm: Achieving I_{ON} of 1.2 A/mm at V_{GS}-V_T=1V and V_{DS}=1 V and g_m of 1.5 S/mm at V_{DS}=1 V
10:50 am	Christopher R. Allemang	8B	Steep Subthreshold Swing ALD ZTO TFTs with *in situ* Gate Insulator
11:10 am	Thomas Anthopolous	8C	(Invited) Large-Area Nanoelectronics Manufactured at a Flash
11:50 am	Kelly Liang	8D	Field-Emission Enhanced Contacts for Disordered Semiconductor Based Thin-Film Transistors
DRC Session 9: Wide Bandgap Devices II			
12:50 pm	Martin Kuball	9A	(Invited) Thermal Modeling for Wide Bandgap Devices
1:30 pm	Aditya Raj	9B	GaN/AlGaN Superlattice Based E-Mode P-Channel MES FinFET
1:50 pm	Reet Chaudhuri	9C	GHz-Speed GaN/AlN P-Channel MIS-HFETs with I_{max} of 0.5 A/mm
2:10 pm	Mina Rais-Zadeh	9D	(Invited) III-Nitride Acousto-Electric Microsystems for Extreme Space Environments
G: Defects and Doping			
1:15 pm	Annalisa Calò	G01	Spatial Defects Nanoengineering for Bipolar Conductivity in MoS_2
1:30 pm	Burcu Ozden	G02	An Alternative Way to Tune the Defects in a Single Layer MoS_2
1:45 pm	Claire Grace Andreasen	G03	(Student) Electron Redistribution at Monovacancy in Graphene
2:00 pm	Julia Tala Hatoum	G04	(Student) Chemical Consequence of Electron Redistribution in Graphene with Grain-Boundary
2:15 pm	James Bork	G05	(LATE NEWS, Student) Improvements in InAlBiAs Morphology and Prospects of InAlBiAs-Based Photon Upconverter
2:30 pm			Break
3:00 pm	Hsien-Lien Huang	G06	(Student) Atomic Scale Investigation of Aluminum Incorporation, Defects and Phase Stability in β-$(Al_xGa_{1-x})_2O_3$ Films
3:15 pm	Pegah Bagheri	G07	(Student) Direct Evidence of Ge Becoming a Deep Donor Instead of a DX- in Al Rich
3:30 pm	Chunyi Huang	G08	(Student) Si Dopants Enable Catalyst-Free n-Type GaAs Nanowire Growth by Modifying Facet Energies
3:45 pm	Qianyu Cheng	G09	(Student) Crystallographic and Defect Characterization of PVT-Grown ZnSe Under Different Growth Configurations
H: Low-Dimensional Structures II			
1:15 pm	Benjamin Diroll	H01	Surface Chemistry Modifies Band Edge Structure of Colloidal Quantum Wells
1:30 pm	Olivia Pavlic	H02	(Student) *Ab Initio* Studies of the Optical Properties of Lead Chalcogenide Nanocrystals
1:45 pm	Maia Mombru Frutos	H03	(Student) A Study of the Optimal Synthesis Conditions in Solution Method for Bismuth Sulpho Iodide Nanorods
2:00 pm	Chappel S Thornton	H04	(Student) Rapid Ge Diffusion Along Si/SiO_2 Interfaces During High Temperature Oxidation for Quantum-Scale Structures
2:15 pm	Pradeep Namboodiri	H05	Fabrication of Single and Few Atom Donor-Based Devices in Silicon
2:30 pm			Break
3:00 pm	Yi Liu	H06	(Student) Self-Selective Formation of Ordered 1D and 2D GaBi Structures on Wurtzite GaAs Nanowire Surfaces
3:15 pm	Sivakumar Vishnuvardhan Mambakkam	H07	(Student) Growth of Topological Insulator Bi_2Se_3 Particles on GaAs via Droplet Epitaxy
3:30 pm	Nicholas Ulizio	H08	(Student) Shape-Effect on Quantum Confinement in Alloy Quantum Dots and Their Applications for Photovoltaic Green Energy
3:45 pm	Pankul Dhingra	H09	(Student) InP Quantum Dot and InGaP Quantum Well Visible Lasers on Si

All times are EDT

I: Silicon Carbide Theory, Characterization and Device Processing			
1:15 pm	Tuerxun Ailihumaer	I01	(Student) Investigation of Dislocations Contrast and Determination of Their Burgers Vectors in Synchrotron Grazing-Incidence X-Ray Topographs in PVT-Grown 4H-SiC Crystals
1:30 pm	Hongyu Peng	I02	(Student) Analysis of Local Lattice Distortion of SiC in Weak Beam Topography
1:45 pm	Zeyu Chen	I03	(Student) Assessment of Lattice Damage in High Energy Ion Implanted 4H-SiC Wafers at Room Temperature
2:00 pm	Lu Wang	I04	(Student) Theoretical and Experimental Analysis of Interfaces Between 4H-SiC and High-κ Dielectrics
2:15 pm	Timothy Sean Wolfe	I05	(Student) Transition Metal Defects 4H-SiC—Optical and Electronic Levels from First Principles
2:30 pm			Break
3:00 pm	Lydia Kuebler	I06	(Student) Investigation of Implant Temperature on Dopant Activation Efficiency for Single Fluence Al+ Implanted 4H-SiC
3:15 pm	Suman Das	I07	(Student) High Temperature Characteristics of NO Annealed P-Channel 4H-SiC MOSFET
3:30 pm	Mathew Kelley	I08	(Student) Spatially Resolved Fourier Transform Impedance Spectroscopy—A Technique to Rapidly Characterize Composite Interfaces and a Study of Quantum Dot/Epitaxial Graphene/SiC Optoelectronic Devices
3:45 pm	Peter A Schultz	I09	Theory for Intrinsic Point Defects in 3C-SiC Reassessed Using Converged Large-Supercell Calculations
4:00 pm	Henry Fidlow	I10	(Student) Atomistic Basis of Anisotropic Poisson's Ratio in 3C-SiC
J: Group III-Nitride Growth—MBE			
1:15 pm	Adam M. Payne	J01	Machine Learning for Evaluation of RHEED Spectra on III-Nitride Films Grown Using Molecular Beam Epitaxy
1:30 pm	Habib Ahmad	J02	(Student) First Experimental Demonstration of P-Type AlN Grown by MME
1:45 pm	Brandon Dzuba	J03	(Student) Anomalous Super-Linear Growth Rate Reduction with Increasing Aluminum Flux in M-Plane Grown by PAMBE
2:00 pm	Ryan Page	J04	(Student) MBE Growth and Transport Properties of Ultra-Wide Bandgap AlGaN on AlN Bulk Substrate
2:15 pm	Elaheh Ahmadi	J05	Growth of High Quality 350nm-Thick InGaN Films on N-Polar GaN Substrates by Plasma-Assisted Molecular Beam Epitaxy
2:30 pm			Break
K: Group III-Nitride MOCVD and Characterization			
3:00 pm	Maliha Noshin	K01	(Student) Characterization of Regrown Interface in Ga-Polar c-Plane GaN with Diverse Growth Interruptions
3:15 pm	Henry Collins	K02	(Student) Planar Porosification of N-Polar GaN for Regrowth of Smooth GaN Films
3:30 pm	Sizhen Wang	K03	Scanning Spreading Resistance Microscopy Characterization of Selective Doped GaN Epitaxial Layer Grown by MOCVD
3:45 pm	Michael Evan Liao	K04	(Student) The Origins of Large Surface Step Features of Homoepitaxial GaN Grown on Dot-Core GaN Substrates
4:00 pm	Caroline E Reilly	K05	(Student) Comparison of AlN/GaN Heterostructures Grown at Low Temperatures with Ammonia or Dimethylhydrazine via Metalorganic Chemical Vapor Deposition
L: Properties of 2D Materials			
1:15 pm	Akshay Balgarkashi	L01	(Student) The Impact of Localized Hot Spots on the Raman Response of Monolayer MoS_2
1:30 pm	Lynn Karriem	L02	(Student) Differential Gene Expression in C2C12 Cells Due to Scaffold Structure-Property-Processing-Performance Correlations
1:45 pm	Jun Yan	L03	Improving Exciton Valley Polarization by Scattering
2:00 pm	Jun Xiao	L04	Berry Curvature Memory Enabled by 2D Ferroelectric Semimetals
2:15 pm	Joel F Siegel	L05	(Student) Large-Area Arrays of Short-Wave-Infrared Graphene Plasmonic Resonators Exhibiting Strong Non-Local and Electron Quantization Effects
2:30 pm			Break
3:00 pm	Matthew C Strasbourg	L06	(Student) Enhanced Multiexciton Formation by an Electron-Hole Plasma in 2D Semiconductors
3:15 pm	Joon-Seok Kim	L07	Dielectric Effects on Exciton Emission of MoS_2/P(VDF-TrFE) Heterostructure—A Correlated Mapping Study
3:30 pm	Elisabeth Mansfield	L08	Surface Morphology and Composition of Hexagonal Boron Nitride Single Crystals Thermally Oxidized in Dry and Ambient Air
3:45 pm	Yuan Li	L09	(Student) Resistive Switching Properties of Single Layer h-BN Film with Different Electrodes
4:00 pm	Daniel Lewis	L10	(Student) Characteristics and Tunability of Electron Emission Sources from Quasi-Freestanding Epitaxial Graphene Microstructures

PROGRAM AT-A-GLANCE

WEDNESDAY

All times are EDT

M: Thermal Transport			
1:15 pm	Joyce H Anderson	M01	Direct Measurement of Thermal Conductivity of Gold from Meso- to Nano-Scale
1:30 pm	Wilarachchige D.C. Bhagya Gunatilleke	M02	(Student) A Fundamental Study of Structural Effects on Thermal Properties of Quaternary Chalcogenides
1:45 pm	Koushik Pal	M03	Microscopic Mechanism of Unusual Lattice Thermal Transport in $TlInTe_2$—Roles of Anharmonic Renormalization and Wave-Like Tunneling of Phonons
2:00 pm	Yiwen Song	M04	(Student) Thermal Conductivity of $Al_{1-x}Sc_xN$ for 5G RF MEMS Filters
2:15 pm	Timothy David Brown	M05	(LATE NEWS) Characterization and Exploitation of Non-Linear Dynamics in Vanadium Dioxide Thermal Memristors
2:30 pm			Break
N: Narrow Bandgap Materials and Devices			
3:00 pm	Aaron J. Muhowski	N01	Minority-Carrier Lifetimes in Digitally-Grown AlInAsSb Alloys
3:15 pm	Oleg Maksimov	N02	High Detectivity PbS_xSe_{1-x} Films for Mid-Wavelength Infrared Detectors
3:30 pm	Kunal Mukherjee	N03	Mid-Infrared Light Emission from PbSe Epitaxial Films on III-V Substrates
3:45 pm	Mark Wistey	N04	Optical Properties and Band Structures of Strained Ge:C
4:00 pm	Seyedeh Fahimeh Banihashemian	N05	SiSn Electronic Band Structure Modelling Using Density Functional Theory for Optoelectronic Applications

DRC POSTER SESSION II

WEDNESDAY

3:00 pm - 5:00 pm (EDT)

Presenter	Paper #	Title
Zehao Lin	PS2.A	Ferroelectric Field-Effect Transistors by Atomic-Layer-Deposited Hafnium Zirconium Oxide and Indium Oxide as Gate Insulator and Channel Semiconductor
Boce Lin	PS2.B	Experimental RF Characterization of Ferroelectric Hafnium Zirconium Oxide Material at GHz for Microwave Applications
Keerthana Shajil Nair	PS2.C	Process Dependent Ferroelectric Switching in Metal-Ferroelectric-Dielectric-Metal FTJ Stack
Saketh Ram Mamidala	PS2.D	Controlling Filament Stability in Scaled Oxides (3 nm) for High Endurance (>106) Low Voltage ITO/HfO_2 RRAMs for Future 3D Integration
Keren Stern	PS2.E	Sub-Nanosecond Partial Reset for Analog Phase Change Neuromorphic Devices
Daniel S Schneider	PS2.F	MoS_2/Graphene Lateral Heterostructure Field Effect Transistors
Shayan Parhizkar	PS2.G	Waveguide-Integrated Photodetectors Based on 2D Platinum Diselenide
Agata Piacentini	PS2.H	Low Hysteresis MoS_2-FET Enabled by CVD-Growth h-BN Encapsulation
Sourish Banerjee	PS2.I	Amorphous ALD-Grown GaO_x TFT for BEOL Integration
Jie Zhang	PS2.J	Crystallinity Engineering of Stoichiometric TiO_2: Transition from Insulator to Semiconductor
Neel Chatterjee	PS2.K	Mobility Boost in Transparent Oxide Semiconductors with High-$_K$ Gated TFTs
Dong Yang	PS2.L	Enhanced Performance of Ultra-Scaled Vertical SiC Gate-All-Around Nanowire 1.2 kV Power MOSFET
Ankit Shukla	PS2.M	Terahertz Auto Oscillations in Non-Collinear Coplaner Metallic Antiferromagnets
Suyogya Karki	PS2.N	Spin-Dependent Electron Transport in Scandium Nitride Magnetic Tunnel Junction Devices Using First Principles
Karam Cho	PS2.O	Exchange-Coupling-Enabled Electrical-Isolation of Compute and Programming Paths in Valley-Spin Hall Effect Based Spintronic Device for Neuromorphic Applications

PS1: POSTER SESSION I

WEDNESDAY

4:45 pm - 5:15 pm (EDT)

Presenter	Paper #	Title
Mayank Bulsara	EP01	(Exhibitor Poster) Taiyo Nippon Sanso
Kathy Wheeler	EP02	(Exhibitor Poster) k-Space Associates, Inc.
Brian Doherty	EP03	(Exhibitor Poster) CuttingEdge Ions, LLC
Gary S Tompa	EP04	(Exhibitor Poster) Structured Materials Industries, Inc.
Paul G. Nalam	PS1.01	(Student) Effect of Post-Deposition Annealing on the Structure, Morphology and Optical Properties of GeO_2 Films
Víctor Eliud Ceniceros-Orozco	PS1.02	(Student) Influence of CaO on Reddish Luminescence of Sm^{3+}-Doped Borosilicate Glasses
Michael Alverson	PS1.03	(Student) Discovery of Novel Crystal Structures via Generative Adversarial Networks
Wafaa Farag Gebril	PS1.04	(Student) CVD Single Layer Graphene-Based Phototransistor with High Responsivity and Detectivity by Photogating Effect
Yongjian Zhou	PS1.05	(Student) Optical Properties of Different Stacking Orders in ReS_2
Yu-Lin Hsu	PS1.06	(Student) Local Photovoltaic Measurements of CdTe Solar Cells Using Microscale Point Back-Contacts
Joel Hubbard	PS1.07	(Student) Electrical Behavior of CNT Epoxy Composites Under Simulated Space Environments
Jessica Nashelly Salgado-Delgado	PS1.08	(Student) Mechanical and Electrical Properties Study of a Composite Biomaterial of PVA-Chitosan / PPy / PEDOT:PSS / MWCNT / CB
Fomina Lioudmila	PS1.10	Synthesis and Characterization of Novel Pyrrole Ferrocene Derivatives and Their Semiconductor Behaviour
Giovanna Angélica Vázquez Hernández	PS1.11	(Student) Synthesis and Characterization of Novel Organic Compound: 1-(p-Fullerene-Phenyl)-2, 5 Diphenylpyrrole and Its Semiconductor Behavior
Marcos Martinez	PS1.13	Parametric Modeling of Self-Winding Helices for Sub-Millimeter Traveling Wave Tube Amplifiers
Mostafa Abdelhamid	PS1.14	(Student) Device Quality P-Type InGaN Relaxed Films
Ping Wang	PS1.15	On the Photoluminescence Emission of ScAlN Grown by Molecular Beam Epitaxy
Marzieh Savadkoohi	PS1.17	(Student) Effect of Active Molecule Edges on Magnetic Transport Properties of Molecular Spintronics Devices (MSD)
Andrew Christopher Grizzle	PS1.18	Monte Carlo Simulation Study of Single Molecular Spin State Effect on Anit-Ferromagnetically Coupled Magnetic Layers of Magnetic Tunnel Junction Based Spintronics Device
Pius Suh	PS1.20	(Student) Monte Carlo Simulations Investigating the Effect of Intra-Molecular Coupling Within Double Segmented Molecules on Magnetic Properties of Molecular Spintronics Devices
Uzma Amir	PS1.22	Ferromagnetic Electrodes Thickness Impacting the Equilibrium Magnetic Properties of the Magnetic Tunnel Junction Based Molecular Spintronics Devices.
Sarah Sheffield	PS1.23	(Student) Fluoropolymer Ionomers as a Dielectric in Rubrene Single-Crystal Transistors for Improved Charge Carrier Mobility
Lu Yu	PS1.24	(Student) Effects of Lignin Precursors and Processing Conditions on the Structures of Carbon Composites as Electrodes for Batteries
Nuwanjula Samarasingha	PS1.26	(Student) Temperature Dependence of Optical Phonon Bands in GaP
Jesus Marquez	PS1.27	(LATE NEWS, Student) Annealing Time Effects with a Fixed Temperature on Thin-Film Perovskite Solar Cells

PS2: POSTER SESSION II

THURSDAY

9:00 am - 10:30 am (EDT)

Presenter	Paper #	Title
Mayank Bulsara	EP01	(Exhibitor Poster) Taiyo Nippon Sanso
Kathy Wheeler	EP02	(Exhibitor Poster) k-Space Associates, Inc.
Brian Doherty	EP03	(Exhibitor Poster) CuttingEdge Ions, LLC
Gary S Tompa	EP04	(Exhibitor Poster) Structured Materials Industries, Inc.
Jung Suk Cha	PS2.01	(Student) Electrical Characteristics of Differently Surface-Treated N-Type AlInP for Red Light-Emitting Diodes
Nayana Remesh	PS2.02	High-Reliability AlGaN/GaN HEMTs for High Voltage Applications Using Nitrogen-Rich Silicon Nitride Passivation and Field Plates
Terje Gunnar Finstad	PS2.03	Engineering Electrical Properties of Reactively Sputtered High Entropy Alloy CrFeNiCoCu Films
Ying Wang	PS2.04	Electrical Conductivity and Effects of Bending of Flexible Amorphous Transparent Conducting CdO–Ga_2O_3 Alloy Films Sputter–Deposited at Room Temperature
Alam Saj	PS2.05	Synthesis and Characterization of Germanium Telluride Nanowires for Memory Application
Sreya Suresh	PS2.06	(Student) Correlated Quantum Materials—Exploring Spin Transport in Iridate Thin Films
Nithin Xavier	PS2.08	(Student) Fabrication and Scaling Up of $Cs_{0.05}(MA_{0.17}FA_{0.83})_{0.95}Pb(I_{0.83}Br_{0.17})_3$ Perovskite Solar Cell at High Moisture and Oxygen Level
Radha Raman	PS2.11	(Student) Conduction-Templated Electrodeposition of Directed Nanostructures on 2D Materials for Axion-Like Evolvable Interconnects
Omid Mohammad Moradi	PS2.12	(Student) Fabrication of Polyvinylidene Fluoride (PVDF) Nanostructures with a Unique Ferroelectric Characteristic Using Initiated Chemical Vapor Deposition (iCVD)
Hiroaki Komatsu	PS2.14	(Student) Photoexcited Carrier Transport Properties of ZnO Nanoparticles-Functionalized Cellulose Nanofiber Films
Malek Mahmoudi	PS2.15	(Student) Developments of Hybrid White Organic Light Emitting Diodes with High Efficiency and Colour Quality Exploiting Exciton Allocation Strategy
Karolis Leitonas	PS2.16	(Student) Investigation of Dibenzo[A,C]Phenazine Derivatives Substituted by Acridan or Carbazole Moieties as Efficient OLED Hosts or Emitters
Jaeho Shin	PS2.18	(Student) Control of Photocurrent Direction by Molecular Dipole Moment in Molecular Heterojunctions with Two-Dimensional Semiconductor
Yang Liu	PS2.19	(Student) Molar Mass Dependence of P3HT on the Molecular Interaction and Performance in a Fullerene-Free Organic Photovoltaic Blend
Indranil Mal	PS2.20	(Student) Effect of Dilute Concentration of Bi on the Optoelectronic Properties of InAs for Long Wavelength Infrared Applications—A First Principle Analysis
Rikuto Nakamura	PS2.21	(Student) Reactive Ion Etching of Mg_2Si Substrate Using CF_4 and SF_6
Hiroto Tsuchida	PS2.22	(Student) Optical Transmission Measurement of *In Situ* Annealed Mg_2Si Crystals
Makoto Chiba	PS2.23	(Student) I-V and C-V Measurements of Metal/n-Mg_2Si Junction
Yudai Ichikawa	PS2.24	(Student) Electrical Property and Photosensitivity of Mesh-Electrode Type Mg_2Si Photodiodes Using Au/Pt P-Side Contact
Eduardas Pečiulis	PS2.26	(Student) Bicarbazole Derivatives Containing Methoxydiphenylamino or Dimethoxycarbazolyl Substituents as Efficient Hole-Transporting Materials
Matas Guzauskas	PS2.27	(Student) Organic Emitters with Photo Induced Conformational Changes for Ratiometric and Colorimetric UV Sensing
Junhee Lee	PS2.28	(Student) Application of p-NiO/n-ZnO Heterojunction PN Diodes as Transparent Temperature Sensors
Yixin Xiao	PS2.29	(Student) Probing the Role of Non-Polar Surfaces of GaN Nanostructures in Efficient and Ultra Stable Photoelectrochemical Water Splitting
Bosun Abbas Roy-Layinde	PS2.30	(Student) Temperature Dependence of Thermophotovoltaic Conversion Using InGaAs Air-Bridge Cells
Ping Wang	PS2.32	Molecular Beam Epitaxy of ScAlN Nanowires—Structural and Optical Properties

Panel on Careers and Post-Graduate Studies in Materials Science

Thursday, June 24 | 7:30 pm – 8:30 pm (EDT)

Zoom Webinar, EMC conference registration NOT required
Moderator: Suzanne Mohney, The Pennsylvania State University

Interested in a career in materials science and want to know more?

- Is graduate school right for you? What paths are there to these careers?
- What does a materials scientist do and where do they work?
- What are the career options in industry, government and academia?

PANELISTS:

Adrienne Stiff-Roberts
Duke University

Wenbing Hu
Applied Materials, Inc.

Samuel Graham
Georgia Institute of Technology

David Estrada
Boise State University

Mona Ebrish
U.S. Naval Research Laboratory

Michael Abraham
Lockheed Martin

This event is organized by the EMC 2021 Officers and was made possible by
National Science Foundation Award DMR-2120668
Program Officer: Debasis Majumdar
PI: Dan Wasserman

Learn more at **mrs.org/63rd-emc**

PROGRAM AT-A-GLANCE

THURSDAY

All times are EDT

O: Water Splitting, Solar Hydrogen and Batteries			
11:15 am	Hyun Uk Chae	O01	(Student) Hot Electron Metal-Free Electrode for Hydrogen Evolution Reaction
11:30 am	Rajashree Konar	O02	(Student) Facile and Scalable Ambient Pressure Chemical Vapor Deposition-Assisted Synthesis of Layered Silver Selenide (β-Ag_2Se) on Ag Foil as a Possible Oxygen Reduction Catalyst in Alkaline Medium
11:45 am	Ishtiaque Ahmed Navid	O04	(Student) Molecular Beam Epitaxy, Carrier Dynamics and Photocatalytic Properties of III-Nitride Nanowall Network
12:00 pm	Soonil Lee	O05	(Student) Low-Cost, Scalable Fabrication of Stable, High Performance Si-Based Metal-Insulator-Semiconductor Photoelectrodes for Solar-Driven Water Splitting
12:15 pm			Break
12:45 pm	Chanyeop Yu	O06	(Student) Surface-Modified Zero-Strain Spinel-Type $Li_2Co_{2-x}Al_xO_4$ (where x = 0, 0.3, and 0.60) Cathodes for Lithium-Ion Batteries
1:00 pm	Lalith Rao	O07	(Student) Multifunctional Composite Binder for High Voltage Lithium-Ion Batteries
1:15 pm	Michelle Salgado	O08	New Long Life/ Safer Lithium Ion Battery with Low Cost/Li-Corrosion Resistant Ultrananocrystalline Diamond-Coated Components
1:30 pm	Sami Ullah	O10	Investigation of Lithiated Tin (Sn/Li Alloy) Thin Film as a Low Work Function Termination on Silicon/Diamond Substrates
P: Synthesis and Processing of 2D Materials			
11:00 am	Madina Telkhozhayeva	P01	(Student) Higher Ultrasonic Frequency Liquid Phase Exfoliation as a More Efficient Method to Deposit Monolayer to Few-Layer Flakes of 2D Layered Materials
11:15 am	Chuanfang (John) Zhang	P02	(Student) High-Quality MXene Inks for Energy Storage
11:30 am	Annika Grundmann	P03	(Student) MOCVD of 2D-WS2 on Conductive TiN/Si Substrates
11:45 am	Rajashree Konar	P04	(Student) Scalable Synthesis of Few-Layered 2D Tungsten Diselenide (2H-WSe_2) Nanosheets Directly Grown on Tungsten (W) Foil Using Ambient-Pressure Chemical Vapor Deposition for Reversible Li-Ion Storage
12:00 pm	Zhehao Zhu	P05	(Student) Towards the Rational Design of Printed 2D Materials
12:15 pm			Break
12:45 pm	Thomas Virgil McKnight	P06	(Student) MOCVD Growth of Tungsten Ditelluride Thin Films
1:00 pm	Gilbert Daniel Nessim	P07	High Yield, Bottom-Up/Top-Down Synthesis of 2D Layered Metal Sulfides, Phosphides and Selenides Using Chemical Vapor Deposition with Applications in Electronics and Electrochemistry
1:15 pm	Ping Wang	P09	Graphene Interface Mediated Lateral Epitaxy of Monolayer Hexagonal Boron Nitride
1:30 pm	Huiran Wang	P10	(Student) Impact of Salt and Solvent Identity on the Deposition of a Cobalt Crown Ether Phthalocyanine Monolayer Electrolyte
Q: Spin Dynamics in Electronic Materials			
11:00 am	Stephen Ross McMillan	Q01	Probing the Coherent Spin Dynamics of Divacancies in Silicon Carbide with Low-Field Magnetoresistance
11:15 am	James P. Ashton	Q02	Ultra-Low Field Frequency-Swept Electrically Detected Magnetic Resonance—Multiple Photon Transitions and Bloch-Siegert Shifts
11:30 am	Eva Mutunga	Q03	Electrode Materials Influence on Molecular Spintronics Devices
11:45 am	Denis R Candido	Q04	Suppression of the Optical Linewidth and Spin Decoherence of a Quantum Spin Center in a p–n Diode
12:00 pm	Emma J. Renteria	Q05	Controlled Synthesis of Screw Dislocations in Semiconductor Nanomembranes for Spintronic Applications
12:15 pm			Break
12:45 pm	I-Hsuan Kao	Q06	(Student) Deterministic Switching of a Perpendicularly Polarized Magnet Using Unconventional Spin-Orbit Torques in WTe_2
1:00 pm	Kwangyul Hu	Q07	(Student) Spin-Wave Edge Modes Excitation in a Tapered Thin Film
1:15 pm	Jonathan Ernesto Valenzuela	Q08	(Student) Neutron Diffraction and Transport Properties of Antiferromagnet $CaFe_2O_4$
1:30 pm	Yueguang Shi	Q09	First Principles Calculation of the Electronic Structure of V(TCNE)2
1:45 pm	Yonatan Calahorra	Q10	Magnetic and Magnetoresistive Properties of Nickel/Nanoporous-GaN Composites

All times are EDT

R: Group III-Nitride Materials and Applications			
11:00 am	Amit P Shah	R01	Rhenium-Based Ohmic Contacts to n-GaN
11:15 am	Elia Palmese	R02	(Student) Characterization of $Al_xIn_{1-x}N$ Mismatched to GaN for Thin Oxide Applications
11:30 am	Amal Das	R03	(Student) Growth and Characterization of Preferential (100) Oriented AlN Thin Films Grown on Mo Coated Si (100) Substrate by Reactive RF Sputtering
11:45 am	Benjamin McEwen	R04	(Student) AlGaN/GaN HEMT-Based Detection of Reactive Oxygen Species Molecule H_2O_2
12:00 pm	Sean Johnson	R05	(Student) Analysis of Patterned GaAsSbN Nanowires via Boltzmann Sigmoidal Model
12:15 pm			Break
S: Metasurfaces and Epitaxially-Grown Optical Materials and Devices			
12:45 pm	Stefan Maier	S01	Metasurface Orbital Angular Momentum Holography
1:00 pm	Milan Palei	S02	Hybridization of Multi-Plasmon Modes on Coupled Nanoridge Array Metasurfaces for Super-Resolution Imaging
1:15 pm	Leland Joseph Nordin	S03	(Student) All-Epitaxial Spectrally Selective Dual-Color Surface Plasmon-Polariton Infrared Detectors
1:30 pm	Angela Cleri	S04	(Student) Mid-Wave to Near-IR Optoelectronic Properties and Epsilon-Near-Zero Behavior in In-Doped CdO
1:45 pm	Priyanka Petluru	S05	(Student) Long-Range Surface Plasmon Polaritons in All-Epitaxial Structures
T: High Electron Mobility Transistors (HEMT) & Characterization of 2-Dimensional Electron, Hole Gases			
11:45 am	Md Didarul Alam	T01	(Student) Influence of Buffer Layer Thickness and Type on Laser Lift-Off of AlGaN/GaN HEMTs Epilayers on Sapphire Substrates
12:00 pm	Mohi Uddin Jewel	T05	(Student) A Comparative Study of Slow Current Transients in $Al_{0.4}Ga_{0.6}N$ Channel MOSHFET's with Back Barriers
12:15 pm			Break
12:45 pm	Jimy Encomendero	T06	Polarization-Induced 2D Electron and Hole Gases Homoepitaxially Grown on Single-Crystal AlN Substrates
1:00 pm	Carsten Beckmann	T07	Two-Dimensional Hole Gases Induced by Spontaneous and Piezoelectric Polarization in Ga-Face GaN-on-AlGaN
1:15 pm	Zexuan Zhang	T08	(Student) Polarization-Induced 2D Hole Gases in Undoped InGaN/AlN Heterostructures Grown on Single-Crystal AlN Substrates
1:30 pm	Athith Krishna	T09	(Student) Effect of Acceptor Traps at Positive Polarization Interfaces on the Charge and Mobility of Holes in N-Polar P-Type GaN/(AlN/AlGaN) Superlattices
1:45 pm	Phillip Dang	T10	(Student) Concurrent Quantum Hall Effect and Superconductivity in an Epitaxial Nitride Semiconductor/Superconductor Heterostructure
U: Diamond, Gallium Oxide and Related Materials			
11:15 am	Nicolas Tappy	U01	(Student) Mapping Boron Concentration in HPHT-Diamond Using Continuous and Time-Resolved Cathodoluminescence Spectroscopy
11:30 am	Dhruba Das	U02	(Student) Making Diamond N-Type with Enhanced Conductivity via Ion Implantation Technique
11:45 pm			Break
12:45 pm	Yixiong Zheng	U06	(Student) β-Ga_2O_3 Nanomembrane and Diamond P-N Heterojunction Integrated with Oxide Quantum Tunneling Layer
1:00 pm	Patrick Taylor	U07	MBE Growth and Optical Characterization of Large E_g Rocksalt-Structured Semiconductors
1:15 pm	Daram N Ramdin	U08	(LATE NEWS, Student) Deep Levels and Self-Trapped Excitons at Iridium/Edge-Fed Grown β-Ga_2O_3 Interfaces
1:30 pm	Nathan Paul Yonkee	U09	(LATE NEWS, Student) Time Dependent Simulations of Defect Kinetics and Thermodynamics in Gallium Oxide
1:45 pm	Menka Jain	U10	(LATE NEWS) Rare-Earth Chromites and Manganites—Structural-Property Relations

PROGRAM AT-A-GLANCE

THURSDAY

All times are EDT

V: Nanoscale Characterization			
3:15 pm	Peter Moeck	V01	Crystallographic Symmetry and Pseudo-Symmetry Quantifications in Atomic and Molecular Resolution Images
3:30 pm	Piran Ravichandran Kidambi	V03	Visualizing Oxidation Mechanisms in Few-Layered Black Phosphorus via *In Situ* Transmission Electron Microscopy
3:45 pm	Elisabeth Mansfield	V04	Transmission Imaging of 2D Materials in a Conventional Scanning Electron Microscope
4:00 pm	Priyanka Ramaswamy	V05	(Student) Doping Assessment of Ga-Assisted MBE Grown Be-Doped GaAs and Te-Doped GaAsSb Nanowires for Infrared Photodetector Application
4:15 pm			Break
4:45 pm	Gabriel Antonio Calderon Ortiz	V06	Identification of Ordered Domains in Organic Semiconducting Polymers Using Variable Probe Size 4-Dimensional Scanning Transmission Electron Microscopy
5:00 pm	Steven Spurgeon	V07	Rapid and Flexible Few Shot Learning-Based Classification of Scanning Transmission Electron Microscopy Data
5:15 pm	Ryan Kowalski	V08	(Student) Identifying Defect Origins of Single-Photon Emitters Using Infrared Nano-Optic Probes
5:30 pm	Mingze Yang	V09	(Student) Measurement of Minority Carrier Diffusion Lengths in Core-Shell GaAs NW p-n Junctions
5:45 pm	Abinash Kumar	V10	(Student) Understanding Relaxor Ferroelectrics at Atomic Scale
W: Organic and Hybrid Materials and Devices I			
3:00 pm	Jacob W. Ciszek	W01	Improving Metal-Top-Contact/Organic Interfaces via Monolayers
3:15 pm	Drona Dahal	W02	(Student) Role of the Injection Barrier on the Performance of Vertical Organic Field Effect Transistors
3:30 pm	Paria Naderi	W03	(Student) Effect of Annealing Printed Electrodes on Gate Dielectric Hydrophobicity and Device Performance in Organic Transistors
3:45 pm	Hamna Haneef	W04	(Student) Elucidating the Role of Water-Induced Traps in the Environmental Stability of Polymer Field-Effect Transistors
4:00 pm	Raj Kishen Radha Krishnan	W05	(Student) Organic Doping at Ultra-Low Concentrations
4:15 pm			Break
4:45 pm	Nolan Concannon	W06	Tuning Exciplex Luminescence Using the Stark Effect in Organic Semiconductors
5:00 pm	Hadi Abroshan	W07	Extending Atomic Scale Simulation for OLED Materials—From Discrete Molecules to Disordered Solid State Morphologies
5:15 pm	Evgeny Pakhomenko	W08	(Student) Understanding the Influence of Spontaneous Orientation Polarization on the Efficiency of Organic Light-Emitting Devices (OLEDs)
5:30 pm	Jonathan Andrew Hopkins	W09	(Student) Synthesis and Characterisation of Phosphonated PEDOT—An Organic Material for Energy-Efficient Bioelectronics
X: 2D Material Devices and Applications			
3:00 pm	Curt A Richter	X01	Reporting and Benchmarking Emerging Field-Effect Transistors
3:15 pm	Zhixian Zhou	X02	Accumulation-Type Ohmic Contacts Between Degenerately Doped and Nearly Intrinsic 2D Semiconductors
3:30 pm	Yuanyue Liu	X03	Why Two-Dimensional Semiconductors Generally Have Low Electron Mobility
3:45 pm	Lun Jin	X04	(Student) Transition Metal Dichalcogenides (TMDCs) Heterostructures Field Effect Transistors (FETs) Fabricated by Sequential Chemical Vapor Deposition (CVD)
4:00 pm	Xiaohan Wu	X05	(Student) Toward Universal 2D Memory—Conductive-Point Resistive Switching in Non-Metallic Atomic Layers
4:15 pm			Break
4:45 pm	Soaram Kim	X06	Rapid Detection of COVID-19 via Epitaxial Graphene Based Sensor
5:00 pm	Arnab Majee	X07	Quantitative Models of Charge Transport in Chemically Vapor Deposited Graphene on Germanium
5:15 pm	Rohan Sengupta	X08	(Student) Investigating the Impact of Dielectric Passivation and Metal Contacts on the Phase Change of 2D $MoTe_2$ via Thermal Annealing
5:30 pm	Riccardo Torsi	X09	(Student) Controlled Rhenium Doping of MoS_2
5:45 pm	Nailah Oliver	X10	(Student) Computational Modeling of Metal Islands for Hybrid Contacts to MoS_2

All times are EDT

Y: Devices and Materials for Power Electronics			
3:00 pm	Shahab Mollah	Y01	Study of Temperature Effect on Performance of Ultrawide Bandgap $Al_{0.4}Ga_{0.6}N$-Channel Depletion and Enhancement Mode MOSHFETs with ZrO_2/Al_2O_3 Gate Insulator
3:15 pm	Mohammad Wahidur Rahman	Y02	(Student) Hybrid $BaTiO_3/SiN_x$/AlGaN/GaN Schottky Barrier Diodes with Low Turn-On and High Breakdown Performance
3:30 pm	Nayana Remesh	Y03	(Student) Re-Engineering of Transition Layer to Achieve Record-High Breakdown Field of 2.05 MV/cm for a Buffer Thickness of 1. 65 µm of AlGaN/GaN HEMT on Si
3:45 pm	Andrew Anthony Aragon	Y04	(Student) Carrier Dynamics in Dry-Etched-and-Regrown Nonpolar M-Plane GaN p-n Diodes—A Small-Signal RF Analysis
4:00 pm	Dennis Edward Szymanski	Y05	(Student) Development of III-Nitride Superjunctions
4:15 pm			Break
4:45 pm	Andrew Anthony Aragon	Y06	(Student) Deep-Level Optical Spectroscopy in Wet-Treated Etched-and-Regrown Nonpolar M-Plane GaN Vertical Schottky Diodes
5:00 pm	Yafei Liu	Y07	(Student) X-Ray Topography Characterization of Selective Area Doping of Gallium Nitride Epitaxial Layers for Power Electronic Devices Development
5:15 pm	Mona Ebrish	Y08	Ion Implanted Edge Termination Designs for High Current 1.2kV GaN Vertical PiN Diodes
5:30 pm	Wenbo Li	Y09	(Student) Characterization of Traps in High-Growth-Rate MOCVD-Grown GaN
5:45 pm	Yuxuan Zhang	Y10	(Student) MOCVD GaN Epitaxy with Fast Growth Rates
Z: Solar Cell Materials and Devices			
3:00 pm	Sara Pouladi	Z01	Sulfur Passivation Effect on Low-Angle Grain Boundaries in Single-Crystal-Like GaAs Flexible Thin Film Solar Cells on Metal Tape
3:15 pm	Falk Niefind	Z02	Nanoscale Morphology of Polymer:Fullerene Blends Investigated by Photoemission Electron Microscopy
3:30 pm	Yu-Lin Hsu	Z03	(Student) Impact of Ar Ion Beam Milling on Metal-Halide Perovskite Solar Cells
3:45 pm	Vinod K. Sangwan	Z04	Impedance Spectroscopy for Emerging Non-Fullerene Acceptor Based Organic Solar Cells
4:00 pm	Laura Nielsen	Z05	Development of Polymers for Scalable Organic Photovoltaics
4:15 pm			Break
AA: Heteroepitaxy on Silicon			
4:45 pm	Eamonn Hughes	AA01	(Student) High-Reliability InAs QD Lasers on Silicon Through Misfit Dislocation Trapping Layers
5:00 pm	Pankul Dhingra	AA02	(Student) Dislocation tolerance of n-InGaP Grown on Si
5:15 pm	Tyler Grassman	AA03	$B_xGa_{1-x}P$/Si Grown via Hybrid Gas/Solid-Source Molecular Beam Epitaxy
5:30 pm	Mario James Dumont	AA04	(Student) Growth of Low Dislocation Density GaAs Films on Silicon Using Bonded III-V Template
5:45 pm	Matthew Dennis Chrysler	AA05	(Student) Tuning Band-Alignment at a Semiconductor-Crystalline Oxide Heterojunction via Electrostatic Modulation of the Interfacial Dipole
BB: Gallium Oxide Processing, Characterization and Defects			
3:00 pm	Yaoyao Long	BB01	(Student) Fin-Waist Formation in β-Ga_2O_3 Fin Arrays Defined by ICP-RIE
3:15 pm	Evan Michael Cornuelle	BB02	(Student) Quantitative Defect Characterization of MOCVD-Grown β-$(Al,Ga)_2O_3$ and Comparison with β-Ga_2O_3
3:30 pm	Md Nazmul Hasan	BB03	(Student) Nanogaps Formation and Recovery Process of Flexible β-Ga_2O_3 Nanomembranes Under Uniaxial Strain
3:45 pm	Michael Evan Liao	BB04	(Student) The Impact of Interfacial Structure on Thermal Transport Characteristics for Wafer Bonded (-201) β-Ga_2O_3 | (0001) 4H-SiC
4:00 pm			Break
CC: Gallium Oxide Epitaxy I			
4:45 pm	Saurav Roy	CC01	(Student) Growth and Characterization of *In Situ* MOCVD-Grown Al_2O_3 Dielectric / (010) β-Ga_2O_3 Interface
5:00 pm	A F M Anhar Uddin Bhuiyan	CC02	(Student) Orientation-Dependent Band Offsets at MOCVD Grown β-$(Al_xGa_{1-x})_2O_3$/β-Ga_2O_3 Heterointerfaces
5:15 pm	Praneeth Ranga	CC03	(Student) Electrical Characterization of MOVPE-Grown Low Sheet Resistance β-$(Al_xGa_{1-x})_2O_3$/β-Ga_2O_3 Heterostructure Channels
5:30 pm	Zixuan Feng	CC04	Expanding Growth Window for MOCVD β-Ga_2O_3
5:45 pm	Kenny Huynh	CC05	(Student) Surface Reaction Dependence of Molecular Beam Epitaxy Grown Al on Various Orientations of β-Ga_2O_3
Panel Discussion			
7:30 pm			PD: Panel on Careers and Post-Graduate Studies in Materials Science Panelists: **Adrienne Stiff-Roberts**, **Wenbing Hu**, **Samuel Graham, Jr.**, **David Estrada**, **Mona Ebrish**, **Michael Abraham**

PROGRAM AT-A-GLANCE

FRIDAY

All times are EDT

DD: Materials for Memory and Logic			
9:15 am	Jun Tao	DD01	(Student) Photo Floating-Gate Field-Effect Transistors for Machine Vision
9:30 am	Diana Sungmin Kim	DD02	(Student) Deterministic Analogue Resistive Memory for Neuromorphic Computing Based on Transition Metal Oxides
9:45 am	Sanghyeon Choi	DD03	(Student) SiO_x Nanorod-Structured Artificial Neuron for Probabilistic Computing Applications
10:00 am	Seonghoon Jang	DD04	(Student) Development of a Single Device-Based Organic Tactile Synapse for Artificial Learning Skin Applications
10:15 am			Break
10:45 am	Yuanshen Qi	DD06	Ferroelectricity of As-Deposited HZO Fabricated by Plasma-Enhanced Atomic Layer Deposition at 300°C by Inserting TiO_2 Interlayers
11:00 am	Oliver Lloyd William McHugh	DD07	(Student) Tackling the Total Spin Hall Conductivity—A Multi-Code Approach for Doped and Alloyed Materials
11:15 am	Marzieh Savadkoohi	DD08	(Student) Effect of Size and Temperature Variation on Magnetic Tunnel Junction-Based Molecular Spintronic Devices (MTJMSDs)
11:30 am	Bishnu R Dahal	DD09	Impact of Anisotropy on the Magnetic Hysteresis of Magnetic Tunnel Junction Based Molecular Spintronics Device (MTJMSD) Properties
11:45 am	Shubham Sukumar Awate	DD10	(Student) High-Speed Two-Dimensional Solid-State Non-Volatile Memory Based on Electric Double Layer Gating Using a Monolayer Electrolyte
EE: Organic and Hybrid Materials and Devices II			
9:00 am	Zhongxiang Peng	EE01	(Student) Manipulation of Morphological, Mechanical and Photovoltaic Properties of Ternary Organic Photovoltaic Blends for Optimum Operation
9:15 am	Kyeong-Yoon Baek	EE02	(Student) Structural and Optical Evolution of Mechanochemically Synthesized Zero-Dimensional Cesium Lead Bromide Perovskite
9:30 am	Colin Tyznik	EE03	(Student) Photocurrent Enhancement in Organic Semiconductor/Metal Halide Perovskite Bilayers
9:45 am	Junwoo Kim	EE04	(Student) Crystallinity-Dependent Device Characteristics of Polycrystalline 2D Ruddlesden-Popper Perovskite Photodetectors
10:00 am	Jonghoon Lee	EE05	(Student) Controllable Deposition of Organic-Inorganic Halide Perovskite Films with Wafer-Scale Uniformity by Single-Source Flash Evaporation
10:15 am			Break
10:45 am	Heebeom Ahn	EE06	(Student) Current Noise Analysis on Organo-Metal Halide Perovskite Resistive Switching Memory
11:00 am	Jung Sun Eo	EE07	(Student) Molecular-Scale Selector Implemented by a Combination of Different Molecular Dipole Orientation and Two-Dimensional Semiconductors
11:15 am	Seonggil Ham	EE08	(Student) Fiber-Shaped Multi-Synapses Enabling an Electronic-Textile Neural Network for Wearable Neuromorphic Applications
FF: Doping and Stoichiometric Effects on Epitaxial Material			
9:00 am	Joshua Andrew McArthur	FF01	(Student) Background Carrier Polarity Switching in $Al_xIn_{1-x}As_ySb_{1-y}$ Digital Alloys
9:15 am	Binjie Chen	FF02	(Student) Reduction of the T_c and Suppression of the $\triangle T_c$ of VO_2 Epitaxial Films on TiO_2 Buffered Sapphire Substrate
9:30 am	Xi Zhang	FF03	Electrochemical-Redox-Modulation of the Oxygen Content in Superconducting $YBa_2Cu_3O_{7-\delta}$
9:45 am	Qian Meng	FF04	(Student) Effect of B Distribution on the Band Structure of BGa(In)As Alloys
10:00 am	Rachel Corey White	FF05	(LATE NEWS, Student) Growth Optimization of InSbBi Alloys for Wavelength Extension on InSb
10:15 am			Break
GG: Oxide Semiconductors: Charge Transport and Optical Properties			
10:45 am	Jade Cowsky	GG01	(Student) Defects and Dopants at Ultra-Thin Film Indium Tin Oxide (ITO) Interfaces
11:00 am	Mian Wei	GG02	(Student) Modulation of Optical and Electronical Properties for Transparent Oxide Semiconductor $ASnO_3$ by the A-Site Ion Substitution
11:15 am	Mingyuan Liu	GG03	(Student) Thermal and Bias Stability of InAlZnO-Based Amorphous Thin-Film Transistors
11:30 am	Maytal Caspary Toroker	GG04	Charge Transport in Ternary Spinel Oxides
11:45 am	Elaheh Kheirandish	GG05	(Student) Charge Transport and Photoconduction Effects in Quasi Two-Dimensional γ-Al_2O_3 Grown by Graphene Assisted Atomic Layer Deposition

All times are EDT

HH: Group III-Nitride LED I			
9:00 am	Evyn Lee Routh	HH01	(Student) Towards Device-Quality Higher Mole Fraction $In_xGa_{1-x}N$ Relaxed Templates ($0 < x < 15\%$)
9:15 am	Keisuke Motoki	HH02	(Student) Observation of Interfacial Strain Relaxation in High Indium, AlInN/GaN Heterostructures by Transmission Electron Microscope
9:30 am	Huabin Yu	HH03	(Student) Micro-Scale AlGaN-Based Deep Ultraviolet Light-Emitting Diodes Emitting at 265 nm
9:45 am	Walter Jin Shin	HH04	(Student) Demonstration of High Q Aluminum Nitride on Sapphire Microring Resonator at Green and UV Wavelengths
10:00 am	Ankit Udai	HH05	(Student) Carrier-Photon Dynamics in InGaN/GaN Quantum-Dots Emitting Green Light
10:15 am			Break
II: Group III-Nitride Photodetectors			
10:45 am	Hoon Jeong	II01	(Student) Low Temperature Geiger-Mode Measurement of Gallium Nitride p-i-n Avalanche Photodiode
11:00 am	Farnood Mirkhosravi	II02	(Student) Characterization of Ga-Polar and N-Polar III-Nitride (GaN) Diodes Under High-Dose Gamma-Ray Irradiation
11:15 am	Danhao Wang	II03	(Student) AlGaN-Based Nanowires for Self-Powered Ultraviolet Photodetectors with High Responsivity
11:30 am	Anisha Kalra	II04	(Student) UV-Stress Induced Degradation in AlGaN Solar-Blind Schottky and p-i-n Photodetectors
11:45 am	Marzieh Bakhtiary-Noodeh	II05	(Student) Growth and Characterization of p-i-n GaN UV 6 × 6 Avalanche Photodiodes Arrays with Large Detection Area
JJ: Printed and Flexible Thin Films			
9:15 am	Benoit Lessard	JJ02	Low Voltage Operation of Flexible Organic Thin-Film Transistors Using Poly(Ionic Liquid) Block Copolymer Based Gating Materials
9:30 am	Annatoma Arif	JJ03	(Student) Inkjet Printed 3D Metal Electrodes on Shape Memory Polymer Towards Improved Electrochemical Bio-Sensing Performance
9:45 am	Nam-In Kim	JJ04	(Student) Skin-Attachable Physical Sensors Using Single-Crystalline III-N Piezoelectric Thin Film for Personal Health and Safety Monitoring
10:00 am	Mohan Panth	JJ05	(Student) High Performance Strain Sensors Based on Zinc Oxide Nanowire Array/Graphene Nanohybrids
10:15 am			Break
KK: MBE: Selective Area Growth and Doping			
10:45 am	Shotaro Kobayashi	KK01	(Student) Control of Nucleation Layers for (110) Oriented ZnTe Thin Film Growth on Sapphire r, S-Plane Nano-Facet Substrates
11:00 am	Ashlee Garcia	KK02	(Student) Experimentally-Calibrated Modeling of Molecular Beam Epitaxy Selective Area Regrowth
11:15 am	Alec Mason Skipper	KK03	(Student) Selective Area Doping and Lateral Overgrowth by Solid-Source Molecular Beam Epitaxy
11:30 am	Kamruzzaman Khan	KK04	(Student) Demonstration of Self-Assembled InGaN/GaN Superlattice on GaN Template Grown by Plasma-Assisted Molecular Beam Epitaxy
11:45 am	Kamruzzaman Khan	KK05	(Student) Investigation of 1μm-Thick InGaN Films Grown on O-Face ZnO by Plasma-Assisted Molecular Beam Epitaxy
LL: Materials Processing and Integration			
9:00 am	Evan M Anderson	LL01	Reduced Temperature Preparation of Atomically Clean Si Surfaces to Augment CMOS with Atomic Precision Devices
9:15 am	Galih R. Suwito	LL02	(Student) Kinetics and Mechanism of Metal-Catalyzed Lateral Epitaxy for Growing Lattice-Mismatched Heterostructures via Vapor-Liquid-Solid
9:30 am	Guohai Chen	LL03	Carbon Nanotube-Cu Through-Silicon-via Interposer for Microelectronic Packaging Applications
9:45 am	Noah Paulson	LL04	Autonomous Optimization of Atomic Layer Deposition via Artificially Intelligent Agents
10:00 am	Rachel Cherry	LL05	(Student) Nanosphere Coatings for Photonic Light Trapping in Ultra-Thin Film Photoconductive Absorber Layers for THz Generation
10:15 am			Break
MM: Gallium Oxide Epitaxy II			
10:45 am	Yuichi Oshima	MM01	In-Plane Orientation Control of (001) κ-Ga_2O_3 by Epitaxial Lateral Overgrowth Through a Geometrical Natural Selection Mechanism
11:00 am	Hitoshi Takane	MM02	(Student) On the Initial Growth Mechanisms of α-Phase Ga_2O_3 on C-Plane Sapphire by Mist CVD
11:15 am	Jingyu Tang	MM03	Phase Composition and Microstructure of Gallium Oxide Heteroepitaxial Films—Effect of MOCVD Growth Conditions
11:30 am	Debabrata Das	MM04	Realization of Self-Assisted Growth of Nano-Columnar β-Ga_2O_3 Thin Film on Silicon Substrate
11:45 am	Jonathan McCandless	MM05	(LATE NEWS, Student) Stabilizing α-Ga_2O_3 and α-$(AlGa)_2O_3$ up to 900°C

PROGRAM AT-A-GLANCE

FRIDAY

All times are EDT

NN: Group III-Nitride Defects			
1:00 pm	Fiaz Ahmed	NN01	(Student) Imaging Photocurrent Distributions from Sub-Bandgap Defects by Polarity Resolved Scanning Photocurrent Microscopy (SPCM) in III-Nitride Devices
1:15 pm	Alexander Chang	NN02	Oxygen Doping Distribution in GaN Lateral Polarity Junction
1:30 pm	Shanshan Hu	NN03	(Student) Characterization of Prismatic Slip in PVT-Grown AlN Crystals
1:45 pm	Vincent E. Meyers	NN04	Microwave-Induced Annealing, Its Impact on Mg Diffusion and Photoluminescence Activity in Implanted and *In Situ* Doped GaN
2:00 pm	Shashwat Rathkanthiwar	NN05	(LATE NEWS) Point Defect Management in Homo-Epitaxially Grown Si-Doped GaN by MOCVD for Vertical Power Devices
OO: Novel Materials			
1:15 pm	Md Rezaul Karim	OO01	(Student) Experimental Determination of Valence Band Offsets of $ZnGeN_2$ and $(ZnGe)_{0.94}Ga_{0.12}N_2$ with GaN
1:30 pm	Mina Moradnia	OO03	(Student) Hybrid Vapor Phase Epitaxy (HybVPE) of Transition-Metal-Alloyed Single-Crystalline Wide-Bandgap Piezoelectric Semiconductor Films
1:45 pm	Benthara Hewage Dinushi Jayatunga	OO04	(Student) Progress in MOCVD Growth and Characterization of $ZnGeGa_2N_4$ Films
2:00 pm	Oleg Maksimov	OO05	Low-Temperature Epitaxial Growth of Anti-Ferromagnetic MnTe at Bi_2Te_3
PP: Oxide Thin Film Transistors			
1:00 pm	Yong Zhang	PP01	(Student) Control of Transistor Operation Modes for SnO-TFT
1:15 pm	Jaesung Jo	PP02	(Student) Understanding the Differences Between Hall Mobility and FE Mobility for P-Type Cu_2O Thin-Film Transistor
1:30 pm	Christopher R. Allemang	PP03	(Student) Temporal Stability of Zinc Tin Oxide TFTs with Active Layers Deposited by Atomic Layer Deposition
1:45 pm	Adam Weidling	PP04	(Student) Photonic Curing of Solution-Processed Indium Zinc Oxide Thin-Film Transistors
2:00 pm	William J Scheideler	PP05	Designing Printed High-k Modulation-Doping Layers for InO_x Transistors to Break Thermal Processing Barriers
QQ: Group III-Nitride LED II			
1:00 pm	Jiaying Lu	QQ01	(Student) Analysis on the Internal Quantum Efficiency of Deep-Ultraviolet Emitting AlGaN Nanowires
1:15 pm	Woncheol Lee	QQ02	(Student) Deep Ultraviolet Luminescence and Charge-Transfer Excitons in Atomically Thin GaN Quantum Wells
1:30 pm	MVS Chandrashekhar	QQ03	AlGaN UVC Micropixel LEDs with Vertical and Slanted Sidewalls
1:45 pm	Haotian Xue	QQ04	(Student) Red-Emitting InGaN/AlGaN/GaN Multiple Quantum Wells with Various Underlayers
2:00 pm	Barbara Anna Kazanowska	QQ05	(Student) Exploring $Al_{(X)}Ga_{(1-X)}N$ Nanostructures Fabricated via Top-Down Chemical Wet Etching
RR: LATE NEWS—Novel Properties, Processing, Modeling and Characterization Methods			
1:00 pm	Christopher M. Matthews	RR01	(LATE NEWS, Student) Kinetic Model of Vertical Indium Segregation During InGaN Epitaxy
1:15 pm	Patrick Ryan Sohr	RR02	(LATE NEWS) Strong Coupling in Semiconductor Hyperbolic Metamaterials
1:30 pm	Barys Korzun	RR03	(LATE NEWS) Preparation by Melt Method and Phase Equilibria in the $CuFeS_2$-δ – $CuAlS_2$ System
1:45 pm	Briana Laubacker	RR04	(LATE NEWS, Student) Nanostructured Semiconductors Prepared Using High Pressure Chemical Vapor Deposition with Mesoporous Templates
2:00 pm	Daniel E. Autrey	RR05	(LATE NEWS) Tuning the Magnetic Properties of Two-Dimensional MXenes by Chemical Etching

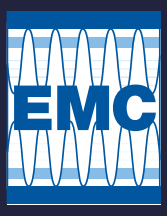

63RD ELECTRONIC MATERIALS CONFERENCE

June 23-25, 2021

WEDNESDAY ORAL PRESENTATIONS

63rd Electronic Materials Conference
June 23 - June 25, 2021

* Plenary

EMC Awards Ceremony and Plenary Session
Session Chairs: Kris Bertness and Lisa Porter
Wednesday Morning, June 23, 2021

9:00 AM EMC AWARDS CEREMONY

9:15 AM *PL01
Abandoning Perfection for Quantum Technologies David D. Awschalom; The University of Chicago, United States

Our technological preference for perfection can only lead us so far: as traditional transistor-based electronics rapidly approach the atomic scale, small amounts of disorder begin to have outsized negative effects. Surprisingly, one of the most promising pathways out of this conundrum may emerge from current efforts to embrace defects to construct quantum devices and machines that enable new information processing and sensing technologies based on the quantum nature of electrons and atomic nuclei. Recently, individual defects in diamond, silicon carbide, and other wide-gap semiconductors have attracted interest as they possess an electronic spin state that can be employed as a solid-state quantum bit at room temperature. These systems have a built-in optical interface in the visible and telecom bands, retain their coherence over millisecond timescales, and can be polarized, manipulated, and read out using a simple combination of light and microwaves. With these well-characterized foundations in hand, we discuss merging electronic, photonic, magnetic, and phononic degrees of freedom to develop coherent atomic-scale devices for transducing information to create multifunctional quantum technologies. We present demonstrations of gigahertz coherent control, single nuclear spin quantum memories, entangled quantum registers, and advances in extending the quantum coherence in both commercial and custom CVD-grown electronic materials for emerging applications in science and technology.

10:00 AM BREAK

SESSION A: Epitaxial Devices
Session Chairs: Adrienne Stiff-Roberts and Randy Tompkins
Wednesday Morning, June 23, 2021

10:45 AM A01
(Student) Growth of B-III-V Alloys for GaAs-Based Optoelectronic Devices Rasha El-Jaroudi[1], Andrew H. Jones[2], Adam A. Dadey[2], Bingtian Guo[2], Xingjun Xue[2], Joe C. Campbell[2] and Seth R. Bank[1]; [1]University of Texas at Austin, United States; [2]University of Virginia, United States

The asymmetric perturbation of the conduction and valence band structure in highly-mismatched dilute-nitride and dilute-bismide III-V alloys has motivated the investigation of highly-mismatched alloy photodiodes. However, the challenging growth of these alloys imposed by limited miscibility of the highly-mismatched elements has often proved deleterious to photodiode device performance, reducing carrier diffusion lengths and mobility,[1] quantum efficiency and responsivity,[2] and increasing the excess noise associated with multiplication gain,[3] ultimately limiting the practicality of dilute-nitride and dilute-bismide photodiodes. Here, we investigate analogous highly-mismatched boron-III-V alloy photodiodes. Recent progress in the growth of dilute-boride alloys has shown that the solid solubility of B significantly exceeds that of dilute-nitride and bismide alloys,[4,5] potentially alleviating the adverse effects previously observed in highly-mismatched alloy photodiodes. The quaternary alloy, BGaInAs, offers the potential for achieving a wide-range of previously inaccessible wavelengths while remaining lattice-matched to GaAs or Si, enabling applications ranging from telecommunication to photovoltaics. However, a thorough exploration of how increasing the B and In composition of these alloys affects device performance remains to be developed. Leveraging a highly kinetically-limited growth regime, BGaInAs films and p-i-n structures were grown by solid-source MBE on exact (100) semi-insulating and n-type GaAs substrates, respectively. High-resolution X-ray diffraction was used to determine the BGaInAs alloy composition and assess structural quality. Dopant activation and carrier mobility in doped BGaInAs films were characterized using Hall measurements in the Van der Pauw configuration. $B_{0.01}Ga_{0.97}In_{0.02}As$ and $B_{0.03}Ga_{0.91}In_{0.06}As$ p-i-n junctions were investigated to understand the effects of increasing the alloy mismatch on photodiode device properties. External quantum efficiency (EQE) measurements from photodiodes fabricated from p-i-n structures showed little decrease in external quantum efficiency as the B and In concentration was increased, suggesting that the high material quality necessary for high-performance devices can be maintained as the B and In concentrations are increased. Fabrication and characterization of thicker intrinsic region devices, as well as higher B and In concentration devices, are underway and will be reported on at the conference. This work was supported by the National Science Foundation (Award Nos. ECCS-1838984 and ECCS-1933836).
[1] S. Fahy et al., Applied Physics Letters (2003)
[2] K. Volz et al., Journal of Crysal Growth (2007)
[3] S.L. Tan et al., Applied Physics Letters (2013)
[4] G.L.W. Hart and A. Zunger, Phys. Rev. B (2000)
[5] K.M. McNicholas et al., 61st Electronic Materials Conference (2019)

11:00 AM A02
(Student) Enhanced Double Heterostructure Infrared LEDs Using Monolithically Integrated Plasmonic Materials Andrew F. Briggs[1], Leland J. Nordin[1], Aaron J. Muhowski[1], Evan Simmons[2], Pankul Dhingra[3], Minjoo L. Lee[3], Viktor A. Podolskiy[2], Daniel Wasserman[1] and Seth R. Bank[1]; [1]University of Texas at Austin, United States; [2]University of Massachusetts Lowell, United States; [3]University of Illinois at Urbana-Champaign, United States

The integration of plasmonic materials with emitters and optoelectronic devices allows for remarkable enhancement and improved understanding of light-matter interaction. Previous approaches to plasmonic integration rely on the noble metals to achieve a plasmonic response near the metal's plasma frequency, limiting plasmonic devices to the near-infrared and visible wavelength range. The noble metals offer strong confinement but with the possibly of greater loss.[1] Since emitters in the near-infrared and visible wavelength ranges already have high optical efficiencies, it is difficult to increase that efficiency with the introduction of a plasmonic material. However, the mid-infrared has few highly efficient light emitting materials.[2] Emission from mid-infrared materials can be significantly enhanced when coupled with a plasmonic material and thus have a strongly enhanced efficiency. The integration of a noble metal in the near-field of an emitter is often incompatible with the electronic requirements of the active device, compromising the device architecture and significantly limiting possible emission enhancement.[3] Each of these drawbacks conspire to limit the design flexibility and potential performance of polylithically-integrated metal-based optoelectronic devices. Molecular beam

epitaxy allows for the engineering of so-called “designed metals” for a monolithic all-epitaxial integration of a plasmonic material and active device in the mid-infrared.[4] Previously we have shown the first all-epitaxial integration of a plasmonic “designer metal” and emitter to produce a cavity-enhanced light-emitting diode (LED).[5] Experimental electroluminescence showed a strong enhancement of emission at the peak wavelength, increasing by a factor of 5.6x when compared to a control LED. The device with the plasmonic virtual substrate showed upper hemisphere powers of 1.45 μW at 300 K, comparable to state-of-the-art mid-infrared LEDs at the same wavelength.[6] In order to increase the efficiency of the cavity-enhanced LEDs, we are integrating our emitters into an AlInAsSb/InAs/AlInAsSb double heterostructure design with a tunnel junction to increase efficiency.[7] The cavity-enhanced LED design was optimized using rigorous coupled-wave analysis. Further simulations and characterization of the double heterostructure cavity-enhanced LED are underway and will be presented at the conference. This work was supported by the National Science Foundation (NSF) under grant EECS-1926187 and performed at the Texas Nanofabrication Facility, supported by NSF grant NNCI-2025227.
[1] J. B. Khurgin and A. Boltasseva, MRS Bulletin, **37**, 768, (2012).
[2] D. Jung, et al., J. Opt., 19, 123001 (2017).
[3] J. B. Khurgin and G. Sun, Nat. Photonics, **8**, 468 (2014)
[4] S. Law, et al., Opt. Express (2012).
[5] A.F. Briggs, et al., Optica, **7**, 1355 (2020).
[6] Boston Electronics, IoffeLED, Optically immersed 7.0 μm optically pumped LED in heatsink optimized housing, OPLED70Sr datasheet.
[7] A. J. Muhowski *et al., 2020 IEEE Research and Applications of Photonics in Defense Conference (RAPID),* (2020).

11:15 AM A03
(Student) Impact of Buffer Traps on Temperature-Dependent Dynamic Ron in AlGaN/GaN HEMT Nayana Remesh, Hareesh Chandrasekar, Srinivasan Raghavan, Muralidharan R and Digbijoy Nath; Indian Institute of Science, India

Over the last decade, GaN-based devices have poised as an excellent candidate in next-generation power electronics as they can withstand high voltage, with low on-resistance and high switching speed. The most critical issue hindering the widespread adoption of GaN-based power devices in the market is reliability, mainly during high voltage and high-temperature operation. One of the major factors affecting device reliability is dynamic Ron i.e., variation in the on-resistance of the device under high voltage or high-temperature stress. Dynamic Ron may result from a trapping mechanism due to the surface or buffer related traps. Several studies depicted the trapping mechanisms related to surface traps, hot electrons, interface traps, and buffer related traps as the reason for dynamic Ron. However, experimental investigation and correlation of the impact of buffer traps on dynamic Ron with buffer growth conditions are still lacking. In the present study, we tried to investigate the impact of variations in growth conditions of AlGaN transition layers on the dynamic Ron/current collapse of the HEMT devices. The growth temperature and carbon doping are varied independently to assess the role of the transition layer in reducing current collapse. While the introduction of high temperature (HT) AlGaN layers is found to alleviate the density of V-pits resulting in the reduction of the injection of carriers into the buffer. The introduction of C-doping in the top AlGaN transition layer with 25% Al-content helps to reduce the trapping of electrons in the GaN buffer. The combination of HT AlGaN (75% Al-content) with C-doped AlGaN (25% Al-content) is found to be the optimal TL design that yielded a minimum buffer induced current dispersion with a 65 % channel recovery when the substrate was swept to -300 V and back. However, the variation in the growth conditions such as carbon incorporation and high growth temperature introduces buffer traps in the epitaxial stack which will affect the dynamic Ron of the device under high temperature and voltage. The buffer traps and their activation energy are characterized using temperature-dependent buffer leakage and dynamic Ron measurements.

11:30 AM A04
Millimeter-Wave pHEMT on Base of Donor-Acceptor Doped Heterostructure Konstantin S. Zhuravlev; Rzhanov Institute of Semiconductor Physics, Russian Federation

The beginning revolution in communication systems has stimulated the development of millimeter wave transistors and integrated circuits. High electron mobility transistors (HEMT) based on III-V heterostructures with highly mobile two-dimensional electron gas (2DEG) are the best candidates for application in communication systems due to the wide frequency range, high output power, efficiency and linearity. To advance GaAs pHEMT in the millimeter range, we proposed the use of a new type of heterostructure with carrier supply layers doped with acceptors located behind donor delta-doped layers on both sides of the InGaAs channel (DA-DpHEMT). The space charge potential creates up to 900 meV high potential barriers around the transistor channel, which increases electrons localization and drift velocity. In a heterostructure with this design, high mobility (5800 $cm^2/(Vs)$) and high density (4.7×10^{12} cm^{-2}) of two-dimensional electron gas at 300 K were obtained. The localization of hot electrons in an external quantum well leads to an increase in their drift velocity and to enhance the DC and RF performances of the device. A field-effect transistor based on such a heterostructure with a T-gate of 0.14 μm in length shows a specific current density of about 0.7 A/mm, transconductance of about 250 mS/mm, gate-drain breakdown voltage in the range 23 – 31 V, which correspond to more than 2 W/mm specific output RF power according to a simple estimate. The transistor demonstrates impressive RF characteristics, the maximum stable gain of more than 15 dB at 40 GHz and more than 10 dB at 67 GHz, ft = 45 GHz and fmax = 250 GHz. The maximum stable gain at 40 GHz increases with increasing distance between the gate in the drain and is almost constant in the range 25 – 55 GHz.

11:45 AM A05
(Student) Mn+3 Rich Nanofiberous Layered δ-Phase MnO2 on Epitaxial Graphene-Silicon Carbide for Selective Gas Sensing Michael Pedowitz[1,1], Soaram Kim[1,1], Daniel Lewis[1,1], Balaadithya Uppalapati[2], Digangana Khan[2], Ferhat Bayram[2], Goutam Koley[2], Rachel Myers-Ward[3] and Kevin Daniels[1,1]; [1]University of Maryland, United States; [2]Clemson University, United States; [3]U.S. Naval Research Laboratory, United States

Mixed valence manganese oxides (MnO_x) have attracted significant research interest in recent years due to the easily reversible redox reactions between manganese oxidations states (Mn^{+2}, Mn^{+3}, Mn^{+4})[1] which enable applications in catalysis[2], energy storage[3], and gas sensing[4]. Manganese dioxide (MnO_2) has been of particular interest due to its wide variety of synthesized structural polymorphs ((β)1x1 tunnel[5], (α)1x2 tunnel[5] (γ) spinel[5], and (δ) layered[5]) which allow for enhanced control of its active surface area and reactivity. Of these structural polymorphs, the α and δ phases exhibit a mixed-valence character with highly reactive Mn^{+3} defects found throughout their crystal structure[5,6]. Layered, or δ phase (MnO_2) in particular contains a large number of Mn^{+3} ions, as the 7Å interlayer contains $Mn^{+2/+3}$ to neutralize the layer charge from Mn^{+3} lattice defects[7]. This makes δ-MnO_2 a desirable candidate for use in gas sensing and energy storage applications, however, its low inherent conductivity limits its use to elevated temperatures exceeding 200°C[4]. To overcome this limitation MnO_2 graphene heterostructures have been formed, which seek to couple the inherent conductivity of graphene with the reactive properties of MnO_2. In this work, we present the growth of nanofibrous layered δ-MnO_2 on quasi-freestanding bilayer epitaxial graphene/silicon carbide and demonstrate its reactive properties through the development of a simple four

contact gas sensor. The δ-MnO_2 was grown via electrodeposition on epitaxial graphene (EG) synthesized on semi-insulating 6H silicon carbide substrates (SiC) utilizing 10mM manganese acetate ($Mn(CH_3CO_2)_2$) solution in a three-electrode electrochemical cell with a platinum counter electrode and a silver/silver chloride reference electrode (Ag/AgCl). The resulting heterostructure was then characterized using Raman spectroscopy, X-ray photoelectron spectroscopy (XPS), atomic force microscopy (AFM), kelvin probe force microscopy (KPFM), and scanning electron microscopy (SEM) to determine its crystal structure and surface morphology. Raman spectroscopy of the heterostructure confirmed the formation of MnO_2 due to the presence of strong peaks at 502cm^{-1}, 575cm^{-1}, and 653cm^{-1} as was found in the literature[8]. The formation of the δ phase is confirmed by the presence of a weak peak at 133cm^{-1} also consistent with the literature[2]. XPS analysis of the heterostructure revealed indicated that the average oxidation state was +3.3 demonstrating the high Mn^{+3} content of the MnO_2. KPFM of the heterostructure also revealed significant hole doping from the MnO_2 with the EG work function shifting upwards by 300meV[9], as well as the formation of a 300meV potential barrier between the EG and the MnO_2.SEM revealed that the heterostructure was made up of micron-sized platelets formed from nanofibrous nanoparticles growing together. AFM confirmed this morphology and indicated the MnO_2 thickness was 50nm. The reactivity of the formed heterostructure was then tested by depositing 4 Ti/Au (30nm/120nm) contacts on the δ-MnO_2/EG/n^+-SiC heterostructures to form a simple gas sensor, which was tested against 5ppm NO_2, 5ppm NH_3, 1000ppm IPA, and 1000ppm methanol. The sensor displayed a remarkably fast response/ recovery time of 3.8s/2.2s to NH_3 and 3.4/6.0s to NO_2 and no response to IPA and methanol successfully demonstrating its reactive properties and indicating its applicability to gas sensing.

References: [1]L. Spinelle et al. *Sensors* 17(7), 1520(2017)[2] F. Cheng et al. *Chem. Mater* 22(3), 898-905(2010)(3) Y.J. Huang et al. *Electrochim Acta* 99, 161-165(2013)[4]N. Joshi et al. *Microchim. Acta* 185, 213(2018)[5]Z. Chang et al. *Proc Natl Acad Sci USA* 115(23), 5261-5268(2018) [6] Julien et al. *Spectrochim Acta A* 60, 3(2004) [7] Drits et al. *Am Mineralogist* 82, 9-10(1997) [8] Julien et al. *Solid State Ionics* 159, 4(2003)[9] Samir Mammadov et al *2D Mater.* 4, 015043(2017)

12:00 PM A06

(LATE NEWS, Student) Dual-Function ZTO Phototransistor Memory with Au Nanoparticles Mediated for Photo-Sensing and Multilevel Photo-Memory Li-Chung Shih[1], Sheng-Rong Lin[1], Ya-Shan Lin[1], Jen-Sue Chen[1], Yen-Hsun Su[1], Jih-Jen Wu[1] and Chao-Cheng Kaun[2]; [1]National Cheng Kung University, Taiwan; [2]Academia Sinica, Taiwan

The processing and storage of optical data have become an imperative issue for developing next-generation communication and computation technologies. Amorphous oxide semiconductors (AOS) have shown the potential for optoelectronic applications owing to their significant photocurrent arising from generation of electron-hole pairs under UV light illumination, or alternatively, from the ionization of neutral oxygen vacancies (V_o) to positively charged oxygen vacancies (V_o^{2+}) and the photoexcited electrons under illumination of visible light of wavelength less than 450 nm. However, it is rather difficult to get significant light response of AOS at wavelengths of greater than 500 nm because the neutral oxygen vacancies are mostly locating at deep levels (>2.5 eV) within the bandgap. Therefore, integrating oxide semiconductors with plasmonic metals provides a promising approach for visible light photodetectors and photocatalysis since the photocurrent can be enhanced by hot electrons generated by local surface plasmon resonance (LSPR). In this work, we report a dual-functional hybrid device which can work as both a photo-sensing transistor and a photo-memory by embedding Au NPs in the zinc-tin oxide (ZTO) thin film transistor. Au NPs not only act as the charge trapping/detrapping layer but also the LSPR media which can transfer hot electrons to ZTO channel layer. The ZTO/Au NPs hybrid device shows a photoresponsivity ~200 % higher than that of bare ZTO thin film transistor under 520 nm light illumination. The photoresponsivity of ZTO/Au NPs hybrid device to 520 nm light is further increased by 1000 % under the negative gate bias because of the effect of electron tunneling from Au NPs to ZTO. Multilevel photo-memory performance is also demonstrated under repeated light and gate bias co-stimulation for 1 s, for at least 6 multiple memory states. The multilevel photo-memory performance of ZTO/Au NPs hybrid device is attributed to Au NPs which donate the hot electrons to ZTO during the co-stimulation. The excess electrons show a superb retention characteristic because there are not many recombination counterparts (i.e., charged oxygen vacancies (V_o^{2+})) in the ZTO channel. This novel ZTO/Au NPs hybrid phototransistor memory exhibits large photoresponsivity and multilevel photo-memory performance to visible light (520 nm) that highlights the promises for both photonic signal detectivity and storage, which will be highly potential for the future optical communication and computation technologies with higher signal transmission speed and lower power consumption.

SESSION B: Low-Dimensional Structures I
Session Chairs: Rainer Timm and George Wang
Wednesday Morning, June 23, 2021

10:45 AM B01

(Student) Scalable III-V Nanowire Networks for IR Photodetection Nicholas P. Morgan, Valerio Piazza, Didem Dede, Martin Friedl, Lucas Güniat, Akshay Balgarkashi, Wonjong Kim, Jean-Baptiste Leran and Anna F. Morral; EPFL, Switzerland

InGaAs is an ideal material for near-infrared (near-IR) photodetection at telecommunications wavelengths. Its direct band gap offers strong absorption and is tunable by varying the alloy composition, making InGaAs versatile for such applications. However, most commercial devices based on this material require InP substrates, which are costly and difficult to process. Moreover, the In content of the InGaAs layer is limited by the requirement for lattice matching.[1] Nanowires are a promising avenue for heteroepitaxy of InGaAs and InAs on common substrates like Si and GaAs, and offer several performance advantages over bulk devices.[2] For example, their thin, anisotropic geometry enables devices to benefit from fast carrier collection and polarization-dependent absorption, making them suitable for fast and efficient multiplexed applications.[3] Nanowires also allow for a significant reduction in the amount of scarce materials, such as In, required to make a device. Typically, nanowires are grown vertically, perpendicular to the substrate, but vertical nanowires are notoriously difficult to incorporate into devices, and a horizontal configuration is often preferred. Recently, horizontal networks of high-quality In(Ga)As nanowires have been demonstrated by growing them on top of GaAs nanomembrane buffers using selective-area epitaxy on III-V substrates.[4,5] In this work we investigate the growth of horizontal In(Ga)As nanowire networks on GaAs substrates by molecular beam epitaxy. An epitaxial GaAs buffer nanomembrane is grown on the substrate to ensure high crystal quality In(Ga)As. Different crystallographic orientations are investigated. For growth on (111) B GaAs substrates, we demonstrate InGaAs nanowire networks positioned atop high aspect ratio GaAs nanomembranes. We show that the In content of the nanowires can be tuned up to 50% of the group III component by controlling growth conditions, but that pure InAs nanowires are not achievable.[6] Next, we demonstrate InAs nanowires grown on low-aspect ratio GaAs nanomembrane on (100) GaAs substrates. The nanowires grow conformally on the nanomembranes, which are dominated by (111) facets, and pure InAs can be achieved with just a narrow intermixed region

near the interface. We compare the nanowires on each of these crystallographic orientations, highlighting their advantages for different applications. Finally, we present preliminary electrical characterization data from basic photodetector devices based on these nanowires. We compare nanowires of different lengths and widths and characterize the photoconductive response for both single nanowires and ensembles in an array. Insights from these preliminary results will guide design choices for future photodetector architectures based on these nanowires.

[1] R. LaPierre et al., *J. Phys. D: Appl. Phys.* **50** (2017)
[2] C. L. Tan et al., *Nanophotonics.* **7** (2018)
[3] A. Dorodnyy et al., *IEEE J. Sel. Top. Quant. Electr.* **24** (2018)
[4] M. Friedl et al., *Nano Lett.* **18** (2018)
[5] F. Krizek et al., *Phys. Rev. Mat.* **2** (2018)
[6] M. Friedl et al., *Nano Lett.* **20** (2020)
Funding from Swiss National Science Foundation, NCCR QSIT

11:00 AM B02
Epitaxial GaAsSbN (Te) NWs for Near-Infrared Region Photodetection Application Rabin Pokharel, Priyanka Ramaswamy, Shisir Devkota, Mehul Parakh, Kendall Dawkins and Shanthi Iyer; North Carolina A&T State University, United States

Ga-assisted self-catalyzed epitaxial growth and demonstration of Te-doped axial GaAsSbN NW-based Schottky barrier photodetector on p-Si (111) in the near-infrared region is reported. The successful growth of improved dilute nitride quaternary GaAsSbN (Te) NWs in axial configuration was achieved by stringent control on NW nucleation conditions, NW stem growth, and exposure of N-plasma on NW growth. Planar defect-free structures were realized with room temperature photoluminescence (PL) characteristics, revealing reduced N-induced point defects and non-radiative recombination centers. N incorporation in the dilute nitride NWs was ascertained from PL and Raman spectral mode shifts and shapes and weak temperature-dependent PL peak energy. The advantage of Te-doping in dilute nitride NW using a GaTe captive source in the compensation of point defects is demonstrated, as evidenced by a significant improvement in PL characteristics, Raman mode shifts, and spectral shape with improved photodetector device performance relative to intrinsic dilute nitride NWs. Te-doped GaAsSbN NW Schottky based photodetectors have been demonstrated on both single and ensemble configurations yielding responsivity of 5 A/W at 860 nm and 3800 A/W at 1100, respectively. Detectivity of $3.2x10^{10}$ Jones was achieved on the Te-doped ensemble NW device. This work showcases rich prospects for engineering bandgap in the near-infrared region for telecommunication wavelength applications using GaAsSb alloy system.

11:15 AM B03
(Student) A Te Doped GaAsSb Ensemble Nanowire Photodetector for Near-Infrared Application Shisir Devkota[1], Mehul Parakh[1], Sean Johnson[2], Priyanka Ramaswamy[2], Michael Lowe[2], Aubrey Penn[3], Lew Penn[3] and Shanthi Iyer[1]; [1]JSNN, United States; [2]North Carolina A&T State University, United States; [3]North Carolina State University, United States

We report on a systematic investigation of the effect of tellurium (Te)-doping on the morphological, optical, and electrical properties of the GaAsSb nanowires (NWs) grown by self-catalyzed molecular beam epitaxy and realization of the ensemble NW photodetector (PD). Qualitative assessment of Te-incorporation in the NWs was made from the structural, optical, and electrical properties, whereas the quantitative assessment was made based on the dark I-V simulations. The single nanowire I-V characterization demonstrated a significant reduction in turn-on voltage with doping. High-resolution transmission electron microscopy image and the selected area electron diffraction patterns of n-GaAsSb NWs revealed the defect-free single-crystal zinc-blende crystal structure. The compositional homogeneity of the NWs is attested by the extended plateau in the energy-dispersive X-ray spectroscopy line scan. An ensemble PD fabricated using n-GaAsSb NWs demonstrated a wide spectral range with the longer wavelength cutoff at ~1.2 µm, with the figure of merits namely, responsivity in the range of 580- 620 A/W and detectivity of $3x\ 10^{12}$ Jones. Low-frequency noise (LFN) spectroscopy revealed the generation-recombination noise being the dominant noise source in the Te doped GaAsSb NWs.

11:30 AM B04
Towards the Growth of 3D Forests of Carbon Nanotubes—Selective Height Control Using Thin-Film Reservoirs and Overlayers Gilbert Daniel Nessim[1,2]; [1]Bar Ilan University, Israel; [2]President Israel Vacuum Society (IVS), Israel

Despite the massive progress achieved in the growth of carbon nanotube (CNT) forests on substrate, apart from lithographic patterning of the catalyst, little has been done to selectively (locally) control CNT height. Varying process parameters, gases, catalysts, or underlayer materials uniformly affects CNT height over the whole substrate surface. We show here how we can locally control CNT height, from no CNTs to up to 4X the nominal CNT height from iron catalyst on alumina underlayer by patterning reservoirs or by using overlayers during annealing or growth. In 2014, we demonstrated how an iron thin film reservoir placed below the alumina underlayer could almost double CNT height.[1] The mechanism is based on the diffusion from the reservoir to the catalytic surface mediated by the thin alumina layer. Leveraging this technology platform consisting of thin film reservoir / alumina / iron catalyst, we placed a copper/silver thin film reservoir under the alumina underlayer to inhibit CNT growth via copper-iron alloying, thus deactivating the iron catalyst.[2] Finally, we show that a thin film reservoir of molybdenum enhances CNT growth by a factor of 4X after alloying with iron and forming a bimetallic catalyst.[3] Combining all the above results into a unique platform, we can lithographically pattern the reservoir material and obtain four different CNT heights during a unique growth process: no growth (Cu/Ag reservoir), nominal growth (no reservoir), 2X growth (Fe reservoir), and 4X growth (Mo reservoir). Using a complementary technique, we show how a copper or nickel overlayer (stencil or bridge) placed above the catalyst surface during pre-annealing or during CNT growth deactivates the catalyst.[4,5] We showed how we could pattern regions with CNTs and without CNTs by simply annealing the sample with a patterned overlayer positioned above its surface. We thus synthesized patterned CNT forests using a simple process, without the need for lithography. We can combine the overlayer technique with one of the above-mentioned reservoirs (no reservoir, Cu/Ag reservoir, Fe reservoir, or Mo reservoir) to further modulate CNT growth by offsetting some or all of the growth enhancements achieved using the reservoirs. We will show examples of growth with patterned regions of CNTs with different CNT heights (or without CNTs) that combine the reservoir and the overlayer techniques. This modulation of the CNT height is a significant improvement compared to the "CNTs (one height) / no CNTs" patterning that has been achieved using lithography of the catalyst, and moves us closer to building 3D architectures of CNTs that could be useful for future electronic devices or sensors.

1. E. Shawat, Mor V., Y. Fleger, L. Oakes, C.L. Pint, and **G.D. Nessim***
What is below the support layer affects carbon nanotube growth: an iron catalyst reservoir yields taller nanotube carpets
Nanoscale, P. 1545-1551, Vol. 6, Jan. 2014
2. E. Shawat Avraham, A.S. Westover, L. Shani, V. Mor, O. Girshevitz, C.L. Pint, and **G.D. Nessim***
Patterned growth of carbon nanotube forests using Cu and Cu/Ag thin film reservoirs as growth inhibitors
Carbon, Vol. 130, 273–280, 2018
3. E. Shawat Avraham, O. Girshevitz, A. Westover, C.L. Pint, and **G.D. Nessim***

Controlling Molybdenum reservoir thickness to enhance the growth of carbon nanotube forests
Nanoscale, Vol.11, P.1929, 2019
4. R. Yemini, M. Muallem, T. Sharabani, E. Teblum, Y. Gofer, **G.D. Nessim***
Patterning of Forests of Carbon Nanotubes (CNTs) Using Copper Overlayers as Iron Catalyst De-Activators
Journal of Physical Chemistry C, Vol. 120 (22), P. 12242−12248, May 2016
5. R. Yemini, A. Itzhak, Y. Gofer, T. Sharabani, M. Drela, and **G.D. Nessim***
Nickel overlayers modify precursor gases to pattern forests of carbon nanotubes
Journal of Physical Chemistry C, *121* (21), 11765–11772, 2017

11:45 AM B05
(LATE NEWS, Student) Surface-Driven Synthesis of Doped Graphitic Nano- and Macro-Tubes Chuanshen Du[1], Paul Gregory[1], Julia Chang[1], Andrew Martin[2,1], Rick Dorn[1], Jingzhe Li[1], Priya Venkatraman[3], E. Johan Foster[4,3], Emily A. Smith[1], Aaron J. Rossini[1] and Martin Thuo[1]; [1]Iowa State University of Science and Technology, United States; [2]Lawrence Berkeley National Laboratory, United States; [3]Virginia Tech, United States; [4]The University of British Columbia, Canada

Graphitic hetero-materials are among one of the fastest growing materials in use due to its unique properties such as high thermal/electrical conductivity and chemical inertness. Due to difficulties and expensiveness associated with scalable synthesis of graphene/graphitic materials, mass-application of such materials has been limited. In this study, we demonstrate a frugal method of synthesizing high aspect ratio oxide-doped tubular graphene structures with nano- to macrometer diameters. We frustrate surface ignition leading to an inverted thermal degradation with concomitant limitation of oxidation leading to partial reduction of C(IV) to C(0). Thermal sintering and stochastic oxidation leads to generation of graphitic/graphene-oxide tubes. Incorporation of endo- or exo-thermic triggers leads to tunable dimension control with concomitant integration of oxides. Felicitous choice of oxide precursors and processing temperatures tunes the paramagnetic properties of the resulting properties or resulting bandgap of the synthesized material..

12:00 PM B06
(LATE NEWS, Student) Enhancement of Integrated Cu-Ti-CNT Conductors via Joule-Heating Driven CVD Dylan J. McIntyre[1], Sarah A. Nadzam[1], Meleni M. Sarantos[1], Anthony P. Leggiero[1], Ryan K. Hirschman[1], Richard K. Hailstone[1], Cory D. Cress[2], Ivan Puchades[1] and Brian Landi[1]; [1]Rochester Institute of Technology, United States; [2]U.S. Naval Research Laboratory, United States

Metal-Carbon Nanotube (CNT) hybrid conductors benefit from the high conductivity provided by metals with the low temperature coefficient of resistance (TCR) for CNTs. Highly conductive metals, such as copper, typically exhibit poor interfacing with CNTs, and thus require an interfacial layer to improve electrical contact and adhesion at elevated temperature. In this work, Ti and Ni were evaluated as adhesion metals by thermally evaporating 10 nm layers onto a CNT conductor, and assessing the evolution of nanoscale morphology upon annealing up to 400 °C. SEM reveals that Ni coalesces upon exposure to temperatures up to 400 °C. Ti, however, maintains a stable coating on the CNTs over the same temperatures. Additionally, a 12% decrease in resistance occurs for a Cu-Ti-CNT hybrid after exposure to 400 °C. Thus, Ti emerges as a promising candidate for enhancing both the adhesion and electrical performance of the metallized hybrids for elevated temperature applications. To enhance the coverage of Ti throughout the CNT network, Joule-heating driven CVD was selected as a delivery route. CVD offers the ability to deposit uniformly over irregular topographies, as well as provide penetrability throughout the thickness of the network. Additionally, Joule-heating driven CVD relies on an applied current to resistively heat the substrate, providing the thermal energy required for precursor decomposition. As a result, deposition occurs favorably at regions which will benefit the most from utilization of metal interconnection. In this study, a cyclopen tadienyl(cycloheptatrienyl) titanium(II) precursor was selected as it is an oxygen-free precursor. Herein, Joule-heating driven CVD was demonstrated to deposit Ti successfully throughout a 30 µm-thick CNT conductor as verified via cross-sectional EDX. The physical morphology of the deposited coatings is analyzed as a function of deposition weight loading, ranging from surface films to coatings localized along the CNT bundle surfaces. The deposition properties are shown to be influenced by the amount of precursor used, inert reactor pressure, and applied current. Furthermore, CNT conductors were purified to remove carbonaceous impurities and residual catalyst to provide a clean surface for CVD deposition and the resultant CVD deposition properties were assessed via EDX and Raman spectroscopy. In addition, temperature dependent electrical modeling was performed to understand the effects of metal interconnection. Electroplating the CVD deposited conductor to form a bulk integrated Cu-Ti-CNT hybrid resulted in conductivities > 30 MS/m, combined with TCR values lower than pure Cu, and outperformed Cu-CNT hybrids fabricated via a similar combination of techniques without the use of a Ti adhesion layer. Thus, Joule-heating driven CVD is shown to be an effective route for the fabrication of integrated Ti-CNT conductors, enabling the advantages of Ti to be realized in bulk CNT networks for advanced conductor fabrication.

SESSION C: Plasmonics, Strong-Coupling and Resonant Optical Structures
Session Chairs: Joshua Caldwell and Anthony Hoffman
Wednesday Morning, June 23, 2021

10:45 AM C01
Long-Lived Modulation of Plasmonic Absorption by Ballistic Thermal Injection John Tomko[1], Evan Runnerstrom[2], Yi-siang Wang[3], Weibin Chu[3], Joshua R. Nolen[4], David Olson[1], Kyle Kelley[5], Angela Cleri[6], Josh Nordlander[6], Joshua Caldwell[4], Oleg Prezhdo[3], Jon-Paul Maria[6] and Patrick Hopkins[1]; [1]University of Virginia, United States; [2]Army Research Office, United States; [3]University of Southern California, United States; [4]Vanderbilt University, United States; [5]North Carolina State University, United States; [6]The Pennsylvania State University, United States

Light–matter interactions that induce charge and energy transfer across interfaces form the foundation for photocatalysis, energy harvesting and photodetection, among other technologies. One of the most common mechanisms associated with these processes relies on carrier injection. However, the exact role of the energy transport associated with this hot-electron injection remains unclear. Plasmon-assisted photocatalytic efficiencies can improve when intermediate insulation layers are used to inhibit the charge transfer or when off-resonance excitations are employed, which suggests that additional energy transport and thermal effects could play an explicit role even if the charge transfer is inhibited. This provides an additional interfacial mechanism for the catalytic and plasmonic enhancement at interfaces that moves beyond the traditionally assumed physical charge injection. In this work, we report on a series of ultrafast plasmonic measurements that provide a direct measure of electronic distributions, both spatially and temporally, after the optical excitation of a metal/semiconductor heterostructure. We explicitly demonstrate that in cases of strong non-equilibrium, a novel energy transduction

mechanism arises at the metal/semiconductor interface. We find that hot electrons in the metal contact transfer their energy to pre-existing free electrons in the semiconductor, without an equivalent spatiotemporal transfer of charge. Further, we demonstrate that this ballistic thermal injection mechanism can be utilized as a unique means to modulate plasmonic interactions. These experimental results are well-supported by both rigorous multilayer optical modelling and first-principle ab initio calculations.

11:00 AM C02
(Student) Enhanced Absorption with Core/Shell Silicon Carbide/Graphene Nanowires for Tunable Mid-Infrared Nanophotonics Patrick Rufangura[1,1], Arti Agrawal[1,1], Thomas G. Folland[2], Joshua D. Caldwell[3] and Francesca Iacopi[1,1]; [1]University of Technology Sydney, Australia; [2]The University of Iowa, United States; [3]Vanderbilt University, United States

Surface plasmon polariton (SPP), which result from the strong coupling of bound electromagnetic (EM) waves and collective charge oscillations, enable subwavelength manipulation of light and matter interaction. Conventional noble metals-based SPP excited in the visible and near-Infrared spectra ranges suffer from large energy losses and cannot be dynamically tuned. Thanks to its 2D nature, graphene has emerged as a promising alternative plasmonic material with well- confined SPPs in the mid-infrared (MIR) and terahertz (THz) ranges and remarkable tunability. On the other hand, polar dielectric materials support low optical losses and sub-wavelength mode in the MIR and THz regions via surface phonon polariton (SPhP)mode' stimulation within the Reststrahlen band, a narrow spectral range between transverse optical (TO) and longitudinal optical (LO) frequencies. Due to the excellent polaritonic responses in both graphene and silicon carbide in the MIR and THz regions, devices combining the two materials are inferred to greatly advance photonics and THz technologies. We have recently theoretically demonstrated the strong confinement and large propagation figures of merit (FOM) for hybrid surface plasmon and surface phonon polariton in the epitaxial graphene on silicon carbide. The ability to confine such MIR light into small volume through excitation of SPP and SPhP has many implications for optoelectronic technologies such as the MIR photodetection[2], sensing[3], and solar cells[4]. Epitaxial graphene(EG) grown on silicon carbide(SiC) on silicon(Si) has been investigated as a suitable platform for graphene growth on semiconductors to meet the prospective technologies [5]. Despite this platform being very advantageous, experimental and theoretical works demonstrating the potentials properties/ applications of EG on SiC on Si are still missing.
Here we combine electromagnetic simulations based on finite elements method (FEM) with attenuated total reflectance Fourier transformed infrared (ATR-FTIR) spectroscopy to indicate improved MIR absorption, E field enhancement, and tunability for graphene-coated SiC nanowires (NWs). As anticipated, low absorption was confirmed from both simulations and measurements on bare SiC NWs, further supported by the calculated weak electric field due to the thin size of SiC NWs being incapable of absorbing sufficient light. On the other hand, enhanced absorption for the SiC NWs was measured by ATR-FTIR after a conformal graphitization of NWs[6]. Our previous study of this material system revealed a low-density oxide layer formed between graphene and SiC NWs[6]. This oxide layer between EG and SiC NW has been implemented in the FEM model, leading to field enhancement of incident EM field and strongly confined in the thin oxide. This substantial absorption and field enhancement originates from the coupling between the incident MIR photon and the plasmon/ phonon in graphene and SiC, respectively, with the oxide layer acting as a coupling medium. Furthermore, we demonstrate the modes' tunability whereby tuning the graphene's Fermi energy, the modes' resonance frequencies can be shifted to ~ 100 cm^{-1}. Lastly, we realize substantial field enhancement, which is achieved by carefully tuning the graphene's Fermi energy and adjusting the spectra position of mode 1(mode on the left of LO frequency) closer to TO frequency. These results hold promise for various photonic applications such as perfect absorber to improve solar cell, MIR photodetectors, and other tunable photonics.
[1]P. Rufangura, et al., *J. Phys. Mater.,* vol. 3, no. 3, p. 032005, 2020. [2]T. Low and P. Avouris, *ACS nano,* vol. 8, no. 2, pp. 1086-1101, 2014. [3]A. G. Brolo, *Nat. Photon.,* vol. 6, no. 11, p. 709, 2012. [4]H. A. Atwater and A. Polman, *Nat. Mater.,* vol. 9, no. 3, p. 205, 2010. [5] N. Mishra et al., *Phys. Status Solidi (a),* vol. 213, no. 9, pp. 2277-2289, 2016. [6]N. Mishra et al., *J. Appl. Phys.,* vol. 126, no. 6, p. 065304, 2019.

11:15 AM C03
(Student) Engineering the Spectral and Spatial Dispersion of Thermal Emission via Strong Coupling Guanyu Lu[1], Christopher R. Gubbin[2], Joshua R. Nolen[1], Thomas G. Folland[1,3], Marko Tadjer[4], Ivan I. Kravchenko[5], Simone D. Liberato[2] and Joshua Caldwell[1]; [1]Vanderbilt University, United States; [2]University of Southampton, United Kingdom; [3]The University of Iowa, United States; [4]U.S. Naval Research Laboratory, United States; [5]Oak Ridge National Laboratory, United States

Phonon polaritons are quasiparticles comprising a photon and a coherently oscillating charge on a polar lattice, which are supported in the form of propagating (SPhP) and localized surface phonon polaritons (LSPhP). The promising properties of LSPhP modes are exceptionally high predicted Purcell enhancements and narrow resonance linewidths, with the potential for near-unity absorption (emissivity). However, one drawback is that as a highly localized mode, they offer no significant degree of spatial coherence (directionality) for thermal emission applications. Alternatively, high spatial coherence can be achieved using propagating SPhPs launched by grating elements. However, the non-localized nature of such propagating modes yields thermal emission into frequency-specific angles across the entire Reststrahlen band where such modes can be supported. The introduction of strong coupling between different polaritonic modes, therefore, provides us an opportunity to combine the virtues of the narrowband LSPhP resonances with the high spatial coherence associated with propagating SPhPs into a novel, mixed character polariton. Further, it has been proposed that strong coupling between LSPhPs with zone-folded longitudinal optic phonons (ZFLO) could provide a mechanism to use the longitudinal fields of an electrical bias to stimulate the transverse fields of SPhPs through Ohmic loss. Thus, we propose that through inducing strong coupling between LSPhPs, propagating SPhPs, and ZFLO phonons, that realization of a narrow-band, spatially coherent emitter amenable to electrically driven emission could be possible. Additionally, through coupling to such a ZFLO mode, the extremely narrow linewidths could be employed via strong coupling to further reduce the linewidths of the SPhP modes. In this work, we report on three-oscillator strong coupling within a SPhP platform using nanopillar arrays fabricated into a 4H-SiC substrate. Here, we experimentally manipulate the dispersion relation of coupled SPhP modes by strongly coupling LSPhPs, propagating SPhPs, with the ZFLO. In the strong coupling regime, the formation of such hybrid modes with mixed character is expected. Furthermore, the strength of the interactions between such optical modes can be precisely controlled through the hybridization of three oscillators. We further report on the influence of such strong coupling upon thermal emission within the long-wave-IR (LWIR), demonstrating significant narrowing of the spectral and spatial dispersion of the individual modes within this strongly coupled regime. In our three-oscillator strong coupling platform, we simultaneously demonstrate a five-fold reduction in the angular spread of the thermally emitted light and a three-fold enhancement of the quality factor over that of the uncoupled LSPhP mode at the anti-crossing point where the splitting occurs. Furthermore, the high Q-factors (over 200) achieved are realized using traditional photolithography, enabling

such devices to be produced at large-scale and reasonable costs. Our results demonstrate that by leveraging three-oscillator strong coupling that the spectral and spatial dispersion of thermal emission can be engineered for a variety of LWIR applications extending from spectroscopy, sensing, to free-space communications.

11:30 AM C04
(Student) Polarization-Selective Modulation of Supercavity Resonances Originating from Bound States in the Continuum
Chan Kyaw[1], Riad Yahiaoui[1], Joshua Burrow[2], Viet Tran[1], Kyron Keelen[3], Wesley Sims[3], Eddie Red[3], Willie Rockward[4], Mikkel Thomas[5], Andrew Saragan[2], Imad Agha[2] and Thomas Searles[1]; [1]Howard University, United States; [2]University of Dayton, United States; [3]Morehouse College, United States; [4]Morgan State University, United States; [5]Georgia Institute of Technology, United States

Bound states in the continuum (BICs) are widely studied for their applications in confining light, producing sharp resonances for sensing applications and serving as avenues for lasing action with topological characteristics. Primarily, the formation of BICs in periodic photonic band gap structures are driven by symmetry incompatibility through structural manipulation or variation of incidence angle from incoming light. In this presentation, we report two methods for driving the formation of BICs in terahertz metasurfaces. For normal incidence, we experimentally confirm polarization driven symmetry-protected BICs by the varying the linear polarization states of light. In addition, we demonstrate through strong coupling of two radiative modes the formation of capacitively-driven Freidrich-Wintgen BICs, exotic modes which occur in off- Γ points not accessible by symmetry-protected BICs. The capacitance-mediated strong coupling at 0° polarization is verified to have a normalized coupling strength ratio of 4.17% obtained by the Jaynes-Cummings model.

11:45 AM C05
Hyperbolic Phonon Polaritons in Calcite Nanopillar and Nanohole Arrays for Nanoscale Infrared Confinement
Vanessa Breslin[1,2], Daniel Ratchford[1], Alexander Giles[1], Adam Dunkelberger[1], Eric Jackson[1], Igor Vurgaftman[1], Chase Ellis[1], Joseph Tischler[3,1] and Jeffrey Owrutsky[1]; [1]U.S. Naval Research Laboratory, United States; [2]NRC Postdoctoral Associate, United States; [3]The University of Oklahoma, United States

Phonon polaritons are collective oscillations resulting from the coupling of photons with optical phonons in polar materials and are supported within a material-specific spectral region called the reststrahlen band, which is bounded by the transverse and longitudinal optical phonons. In this region, the material behaves optically like a metal; it is highly reflective and has a negative real part of the permittivity. When polar materials are nanostructured, phonon polaritons can enable a variety of near-field optical effects such as sub-diffraction light confinement. Polar materials that support phonon polaritons can also have anisotropic optical properties, such that the optical constants depend on the propagation direction and polarization of the incoming light. When the principal components of the permittivity tensor have opposite signs, the material is referred to as hyperbolic. Hyperbolic materials are somewhat unusual as they behave optically like a dielectric and metal along different crystal axes, and this anisotropy of the metal-like response has important implications for the physics of its supported modes. Here, we report on the first experimental observation of hyperbolic phonon polaritons (HPs) in calcite nanopillar arrays, demonstrate the aspect ratio dependence of the HP resonance frequencies, discuss fabrication challenges, observe a new, possibly higher order mode as the pitch is reduced, and compare our results to both numerical simulations and an analytical model. We also found that the simulated electric field distributions for the HP modes are not localized to the pillars but extend appreciably into the calcite substrate. In addition, we have fabricated nanohole arrays in calcite, which also support HPs. However, the HP resonances appear to exhibit a slight aspect ratio dependence but opposite in trend to what was observed for the nanopillars. Additionally, the nanohole arrays have fewer HP modes and these modes are blueshifted in comparison to the nanopillars. We are currently using finite difference time domain simulations to characterize the HP modes supported in the nanohole arrays and to understand the differences between these modes and the HP modes confined within the nanopillars. Calcite is an ideal low-loss material for studying HPs that could find applications in mid-IR nanophotonic devices, and so these results are an important step toward creating a library of materials with the appropriate phonon properties to span the infrared.

12:00 PM C06
(Student) Long-Wave Infrared Topological Phonon Chain
Abhilasha Kamboj[1], Monica Allen[2], Jeffery Allen[2] and Daniel Wasserman[1]; [1]University of Texas at Austin, United States; [2]Air Force Research Laboratory, United States

Topological photonic or plasmonic systems have recently gained significant interest for their unique optical properties and potential applications in unidirectional waveguides, field enhancement, and lasing from topologically protected states. One of the simpler models available to investigate topological systems is a 1-D diatomic staggered chain of period Δ, the Su-Schrieffer-Heeger (SSH) model where adjacent resonant particles are spaced by βΔ/2 & (2-β)Δ/2, (β/2 ∈ (0,1)). In the commonly studied quasi-static (QS) limit, radiative damping is typically neglected and only the nearest neighbor effects are considered. Such an approach is reasonably accurate when the size of an individual particle is much smaller than either of the inter-particle spacings. However, as we approach experimental sizes, where the particle radii are on the order of the interparticle gap, radiative damping and long-range effects can become too significant to neglect[1]. In this work we investigate sub-wavelength resonators leveraging localized surface *phonon* resonances (LSPhR), taking into account radiative damping and long-range effects. We design, fabricate and characterize topological phononic chains consisting of aluminum nitride (AlN) pillars on a molybdenum (Mo) ground plane which support edge modes in the long-wave infrared regime. AlN has a negative permittivity in the spectral range bridging AlN longitudinal optical (LO) and transverse optical (TO) phonon energies (AlN Reststrahlen band). In this spectral range, AlN can support propagating and/or localized surface phonon modes at the interface between AlN and a dielectric medium.
In the QS approach, an infinite staggered chain of particles is assumed, with periodic boundary conditions. Using the nearest neighbor model, one solves the 2×2 Bloch Hamiltonian matrix to obtain the dispersion relation for the chain. The edge mode, however, cannot be observed for such a case (infinite chain assumption). In order to do so, we must apply an open boundary condition, where each particle has a unique polarization due to its interaction with all the other particles in the chain, including those at the end of the chain. Therefore, for an N-particles chain, we obtain an N×N matrix. The solution for this system gives the dispersion relation, or the allowed frequencies of the finite chain for a given Δ, r & β. One observes that set of allowed frequencies, and the phononic band gap, are the same for β & (2 – β), however, presence of the edge modes is only observed (in the band gap) for β >1. The fabricated sample consists of 1.2μm thick AlN over 200nm of Mo on a silicon substrate. The topological chain of AlN pillars of radius, r = 1.5μm, Δ = 20μm is etched using a standard photo-lithography & ICP RIE process. Similarly, an isolated 3μm wide strip of Mo is etched under the AlN pillars on the edge of the sample, to be used for thermal excitation of the topological chain. The reflectance spectrum of the pillars is measured using a Bruker V80v Fourier transform infrared (FTIR) spectrometer. The collected spectra are compared to RCWA-simulated reflection spectra, as well as reflection from a bulk AlN sample. While the

bulk sample shows the absorption feature at $\lambda \approx 11.2\mu m$ corresponding to the AlN Berreman mode[2], the pillar spectra show coupling to LSPhR modes at $\lambda \approx 12.1\mu m$, in excellent agreement with the plasma frequency calculated for the pillars and our numerical simulations. Future work will look to collect the edge mode emission from one end of chain by thermal excitation of the chain's opposite end. Authors AK and DW gratefully acknowledge Air Force award #FA8075-18-D-0002 via Macauley-Brown Inc subcontract. Authors MSA and JWA are thankful for the funding support through AFOSR Lab Task 20RWCOR090 and the AFRL Munition Directorate's Chief Scientist Office. 1. S. R. Pocock et al. ...V. Giannini, ACS Photonics, 5(6):2271–2279, 2018. 2. L. Nordin et al. ... D. Wasserman.Applied Physics Letters, 111(9):091105, 2017.

SESSION D: Scandium Nitride
Session Chairs: Leonard Brillson and Christian Wetzel
Wednesday Morning, June 23, 2021

10:45 AM D01
Stress and Crystal Quality Control in Heteroepitaxial ScAlN Grown on SiC by Molecular Beam Epitaxy Matthew Hardy, Brian P. Downey, Andrew C. Lang, Eric N. Jin, Neeraj Nepal, D. S. Katzer and David J. Meyer; U.S. Naval Research Laboratory, United States

ScAlN thin films have attracted significant attention due to their factor of five increase in piezoresponse over AlN for $Sc_xAl_{1-x}N$ compositions of $x = 0.43$ [1]. The strong piezoresponse makes ScAlN a likely candidate for future broadband filters for 5G telecom applications. The large spontaneous polarization of epitaxial ScAlN barrier layers in GaN-based high-electron-mobility transistors (HEMTs), can provide a 3–5× higher channel carrier density than conventional AlGaN/GaN HEMTs. Recently, sputtered $Sc_xAl_{1-x}N$ thin films with $x \geq 0.27$ has been experimentally confirmed to exhibit ferroelectricity [2], marking the first demonstration of ferroelectricity in a III-V semiconductor material. Maintaining phase-pure and high crystal quality $Sc_xAl_{1-x}N$ at high x is critical to improve resonator bandwidth and insertion loss and reduce the coercive field and leakage in ferroelectric devices. At the same time, control of film stress is needed to allow thicker $Sc_xAl_{1-x}N$ films, stabilize suspended ScAlN membranes for resonator structures, and to modify the ferroelectric coercive field. In this work we investigate the interplay between growth conditions, namely group-III/V flux ratio and growth temperature, with $Sc_xAl_{1-x}N$ composition, crystal quality, and film stress for films grown heteroepitaxially on SiC substrates using plasma-assisted molecular beam epitaxy. Using a thin AlN interlayer, and a III/V ratio of 0.8, high quality $Sc_{0.18}Al_{0.82}N$ films can be grown at or slightly below typical GaN growth temperatures (600–700 °C) with X-ray diffraction (XRD) 0002 reflection rocking curve full-width at half-maximum (FWHM) of less than 1000 arcsec. However, these films have a cracking critical thickness between 150–200 nm in spite of nominally compressive misfit strain. We show that reduction in growth temperature results in a small increase in the cracking critical thickness. Comparison to calculated stress results from coefficient of thermal expansion (CTE) mismatch suggests minimal contribution from CTE mismatch, suggesting another mechanism such as dislocation inclination or volumetric defect annihilation is dominant. In addition to changes in stress state, lower growth temperature also enables growth of wurtzite phase-pure $Sc_xAl_{1-x}N$ with x up to 0.32, as demonstrated by XRD and transmission electron microscopy (TEM). These films show XRD FWHM as low as 4000 arcsec and tensile stresses as high as 2.7 GPa for 150-nm films. $Sc_xAl_{1-x}N$ thin films with $x = 0.4$ show signs of a second phase in the early stages of ScAlN nucleation, as seen in reflection high-energy electron diffraction (RHEED) and TEM, although the RHEED pattern improves as the film growth progresses. A novel two-step growth process enables improved phase purity as well as a reduction in film stress from 1.4 to 0.9 GPa with an XRD FWHM of 5800 arcsec for a film only 150-nm-thick.
[1] M. Akiyama, K. Kano, A. Teshigahara, Appl. Phys. Lett., 95 (2009) 162107.
[2] S. Fichtner, N. Wolff, N. Lofink, L. Kienle, B. Wagner, J. Appl. Phys., 125 (2019) 114103.

11:00 AM D02
(Student) Physical Properties of ScxAl1-xN/GaN Heterostructures by Molecular Beam Epitaxy Joseph Casamento[1], Hyunjea Lee[1], Celesta S. Chang[1,1], Takuya Maeda[1,1], Matthew F. Besser[2], David A. Muller[1,1], Huili Grace Xing[1,1,1] and Debdeep Jena[1,1,1]; [1]Cornell University, United States; [2]Ames Laboratory, United States

Scandium aluminum nitride ($Sc_xAl_{1-x}N$) has gained tremendous interest in recent years due to enhanced piezoelectric and ferroelectric behavior from isoelectronic alloying of AlN with Sc. [1,2] However, realization of $Sc_xAl_{1-x}N$ with low defect levels remains challenging, in part due to the high oxygen affinity of scandium (Sc). [3] As $Sc_xAl_{1-x}N$ continues to garner merit in epitaxial electronic and photonic device applications on the GaN platform, reduction of structural and chemical defects becomes vital to realize the optimal properties of this novel materials system. In this work, we report the first comparison of the chemical, electrical, and structural properties of epitaxial $Sc_xAl_{1-x}N$ (x=0.1 to 0.45)-GaN heterostructures grown by plasma-MBE on metal polar GaN (0001) substrates using two different Sc metal sources. One Sc source is nominally a 99.99 % (4N) pure on a rare metals basis and another Sc source from Ames Laboratory is nominally 99.9% (3N) total purity, including carbon and oxygen. This leads to the Sc source from Ames having a higher purity. Sc was supplied via E-Beam evaporation and Al, Ga, and Si were supplied using Knudsen effusion cells. Growth temperatures measured by a thermocouple were 700C and 600C for GaN and $Sc_xAl_{1-x}N$, respectively. Corresponding film growth rates were ~5 nm/minute. *In situ* reflection high energy electron diffraction (RHEED) tracked surface crystallinity. Secondary ion mass spectrometry (SIMS) measurements were calibrated by Rutherford backscattering spectrometry (RBS). Structural characterization was performed via high annular dark field scanning transmission electron microscopy (HAADF-STEM). Electrical characterization consisted of quasi static current-voltage (I-V) measurements on lithographically patterned Ti/Au electrodes. *In situ* RHEED images suggested the $Sc_xAl_{1-x}N$ layers remained epitaxial throughout the growth and the subsequent GaN layers grown on $Sc_xAl_{1-x}N$ retained their hexagonal crystal structure. Atomic force microscopy (AFM) images showed surfaces with an RMS roughness of less than 2 nm, with hillocks related to extended defects. SIMS analysis showed a reduction of carbon, oxygen, and fluorine impurities of two to three orders of magnitude for the sample grown with the Ames Sc source. An oxygen content of ~$6x10^{17}$ atoms/cm^3 at 34% Sc content (x=0.34) is the lowest oxygen content reported to date for $Sc_xAl_{1-x}N$. This is in accordance with the Sc source design as Ames Laboratory utilizes a process designed to reduce fluorine, oxygen, and carbon. The reduction in the unintentional doping led to a significant decrease in leakage current levels in quasi static I-V measurements. A 4-7 order of magnitude reduction in current densities across all samples studied was observed. The current density was lowest for the ~18% Sc content (x=0.18) near lattice-matched heterostructures, which increased with the Sc content. The low leakage current in the higher purity Sc source enabled, for the first time, direct and accurate measurements of the relative dielectric constant of epitaxial $Sc_xAl_{1-x}N$, which is found to be ~15 for $0.18 < x < 0.3$. The higher purity of Sc source is thus expected

to gradually help reveal several properties of this transition-metal nitride alloy for electronic and photonic device applications. This work was supported by the DARPA TUFEN program monitored by Dr. Ron Polcawicz.
[1] Akiyama, M et al. Adv. Mater. 21, 593 (2009).
[2] Fichtner, S et al. J. Appl. Phys. 125, 114103 (2019).
[3] Casamento, J et al. Phys. Status Solidi B 257, 1900612 (2020).

11:15 AM D03
(Student) Cathodoluminescence and X-Ray Photoelectron Spectroscopy of ScN: Dopant, Defects and Band Structure
Micah Haseman[1], Brenton A. Noesges[1], Seth Shields[1], John Cetnar[2], Amber Reed[2], Hayder A. Al-Atabi[3,4], James H. Edgar[3] and Leonard J. Brillson[1,1]; [1]The Ohio State University, United States; [2]Air Force Research Laboratory, United States; [3]Kansas State University, United States; [4]The University of Technology, Iraq

The rocksalt-structure semiconductor ScN is a relatively unexplored group IIIB transition metal nitride with outstanding physical properties that, combined with its III-nitride counterparts, has the potential to dramatically expand the range of their electrical, optical, and thermoelectric device applications. Recent works have focused on the degenerate nature of ScN by substitutional impurities O_N and F_N, which shift the direct (X–X) gap transition to higher energies via the Burstein–Moss effect. Here, we used cathodoluminescence spectroscopy (CLS) to observe optical signatures of both the midgap V_N precursor to O_N doping as well as signatures above the direct (X–X) bandgap corresponding to band-to-band transitions from four separate conduction bands near the Γ point with the valence band minimum, in agreement with calculated band structure diagrams. Thin film ScN grown by reactive magnetron sputtering displays mild degenerate doping by substitutional oxygen as indicated by elevated (X–X) transition energies and the presence of Sc–O bonding determined via x-ray photoelectron spectroscopy (XPS), while ScN grown by physical vapor transport exhibited the intrinsic, non-degenerate (X–X) bandgap predicted by theory. CLS reveals a sharp, sub-bandgap emission at 1.26 eV for sputter grown ScN on GaN, which we attribute to nitrogen vacancies (V_N) based on surface sensitive CLS and XPS chemical trends. This finding is in strong agreement with theoretical calculations for V_N predicting the formation of a defect energy level within the gap. Since O substitution into V_N defects creates the shallow donor level responsible for degenerate doping, optical identification of this doping precursor can help understand the growth and processing that influence ScN doping. L.J.B., M.S.H., and S.S. acknowledge the support from the National Science Foundation, Grant No. DMR 18-00130. A.H. and J.H.E. acknowledge the support for ScN crystal growth from the National Science Foundation under Grant No. DMR-1508172. This research was also supported by the Air Force Office of Scientific Research through Project No. FA9550-RY17COR490 (J.S.C. and A.N.R.).

11:30 AM D04
(Student) Plasma-Assisted Epitaxy of Piezoelectric $Sc_xAl_{1-x}N$ Films for Use in Harsh Environment Microwave Acoustic Sensors Morton Greenslit[1,2], Mauricio Pereira da Cunha[1,2] and Robert J. Lad[1,2]; [1]University of Maine, United States; [2]Frontier Institute for Research in Sensor Technologies, United States

The AlN wurtzite structure retains piezoelectricity to at least 1000°C and AlN films can be grown using a wide range of techniques, making AlN an attractive high temperature piezoelectric material for harsh environment microwave acoustic sensor applications. Several theoretical predictions and experimental thin film growth studies reported in the literature have indicated that the addition of ScN into the AlN wurtzite lattice to form a $Sc_xAl_{1-x}N$ alloy can increase the value of the piezoelectric coupling coefficient, d_{33}. The most common method that has been used for $Sc_xAl_{1-x}N$ film synthesis is RF magnetron sputtering from a fixed target composition which allows uniform film growth over large wafer areas. In this work, a plasma-assisted epitaxial growth method has been used to synthesize highly oriented (0002) $Sc_xAl_{1-x}N$ films on pre-nitrided c-sapphire substrates over a range of stoichiometries from x = 7 at.% to 55 at.% by co-evaporating Sc and Al high purity metal sources in the presence of a nitrogen plasma generated by an RF plasma source within a highly controlled ultra-high vacuum environment. This plasma-assisted epitaxy approach allows $Sc_xAl_{1-x}N$ films to be produced with the desired highly oriented (0002) grains needed for piezoelectric activity using precisely controlled Sc, Al, and N-plasma fluxes, and the method easily allows synthesis of many $Sc_xAl_{1-x}N$ film compositions. $Sc_xAl_{1-x}N$ film stoichiometries are dictated by the Sc and Al arrival rates on the 930°C growth surface during the plasma epitaxy process and were verified by in situ X-ray photoelectron spectroscopy analysis immediately after growth. X-ray diffraction pole figures and in situ RHEED indicate that the desired highly oriented ScAlN (0002) grains epitaxially nucleate on prenitrided c-sapphire substrates for Sc concentrations below 20 at.%. At Sc concentrations above 20 at.% the (0002) film texture becomes less pronounced, and above ~45 at.% the ScAlN (0002) wurtzite structure becomes unstable and non-wurtzite phases are produced. The piezoelectric activity of the $Sc_xAl_{1-x}N$ films was evaluated by measuring the response of one-port surface acoustic wave resonators (SAWRs) that were fabricated on top of the $Sc_xAl_{1-x}N$ epitaxial films with Pt-Ni interdigitated transducer electrodes patterned by a photolithographic lift-off process. To successfully fabricate the SAWRs, a 10nm thick PE-CVD Si_xN_y layer was needed to prevent etching of the ScAlN film by the photoresist developer. The degree of piezoelectric coupling was inferred by measuring the reflection coefficient ($|S_{11}|$) response of one-port resonators and calculating the respective conductance and susceptance values for the SAWR devices. In addition to the quality of (0002) epitaxy and grain mosaic spread, other ScAlN film characteristics affect the amount of piezoelectric coupling including the Sc concentration, oxygen impurity content, and other grain distributions and defects within the films, as evidenced by high resolution x-ray diffraction, RHEED, and x-ray photoelectron spectroscopy data.

11:45 AM D05
Composition and Electrical Characterization of $Sc_xAl_{1-x}N$ Grown on Si Substrate by DC Sputtering Clarissa Vazquez-Colon, Stefan Nikodemski, Bruce Claflin, John Cetnar and Amber Reed; Air Force Research Laboratory, United States

Alloys made of III-nitrides such as GaN, AlN, InN have been and continue to be of large technological and economic importance. They have found use in devices such as light-emitting diodes and High Electron Mobility Transistors. However, lattice mismatches limit the performance of III-nitride-based devices. One proposed solution that has received interest in recent years is the incorporation of ScN to enhance optical and electronic properties. In particular, scandium aluminum nitride ($Sc_xAl_{1-x}N$) has been demonstrated to exhibit spontaneous polarization, high piezoelectricity, a wide bandgap, and an excellent lattice match to GaN. These properties have been demonstrated to be dependent on the Sc content and growth parameters such as temperature, pressure, and sputtering mode. $Sc_xAl_{1-x}N$-based devices are expected to find use in applications such as filters and resonators, microelectromechanical systems and transistors, among others. This work reports the characterization of $Sc_xAl_{1-x}N$ films deposited on oxidized silicon substrates by a pulsed DC magnetron sputtering technique. The Sc and Al sources used were 99.999% pure Sc and 99.9995% pure Al targets. Sample composition and crystalline orientation were investigated using X-ray photoelectron spectroscopy and X-ray diffraction. Investigation on surface roughness was conducted using atomic force microscopy. Our results contribute to the understanding and development of $Sc_xAl_{1-x}N$ synthesis and characterization for the next generation of electronic devices and sensors.

12:00 PM D06
Molecular Beam Epitaxy of N-Polar ScAlN and HEMT Structures Ping Wang, Ding Wang, Boyu Wang, Sandra M. Diez, Elaheh Ahmadi and Zetian Mi; University of Michigan–Ann Arbor, United States

ScAlN has been proposed as a promising candidate for next-generation ultrawide bandgap devices, such as high-power and high-frequency electronic devices. The incorporation of Sc offers new opportunities for bandgap, polarization, piezoelectric, and ferroelectric engineering in nitride semiconductors. In past years, enhanced spontaneous polarization, increased piezoelectric coefficient, and ferroelectric behaviors have been experimentally demonstrated in ScAlN. Among the broad range of applications, ScAlN-based high electron mobility transistors (HEMTs) stand out as a strong competitor in future power electronics. Improving the HEMT current density is an efficient approach to achieve high output power. For $Sc_{0.18}Al_{0.82}N$, which is theoretically predicted to be lattice-matched with GaN, the spontaneous polarization is ~6 times larger than that of GaN, leading to high channel charge densities in the range of 2-3 × 10^{13} cm^{-2}, which has been demonstrated in metal-polar ScAlN-based HEMTs. Typically, for metal-polar HEMTs, the barrier thickness is constrained to enable sufficient gate control, thus limiting the channel carrier density. Thanks to the lattice-matched feature, thick ScAlN can be grown as a back-barrier in N-polar HEMT structures, resulting in much higher electron density in the channel and favoring the downscaling of HEMTs. However, the growth of N-polar ScAlN and corresponding HEMTs have not been reported yet, which possess great potential for further improving the operating frequency while maintaining high output power.
In this context, we have investigated the molecular beam epitaxy (MBE) of N-polar ScAlN on sapphire substrates. The lattice-polarity of ScAlN is controlled by the underlying N-polar GaN, which was grown by MBE as well. Wurtzite phase N-polar ScAlN with Sc content up to 0.4 is achieved, which is comparable with the previously reported values for metal-polar ScAlN grown by MBE. Reciprocal space mapping x-ray diffraction confirms the coherent growth of lattice-matched $Sc_{0.18}Al_{0.82}N$ on GaN, while the ScAlN with lower or higher Sc content is partially or fully relaxed. The wurtzite structure, lattice-polarity, and in- and out-of-plane strain are characterized in detail using a high spatial resolution transmission electron microscope. Furthermore, N-polar HEMT structures were grown with a 40-nm-thick GaN channel, 2/1-nm-thick AlN/GaN interlayer, 4 to 30-nm-thick $Sc_{0.18}Al_{0.82}N$ barrier, 4-nm-thick AlN electron blocking layer (EBL), and 100-nm-thick GaN regrowth layer. The sheet electron concentration gradually increases with varying $Sc_{0.18}Al_{0.82}N$ barrier thickness from 4 to 30 nm, agreeing well with the simulated results. A sheet electron concentration of 4.1 × 10^{13} cm^{-2} with electron mobility of 564 cm^2/Vs and sheet resistance of 271 W/sq was achieved with a 15-nm-thick $Sc_{0.18}Al_{0.82}N$ barrier. These results demonstrate the potential applications of N-polar ScAlN in next-generation electronic devices.

SESSION E: Nanostructured Materials
Session Chairs: Matt Brubaker and Parsian Mohseni
Wednesday Morning, June 23, 2021

10:45 AM E01
Gallium Desorption from Selective Epitaxy Growth Mask Surfaces Determined by *In Situ* Reflectance Measurements Matt Brubaker, Alexana Roshko, Todd Harvey and Kris Bertness; National Institute of Standards and Technology, United States

Selective epitaxy of gallium nitride nanostructures enables the fabrication of engineered nanoscale optical and electrical devices. This process relies on re-evaporation of fluxes incident on the growth mask and is very sensitive to the substrate temperature, resulting in a process window that can be quite narrow. Transposing the selective epitaxy process between different substrate types presents challenges related to the heater-to-substrate thermal coupling and depends on transparency and emissivity variations between the substrates. In this work we examine the gallium desorption rate from silicon nitride growth masks using in-situ reflectance measurements as a means for determining the real surface temperature. This links the actual surface temperature to a physical process, thereby avoiding some of the challenges encountered with conventional optical measurements on substrates with complex buffer and mask layer stacks. Furthermore, having an accurate assessment of the Ga desorption rate provides a critical parameter required for growth process modeling. Reflectance measurements were obtained for a variety of substrates in a molecular beam epitaxy (MBE) growth system, using a red laser (635 nm) incident at 15° to the substrate plane. The incident beam intensity was modulated at 1 kHz and a manually adjustable filter was used to set the polarization. The reflected beam intensity was measured by a photodiode and lock-in detection was used to reject the steady-state blackbody radiation from the signal. The substrates were dosed with gallium from a calibrated effusion cell in order to correlate the reflectance change to the gallium layer thickness. After dosing, the reflectance signal was recorded as the gallium layer evaporated and was used to calculate the desorption rate. Measurements were obtained at various substrate temperatures (after a high-temperature surface refresh) in order to generate Arrhenius curves of the desorption process. These reflectance measurements were first validated for gallium desorbed from a Ga-polar GaN surface, for which there is existing published data from a variety of techniques. The temperature for this GaN-on-sapphire substrate was determined by band-edge thermometry and the activation energy for desorption derived from the reflectance measurements (~2.7 eV) was found to be in good agreement with literature values. This technique was then applied to a GaN-on-silicon selective area growth substrate with a silicon nitride growth mask. The surface temperature was estimated from a calibration based on blackbody radiation spectral measurements of a bare silicon wafer. The reflection measurements for this Si_3N_4-GaN-on-silicon wafer were also found to produce an activation energy consistent with literature values (~2.8 eV). The near-identical results from these two different substrate types suggests that Ga desorption is independent of the actual surface chemistry (which has been suggested by others for the gallium droplet growth regime) and likely is a consequence of the thick liquid gallium layers used in this study. As such, the Arrhenius fitting parameters were assumed valid across samples and were used to determine surface temperature offsets between substrates with and without independent temperature calibrations. As a demonstration, these reflectance measurements were applied to bulk GaN substrates to assess the efficacy of various back-surface coatings in enhancing heater-to-substrate thermal coupling.

11:00 AM E02
(Student) Growth and Characterization of Mixed-Dimensional InAs/MoS2 Heterostructures Alireza Abrand[1], Mohadeseh A. Baboli[1], Benjamin P. Huet[2], Zackary Santos[1], Pratik P. Dholabhai[1], Joan M. Redwing[2] and Parsian Mohseni[1,1]; [1]Rochester Institute of Technology, United States; [2]The Pennsylvania State University, United States

Epitaxial integration of III-V semiconductor nanostructures with two-dimensional (2D) materials enables tremendous freedom in the synthesis of widely tunable mixed-dimensional heterostructures. Such III-V/2D hybrid nanosystems give rise to otherwise inaccessible physical properties stemming from novel interlayer coupling effects and heterojunction carrier dynamics. They also provide opportunities for discovery of new crystal growth mechanisms. Direct integration of III-V compounds with foreign lattices, and in a manner that allows pristine interfaces to

be preserved, is very challenging by conventional epitaxy. However, dislocation-free and electronically clean interfaces can be realized via the van der Waals (vdW) epitaxial integration approach for III-V crystal growth on various monolayer nanomaterials. Of particular interest is the InAs/MoS_2 nanosystem, which provides a type-I heterojunction band alignment and tunable interlayer band structure that depends largely on lattice polarity and presence of vacancy defects at the heterointerface. Here, we present the self-assembly of InAs nanostructures via metalorganic chemical vapor deposition (MOCVD) on continuous MoS_2 monolayers on sapphire substrates. We show that MOCVD growth conditions dramatically influence the morphology and number density of InAs nanostructures grown on MoS_2. Whereas self-assembly of vertical nanowires is favored at a growth temperature 600 °C, triangular nanoplates with two common self-aligned in-plane orientations are observed at 750 °C. We compare growth of InAs on epitaxial MoS_2/sapphire to growth on bare sapphire and on MoS_2/oxide, as well as to growth on graphene/sapphire and graphene/oxide systems, in order to discern the role of remote epitaxy effects. We present a model for coincident sub-lattice registry between InAs and MoS_2 that describes their epitaxial arrangement. We investigate the interfacial atomic order at the InAs/MoS_2 heterojunction by transmission electron microscopy and we explore the optical properties of the mixed-dimensional heterostructures by photoluminescence and Raman spectroscopy. Finally, we describe the observed structural and optical properties based on first principles density functional theory calculations of the interfacial density of states. We highlight the benefits of such III-V/2D nanosystems for emerging device applications in flexible optoelectronics.

11:15 AM E03
Structural Symmetry Breaking and Fast Chemical Diffusion in the Lead-Cadmium Sulfide Cation Exchange System
Andrew Nelson[1], Shreyas Honrao[1,2], Richard Hennig[2,1] and Richard Robinson[1]; [1]Cornell University, United States; [2]University of Florida, United States

In the synthesis and utilization of complex nanostructured solids, precise control over their transformation by atomic transport, especially by diffusion, is necessary to realize reliable devices depending on these materials. Knowledge of the thermodynamics of the system components will explain why atomic migration and (de)mixing takes place, but experiments probing transformation kinetics are required to determine the mode through which these processes occur. The cation exchange of colloidal lead sulfide nanocrystals with cadmium to form core-shell nanostructures provides a useful test case for monitoring the evolution of semiconductor interfaces by the migration of cations to and from the CdS-PbS interface. Monitoring the reaction through in-situ x-ray diffraction, we show that the epitaxial relationship of CdS and PbS breaks the symmetry of the crystal, producing peak shifts without non-cubic distortions of the unit cells. Reaction kinetics, quantified by Bragg diffraction peak parameters, indicate cation exchange proceeds through three stages. First, a metastable rocksalt CdS shell forms by displacement of surface Pb ions with Cd. Next, the shell recrystallizes to the more stable zincblende phase. Further exchange, up to complete conversion of the particles, proceeds through diffusive transport of Cd and Pb ions across the completed shell. The interdiffusion coefficients, D, for cation diffusion in the shell have an activation energy of 160-180 kJ/mol, like those in bulk solids, indicating that point defect formation likely governs the exchange kinetics. The magnitude of D, however, is larger by a factor of 10^4 or more relative to values extrapolated from bulk data for diffusion of the slowest component (Cd in CdS). Fast interdiffusion in nanocrystals shows the distinction between chemical diffusion in a chemical potential gradient and equilibrium self-diffusion has not been fully appreciated: the sharp change in composition over a thin interface strongly affects the population of defects and thus the diffusivity of ions. These results advance the methodology for quantifying solid interface stability and migration at the nanoscale.

11:30 AM E04
(Student) Self-Assembly of Hybrid Nanomembranes via Reconfiguration of Amorphous Complex Oxides
Divya J. Prakash[1,1], Mengistie Debasu[1], Yajin Chen[2], Donald Savage[2], Chaiyapat Tangpatjaroen[2], Christoph F. Deneke[3], Angelo Malachias Da Souza[4], Adam D. Alfieri[2], Izabela Szlufarska[2], Paul G. Evans[2] and Francesca Cavallo[1,1]; [1]The University of New Mexico, United States; [2]University of Wisconsin–Madison, United States; [3]Universidade Estadual de Campinas, Brazil; [4]Universidade Federal de Minas Gerais, Brazil

This work shows that reconfiguration of amorphous complex oxides provides a readily controllable source of stress that can be leveraged in nanoscale assembly. The study focuses on the assembly of $SrTiO_3$/group IV semiconductor nanomembranes (NMs), but our synthesis process and conclusions are applicable beyond this specific materials combination. We demonstrate that amorphous $SrTiO_3$ layers deposited on Si/SiGe heterostructures on bulk Si are reconfigured at the atomic scale upon heating, exhibiting a change in volume of several percents and accompanying biaxial stress. The hybrid oxide/semiconductor NMs are fabricated by molecular beam epitaxy of the semiconductor bilayer on bulk Si at 500 °C followed by sputter deposition of $SrTiO_3$ at room temperature. Upon release from the substrate, NMs bend into scrolls with a few micrometer radii of curvature, consistent with the stress imparted in Si/SiGe through epitaxial growth. Heating a freestanding $SrTiO_3$/Si/SiGe NM to 600 °C leads to the formation of swiss rolls structures with a few hundred nanometers inner radii of curvature. Continuum mechanical modeling predicts the geometry of the hybrid oxide/semiconductor NM at various stages of the heat treatment, including increasing the tempearture from 20 to 600 °C, annealing at 600 °C, and cooling the structure back to room temperature. Analytical modeling shows that the measured radius of the curvature of the NM upon heating is consistent with the development of a large compressive biaxial stress during the reconfiguration of $SrTiO_3$. X-ray reflectivity, X-ray diffraction, and transmission electron microscopy probe changes in the structure of the $SrTiO_3$ layer that are consistent with densification of the amorphous $SrTiO_3$. Based on our experimental results and continuum mechanics modeling, we predict that a variety of complex oxides-based heterostructures can be obtained via reconfiguration-driven self-assembly of amorphous oxides, including $SrTiO_3$/Si and $SrTiO_3$/$LaAlO_3$. Our results have significant implications from a technology and a fundamental science standpoint. We have shown that complex oxides can be combined with different materials in a radial geometry and through scalable processes on large area semiconductor substrates. By altering the structure and composition of the as-grown NM one could obtain a wide palette of heterostructures. A broad palette of electronic band structures can be obtained by tailoring the curvature of the self-assembled NMs and the materials that the heterostructure comprises. Additionally, high strain gradients across the thickness of a bent oxide sheet will potentially generate significant flexoelectric effects. Strain and confinement in a curved geometry are also expected to create curvature-induced potentials and electrical transport features.
ACKNOWLEDGEMENT. This research was supported by the U.S. Department of Energy (DOE), Office of Science, Basic Energy Sciences (BES), under Award # DE-SC0020186 (electron microscopy, data analysis, and mechanical modeling) and by the National Science Foundation (NSF) under Award # DMR-1720415 (synthesis of the samples). This work was performed, in part, at the Center for Integrated Nanotechnologies, an Office of Science User Facility operated for the U.S. Department of Energy (DOE) Office of Science by Los Alamos National Laboratory (Contract 89233218CNA000001) and Sandia National Laboratories (Contract DE-NA-KE,0003525). X-ray diffraction

was performed at the XRD2 beamline within the Laboratorio Nacional de Luz Sincrotron.

11:45 AM E05
Graphene-Templated Growth of Surfactant-Free Gold Nanostructures for SERS Applications Wenbo Xin[1,2], Zuo Xiao[1] and Igor M De Rosa[2]; [1]Nanjing Tech University, China; [2]University of California, Los Angeles, United States

Gold nanocrystals with isotropic structures, e.g., nanoparticles with spherical shape, are thermodynamically favorable and stable. To obtain anisotropic Au nanocrystals in a wet chemistry synthesis, surfactants or capping agents are indispensable. However, ligands passivating surfaces of nanocrystals restrict their applications that require bare metal facets, such as catalysis and surface-enhanced Raman scattering (SERS) sensors. Removal of these surfactants costs tedious treatment processes and may lead to environmental issues as well. In the present work, we report a surfactant-free approach to synthesize a variety of anisotropic Au nanocrystals with the direction of graphene template under appropriate conditions. Sizes, dimensions and shapes of Au nanostructures are well controllable through this strategy, based on which graphene supported Au nanowires, nanoribbons, nanoplates, nanobelts, and nanoframes are successfully obtained, respectively, as shown in Figure 1. The role of graphene template playing in the syntheses is systematically investigated. We reveal that graphene serves as the reductant for gold precursor that reduces Au^{3+} to Au^0, the pre-step for the nucleation of gold clusters. Graphene provides the nucleation sites for gold clusters, which gradually leads to the epitaxial growth of Au nanobelts and nanoplates. For Au nanowires and Au nanoribbons, graphene template facilitates the coalescence of gold clusters by virtue of "oriented attachment", which is the unclassical mechanism of paramount importance in the formation of anisotropic structures. Finally, we demonstrate that graphene supported Au nanocrystals can be fabricated to a series of flexible SERS sensors, which shows greatly enhanced sensitivity to detect analytes at the ppm levels. For instance, A SERS substrate made of graphene/Au nanoframes can detect the analyte R6G at the concentration as low as 10^{-9} M (Figure 2). The mechanism for the sensitivity enhancement could be attributed to the homogenous distribution of Au nanoframes on the graphene support as well as the strong adsorption of analytes to the graphene substrate.

12:00 PM E06
(LATE NEWS, Student) Realization of High-Efficiency Green InGaN Nanowire Light-Emitting Diodes Using a Novel Dry-Etch Hardmask Removal Process Bryan Melanson, Matthew Hartensveld, Vijaygopal T. Vangipuram, Matthew Seitz and Jing Zhang; Rochester Institute of Technology, United States

Nanowire light-emitting diodes (LEDs) have long been investigated as alternatives to conventional mesa LEDs, as they allow for increased light extraction efficiency (LEE) and a reduction of the internal electric field strength in AlInGaN alloys. Nanowires also show potential for use as single pixels in micro-LED (µLED) displays and photonic crystal surface-emitting laser diodes (PCSELs). While epitaxially grown nanowires allow for higher material quality in the active region and reduction of the quantum confined Stark effect, they often suffer from uniformity and yield issues, and are difficult to fabricate into ordered, addressable arrays. Nanowires can alternatively be formed through dry-etching of epitaxially grown light emitting layers, taking advantage of processes and tools developed by the semiconductor industry. The general process for fabricating a nanowire array LED involves dry-etching of an n-i-p epitaxial stack to form high aspect ratio structures, followed by deposition of the n-contact metal, application of an interlayer dielectric, and deposition of the p-contact material. As most LEDs emitting in the visible range are based on the AlInGaN material system, an aggressive Cl_2 plasma must be used to perform the dry-etch. The poor selectivity of Cl_2 plasmas against conventional dry-etch hardmask materials such as photoresist and SiO_2 necessitates the use of a metal hardmask such as Ni, which is capable of withstanding the extended etch times required to form nanowires with heights greater than 1 µm. This thick Ni hardmask must be removed from the nanowires in order to maximize LEE. In devices which use self-masked n-metal deposition, in which the nanowires themselves act at the mask for deposition of a universal n-contact, wet etching of the Ni hardmask following deposition of the n-metal (which itself often contains Ni) is not possible, because the chemistries commonly used to etch Ni will also attack the other metals in the n-metal stack (Ti, Al, Ni, etc.). For this reason, an alternative method of removing the Ni hardmask is desired. In this work, we present a novel method for removing a metal hardmask from the tops of dry-etched GaN nanowires which does not involve metal etch chemistry, but instead relies upon an underlying "liftoff" layer to separate a thick metal "cap" from the tops of the nanowires. A 300 nm layer of SiO_2 is deposited on the wafer, followed by patterning of the Ni hardmask through a liftoff process. The Ni is then used to mask a CF_4/CHF_3 dry-etch of the underlying SiO_2, and a subsequent Cl_2/Ar dry-etch of the GaN, with ~200 nm of Ni capable of withstanding etch depths of more than 7 µm. The nanowires are then etched in a KOH solution to remove dry-etch damage and smooth the sidewalls of the nanowires. A universal n-metal (Ti/Al/Ni/Ag) contact, masked by the nanowires themselves, is then deposited and annealed. A buffered oxide etch (BOE) solution is then used to remove the SiO_2 layer, releasing the thick metal caps (Ni/Ti/Al/Ni/Ag) which are washed away in the etch solution. Polydimethylsiloxane (PDMS) is then coated over the "bare" nanowires and etch-back to expose the p-GaN nanowire tips. A transparent top contact, either ITO or thin (<20 nm) Ni is then deposited, making contact to the tops of the nanowires and linking many of them in series, allowing for electrical excitation of arbitrarily large arrays simultaneously. Using this process, we have fabricated high brightness arrays of 2.5 µm diameter electrically driven nanowires emitting at 550 nm with a linewidth of ~40 nm. Removal of the metal cap from the nanowires allows for increased LEE from extremely uniform arrays, while the use of a universal n-metal contact allows for decreased series resistance and more uniform emission intensity from larger arrays. This novel fabrication approach can allow for more efficient top-down fabricated light-emitting nanowire arrays, which are of interest for use in LEDs, µLED displays, and PCSELs.

SESSION F: Gallium Oxide Devices
Session Chairs: Marko Tadjer and Huili Grace Xing
Wednesday Morning, June 23, 2021

10:45 AM F01
Growth and Characterization of Deep Acceptor Mg-Doped/N-Type β-Ga_2O_3 Junctions Andreas Fiedler, Zixuan Feng, A F M Anhar Uddin Bhuiyan, Nidhin Kurian Kalarickal, Sushovan Dhara, Ashok Dheenan, Hongping Zhao and Siddharth Rajan; The Ohio State University, United States

Monoclinic gallium sesquioxide (β-Ga_2O_3) is deemed to be the future material for high power electronics and radio frequency device applications due to the large, estimated break down field of 8 MV/cm, a reasonable electron mobility of up to about 200 cm^2/Vs at room temperature, and the feasibility to dope it n-type over a wide range from 10^{14} to 10^{20} cm^{-3}. While acceptors in Gallium Oxide are expected to be relatively deep, there are still several possibilities for using acceptor-like impurities to create space-charge regions for improved performance and functionality devices such as rectifying diodes, transistors, and sensors. Among

the various acceptor-like defects, Mg is one of the deepest, and is predicted to have an energy level 1.1 eV above the valence band. In this work, we report on the growth and electrical characteristics of deep acceptor Mg-doped/n-type β-Ga_2O_3 based junctions. We investigate the electrostatics and current characteristics of these junctions, and the temporal response of the acceptor ionization. Our results indicate that Mg-doped layers can be used to create stable negative space charge regions for applications in future Gallium Oxide devices. The Mg-doped/n-type β-Ga_2O_3 based junctions were grown by MOCVD (Agnitron Agilis R&D oxide system) on (010) oriented Sn-doped conductive substrates at 700 °C. While the 500 nm thick n-type layer was similarly grown for all samples with a Si doping of $9x10^{17}cm^{-3}$, the 30 nm thick Mg-doped cap layer was doped with$7.6x10^{17}$ cm^{-3}, $1.24x10^{18}$ cm^{-3} and $1.42x10^{18}$ cm^{-3}, respectively (estimated). A Ti/Au (30/100 nm) metal stack was deposited on the whole back side of the substrate and annealed for 1 min at 470 °C (N2 ambient) to form ohmic contacts. Circular contacts with diameters ranging from 30 µm to 300 µm were defined by laser lithography on the front side. Pt Schottky diodes (30 nm) were deposited by electron beam evaporation. Capacitance voltage characteristics were used to infer the electrostatics and band line-up the structures. In the probed channel region (30 nm away from the interface) N_D-N_A is constant and matching the Si doping of $9x10^{17}$ cm^{-3}. The C-V curves, and the extracted carrier density profiles show that the negative space charge, depletion region width, and built-in voltage in the n-type region scale with the Mg doping, as expected. To investigate if the Mg-doped layers remain in a stable charge state, we carried out stress tests of the devices by applying voltages and measuring shifts in the capacitance-voltage profile. We do not see no change of charge state under reverse bias (25 V/15 min/3 MV/cm) and forward bias (5 V/5 min/200 A/cm2), showing that the Mg acceptor levels remain stable and do not change their ionization even under these stress conditions. This suggests that Mg doping can be used as fixed charges for electrostatic engineering in Gallium Oxide devices. I-V forward measurements reveal a rectifying diode behavior, with ideality factors of about 1.7. The on-resistance increases with higher Mg doping. For the lowest Mg-doped planar diodes ([Mg]=$7.6x10^{17}cm^{-3}$) a maximum parallel plate breakdown field of 3.7 MV/cm was achieved, with repeatable reverse characteristics. In summary, we have demonstrated the growth of Mg-doped cap layers enabling band engineering by pinning the fermi level. This can be applied for field management in rectifiers and sensors, and for the design of β-Ga_2O_3 based E-mode devices.

11:00 AM F02

(Student) MOVPE-Grown β-Ga_2O_3 High Current Density (130 mA/mm) MESFET with a Record Metal/Ga_2O_3 Specific Contact Resistance of 8.3×10^{-7} Ω.cm²

Arkka Bhattacharyya[1], Praneeth Ranga[1], Saurav Roy[1], Daniel Shoemaker[2], Yiwen Song[2], Sukwon Choi[2] and Sriram Krishnamoorthy[1]; [1]University of Utah, United States; [2]The Pennsylvania State University, United States

With the advantage of being able to grow β-Ga_2O_3 homoepitaxial films with high room-temperature electron mobility values that are close to the theoretical limit of ~ 200 cm^2/Vs, metalorganic vapor phase epitaxy (MOVPE) as an epitaxial growth technique has drawn a lot of attention for fabricating β-Ga_2O_3 lateral FETs with high current densities [1]. Using the selective area epitaxy approach, we demonstrate the realization of low resistance regrown source/drain (S/D) contacts in a fully MOVPE-grown β-Ga_2O_3 lateral MESFET for the first time. The fabricated devices show high current densities (~ 130 mA/mm) and a high ON/OFF ratio exceeding 10^{10}. The epitaxial structure consisting of a 500 nm thick lightly Si-doped ($n_s = 5.7\times10^{12}$ cm^{-2}) β-Ga_2O_3 channel was grown on a (010) Fe-doped semi-insulating Ga_2O_3 substrate (NCT Japan) at a temperature of 810°C using triethylgallium, O_2 and silane gases as precursors and Ar as the carrier gas, using an Agnitron Agilis MOVPE reactor. A selective area MOVPE regrowth process was developed to obtain low-resistance S/D ohmic contacts using a Ni/SiO_2 mask. From the cross-sectional SEM image, n^+-Ga_2O_3/channel interface was found to be very conformal with no cracks or crevices. The low-temperature (600°C) heavy (n^+) Si-doped MOVPE-regrown layers exhibit high conductivity with sheet resistance as low as 73Ω/■, a record metal/n^+- Ga_2O_3 contact resistance of 0.08 Ω.mm and a record specific contact resistivity of 8.3×10^{-7} Ω.cm². The fabricated MESFETs show a maximum drain-to-source current of 130 mA/mm, a high I_{ON}/I_{OFF} of $>10^{10}$ and a maximum power FOM of 25 MW/cm^2 was achieved without any field plates. Using a 2D Sentaurus TCAD simulation, the peak and average breakdown fields were estimated to be 7 MV/cm and 1.9 MV/cm, respectively, for a device with L_{GD} of 1.6 µm which showed a three terminal breakdown voltage of 267 V. Breakdown voltage increased to 768 V and the peak current reduced to 76 mA/mm for the device with L_{GD} of 20 µm. A high I_{ON}/I_{OFF} and subthreshold slope of 122 mV/dec was achieved possibly due to low-charge and high mobility in the MOVPE-grown channel along with excellent control of the parasitic charge at the substrate-epilayer interface. For these long channel devices, the absolute $I_{DS,MAX}$ values scaled linearly with W/L. The $I_{DS,MAX}$ values were limited due to self-heating in these devices evident from the reduction of I_{DS} at higher V_{DS} values. To estimate the channel temperature at which self-heating induced current droop occurs (V_{GS}=0 V, V_{DS}= 15 V, P=0.96W/mm), a three-dimensional (3D), finite element device thermal model was constructed [2]. At the current inflection point (P = 0.96 W/mm), the estimated channel temperature rise was ~ 310°C. Detailed analysis of the DC resistance components will be presented. This demonstration is very promising for the development of MOVPE-grown β-Ga_2O_3 high performance devices. Further improvement in device performance can be achieved by implementing field-management techniques (MOSFETs) and effective thermal management solutions.

Acknowledgement: This work was supported by II–VI foundation Block Gift Program. We also thank the Air Force Office of Scientific Research under Award No. FA9550-18-1-0507 (Program Manager: Dr. Ali Sayir) for financial support. Funding for Penn State was provided by the AFOSR Young Investigator Program (Grant No. FA9550-17-1-0141, Program Officers: Dr. Brett Pokines and Dr. Michael Kendra, also monitored by Dr. Kenneth Goretta) and NSF (CBET-1934482, Program Manager: Dr. Ying Sun)

References:

[1] A. Bhattacharyya *et al. Appl. Phys. Lett.* 117, 142102 (2020).
[2] B. Chatterjee *et al. Appl. Phys. Lett.* 117, 153501 (2020).

11:15 AM F03

(Student) Modulation-Doped β-$(Al_xGa_{1-x})_2O_3$/Ga_2O_3 HEMTs: Design Principles and Performance Optimization via TCAD

Dawei Wang and Houqiang Fu; Iowa State University of Science and Technology, United States

Recently, beta-phase gallium oxide (β-Ga_2O_3) has attracted significant research attention for high-power, high-voltage, and high-frequency applications due to its ultra-wide bandgap (~4.8 eV), high critical breakdown field of 8 MV/cm, and large Baliga's figure of merit (FOM). The research of Ga_2O_3 based high electron mobility transistors (HEMTs) are still in its infancy, mainly because the electron mobility of bulk Ga_2O_3 is relatively low. To address this issue, modulation doping scheme has been adopted. Delta-doped β-$(Al_xGa_{1-x})_2O_3$/Ga_2O_3 HEMTs have been experimentally demonstrated with high quality electron channel and high channel electron mobility (>500 cm^2V^{-1}). Delta doping regulates the electrical characteristics of β-$(Al_xGa_{1-x})_2O_3$/Ga_2O_3 HEMTs since it is responsible for the formation of two-dimensional electron gas (2DEG) in the channel. This means that delta doping is the key design parameter in Ga_2O_3 based high power HEMTs. However, the effects of delta doping on the device performance are still lacking comprehensive investigations. In this work, we explore the design and optimization of β-$(Al_xGa_{1-x})_2O_3$/

Ga_2O_3 delta-doped HEMTs via TCAD SILVACO simulation, which can serve as critical guidance for experimental realizations. To date, there are very few reports on the simulation of $(Al_xGa_{1-x})_2O_3/Ga_2O_3$ HEMTs, partly due to the immature status of Ga_2O_3 and $(Al_xGa_{1-x})_2O_3$ research and the lack of accurate material properties. In the simulation, we first used the experimental electrical characteristics of β-$(Al_xGa_{1-x})_2O_3/Ga_2O_3$ HEMT (such as their transfer and transconductance curves) to calibrate our model. Then a series of comprehensive study and optimized designs of delta doping in the HEMTs are carried out, including delta-doping concentration, delta-doping position, delta-doping width and multiple delta-doping channels. The simulated HEMT structure consisted of a Ga_2O_3 substrate, a 130 nm unintentionally doped (UID) Ga_2O_3 layer, and a 27 nm $(Al_xGa_{1-x})_2O_3$ layer, and two n^+-Ga_2O_3 contact regions for the source and drain. The delta-doping region was modeled by a thin n-$(Al_xGa_{1-x})_2O_3$ slab, which are positioned inside the $(Al_xGa_{1-x})_2O_3$ layer at 4 nm distance from the $(Al_xGa_{1-x})_2O_3/Ga_2O_3$ interface. With increasing delta-doping concentration, the transconductance and drain current of the devices increased significantly. When the delta-doping concentration was over 1e19 cm^{-3}, the device exhibited large leakage from the delta-doping region. This was because at significantly high doping, the conduction band at the delta doping position was lower than that of the channel. The position of the delta doping also played an important role. The largest breakdown voltage was obtained when the delta doping was the nearest to the $(Al_xGa_{1-x})_2O_3/Ga_2O_3$ interface. We also simulated the effect of delta doping diffusion across the interface on the HEMT Performance. This is a great concern during the device epitaxial growth and needed to be studied. The breakdown voltage decreased sharply when there was a portion of the delta-doping region diffusing into the Ga_2O_3 layer because the high donor concentration from the delta doping made it difficult to pinch off the channel, resulting in low breakdown voltages. In addition, the multiple delta-doping channels can also significantly impact device threshold voltage and breakdown voltages. In summary, we comprehensively studied the effects of delta doping on the performance of β-$(Al_xGa_{1-x})_2O_3/Ga_2O_3$ HEMTs. These results can provide critical references for the future development of high-performance Ga_2O_3 high-power and high-frequency electronics.

11:30 AM F04
(Student) Vertical Wide Bandgap β-Ga2O3/GaN p-n Heterojunction with Mesa Based Edge Termination Dinusha Herath Mudiyanselage and Houqiang Fu; Iowa State University of Science and Technology, United States

Newly emerged wide bandgap semiconductor (WBG) β-Ga_2O_3 has been extensively researched for power electronics, RF electronics and optoelectronics due to its large bandgap of 4.7- 4.9 eV and high breakdown field of ~ 8 MV/cm. Due to the absence of p-type Ga_2O_3, most of demonstrated β-Ga_2O_3 devices are unipolar devices such as high electron mobility transistors (HEMTs) and Schottky barrier diodes. To overcome this limitation, other p-type materials, such as GaN and NiO, have been investigated to produce Ga_2O_3 based p-n heterojunctions. Among these p-type materials, p-GaN has attracted especial interests since GaN is also a WBG semiconductor and has a clear crystallographic relationship to β-Ga_2O_3 for epitaxial growth. In addition, both β-Ga_2O_3 and GaN can be produced in the industrial standard tools, i.e., the metalorganic chemical vapor deposition (MOCVD). The growth of high-quality GaN on Ga_2O_3 by MOCVD has been recently reported. β-Ga_2O_3/GaN p-n heterojunction via mechanically exfoliation also showed decent rectifying behaviors. However, the breakdown capability of the β-Ga_2O_3 based p-n heterojunctions is still far from expectations due to the lack of effective edge terminations. Here we design and simulate mesa based edge terminations for the vertical β-Ga_2O_3/GaN p-n heterojunctions using SILVACO TCAD simulator. The model was first calibrated by the experimental results, including the conduction and valance band offsets of the heterojunction and electrical properties. The device structure consisted of n^+-Ga_2O_3 n-contact layer, 5 µm unintentionally doped (UID) β-Ga_2O_3 drift layer and 500 nm p-GaN layer. The ideal breakdown voltage (BV) of the heterojunction was 1.37 kV, while the BV of the reference device without effect mesa edge termination dropped dramatically to 300 V due to the electric field crowding at the device edge. Therefore, it is critical to design and optimize the mesa edge termination to improve the BV of the β-Ga_2O_3/GaN p-n heterojunctions. Three mesa edge termination structures were investigated in this work: beveled mesa, step mesa, and deeply-etched mesa. The beveled mesa angle θ is the key parameter in determining the device BV. When θ was varied from 15° to 90°, the highest BV of 1224 V was obtained for θ =15°. For the step mesa edge termination, the width (*W*), depth (*D*), and the number of steps define the mesa structure. It was found that the BV of the devices increased with increasing number of steps. The combination of (*W*, *D*) values of (0.5,0.5) and (0.5,1.0) and (1.0,1,0) was investigated, where all the values are in µm. The highest value was obtained for $W = 0.5\mu m$, $D = 1.0\mu m$ and the number of steps = 5. Smaller *W* and larger *D* led to better BV. The electric field distributions of devices with different mesa edge terminations were compared at –300V. Without effect mesa edge termination, the peak electric field at the junction edge was ~ 4.2 MV/cm. By incorporating the mesa edge termination techniques, the electric field crowding at the device edge was mitigated, and the peak electric fields were reduced to 1.8 MV/cm and 2.4 MV/cm for the beveled and step mesa edge terminations, respectively. For the deeply-etched mesa structure, it was found that a more uniform electric field distribution was observed when the mesa depth was increased from 0.5,1.0, 2.0, to 3.0 µm, where the peak electric fields were decreased from 2.1, 1.8 ,1.5 to 1.2 MV/cm, respectively. In summary, this work presents a comprehensive design and optimization of mesa edge terminations for the wide bandgap vertical β-Ga_2O_3/GaN p-n heterojunctions, which is first of its kind. Three mesa structures were explored, including beveled mesa, step mesa and deeply-etched mesa. It was found that these mesa edge terminations can alleviate the electric field crowding at the junction edge and increase the device BV. This work can provide critical guidance for the development of high-performance β-Ga_2O_3 based bipolar high voltage and high power devices.

11:45 AM F05
Temperature Dependent Current Stress of β-Ga_2O_3 Schottky Devices Rujun Sun[1], Arkka Bhattacharyya[1], Caixia Hou[2], Martin Allen[2], Sriram Krishnamoorthy[1] and Michael Scarpulla[1,1]; [1]The University of Utah, United States; [2]University of Canterbury, New Zealand

β-Ga_2O_3 is of high interest for high voltage and high-power DC and microwave applications. Point defects and extended structural defects in bulk crystal and epitaxy layer are likely responsible for poor device performance. The fundamental properties of instability under high reverse bias (device degradation mechanism) are still poorly understood. Here, changes of I-V and C-V curves of schottky diodes based on MOVPE films and UID crystals can be observed at relatively low temperature after a high current density (0.1 mA/cm^2) stress. About 1.6um-thick UID Ga_2O_3 epitaxial film were grown by MOVPE on (010)-oriented NCT Fe-doped substrate using triethyl gallium, diluted silane and oxygen precursors. UID crystals were grown by Czochralski method. The defect properties for the pristine and stressed devices will be investigated by deep level transient spectroscopy (DLTS).

12:00 PM F06

(LATE NEWS, Student) Electrical Properties of MOCVD-Grown AlSiO Gate Dielectric on (001) β-Ga_2O_3

Zhe Ashley Jian[1], Islam Sayed[2], Wenjian Liu[2], Subhajit Mohanty[1] and Elaheh Ahmadi[1]; [1]University of Michigan–Ann Arbor, United States; [2]University of California, Santa Barbara, United States

β-Ga_2O_3 has become a promising semiconductor for high power applications. High-quality dielectrics are crucial for enabling high performance β-Ga_2O_3 field-effect transistors (FETs) especially because achieving p-type doping does not seem feasible for this material system. The material properties of high-quality gate dielectric include high dielectric constant, negligible gate leakage, low density of interface and bulk traps, and large breakdown field. Recently, aluminum silicon oxide (AlSiO) has been proposed as a high-performance and reliable gate dielectric for GaN-based devices [1], [2]. Previous studies showed that the alloying of Al_2O_3 with silicon to form AlSiO has the potential to combine the merits of both SiO_2 and Al_2O_3 thus realizing low density of interface traps (D_{it}), high conduction/valence band offset and high breakdown strength [3], [4]. The promising results of AlSiO as a dielectric for GaN-based devices motivated us to expand its applications to Ga_2O_3. In this work, the interface and bulk properties of aluminum-silicon-oxide (AlSiO) dielectric grown by metal-organic chemical vapor deposition (MOCVD) on (001) β-Ga_2O_3 were investigated systematically using a deep UV-assisted capacitance-voltage methodology. The AlSiO dielectric, with a silicon composition of 40%, was grown by metal organic chemical vapor deposition (MOCVD) in a close coupled showerhead chamber. The AlSiO deposition temperature was 700 °C, and the TMAl, Si_2H_6, and O_2 flows were 3.2 µmol/min, 3.2 µmol/min, and 4.4 mmol/min, respectively. AlSiO with various thicknesses (10 nm, 20 nm, and 30 nm) were deposited on three different Ga_2O_3 samples treated by UV-ozone followed by an HF dip. This improved surface preparation with a combination of UV-ozone and wet chemical treatment reduced near-interface traps resulting in a negligible hysteresis. The fast trap density was extracted to be 2.18×10^{11} cm^{-2}, and the slow trap density excluding the contribution from fast traps was calculated to be 2.73×10^{11} cm^{-2}. A net positive interface fixed charge of 1.56×10^{12} cm^{-2} was measured. The D_{it} was extracted accurately by accounting for dielectric bulk traps employing deep UV-assisted C-V method and physical models. An average interface state density of 6.63×10^{11} cm^{-2} eV^{-1} and AlSiO bulk trap density of 4.65×10^{17} cm^{-3} eV^{-1} were quantified, which is half of that for Al_2O_3 deposited by atomic layer deposition (ALD). In addition, a high dielectric breakdown field of ~7.8 MV/cm and more effective suppression of gate leakage were achieved on these devices compared with ALD-Al_2O_3 on similar metal-oxide-semiconductor (MOS) structures. The negligible hysteresis, lower interfacial trap density, low leakage current and high breakdown electric field achieved on AlSiO/Ga_2O_3 MOSCAPs reveals MOCVD AlSiO as a promising gate dielectric for high-performance Ga_2O_3 devices.

[1] S. H. Chan et al., Jpn. J. Appl. Phys., vol. 55, no. 2, p. 021501, Feb. 2016. [2] D. Kikuta et al., J. Vac. Sci. Technol., vol. 35, no. 1, p. 01B122, Jan. 2017. [3] C. Gupta, et al., IEEE Electron Device Lett., vol. 38, no. 11, pp. 1575–1578, Nov. 2017. [4] I. Sayed et al., Appl. Phys. Lett., vol. 115, no. 17, p. 172104, Oct. 2019.

SESSION G: Defects and Doping
Session Chairs: Lincoln Lauhon and Burcu Ozden
Wednesday Afternoon, June 23, 2021

1:15 PM G01
Spatial Defects Nanoengineering for Bipolar Conductivity in MoS_2 Annalisa Calò[1,2]; [1]Universidad Barcelona, Spain; [2]IBEC, Spain

Two-dimensional transition metal dichalcogenides show great potential as a new class of atomically thin semiconductors for electronics and optoelectronics. Understanding the atomistic origin of defects in these materials and their impact on the electronic properties, as well as finding viable ways to dope them is matter of intense scientific and technological interest. In particular, controlling defects could be envisioned as a strategy for the design of ad-hoc electronic and optoelectronic properties. Here, we demonstrate a new integration of thermochemical scanning probe lithography (tc-SPL) with a flow-through reactive gas cell to achieve a nanoscale control of the local thermal activation of defects in monolayer MoS_2. The tc-SPL activated nanopatterns can present either p- or n-type doping on demand, depending on the used gasses, allowing the realization of field effect transistors, and p-n junctions with precise sub-mm spatial control and a rectification ratio over 10^4. Doping and defects formation mechanisms are elucidated at the molecular level by means of X-Ray photoelectron spectroscopy, scanning transmission electron microscopy, and density functional theory. The p-type doping of locally heated MoS_2 in HCl/H_2O atmosphere is found to be related to the rearrangement of sulfur atoms and the formation of new protruding covalent S-S bonds on the surface, which produce a band structure with p-character. Alternatively, local heating MoS_2 in N_2 produces n-character.

1:30 PM G02
An Alternative Way to Tune the Defects in a Single Layer MoS_2 Burcu Ozden; The Pennsylvania State University, Abington, United States

Two-dimensional materials (2DMs) have attracted considerable attention for space applications due to potential use as a replacement of traditional semiconductors for next-generation electronic devices and circuits. Among these materials, molybdenum disulfide (MoS_2) is a promising candidate due to its attractive semiconducting properties, including high mobility, strong light emission and remarkable mechanical properties. In high radiation environments, radiations may damage MoS_2 layers by breaking atomic bonds and ionizing atoms and end up creating defects. The performance and functionalities of these devices strongly depend on the quality and defect morphology of MoS_2 layers. Previous studies has already the address the question of how the defects alters the properties of MoS_2. However there are still missing links in connecting the presence of different types of radiation induced defects to the optical, morphological and chemical properties of the MoS_2. In this study, up to our knowledge for the first time we used different energy (150 keV) and (590keV) proton beam radiation with the fluence of 1×10^{12} protons/cm^2 rather than different fluences to modulate the defects in monolayer MoS_2. . We found that lower proton energy irradiations exhibited signs of higher damages to monolayer MoS_2. Our AFM and SEM results demonstrated that by varying the proton energy two distinct morphological changes can be fabricated in single layers of MoS_2 by individual ions. AC-HSTEM studies confirmed that selective proton energies create different types of defects. We were able to tune the defect concentrations in MoS_2 by varying the energy of proton irradiation as shown by XPS and PL measurements. Observed intensity changes in PL spectra is considered to be negligible relative to conventional semiconductor materials. Raman spectroscopy data unveiled no major structural changes indicating its substantial tolerance to low fluence proton irradiation. The relatively low damage resulting from these low radiation energies can be attributed mainly to the ions' electronic energy loss and atomically thin nature of MoS_2.This work inspires future research of defect engineering in tailoring the chemical, morphological and optical properties of MoS_2 as well as other 2D materials to establish more stable and reliable optoelectronic devices for space, defense and energy applications.

1:45 PM G03
(Student) Electron Redistribution at Monovacancy in Graphene Claire G. Andreasen, Zubaer Hossain and Julia Hatoum; University of Delaware, United States

Vacancy defects are unavoidable in 2D materials due to the challenges involved in fabricating defect-free lattice from experimental methods. While defects are known to degrade the mechanical properties of a lattice, they offer unique opportunities to tailor the electronic and thermal properties by controlling the mean free path of electrons and phonons. It is therefore important to develop a fundamental understanding of the role of defects in modulating the local electronic character of a lattice. Nevertheless, the understanding of defect-induced alteration of electronic properties (the electronic states for example) remains less understood, particularly under finite deformation. Although researchers have investigated the mechanical and electronic properties of pristine graphene under stress, there is little research on the chirality effects on electron distribution at defective sites in 2D materials under applied stress. In this work, we use the density functional theory simulations and the Mulliken charge population analysis to investigate the electronic behavior of an isolated defect in graphene under the uniaxial loading condition for five different chiralities of the lattice. We analyze how chirality and intensity of loading affect the mechanical properties, bond length and bond angle change, charge distributions, the density of states, and the partial density of states surrounding the vacancy. Our results show that there is a uniform pattern for bond length redistribution as well as electron redistribution at all orientation angles and that such bond and electron redistributions are directly correlated. During all simulations, we observe a bond reconstruction at the defective site at higher deformation. In terms of the orientation angle, we demonstrate that increased orientation angle yields changes in the strength, toughness, stiffness, bond distributions, and electronics surrounding a mono vacancy. We find that differing orientation angles result in different failure processes and speeds. Additionally, the redistribution at the defective site is chirality-dependent, and there is a significant localization of electronic states at the defective site. The pattern of density of states is deformation-dependent. This talk will present a comprehensive view on the specific effects of electron redistribution on mechanical and electronic characteristics of the defective lattice.

2:00 PM G04
(Student) Chemical Consequence of Electron Redistribution in Graphene with Grain-Boundary Julia T. Hatoum, Claire G. Andreasen and Zubaer Hossain; University of Delaware, United States

In recent years, graphene has captured wide attention among engineers and researchers for its unique electronic, thermal, chemical, and mechanical properties, which could revolutionize a number of application areas including electronics, nanotechnology, drug delivery, sensors, and catalysis. Since discovery, extensive research has been conducted theoretically, experimentally, and computationally to investigate the behavior of pristine graphene under no strain conditions. With the goal of applications in mind, it is critical to develop a fundamental understanding of the properties of defective graphene under

deformed or strained conditions. While line-defects (such as grain boundary) within the graphene lattice are known to degrade its mechanical properties, they can serve as an important source for making the graphene layer function as a chemically reactive 2D material which may be unattainable otherwise. Under defect-free conditions, an ideal and infinite graphene lattice can be deemed non-polar, due to its symmetry preservation across the sheet, which can prevent any measurable interaction with external molecules that may come in contact with. In this work, using density functional theory simulations, we investigate the energetics of an isolated H_2O molecule at a grain-boundary formed between armchair and zigzag graphene sheets. By placing the molecule at different heights from the graphene lattice, we calculate the total groundstate energy of the system. Our findings suggest that if the initial placement of the molecule is parallel to the lattice within the van der Waals interaction distance, the molecule undergoes a reorientation, and the O atom faces the graphene lattice. On the other hand, if the initial position of the molecule is parallel but closer to the graphene lattice, the H atoms become more reactive and they face toward the graphene lattice. We considered six different sites on the hexagon and found similar behavior. An electronic structure analysis suggests that the electron redistribution at the grain boundary affects the behavior of the molecule. Also, due to a separation-distance dependent distinct chemical affinities between the C-O atom vs. C-H atom pairs, the groundstate interaction is strongly affected by the initial position of the molecule. The results are expected to have important implications to our understanding of strain-chemistry of defective graphene. This talk will present the analysis of the results from an electronic structure perspective.

2:15 PM G05
(LATE NEWS, Student) Improvements in InAlBiAs Morphology and Prospects of InAlBiAs-Based Photon Upconverter James Bork, Wilder Acuña González, Matthew Doty and Joshua Zide; University of Delaware, United States

The dilute bismuthides are highly-mismatched alloys in which III-V semiconductors contain bismuth. The large difference in electronegativity and size between bismuth and traditional III-V elements provides bismuthides with significant tunability of bandgap, band alignment, lattice constant.[1] This makes bismuthides useful for infrared lasers, photodetectors, solar cells, and other (opto)electronic devices.[2,3,4] However, the same mismatch that enables their tunability makes dilute bismuthides challenging to grow with good uniformity, high interface quality, and relatively large bismuth incorporation.[5] This obstacle necessitates the systematic investigation of bismuthide growth conditions. The InP-based InAlBiAs is of particular interest for improving solar cell efficiency through photon upconversion.[4,6] We present on recent improvements in morphology of InAlBiAs and on approaches to bismuth incorporation. To date, there has been little reported on growth morphology and resulting electrical properties.[7] Through systematic exploration of the V/III and Bi/As flux ratios used during growth, we have improved InAlBiAs morphology and increased the maximum bismuth incorporation to 4% with a n-type background doping of $3x10^{13}$ cm^{-3}. By varying the growth parameters near the stoichiometric point, we have identified several growth regimes and their impacts on morphology, including regions of droplet-free, group-V, and group-III droplets. Beyond morphology improvements, we are also actively engineering the use of these (and related) materials in a nanostructure for designer photon upconversion.
[1] *Crystals.*17, 7, 63 (2017) [2] *Semicond. Sci. Technol.* 27, 094011 (2012) [3] *Appl. Phys. Lett.* 88, 201112 (2006) [4] *Sol. Ener. Mat. and Sol. Cells.* 155, 446-453 (2016) [5] *Jour. of Appl. Phy.* 120, 125310 (2016) [6] *Jour. of Photovol.* 6, 1183-1190 (2016) [7] *Jour. of Appl. Phy.* 126, 095704 (2019)

2:30 PM BREAK

3:00 PM G06
(Student) Atomic Scale Investigation of Aluminum Incorporation, Defects and Phase Stability in β-(AlxGa1-x)2O3 Films Hsien-Lien Huang, Jared Johnson, A F M Anhar Uddin Bhuiyan, Zixuan Feng, Nidhin Kurian Kalarickal, Siddharth Rajan, Hongping Zhao and Jinwoo Hwang; The Ohio State University, United States

Beta-gallium oxide (β-Ga_2O_3) has emerged as an excellent candidate for transparent conducting oxides (TCO) applications such as ultraviolet photodetectors and optoelectronics due to its high electrical conductivity and transparency. To fulfill the extensive potential as an electronic material, β-Ga_2O_3 can be alloyed with Al_2O_3 for the tunability of a large bandgap up to 8.8 eV and modifiable photoresponse spectral range. The crystal structure of ground state Al_2O_3 is corundum phase (a), which is extensively different from the monoclinic phase of ground state Ga_2O_3. Density functional theory (DFT) calculations have denoted the monoclinic phase of $(Al_xGa_{1-x})_2O_3$ is as an energetically preferred structure for up to 71% Al incorporation [1], despite the structural variations between these two materials. However, previous studies on the growth of $(Al_xGa_{1-x})_2O_3$ heterostructures with high Al composition indicated impaired film quality or phase transformations [2], indicating the challenges in the controlling point and extended defects and achieving the theoretical maximum Al content while maintaining the monoclinic phase. These limitations have demonstrated the demand for direct characterization of Al incorporation and defects in beta-$(Al_xGa_{1-x})_2O_3$ thin films. In this report, we investigated the atomic structure and defects in beta-$(Al_xGa_{1-x})_2O_3$ thin films using scanning transmission electron microscopy (STEM). Our quantitative STEM analysis for beta-$(Al_xGa_{1-x})_2O_3$ films grown by molecular beam epitaxy (MBE) and metal organic chemic vapor deposition (MOCVD) revealed two significant pieces of information for atomic-scale origins of growth characteristics and properties of the heterostructures. Our characterization indicated that 54% of the incorporated Al occupied the octahedrally coordinated Ga_2 site, suggesting the non-equilibrium growth conditions lead to a higher energy structure. DFT calculations have shown that Al can be incorporated on the less thermally favorable tetrahedral Ga_1 site due to its occupation in particular configurations on the surface and kinetic limitations. On the other hand, the formation of a planar defect perpendicular to the growth direction associated with a larger Al concentration corresponded to a local inclusion of the gamma phase. We have identified the local Al content reaches a critical value of about 50%, which could destabilize the monoclinic phase of $(Al_xGa_{1-x})_2O_3$ films. DFT calculations have demonstrated these planar defects are thermally stable at higher Al compositions, and its formation reduces the in-plane stress of tensile-strained films. The projection of cation columns identically match with the recently observed divacancy-interstitial complex structures [3]. In summary, our STEM research offers essential atomic scale insights on exact control of impurity incorporation for semiconductor bandgap engineering, and eventually provides guidance to the future epitaxial growth of $(Al_xGa_{1-x})_2O_3$ for high-performance power electronics applications. We acknowledge support by the Department of Defense, Air Force Office of Scientific Research GAME MURI Program (Grant No. FA9550-18-1-0479). [1] H. Peelaers, J. B. Varley, J. S. Speck, and C. G. Van De Walle, *Structural and Electronic Properties of Ga2O3-Al2O3 Alloys*, Appl. Phys. Lett. **112**, 242101 (2018).
[2] A. F. M. A. U. Bhuiyan, Z. Feng, J. M. Johnson, H. L. Huang, J. Sarker, M. Zhu, M. R. Karim, B. Mazumder, J. Hwang, and H. Zhao, *Phase Transformation in MOCVD Growth of (AlxGa1-x)2O3 Thin Films*, APL Mater. **8**, 031104 (2020).
[3] J. M. Johnson, Z. Chen, J. B. Varley, C. M. Jackson, E. Farzana, Z. Zhang, A. R. Arehart, H. L. Huang, A. Genc, S. A. Ringel, C. G. Van De Walle, D. A. Muller, and J. Hwang, *Unusual Formation of Point-Defect Complexes in the Ultrawide-Band-Gap Semiconductor β-Ga2 O3*, Phys. Rev. X **9**, 041027 (2019).

3:15 PM G07
(Student) Direct Evidence of Ge Becoming a Deep Donor Instead of a DX- in Al Rich AlGaN Pegah Bagheri[1], Pramod Reddy[2], Seiji Mita[2], Dennis E. Szymanski[1], Ji Hyun Kim[1], Yan Guan[1], Dolar Khachariya[1], Spyridon Pavlidis[1], Ronny Kirste[2], Ramón Collazo[1] and Zlatko Sitar[1,2]; [1]North Carolina State University, United States; [2]Adroit Materials, United States

Controllable n-type doping in AlGaN and AlN is crucial for applications in electronics, optoelectronics, and power electronics. Si and recently Ge have been utilized as n-type dopants in $Al_xGa_{1-x}N$ with low ionization energy for x<0.8 and x<0.5, respectively.[1,2] However, the transition of the Si and Ge shallow donors to deep states occurs at x>0.8 and x>0.5, presenting challenges for novel applications employing Al rich AlGaN and AlN. While such a transition was previously observed in the AlGaAs system, it was confirmed to be an acceptor type DX^{-1}. However, no such direct proof of the Si and Ge charge states in Al rich AlGaN and AlN exists. In this work we present direct evidence of single electron occupancy in the Ge deep state in $Al_xGa_{1-x}N$ (x>0.5) i.e., Ge transitions to a deep neutral donor. Co-doping with the shallow donor Si (at x < 0.8) was used as a source of free electrons in Ge doped AlGaN grown via MOCVD to follow on the charge state of Ge. The measured carrier concentration (n) in Al rich AlGaN shows whether Ge is a shallow donor (n~[Si]+[Ge]), neutral deep donor (n~[Si]) or a compensating acceptor type DX^{-1} (n~[Si]-[Ge])). Temperature dependent carrier concentration measurements suggested an increase in the ionization energy of Ge: AlGaN with increase in Al content and a sudden drop in the carrier concentration was shown to occur at x>0.5 showing that Ge transitions to a deep state.[1] Si remained a shallow donor with low ionization energy up to x~0.8. Therefore, both dopants are expected to be shallow donors in $Al_{0.4}Ga_{0.6}N$ forming a d^+ state. However, possible electron compensation in Si and Ge codoped $Al_{0.65}Ga_{0.35}N$ where Ge transitions into a deep state, would directly show the charge sate of the deep state Ge, either D^0 or DX^{-1}. Carrier concentration measurements versus Al content under constant Si and Ge concentrations of 1×10^{19} cm^{-3} and 8×10^{18} cm^{-3}, respectively, were realized at RT and 600°C. Negligible compensation and a temperature independent carrier concentration are observed in $Al_{0.4}Ga_{0.6}N$ were both Ge and Si are expected to be in their shallow states. Interestingly, a reduction in carrier concentration at x~0.65 corresponding only to the Ge concentration was observed, indicating that Ge is not providing free electrons nor compensating the free electrons provided by Si. This is the signature of a deep donor having a higher ionization energy and not of an acceptor state. At higher temperatures, the ionization of the deep donor Ge provides higher carrier concentrations as expected for such a donor. Contrary to the formation of a stable DX^{-1}, which is expected to pin the Fermi level at the (-/+) thermodynamic transition[3], transition to a deep donor allows for the possibility of highly conducting AlN and Al rich AlGaN by degenerately doping the system. Hence, this work cast light on the true nature of donor related deep states in nitrides, further opening pathways for doping engineering and achievement of high conductivity in Al rich AlGaN and AlN.

1. Bagheri, P. *et al.* The nature of the DX state in Ge-doped AlGaN. *Appl. Phys. Lett.* **116**, 222102 (2020).
2. Collazo, R. *et al.* Progress on n-type doping of AlGaN alloys on AlN single crystal substrates for UV optoelectronic applications. *Phys. Status Solidi C* **8**, 2031–2033 (2011).
3. Gordon, L., Lyons, J. L., Janotti, A. & Van de Walle, C. G. Hybrid functional calculations of D X centers in AlN and GaN. *Phys. Rev. B* **89**, 085204 (2014).

3:30 PM G08
(Student) Si Dopants Enable Catalyst-Free n-Type GaAs Nanowire Growth by Modifying Facet Energies Chunyi Huang[1], Daniel Ruhstorfer[2], Gregor Koblmüller[2] and Lincoln Lauhon[1]; [1]Northwestern University, United States; [2]Technical University of Munich, Germany

Control over dopant concentration and distribution is essential to engineering nanowire-based devices. However, controllable n-type doping has remained challenging for GaAs, which is the foundation for many important III-V heterostructures. In particular, silicon behaves as a p-type dopant in GaAs nanowires grown by a vapor-liquid-solid (VLS) process in molecular beam epitaxy (MBE) conditions. Recently, it was shown that Si can act as a donor when incorporated in a catalyst free vapor-solid (VS) growth process,[1] highlighting the importance of understanding the growth and dopant incorporation mechanisms to controlling conductivity and carrier type. Here we present evidence that Si stabilizes the nanowire facets necessary for nanowire elongation, leading to uniform doping in a core region and enhanced doping at the nanowire surface. The growth conditions used here produce crystalline clusters of GaAs on Si (111) substrates in the absence of a Si flux. The introduction of Si leads to a high yield of uniform vertical nanowires (Figure 1(b)). We used atom probe tomography (APT) to measure the Si distribution in three dimensions and resolve variations in doping across the diameter of the nanowire. The reconstructions in Figure 2(a) and Figure 3(a) show a portion of the GaAs nanowire and the AlGaAs passivation layer (the entire diameter is not within the field of view). The dopant concentration increases from the nanowire center to the edge and peaks near the interface between GaAs core and AlGaAs shell (Figure 2(b)), indicating that different incorporation rates may be associated with distinct facets whose prevalence is influenced by the Si dopant itself. Additionally, Si-enriched regions and clusters appear at the intersection of {110} facets of some nanowires (Figure 3(b)), which maybe be linked to variations in surface faceting. The above observations suggest that Si alters the surface energy of GaAs and stabilizes the facets that promote nanowire growth via preferential incorporation. Si has previously been observed to induce twin-defect mediated growth in GaAs,[2] which may also be related to modification of surface energies. Surface etching to remove Si enriched layers provides a pathway to uniformly doped n-type GaAs nanowires that are free of catalyst impurities.

References:
[1] Ruhstorfer, D., *et al.* Demonstration of n-type behavior in catalyst-free Si-doped GaAs nanowires grown by molecular beam epitaxy. *Applied Physics Letters,* **2020,** *116,* 052101.
[2] Keitaro Ikejiri, *et al*, Growth characteristics of GaAs nanowires obtained by selective area metal-organic vapor-phase epitaxy. *Nanotechnology,* **2008,** *19,* 265604.

3:45 PM G09
(Student) Crystallographic and Defect Characterization of PVT-Grown ZnSe Under Different Growth Configurations Qianyu Cheng, Zeyu Chen, Balaji Raghothamachar and Michael Dudley; Stony Brook University, The State University of New York, United States

Zinc Selenide (ZnSe) is a prominent II-VI semiconductor known for its effective utilization for electronic and optoelectronic devices such as blue light-emitting diodes [1], lasers [2], blue/ultraviolet-light-sensitive photodetectors [3], solar cells [4], and thin film transistors [5]. Its excellent performance on various applications is based on the unique properties of ZnSe, including wide bandgap (2.68 eV at 300K), high refractive index, good thermal shock resistance ($5.3 W/m^{1/2}$), low optical absorption in the visible and infrared spectral region, and intense edge luminescence in the short-wavelength spectral region [6, 7]. In order to overcome limitations and continuously fulfill the requirement of modern device applications, understanding the crystallographic

structure and defects of ZnSe crystal grown under different conditions become crucial. In this study, the crystalline quality and defect structures in physical vapor transport (PVT) grown ZnSe and Fe-doped ZnSe boules are characterized by adopting synchrotron white beam X-ray topography (SWBXT) in conjunction with optical microscopy and high-resolution triple X-ray diffraction (HRTXD). The effect of seeding condition and gravity vector with respect to growth geometry on crystal quality is investigated. The impact of hydrofluoride (HF) acid etching pretreatment of growth ampoule on crystal quality improvement is verified. The presence of grains and the occurrence of twinning is revealed and analyzed. This study can provide a clear understanding of factors that influence the ZnSe crystal quality during the growth process, which contributes to pursuing crystal quality enhancement.

References:
[1]: Robinson, R.J. and Z.K. Kun, *p-n junction zinc sulfo-selenide and zinc selenide light-emitting diodes.* Applied Physics Letters, 1975. **27**(2): p. 74-76.
[2]: Macdonald, J.R., et al., *Compact mid-infrared Cr:ZnSe channel waveguide laser.* Applied Physics Letters, 2013. **102**(16): p. 161110.
[3]: Fang, X., et al., *High-Performance Blue/Ultraviolet-Light-Sensitive ZnSe-Nanobelt Photodetectors.* Advanced Materials, 2009. **21**(48): p. 5016-5021.
[4] Huang, F., et al., *High Efficiency CdS/CdSe Quantum Dot Sensitized Solar Cells with Two ZnSe Layers.* ACS Applied Materials & Interfaces, 2016. **8**(50): p. 34482-34489.
[5]: Chiu, M.-Y., et al., *An optical programming/electrical erasing memory device: Organic thin film transistors incorporating core/shell CdSe@ZnSe quantum dots and poly(3-hexylthiophene).* Organic Electronics, 2009. **10**(5): p. 769-774.
[6]: Sushkevich, K., et al., *Photoluminescence of ZnSe samples doped with antimony and iodine.* Physica B: Condensed Matter, 2021. **602**: p. 412466.
[7]: Ou, K., et al., *Investigation on annealing temperature-dependent optical properties of electron beam evaporated ZnSe thin films.* Thin Solid Films, 2019. **669**: p. 247-252.

SESSION H: Low-Dimensional Structures II
Session Chairs: Paul Simmonds and Daniel Wasserman
Wednesday Afternoon, June 23, 2021

1:15 PM H01
Surface Chemistry Modifies Band Edge Structure of Colloidal Quantum Wells Benjamin Diroll; Argonne National Laboratory, United States

Similar to epitaxial quantum wells, colloidal quantum wells display electron intersubband transitions when photoexcited or electrochemically charged. Compared to epitaxial quantum wells, the strong confinement effect of thin, monodisperse colloidal quantum wells results in narrow intersubband transitions which reach high energies spanning the near-infrared spectral range. The composition of surface ligand chemistry subtly tunes the strain of the colloidal quantum wells to generate intersubband transitions over nearly continuously tunable energies. The divergent behavior of the band gap energy and intersubband transition energy implicates a substantial role of biaxial (in-plane) strain on the valence band structure. Multiple pump transient spectroscopy was furthermore employed to examine the lifetime of intersubband transitions, which is critical to their implementation in quantum cascade lasers or infrared detectors. In all cases, including core/shell samples, the lifetime of intersubband transitions is limited by surface or LO phonons to 1 ps or less, much shorter than comparable intraband transitions in quantum dots.

1:30 PM H02
(Student) *Ab Initio* Studies of the Optical Properties of Lead Chalcogenide Nanocrystals Olivia Pavlic; NSWC Crane/WVU, United States

Lead chalcogenide (PbX, X = S, Se, Te) colloidal quantum dots (CQDs) support rich optoelectronic phenomena, offering an attractive platform for advanced optoelectronics based on low-dimensional materials. Experimental results have shown a change in CQD shape and optical characteristics as the CQDs grow in size. This work aims at understanding the effect of size, shape, and composition on the sensitive optical behavior in this particular class of CQDs using density functional theory (DFT) code Octopus. Resonant optical transitions and energy relaxation pathways are elucidated, with emphasis towards activity in the 3-5 µm mid-wave infrared (MWIR) spectrum. Optoelectronic results are presented for the bulk material, isolated slabs representative of specific crystalline facets, and for the octahedral through cubic morphologies that evolve with CQD growth.

1:45 PM H03
(Student) A Study of the Optimal Synthesis Conditions in Solution Method for Bismuth Sulpho Iodide Nanorods Maia Mombru Frutos, Carolina Grosso, Heinkel Bentos Pereira, Alvaro Olivera, Laura Fornaro and Ivana Aguiar; Universidad de la República, Uruguay

BiSI is a ternary semiconductor which has gained attention lately due to its suitable properties as an absorber material for photovoltaics. With a band gap of 1.57 eV, and comprising elements which are not in a critical supply state, BiSI is a promising candidate not only for photovoltaics applications but also in ionizing radiation detection and others. However, given its ternary nature, the synthesis of this compound presents several challenges, the most important being the competition of other iodided compounds such as BiOI or BiI_3. This work presents the optimization of the synthesis of BiSI nanorods (NR) in a solution method, dispensing the equipment needed for a solvothermal synthesis, the most popular reported when dealing with BiSI nanostructures. Bi_2S_3 nanoflowers (NF) and powdered I_2 as precursors provide the elements Bi and S, and I, respectively, limiting the by-products generated during the reaction. As for the solvent, mono ethylene glycol (MEG) proved to be the best option for a pure yield of BiSI NR. This signifies not only the use of a green solvent, but the avoidance of complicated media such as H_2S currents. Different conditions were tested to determine the best route for the production of nanorods, such as the morphology of the Bi_2S_3 precursor, reaction time, temperature, as well as the comparison with a solvothermal system. The best synthesis conditions to obtain BiSI NR with the least energy expenditure proved to be in solution method using Bi_2S_3 NF (3 um in diameter) for a minimum of 1 h of reaction at 180ºC. XRD characterization followed by Rietveld refinement showed that while for a solvothermal synthesis method 10 h are at least necessary for a complete conversion of Bi_2S_3 to BiSI, in solution this time shortens to 1 h. An important factor is the greater control of temperature achieved by using a hot plate instead of a solvothermal reactor. Furthermore, it was noted that increasing the temperature to 220 ºC only produced BiSI up to 3 h. After that, competition with BiI_3 started to appear. In these cases the size distribution of BiSI NR was wider than for 180 ºC, with an average width of 390 nm, as opposed to 340 nm. When the Bi_2S_3 NF precursor was changed to Bi_2S_3 smaller nanoparticles (10 nm in diameter), the synthesis was incomplete, with remaining Bi_2S_3, regardless of the reaction time (up to 20 h). This was attributed to the fact that in order to obtain such small Bi_2S_3 nanoparticles, oleylamine was used as a capping agent and it would obstruct the reaction. Finally, when amorphous Bi_2S_3 was used as the precursor, a mixture of BiSI and BiOI was obtained. Furthermore, the function of the iodine source was also studied, determining that with I_2 the species present in the solution are I_2, I^-, and I_3^-. Not

only I_2 needs to be added in excess to complete the transformation to BiSI, but when only the species I^- was tested, in the form of NH_4I, the reaction did not take place at all. In addition to this, spectroscopic and Raman microscopy data was gathered to assess the nature of iodine before and after the reaction. This data allowed us to propose a BiSI formation mechanism which involves a synergistic effect of the three elements at play: MEG, Bi_2S_3, and I_2. While Bi_2S_3 is virtually insoluble in polar solvents, the action of I_2 in excess allows for a partial dissolution of this compound. In turn, the iodine, which is reduced to I^- form, attacks the Bi_2S_3 crystal structure, which comprises double chained structures, analogous to BiSI's. This prompts the growth of BiSI NR from the NF, that once they are fully formed, they stop growing further. The BiSI obtained was determined to have a band gap of 1.6 eV, in close agreement with reported values, which makes it a suitable material for applications such as the aforementioned. This work delves deep into the production of a novel material which has promising applications in many technological fields and warrants further investigation.

2:00 PM H04
(Student) Rapid Ge Diffusion Along Si/SiO2 Interfaces During High Temperature Oxidation for Quantum-Scale Structures
Chappel Sharrock Thornton[1], Benjamin Hicks[1], Emily Turner[1], George T. Wang[2], Mark Law[1] and Kevin S. Jones[1]; [1]University of Florida, United States; [2]Sandia National Laboratories, United States

There is continued interest in the combination of Si and Ge in unique geometries to further improve the performance of transistors [1]. A novel diffusion mechanism of Ge along an oxidizing Si/SiO_2 interface was reported, which resulted in the formation of strained Si nanowires [2]. By taking advantage of this diffusion mechanism, there is the potential of forming site-controlled nanowires, quantum dots, and arbitrary nanoshapes. However, there is limited understanding of the diffusion mechanism that results in the formation of these nanostructures. To investigate this mechanism, alternating 15nm thick layers of Si and $Si_{0.7}Ge_{0.3}$were grown in a superlattice and patterned into fins via electron beam lithography. The final pattern contained multi-layered Si/SiGe fins with widths varying from 70 to 280nm with a 100nm layer of Si substrate exposed at the base. This extended Si surface enabled the observation Ge's diffusion down the fin's sidewall during high temperature oxidation. Ge's lateral diffusion was observed over a range of times at temperatures between 800 and 950°C. Cross-sectional TEM samples were prepared after each anneal and the diffusion length was measured through analysis of HAADF-STEM images, utilizing z-contrast. The diffusion length was measured after four different oxidation times at each temperature and the diffusivity was extracted. An Arrhenius plot of the data indicated the activation energy of Ge diffusion down the oxidizing interface is 2.50 +/- 0.3 eV. This is approximately half of activation enthalpy for Ge's movement into bulk Si or through the oxide [3], [4]. We propose that the Ge may be diffusing through the suboxide along the Si/SiO_2 interface and is subsequently reinserted back into the Si during oxidation. This is further supported by the linear correlation between the thickness of the thermally grown oxide and the distance the Ge diffuses down the Si sidewall. The difference in the activation energy compared to bulk interdiffusion helps to explain why the nanowires and quantum dots are formed within these materials during oxidation. In addition to dry oxidation anneals, anneals in a wet oxidizing ambient (steam) will be discussed. A model for the diffusion using the Florida object-oriented process and device simulator (FLOOXS) was developed. This model was used to assist in the extraction of diffusivities and is being further developed to help predict possible structures using this phenomenon. Preliminary results using the process simulator's model will be compared to the experimentally observed evolution of the nanostructures. *This work is supported by Sandia National Laboratories, which is managed and operated by NTESS under DOE NNSA contract DE-NA0003525.*

[1] T. David *et al.*, "New strategies for producing defect free SiGe strained nanolayers," *Sci. Rep.*, vol. 8, no. 1, pp. 1–10, Feb. 2018, doi: 10.1038/s41598-018-21299-9.
[2] W. M. Brewer, Y. Xin, C. Hatem, D. Diercks, V. Q. Truong, and K. S. Jones, "Lateral Ge Diffusion During Oxidation of Si/SiGe Fins," *Nano Lett.*, vol. 17, no. 4, pp. 2159–2164, Apr. 2017, doi: 10.1021/acs.nanolett.6b04407.
[3] R. Kube *et al.*, "Composition dependence of Si and Ge diffusion in relaxed Si1−xGex alloys," *J. Appl. Phys.*, vol. 107, no. 7, p. 073520, Apr. 2010, doi: 10.1063/1.3380853.
[4] Y. Dong, Y. Lin, S. Li, S. McCoy, and G. Xia, "A unified interdiffusivity model and model verification for tensile and relaxed SiGe interdiffusion over the full germanium content range," *J. Appl. Phys.*, vol. 111, no. 4, p. 044909, Feb. 2012, doi: 10.1063/1.3687923.

2:15 PM H05
Fabrication of Single and Few Atom Donor-Based Devices in Silicon
Pradeep Namboodiri[1], Ranjit Kashid[1], Alessandro Restelli[2], Xiqiao Wang[1,2], Jonathan Wyrick[1], Fan Fei[3,1] and Richard Silver[1]; [1]National Institute of Standards and Technology, United States; [2]Join Quantum Institute (JQI), United States; [3]University of Maryland, United States

Fabrication of quantum devices by atomic scale patterning using Scanning Tunneling Microscopy (STM) has led to the development of single/few atom transistors, few-donor/dot devices for spin manipulation, and arrayed few-donor devices for analog quantum simulation. We have developed high precision lithography, dopant incorporation, device encapsulation, ex situ device relocation, and contact processes that enabled us to have a high yield device fabrication. Material properties at the atomic scale including cleanliness, near perfect atomic order, dopant layer confinement and low-temperature epitaxial silicon overgrowth determine the operation and performance of quantum devices. We present a complete fabrication process for the creation of robust nano and atomic scale devices with atomically aligned gates and contact pads on clean silicon surfaces in an ultrahigh vacuum environment (10^{-11} Torr). Device stability is the direct result of controlling materials and process conditions at the atomic scale. Alignment of ohmic contacts to the sub surface nanoscale device pads is achieved using Kelvin Probe Force Microscopy (KPFM) and subsequent e-beam lithography. We will discuss low temperature transport measurements of atomic-scale tunnel junctions and single electron transistors that demonstrate stable coulomb blockade oscillations.

2:30 PM BREAK

3:00 PM H06
(Student) Self-Selective Formation of Ordered 1D and 2D GaBi Structures on Wurtzite GaAs Nanowire Surfaces
Yi Liu[1], Sandra Benter[1], Elliot Young[2], Sebastian Lehmann[1], Kimberly Dick[1], Chris Palmstrom[2], Anders Mikkelsen[1] and Rainer Timm[1]; [1]Lund University, Sweden; [2]University of California, Santa Barbara, United States

Bismuth (Bi) incorporation and alloying in III-V semiconductors such as InAsBi and GaAsBi have become a popular topic during recent years, due to a number of promising properties including band gap engineering, a large spin-orbit splitting, and predicted band inversion and topological behavior in the case of high Bi concentrations [1]. However, the realization of alloys with high Bi content by epitaxial growth has remained challenging, and GaBi bonds have been considered to be unstable [2]. We follow a different approach and deposit Bi onto clean surfaces of GaAs nanowires (NWs) containing both zinc blende (Zb) and wurtzite (Wz) segments, allowing us to study the incorporation of Bi atoms in different surface facets by low-temperature scanning tunneling microscopy and spectroscopy (STM/S). Our previous STM

studies have shown that the most common Zb{111} and Wz {11-20} and {10-10} NW facets are non-polar and typically unreconstructed [3,4]. Here, we observe that Bi atoms tend to replace As atoms in the GaAs NW surfaces via group-V exchange reaction and form GaBi bonds. What is more, we also find a crystal structure dependent surface alloying process, where ordered GaBi structures such as 2D islands and 1D atomic chains are formed on Wz {11-20} facets, while randomly distributed single Bi sites are found on Zb {110} facets. This self-selective formation process of ordered GaBi nanostructures is attributed to different diffusion barriers and different surface geometries of the different surface facets. Lastly, signs of a length-dependent energy confinement effect in Bi-chains on Wz {11-20} facets are observed via STS, which also indicates a reduced band gap on GaBi islands as compared to GaAs surfaces on the same nanowire. Our results indicate a promising way to realize stable and ordered 3D GaBi nanostructures with atomic-scale precision using nanowire templates and radial overgrowth, which open the path towards monolayer thin nanostructures with variable width, atomically sharp borders, and promise for exotic electronic phases of matter.

References:
[1] Chuang et al., Nano Lett. 14, 2505 (2014)
[2] Ferhat et al., Phys. Rev. B 73, 115107 (2006)
[3] Hjort et al., ACS Nano 8, 12346 (2014)
[4] Hjort et al., Nano Lett. 17, 3634 (2017)

3:15 PM H07
(Student) Growth of Topological Insulator Bi2Se3 Particles on GaAs via Droplet Epitaxy Sivakumar V. Mambakkam and Stephanie Law; University of Delaware, United States

With the discovery of topological insulators, a wide list of potential applications for their unique spin-momentum locked surface states have been proposed. Among these possibilities, it has been posited that electrons occupying these surface states might be useful as information carriers, since they cannot be scattered by a non-magnetic perturbation. A quantum dot-like system with discrete states that features these properties is of interest. To explore the potential of producing such a device, we first must learn more about how to make topological insulator quantum dots, and then study whether the topologically-protected surface states exhibit discretization while maintaining their unique properties. This study focuses on the growth and characterization of self-assembled, selenized bismuth particles on GaAs via droplet epitaxy in a molecular beam epitaxy system. In droplet epitaxy, we first deposit a small amount of bismuth which has a high surface tension and does not wet the substrate, resulting in the formation of bismuth clusters. These clusters are then exposed to a selenium flux, forming Bi_2Se_3 nanoparticles. For this study, growth time and substrate temperature during deposition were varied, and final particle density, average height and area were measured via a combination of atomic force microscopy and scanning electron microscopy. Within the substrate temperature (250-285 ^{o}C) and bismuth deposition time (20-100 seconds) ranges, we observed variations in average height, area, particle density, and polydispersity. Within the growth window, particles are generally 5-15 nm tall, and 500-3000 nm^2 in area (equivalent circular radius ~12-30 nm). When the amount of bismuth initially deposited increases, the nanoparticle density also increases, though this effect becomes less significant at higher substrate temperatures. Above 275 ^{o}C, the average particle height and area settle around 10 nm and 500-1000 nm^2 (equiv. circular radius ~12-17 nm). Polydispersity in particle height and area tends to drop relatively significantly above 275 ^{o}C as well. There also appears to be some correlation between particle height and area when changing growth conditions: in general, if particles are becoming taller on average, they are also becoming larger in radius. We demonstrated that adding a long anneal step between the bismuth deposition and selenium exposure steps resulted in smaller, shorter, and more numerous particles. These observations support our over-arching theory that the nanoparticle size is determined by bismuth adatom mobility and rate of bismuth removal from an existing nanoparticle rather than nanoparticle mobility. We have demonstrated the ability to affect the properties of particle height, area, density, and polydispersity by changing the initial bismuth deposition time and substrate temperature. These results should prove useful to those interested in creating topological insulator devices through epitaxial growth. **Acknowledgments**: National Science Foundation, Division of Materials Research under Award No. 1838504 and the Brookhaven National Laboratory/University of Delaware Seed Program under Award No. 20A00145. We also acknowledge the use of the Materials Growth Facility (MGF) at the University of Delaware, which is partially supported by the National Science Foundation Major Research Instrumentation under Grant No. 1828141 and is a member of the Delaware Institute for Materials Research (DIMR).

3:30 PM H08
(Student) Shape-Effect on Quantum Confinement in Alloy Quantum Dots and Their Applications for Photovoltaic Green Energy Zubaer Hossain and Nicholas Ulizio; University of Delaware, United States

Alloy quantum dots (aQD) represent a new class of low-dimensional materials whose electron confinement is determined not exclusively by size, but also by composition field. While homogeneous quantum dots have been more widely explored for applications in photonics, optoelectronics, and photovoltaics, aQDs remain less investigated. The differences in both size and composition field across aQDs lead to differences in material properties. These variations in material properties present compelling potential applications, specifically in the field of energy generation and photovoltaics. This is primarily because of the complexity in characterizing nonuniform fields and establishing the correlation between inhomogeneity and confinement. In order to effectively analyze the varied electron confinement of these materials, we employ a combination of density functional theory based quantum simulations, and finite element analysis based k.p calculations to determine the electron energy levels for a number of uniform and nonuniform physical variables. As a part of the analysis, composition maps were constructed for each of the different aQD shapes, namely, the steep cone, normal cone, hut, and dome. Each of these compositions maps was fitted with an analytical function that was then used to analyze the electronic properties of the aQDs. Results show that a generic expression for all four of the aQDs exists such that modification of this equation allows each of the disparate aQDs to be modeled. The steep cone shaped aQD with a 15° sidewall angle corresponds to a composition map where spatial decay occurs from the tip of the cone to the bottom. The normal cone shaped aQD exhibits a similar behaviour, but the sidewall angle is instead 30°, and the fitting function is modified to a product of a quadratic and a linear function. For the hut shaped aQD, the composition map takes the shape of a “hut” where decay occurs from the top edges towards the bottom edges in a non-linear fashion. For the final shape, the dome, spatial decay emanates from the top tip of the dome. The dome is fitted by two sidewalls per side that have angles of 11° and 30° respectively. For each of the quantum dots above, composition maps obtained are independent of size to determine the singular effects of the compositional variation. Our results suggest that inhomogeneity in composition field has a consequential role in controlling the confinement energy levels. Thus, the shape of aQDs can play a critical role in tailoring the effective electronic behavior. Furthermore, a larger alloy quantum dot, can behave electronically like a smaller quantum dot, if the composition field is inhomogeneous. By engineering quantum dots with certain composition maps, the photon absorption properties of the respective quantum dot can thus be tailored substantially. In particular, the most apparent application of this is to solar cells and spintronics; engineering the properties of the quantum dot

allows us to increase the absorption efficiency of the photovoltaic cell, which directly leads to greater potential for green energy generation.

3:45 PM H09
(Student) InP Quantum Dot and InGaP Quantum Well Visible Lasers on Si Pankul Dhingra[1], Aaron J. Muhowski[2], Brian Li[1], Patrick Su[1], Ryan D. Hool[3], John Dallesasse[1], Daniel Wasserman[2] and Minjoo L. Lee[1]; [1]University of Illinois Urbana Champiagn, United States; [2]The University of Texas at Austin, United States; [3]University of Illinois at Urbana-Champaign, United States

We present InP quantum dot (QD) and $In_{0.6}Ga_{0.4}P$ quantum well (InGaP QW) lasers on Si with continuous wave (CW) operation at room temperature (RT). Applications such as trapped-ion quantum computing could benefit greatly from Si/SiN_x photonic chips with integrated optical gain in the visible spectrum. The past few years have seen tremendous progress in the development of 1.3 µm InAs QD lasers on Si with low threshold current density (J_{th}) and high reliability.[1] Epitaxial InP QD and $In_xGa_{1-x}P$ QW lasers on GaAs grown by molecular beam epitaxy (MBE) and metalorganic vapor phase epitaxy (MOVPE) offer widely tunable visible emission from 645-750 nm [2] but there have been very few reports about the monolithic integration of red lasers on Si.[3] Here, we first show record InGaP QW and InP QD lasers on GaAs working CW with J_{th} of 180 A/cm^2 and 310 A/cm^2. Leveraging these device results, we then go on to demonstrate the first CW red InGaP QW and InP QD laser on Si at RT with J_{th} ~ 600 A/cm^2 and 1300 A/cm^2, despite an elevated threading dislocation density (TDD) of ~ 1×10^7 cm^{-2}. We grew InGaP QW and InP QD lasers on bulk GaAs (001) and GaAs/Si (001) templates by MBE. The GaAs/Si templates were grown on commercially available GaP/Si (001) templates using a 1.5 µm GaAs buffer subjected to thermal cycle annealing and $In_{0.1}Ga_{0.9}As$ dislocation filter layers. The InGaP QW lasers utilize a single, compressively strained 7 nm InGaP QW surrounded by an $(Al_xGa_{1-x})_{0.52}In_{0.48}P$ waveguide sandwiched between $Al_{0.51}In_{0.49}P$ cladding layers. InP QD lasers utilize 3.5 monolayers (ML) of InP QDs buried by a 7 nm InGaP QW to form a dot in a well (DWELL) structure. The active region of InP QD lasers consisted of either 3 or 5 DWELL layers separated by 16 nm of $Al_{0.17}Ga_{0.35}In_{0.48}P$ spacers. The lasers were subjected to rapid thermal annealing (RTA) at 950C for 1 s after growth for optical improvement. Uncoated, broad-area lasers (40-100 µm wide, ~ 1.5 mm length) were fabricated using standard techniques and characterized at RT with CW injection.
RTA reduces J_{th} of InGaP QW and InP QD lasers on GaAs by 1.5× and 6×, respectively. InGaP QW lasers on GaAs operate with a low J_{th} of 180 A/cm^2 at RT, lowest reported for CW InGaP QW lasers on GaAs by any growth technique. InP QD lasers on GaAs operate CW with a J_{th} of 310 A/cm^2 at RT with emission at 726 nm, ~ 8× lower J_{th} than previous InP QD lasers grown by MBE (pulsed, RT) [4] and comparable to their MOVPE-grown counterparts (pulsed, RT) grown on 10° offcut GaAs. [2] Annealed InGaP QW lasers on Si emitting at 693 nm show a J_{th} of 600 A/cm^2, 2.4× higher than InGaP QW laser grown on GaAs. These are the first CW and the lowest threshold InGaP QW lasers on Si to the best of our knowledge and operate with an output power of > 15 mW/facet. We also report the first demonstration of InP QD lasers on Si emitting at 726 nm showing a J_{th} of 1300 A/cm^2 (CW, RT), 4.3× higher than InP QD laser grown on GaAs. The J_{th} increase of InP QD lasers on Si can be partly attributed to poor facet quality and shorter cavity length of lasers on Si, in addition to the effect of TDD. We believe that with further design and process optimization, InP QD lasers on Si have the potential of demonstrating similar J_{th} as InP QD on GaAs.
[1] S. Chen, W. Li, J. Wu, Q. Jiang, M. Tang, S. Shutts, S. Elliot, A. Sobiesierki, A. Seeds, I. Ross, P. Smowton, H. Liu, *Nat. Photonics*, 10, 307 (2016)
[2[J. Lutti, P. Smowton, G. Lewis, A. Krysa, J. S. Roberts, P. Houston, Y. Xin, Y. Li, L. Lester, *Electron. Lett.,* 41, 5, 247 (2005)
[3] J. A. Carlin, C. L. Andre, O. Kwon, M. Gonzalez, M. R. Lueck, E. A. Fitzgerald, D. M. Wilt, S. A. Ringel, *ECS Trans.,* 3, 7, 729 (2006)
[4[Y. M. Manz, O. G. Schmidt, K. Eberl, *Appl. Phys. Lett.* 76, 3343 (2000)

4:00 PM H10
Generation of Water-Stable Zinc Sulphide Nanoparticles for Destruction of Emerging Contaminants Josian Luciano-Velázquez[1], Sonia J. Bailón-Ruiz[2] and Kevin D Correa-Vargas[1]; [1]University of Puerto Rico at Mayagüez, United States; [2]University of Puerto Rico in Ponce, United States

Thousands of drugs, analgesics and anti-inflammatories, are deposited in the bodies of water and ingested by the fauna of the ecosystems and river bodies. These drugs are metabolized and transformed into other compounds that are deposited back into the environment and they can reach drinking water treatment plants. Currently many of these drugs do not have regulations for water bodies and the ecotoxic effects are not known. Photo-catalysis is an emerging alternative for the destruction and removal of drugs and secondary metabolites. This technique, based in advanced oxidation processes, includes rapid oxidation of drugs, a decrease in the generation of aromatic products and finally the destruction of compounds and, generation of eco-friendly products as carbon dioxide and water. This technology is based on the activation of nanomaterials (i.e. semiconductors) in presence of electromagnetic radiation and subsequent generation of radicals from water to directly oxidize the contaminants. Based on the above considerations, this research is an attempt at the use of Zn-based nanomaterials (i.e. ZnS NPs) for the degradation of emerging contaminants from aqueous matrices. The specific goals of this project were: i) Generate and characterize nanomaterials of ZnS with photoactive properties, ii) Study the photo-chemical stability of photoactive nanomaterials, and iii) Demonstrate the degradation of emerging contaminants in presence of photoactive nanomaterials and the reuse of the nanostructures.

SESSION I: Silicon Carbide—Theory, Characterization and Device Processing
Session Chairs: Joshua Caldwell and Nadeemullah Mahadik
Wednesday Afternoon, June 23, 2021

1:15 PM I01
(Student) Investigation of Dislocations Contrast and Determination of Their Burgers Vectors in Synchrotron Grazing-Incidence X-Ray Topographs in PVT-Grown 4H-SiC Crystals Tuerxun Ailihumaer, Hongyu Peng, Yafei Liu, Balaji Raghothamachar and Michael Dudley; Stony Brook University, United States

The contrast of dislocations on the Si face of off-axis 4H-SiC crystals observed in synchrotron grazing-incidence X-ray topographs has been simulated by ray tracing based on orientation contrast mechanism [1-7]. The image contrast of dislocations, such as basal plane dislocations, deflected threading screw and mixed dislocations have been simulated. In order to further evaluate the factors contributing to the dislocation contrast formation, a more sophisticated simulation model is developed based on the principle of ray tracing by applying the effects of surface relaxation combined with X-ray absorption. Comparing the simulated results with the actual topographic dislocation images reveals that the dislocation contrast is dominated by surface relaxation effect, which mainly occurs for diffractions near the crystal surface. Depth analysis shows that the diffracted X-ray beam from regions below the dislocation contribute additional contrast to the image. By taking into account X-ray absorption,

the simulated contrast of the dislocation gradually weakens as the diffraction position gets deeper into the crystal. Based on the characteristic contrast of screw BPDs, Si-core and C-core edge BPDs, the full BPD loop contrast is also simulated and thus the Burgers vectors of all types of BPDs can be determined by comparing with the simulated results.
[1] X. R. Huang, M. Dudley, W. M. Vetter, W. Huang, S. Wang, and C. H. Carter, Jr., Appl. Phys. Lett. 74, 353 (1999).
[2] Y. Chen and M. Dudley, Appl. Phys. Lett. 91, 141918 (2007).
[3] I. Kamata, M. Nagano, H. Tsuchida, Y. Chen, M. Dudley, Mater. Sci. Forum 600-603, 305 (2009).
[4] X.R. Huang, D.R. Black, A.T. Macrandar, J. Maj, Y. Chen, M. Dudley, Appl. Phys. Lett. 91, 231903 (2007).
[5] F. Wu, S. Byrappa, H. Wang, Y. Chen, B. Raghothamachar, M. Dudley, E.K. Sanchez, G. Chung, D. Hansen, S.G. Muller, M.J. Loboda, MRS Proc. 1433 (2012).
[6] J. Guo, Y. Yang, F. Wu, J. Sumakeris, R. Leonard, O. Goue, B. Raghothamachar and M. Dudley, J. Electron. Mater. 45, 2045 (2016).
[7] Y. Yang, J. Guo, O. Goue, J. Kim, B. Raghothamachar, M. Dudley, G. Chung, E. Sachez, I. Manning, J. Electron. Mater. 47, 1218 (2018).

1:30 PM I02
(Student) Analysis of Local Lattice Distortion of SiC in Weak Beam Topography Hongyu Peng, Tuerxun Ailihumaer, Yafei Liu, Balaji Raghothamachar and Michael Dudley; Stony Brook University, The State University of New York, United States

The non-destructive characterization technique, synchrotron X-ray topography, is widely used to investigate extended crystal defects such as dislocations, inclusions, stacking faults and grain/twin boundaries [1]. Many studies have been carried out of the contrast of dislocations in 4H-SiC crystals using monochromatic synchrotron X-ray topography in grazing incidence. Such images are usually characterized by the presence of "so-called" Bragg contours resulting from mild distortions in the crystal such that only a limited region diffracts the X-rays for a given incidence direction. However, the contrast of dislocations in 4H-SiC crystals shows distinctive features for diffraction at different positions on the operative rocking curve. Ray tracing simulations have previously been successfully applied to describe dislocation contrast at the peak of the rocking curve [2-4]. And recent work shows that under weak diffraction conditions (i.e. diffraction takes place off rocking curve peak), the observed dislocation images can also be simulated using the ray tracing method, indicating the contrast of dislocations is dominated by orientation contrast, which is defined as the separation or overlap of diffracted X-rays arising from local lattice distortion. In this study, we will show that the contrast of threading screw dislocations under weak diffraction conditions can be directly correlated to its lattice displacement (negative effective misorientation or positive effective misorientation will result in either enhanced or reduced contrast). And the fundamental contrast formation analysis enables us to understand the local lattice distortion generated by other defects as well, extending potential applications of X-ray topography.
Reference:
[1] B. Raghothamachar, M. Dudley, X-Ray Topography, in ASM Handbook, DOI: https://doi.org/10.31399/asm.hb.v10.a0006644, pp 459-477, ASM International (2019)
[2] Y. Chen & M. Dudley, Appl. Phys. Lett. 91, 141918 (2007)
[3] F. Wu, S. Byrappa, H. Wang, Y. Chen, B. Raghothamachar, M. Dudley, E. Sanchez, G. Chung, D. Hansen, S. Mueller & M. Loboda, MRS online Proceedings Library 1433, 53-58 (2012)
[4] J. Guo, Y. Yang, F. Wu, J. Sumakeris, R. Leonard, O. Goue, B. Raghothamachar & M. Dudley, J. Electron. Mater. 45, 4 (2016)

1:45 PM I03
(Student) Assessment of Lattice Damage in High Energy Ion Implanted 4H-SiC Wafers at Room Temperature Zeyu Chen, Yafei Liu, Hongyu Peng, Tuerxun Ailihumaer, Qianyu Cheng, Balaji Raghothamachar and Michael Dudley; Stony Brook University, The State University of New York, United States

Silicon Carbide (SiC) is a promising wide bandgap semiconductor for power devices. Due to excellent properties of SiC, such as wide band gap, high break down voltage and thermal stability, SiC devices are able to be operated under harsh environment, such as high temperature, high voltage and high frequency environment [1]. To control the conductivity, SiC wafers are usually doped with impurities, such as Aluminum for P type and Nitrogen for N type, by ion implantation. For conventional ion implantation, the implantation energy is of the order of few hundred KeVs and the depth of the junction is within 1 micron. However, deeper implantation profiles are necessary for the development and fabrication of future generation of SiC power devices such as the high voltage SiC superjunction FETs, To achieve this, high energy ion implantation with energy level of several MeVs, is gaining interest. By using MeV implantation energy, implantation depths up to 10um or more has been achieved [2]. During the ion implantation process, accelerated dopant atoms will bombard and penetrate the SiC wafer. Therefore, the implantation process will introduce damage in the SiC lattice [3]. One of the ion implantation damages is introducing lattice strain into the SiC wafer since the incoming accelerated dopants will displace the original Si or C atoms [4]. Higher energy used for implantation can potentially introduce higher damage than conventional lower energy implantation processes. Therefore, characterizing damages due to high energy ion implantation is critical to the fabrication of SiC devices. In this paper, we characterized lattice strain of as-implanted 4H-SiC implanted with energies as high as 59.8 MeV, by using Synchrotron Rocking Curve X-ray Topography and Reciprocal Space Mapping. Results from samples implanted by Al and N dopants will be compared with unimplanted samples to assess the lattice damage ahead of annealing experiments.
[1] Jianqiu Guo, Yu Yang, Balaji Raghothamachar, Taejin Kim, Michael Dudley, Jungyu Kim, Journal of Crystal Growth 480 (2017) 119–125
[2] P. Thieberger, C. Carlson, D. Steski, R. Ghandi, A. Bolotnikov, D. Lilienfeld and P. Losee, Nuclear Inst. and Methods in Physics Research B 442 (2019) 36–40
[3] Kumiko Konishi et al 2018 Semicond. Sci. Technol. 33 125014
[4] L.Q. Zhang, Y.G. Chen, H.P. Liu, L. Kang, T.M. Zhang, J.Y. Li, C.L. Xu, X.L. Zhang, J.Y. Li, Z.N. Ding, C.H. Zhang, Nuclear Inst. and Methods in Physics Research B 474 (2020) 15–2

2:00 PM I04
(Student) Theoretical and Experimental Analysis of Interfaces Between 4H-SiC and High-κ Dielectrics Lu Wang[1], Ryan Thorpe[2], Sarit Dhar[1], Leonard C. Feldman[3] and Marcelo A. Kuroda[1]; [1]Auburn University, United States; [2]Lehigh University, United States; [3]Rutgers, The State University of New Jersey, United States

4H-SiC MOSFETs suffer from low channel mobility that is primarily attributed to the poor SiC/SiO_2 interface quality [1]. Although various chemical treatments have been adopted to reduce the interface trap densities, the channel mobility is still low. Alternatively, high-κ dielectrics with suitable band gaps offer another possibility to replace the conventional SiO_2 as a gate insulators. To this end, these material candidates must have adequate band alignments and low density of interfacial traps. This study assesses both theoretically and experimentally a variety of high-κ dielectrics for 4H-SiC MOSFETs that includes MgF_2 and Al_2O_3. Using first principles calculations within the density functional theory (DFT) for binary compounds we established that most alkaline earth metal fluorides (AF_2), and Al_2O_3 can be

promising high-κ/larger band gap dielectrics candidates. From tens of phases of alkali earth metal halides found in the AFLOW database [2], the fluoride compounds were screened based on their electronic and thermal properties for the most stable phases. Subsequently, interface models of the Si-face of 4H-SiC with CaF_2, MgF_2, and Al_2O_3 were produced and their valence band ($\triangle E_V$) and conduction band ($\triangle E_C$) offsets were quantified by aligning local band edges with respect to the local electrostatic potential [3]. Experimentally, the band alignments for SiC/MgF_2 and SiC/Al_2O_3 interfaces were measured using x-ray photoelectron spectroscopy (XPS) for comparisons. We find that MgF_2 and Al_2O_3 exhibit band gaps that are consistent with experiment. The SiC/Al_2O_3 interface model has adequate band offsets (for both $\triangle E_V$ and $\triangle E_C$) and shows values comparable to the experiments. In contrast, XPS measurements suggests sizable offsets for electrons and holes in SiC/MgF_2 interfaces which do not agree with our model interfaces. The possible origins of these discrepancies will be discussed. Overall, this work offers insights on the potential use of alternative high-κ dielectric materials in wide band gap electronic applications, The authors gratefully acknowledge the funding support from Army Research Lab grant ARMY-W911NF-18-2-0160, computational resources from AU Hopper HPC.
[1] T. Kimoto and J. A. Cooper, *Fundamentals of silicon carbide technology* (Wiley, Singapore, 2014).
[2] S. Curtarolo et al., Comput. Mater. Sci. 58, 218 (2012).
[3] L. Weston et al., Comput. Mater. Science 151, 174 (2018).

2:15 PM I05
(Student) Transition Metal Defects 4H-SiC—Optical and Electronic Levels from First Principles Timothy S. Wolfe[1], Renee Van Ginhoven[2] and Alejandro Strachan[1]; [1]Purdue University, United States; [2]Air Force Research Laboratory, United States

Electronic structure calculations of 4H-SiC doped with various transition metals reveal dilute magnetic semiconductor (DMS) behavior in a material suitable for high-power and high-frequency semiconductor devices. Our results are consistent with prior work on V, Cr, and Mn doping and explore additional metals: Fe, Co, and Ni. Charge-state calculations show that the latter maintain amphoteric semi-insulating properties while offering a higher stable spin polarization and also greater asymmetry in the spin density of states than previously studied dopants. This indicates possible enhanced half-metal properties. We then use these discoveries to inform the first calculations of the phonon-assisted optical properties of doped 4H-SiC systems, using the approach first published by Noffsinger et al. [1] based on Maximally Localized Wannier Functions to assist overcoming the numerical challenge.
[1]: Phonon-Assisted Optical Absorption in Silicon from First Principles Jesse Noffsinger, Emmanouil Kioupakis, Chris G. Van de Walle, Steven G. Louie, and Marvin L. Cohen Phys. Rev. Lett. **108**, 167402 – Published 20 April 2012

2:30 PM BREAK

3:00 PM I06
(Student) Investigation of Implant Temperature on Dopant Activation Efficiency for Single Fluence Al+ Implanted 4H-SiC Lydia Kuebler[1], Christopher Hatem[2], Hans Gossmann[2], Wei Zhao[2], Supakit Charnvanichborikarn[2] and Kevin S. Jones[1]; [1]University of Florida, United States; [2]Applied Materials, Inc., United States

As a wide bandgap semiconductor, silicon carbide (SiC) possesses unique properties that make it an advantageous replacement for silicon in high power, high frequency, and high temperature electronic devices. Ion implantation followed by high temperature annealing (>1600°C) is often used to introduce and activate dopants in the material. However,the high concentration of point defects created from implantation evolve into extended defects upon annealing, resulting in device failure. In order to address this issue, elevated temperature implants have been used extensively to prevent amorphization but little is known about higher temperature implant effects on defect evolution and how this correlates with dopant activation efficiency. In this study, 60 keV Al^+ was implanted into single crystal n-type 4H-SiC wafers to a fluence of either $5x10^{13}$ or $1x10^{15}$ cm^{-2}. The implant temperature was varied between 300°C and 700°C. High temperature furnace annealing was performed with a carbon cap from 1300°C to 1680°C for 30 minutes. Structural characterization using cross-sectional and plan-view BF-TEM and DF-TEM was performed for extended defect analysis. Ohmic contacts were created from sputter deposition of a Ti/Al/Ni metal stack followed by alloying at 1000°C for 1 minute. Electrical characterization using variable-temperature Hall Effect was performed to study dopant activation. As implanted cross-sectional TEM analysis showed amorphization is avoided for the low fluence ($5x10^{13}$ cm^{-2}) implants at all implant temperatures. For the high fluence case ($1x10^{15}$ cm^{-2}), amorphization is avoided above 400°C due to the increasing effects of dynamic annealing. The reduction of lattice damage with increasing implant temperature can be seen in UV/Vis/NIR measurements for the unannealed samples. The absorption peaks corresponding to lattice damage show a consistent reduction as the implant temperature is increased up to 700°C. A carbon cap was introduced to reduce surface decomposition during the high temperature annealing process with a variety of capping methods studied. Graphitized photoresist was shown by AFM measurements to result in the least amount of surface roughening upon annealing at around 1 nm. Extended defects were observed by TEM for the high fluence implants at all implant temperatures after annealing but were absent for the low fluence case. The loops are seen to coarsen with implant temperature as expected but are not eliminated by the anneal. TEM results suggest the concentration of trapped interstitials in the extended defect decreases with increasing implant temperature. Further analysis on the effect of implant temperature on the evolution of these extended defects will be presented. In addition to structural characterization, electrical measurements were carried out. Ohmic contacts were successfully created from the combination of an effective annealing cap and from the optimal metal thickness ratios in the metal stack. However, initial Hall effect measurements at room temperature were not successful in determining the dopant activation values even after 1680°C annealing. This is thought to be due to the relatively deep acceptor level associated with Al in SiC. Subsequently, variable field measurements at 400°C showed a dopant type change from the n-type substrate to the p-type implant enabling dopant activation values to be determined. These electrical results will be compared with structural images to highlight correlations between extended defect evolution and dopant activation efficiency.

3:15 PM I07
(Student) High Temperature Characteristics of NO Annealed P-Channel 4H-SiC MOSFET Suman Das, Tamara Isaacs-Smith, Ayayi C. Ahyi, Marcelo A. Kuroda and Sarit Dhar; Auburn University, United States

Superior material qualities of 4H-SiC such as wide bandgap, high thermal conductivity, and large breakdown electric field make devices capable of operating with high power at high temperature. In this work, the behavior of p-channel 4H-SiC metal-oxide-semiconductor field-effect transistor (MOSFET), where holes are the channel charge carriers; has been investigated. The experimental results confirm that post oxidation Nitric Oxide (NO) annealing reduces SiO_2/4H-SiC interface trap densities (D_{it}) in the upper half of the 4H-SiC bandgap as widely reported. In addition, D_{it} is also significantly reduced in the lower half, which is critical for p-channel MOSFETs. This result is corroborated by capacitance-voltage (CV) measurements conducted on p- and n-type 4H-SiC MOS capacitors from room temperature to 300°C,

as well as under UV illumination, which allows estimation of the D_{it} profile throughout the large 4H-SiC bandgap. Thereafter, p-channel 4H-SiC MOSFETs were fabricated and measured from room temperature through 300°C. The MOSFETs without NO annealing turn on at very large negative voltages with high dielectric leakage currents, making it difficult to get reliable high temperature data. In contrast, the NO annealed MOSFETs turn on at a much lower voltage, with low leakage, consistent with the reduction of D_{it} due to NO annealing. With the rise of temperature, the threshold voltage drops as the number of occupied interface traps reduce with the increase of temperature. However, the temperature dependence of the hole channel mobility is not obvious from these measurements. The weak temperature dependence can be explained considering the behavior of the phonon and Coulomb scattering components. The phonon scattering limited hole mobility reduces from ~120 cm^2/Vs at room temperature to less than 25 cm^2/Vs at 300°C in lightly doped bulk p-type 4H-SiC. On the other hand, the Coulomb scattering limited surface hole mobility increases weakly with temperature. The competition between the two mechanisms increases at higher temperatures and the overall field-effect mobility shows an almost temperature-independent behavior in the 25°C - 300°C range. While NO annealing realizes high temperature operation, the negative bias temperature instability (NBTI) is a major shortcoming. This is a result of hole injection and trapping in the oxide under high temperature and negative bias stress. In this presentation, the results from the NBTI experiments will be reported and the main mechanisms related to high temperature NBTI will be discussed. The authors gratefully acknowledge the funding support from US Army Research Laboratory grant ARMY-W911NF-18-2-0160 and National Renewable Energy Laboratory/ US Department of Energy grant NREL-AHL-9-92362-01.

3:30 PM I08
(Student) Spatially Resolved Fourier Transform Impedance Spectroscopy—A Technique to Rapidly Characterize Composite Interfaces and a Study of Quantum Dot/Epitaxial Graphene/SiC Optoelectronic Devices Mathew Kelley, Grigory Simin, Mohammad K. Hussain, Asif Khan, Andrew Greytak and MVS Chandrashekhar; University of South Carolina, United States

We demonstrate a technique to spatially map and quickly build the frequency response of optoelectronic devices using optical probes. The transfer function of a linear system is the Fourier transform of its impulse response, which may be obtained from transient photocurrent measurements of devices such as photodetectors and solar cells. We introduce and apply Fourier Transform Impedance Spectroscopy (FTIS) to a PbS colloidal quantum dot (QD)/SiC heterojunction photodiode and corroborate results using intensity-modulated photocurrent spectroscopy. The cutoff frequencies of the QD/SiC devices were as high as ~10kHz, demonstrating their utility in advanced flexible and thin film electronics. The practical frequencies for FTIS lie in the mHz-kHz range, ideal for composite or novel materials such as QD films that are dominated by interfacial trap states. These can lead to characteristic lengths for charge collection ~20-500 µm dominated by transmission line effects, rather than intrinsic diffusion and drift length scales, enabling extraction of interfacial capacitances and series/parallel resistances.

3:45 PM I09
Theory for Intrinsic Point Defects in 3C-SiC Reassessed Using Converged Large-Supercell Calculations Peter A. Schultz[1], Renee Van Ginhoven[2] and Arthur H. Edwards[2]; [1]Sandia National Laboratories, United States; [2]Air Force Research Laboratory, United States

Silicon carbide a wide band gap semiconductor, with potential advantages for use in high-power, high-frequency electronics in extreme environments. Its higher breakdown fields and reduced sensitivity to radiation and thermal effects (vs. silicon) make it an auspicious candidate for high-temperature applications and in radiation environments (e.g., in space). Given the importance of atomic defects for SiC device performance, surprisingly little is definitively known about individual defects in any SiC polytype. Even in the simplest 3C-SiC polytype, despite numerous experimental and computational efforts, properties a "simple" defect such as the Si vacancy remain a mystery. We present results for a comprehensive set of intrinsic defects in 3C-SiC using fully converged density functional theory methods that (1) explicitly fix the boundary condition problem in supercell calculations, (2) eliminate finite size errors and converge to a bulk limit, demonstrated in supercell models up to 1000 atoms, and (3) avoid a band gap problem in computation of defect levels, thereby obtaining <0.2 eV accuracy in predictions of defect levels (Schultz, 2006, 2015)[1,2]. The computed levels span the band gap of 3C-SiC and offer new insights into properties of defects in SiC. For example, the simple silicon vacancy is an iconic defect in 3C-SiC. The negatively charged v(1-) is well-understood, experiment and theory converging to a high-spin quartet with T_d structure. For v(0), however, standard DFT predicted a high-spin triplet (Torpo, 1999)[3] that, despite a Jahn-Teller degeneracy, remained an undistorted T_d. This conflicted with experiments (e.g., Itoh, 1997; Son 1997)[4,5] which found no such T_d triplet. This absence prompted use of more exotic electronic structure approaches (Deak, 1999; Zywietz, 2000 Oda 2013)[6,7,8], which found a lower energy singlet-spin v(0), in principle invisible to spin-sensitive experiments such as EPR. We find a lower energy yet for a high-spin triplet v(0), distorted from T_d, due to the Jahn-Teller instability, confirmed in calculations up to large 1000-site supercells using DFT. This gives a description of the v(0) more consistent with observations. The divacancy, interesting for quantum applications, is discovered in these large-cell models to exhibit an unanticipated bistability with a site-shift structure that will dominate in p-type material. This site-shift is analogous to the site-shift bistability in the single Si vacancy that complicates the its range of stability with respect to the Fermi level. We find that other defects also are inadequately described in the smaller cells historically used in DFT calculations. The larger supercells, with explicit correction of the boundary condition problem and avoidance of the band gap problem, reveal more accurately the character of SiC defects.--- SNL is managed and operated by NTESS under DOE NNSA contract DE-NA0003525.
[1] P.A. Schultz, Phys. Rev. Lett. **96**, 246401 (2006).
[2] P.A. Schultz, J. Phys.: Condens. Matter **27**, 075801 (2015).
[3] L. Torpo, R.M. Nieminen, L.E. Laasonen, and S. Pöykkö, Appl. Phys. Lett. **74**, 221 (1999).
[4] H. Itoh, et al., Phys. Stat. Sol (a), **162**, 173 (1997).
[5] N.T. Son, et al., Phys. Rev. B **55**, 2863 (1997).
[6] P. Deak, et al., Appl. Phys. Lett. **75**, 2103 (1999).
[7] A. Zywietz, J. Furthmüller, and F. Bechstedt, Phys. Rev. B **62**, 6854 (2000).
[8] T. Oda, Y. Zhang, and W.J. Weber, J. Chem Phys. **139**, 124707 (2013).

4:00 PM I10
(Student) Atomistic Basis of Anisotropic Poisson's Ratio in 3C-SiC Zubaer Hossain and Henry Fidlow; University of Delaware, United States

Poisson's ratio (PR) of a material plays an important role in governing the lateral response of a solid subjected to symmetry-breaking deformation. Traditionally, PR is represented as a single material constant which, by construction, refers to the linear part of the stress-strain curve. The understanding of a possible coupling between crystallographic direction and PR remains more elusive. Here, we report the observation of anisotropic PR in defect-free 3C-SiC lattice, using quantum simulations based on the Density Functional Theory. We analyze the lateral response of 3C-SiC to an applied strain along the three high-symmetry

crystallographic directions, [100], [110], and [111]. From our ab initio calculations, we use the linear and nonlinear regimes of mechanical deformation to determine Poisson's ratio as a function of applied strain for a given axial and transverse direction. Asymmetric deformation in the lattice of the [110] direction results in two Poisson functions dependent on the lateral orientation. One of these indicates a positive value, while the other a negative value (regardless of the strain state of the lattice). This suggests simultaneous existence of both positive and negative PRs in the material. Conversely, uniaxial loading along either of the other two high-symmetry directions, the [100] and [111] directions, yields identical lateral behavior, allowing for a single Poisson function. From the four Poisson's functions, the maximum and minimum Poisson's ratios are reached in the two different lateral directions of the [110] direction. The first function reaches a maximum Poisson's ratio of 0.5, indicating incompressibility and maximum contraction of the lateral direction for applied tensile loads. The second function is auxetic, exhibiting purely negative Poisson's ratios throughout the true strain range. This translates to lateral expansion in tension and lateral contraction in compression. In both the [100] and [111] directions, all values of the Poisson's functions exist within the range of 0 to 0.3. Anisotropic behavior is similarly witnessed in the strength and toughness of 3C-SiC for the three high-symmetry directions. Here it can be noted that loading along the [100] direction exhibits optimal strength and toughness while loading in the [111] direction displays maximum stiffness. Analysis at the atomic scale reveals relationships between crystallographic structure and anisotropy of Poisson's ratio. Linear and angular bond deformation influences the lateral strain behavior based on lattice symmetry with respect to the axial direction. Additionally, further investigation of the electron redistribution properties of both silicon and carbon atoms was investigated to determine relationships between Poisson's ratio and electron density in the various orbitals. Coupled with improvements in grain manufacturing technologies, these observations can be utilized toward the optimization of mechanical properties of 3C-SiC and other diamond cubic structures in practical applications.

SESSION J: Group III-Nitride Growth—MBE
Session Chairs: Theeradetch Detchprohm and Zetian Mi
Wednesday Afternoon, June 23, 2021

1:15 PM J01
Machine Learning for Evaluation of RHEED Spectra on III-Nitride Films Grown Using Molecular Beam Epitaxy Adam M. Payne[1], Terence Brown[1], Alexander H. Rao[1,2] and W. Alan Doolittle[1,2]; [1]Innovative Advanced Materials, United States; [2]Georgia Institute of Technology, United States

RHEED spectra taking during molecular beam epitaxy of GaN and related alloys on sapphire substrates were analyzed using a convolutional neural network. An existing image-classifying convolution neural network (CNN)— AlexNet— was employed for the analysis. The RHEED images during various stages of growth were manually categorized to train the CNN. The CNN only works on images, so video frames of RHEED during growth had to first be extracted from the video. These images were then separated into a training set and a validation set for use in training the network and in validating it. Mobility, deposition temperature, X-ray diffraction, atomic force microscopy, and Hall measurements were taken on the resulting films. After training on the manually categorized images and videos, the CNN achieved a proper categorization rate of 97% on the validation data and employing mobility and various growth stages as categorical outputs. Other machine learning techniques were applied as well to analyze RHEED spectra, such as principal components analysis and k-means clustering. Initial results from growth of ternary ($Al_xIn_{1-x}N$) and quaternary (AlGaInN) alloys will also be presented at the conference.

1:30 PM J02
(Student) First Experimental Demonstration of P-Type AlN Grown by MME Habib Ahmad, Zachary Engel, Christopher M. Matthews, Keisuke Motoki and W. Alan Doolittle; Georgia Institute of Technology, United States

Both MOCVD and MBE have achieved moderately doped p-GaN. Furthermore, metal modulated epitaxy (MME) has achieved hyper p-type GaN by improved growth kinetics at low substrate temperature and low III/V ratio. These growth kinetics have been previously applied to GaN:Be films as well[1] showing abrupt step-doped Be incorporation. Bulk Be doping resulted in semi-insulating GaN suitable for high power devices but highly p-type GaN could not be achieved due to the high experimental activation energy (~700 meV). The high activation energy of Be in GaN is due to lattice strain resulting from the high atomic radius mismatch of Be (112 *p*m) vs Ga (136 *p*m). As compared to GaN, AlN is much harder to dope, especially p-type because Mg has a higher activation energy (~510 meV) in AlN presumably due to the high atomic radii difference of Mg (145 *p*m) as compared to Al (118 *p*m). Be is a potentially suitable candidate for p-type doping of AlN due to the close atomic radii match of Be to Al. Also AlN:Be has theoretically shown a much lower activation energy (330 meV) as compared to AlN:Mg. We applied the growth kinetics used for Mg doping of GaN to the growth of AlN:Be films in the range of Be dopant concentrations of 0 (N4436), 2×10^{17} (N4434), 7×10^{18} (N4435), and 1×10^{20} cm^{-3} (N4433) grown on HVPE AlN templates. Pt/Pd/Au (10 nm/ 10 nm/ 100 nm) Van der Pauw contacts were deposited via e-beam evaporation. Before annealing all the samples showed non-ohmic behavior with current at the noise floor of the latest Lake Shore FastHall M91 Hall Effect Measurement equipment. The samples were then annealed at 700 °C for 10 minutes under nitrogen. After annealing, N4433 and N4436 still showed non-ohmic behavior. However, N4434 and N4435 exhibited highly ohmic behavior with currents 4-5 decades higher than pre-annealing. Hot probe measurements performed via a high impedance Keithley 6517A electrometer showed n-type behavior for N4433 and N4436 while p-type behavior was observed for N4434 and N4435. Four-point resistivity and Hall measurements of N4433 and N4436 could not be performed due to contacts' failure. 100 repeated measurements were taken for both resistivity and Hall measurement of both N4434 and N4435 for increased reliability and statistical validation of the results. Longer measurement times of several hours were employed to cater for RC time constants of the contacts. Validating the thermal probe results of p-type conduction, Hall measurements showed p-type conductivity for all the 100 repeated measurements of both N4434 and N4435 with hole concentrations of 4.65×10^{16} and 1.4×10^{17} cm^{-3} respectively. In Hall measurements, the current flows through different contacts than the Hall voltage is measured, and since contacts were absent of rectification and symmetric in repeated trials with reversed polarities per NIST standards, the Hall results are accurate to +/- 2×10^{14} and 4×10^{14} cm^{-3}, respectively. Four-point resistivity of N4434 and N4435 showed resistivity values of 12.2 and 6.5 mΩ-cm, respectively but could be underestimates of the actual values due to linear but very high contact resistances of ~15 and 6 MΩ, respectively. Hall voltages of the measurements were verified with Lake Shore staff and were found above the noise levels with SNR of 203 and 316, respectively. Purlieu (full-width at fractional peak heights to delineate the thin film from the bulk material) symmetric and asymmetric XRD rocking curves showed the regrown films closely matched the crystalline quality of the underlying templates. Furthermore, the (002) symmetric quality of AlN slightly decreased with Be concentration, however, both (105) and (102) asymmetric quality improved slightly with Be concentration suggesting a modest change in defect structure.

This work successfully showed MME grown p-type AlN:Be suggesting huge potential for future AlN-based high temperature, high voltage transistors, and, DUV photodetectors and light sources. References:
1. Ahmad et al. *JAP,* 127, 215703, 2020

1:45 PM J03
(Student) Anomalous Super-Linear Growth Rate Reduction with Increasing Aluminum Flux in M-Plane AlGaN Grown by PAMBE Brandon Dzuba, Trang Nguyen, Yang Cao, Rosa Diaz, Michael Manfra and Oana Malis; Purdue University, United States

III-Nitride materials have long been promising candidates for the development of infrared optoelectronic devices. However, design of multiple quantum well (MQW) structures on conventional c-plane (0001)-oriented GaN substrates is hindered by the spontaneous and piezoelectric polarization fields associated with lack of inversion symmetry. Low-defect density free-standing m-plane (10-10) GaN substrates have enabled the growth of non-polar MQW structures without strong built-in polarization fields. We have previously demonstrated the potential of m-plane $Al_{0.16}Ga_{0.84}N$/GaN heterostructures grown by plasma-assisted molecular-beam epitaxy (PAMBE) for terahertz devices [1]. To support higher energy near-infrared optical transitions, though, a larger conduction band offset (CBO) is required. This can be achieved through higher Al composition in the barriers. However, m-plane AlGaN layers with aluminum fractions above 0.2 grown under conventional gallium-rich PAMBE conditions exhibit severe material inhomogeneities [2]. Recently, we demonstrated that growth of m-plane AlGaN by indium surfactant assisted epitaxy (ISAE) at low temperature significantly reduces composition inhomogeneities [3]. Here, we present an in-depth comparison of the PAMBE growth of m-plane AlGaN with and without indium surfactant at 565°C. We investigated the compositions and growth rates of low temperature m-plane AlGaN layers grown by conventional gallium-rich epitaxy and by ISAE across a range of aluminum fluxes. It is expected that under nitrogen-limited growth conditions the growth rate would be independent of metal flux. We find the opposite to be true: as aluminum flux increases, the growth rate of AlGaN decreases rapidly. We attribute this phenomenon to nitrogen loss during PAMBE of m-plane AlGaN that increases super-linearly with increasing aluminum flux. These films also show a super-linear increase in aluminum content with increasing aluminum flux. Transmission Electron Microscopy (TEM) images indicate that these effects are correlated with high aluminum containing defects within the material. Our results indicate that ISAE mitigates this effect almost entirely. Films grown by ISAE with identical aluminum fluxes to the gallium-rich layers do not exhibit a significant decrease in growth rate with increasing aluminum flux, and their aluminum compositions increase linearly with aluminum flux. TEM images show the ISAE layers are thicker, and exhibit a higher degree of material uniformity up to 0.30 aluminum metal fraction. X-ray diffraction (XRD) measurements suggest minimal indium incorporation in the ISAE AlGaN layers. The CBO of MQWs can be further increased by using InGaN as the quantum well (QW) material. We have recently demonstrated the growth of high-quality m-plane InGaN with up to 0.16 indium metal fraction [4], enabling the growth of $In_{0.055}Al_{0.19}Ga_{0.755}N/In_{0.16}Ga_{0.84}N$ MQW structures using the ISAE technique [3]. We will also present results of structural and optical characterization of m-plane (In) $Al_{0.3}Ga_{0.7}N/In_{0.16}Ga_{0.84}N$ MQW structures. Due to the anisotropic nature of strain in m-plane structures, AlGaN/InGaN structures cannot be perfectly strain-balanced. We will discuss the method used to control strain accumulation along the (0001) and (11-20) directions below the level for defect formation in both the InGaN QWs and AlGaN barriers.
[1] C. Edmunds et al., Appl. Phys. Lett. 105, 021109 (2014).
[2] M. Shirazi-HD et al., J. Appl. Phys. 123, 161581 (2018).
[3] B. Dzuba et al., J. Appl. Phys. 128, 115701 (2020).
[4] A. Senichev et al., APL Mater. 7, 121109 (2019).

2:00 PM J04
(Student) MBE Growth and Transport Properties of Ultra-Wide Bandgap AlGaN on AlN Bulk Substrate Ryan Page[1], Kevin Lee[1], Len van Deurzen[1], Connor Gerlach[1], Huili Grace Xing[1,1,2] and Debdeep Jena[1,1,2]; [1]Cornell University, United States; [2]Kavli Institute at Cornell for Nanoscale Science, United States

As III-N power electronics and deep ultraviolet photonics require materials with larger and larger bandgaps, they are faced with many novel challenges, such as prohibitively high voltage drops across transport layers and the requirement that these layers be transparent to UV photons in light emitting devices. Additionally, the limited availability of low dislocation density substrates suitable for growing thick layers of high Al-composition AlGaN has led to devices with deleteriously high dislocation densities, which degrades both the carrier transport in doped layers and the performance of subsequent active layers[1]. Here, high (>50%) Al-composition n-type AlGaN layers are grown by molecular beam epitaxy (MBE) on single crystal aluminum nitride substrates with low, 10^4 cm^{-2} dislocation densities. Films of 60% to 80% Al-content AlGaN have been grown with room temperature resistivities ranging between $6x10^{-3}$ and $7.5x10^{-3}$ ohm-cm, all comparable to or below the lowest reported resistivity in 70% AlGaN by Fan et al[2]. Additionally, these films exhibit temperature-independent carrier concentrations and mobilities, indicating that they are doped beyond the Mott transition. Optically, these AlGaN layers retain transparency deep into the UV-C spectrum, with optical bandgaps, as measured by the Tauc method, exceeding 5 eV, validating that these materials are well-suited for electron transport layers in deep ultraviolet photonic devices. High crystalline quality and a smooth surface are particularly important to the n-type transport layer, since the active region of the device is grown above the n-layer in many LED and vertical power transistor device geometries, epitaxially inheriting the interface roughness of the previous layer any threading dislocations generated or propagated within. Owing to earlier research on bulk aluminum nitride substrate surface preparation and subsequent homoepitaxy, these AlGaN layers maintain highly smooth surfaces and interfaces[3,4]. Atomic force microscopy (AFM) reveals exceptionally smooth surfaces with clear, parallel atomic steps and no visible screw dislocation features. Additionally, 2theta-omega coupled x-ray diffraction measurements demonstrate sharply resolved Pendellösung fringes, indicating a sharp AlGaN/AlN interface under the surface.
To realize the full advantage of low-dislocation bulk substrates, the generation of new dislocations in these layers must be minimized, a major source being crystal relaxation in epitaxially-grown films. To investigate the strain state of the compressively strained AlGaN layers on bulk AlN substrates, reciprocal space maps (RSMs) around the asymmetrical, (10-15) peak of AlN were measured. The RSMs of all the AlGaN layers indicate that films are fully strained to the AlN substrate, up to 300nm films of 70% AlGaN. While there are still many challenges to overcome, namely hole transport and contact layers, this work represents another important step towards the realization of improved deep UV photonic and power electronic devices enabled by low defect density AlN substrates. The authors acknowledge the following funding sources: NSF grant DMR-1719875 and MRI DMR-1631282, DOE award DE-SC0021230, and AFOSR grant FA9550-20-1-0148.
1. Bryan, I., Bryan Z., Washiyama, S. et al. *Appl. Phys. Lett.* **112**, 062102 (2018)
2. Fan, Z., Lin J., and Jiang H., in Quantum Sens. Nanophotonic Devices IV, edited by M. Razeghi and G.J. Brown (2007), p. 64791I.
3. Cho, Y., Chang, C., Lee, K., et al. *Appl. Phys. Lett.* **116**, 172106 (2020)
4. Lee, K., Cho, Y., Schowalter, L., et al. *Appl. Phys. Lett.* **116**, 262102 (2020)

2:15 PM J05
(Student) Growth of High Quality 350nm-Thick InGaN Films on N-Polar GaN Substrates by Plasma-Assisted Molecular Beam Epitaxy Sandra M. Diez[1], Kamruzzaman Khan[1], Christian Wurm[2], Umesh Mishra[2] and Elaheh Ahmadi[1]; [1]University of Michigan–Ann Arbor, United States; [2]University of California, Santa Barbara, United States

A parametric analysis of growth conditions on the structural properties of N-Polar InGaN films was studied. Three series of N-polar InGaN films were grown on bulk GaN substrates by plasma-assisted molecular beam epitaxy (PAMBE) to study the effect of substrate temperature, Ga, and In fluxes. For all series, the surface morphology was measured by atomic force microscopy (AFM), and the composition and strain were determined by high resolution X-ray diffraction (HRXRD) and XRD reciprocal space mapping (RSM). All the samples in this study were 350 nm thick. First, a series of samples was grown at temperatures varying from 620 °C to 690 °C. The Ga flux for all samples in this series was kept at 3.8E-7 Torr and the In flux was increased by temperature to ensure metal-rich growth conditions. The surface morphology improved significantly by increasing the temperature, and the indium content was reduced as expected. The samples grown at 670 °C and 690 °C showed surprisingly smooth surface morphologies with surface roughness <0.7 nm which has never been reported before on such thick InGaN films. An In content of 16.5% and 13.6% was measured on samples grown at 670 °C and 690 °C, respectively. These temperatures are significantly higher than growth temperatures (<600 °C) typically used for the growth of InGaN films on Ga-polar GaN.
In the next step, samples were grown with In fluxes of 3E-7 Torr and 4E-7 Torr. The Ga flux was kept at 3.8E-7 Torr and both samples were grown at a substrate temperature of 670 °C. Both samples showed step flow growth and low surface roughness despite the large difference in In flux. Nonetheless, increasing the In flux from 3E-7 Torr to 4E-7 Torr resulted in an improved surface morphology, and increased In composition and strain relaxation. These results indicate that the In flux can be tuned within an ample window to obtain specific sample properties.
For the last series, three samples were grown at 660 °C and with In flux of 4E-7 Torr, while the Ga flux was varied from 3.2E-7 Torr to 3.6E-7 Torr. The surface morphology degraded with decreasing Ga flux. The Indium composition simultaneously increased due to the limited availability of Ga during growth. This indicates that the strain caused by increased In incorporation is relaxed by generating dislocations which in turn results in further increase in In incorporation as relaxation proceeds (the In pulling effect).

SESSION K: Group III-Nitride MOCVD and Characterization
Session Chairs: Theeradetch Detchprohm and Christian Wetzel
Wednesday Afternoon, June 23, 2021

3:00 PM K01
(Student) Characterization of Regrown Interface in Ga-Polar c-Plane GaN with Diverse Growth Interruptions Maliha Noshin, Rohith Soman, Xiaoqing Xu and Srabanti Chowdhury; Stanford University, United States

Vertical gallium nitride (GaN) devices [1] are strong candidates for next generation power electronics [2]. Such vertical devices require epitaxial regrowth of GaN [3,4]. These regrown devices typically exhibit electric field peak and hence higher leakage current than continuously grown ones due to impurities at the regrowth interfaces [3,4]. However, to-date very few studies [3] have been performed on the characterization of such impurities, thus inspiring an in-depth investigation of the regrowth interfaces in GaN. Hence, in this study we perform a detailed characterization of the impurities at regrowth interface of Ga-polar GaN on c-plane sapphire substrate under various growth interruptions. To analyze the impact of impurities at the regrowth interface of vertical GaN device, we performed device simulation using Atlas Silvaco. First, for an impurity free pn-junction diode under 400V reverse bias, the simulated E field shows uniform distribution in the n-GaN region without any local peak. Next, a regrown pn-junction was simulated with an ionized donor of 2×10^{13} cm^{-2} at the interface of the p and n regions to mimic the anticipated regrown interface. This resulted in ~50% higher peak E field compared to the E field in first simulation. This peak E field will lead to higher leakage current and premature breakdown of the device further delineating the importance of a thorough investigation of the regrown interfaces in GaN. This interfacial impurity impacts 3-terminal devices even more acutely, leading to parasitic channels that are not controlled by the gate. In this context, an unintentionally doped (UID) Ga-polar GaN sample has been grown with epitaxial regrowth on a c-plane sapphire substrate using MOCVD growth technique. Epitaxial growth and regrowth were performed with a growth rate of 2.55 µm/h (using NH_3: 6000 sccm, TMGa: 58.5 sccm, temperature: 1230°C and pressure: 250 mbar). AFM images for as-grown and regrown GaN show an RMS surface roughness of 0.172 nm and 0.229 nm, respectively. To characterize the regrowth interface, we performed different growth interruptions (exposing the regrowth interface to air or in glovebox for varying amount of time) after 1.2 µm of UID GaN growth. The regrown surfaces are characterized using secondary ion mass spectrometry (SIMS). The SIMS profiles reveal the strong incorporation of silicon (Si) impurities at the regrowth interface when exposed to air or glovebox. Moreover, ~1.9× higher peak Si impurity concentration is measured for 10 minutes exposure in air (1.42×10^{17} cm^{-3}) vs. in glovebox (7.57×10^{16} cm^{-3}) pointing at the inevitably higher impurity incorporation when exposed to air. Even a very short exposure of 2 minutes in the glovebox (filled with nitrogen at a higher pressure than atmosphere) resulted in a peak Si concentration of 2.66×10^{16} cm^{-3} delineating the strong Si incorporation from the environment during the growth interruption. However, the carbon (C) and oxygen (O) impurity concentrations remained relatively unchanged in all cases compared to their background concentration. This is in contrast with the m-plane GaN regrowth where both O and Si peaks have been shown to be dominant [3]. Our result confirms that a longer time exposure either in air or in glovebox increases the Si peak. Also, higher Si peak is observed for exposure in air vs. glovebox, consistent with the finding for m-plane GaN regrowth [3]. In summary, we demonstrated that Si impurity at the regrowth interfaces of GaN structures are almost inevitable during the regrowth process. This study would bring fundamental understanding of the regrowth interfaces needed to address challenges for vertical GaN-based power electronics.
Ref: [1] Kim, H. *et al*. *J. Appl. Phys.* **107**, 113707 (2010). [2] Hu, J. *et al. Mater. Sci. Semicond. Process.* **78**, 75–84 (2018). [3] Stricklin, I. *et al.* in *Proc.SPIE* **10754** 1075402 (2018). [4] Fichtenbaum, N. A. *et al*. *J. Cryst. Growth* **310**, 1124–1131 (2008)

3:15 PM K02
(Student) Planar Porosification of N-Polar GaN for Regrowth of Smooth GaN Films Henry Collins, Islam Sayed, Wenjian Liu, Nirupam Hatui, Shubhra S. Pasayat, Aidan A. Taylor, Weiyi Li, Stacia Keller and Umesh Mishra; University of California, Santa Barbara, United States

The porosification of GaN has emerged as a promising method for growing strain relaxed III-Nitride films for optoelectronic and electronic devices. Growth of InGaN and AlGaN with strain relaxation of up to 71% and 85%, respectively, on Ga-polar porous GaN tile templates have been reported[1,2]. These advancements in strain-relaxed III-Nitride growth enable further

improvement in electronic device performance. For example, an InGaN/GaN High Electron Mobility Transistor (HEMT) fabricated on a porous GaN buffer demonstrated a 9.6% increase in 2D electron gas mobility compared to a similar HEMT fabricated on a standard GaN buffer[3]. With these promising results shown for the Ga-polar orientation, attention should now be turned to N-polar GaN. The benefits of fabricating mm-wave and high-power HEMTs on N-polar GaN include: reduced ohmic contact resistance, a stronger natural back-barrier, and greater scalability[4]. Recently, an N-polar HEMT exhibited a record W-band power density of 8.84 W/mm at 94 GHz[5]. The inherent benefits of the N-polar orientation encourage development of a process for epitaxial growth of strain-relaxed III-Nitrides atop N-polar porous GaN. This investigation was directed towards the optimization of the surface porosification conditions of planar N-polar n+ GaN allowing the regrowth of a smooth 100 nm unintentionally doped (UID) GaN film on top of the porous layer. Porosification was carried out via electrochemical (EC) etching of Ti-contacted GaN:Si in oxalic acid. The pore morphology at different anodization voltages was evaluated by SEM, while AFM was used to examine the surface morphology of the regrown GaN films. For a Si doping of 4.5 x 10^{18} cm^{-3}, an increase in anodization voltage up to 17 V optimized the pore shape (analyzed by FIB-SEM) and suppressed hexagonal hillock formation and enabled the regrowth of smooth GaN. Finally, 100 nm of $In_{0.07}Ga_{0.93}N$ was grown atop the 100 nm regrown GaN. AFM scans show no degradation of surface quality, encouraging further investigation of InGaN growth and strain relaxation on these porous N-polar GaN templates. A comprehensive analysis of the relationship between anodization voltage, pore morphology, and the resulting regrown film quality will be presented at the conference. Furthermore, strain-relaxation experiments involving InGaN regrowth on tiles fabricated on N-polar porous GaN templates will be presented.

References
[1] S.S. Pasayat, C. Gupta, Y. Wang, S.P. DenBaars, S. Nakamura, S. Keller, and U.K. Mishra, Materials **13**, 213 (2020).
[2] S.S. Pasayat, N. Hatui, W. Li, C. Gupta, S. Nakamura, S.P. Denbaars, S. Keller, and U.K. Mishra, Appl. Phys. Lett. **117**, 062102 (2020).
[3] W. Li, S.S. Pasayat, M. Guidry, B. Romanczyk, X. Zheng, C. Gupta, N. Hatui, S. Keller, and U.K. Mishra, Semicond. Sci. Technol. **35**, 075007 (2020).
[4] M.H. Wong, S. Keller, S.D. Nidhi, D.J. Denninghoff, S. Kolluri, D.F. Brown, J. Lu, N.A. Fichtenbaum, E. Ahmadi, U. Singisetti, A. Chini, S. Rajan, S.P. DenBaars, J.S. Speck, and U.K. Mishra, Semicond. Sci. Technol. **28**, 074009 (2013).
[5] B. Romanczyk, X. Zheng, M. Guidry, H. Li, N. Hatui, C. Wurm, A. Krishna, E. Ahmadi, S. Keller, and U.K. Mishra, IEEE Electron Device Letters **41**, 349 (2020).

3:30 PM K03
Scanning Spreading Resistance Microscopy Characterization of Selective Doped GaN Epitaxial Layer Grown by MOCVD
Sizhen Wang, Bingjun Li and Jung Han; Yale University, United States

Dopant characterization of selective doped GaN epitaxial thin film is very critical to reveal the Mg atom distribution and to understand the electrical performance of formed lateral GaN p-n diode. This GaN p-n junction is the key building block to prepare edge termination and tune electrical field distribution for III-nitride based power device technology. Usually Secondary Ion Mass Spectrometry (SIMS) was used for dopant profile analysis, but this technique can not provide two-dimensional dopants or conductivity map. We applied the Scanning Spreading Resistance Microscopy (SSRM) to investigate the GaN p-n junction, which was prepared by selective area epitaxy growth of Mg-doped GaN in MOCVD reactor. The diagram and cross-section SEM image of regrown GaN diode was presented in Figure (a) and (b). As an AFM-based technique, SSRM detects the resistance of current spreading layer just below the tip-semiconductor contact region. Based on the Schottky barrier height between the probe tip and the underlaying GaN layers, two different voltages were applied to the trench region: -1.0 V for n-GaN or UID GaN, and +3.0 V bias for p-GaN. By applying proper tip deflection force, two-dimensional mapping of Log(R) was successfully obtained to delineate the junction profile, as shown in Figure (c) and (d). The cutline plots of Log(R) at site 1 and site 2 were shown in Figure (e), clear p-type conductivity variation was observed in vertical direction, and unintentional impurity doping at epitaxial growth interface was also detected, which was related to outgassing of mask. Effective doping concentration can be further extracted with reference to the SSRM doping calibration curve.

3:45 PM K04
(Student) The Origins of Large Surface Step Features of Homoepitaxial GaN Grown on Dot-Core GaN Substrates
Michael E. Liao[1], Kenny Huynh[1], Yekan Wang[1], Andrew Allerman[2] and Mark Goorsky[1]; [1]University of California, Los Angeles, United States; [2]Sandia National Laboratories, United States

X-ray topography and surface imaging techniques were employed to study the origins of surface step formation on homoepitaxial GaN grown on c-plane dot-core GaN substrates. We observe features with ~100 µm step lengths and ~400 nm step heights after growth. Step-bunching has been reported in the literature for GaN epitaxially grown on miscut substrates,[1,2] but the dimensions of the features are significantly smaller – with step lengths of ~0.2 µm and step heights of ~1-2 nm. Furthermore, there does not seem to be any reports in the literature of step formation for GaN growth on dot-core substrates. In this study, 11 µm of Metal Organic Chemical Vapor Deposition GaN was grown on 2-inch c-plane dot-core GaN substrates. Prior to growth, no step features were present on the as-received polished bare substrates. After the 11 µm growth, there were parts of the surface that appeared optically hazy and other parts that were specular. The hazy regions corresponded to a high density of stepped features bunched together that obscured the origins of these features. Within the specular regions of the surface, we observed surface stepped features confined within a ~0.15 mm radius all spaced apart by ~0.8 mm; the cores from the underlying dot-core substrate are also separated by ~0.8 mm. Both optical images and profilometer measurements revealed that the step features nucleate at the centers of the cores. Our previous work on dot-core GaN substrates used topography to show that the cores consist of highly distorted and tilted lattice planes.[3] These large step features nucleate at the centers of these cores due to the high lattice tilt distortions, analogous to the step bunching formation of GaN grown on vicinal substrates, and coalesce with increasing GaN thickness during epitaxial growth, which eventually gives rise to the optically hazy appearance. X-ray topography images were generated at the 1-BM beamline of the Advanced Photon Source, Argonne National Laboratory using an X-ray energy of 8.05 keV to measure the (11$\underline{2}$4) GaN reflection in the glancing incidence geometry to generate rocked images (step size of 0.012°). The topography images were then used to correlate with the surface morphology observed with optical images and profilometer measurements. The cores from GaN dot-core substrates enables us a pathway to engineer and fundamentally study these structural defects with GaN growth.

References:
1. H. Fujikura, et al., Appl. Phys. Lett., 113, 152101 (2018).
2. X.Q. Shen, et al., J. of Crys. Growth, 300, 75 (2007).
3. M.E. Liao, et al., ECS Trans., 98(6), 15 (2020).

This research was supported through the ARPA-E PNDIODES program under contract DE-AR0001116 at UCLA. This research used resources of the Advanced Photon Source, a U.S. Department of Energy (DOE) Office of Science User Facility operated for the

DOE Office of Science by Argonne National Laboratory under contract no. DE-AC02-06CH11357.

4:00 PM K05
(Student) Comparison of AlN/GaN Heterostructures Grown at Low Temperatures with Ammonia or Dimethylhydrazine via Metalorganic Chemical Vapor Deposition Caroline E. Reilly, Nirupam Hatui, Shuji Nakamura, Steven DenBaars and Stacia Keller; University of California, Santa Barbara, United States

Continuously improving results for electronic devices comprised of III-nitride materials, such as high-electron mobility transistors (HEMTs), have led to increasing interest in the integration of the nitrides with other materials systems. In particular, the heterogenous growth of nitride materials on foreign substrates would enable new device designs and integration schemes, where currently integration would largely be conducted post-growth via processing-based transfer techniques. Direct growth on other materials would require the growth conditions used to be compatible with constraints of the substrates, including any temperature sensitivity. Many processed wafers or other potential substrates will degrade at temperatures above ~500 °C, while high-quality AlN and GaN are typically grown at temperatures above 1000 °C by metalorganic chemical vapor deposition (MOCVD). Other growth techniques such as molecular beam epitaxy can be used to grow high-quality nitrides at reduced temperatures, however MOCVD has the advantage of being more scalable and highly used in industry. In this work, low temperature (LT) MOCVD growth of AlN and GaN was conducted using NH_3 and dimethylhydrazine (DMHy) as N-precursors, with a specific focus on the analysis of AlN/GaN heterostructures for use in electronic applications. Growth rates were determined as a function of growth temperature using trimethylaluminum and triethylgallium as group III precursors. Semiinsulating GaN-on-sapphire was used as a base layer for the remaining LT growth experiments and films were characterized using Hall measurements, X-ray diffraction (XRD), transmission electron microscopy (TEM), and atomic force microscopy (AFM). The thermocouple-read growth temperature was 550 °C, with the expected surface temperature being ~50 °C colder. A flow-modulation epitaxy (FME) scheme was utilized, which involved pulsing group III precursors to enhance surface adatom migration. Previous studies also showed lower C and O impurities when an FME scheme was employed for the deposition of LT GaN using NH_3. LT AlN was deposited via FME on the semiinsulating GaN base layers using NH_3, DMHy, and a combination of N-precursors. Electronical characterization via Hall measurements showed that samples grown with either DMHy or both DMHy and NH_3 were resistive, whereas the AlN sample grown with NH_3 showed the formation of a two dimensional electron gas (2DEG) with a charge of 3.7 x 10^{13} cm^{-2} and a mobility of 540 cm^2/Vs, comparable to previous reports for MBE grown samples. For the sample grown with only DMHy, an ω-2θ scan about the (004) GaN peak showed no AlN layer peak. In contrast, the samples in which NH_3 or both precursors were used showed XRD signals. TEM of the DMHy sample indicated that the AlN layer was polycrystalline, explaining the lack of signal from XRD. In the case of the best LT AlN film, grown with NH_3, crystalline films were observed via TEM. LT FME GaN growth, optimized using NH_3 in a separate study, was also attempted using DMHy. However, GaN films were not obtained under these conditions. Most likely, the vapor pressure of DMHy in the gas phase was too low to satisfy GaN growth because of the higher equilibrium pressure of nitrogen over GaN compared to AlN. A full LT heterostructure of GaN/AlN was grown using NH_3. The Hall measurements showed a charge of 1.6 x 10^{13} cm^{-2} and a mobility of 230 cm^2/Vs. The charge was less than half that of the charge found for the LT AlN grown directly on GaN base layers and was likely compensated by a higher level of impurities in the LT GaN. The decrease in mobility may be attributed to the smaller distance between steps in the LT GaN as compared to the GaN base layers, effectively increasing the interface roughness seen by the 2DEG. Additional film characterization using Hall, XRD, TEM, and AFM will be presented in the talk. This work is partially supported by the Solid State Lighting and Energy Electronics Center and Intel Corporation.

SESSION L: Properties of 2D Materials
Session Chairs: Mona Ebrish and James Edgar
Wednesday Afternoon, June 23, 2021

1:15 PM L01
(Student) The Impact of Localized Hot Spots on the Raman Response of Monolayer MoS2 Akshay Balgarkashi, Mirjana Dimitrievska, Jin Jiang, Shreyas Joglekar, Didem Dede, Mitali Banerjee and Anna F. Morral; EPFL, Switzerland

Transition-metal dichalcogenides (TMDs) have attracted a lot of interest owing to their direct bandgap as they are reduced down to thickness of a monolayer (ML) [1]. Thus, they have potential for numerous applications in electronic and optoelectronic devices such as transistors, photodetection and sensing [2]. MoS_2 is probably one of most investigated TMD material due to the ability to tune its band structure with applied strain or electric field [3, 4]. As a naturally occurring crystalline mineral, tuning the properties of MoS_2 as a representative TMD material provides further insights into the effects of strain and doping on its properties before moving on to investigate rare and more complex TMD materials. The strain and doping in MoS_2 can be modulated in various ways such as mechanical bending [5], use of different substrates [6] or by introducing a metal- MoS_2 interface [7]. A metal-semiconductor interface provides an interesting platform to investigate the plasmon-exciton interactions and the charge transfer mechanism between the metal and the semiconductor. In this work, we create plasmonic hot spots between gold nanoparticles to modify the Raman and luminescence response of ML MoS_2. Nominal 2, 4 and 7 nm of Au and 2nm of Al were evaporated on SiO_2/Si (oxidized silicon). Au and Al do not wet well SiO_2, resulting in the formation of nanoparticles. Au and Al nanoparticle films exhibit a plasmonic band centered around 550 nm and 300 nm respectively. Plasmonic hot spots are created upon excitation within the band of plasmonic response of the nanoparticles. Monolayers of MoS_2 were mechanically exfoliated directly on the nanostructured metallic layers and on SiO_2/Si as a reference sample. Raman spectroscopy and photoluminescence were performed to characterize the optical response of the MoS_2 to the plasmonic hot spots and compared to the reference sample. By varying the thickness of the Au film from 2nm to 7nm, we observe a shift and splitting of the E^1_{2g} Raman modes into E^1_{2g} and E^1_{2g}'. The A_{1g} mode also red shifts. The shift and splitting are only observed when the plasmonic resonance is excited during the optical measurements, indicating a plasmonic hot spot effect.
We also investigate the effect on the photoluminescence (PL). In comparison to the reference ML MoS_2, the PL intensity from the ML MoS_2 on Au is drastically reduced. As the thickness of the Au film increases, the PL emission from A and B excitonic peaks is quenched until the B-exciton is no longer seen for ML MoS_2 on a 7nm Au film. This can be explained by the electron transfer from MoS_2 to Au, which hinders the recombination of electron−hole pairs created by the photoexcitation. As the work function of MoS_2 is lower than that of Au, the electrons in the excited state of MoS_2 transfer to Au, leaving a hole behind, which causes p-doping in MoS_2. The charge transfer phenomena, along with the strain effects on optoelectronic properties of MoS_2 MLs will be presented and dicussed. This work shows the potential of combining plasmonics with 2D materials to modify their optical and phonon response.
[1] Choi, W. et al. Mater. Today 20, 116–130 (2017).
[2] Lorenz, T., Joswig, J.-O. & Seifert, G. 2D Mater. 1, 011007 (2014).
[3] Castellanos-Gomez, A. et. Al. Nano Lett. 13, 5361–5366 (2013).
[4] Chakraborty, B. et al. Phys. Rev. B 85, 161403 (2012).
[5] Conley, H. J. et al. Nano Lett. 13, 3626–3630 (2013).
[6] Sun, Y., Wang, R. & Liu, K. Appl. Phys. Rev. 4, 011301 (2017).

[7] Moe, Y. A., Sun, Y., Ye, H., Liu, K. & Wang, R. ACS Appl. Mater. Interfaces 10, 40246–40254 (2018).
Acknowledgement: This work is part of a project that has received funding from the European Union's Horizon 2020 research and innovation programme under the Marie Sklodowska-Curie grant agreement No 765075 (Project LIMQUET). Funding from Swiss National Science Foundation (project 196948) is also acknowledged.

1:30 PM L02
(Student) Differential Gene Expression in C2C12 Cells Due to Scaffold Structure-Property-Processing-Performance Correlations Lynn Karriem[1], Stephanie Frahs[1], Domenica Convertino[2], Marissa Hondros[1], Twinkle Pandhi[1], Ashita Chandnani[1], Harish Subbaraman[1], Camilla Coletti[2], Julia Oxford[1] and David Estrada[1]; [1]Boise State University, United States; [2]Instituto Italiano de Tecnologia, Italy

Graphene – an atomically thin layer of carbon atoms arranged in a hexagonal lattice – has gained interest as a bioscaffold for tissue engineering for its exceptional mechanical, electrical, and thermal properties[1-5]. Graphene's structure and properties– tightly coupled to synthesis and processing conditions[4]– are thought to influence biomolecular interactions at the graphene-cell interfaces. In this study, C2C12 cells, a multipotent mouse myoblast cell line, were grown on graphene bioscaffolds with specific structure–property–processing–performance (SP3) correlations. We found that SP3 correlations significantly influenced C2C12 differentiation, myotube formation, and gene expression, suggesting that graphene–cell interfaces can be engineered to control biomolecule structure and function in adherent cells. The experiments performed are the first to make a direct comparison on scaffold SP3 correlations and their impact on genetic expression of multipotent myoblast cells. **METHODS:** Chemical vapor deposition (CVD) grown graphene film, transferred to quartz glass slides, resulted with surface roughness (Ra) of 2.37 nm and graphene ink– produced by solvent assisted exfoliation– was printed using a Dimatix inkjet printer onto glass coverslips (Ra of 10.0 nm). Epitaxial graphene on SiC wafers, produced by Si sublimation (Istituto Italiano de Tecnologia, Pisa, Italy) (Ra of 2.24 nm). Prior to cell integration, cell attachment was facilitated with agarose gel applied to the edges of all graphene bioscaffolds and corresponding control bioscaffolds (quartz glass, glass coverslips and SiC wafers). C2C12 cells, maintained in a humidified incubator at 37°C and 5% CO_2, were seeded onto the scaffolds at 1.3 x 10^4 cells/cm^2 in Dulbecco's Modified Eagle Medium (DMEM) with 10% fetal bovine serum (FBS) and 1% penicillin/streptomycin (P/S). Cell growth and proliferation were monitored by transmitted light microscopy with images captured to study cell morphology. Gene expression patterns for each bioscaffold were analyzed for muscle myogenesis via qRT-PCR using a PCR array for muscle myogenesis and myopathy. Preliminary results show differences in cell morphology varied in a manner dependent upon the specific bioscaffold used. Myotube-like structures were evident in the control, CVD and epitaxial graphene (Fig.1A). Each of the three graphene bioscaffolds resulted in a unique overall genetic profile related to muscle myogenesis. However, four up-regulated genes were common to all biosaffolds when compared to their control. These genes are as follows: dystrophin (Dmd), myostatin (Mstn), leptin (Lep), pyruvate dehydrogenase kinase isoenzyme 4 (Pdk4) and Utrophin (Utm) (Fig. 1B). **DISCUSSION:** This preliminary work successfully shows that epitaxial, CVD, and printed graphene bioscaffold's SP3 correlations impact the gene expression of C2C12 cells in culture. Each graphene bioscaffold presented with different and unique muscle gene expression profiles when compared to the control. The different morphologies of the cells as viewed in the transmitted light microscopy images confirms that the C2C12 cells grown on each bioscaffold, are uniquely different than the control. The following biomarkers: dystrophin, myostatin, leptin, pyruvate dehydrogenase kinase isoenzyme 4, and Utrophin were all upregulated in each of the graphene bioscaffolds. Epitaxial graphene shows the most genes upregulated that correlate to the muscle genotype followed by printed graphene and CVD graphene which showed the least number of upregulated genes relating to muscle (Fig. 1C).
1. Nayak et al., ACS Nano., 2011. 2. Li et al., Sci Rep., 2013. 3. Krueger et al., ACS Biomaterials Science & Engineering, 2016. 4. Novoselov et al., Nature, (2012): 192-200. 5. Nieto et al., Advanced Functional Materials, 2015.
Support kindly provided by NIGMS under P20GM103408 and P20GM109095 and NSF under 0619793 and 0923535

1:45 PM L03
Improving Exciton Valley Polarization by Scattering Yueh-Chun Wu[1], Kenji Watanabe[2], Takashi Taniguchi[2] and Jun Yan[1]; [1]University of Massachusetts Amherst, United States; [2]National Institute for Materials Science, Japan

Scattering in a device typically causes performance degradation. Here we experimentally demonstrate a counter-intuitive enhancement of device performance induced by scattering. In monolayer MoS_2, we show that scattering can markedly improve its excitonic valley polarization. We report seven- and twelve-folds of valley polarization enhancement due to thermally activated and charge doping induced scattering respectively. This interesting effect is attributed to the reduction of valley pseudospin precession arising from rapid modulation of exciton momentum and concomitant exchange interaction field, which can be viewed as a type of motional narrowing. Our work advances understanding of valley depolarization mechanisms in transition metal dichalcogenide atomic layers and illustrates a novel approach for controlling and improving valleytronic devices.

2:00 PM L04
Berry Curvature Memory Enabled by 2D Ferroelectric Semimetals Jun Xiao[1,2] and Aaron Lindenberg[1,2]; [1]Stanford University, United States; [2]SLAC National Accelerator Laboratory, United States

Quantum materials with novel phases of matter are the key building blocks of energy efficient quantum electronics and powerful quantum computation. Exploiting control of those materials is fascinating to achieve new functionalities and information algorithm in future quantum devices. Quantum nanomaterials like layered materials, has revealed many exotic properties such as extremely large magnetoresistance (MR)[1], type-II Weyl electron transport and diverging Berry curvature[2,3]. On the other hand, the nature of layered materials leads to ultra large tunability of physical properties via external stimuli. Here we report the manipulation of quantum geometrical properties in a ferroelectric semimetal (WTe_2) belonging to layered Weyl materials. With such control and various characterization means, we observed substantial modulation in optical and electrical responses associated the unique stacking orders in such exotic ferroelectric semimetal. Further nonlinear Hall transport measurements show the observed transitions are locked with the variation of topological and geometrical property. Our findings demonstrate a new low-energy-cost, electrically controlled topological memory in the atomically thin limit[4].
1. Ali, M. N. *et al.* Large, non-saturating magnetoresistance in WTe2. *Nature* **514**, 205–8 (2014).
2. Soluyanov, A. A. *et al.* Type-II Weyl semimetals. *Nature* (2015). doi:10.1038/nature15768
3. Armitage, N. P., Mele, E. J. & Vishwanath, A. Weyl and Dirac semimetals in three-dimensional solids. *Rev. Mod. Phys.* **90**, 015001 (2018).
4. Xiao, J. *et al.* Berry curvature memory through electrically driven stacking transitions. *Nat. Phys.* **16**, 1028–1034 (2020).

2:15 PM L05
(Student) Large-Area Arrays of Short-Wave-Infrared Graphene Plasmonic Resonators Exhibiting Strong Non-Local and Electron Quantization Effects Joel F. Siegel, Jonathan H. Dwyer, Anjali Suresh, Nathaniel Safron, Margaret Fortman, Chenghao Wan, Jonathan W. Choi, Wei Wei, Vivek Saraswat, Wyatt A. Behn, Mikhail A. Kats, Michael S. Arnold, Padma Gopalan and Victor W. Brar; University of Wisconsin–Madison, United States

Graphene plasmonic resonances have been broadly studied in the terahertz and mid-infrared (MIR) ranges because of their electrical tunability and large confinement factors, which can enable dramatic enhancement of light-matter interactions, among other optoelectrical applications. Plasmonic resonances occur in graphene when it is patterned into nanostructures (e.g. ribbons) which confine the graphene plasmons and enables coupling to free-space radiation. For nanostructures with dimensions greater than 15 nanometers, the characteristic scaling laws of the graphene plasmons are well approximated by the local model of graphene's conductivity. However, we experimentally demonstrate that those scaling laws change for structures smaller than 15 nanometers due to non-local and quantum effects in the graphene. Those changes blue-shift the frequencies of the graphene plasmons, pushing their operational range from the MIR into the short-wave-infrared (SWIR). We realize these effects in centimeter-scale arrays of graphene nanoribbons as narrow as 12 nanometers that are created using a novel, bottom-up block copolymer lithography method. The devices we create exhibit tunable plasmonic resonances at wavelength as short as 2.2 μm, almost double the energy of the previous experimental works. Furthermore, the confinement factors of our resonators reach 137 ± 25, which is amongst the largest reported in literature for any type of 2D optical resonator. The combined SWIR response and large confinement factors coupled to a scalable and efficient fabrication method makes these graphene nanostructures an attractive platform to explore next-generation optoelectrical devices and strongly enhanced spontaneous emission in the SWIR.

2:30 PM BREAK

3:00 PM L06
(Student) Enhanced Multiexciton Formation by an Electron-Hole Plasma in 2D Semiconductors Matthew C. Strasbourg[1], Cory Johns[1], Zoe Nobel[1], Thomas Darlington[2], Emauil Yanev[2], James Hone[2], P. James Schuck[2] and Nicholas J. Borys[1]; [1]Montana State University, United States; [2]Columbia University, United States

Transition metal dichalcogenide (TMD) semiconductors are layered van der Walls materials that exhibit exceptional optoelectronic properties in monolayer form. Their atomically thin nature and reduced long-range dielectric screening make them ideal systems in which to study many-body electronic states. Notably, excitonic many-body phenomena govern the light-matter interactions in TMD semiconductors and open up new possibilities for novel optoelectronic devices, including new classes of quantum light sources. Thus, understanding the rich suite of many-body phenomena in these systems is motivated by potential applications in on-chip optoelectronics and by the insights that can be gained into the fundamental interactions that govern TMD material properties. Here, the dynamics of several higher-order excitons including trions, biexcitons, and charged biexcitons in monolayer-WSe_2 are probed using temperature-, energy-, and power-dependent time-resolved optical spectroscopy. We find that the formation of multiexciton complexes is enhanced by increasing the optical excitation energy for a given density. This enhancement is attributed to formation from an electron-hole plasma which generates 200% more multiexcitons than a lower-energy exciton gas. We further find that the multiexciton enhancement is robust over many samples and diminished with increasing temperature. These studies reveal a complex interplay between the multiexcitons and single-excitons that depends on both the density and excitation energy of the initial exciton population and open new doors to a number of applications such as entangle photon pair production and lasing, highlighting the importance of understanding the formation and relaxation dynamics of the rich manifold of excitons in order to leverage 2D semiconductors for advanced technologies.

3:15 PM L07
Dielectric Effects on Exciton Emission of MoS_2/P(VDF-TrFE) Heterostructure—A Correlated Mapping Study Joon-Seok Kim, Jack N. Olding, Emily A. Weiss and Lincoln Lauhon; Northwestern University, United States

Semiconducting two-dimensional (2D) materials possess intriguing optoelectronic properties owing to the unique layered confined structure, such as strong light-matter interaction and large exciton binding energies. Especially, their excitonic binding energies far exceeding thermal energy will allow for room-temperature optoelectronic applications, such as excitonic computing applications and optical interconnects. It is therefore of significant importance to engineer excitonic properties and dynamics. The most widely used approaches to modulate the semiconducting 2D materials' excitonic dynamics include modifying the dielectric environment,[1] applying strain,[2] and gate-tuning.[3] In this study, we study modulation of exciton dynamics in monolayer MoS_2 via dielectric Coulomb engineering and local strain by correlating photoluminescence (PL) mapping and scanning probe microscopy characterization. A mixed-dimensional heterojunction (MDHJ) was fabricated consisting of monolayer MoS_2, sub-μm 0-dimensional P(VDF-TrFE) copolymer islands, and hBN. An optical microscope image, AFM topography map, and side view schematic of the MDJS are showing in Figures 1a, 1b, and 1c, respectively. Photoluminescence (PL) maps were obtained; A and B exciton emissions were fitted to Gaussians for parameter extraction (Figure 2a and 2b) and correlated with the topography data (Figure 2c). A clear blueshift of A exciton emission energy was observed on 1L-MoS_2 on P(VDF-TrFE) islands with respect to 1L-MoS_2 on hBN (Figure 2b). MoS_2 on the polymer islands (red scatter plot; draped over polymer islands) showed a noticeable blueshift of ~3 meV compared to that of planar MoS_2 on hBN (blue scatter plot) (Figure 2c). The bandgap increase can be attributed to the band structure renormalization and binding energy decrease due to the strong dielectric screening of the P(VDF-TrFE) substrate ($\varepsilon_r \approx 13$).
[1] Effects of dielectric environment and local strain on excitonic dynamics were examined by analyzing the A and B exciton intensity ratio; a high A-to-B intensity ratio is a sign of low nonradiative recombination.[4] Regions of increased A/B ratio (up to 2x) correlate well with the P(VDF-TrFE) islands locations (Figure 3a). Suppressed B exciton from the MoS_2/P(VDF-TrFE) region contributes to the majority of the A/B ratio enhancement. Moreover, the B intensity showed a negative correlation with height, suggesting that large substrate screening combined with higher strain from the morphology enhances the intravalley scattering from the B exciton state to the A exciton state (Figure 3b). The A and B exciton energy difference map (Figure 3c) demonstrates that in contact with P(VDF-TrFE), the spin-orbit coupling-induced valence band splitting reduces, which may lead to an increased intravalley scattering rate. The correlation of PL and topography map revealed that the substrate dielectric screening and local strain affect the exciton dynamics of monolayer MoS_2.
[1] A. Raja *et al.*, "Coulomb engineering of the bandgap and excitons in two-dimensional materials," *Nat. Commun.*, vol. 8, no. May, p. 15251, May 2017.
[2] A. Castellanos-Gomez *et al.*, "Local Strain Engineering in Atomically Thin MoS 2," *Nano Lett.*, vol. 13, no. 11, pp. 5361–5366, Nov. 2013.
[3] Z. Qiu *et al.*, "Giant gate-tunable bandgap renormalization and excitonic effects in a 2D semiconductor," *Sci. Adv.*, vol. 5, no. 7,

p. eaaw2347, Jul. 2019.
[4] K. M. McCreary, A. T. Hanbicki, S. V. Sivaram, and B. T. Jonker, "A- and B-exciton photoluminescence intensity ratio as a measure of sample quality for transition metal dichalcogenide monolayers," *APL Mater.*, vol. 6, no. 11, p. 111106, Nov. 2018.

3:30 PM L08
Surface Morphology and Composition of Hexagonal Boron Nitride Single Crystals Thermally Oxidized in Dry and Ambient Air Elisabeth Mansfield[1], Jason Holm[1], Neelam Khan[2], Michael Katz[1], Albert Davydov[1], Eli Janzen[3] and James H. Edgar[3]; [1]National Institute of Standards and Technology, United States; [2]Georgia Gwinnett College, United States; [3]Kansas State University, United States

Hexagonal boron nitride is frequently employed as a protective encapsulate for 2D materials due to its excellent thermal and chemical stability. Here we report on the effects of heating hBN single crystals in dry and ambient air with 30% relative humidity over temperatures from 400 °C to 1000 °C, for times of 20 minutes to 60 minutes. Using single crystals and variety microscopy methods (AFM, SEM, TEM) make it possible to establish hBN's oxidation behavior and ultimate thermal stability. At 900 °C, pits formed, with shapes that were characteristic of the oxidation environment. For example, oxidation in dry air produced irregular shaped pits that appeared to be formed in the trail of the oxide particles as they moved across the surface. In contrast, the pits formed in ambient air were hexagon shape, and the oxide particles were retained within the etch pit. Often, multiple steps exposing different layers of the hBN were seen in these etch pits. Thermodynamic calculations were performed to assess phase equilibria as a function of temperature and air humidity levels and to gain insights into the chemical species forming during oxidation. In dry air, the primary compound formed is B_2O_3, which melts at 450 °C, thus, it is liquid at > 500 °C process conditions. The presence of water from moisture in the air made additional chemical reaction product possible. For both cases, hBN loses mass during oxidation due to the volatile products formed. This study demonstrates that hBN oxidation occurs in a highly localized manner.

3:45 PM L09
(Student) Resistive Switching Properties of Single Layer h-BN Film with Different Electrodes Yuan Li, Yanwei He and Zhenjun Cui; University of California, Riverside, United States

The two-dimensional insulating material hexagonal boron nitride (h-BN) has attracted much attention for resistive switching applications, yet its performance needs to be improved. In this work we present our comprehensive study of the resistive switching behavior of monolayer h-BN films with different electrode materials. The h-BN monolayers and h-BN/graphene heterostructure are synthesized on Ni substrates using molecular beam epitaxy (MBE), then Ni and Al are deposited as top electrodes. Three types of resistive switching devices are fabricated, namely, the symmetric metal-insulator-metal (MIM) device with Ni/h-BN/Ni, asymmetric MIM devices with Al/h-BN/Ni, and metal-insulator-graphene devices with Ni/h-BN/graphene and Al/h-BN/graphene structures. The symmetric Ni/h-BN/Ni devices demonstrate a polarity independent bipolar resistive switching behavior, a good durance with up to 97 cycles at 100 mA compliance current, an average on/off window of 10^3, and a low set and reset voltage variability. The asymmetric Al/h-BN/Ni devices demonstrate polarity dependent set voltage, with the larger set voltage observed when positive bias is applied on Ni. The metal/h-BN/graphene devices demonstrate self-compliant current bipolar resistive switching. The formation of conductive filaments is attributed to the diffusion of metallic ions and trapped charges. Our work reveals the influence of electrodes on resistive switching devices and provide ways to control the resistive switching behavior of two-dimensional h-BN based devices.

4:00 PM L10
(Student) Characteristics and Tunability of Electron Emission Sources from Quasi-Freestanding Epitaxial Graphene Microstructures Daniel Lewis and Kevin Daniels; University of Maryland, United States

Graphene microstructures have been shown to exhibit controllable directional electron emission when carrying a current under an accelerating electric field. Through Phonon-Assisted Electron Emission (PAEE), graphene microstructures demonstrate electron emission at electric field intensities and lattice temperatures below what would be expected for carbon to demonstrate field emission or thermionic emission, respectively. Furthermore, such emissions tend to be out of the plane of the graphene microstructure, giving some control of the directionality of the emission current even before being directed with an applied electric field Thus far, such arrangements have tended to involve structural dimensions in the range of a handful of μm, commonly with CVD transferred graphene, flakes, or carbon nanotubes, with applied fields that can get up to the order of hundreds of kV/cm, and emission currents rarely exceeding a few nA. Herein are some examples of the characteristics and tunable variables demonstrated by multiple graphene structures with some dimensions up to cm, in fields below 4 kV/cm, and producing >1 μA emission currents. Quasi-freestanding epitaxial graphene on a silicon carbide substrate offers several advantages compared to transferred graphene or unzipped nanotubes, including lower defect density, greater structural integrity, ease of handling, and compatibility with simple photolithography fabrication techniques. The devices presented here were fabricated with a low-cost, wafer scalable, single-photomask process that does not require material transfer to a secondary substrate and is easily tailored to create variations in design parameters, which allowed multiple batches of devices to be rapidly manufactured with precise variations for the purpose of performance testing. The devices exhibited recognizable patterns of emission that seem to be influenced by several factors including, but not limited to shape and orientation, resistivity, input power, active time and on/off cycling frequency, device and substrate temperature, applied electric field, and both total device length and width dimensions (relative to current flow). Emission current seemed to show its most substantial dependence on input power, sometimes as much as doubling output with only a 25% increase in input; it is unknown if this relation holds for devices that vary other parameters alongside power input, necessitating further testing. The devices strongly imply a direct relationship between emission current density and device and substrate temperature, as some devices produced current outputs that exceeded measuring limits. Devices with larger dimensions also tended to produce more significant emission currents. However, the trends between increasing length and increasing width were not symmetrical: increasing device length (along the path of the input current) showed a stronger corresponding increase in output relative to % change in dimension than did changes in device width, and preliminary simulation results indicate both factors to have a roughly linear positive trend. While a general trend of larger dimensions and higher applied power levels tended to accompany higher emission currents, the output variations that may be attributed to other variables will allow for a broader range of device optimization parameters or tailoring of devices for specific purposes. Graphene microstructure electron sources may provide a means for device implementation in a 2D heterostructure environment or as a vehicle for further miniaturization of constructs requiring controllable electron emissions, such as electron microscopy or X-ray generation.

SESSION M: Thermal Transport
Session Chairs: Sukwon Choi and Samuel Graham
Wednesday Afternoon, June 23, 2021

1:15 PM M01
Direct Measurement of Thermal Conductivity of Gold from Meso- to Nano-Scale Joyce H. Anderson[1], Mark W. Holtz[1] and Sanjeeva Maithripala[2]; [1]Texas State University, United States; [2]University of Peradeniya, Sri Lanka

Conductors having at least one dimension at the nanoscale have properties that differ substantially from their bulk counterparts. In particular, electrical resistivity increases significantly when size is reduced while thermal conductivity (κ) decreases. These factors present a critical technological barrier to miniaturization, since the former increases self-heating when current is driven while the latter limits dissipation of that heat from device-active regions. Despite the prominent role of metallic nanostructures in current and future electronics and photonics, large gaps exist in understanding the influence of "size effects" on thermal characteristics at small dimensions. In particular, there is a paucity of direct measurements of thermal conductivity for technologically-relevant materials. This study focuses on development and test of a method for directly measuring κ for conducting nanofilms and nanowires. We report on design, fabrication, test, and application of this approach to 50 and 100 nm thick evaporated gold structures with lateral dimensions ranging from 74 to 720 nm, thereby spanning the nano- to meso-scale. Measurements are carried out at ambient room and 100° C temperatures, i.e., in the standard operating range of low-power electronics. A decrease in κ is observed as gold thickness is reduced. At large lateral width, corresponding to the microscale and analogous to thin films, κ values are found to be 200 and 280 W/mK for thicknesses of 50 and 100 nm, respectively (room temperature). These are to be compared with the accepted value of 317 W/mK for κ of bulk gold. In addition, as the width is reduced, for either thickness, a dramatic decrease in κ is observed beginning at ~ 300 nm width. For the smallest nanowire investigated, 50 nm in thickness and 74 nm in width, a value of κ = 56 W/mK is obtained. At higher test temperature, the thermal conductivities are found to decrease, as expected. The decrease in κ with diminishing size are primarily attributed to grain boundary and surface/interface scattering of electrons—that conduct most of the heat in gold—and quantitatively interpreted using the Boltzmann Transport Equation (BTE).

1:30 PM M02
(Student) A Fundamental Study of Structural Effects on Thermal Properties of Quaternary Chalcogenides Wilarachchige D. Gunatilleke and George S. Nolas; University of South Florida, United States

A material with a high thermoelectric figure of merit plays an important role in the development of efficient thermoelectric devices. Modification of thermal transport in a crystal lattice is one of the most sought-after methods of developing novel thermoelectric materials. Increasing phonon scattering in a crystalline material to lower thermal transport is one way of achieving this objective. A fundamental understanding of the effects of structural features on the thermal properties is a significant first step towards enhanced thermoelectric properties of a material. Although certain quaternary chalcogenides have been examined for their applications as thermoelectric materials, fundamental research into altering the thermal conductivity of this large class of materials remains to be explored. This work contributes towards this area of research by investigating the thermal conductivity and heat capacity of select quaternary chalcogenides to analyze their structure-property relationships. Phenomenological models were utilized to examine the thermal conductivity, κ, and heat capacity, C_p, of $BaCu_2SnQ_4$ (Q = S, Se) and $BaCdSnSe_4$. The Debye-Callaway model was employed to investigate the phonon scattering phenomena that occur in these materials. Our analyses indicate similar anharmonicity in all crystal lattices. Furthermore, highly distorted corner-sharing chalcogen tetrahedra encompassing Cu/Cd atoms give rise to large thermal parameters for Cu/Cd in these materials. Relatively high scattering from soft modes in $BaCu_2SnS_2Se_2$ was identified, such dynamic disorder resulting in very low κ values. Additional disorder for $BaCu_2SnS_2Se_2$ is due to alloying, causing the lowest κ among the quaternary chalcogenides. The Debye and Einstein temperatures from C_p data corroborated the results obtained from our analyses of the κ data. The large primitive cells with complex lattice vibrations these materials possess lead to an increase in optical modes that further suppress κ. These results and analyses, as well as further recent results on other quaternary chalcogenides, demonstrate the direct impact of complex structural features on phonon dynamics, enhancing our fundamental understanding of the thermal properties of these materials. With material property developments being a significant aspect of thermoelectrics research, our results will aid investigations of other quaternary chalcogenides of interest for thermoelectric applications, as will be described in this presentation.

1:45 PM M03
Microscopic Mechanism of Unusual Lattice Thermal Transport in $TlInTe_2$—Roles of Anharmonic Renormalization and Wave-Like Tunneling of Phonons Koushik Pal, Yi Xia and Chris Wolverton; Northwestern University, United States

$TlInTe_2$ represents a class of chain-like crystalline semiconductors (InTe, TlSe, $TlGaTe_2$) that exhibit ultralow lattice thermal conductivity (κ_l), and promising thermoelectric performance. Although it was shown that these compounds contain rattler cations and exhibit strong anharmonicity, the underlying origin behind their unusual thermal transport properties has remained unclear. Here, we investigate the microscopic mechanism of the ultralow-κ_l in $TlInTe_2$ using an advanced and unified theory of lattice heat transport that considers contributions arising from the particle-like propagation as well as wave-like tunneling of phonons. While the former term is calculated within the Peierls-Boltzmann transport equation (PBTE), the later quantity has been determined by explicitly calculating the off-diagonal (OD) components in the heat-flux operator within a first-principles framework based on density functional theory. At each temperature, T, we anharmonically renormalize the phonon frequencies using the self-consistent phonon theory including quartic anharmonicity and utilize them to calculate κ_l. With the combined inclusion of the particle-like contributions, the OD term, and additional grain boundary scatterings, our calculations successfully reproduce available experimental measurements of κ_l in $TlInTe_2$. Our analysis shows that the presence of the large quartic anharmonicity (a) strongly hardens the rattling phonon branches, (b) diminishes the three-phonon scattering processes at finite T, and (c) recovers the correct T-dependence of κ_l that deviates from T^{-1} behavior found in weakly anharmonic solids. Our work signifies the importance of including phonon renormalization and a unified theory of lattice thermal conductivity to uncover the lattice heat transport mechanism in low-dimensional crystalline solids with strong anharmonicity, facilitating the rational design and discovery of new ultralow-κ_l materials.

2:00 PM M04
(Student) Thermal Conductivity of Al1-xScxN for 5G RF MEMS Filters Yiwen Song[1], Carlos Perez[1], Giovanni Esteves[2], James Spencer Lundh[1], Christopher B. Saltonstall[2], Thomas E. Beechem[2], Jung In Yang[1], Kevin Ferri[1], Joseph E. Brown[1], Zichen Tang[3], Roy H. Olsson III[3], David W. Snyder[1], Jon-Paul Maria[1], Benjamin A. Griffin[2], Brian M. Foley[1], Susan E. Trolier-Mckinstry[1] and Sukwon Choi[1]; [1]The Pennsylvania State University, United States; [2]Sandia National Laboratories, United States; [3]University of Pennsylvania, United States

Global fifth-generation (5G) coverage has the potential to underpin the internet-of-things (IoT) ecosystem. Radio frequency (RF) microelectromechanical system (MEMS) filters based on $Al_{1-x}Sc_xN$ are replacing AlN-based devices because of the higher achievable bandwidths. [1] However, overheating of $Al_{1-x}Sc_xN$ film bulk acoustic wave resonators (FBARs) used in RF MEMS filters limits power handling and thus the phone's ability to operate in an increasingly congested RF environment while maintaining its maximum data transmission rate. Despite this, the factors limiting thermal transport within $Al_{1-x}Sc_xN$ have not been examined. This work investigated the physics that govern the thermal transport within $Al_{1-x}Sc_xN$, a fundamental building block for 5G RF MEMS. The thermal conductivities of c-axis textured $Al_{1-x}Sc_xN$ films were found to be one order of magnitude lower than similarly textured polycrystalline AlN films and two orders of magnitude lower than single crystal and/or bulk AlN. This abrupt reduction of thermal conductivity with incorporation of Sc atoms into the AlN crystal can be understood in terms of phonon-alloy/disorder scattering, in the context of the phonon gas theory. Increasing the Sc composition results in a further decrease in the thermal conductivity due to structural frustration and lattice softening, which is an effect absent in isomorphs such as $Al_{1-x}Ga_xN$. [2] A relatively strong film thickness dependence of the thermal conductivity was observed for the $Al_{1-x}Sc_xN$ films. However, thermal conductivity measurement at varying ambient temperatures exhibited a weak temperature dependence. The impact of abnormally oriented grains on the cross-plane thermal conductivity was found to be negligible for the piezoelectrically functional $Al_{1-x}Sc_xN$ films tested in this work. Outcomes of this work support the electro-thermo-mechanical co-design of 5G $Al_{1-x}Sc_xN$-based RF acoustic filters. From a thermal standpoint, for $Al_{1-x}Sc_xN$-based bulk acoustic wave (BAW) filters, the solidly mounted resonator (SAW) configuration would be preferred over the FBAR (free-standing membrane) configuration due to the poor thermal conductivity of $Al_{1-x}Sc_xN$. The thermal property data set generated in this work reveals design trade-offs for (i) increasing the Sc composition of $Al_{1-x}Sc_xN$ to maximize the electromechanical coupling factor, (ii) decreasing the film thickness to achieve higher GHz-range resonance frequencies, (iii) higher operating temperatures resulting from higher integration density and RF input powers. The thermal conductivity data will allow construction of multi-physics device models that will enable the design and development of $Al_{1-x}Sc_xN$ RF filter technologies with enhanced device performance and improved lifetime.
Acknowledgment: This material is based upon work supported by the National Science Foundation, as part of the Center for Dielectrics and Piezoelectrics under Grant Nos. IIP-1361571, IIP-1361503, IIP-1841453, and IIP-1841466. This work was performed, in part, at the Center for Integrated Nanotechnologies, an Office of Science User Facility operated for the U.S. Department of Energy (DOE) Office of Science. G.E. would like to gratefully thank Sara Dickens and Joseph Michael at Sandia for conducting the EBSD analysis. Sandia National Laboratories is a multimission laboratory managed and operated by National Technology & Engineering Solutions of Sandia, LLC, a wholly owned subsidiary of Honeywell International, Inc., for the U.S. DOE's National Nuclear Security Administration under contract DE-NA-0003525. The views expressed in the article do not necessarily represent the views of the U.S. DOE or the United States Government.

References:
[1] G. Piazza, V. Felmetsger, P. Muralt, R. H. Olsson III, R. Ruby, MRS Bull. 2012, 37, 1051.
[2] K. R. Talley, S. L. Millican, J. Mangum, S. Siol, C. B. Musgrave, B. Gorman, A. M. Holder, A. Zakutayev, G. L. Brennecka, Phys. Rev. Mater. 2018, 2, 63802.

2:15 PM M05
(LATE NEWS) Characterization and Exploitation of Non-Linear Dynamics in Vanadium Dioxide Thermal Memristors Timothy D. Brown[1], Suhas Kumar[2] and Richard S. Williams[1]; [1]Texas A&M University, United States; [2]Sandia National Laboratories, United States

As Moore's Law reaches its natural saturation, it has become crucial to investigate novel devices and materials for high-performance computing. One promising approach is to develop brain-like connected neuromorphic architectures composed of elemental devices capable of non-linear phenomena, such as spiking and potentiation. Much progress towards this end has been made using oxide materials like VO2 and NbO2, in which memristive behavior arises as a consequence of non-linear conductance mechanisms and of the inherent metal-insulator transition (MIT). However, much work remains to be done to correlate device properties, especially performance versus energy cost, to underlying materials properties like effective energy barriers and conductance changes across the MIT. In this work, we investigate these issues by developing a compact model for individual vanadium dioxide devices, so as to link complex dynamic behavior to underlying material and device properties. Using a combination of steady-state current-voltage sweeps, time-varying oscillations, and a novel thermoreflectance temperature-measuring technique, we extract thermal and electrical conductance and capacitance model parameters, and show that the model reproduces all observed device behavior. Finally, we exploit the link between dynamics and materials parameters embodied by the compact model to develop non-trivial device scaling laws, and also experimentally demonstrate a capacitance-controlled bifurcation from stable to unstable oscillating dynamics. This work lays the foundation for future studies allowing disparate memristive materials to be compared through the compact model framework, as well as to begin investigating the even more complex dynamical behaviors arising from couplings of pairs or networks of non-linear devices.

SESSION N: Narrow Bandgap Materials and Devices
Session Chairs: Ganesh Balakrishnan and Mark Wistey
Wednesday Afternoon, June 23, 2021

3:00 PM N01
Minority-Carrier Lifetimes in Digitally-Grown AlInAsSb Alloys Aaron J. Muhowski, Stephen D. March, Scott J. Maddox, Seth R. Bank and Daniel Wasserman; The University of Texas at Austin, United States

Digitally-grown AlInAsSb alloys have recently emerged as a platform for high performance short- avalanche photodiodes (APDs) with potential applications in chemical sensing, security, and LIDAR [1,2]. While the impact ionization of APDs grown with a single composition has been shown to be nearly perfectly electron-initiated [2,3], AlInAsSb also enables sophisticated bandgap engineering to create a "staircase" APDs – a solid-state analogue of the photomultiplier tube wherein impact ionization only occurs in spatially-localized, narrow-gap wells [4, 5]. Carrier trapping phenomena in the narrow-gap regions, coupled to non-

radiative Shockley-Read-Hall recombination, can reduce the efficiency of impact ionization and reduce the maximum achievable gain in staircase APDs. Unfortunately, due to the miscibility gap associated with conventionally grown AlInAsSb, the carrier lifetime of AlInAsSb materials is largely unknown. Furthermore, the SWIR and MWIR spectral regions spanned by AlInAsSb remain an active area of research for high-performance unity-gain photodiodes and emitters for chemical sensing and security applications; high performance in either class of devices depends critically on the carrier recombination dynamics. Thus, there is a need to measure the carrier lifetime in digitally-grown AlInAsSb to foster improved staircase APD performance, as well as to evaluate AlInAsSb more broadly as a candidate material for SWIR and MWIR detection and emission. Here, we present an investigation of carrier recombination dynamics of SWIR and MWIR AlInAsSb digital alloys with alloy compositions ranging from 0% Al to 30% Al, at temperatures between 77K and room temperature. Bright photoluminescence was observed from all samples at all temperatures, spanning wavelengths from 1.8µm to 5µm. Minority carrier lifetimes were measured from time-resolved photoluminescence ranging from 75ns to 260ns at 77K, and 25ns to 75ns at room temperature. Samples containing more than 0% Al displayed a 'U' shaped dependence on the temperature, with the minima occurring around 200K and ranging from 20ns to 50ns. The minority carrier lifetime of the 0% Al sample, however, monotonically increased with decreased temperature. Further characterization and analysis will be presented at the conference. This work was supported by ARO (W911NF-17-1-0065), DARPA (HR0011-20-9-0087), and NSF (ECCS-1926187).
[1] S.R. Bank *et al.*, IEEE J. Sel. Top. Quantum Electron. **24**, 3800407 (2018) [2] M. Ren *et al.*, … J. C. Campbell, J. Light. Technol. **35**, 2380 (2017) [3] Y. Yuan *et al.*, … J. C. Campbell, IEEE Photon. Technol. Lett. **31**, 315 (2019) [4] F. Capasso and G. F. Williams, IEEE Trans. Nucl. Sci. **30**, 381 (1983) [5] M. Ren *et al.*, … S. R. Bank, Appl. Phys. Lett. **108**, 081101 (2016).

3:15 PM N02
High Detectivity PbS_xSe_{1-x} Films for Mid-Wavelength Infrared Detectors Oleg Maksimov[1], Peter Su[2], Pijush Bhattacharya[1], Katherine Stoll[2], Kazumi Wada[2], Lionel Kimerling[2], Anuradha Agarwal[2,2] and Harish Bhandari[1]; [1]Radiation Monitoring Devices, United States; [2]Massachusetts Institute of Technology, United States

There is significant technological interest in binary lead chalcogenides (PbS, PbSe, PbTe) due to their application as mid-wavelength infrared detectors (MWIR) at near room temperature. Ternary alloys are attractive due to the possibility to shift the cut-off wavelength via bandgap engineering. Particular attention is dedicated to ternary $PbS_{1-x}Se_x$ to merge high detectivity reported for PbS and long cut-off wavelength characteristic for PbSe. Importantly, unlike $Hg_xCd_{1-x}Te$ and InSb, even polycrystalline lead chalcogenide films demonstrate high detectivity at temperatures close to the room temperature. This is achieved through a special sensitization process – a step that involves annealing sample in Oxygen atmosphere. This leads to the growth of lead oxides along the grain boundaries of polycrystalline chalcogenide. Sensitized polycrystalline films get composed of two stacked material layers: narrow bandgap lead chalcogenide wide bandgap oxide. This is believed to be responsible for the carrier inversion and increase in carrier lifetimes in the sensitized films. Oxygen transport during the sensitization process should depend on the morphology, crystalline structure, and grain size of the lead salt films. It is expected to be more effective in the films with smaller grains. Film grain size and microstructure can be controlled via deposition conditions, among them the growth temperature being the most important one. The ability to control lead chalcogenide grain size and orientation will help to simplify and optimize the sensitization process. This will be a step forward towards and producing IR detectors with superior performance for imaging. To test this approach, we investigated growth of $PbSe_{0.6}S_{0.4}$ at different substrate temperatures. $PbSe_{0.6}S_{0.4}$ films were deposited via physical vapor deposition at (111) BaF_2 at 200 ^{0}C and 50 ^{0}C. High-temperature growth produced films with near-columnar fiber-like microstructure with grains preferentially growing along the [111] direction. Low temperature growth resulted in films with smaller grain size that did not demonstrate texture. Importantly, there was a significant improvement in the photoresponse of the sensitized films with the decrease of the $PbSe_{0.6}S_{0.4}$ growth temperature. A peak Johnson-noise-limited detectivity, measured at -40 ^{0}C, increased from 1.0 x 10^8 Jones for high-temperature grown film to more than 1.0 x 10^{10} Jones for the low-temperature grown film. We attribute this to the more efficient oxide formation in the films with small grains. These findings highlight importance of grain size control to produce high detectivity lead salt detectors operating at room temperature. The work was supported by ONR under the SBIR award number N68335-19-C-00. It made use of the MRSEC Shared Experimental Facilities at MIT, supported by the National Science Foundation under Award No.DMR-1419807.

3:30 PM N03
Mid-Infrared Light Emission from PbSe Epitaxial Films on III-V Substrates Kunal Mukherjee[1,2], Brian B. Haidet[2], Eamonn T. Hughes[2], Leland J. Nordin[3], Aaron J. Muhowski[3], Jarod Meyer[1], Kevin Vallejo[4], Paul Simmonds[4] and Daniel Wasserman[3]; [1]Stanford University, United States; [2]University of California, Santa Barbara, United States; [3]The University of Texas at Austin, United States; [4]Boise State University, United States

The unusual mix of covalent, metallic, and ionic bonding in the narrow gap rocksalt semiconductor PbSe sets it apart from covalently bonded III-V semiconductors.[1] Specific to efficient mid-infrared (mid-IR, 3–5 µm) light emission, the mixed-bonding character is responsible for PbSe having unusual degenerate and anisotropic L-valley band edges in both the conduction and valence band. This leads to 1–2 orders of magnitude lower direct Auger recombination coefficients compared to III-V materials of the same bandgap, traditionally a key limiter of mid-IR light emission.[2] In this work, we explore two additional benefits of PbSe's unusual bonding—(1) significant tolerance of minority carriers to threading dislocations and (2) highly mobile dislocations for strain engineering. We grow epitaxial thin films of PbSe on (001) GaAs substrates by molecular beam epitaxy at temperatures in the 300–330 °C range. We have previously demonstrated a route to sharp interfaces using an in-situ high-temperature substrate surface treatment prior to PbSe nucleation that helps overcome the heterovalent and dissimilar crystal structures.[3] Yet, the 8% lattice-constant mismatch between PbSe and GaAs results in excess of 10^9 threading dislocations/cm^2 and misfit dislocations with an average spacing of a few nanometers. Despite this high defect density, we measure strong room temperature band-edge photoluminescence at 4 µm from uncapped-PbSe films as thin as 50 nm. To further understand our film's strong room temperature photoluminescence, we performed time-resolved and power-dependent photoluminescence. Using time-resolved photoluminescence, we measure a low-injection minority carrier lifetime at room temperature is in the range of 20–200 ns, strongly deviating from picosecond lifetimes one would expect for III-V materials with these dislocation densities. Using power-dependent photoluminescence, we measure that bimolecular recombination is the dominant process in our films, further suggesting a carrier recombination mechanism that does not appear to be defect limited. The unusual bonding also confers PbSe with a thermal expansion coefficient of 19 ppm/K, about four times higher than that of GaAs. Nevertheless, we show (111)-oriented films of PbSe on III-V substrates relieve thermal-expansion mismatch strain efficiently thanks to highly mobile threading dislocations that glide even below room temperature. Photoluminescence measurements coupled with x-ray diffraction show (001)-oriented PbSe samples do not have an active slip system and become strained upon cool down, whereas the (111)-oriented samples remain strain free even at LN_2 temperatures.

Essentially, we are learning that dislocation motion in PbSe requires far less thermal activation compared to III-V materials. This presents unique opportunities to engineer strain states and control the color of light emission. This preliminary work shows that luminescence from PbSe films tolerates extended defects and thermal mismatch. In combination with low growth temperatures, this means that PbSe could be suitable for back-end-of-line integration of mid-IR emitting materials on low-cost lattice-mismatched substrates like Si or Ge for a range of applications. At the same time, we still have much to learn about the properties of PbSe. [1] P.B. Littlewood, Critical Reviews in Solid State and Materials Sciences **11**, 229 (1983). [2] P.C. Findlay, C.R. Pidgeon, R. Kotitschke, A. Hollingworth, B.N. Murdin, C.J.G.M. Langerak, A.F.G. van der Meer, C.M. Ciesla, J. Oswald, A. Homer, G. Springholz, and G. Bauer, Phys. Rev. B **58**, 12908 (1998). [3] B.B. Haidet, E.T. Hughes, and K. Mukherjee, Phys. Rev. Materials **4**, 033402 (2020).

3:45 PM N04
Optical Properties and Band Structures of Strained Ge:C
Mark Wistey[1,1], Qian Meng[2], Tuhin Dey[1], Mohammed S. Reza[1] and Seth R. Bank[2]; [1]Texas State University, United States; [2]The University of Texas at Austin, United States

Dilute germanium carbides (Ge:C) are promising optical materials for active silicon photonics since they can be grown directly on Si at temperatures compatible with post-metal CMOS fabrication. Although Ge and diamond-lattice C both have an indirect bandgap, substitution of ~1% C into Ge creates a direct bandgap suitable for lasers and modulators. However, there is disagreement in the literature about whether C creates a true direct bandgap or merely a pseudo-direct bandgap in which symmetry prevents optical emission even at Gamma (k=0). In this work, we studied the effects of strain and defects on the optical properties of Ge:C using ab initio techniques. We find Ge:C is similar to other highly mismatched alloys such as $GaAs_{1-x}N_x$ in many ways, but it also presents several curious differences. The Vienna Ab initio Simulation Package (VASP) was used to model 128 atom supercells of Ge:C with different periodicities, as well as 128 atom supercells with a single Ge vacancy. The use of HSE06 hybrid functionals provided good agreement with experiment in both the direct and indirect bandgaps in unstrained Ge. To study whether periodic boundary conditions artificially affected the results, supercell lattice vectors were varied; the center of each supercell might align with the face, edge, or vertex of the next supercell. This changed the spacing between C atoms in different directions, mimicking a random alloy at a far lower computational cost than doubling the supercell sizes. Other groups have reported that the new conduction band edge created by C is dominated by indirect (L) states. We found instead that the conduction band splits into two bands, E^- and E^+, that are similar to each other (consistent with band anticrossing, BAC) but retain a predominantly Ge Γ character. The optical transitions in Ge:C are comparable with those of the direct bandgap transition (Γ) in Ge. Spectral weights after band unfolding show comparable or more weight at Γ than L for both E^+ and E^- states. We also ran a few validation jobs with spin-orbit coupling, compressive strain, or harder Ge potentials, and these all showed similar results. In particular, the band-to-band optical transition strength in Ge:C is within a factor of 2 of that in Ge, and it is comparable with common III-V materials currently used for lasers. We found that the pressure dependence of the band structure can be highly misleading when trying to interpret band identities. In particular, the E- band shifts with strain almost identically with the Ge CB L valley, but this is pure coincidence. Instead, the slow shift with strain comes from a carbon "defect" state near E_{VB}+0.79 eV that varies relatively slowly, more or less tracking the vacuum level rather than the conduction band edge, unlike traditional impurity states. Because the C "defect" state is so close to the native Ge direct bandgap (0.80 eV), the splitting in bands is very strong, driving the direct bandgap more than 0.2 meV below the indirect L valley. This agrees with the deep state model of Hjalmarson and Dow and BAC models near Γ. However, BAC fails to explain the bands away from k=0, and it also does not explain the appearance of a third CB state between the E+ and E- bands. In summary, these results strongly support the development of Ge:C as a strongly optically active material for silicon photonics, with a strongly direct bandgap and optical transitions comparable with III-V materials. Furthermore, these strain results offer a route to test the computational models against experiments, using a diamond anvil cell. These tests are currently underway.

4:00 PM N05
SiSn Electronic Band Structure Modelling Using Density Functional Theory for Optoelectronic Applications Seyedeh Fahimeh Banihashemian[1], Murtadha Alher[2], Mehrshad Mehboudi[3], Aboozar Mosleh[1] and Hameed Naseem[1]; [1]University of Arkansas, Fayetteville, United States; [2]University of Kerbala, Iraq; [3]McDaniel College, United States

Investigation of new group IV alloys to find a direct bandgap material that can emit and detect light efficiently has been pursued by Si photonics in the past decades. The integration of optoelectronics on the electronics chips enables high-speed data transfers through emitters and detectors that are compatible with Si technology [1]. Although GeSn has been shown as a group IV that can achieve the above-mentioned goals by different groups [2], other alloys of group IV have not been yet fully investigated due to technical challenges such as insolubility, lattice mismatch, unavailability of proper precursor, etc. Theoretical calculations show that Si_xSn_{1-x} alloys can also be a direct bandgap material like GeSn with the difference of having a larger bandgap due to high direct band edge of Si at 3.2 eV (Γ-valley)[3]. However, the theoretical study of this material is not well developed. The estimation of Sn concentration needed to achieve direct bandgap varies in the range of 40-60% while the experimentalist are expecting that to be in the 25% range.[3] In this paper we have studied both material properties as well as electronic band structure using density functional theory (DFT) calculations. We have adopted generalized gradient approximation- Perdew–Burke–Ernzerhof (GGA-PBE) [4] with Vienna Ab-initio Simulation Package (VASP).[5] The 16-atom cubic supercells of Si and Sn, as well as the unit cell, were used in this modeling in order to find the atomic configurations and energetics. The supercells were relaxed for all the atoms with a residual force of less than 5×10^{-5} eV/Å for each atom. A (4×4×4) Monkhorst−Pack mesh of k-points for a periodic 16-atom supercell was adopted to generate the Brillouin zone. We calculated the lattice constant and its formation energy for all compositions using the GGA–PBE exchange-correlation potential considering the structural relaxation of an isotropic stress for the supercell. The change in the lattice follows the Vegard's law and a slight bowing (=0. 05 Å) is observed across the full range which is close to previously reported values 0.02-0.084 Å [3, 6]. The lattice constants of Si and α-Sn were estimated to be 5.47 and 6.65 Å, respectively. These values are in close agreement with previously reported values of 5.47Å for Si[7] and 6.65–6.74 Å for α-Sn [8] using a similar modeling method of GGA–PBE. It is noteworthy that compared to other group IV binary alloys such as SiGe and GeSn, the proposed bowing parameter is slightly lower. The band structure of all compositions of Si_xSn_{1-x} is calculated for both unit cell and supercell of 16 atoms. The electronic properties of the alloys are affected by the displacement of $Si_{1-x}Sn_x$ atoms; therefore, structural relaxation of the structures plays an important role in the band structure. These structures were relaxed to a high extent as stated above. Since the GGA-PBE method underestimates the bandgap of Si_xSn_{1-x} alloys, different methods have been applied to bring the calculations closer to the real bandgap. In our calculations, we have included the valence band offset of Si_xSn_{1-x} alloys. The valence band offset is attributed to the electronic interaction between the occupied and unoccupied orbitals of $Si_{1-x}Sn_x$. Therefore, by considering an Sn dependent valence band offset as well as heavy, light, and split-off

hole bands, the calculations are closer to the real bandgaps. More details of the material properties along with the electronic band structure calculations will be presented at the conference.

References

[1] A. Atabaki et al., Nature 556, 349 2018
[2] A. Mosleh et al. J Electron Mater 43, 938 2014
[3] J. Tolle et al., Appl. Phys. Lett. 89, 231924 2006
[4] J. P. Perdew et al. Physical Review B 46, 6671 1992
[5] G. Kresse et al. Physical Review B 54, 11169 1996
[6] P. Yakibchuk et al. J Physical Studies 23, 2703 2019
[7] SQ Wang et al. J Physics: Cond. Matt. 15, L197 2003
[8] R. Pandey et al. Appl. Phys. Lett. 75, 4127 1999

63RD ELECTRONIC MATERIALS CONFERENCE

June 23-25, 2021

POSTER PRESENTATIONS

SESSION PS1: Poster Session I
Wednesday Afternoon, June 23, 2021
4:45 PM - 6:15 PM

EP01
(Exhibitor Poster) Taiyo Nippon Sanso Mayank Bulsara; Matheson Tri-Gas, Inc., United States

List of Products
MOCVD reactors, specialty gas sources, gas purifiers, and gas abatement solutions

Business Description
Taiyo Nippon Sanso is an industrial gas manufacturer established in 1910. As an innovator in the compound semiconductor industry, Taiyo Nippon Sanso was the first company to introduce commercial MOCVD systems, in 1983. Taiyo Nippon Sanso is uniquely qualified to provide total solutions for compound semiconductor fabrication, with MOCVD equipment, gas handling and purification equipment, exhaust abatement solutions, and custom piping and installation services. The SR4000 series GaN MOCVD reactors, originally introduced in 2002, are highly regarded worldwide for their exceptionally stable performance for HEMT, PN Diode, Laser, and RBG/UV LED applications. The SR4000HT (maximum 1350 °C process temperature) can be configured interchangeably for 2" and 4" wafer processing at growth pressures of 10 kPa up to 100 kPa. The newly introduced SR4000HT-RR has a compact design especially suited for university and research environments while maintaining high performance capability. The UR series GaN MOCVD reactors, available since 2008, are workhorse solutions for production applications. The UR25K is configurable for multi-4" or 6" wafer processing and the UR26K is configurable for multi-6" or 8" wafer processing. The UR series reactors can process high quality films at growth pressures from 10 kPa to 100 kPa. With high growth rate capability, cassette-to-cassette wafer handling options, and other features, the UR series offer customers excellent uptime and throughput.

EP02
(Exhibitor Poster) k-Space Associates, Inc. Kathy Wheeler; k-Space Associates, Inc., United States

Key Products: In situ and Ex situ Metrology Tools for Epitaxy
k-Space Associates, Inc. is a leading provider of optical metrology tools. kSA 400 is an **analytical RHEED acquisition and analysis** tool offering real-time growth rate and atomic spacing. kSA BandiT offers **band edge substrate temperature** for semiconductor substrates such as GaAs, InP, Si, CZT, GaP, SiC, GaN, Ga2O3, and AlN. kSA MOS measures **film stress** during deposition or thermal processing. kSA ICE is a modular, in situ system for MBE and MOCVD, offering real-time wafer curvature, temperature, and reflectivity. kSA SpectR is a complete metrology solution for measurement of absolute **spectral reflectance**, growth rate and end point detection to determine device spectral features for DBRs or VCSELs. kSA ICE (**integrated control for epitaxy**) combines these tools in modules on one optics head for a compact measurement solution. kSA MOS UltraScan provides **ex situ full wafer stress mapping** with adjustable optics for measurement of smaller samples. kSA ACE (**atomic control for epitaxy**) will be released soon.
requestinfo@k-space.com | www.k-space.com

EP03
(Exhibitor Poster) CuttingEdge Ions, LLC Brian Doherty; CuttingEdge Ions, LLC, United States

Specialty Ion Implant Services:
* Most elements of the periodic table
* Also molecules
* Capabilities:
° LN2 cooled implants
° Chilled stage to -15C
° Heavy dose implants for exfoliation
° Nitrogen vacancy implants into single crystal diamonds – N15 and N14
° Heated implants for SiC and other materials up to 1000C on small samples and full wafers of up to 6 inch
° $LiNbO_3$ exfoliation implants using Helium or other species
° 8 different implanters covering 1keV to 1MeV
° Special beam filters as required by some species
° Flux control capabilities down to the nanoamp range – useful for control of lattice damage
° Tilt and twist angle control of any angle – useful for trench implants and also to eliminate "channeling"
° Masking of samples to allow for different sections to have different implant specs
° 4 quadrant rotation of samples
° Plus and minus tilt angles
° Many specialty gasses kept in stock: e.g. 3He, 17O, 18O, Deuterium 2H etc.
° Implantation of species for surface hardening of medical devices
° Modeling services – including achieving a box profile using multiple implant energy/dose combinations
° Guidance on other process steps including annealing parameters
° Fast turnaround is normal – typically 3 days
° Support for researchers and students, no job too small, we are here to help
° Production implants with very fast turnaround – 24 hour 3 shift operations for one day/same day expedite options
° Special packing capabilities as needed – e.g insulated with cool-pak
° Overseas shipments with rapid customs clearance protocols

EP04
(Exhibitor Poster) Structured Materials Industries, Inc. Gary S Tompa[1]; [1]Structured Materials Industries, Inc., United States

Your one stop resource for custom Metal Organic Chemical Vapor Deposition (MOCVD) Systems, Alternating Layer Depository (ALD) systems, Plasma Enhanced CVD (PECVD) systems, Hydride Vapor Phase Epitaxy (HVPE) Systems, and supporting Processes, Services, and Components, and Contract Service Support. We do it all!

PS1.01
(Student) Effect of Post-Deposition Annealing on the Structure, Morphology and Optical Properties of GeO2 Films
Paul G. Nalam, Francelia S. Escobar, Debabrata Das and Chintalapalle Ramana; The University of Texas at El Paso, United States

Germanium dioxide (GeO_2) is a versatile, wide band gap material that has been explored in depth due to its promising thermal, optical and electrical properties. GeO_2, which is thermally a stable oxide of Ge, exhibits quite interesting electronic properties, such as a high dielectric constant and refractive index. GeO_2 thin films find numerous applications in optoelectronics and photonics. However, understanding the processing-property correlation is the key to tailor the performance of GeO_2 thin films in practical device applications. In this work, ~100 nm thick GeO_2 films were deposited using sputtering under variable oxygen content. The effect of post-deposition annealing (700-1000 oC) on the structure, morphology and optical properties of GeO_2 films has

been studied in detail. While the as-deposited GeO_2 films were amorphous, increasing annealing temperature induces amorphous-to-crystalline transformation. Corroborating with microstructure changes, the optical quality and band gap also increases dramatically for the annealed GeO_2 films. The structure-property correlation in annealed GeO_2 films is discussed in detail.

PS1.02
(Student) Influence of CaO on Reddish Luminescence of Sm^{3+}-Doped Borosilicate Glasses Víctor E. Ceniceros-Orozco, José Escorcia-García and Carlos A. Gutiérrez-Chavarría; Centro de Investigación y de Estudios Avanzados del Instituto Politécnico Nacional, Mexico

Rare-earth ion doped borosilicate glasses are attractive for solid-state lighting since they exhibit high optical transparency, mechanical, chemical, and thermal stability. Furthermore, glasses can be obtained through the melting-quenching, a low-cost manufacturing technique with the ease of producing glasses in intricate forms. In this work is presented the synthesis of Sm^{3+}-doped luminescent borosilicate glasses by melting-quenching technique varying the CaO content, according to the following formula: $[60 – (x + y)]\ SiO_2 – 20\ B_2O_3 – x\ CaO – 20\ Na_2O – y\ Sm_2O_3$ (where x=0-30 and y=0-2 mol%). The raw materials were SiO_2, H_3BO_3, Na_2CO_3, $CaCO_3$, and Sm_2O_3. These precursors were weighed, mixed, and grilled in an agate mortar to get the batches (15-20 g). The mixture was then taken into an alumina crucible and kept in an electric furnace at temperatures between 1300-1400 °C, depending on CaO content, for 2 h. Later, the melt was cast into two preheated (450 °C) stainless steel plates and slowly cooled until room temperature. Finally, the glass pieces were crushed and sieved to particle size fractions less than 74 μm to make their further characterization in XRD, XPS, FTIR, UV-Vis spectroscopy, and photoluminescence (PL). XRD results of glasses varying CaO showed a wide halo at 15-40° without any intense diffraction peaks that indicate the presence of undesired crystalline phases. Therefore, borosilicate glasses are amorphous. Analysis of the XPS survey corroborated the presence of Si 2p, B 1s, O 1s, Ca 2p, Na 1s, and Sm 3d in glasses. Deconvolution of high-resolution spectra of O 1s region showed an increase in the peak associated with B-O-B bond (533.4 eV), increasing the CaO from 0 to 30 mol%. On the contrary, the bridging oxygen (531.9 eV) and non-bridging oxygen (519.5 eV) peaks decreased. Similar results were obtained in the FTIR spectra of glasses. The absorption band associated with BO_3 (1390-1317 cm^{-1}) increased with the CaO, while the absorption bands associated with Si-O-Si and B-O-Si reduced (975-925 cm^{-1}). These results demonstrate that CaO promotes phase separation in borosilicates, resulting in a borate phase (B_2O_3) (apart from the borosilicate phase) for high CaO content. Furthermore, FTIR indicated an increase in the absorption band around 698 cm^{-1} associated with the Sm-O bond. According to XPS, this bond is related to Sm^{3+} due to the identification of Sm $3d_{5/2}$ and Sm $3d_{3/2}$ orbitals with binding energies of 1083 and 1109 eV, respectively. UV-Vis and excitation PL spectroscopy exhibited several characteristic absorption peaks of Sm^{3+}, being the most intense peak located at 401 nm ($^6H_{5/2} \rightarrow {}^4F_{7/2} + {}^6P_{3/2}$ transition). Furthermore, the 401 nm peak intensity increased with the addition of CaO. On the other hand, the emission PL spectrum showed 4 peaks with wavelengths at 567, 604, 651, and 712 nm corresponding to the transitions $^4G_{5/2} \rightarrow {}^6H_{5/2}$ (yellow-green), $^4G_{5/2} \rightarrow {}^6H_{7/2}$ (reddish-orange), $^4G_{5/2} \rightarrow {}^6H_{9/2}$ (red), and $^4G_{5/2} \rightarrow {}^6H_{11/2}$ (dark red), respectively. The most intense peak was identified at 604 nm. Moreover, the increase of CaO promoted a higher luminescence on Sm^{3+}-doped borosilicate glasses. The coordinates in the chromaticity diagram showed a color emission in the reddish-orange region. In conclusion, the PL enhancement with the increase of CaO was due to the formation of phase separation (spinodal composition) in the glasses, which lets to host a higher amount of Sm^{3+} ions in the borate phase. Finally, these glasses could be used in applications such as high-density optical storage, undersea communication, and color displays.

PS1.03
(Student) Discovery of Novel Crystal Structures via Generative Adversarial Networks Michael Alverson, Taylor Sparks and Ryan Murdock; The University of Utah, United States

The idea of material discovery has excited and perplexed research scientists for centuries. Several different methods have been employed to find new types of materials, ranging from the arbitrary replacement of atoms in a crystal structure to advanced machine learning methods for predicting entirely new crystal structures. In this work, we investigate and analyze the performance of various Generative Adversarial Network (GAN) architectures to find an innovative and effective way of generating theoretical crystal structures that are synthesizable and stable. Over three hundred thousand Crystallographic Information Files (CIFs) from Pearson's Crystal Data are used for the training of each GAN. The space group number, atomic positions, and lattice parameters are parsed from the CIFs and used to construct an input tensor for each of the different network architectures. Several different GAN layer configurations are designed and analyzed, including Wasserstein GANs with weight clipping and gradient penalty, in order to identify a model that can adequately recognize and discern symmetry patterns that are present in known material crystal structures and are imperceptible to humans. This work will detail the process and techniques that were used in an attempt to generate never-before-seen crystal structures that are both stable and synthesizable, as well as reveal a plethora of guiding questions for future work.

PS1.04
(Student) CVD Single Layer Graphene-Based Phototransistor with High Responsivity and Detectivity by Photogating Effect Wafaa F. Gebril[1,2] and Omar Manasreh[3]; [1]University of Arkansas, United States; [2]University of Benghazi, Libya; [3]University of Arkansas, Fayetteville, United States

A phototransistor based on CVD single layer graphene on light p-doped Si/SiO_2 substrate was investigated. The p-Si/SiO_2 interface helped to create a photogating effect that produces high responsivity photodetection. The p-doped Si in the substrate was utilized as a photosensitizer and a back gate to tune the photoresponse of the graphene phototransistor at room temperature. The phototransistor was fabricated with a simple structure of a single graphene channel formed by two metal electrodes on the substrate. Additionally, a metal was deposited on the back of the substrate to connect the p-Si back gate. The grown graphene was found to be high-quality single layer graphene by measuring its Raman spectroscopy. The performance of the fabricated devices was investigated based on measuring their current-voltage (I-V) characterization. The device's I-V curves were measured in the dark and under the illumination of a broadband light source to exam their photoresponse. The device's response was also examined as a function of applied gate voltage. A remarkable tunability of the obtained photocurrent was observed by changing the gate voltage. The responsivity and the detectivity were calculated using the measured dark and photocurrents of a device with a 5 μm length channel. The investigated phototransistor was found to reach high responsivity of 2.5×10^3 A/W and detectivity of 5×10^{12} $cmHz^{0.5}/W$ at a gate bias voltage of -20 V and drain bias voltage of 1 V. Moreover, the investigated phototransistor works as a self-powered device by biasing the drain at 0 V and applying a voltage on the back gate. The photocurrent and the responsivity of the device were also studied as functions of the incident power density of a 632.8 nm red laser.

PS1.05
(Student) Optical Prosperities of Different Stacking Orders in ReS2 Yongjian Zhou and Yaguo Wang; The University of Texas at Austin, United States

Two stacking orders, AA stacking and AB stacking, of ReS_2 are identified by scanning transmission microscopy. The Raman spectrum of these two stacking orders can be an excellent tool to differentiate them. The photoluminescence spectrum shows different exciton positions and widths, which suggests that the dielectric environment is different. The First-principles calculations reveal that the two stacking orders are the two energy minimum when shifting the upper layer along the ***a*** axis. To better understand the excitons, polarization-dependent fs-second pump-probe are performed, which shows drastically different carrier dynamics when laser polarization perpendicular to the ***b*** axis.

PS1.06
(Student) Local Photovoltaic Measurements of CdTe Solar Cells Using Microscale Point Back-Contacts Kaden Powell, Yu-Lin Hsu, David J. Magginetti and Heayoung P. Yoon; The University of Utah, United States

Cadmium telluride (CdTe) thin-film semiconductors exhibit many desirable properties for low-cost and high-efficiency photovoltaic (PV) technology, including inherent robustness of the inorganic absorber, a direct bandgap that allows full absorption of the solar spectrum with thicknesses of only a few microns, and inexpensive and high-throughput manufacturing processes. At the best efficiency of 22 %, the power conversion efficiency of CdTe PVs is still well below the maximum theoretical limit (approximately 30 %). It has been suggested that the inferior efficiency is mainly due to the inherent polycrystalline nature of the CdTe absorber (e.g., grains, grain boundaries). Understanding local photocarrier dynamics is vital to overcoming roadblocks toward higher efficiency CdTe PVs. However, conventional cell-level PV measurements often limit the microstructural analysis. In this work, we present a local PV characterization technique using point back-contacts. The thin-film CdTe solar cells used in this work were prepared by CSS (close-spaced sublimation) on a stack of *n*-type window layer (e.g., CdS) / transparent conductive layer (TCO; e.g., SnO_2) / glass substrate. To fabricate microscale point back-contacts, we used conventional photolithography or a shadow mask technique. In the first method, CdTe samples were spin-coated with photoresist (Microposit 1813; ≈1.5 µm) and patterned using a laser writer (375 nm, 10 mW power laser with 60 % pixel energy). After development, an O_2 plasma descum was performed. The contact metal (Au or Au-Pd) was deposited onto CdTe via either evaporation or sputtering. Liftoff was then performed, leaving localized metal back-contacts on the CdTe surface. For the second method, a shadow mask with an array of square holes (40 µm × 40 µm) was used. An evaporated Au film was deposited onto the sample through the openings in the shadow mask, forming microscale point contacts. For both contact patterning methods, the front contact was formed by exposing the TCO and applying melted indium. A control CdTe cell with contacts 0.8 cm × 0.6 cm was also used for the comparison of PV parameters (e.g., open-circuit voltage [V_{oc}], short-circuit current [J_{sc}], fill-factor [*FF*], efficiency [η)]). We collected dark and light current-voltage (*I-V*) characterizations by probing the microscale back-contacts and the TCO front contact. CdTe samples were illuminated under 1-sun (AM 1.5G) to extract the PV parameters. The photolithography samples showed significantly inferior *I-V* characteristics. The series resistance was higher than expected, and a poor light response was observed. We speculate that photoresist residue remaining between the rough surface of CdTe and the metal contact layer is likely to cause the undesirable carrier behaviors. By contrast, the microscale back-contacts formed with a shadow mask displayed good diode characteristics and light responses. We measured the V_{oc} of 0.66 V, *FF* of 0.37, and I_{sc} of 0.43 µA for the 40 µm square contacts. The estimated J_{sc} is 27.0 mA/cm^2. This measured J_{sc} value is consistent with the control CdTe device (J_{sc} ≈ 26), and over three-times higher than that of the photolithography devices (J_{sc} ≈ 8.1). We will discuss our on-going fabrication methods to produce the point back-contacts with sizes of 1 µm, improving series resistance of the contacts, and subsequent local PV characterizations.
This work was supported by the U.S. Department of Energy's Office of Energy Efficiency and Renewable Energy (EERE) under the DE-FOA-0002064 program award number DE-EE0008983. We also acknowledge the support by the National Science Foundation (NSF) under Grant No. 1711885. We thank Dr. C. Lee and Dr. G. Xiong at First Solar for providing part of the CdTe samples studied in this work.

PS1.07
(Student) Electrical Behavior of CNT Epoxy Composites Under Simulated Space Environments Joel Hubbard[1], Claudia Luhrs[1,1], Brian Earp[1,2], Alexander Tracy[1] and Dan Sakoda[1]; [1]Naval Postgraduate School, United States; [2]U.S. Naval Academy, United States

The properties of CNT composites are known to suffer changes when exposed to space conditions or simulated space environments. An in-depth understanding of the magnitude of those changes could help improve the design of systems that contain them, produce more accurate predictions of their performance, or even open the possibility of new applications. In this study, the electrical properties of CNT epoxy conductive composites containing low CNT loadings (<1%) were measured in-situ while the specimens were exposed to diverse simulated space conditions. A thermal vacuum chamber was employed to produce the low pressures and temperatures associated with low earth orbit. A solar simulator was used to replicate solar irradiance. A convection oven was used to determine the effects that could only be attributed to temperature variations. The changes in resistivity exhibited by the composite specimens are reported for each scenario along with possible mechanisms that could explain the observed behavior. The microstructural and thermogravimetric characterization of the composites for the diverse loadings is also presented. Resistivity reductions of up to 40% were observed by the simultaneous application of high temperatures and low pressures, while the application of simulated sunlight with the concomitant surge in temperature, showed a maximum decrease of 58%. Outgassing and an increase in the number of charge carriers at the higher temperatures promoted by the simulated sunlight treatment are believed to be responsible for the recorded reductions in resistivity. A qualitative analysis of the resistivity changes noted when the composites are exposed back to atmospheric conditions is included.

PS1.08
(Student) Mechanical and Electrical Properties Study of a Composite Biomaterial of PVA-Chitosan / PPy / PEDOT:PSS / MWCNT / CB Alfredo Olarte-Paredes, Jessica N. Salgado-Delgado, Areli M. Salgado-Delgado, René Salgado-Delgado, Zully Vargas-Galarza and Edgar García-Hernández; Tecnológico Nacional de México/Instituto Tecnológico de Zacatepec, Mexico

Technologies based on conductive polymers have been development in recent years. these conductive materials have adequate mechanical and electrical properties to generate new high impact materials than existing materials. These materials have a wide variety of applications, such as in photovoltaic appliances, storage and transportation of electric charge, etc. The most conductive polymers, polythiophene derivative poly (3,4-ethylenedioxythiophene)-polystyrene sulfonate (PEDOT:PSS), carbon black (CB), have high conductivity, electrochemically and thermally stable, multiwall carbon nanotubes (MWCNT) and polypyrrole (PPy) have high mechanical properties compared to conventional materials. These materials improve the transfer kinetics of electrons and the magnitude of the analytical signal

when used as an electrochemical sensor. Polyvinyl alcohol (PVA) in structural applications has low mechanical properties and its use has been limited, so in this work has been reinforced with chitosan (Cs), films were made by the method of casting, we used a matrix of PPy (0.1 g, 0.2 g, 0.3 g), PEDOT:PSS, CB and MWCNT (0.1 g, 0.2 g) each, and films with PPy/CB/MWCNT/PEDOT:PSS together at different concentrations, to increase some properties as elastic modulus, strength, hardness and further improves properties as electrode materials (including capacitance, conductivity, stability and mechanical strength). The analysis of the mechanical properties with the standard ASTM (American Society for Testing Materials): tension ASTM D882; At the end of the test, in addition to having the stress-strain curve, the value of the maximum stress reached during the test, Young's modulus value is obtained using the ASTM E111 standard, comparing the results with those thrown by the software. Composite material with good mechanical properties compared to the PVA-Cs material, by adding the conductive charges a material with greater mechanical resistance was obtained, so the PVA-Cs / PPy 0.3 g / PEDOT: PSS 0.1 g / MWCNT 0.1 g / CB 0.1 g, was the one that presented the best performance in the mechanical tests, having Young's modulus of 17.743 MPa, resulting in a material with higher mechanical resistance, compare to the material PVA-Cs with Young's modulus of 10.858 MPa. In contact angle analysis, observed all composite materials had a hydrophilic character, due to the influence of the molecules of the conductive charges.
The Electrochemical Impedance Spectroscopy (EIS) study was performed in a range of 0 Hz- 7 MHz, allows observing the behavior of the spectrum. The following impedance diagrams Z were made: Nyquist diagrams and bode diagrams. The film containing PPy 0.1 g/PEDOT:PSS 0.1 g/MWCNT 0.1 g/CB 0.1 g has Z = 78.66 kilohm, shown with a semicircle in the high frequency region, represents the interracial load transfer resistance (Rct), this is due to the transfer of electrons and diffusion of charges. Analysis Fourier Transform Infrared Spectroscopy (FTIR), in the area of 4000 to 600 cm^{-1}, present bands tension and stretching vibration of the hydroxyl group -OH, C-H stretching, C=O stretch band, vibration by O-H bending could be water absorption. C-O-C and C-OH vibration.

PS1.10
Synthesis and Characterization of Novel Pyrrole Ferrocene Derivatives and Their Semiconductor Behaviour Fomina Lioudmila, Roxana Carolina Delgado Cruz and Roberto Salcedo; Universidad Nacional Autónoma de México, Mexico

In the last decades, the study of organic semiconductors has been of great importance due to their potential applications in electronic devices, such as organic light-emitting diodes (OLEDs), field-effect transistors, sensors and solar cells. It is now possible to design organic semiconductor materials with adjustable HOMO-LUMO levels in order to have control over the electronic properties of the material and its potential performance in different devices. The present work consists of designing, synthesizing and characterizing new organic semiconductor materials derived from the compound 1-(p-amino-phenyl)-2,5 -diphenyl-pyrrole, using the electronic band gap value reduction strategy by introducing electron-withdrawing substituents in the molecule.
To obtain the trisubstituted pyrroles, the precursor 1,4-diphenyl-1,3-butadiyne was prepared by the Glaser-Hay reaction which consists of an oxidative coupling of terminal alkynes, in this case phenylacetylene. Subsequently trisubstituted pyrroles were synthesized using the Reisch-Schulte reaction involving the addition of aromatic amines substituted to 1,4-diphenyl-1,3-butadiyne. Finally, the group-NO_2 in the compound obtained (1-(4-nitro-phenyl)-2,5-diphenyl-1-pyrrole) was reduced to the derivative which includes-NH_2. From the compound (1-(4-amino-phenyl)-2,5-diphenyl-1-pyrrole) the formation reaction of diazonium salts was performed to obtain the compounds functioned with ferrocene. The synthesized compounds were characterized by infrared spectroscopy, nuclear magnetic resonance spectroscopy and thermal analysis. In addition, one of pyrrole ferrocene derivative was characterized by electron paramagnetic resonance spectroscopy. Theoretical calculations were also carried out for the optimizations of geometry of new pyrrole ferrocene derivatives. The values of bandgap obtained are located in the range of organic semiconductors, so these materials could have potential applications in optoelectronics.

PS1.11
(Student) Synthesis and Characterization of Novel Organic Compound: 1-(p-Fullerene-Phenyl)-2, 5 Diphenylpyrrole and Its Semiconductor Behavior Giovanna Angélica Vázquez Hernández[1], Lioudmila Fomina[1], Roberto Salcedo Pintos[1] and María Elena Sánchez Vergara[2]; [1]Universidad Nacional Autónoma de México, Mexico; [2]Universidad Anáhuac, Mexico

Organic semiconductors are a novel material class which has recently been investigated in detail due to very promising application possibilities. Since flexible and transparent substrate can be used, organic electronics open many new application and integration perspectives. The present work consists of designing, synthesizing, and characterizing a new organic semiconductor material:*1- (p-fullerene-phenyl) -2,5-diphenyl pyrrole* molecule. This synthesis was carried out from the reaction of diazonium salts. The product obtained was characterized by Fourier transform infrared spectroscopy (FT-IR) and Carbon Nuclear Magnetic Resonance ^{13}C NMR in solid to corroborate the formation of the compound and its structure, as well as by thermogravimetric analysis (TGA and DSC) to check its thermal stability. The thin film of the product was manufactured by thermal evaporation technique and characterized by FT-IR, UV-Vis, X-ray Diffraction and Scanning Electron Microscopy (SEM). It was found that the experimental band gap value by the Kubelka-Munk method for direct product transitions is 1.86 eV, which is in the range of those reported for organic semiconductors so that the compound obtained could be used for optoelectronic applications.

PS1.13
Parametric Modeling of Self-Winding Helices for Sub-Millimeter Traveling Wave Tube Amplifiers Marcos Martinez[1], Divya J. Prakash[2], Danier van der Weide[1] and Francesca Cavallo[2]; [1]University of Wisconsin–Madison, United States; [2]The University of New Mexico, United States

We have recently shown that helices formed by guided self-assembly of conductive nanomembranes (NMs) hold the promise to enable low-weight, reliable, and affordable traveling wave tube amplifiers (TWTA) that provide high field strength at THz frequencies[1] . These devices will potentially combine unique THz capabilities and vast deployment opportunities that will benefit high-data-rate and secure communications, radar, and electronic countermeasures. Designing a beam-wave interaction device based on a self-winding helix requires a reliable simulation approach to calculate cold-circuit (beam-free) parameters and gain resulting from beam-wave interaction. However, accurate parametric modeling of slow-wave structures obtained from guided self-assembly of NMs presents a unique set of challenges related to the reduced thicknesses and lateral dimensions of the NMs, and microscale diameter and pitch of the helices.
Here we present an in-depth parametric simulation analysis of self-assembled and conductive helices in the context of TWTA. Our study combines 3D numerical simulations of traveling waves in self-assembled structures with the evaluation of beam-wave interaction using a particle in cell solver. We perform simulations using CST microwave studio (CST-MS). We evaluate cold-circuit parameters as well as total gain, output saturation power, and bandwidth for helices formed via self-assembly of Cr/Au-based NMs. The helices diameters and pitch range from tens to few hundreds of micrometers. On the other hand, the helices are a few millimeters long. The NM thickness is of the order of 30-400 nm. Our work evaluates the sensitivity of the simulated performance

parameters of the TWTA to changes in the meshing techniques and the attributes of a given mesh. Additionally, we perform a comparative analysis of simulation results obtained via time-domain and frequency-domain solvers. [1] Prakash, Divya J., Matthew M. Dwyer, Marcos Martinez Argudo, Mengistie L. Debasu, Hassan Dibaji, Max G. Lagally, Daniel W. van der Weide, and Francesca Cavallo. 2020. "Self-Winding Helices as Slow-Wave Structures for Sub-Millimeter Traveling-Wave Tubes." *ACS Nano*, December. American Chemical Society (ACS). doi:10.1021/acsnano.0c08296.

PS1.14
(Student) Device Quality P-Type InGaN Relaxed Films
Mostafa Abdelhamid, Evyn L. Routh, Ahmed Shaker, Nadia El-Masry and Salah Bedair; North Carolina State University, United States

Conventional InGaN/GaN LEDs utilize p-type GaN with hole concentration in the low to mid $10^{17}cm^{-3}$ due to the high activation energy of the Mg dopant in GaN. This results in low hole injection in the multiple quantum wells (MQWs) active region. On the other hand, Si-doped n-type GaN electron concentration is in the mid 10^{18} cm^{-3}. This asymmetry in electron and hole concentrations and in carrier transport parameters has been reported to cause electron leakage. Electron leakage and thus, droop, can be eliminated for symmetrical LEDs with the same n- and p-type doping densities. Also, the performance of red emitting LEDs can be highly improved by an increase of an order of magnitude of p-type doping. For p-doped bulk $In_xGa_{1-x}N$ with In-content of about 15%, hole concentration in the mid to high 10^{18} cm^{-3} range were reported [1]. The high hole concentration is a result of the reduced activation energy of Mg with the increase in indium concentration in the ternary alloy, However, bulk $In_xGa_{1-x}N$, suffers from poor material quality, with many structural defects and have not been used as a part of pn-junctions, except for low values of In-content. Also, bulk InGaN has surface roughness that can be as high as 30 nm, thus not suitable for layered structures such as tandem solar cells and inverted n/p structures used to reduce polarization charges in LEDs.We report on device quality p-InGaN, using Mg doping of the Semi Bulk (SB) approach grown on GaN by MOCVD. A SB template of 20-30 periods of an $In_xGa_{1-x}N$ layer (15-25 nm) followed by a GaN interlayer (1-4 nm) is used. The cycle is repeated to achieve p-type InGaN films in the thickness range from 0.6 to 1 µm. The SB template allows for a gradual relaxation of the lattice parameter, while the GaN interlayer acts as a mitigating mechanism for the forming *V-pits* as the material is strain relaxed; the GaN interlayer is able to back fill the *V-pits* as the growth progresses. We have shown, by TEM studies that relaxation was mainly due to *V*-pit formation rather the generations of misfit dislocations [2]. P-type InGaN templates are characterized by photoluminescence (PL), atomic force microscopy (AFM), x-ray diffraction (XRD) and Hall measurements to determine the In-content, surface roughness, and hole concentration. We have achieved device quality p-$In_xGa_{1-x}N$ templates by the SB approach with indium content up to 12% and hole concentration of $3x10^{18}$ cm^{-3}. Surface roughness of 3-5 nm was measured by AFM. We will report on the dependence of hole concentration and surface roughness on the In-content for InGaN templates with In-content in the range of 5-15%. The impact of these p-type InGaN layers grown lattice matched to n-type InGaN templates in LED structures emitting in the green gap will be discussed. The SB p-type was tested as part of a green/yellow LED and the I-V is comparable to that of standard LED with p-type GaN. We will present methods to achieve device quality p-InGaN templates with hole concentration approaching $10^{19}cm^{-3}$
[1] K. Kumakura, T. Makimoto, and N. Kobayashi, Jpn. J. Appl. Phys., Part 2 39, L195 (2000).
[2] T. B. Eldred, M. Abdelhamid, J. G. Reynolds, N. A. El-Masry, J. M. Lebeau, and S. M. Bedair, Appl. Phys. Lett. 116, 102104 (2020).

PS1.15
On the Photoluminescence Emission of ScAlN Grown by Molecular Beam Epitaxy Ping Wang, Boyu Wang, David A. Laleyan, Ayush Pandey, Yuanpeng Wu, Yi Sun, Xianhe Liu, Zihao Deng, Emmanouil Kioupakis and Zetian Mi; University of Michigan–Ann Arbor, United States

Recent studies have shown that incorporating IIIB Sc atoms into the lattice of traditional IIIA-nitrides can significantly expand their functionality, such as bandgap and polarization engineering, and ferroelectric properties. Abnormal enhancement of electromechanical response has been observed in ScAlN, enabling a broad range of applications in surface acoustic wave (SAW) resonators, high electron mobility transistors (HEMT), micro-electromechanical systems (MEMS), and polarization engineered deep ultraviolet (UV) optoelectronics. The theoretically predicted bandgap of ScAlN has been experimentally demonstrated by employing pulsed DC magnetron co-sputtering and plasma-assisted molecular beam epitaxy (MBE). To date, however, there have been no reports on the optical emission properties of ScAlN, either under optical excitation or electrical injection. The nonluminous ScAlN suggests the dominance of nonradiative recombination, resulting from the presence of extensive defects and impurities. Due to the large affinity of Sc and the refractory nature of Sc_2O_3, ScAlN is more susceptible to oxygen impurity incorporation than GaN and AlN. The non-steep absorption spectra reported in ScAlN indicated the existence of interband defect levels as well. The undesirable incorporation of oxygen not only prevents bandgap engineering in optoelectronic devices, but also introduces electrical leakage path in electronic devices, and further deteriorates the ferroelectric properties. Exploring the defect-related emissions of ScAlN, therefore, are essential for its applications in next generation optoelectronic and electronic devices. In this work, we have investigated the photoluminescence emission of ScAlN grown by MBE with varying growth temperatures and Sc contents. ScAlN/AlN epilayers were excited using a 193 nm (6.42 eV) ArF excimer laser (with a repetition rate of 100 Hz with a pulse energy of 0.1 mJ). Employing this above-band photoexcitation, a bright and broad emission was measured, with a dominant peak at ~3.52 eV and a weak peak at ~2.90 eV for $Sc_{0.05}Al_{0.95}N$. The peak energy of the dominant peak is independent of the excitation power and measurement temperature, suggesting a highly localized nature of its emission state. Comparing with the well-studied defect-related emissions in AlN, the origin of the 3.52 eV emission line is attributed to charge carrier recombination from the localized excited state of $(V_{cation}\text{-}O_N)^{2-/-}$ to its ground state, whereas the second peak at ~2.90 eV results from charge carrier recombination of isolated to valance band. With increasing growth temperature, the oxygen defect-related emission can be suppressed significantly. This work sheds light on the recombination dynamics of photoexcited carriers in ScAl, and further offers insight on how to improve the optical and electrical properties of ScAlN that are relevant for a broad range of applications.

PS1.16
Investigation of Ferroelectric Properties in $Al_xSc_{1-x}N$ Thin Films via *In Situ* Transmission Electron Microscopy Stefan Nikodemski[1], Amber Reed[2], John Cetnar[2], David Look[3], Vladimir Vasilyev[2] and Clarissa Vazquez-Colon[1]; [1]KBR, United States; [2]Air Force Research Laboratory, United States; [3]Semiconductor Research Center, Wright State University, United States

Recently, there has been a demand for high quality thin film materials possessing ferroelectric properties that can be integrated with current semiconductor devices as well as other emerging technologies. Herein, we investigate the recent claims of ferroelectric switching in $Al_{1-x}Sc_xN$ using *in-situ* transmission electron microscopy (TEM). Direct observation of the dynamic process of electric field induced transitions in ferroelectrics is of great importance in verifying the underlying mechanisms of the

residual polarizations in these materials. We began by preparing polycrystalline thin films of AlScN with various Al/Sc ratios spanning the entire composition range via low temperature magnetron co-sputtering. Composition was verified via x-ray photoelectron spectroscopy measurements. Wurtzite-type crystal films particularly close to the wurtzite-rocksalt phase transition were prioritized as prior reports indicate the most pronounced ferroelectric properties in these films. *In-situ* TEM measurements were performed by a series of electrical biasing experiments through the films parallel to the wurtzite c-axis in order to observe changes in the crystal structure as a function of applied voltage. Additionally, the influence of temperature was investigated via dynamic heating. Bulk-like film structure and roughness was measured using x-ray diffraction and atomic force microscopy.

PS1.17
(Student) Effect of Active Molecule Edges on Magnetic Transport Properties of Molecular Spintronics Devices (MSD) Joshua Dillard, Kymani Brown, Marzieh Savadkoohi, Andrew C. Grizzle, Christopher D'Angelo and Pawan Tyagi; University of the District of Columbia, United States

The Magnetic Tunnel Junction Molecular Spintronics Device (MTJMSD) approach provides an opportunity to resolve decades-old mass-production difficulties in fabrication of spintronic-based computer devices. The MTJMSD consists of two ferromagnetic electrodes (FMEs) connected by a nanoscale insulator film and molecular channels along the exposed side edges. Given the large number of molecules known today, the device can be idealized by using molecular combinations with ideal transport properties. In previous studies we have found that single molecular magnets produced strong antiferromagnetic coupling between electrodes. Herein the strength and nature of ferromagnetic coupling between paramagnetic molecules and two ferromagnetic electrodes is altered. As the magnitude and nature of coupling changes, the temporal evolution of total device magnetization is studied as individual vector components—left electrode magnetization, right electrode magnetization and molecular magnetization. In our previous studies we have investigated the molecular-induced magnetic properties of MTJMSD using four edges of the rectangular shaped molecular plane. There exists a knowledge gap about the role of number of active edges on the MTJMSD equilibrium properties. In this paper we are exploring the effect of selectively turning on one, two, three, and four edges of the MTJMSD. We focus on investigating the effect of number of active edges on temporal evolution process. We also study the effect of active molecular edges on global and localized magnetic susceptibility and heat capacity of MTJMSD. In this paper we utilize Monte Carlo simulation (MCS) to study the MTJMSD Ising model composed of 2500 atoms and individual spin states. The simulation allows for changing the magnitude and nature of FME-molecules-FME couplings. Molecule-FM interaction is represented by Heisenberg exchange coupling with left (JmL) and right electrodes (JmR). The magnetization can be an indicator of various types of couplings (e.g., antiferromagnetic, ferromagnetic) via bridging molecules when the competing coupling via insulator is minimized. This study is part of ongoing effort to discover an MTJMSD magnetic configuration wherein the effect of the variation in the molecular exposed edges can be fully understood. Our preliminary results suggested that at least 200 million simulation is required to achieve the equilibrium state for extreme cases where there is a strong molecular coupling between molecules and left and right electrodes. However, higher number of simulations might be needed to gain the equilibrium state when studying temporal evolution of magnetic moment with weaker Heisenberg FMEs-molecules exchange couplings. Furthermore, the spatial distribution of magnetic moment was studied using the Ising Model of MTJMSD. We observed that only four molecules on the right exposed edge are able to form ferromagnetic coupling with the left electrode and antiferromagnetic coupling with the right FM electrode.

PS1.18
Monte Carlo Simulation Study of Single Molecular Spin State Effect on Anit-Ferromagnetically Coupled Magnetic Layers of Magnetic Tunnel Junction Based Spintronics Device Andrew C. Grizzle, Christopher D'Angelo, Bishnu R. Dahal and Pawan Tyagi; University of The District of Columbia, United States

Molecular spintronics devices (MSDs) are created by connecting molecular channels between two ferromagnetic (FM) electrodes. Utilizing a magnetic tunnel junction (MTJ), single molecular magnets (SMMs) provide a robust molecular channel between the FM electrodes, thereby producing a magnetic tunnel junction based molecular spintronics device (MTJMSD). Our prior experimental studies showed that the SMM-based MTJMSDs produced unprecedented strong anti-ferromagnetic coupling between the FM electrodes and consequently resulted novel electrical, optical, and magnetic device properties. While the spin states of isolated SMMs have been experimentally verified, it is challenging to quantify their spin state while connected to two FM electrodes. Here we show the variable molecular spin states of the SMM and the impact on producing strong anti-ferromagnetic and ferromagnetic coupling between the first and second FM electrodes of the MTJMSD, ultimately leading to an overall robust anti-FM coupling around room temperature regime. Using Monte Carlo Simulations (MCS), following a Markov process, and analogous 11x50x50 3D Ising models of the MTJMSD, we analyzed the devices' temporal and spatial magnetic moments as a function of the SMM's spin state, molecular exchange coupling strength, and thermal energy. We also show the SMM's impact on the MTJMSDs' spatial correlation factor, heat capacity, and magnetic susceptibility. Our findings suggest that the magnitude of the SMM's spin state should be at least ~0.2 to impact the magnetic properties of the MTJMSD significantly. With increasing molecular spin magnitude, we observed more pronounced effect due to molecular coupling. Higher molecular spin magnitude also expedited the stabilization process.

PS1.19
(Student) Effect of Biquadratic Coupling Due to Molecular Magnet Channels Between Ferromagnetic Electrodes of a Magnetic Tunnel Junctions Hayden Brown, Bishnu R. Dahal, Andrew C. Grizzle, Marzieh Savadkoohi, Christopher D'Angelo and Pawan Tyagi; University of the District of Columbia, United States

Molecular spintronics devices (MSD) utilizing magnetic tunnel junctions (MTJ) as the testbed may prove to be a revolutionary technology. MTJ based MSD(MTJMSD) can utilize the optimization efforts towards commercializing the MTJ technology in the current readaheads of present-day computers. Hence, MTJMSD method can solve difficulties of reliability and mass production of molecular devices. Under MTJMSD approach organic molecules bridge an insulator along the exposed side edges of a prefabricated MTJ. MTJMSD is in this complete setup, have potential to utilize any molecule which could bond to ferromagnets. In our previous theoretical studies, we have investigated the Heisenberg type molecule induced exchange coupling between ferromagnetic electrodes to explain the experimentally observed molecule effect. However, it is well known a nanostructure placed between ferromagnetic electrodes also produce biquadratic type magnetic coupling. this paper focus on studying the effect of biquadratic coupling on MTJMSDs for the first time. We have investigated the biquadratic coupling induced by molecules and any potential defect causing direct coupling in the planar junction area. To make this study relevant to our experimental setup we have focused on Ising model of the cross junction shaped MTJMSD. We performed Monte Carlo Simulations (MCS) using continuous spin model. MCS studies focus on varying the magnetic molecule induced biquadratic coupling with two ferromagnetic electrodes over –1 to 1 range. By this provision, our MCS study cover a wide range of possibilities

arising due to the several combinations of molecule interaction with two metal electrodes. We also study the impact of competition between biquadratic coupling and Heisenberg type exchange coupling due to the magnetic molecules. We mainly study the impact of biquadratic coupling in the strong coupling regime of Heisenberg type exchange coupling. For the case when molecules produced antiferromagnetic type Heisenberg coupling, we observed that strong biquadratic coupling dominated the magnetic phases on the ferromagnetic electrodes. One of the ferromagnetic electrodes assumed repetitive phases comprised of high and low spin states. Future study focuses on exploring the wide range of combinations of Heisenberg and biquadratic coupling to explore new science of highly correlated magnetic states on MTJMSDs. This research is supported by National Science Foundation-CREST Award (Contract # HRD- 1914751), Department of Energy/ National Nuclear Security Agency (DE-FOA-0003945).

PS1.20
(Student) Monte Carlo Simulations Investigating the Effect of Intra-Molecular Coupling Within Double Segmented Molecules on Magnetic Properties of Molecular Spintronics Devices Pius Suh, Marzieh Savadkoohi, Andrew C. Grizzle, Bishnu R. Dahal, Christopher D'Angelo and Pawan Tyagi; University of the District of Columbia, United States

Paramagnetic molecules, with a net spin state, can tailor magnetic exchange coupling between two ferromagnetic (FM) electrodes in magnetic tunnel junction based molecular spintronics devices (MTJMSD). Magnetic coupling between paramagnetic molecules and two FM electrodes in MTJ-based devices is dependent on a net molecular spin state. In our prior studies, we have extensively studied the atomic analog of the single molecular magnet. That means whole molecular geometry and internal features were approximated to appear as one atom representing that molecule. To advance the understanding of the impact of internal molecular structure on MTJMSD, we have focused on multi-segmented molecules. This research aims to fill the knowledge gap about the intramolecular coupling role on the magnetic properties of the MTJMSD. This study explored a double segmented molecule containing two sections, each with a net spin state. In this research, we tested the hypothesis that variation in the strength and nature of intra-molecular coupling among multiple segments of a molecule can produce a novel testbed to observe the novel phenomenon. This paper investigates the effect of intra-molecular coupling (Jm) on the MTJMSD magnetic properties using Monte Carlo Simulation (MCS). We varied Jm magnitude and sign and studied its subsequent impact on the MTJMSD magnetic properties at different thermal energies. We also examined the effect of Jm on the MTJMSD evolution under varying Jm. Device magnetization was recorded as a function of time for various simulation counts (10000 to 500 million) to achieve device stabilization and to capture temporal evolution. Our MCS results showed that Jm yielded an impact localized around the junction area at low thermal energy. At increased thermal energy, we observed the entire system was set into chaos with random spin directions. These studies may create a platform for more investigations on the effect of intra-molecular coupling on the magnetic properties of the MTJMSD. This research is supported by National Science Foundation-CREST Award (Contract # HRD-1914751), Department of Energy/ National Nuclear Security Agency (DE-FOA-0003945).

PS1.22
Ferromagnetic Electrodes Thickness Impacting the Equilibrium Magnetic Properties of the Magnetic Tunnel Junction Based Molecular Spintronics Devices. Uzma Amir, Andrew C. Grizzle, Christopher D'Angelo, Marzieh Savadkoohi, Bishnu R. Dahal and Pawan Tyagi; University of the District of Columbia, United States

The magnetic tunnel junction based molecular spintronics device (MTJMSD) approach is capable of integrating a vast range of electrode materials and molecules thus offers limitless opportunities. MTJMSD is formed by placing magnetic molecular channels along the exposed sides of a magnetic tunnel junction. Previous research have shown that variation in ferromagnetic electrode thickness can produce significant different in magnetic coercivity[1]. Difference in magnetic electrode coercivity has been a major goal in designing and fabricating molecular spintronics devices showing highly intriguing Kondo Level splitting like attributes [2]. MTJMSD is relatively new field where limited experimental studies have been performed to investigate the effect of magnetic electrode thickness. Under MTJMSD approach, molecules appear in the form of a ring around the tunnel barrier of a MTJ with exposed side edges. However, it is extremely challenging to investigate the effect of wide range of FM electrode thicknesses up to monolayer scale experimentally. We have utilized continuous Monte Carlo simulations to investigate the Ising Model representation of cross junction shaped MTJMSD. This paper provides insights into the effect of placing the molecular layer between two FM electrodes of different thicknesses. We conducted MCS while varying exchange coupling between molecules and the FM electrodes at different thermal energies. The effect of FM electrode thickness was strongly dependent of the magnetic molecule coupling with the two FM electrodes. Thinner FM electrodes reached in the equilibrium state quicker as compared to thicker FM electrodes. As a result, overall MTJMSD stabilization, depending on the equilibrium state on both FM electrodes, was governed by thicker FM electrode. The spatial correlation of the magnetic molecular spin with FM electrodes spins was dependent on the FM electrode's thickness. The FM electrode's thickness impact was influenced by the thermal energy (kT). To explore the switching potential of MTJMSD among multiple equilibrium magnetic states we also simulated the spatial distribution of magnetic susceptibility and heat capacity. We strived to find the combination of film thickness, molecular coupling strengths and nature, and thermal energy to seek a large difference in magnetic susceptibility of the molecule and the ferromagnetic electrodes. This MCS research may enable the designing of futuristic MTJMSD or molecular spintronics device based spin valves for memory devices.

PS1.23
(Student) Fluoropolymer Ionomers as a Dielectric in Rubrene Single-Crystal Transistors for Improved Charge Carrier Mobility Sarah Sheffield, Michael Hickner and Enrique D. Gomez; The Pennsylvania State University, United States

Organic transistors have a significant potential in emerging modern electronics, such as bioelectronics due to their ability to amplify low electrical signals. As organic transistors are applied to these new applications, various gating mechanisms are being explored to achieve the desired device performance. Electrolyte-gated transistors (EGTs) and organic electrochemical transistors (OECTs) are gated using electrolytic or ionic materials as their dielectric layer, which has been shown to produce good signal amplification and sensitivity to low voltages. Solid-state ionic materials, such as ionomers, are currently of interest due to being more processable than liquid ionic materials for EGTs. In EGTs, the conduction channel is formed at the semiconductor-dielectric interface due to the induction of the ions within the electrolyte layer. To isolate studying the properties of the dielectric layer,

rubrene organic single crystals are used as the semiconductor in the fabricated EGTs as their complete crystallinity prevents any ion injection into the semiconductor. Rubrene single crystals are formed through physical vapor transport (PVT), which produces high-purity crystals with minimal to no grain boundaries, and are known to exhibit high charge carrier mobilities for an organic material. This work uses Nafion, a fluoropolymer consisting of a hydrophobic polytetrafluoroethylene (PTFE) backbone with a perfluorinated ether side chain capped with a hydrophilic sulfonic acid, as the dielectric material in the EGTs, as it is known to be a good proton conductor. Additional modifications to the Nafion layer can be employed to better improve charge carrier mobility, such as adding ionic liquids to increase the ionic concentration. This work examines the properties of using an ionomer, Nafion, as an electrolyte gate insulating layer in single-crystal transistors for the improvement of charge carrier mobility and overall device performance.

PS1.24
(Student) Effects of Lignin Precursors and Processing Conditions on the Structures of Carbon Composites as Electrodes for Batteries Lu Yu, Kendhl Seabright, Valerie García-Negrón, Dayton G. Kizzire, David J. Keffer and David P. Harper; University of Tennessee, United States

Lignin as a natural abundant polymer with high carbon content and unique aromatic structure has demonstrated promise as energy dense electrode materials in electrochemical devices. As such, these materials demonstrate ion binding that differs from intercalation. Understanding the structural changes and relationship to the performance of these carbon composites from lignin has been a challenge due to lignin's highly complex structure that varies as a function of the biomass source and the isolation method. In this work, yellow pine (YP, softwood lignin), hybrid poplar (HP, hardwood lignin) and switchgrass (SG, grass lignin), were adopted as the carbon precursors. Lignin precursors with various functional groups and syringyl (S), guaiacyl (G) and p-hydroxyphenyl (H) contents were characterized using ^{31}P nuclear magnetic resonance (NMR) and two-dimensional HSQC NMR. For the produced carbon composites, neutron scattering data was collected at a spallation neutron source in Oak Ridge National Laboratory. The changes in the pair distribution functions corresponds to the samples from different precursors and processed under varying conditions. The morphology obtained from total neutron scattering were investigated and compared with our previous synchrotron data as well as molecular dynamics simulation results.

PS1.26
(Student) Temperature Dependence of Optical Phonon Bands in GaP Nuwanjula Samarasingha and Stefan Zollner; New Mexico State University, United States

We explore the effect of temperature on the frequency and linewidth of transverse (TO) and longitudinal (LO) optical phonons in bulk gallium phosphide (GaP) using FTIR ellipsometry from 0.03 to 0.80 eV from 80-720 K. We extract the optical phonon features of GaP by fitting our ellipsometric spectra with the Lowndes–Gervais model, which applies two different broadening parameters to the TO and LO phonons. In GaP, the two-phonon density of state is larger for the decay of TO phonons than for LO phonons. Therefore, we observed a large TO phonon broadening and an asymmetric reststrahlen line shape (compared to the LO phonon). This leads to a negative dielectric constant (ε_2) just above the LO phonon. Two-phonon absorption can be added in the model to avoid this negative ε_2. We find a temperature dependent redshift and broadening of TO and LO phonons with increasing temperature due to anharmonic phonon-phonon decay [1]. These temperature dependent phonon features can be described by three and four phonon decay processes. Also, we investigate the temperature-dependence of the high-frequency dielectric constant. Its variation is explained by thermal expansion and the temperature dependence of the band gap.

Reference

[1] M. Balkanski, R. F. Walls, and E. Haro, Phys. Rev. B **28**, 1928 (1983).

PS1.27
(LATE NEWS, Student) Annealing Time Effects with a Fixed Temperature on Thin-Film Perovskite Solar Cells Jesus Marquez, Yves A. Ramirez, German Rodriguez-Ortiz and Deidra Hodges; The University of Texas at El Paso, United States

Current $FA_xCs_{(1-x)}Pb(I_yBr_{(1-y)})_3$ perovskite solar cells are improving its results every year. It is a matter of time until they approach the maximum theoretical single layer efficiency of 31%. The process to achieve cheap commercial perovskite solar panels is divided in three main categories: power conversion efficiency, scalability, and lifetime. Power conversion efficiency is sub-divided in low-bandgap, high-bandgap, and tandem solar cells. A tandem solar cell is required to surpass the single layer theoretical efficiency. However, before reaching any of these steps, a high bandgap perovskite solar cell with a high efficiency must be developed. High bandgap solar cells require a bandgap as close to 1.5 eV to absorb most of the visible wavelength. During the deposition processes, a stable process such as chemical vapor deposition or physical vapor deposition is required to deposit either SnO2 or ZnO2 as the n-dopant. The proposed research in this project will vary time, temperature, and thickness to achieve an efficiency above 20%. In this paper, we discuss how the smallest change in the deposition processes of a perovskite solar cell can change the results very abruptly. In this experiment, the varying factor during the perovskite deposition process is annealing time. There was a variation of the time between 30- and 80-minutes for six samples with a difference of 10 minutes each at a fixed temperature of 100°C. The main difference between the samples is that the efficiency, open circuit voltage, fill factor, and current density start to decay when the annealing surpasses the inflection point. If the annealing time is less than 50 minutes or if it exceeds 70 minutes, the key solar cell parameters decay. If the annealing time is less than 50 minutes, the grains do not have enough time to form, or they are very small. These devices result in low efficiencies. When the annealing time exceeds 70 minutes, the grains are larger with voids, negatively affecting the overall device performance. There is an efficiency decay of 59% between a device annealed during 40 and 50 minutes while there is a drop of 23% between 70 and 80 minutes. These limits leave the process with an optimization time between 50 and 70 minutes. However, there are small differences between 50, 60, and 70 minutes. Fill factor, current density, and power conversion efficiency are higher at 50 minutes of annealing while the open circuit voltage is higher at 70 minutes. This is attributed to the grain size at a shorter time, allowing for a higher current density. A high current density maintains a relatively high fill factor and power conversion efficiency. With a fixed temperature of 100°C, the optimum annealing time to achieve the highest power conversion efficiency is between 50 and 70 minutes where the current density is higher at 50 minutes while the voltage is higher at 70 minutes. The obtained results will be very beneficial as a reference for future $FA_xCs_{(1-x)}Pb(I_yBr_{(1-y)})_3$ perovskite solar cell characterization and research.

SESSION PS2: Poster Session II
Thursday Morning, June 24, 2021
9:00 AM - 10:30 AM

EP01
(Exhibitor Poster) Taiyo Nippon Sanso Mayank Bulsara; Matheson Tri-Gas, Inc., United States

List of Products
MOCVD reactors, specialty gas sources, gas purifiers, and gas abatement solutions

Business Description
Taiyo Nippon Sanso is an industrial gas manufacturer established in 1910. As an innovator in the compound semiconductor industry, Taiyo Nippon Sanso was the first company to introduce commercial MOCVD systems, in 1983. Taiyo Nippon Sanso is uniquely qualified to provide total solutions for compound semiconductor fabrication, with MOCVD equipment, gas handling and purification equipment, exhaust abatement solutions, and custom piping and installation services. The SR4000 series GaN MOCVD reactors, originally introduced in 2002, are highly regarded worldwide for their exceptionally stable performance for HEMT, PN Diode, Laser, and RBG/UV LED applications. The SR4000HT (maximum 1350 °C process temperature) can be configured interchangeably for 2" and 4" wafer processing at growth pressures of 10 kPa up to 100 kPa. The newly introduced SR4000HT-RR has a compact design especially suited for university and research environments while maintaining high performance capability. The UR series GaN MOCVD reactors, available since 2008, are workhorse solutions for production applications. The UR25K is configurable for multi-4" or 6" wafer processing and the UR26K is configurable for multi-6" or 8" wafer processing. The UR series reactors can process high quality films at growth pressures from 10 kPa to 100 kPa. With high growth rate capability, cassette-to-cassette wafer handling options, and other features, the UR series offer customers excellent uptime and throughput.

EP02
(Exhibitor Poster) k-Space Associates, Inc. Kathy Wheeler; k-Space Associates, Inc., United States

Key Products: In situ and Ex situ Metrology Tools for Epitaxy
k-Space Associates, Inc. is a leading provider of optical metrology tools. kSA 400 is an **analytical RHEED acquisition and analysis** tool offering real-time growth rate and atomic spacing. kSA BandiT offers **band edge substrate temperature** for semiconductor substrates such as GaAs, InP, Si, CZT, GaP, SiC, GaN, Ga2O3, and AlN. kSA MOS measures **film stress** during deposition or thermal processing. kSA ICE is a modular, in situ system for MBE and MOCVD, offering real-time wafer curvature, temperature, and reflectivity. kSA SpectR is a complete metrology solution for measurement of absolute **spectral reflectance**, growth rate and end point detection to determine device spectral features for DBRs or VCSELs. kSA ICE (**integrated control for epitaxy**) combines these tools in modules on one optics head for a compact measurement solution. kSA MOS UltraScan provides **ex situ full wafer stress mapping** with adjustable optics for measurement of smaller samples. kSA ACE (**atomic control for epitaxy**) will be released soon.
requestinfo@k-space.com | www.k-space.com

EP03
(Exhibitor Poster) CuttingEdge Ions, LLC Brian Doherty; CuttingEdge Ions, LLC, United States

Specialty Ion Implant Services:
* Most elements of the periodic table
* Also molecules
* Capabilities:
° LN2 cooled implants
° Chilled stage to -15C
° Heavy dose implants for exfoliation
° Nitrogen vacancy implants into single crystal diamonds – N15 and N14
° Heated implants for SiC and other materials up to 1000C on small samples and full wafers of up to 6 inch
° $LiNbO_3$ exfoliation implants using Helium or other species
° 8 different implanters covering 1keV to 1MeV
° Special beam filters as required by some species
° Flux control capabilities down to the nanoamp range – useful for control of lattice damage
° Tilt and twist angle control of any angle – useful for trench implants and also to eliminate "channeling"
° Masking of samples to allow for different sections to have different implant specs
° 4 quadrant rotation of samples
° Plus and minus tilt angles
° Many specialty gasses kept in stock: e.g. 3He, 17O, 18O, Deuterium 2H etc.
° Implantation of species for surface hardening of medical devices
° Modeling services – including achieving a box profile using multiple implant energy/dose combinations
° Guidance on other process steps including annealing parameters
° Fast turnaround is normal – typically 3 days
° Support for researchers and students, no job too small, we are here to help
° Production implants with very fast turnaround – 24 hour 3 shift operations for one day/same day expedite options
° Special packing capabilities as needed – e.g insulated with cool-pak
° Overseas shipments with rapid customs clearance protocols

EP04
(Exhibitor Poster) Structured Materials Industries, Inc. Gary S Tompa[1]; [1]Structured Materials Industries, Inc., United States

Your one stop resource for custom Metal Organic Chemical Vapor Deposition (MOCVD) Systems, Alternating Layer Depository (ALD) systems, Plasma Enhanced CVD (PECVD) systems, Hydride Vapor Phase Epitaxy (HVPE) Systems, and supporting Processes, Services, and Components, and Contract Service Support. We do it all!

PS2.01
(Student) Electrical Characteristics of Differently Surface-Treated N-Type AlInP for Red Light-Emitting Diodes Jung Suk Cha and Tae-Yeon Seong; Korea University, Korea (the Republic of)

For micro-based display application, the development of high-efficiency full color micro- light-emitting diodes (LEDs) (e.g., red, green, and blue emitters) is critical. In particular, despite the importance for the realization of high-efficiency red emitters, the performance of AlGaInP-based red micro-LEDs has not been extensively investigated. Further, the surface recombination velocity and carrier diffusion length of AlGaInP-based red LEDs was known to be much larger than those of InGaN. Therefore, the surface characteristics of an n-type AlInP contact layer are considerately affected by the presence of surface states (defects). Thus, in this study, we have investigated surface Fermi level pinning behaviour at n-AlInP/metal interfaces, where four different metal layers (Ti, Cr, Au and Pt) with different work

functions were used. In other words, Schottky barrier heights (SBHs) and their dependence on metal work function at (001) n-AlInP surfaces were investigated. The SBHs and ideality factors were obtained using current-voltage-temperature (I-V-T), Norde model, and barrier inhomogeneity model. Further, three different sets of samples were prepared, namely, as-cleaned, buffer-oxide-etch (BOE)-treated, and BOE-$(NH_4)_2S$-treated. It was shown that for regardless of the surface treatments, the SBHs of all samples increased and the ideality factors decreased with increasing temperature. For the as-cleaned samples, the SBHs estimated using the I-V characteristics were in the range of 0.78–0.83 eV, depending on the metals. On the other hand, for the BOE and BOE-sulphur-treated samples, the SBHs were in the range of 0.78–2.1 eV, depending on the metals. The S-parameters (Φ_B/Φ_M) (the mean barrier height vs. the metal work functions) indicate that the as-cleaned sample exhibits almost perfectly pinned surface Fermi level, the BOE-sulphur-treated sample shows no pinning, and the BOE-treated sample reveals somewhat unpinned. On the basis of the electrical results by the I-V and inhomogeneity model, the dependence of the SBH characteristics on the surface treatments is discussed in detail.

PS2.02
High-Reliability AlGaN/GaN HEMTs for High Voltage Applications Using Nitrogen-Rich Silicon Nitride Passivation and Field Plates Nayana Remesh, Khawaja N. Subhani, Niranjan S, K N. Bhat, Srinivasan Raghavan, Muralidharan R and Digbijoy Nath; Indian Institute of Science, India

Despite its maturity and growing competitiveness in the emerging power electronics market, GaN-on-Silicon transistors face a host of challenges in material quality and device performance, namely, current collapse and reduced reliability due to permanent breakdown. Current collapse occurs mainly due to surface states and bulk trapping. The former can be controlled by appropriate passivation and field plate design. Improper passivation between the gate-source region and gate-drain region leads to degradation of device performance due to interfacial traps This will result in channel current modulation by these interfacial traps with time, temperature, and electric field. These traps will also lead to an increase in the gate leakage which will result in degradation of the breakdown characteristics of the device. It is very crucial to realize a pristine interface between SiN and the semiconductor (GaN) to achieve high breakdown voltage and low current collapse. There has been a lot of studies on reducing these interfacial and bulk traps in SiN to achieve low current collapse and low surface/gate leakage in III-V devices. In this work, we have investigated the material properties of PECVD (plasma-enhanced vapor deposition) deposited amorphous SiN films and their influence on leakage current and passivation of AlGaN/GaN HEMT grown on Si to obtain reliable devices with a low coefficient of dispersion. We have studied the effect of gas flow (SiH_4/NH_3) on the structural and compositional properties of SiNx deposited on crystalline Si. The optimized SiNx is N-rich with a refractive index of 1.83, tensile stress of 681 MPa, and NH_3/SiH_4 ratio of 18, and showed a substantial reduction in terms of gate leakage and three-terminal leakage compared to the reference samples. We have fabricated AlGaN/GaN HEMTs with gate connected field of length 800 nm using the optimized SiNx. The fabricated HEMTs demonstrated high reliability in terms of 3-Terminal Breakdown Voltage up to 400 V @ 10 μA/mm with a 3.6 % coefficient of variance over 25 devices.

PS2.03
Engineering Electrical Properties of Reactively Sputtered High Entropy Alloy CrFeNiCoCu Films Jeyanthinath Mayandi[1,1], Terje G. Finstad[1,1], Marit Stange[2], Giovanni Vasque[1], Martin F. Sunding[2], Ole M. Løvvik[1,2], Spyros Diplas[2,1] and Patricia Carvalho[2]; [1]University of Oslo, Norway; [2]SINTEF Industry, Norway

Oxide containing films were deposited by reactive sputtering using a high entropy alloy (HEA) target made of equal concentrations of the five 3d-transion metals: Cr, Fe, Co, Ni, and Cu. We report on controlled alterations to the electrical properties made by post-deposition heat treatments in oxidizing and reducing atmospheres respectively. The temperature coefficient of resistivity of the films could be varied between -1.2×10^{-3} K^{-1} through 0 and to $+0.7\times10^{-3}$ K^{-1}, while the measured effective resistivity could be varied between 1.3×10^{-4} Ωcm and 1.2×10^{-3} Ωcm by post deposition processing. To study the transport mechanisms, we performed temperature dependent Hall effect measurements down to 10 K. We correlated the electrical behavior with structural measurements by a combination of X-ray diffraction (XRD), scanning electron microscopy (SEM) with energy dispersive X-ray spectroscopy (EDS) for elemental mapping at various length scales and secondary ions mass spectroscopy (SIMS). The key to engineering the resistivity is controlling the topology of the film. The topology of the as-deposited thin films can be controlled by the oxygen flow during reactive sputtering as the most important parameter. For zero oxygen flow we have obtained a homogenous HEA film having a FCC structure with the CrFeNiCoCu target. For high oxygen flow we have observed a high entropy oxide with a rock salt crystal structure. Here we report on the case of intermediate flow of oxygen. The as-deposited structure is then complex. There are nano sized regions with oxides and regions with FCC HEA alloys with different compositions of all the 3d-metals but also supersaturated with oxygen. The topology of these regions, and also their concentration, can be altered by post-deposition heat treatment. The transport in the HEA regions are dominated by alloy scattering. The potential in the FCC HEA has disorder due to the random mixing of the elements, which also gives distortion of the individual atom sites. This gives resistivities above the Mott-Ioffe-Regel limit while still having a positive TCR. These disorder effects will be further enhanced by the uptake of oxygen atoms. For these cases one gets weak localization, yielding a negative TCR. The oxides may be insulating but may also conduct by variable range hopping of the Efros–Shklovskii-type or the Mott-type yielding characteristic negative TCR. The post-deposition yields oxide segregation, of for example of spinel type containing Cr. This reduce the entropy and stability of the metal alloy, creating FCC and BCC metal alloys of different compositions. In the case of reducing the heat treatment in a reducing atmosphere, the oxides are reduced. The experimental resistivities are in excellent agreement with the model for the conduction.

PS2.04
Electrical Conductivity and Effects of Bending of Flexible Amorphous Transparent Conducting CdO–Ga_2O_3 Alloy Films Sputter–Deposited at Room Temperature Ying Wang, Cheuk Kai G. Kwok, Shil Sujit H. Kumer and Kin Man Yu; City University of Hong Kong, Hong Kong

Wide band gap amorphous ionic oxide semiconductors (AIOSs) with high electron mobility(>10 cm^2/V-s) and low electrical resistivity have attracted much recent attention due to their potentials as materials for a wide range of next-generation flexible and transparent optoelectronic devices. AIOSs are typically ternary or quaternary oxides grown at low temperature with large area uniformity, and hence are compatible with the fabrication of flexible and organic devices. In this study, we synthesize a new class of AIOS, CdO-Ga_2O_3 alloys on both glass and polyethylene terephthalate (PET) substrates by radio frequency magnetron

sputtering at room temperature and explore their properties for flexible electronic applications. Our experimental results show that $Cd_{1-x}Ga_xO_{1+\delta}$ alloy films are amorphous with Ga content x>0.3 and within the amorphous composition range of 0.3<x<0.4 the films exhibit a high electron mobility of ~20 cm^2/V-s and a low resistivity of ~2×10^{-3} Ω-cm with a wide optical gap of ~3.4 eV. In order to determine if the $Cd_{1-x}Ga_xO_{1+\delta}$ alloy films are suitable for flexible electronic applications, effects of mechanical bending on their resistivity were evaluated as a function of the bending radius R_b and number of bending cycles. We find that amorphous $Cd_{1-x}Ga_xO_{1+\delta}$ films are more resilient to repeated compressive (inner) bending than that of crystalline film. No change in the electrical resistivity of the amorphous films is observed for compressive bending with $R_b \geq 10$ mm. On the other hand, crystalline films experience much less electrical degradation after tensile (outer) bending. SEM and AFM studies confirm that crystalline films with large grain size easily delaminate from the substrate under compressive bending, giving rise severe electrical degradation. On the other hand, amorphous films degrade most likely through developing microcracks under repeated tensile bending. Our results suggest that amorphous $Cd_{1-x}Ga_xO_{1+\delta}$ alloy films with 0.3<x<0.4 have the desired electrical, optical and mechanical properties as transparent conductors for flexible optoelectronic devices.

PS2.05
Synthesis and Characterization of Germanium Telluride Nanowires for Memory Application Alam Saj, Sumayya Ansari, Shaikha Mohammad Ayed Alketbi and Haila M. Aldosari; United Arab Emirates University, United Arab Emirates

The phase change material germanium telluride (GeTe) has garnered the attention of researchers because of its appealing properties, which include a high crystallization temperature, high OFF/ON resistance ratio, and a low ON-state resistivity. Despite the promising applications envisioned for this material, such as radio-frequency switches and random-access memory, the fabrication of GeTe-based devices has been challenging because the underlying nucleation and growth mechanisms are still unclear. Moreover, fabrication and characterization of the nanoscale phase-change materials can have useful knowledge on the size-scaling of phase-switching properties and can provide insight into the process that cannot be gleaned experiments on bulk materials. In this context, the GeTe nanowires were grown using the modified Au-catalyzed vapor-liquid-solid (VLS) method. Au thin film with 2-8 nm nominal thickness were thermal evaporated on 90 nm SiO_2/Si substrate using Mantis Magnetron Sputtering system. Then annealed in tube furnace at 700 °C for 20 min and purged with argon (Ar). Annealing caused the Au film to agglomerate into nanoparticles through Ostwald Ripening which then served as the nucleation site for the growth of the nanowires. GeTe source powder (99.999%) sublimated at the center of a tube furnace was transported by ~ 120 sccm Ar downstream to a SiO_2 substrate covered with Au nanoparticles. The source was kept at 400 °C and the receiving substrates were kept at ~400 °C for 8 h with pressure of 0.01 MPa and then allowed to cool naturally. Morphological study using scanning electron microscopy (SEM) and Energy Dispersive Spectroscopy (EDS) along with elemental mapping reveals that three distinct phase transition cases have been found. In the first form, the GeTe nanowire in size of 500-800 nm is still connected to the Au catalyst. Second, the Ge-based nanowire with secondary growth with and without Au was observed and, eventually, the Te-based nanowire with secondary growth with and without Au was also observed. Furthermore, detailed investigation will be carried out using transmission electron microscopy to understand the nucleation and growth mechanism of stoichiometric GeTe nanowire and still further experimental parameter optimize to achieve reproducible and ideal stoichiometric GeTe nanowire for memory applications.

PS2.06
(Student) Correlated Quantum Materials—Exploring Spin Transport in Iridate Thin Films Sreya Suresh, Suraj T.S., Vidya P. Bhallamudi, Sethupathi Kanikrishnan and M. S. Ramachandra Rao; Indian Institute of Technology Madras, India

Spin current generation and detection have become intriguing areas of research in spintronics. Spin current generated through the spin-Hall magnetoresistance (SMR) technique has been proved as a tool to probe the interfacial magnetic ordering in a Metal/Magnetic Insulator (MI) heterostructures, which otherwise requires sophisticated synchrotron facilities. The strongly correlated oxides exhibit a plethora of exotic properties from unconventional superconductivity to topological phases due to their strong interplay between the strong SOC (ζ_{SO}) and other interactions like the crystal field (△) and the electron correlation (U), due to their comparable energy scale in these materials [1]. $SrIrO_3$ (SIO) has become one of the interesting perovskite compounds due to the high spin-orbit coupling and metallicity in the Ruddlesden Popper series [2]. Among the Iridate family tree, $SrIrO_3$ (SIO) has the highest J_{eff} =1/2 bandwidth. This higher bandwidth drives the half-filled band to be metallic and as one expects all the half-filled bands should have a large Fermi surface, however, it is not the case here as the strong interplay between spin-orbit coupling and Coulomb interaction drives the system to be semi-metallic [3]. In iridates, the oxygen non-stoichiometry will have drastic effects in changing Ir-O-Ir bond angle which will affect the whole structural and electronic band structure that can, in turn, change the spin hall conductivity which is proposed theoretically. Recent studies have revealed that oxygen content evolution can drive the system to novel ground states as Ir^{5+} has an intrinsic magnetic order. The systematic SMR studies on $SrIrO_3$ thin film will help the scientific community to bridge a gap between probing novel magnetic phases in conjunction with synchrotron measurements which needs to be addressed through experiments and theoretical studies [4]. We have deposited SIO thin films on $SrTiO_3$ substrate by pulsed laser deposition (PLD) by varying the oxygen annealing partial pressure of the film. X-ray Photoelectron Spectroscopy has been carried out to analyze the stoichiometry and valence state of Iridium in the SIO film. High-resolution X-ray studies were carried out to study the structural quality of the thin films. We observed that the metallicity of the SIO thin film decreases with the decrease in O_2 annealing partial pressure. Further, we have carried out magneto-transport studies in SIO thin films as a function of oxygen content.

References:

1.Kondo, Takeshi, M. Nakayama, R. Chen, J. J. Ishikawa, E-G. Moon, T. Yamamoto, Y. Ota, *et al*, *Nature Communications* 6 (2015): 10042.
2. Tokiwa, Y., Ishikawa, J. J., Nakatsuji, S. & Gegenwart, P. Quantum criticality in a metallic spin liquid. Nat. Mater. 13, 356–359 (2014).
3. Takayama, T., A. N. Yaresko, and H. Takagi. “Monoclinic SrIrO3—a Dirac semimetal produced by non-symmorphic symmetry and spin-orbit coupling.” Journal of Physics: Condensed Matter 31.7 (2018): 074001.
4. T. S. Suraj and M. S. Ramachandra Rao *et al*. Phys. Rev. B 102, 125145 (2020).

PS2.08
(Student) Fabrication and Scaling Up of $Cs_{0.05}(MA_{0.17}FA_{0.83})_{0.95}Pb(I_{0.83}Br_{0.17})_3$ Perovskite Solar Cell at High Moisture and Oxygen Level Nithin Xavier; Indian Institute of Technology Madras, India

Hybrid organic-inorganic metal halide perovskites based solar cells (PSC) have drawn considerable attention due to a steep improvement of power conversion efficiency from 3.8% in 2009 to 25.2% in May 2020. Owning to the advantages of tuneable direct bandgap, wider absorption range, high absorption coefficient, high diffusion length (~ 1μm) and high V_{OC}, PSC has

emerged as a promising candidate offering highest efficiency advancement per year in the history of photovoltaic technology. However, like any new technology, PSC also suffers from several issues including the sensitivity to humidity, oxygen, temperature etc. Hence all the high-efficiency PSCs have been typically fabricated in a controlled atmosphere with less humidity and oxygen level. This work focuses on the fabrication and scaling of $Cs_{0.05}(MA_{0.17}FA_{0.83})_{0.95}Pb(I_{0.83}Br_{0.17})_3$ perovskite-based solar cells (unencapsulated) at comparatively high H_2O level (7- 8 % RH) and high oxygen level (3000 ppm). Perovskite solar cells in direct mesoscopic architecture FTO/c-TiO_2/ m-TiO_2/ perovskite/ Spiro-OMeTAD/ Au, as shown in Figure 1(a), is demonstrated with 0.09 cm^2 area. The average efficiency of 13.9 ± 0.53 % with the highest efficiency of 14.5 % (in the reverse scan) is achieved. The corresponding I-V curve is shown in Figure 1(b). Large area (1 cm^2) PSCs with maximum PCE of ~ 7% incorporating negligible degradation even after keeping > 2000 hours in the glove box is demonstrated.

PS2.11
(Student) Conduction-Templated Electrodeposition of Directed Nanostructures on 2D Materials for Axion-Like Evolvable Interconnects Radha Raman[1,2,3], Ding-Rui Chen[1], Ya-Ping Hsieh[1] and Mario Hofmann[4]; [1]Institute of Atomic and Molecular Sciences, Academia Sinica, Taiwan; [2]Taiwan International Graduate Program, Taiwan; [3]National Central University, Taiwan; [4]National Taiwan University, Taiwan

The production of nanostructures with adjustable composition, morphology, and location represents the main challenge of integrating nanotechnology into future applications, such as nanoelectronics, bio-sensing, photonics, and plasmonics. Electrodeposition is a promising route with high potential for materials interfaces with electronic devices that could enable future memory, brain-inspired devices, and evolvable circuitry. Unfortunately, current electrodeposition approaches lack the ability to control the orientation of nanostructures and are limited to templated deposition processes. We here introduce a novel conductance-templated electrodeposition approach. By exploiting the spatially varying conductance of a 2D material within the electrode gap, complex electrodeposition patterns can be dynamically created by adjusting the electric field distribution. The spatial selectivity and time evolution of deposition can be controlled by the 2D materials' functionalization and time-varying deposition parameters as investigated by in-situ optical microscopy. Our novel approach opens up novel routes for the formation and manipulation of nanostructures, and we demonstrate the potential by forming neural network-type interconnects with adjustable weight and location that form a circuit representation of axions for evolvable brain-like electronics architectures.

PS2.12
(Student) Fabrication of Polyvinylidene Fluoride (PVDF) Nanostructures with a Unique Ferroelectric Characteristic Using Initiated Chemical Vapor Deposition (iCVD) Omid Mohammad Moradi[1], Umit Çelik[2], I. Burc Misirlioğlu[1,3] and Gozde Ozaydin Ince[1,3,4]; [1]Sabanci University, Turkey; [2]Firat University, Turkey; [3]Center of Excellence for Functional Surfaces and Interfaces (EFSUN), Sabanci University, 34956 Istanbul, Turkey, Turkey; [4]Sabanci University Nanotechnology Research and Application Center (SUNUM), Orhanli/Tuzla, 34956 Istanbul, Turkey, Turkey

Initiated chemical vapor deposition (iCVD) is a well-known method for polymeric thin-film fabrication. In this study, we demonstrated successful deposition of thin (<100 nm) Polyvinylidene fluoride (PVDF) film on a silicon substrate with a unique surface microstructure. These spontaneously forming microstructures exhibit enhanced ferroelectric behavior compared to the smooth regions. Scanning Electron Microscopy (SEM) measurements revealed the topography of the surface. Chemical composition of microstructures was checked with FTIR, RAMAN and Energy-Dispersive X-ray spectroscopy (EDS). FTIR spectroscopy results confirmed the formation of polar and non-polar phases of PVDF on the surface. RAMAN spectroscopy results showed that higher ratio of polar phase formed on the microstructure. EDS results revealed higher ratio of Florine on the microstructure compared to smooth regions. Furthermore, Atomic Force Microscopy modes were utilized to locally characterize both mechanical and electrical properties. Quantitative Nanoscale Mechanical (QNM) mapping results revealed the Elastic modulus (<50KPa) of the microstructures were lower compared to adjacent smooth regions. Electrostatic Force Microscopy (EFM) with a cyclic voltage bias sweep showed different oscillation phase response from the microstructures which was correlated to ferroelectric characteristics of PVDF.

PS2.13
Flower-Like α-Fe_2O_3 Nanostructures for Waste Water Treatment Mohammad S. Anwar; Aligarh Muslim University, India

Nanomaterials have been long researched for exploring their unique physical and chemical properties that are different from those of the corresponding bulk materials or constituting atoms. The properties that result by shrinking down materials to the nanoscale, in many cases, are caused by the quantum confinement effect and/or the large surface-to volume ratio. A vast number of studies have been devoted to the preparations of various nanostructures. Tremendous progresses have been made in the synthetic control of the size and shape of different nanostructures. Herein, flower-like α-Fe_2O_3 nanostructures were synthesized via a template-free microwave-assisted solvothermal technique, and were applied as adsorbents for the removal of organic impurities from aqueous solutions. The results indicated that the synthesized flower-like α-Fe_2O_3 showed photodegradation of methylene blue (MB) and exhibited very high photocatalytic performance for the photodegradation of MB and that the as-obtained flower-like α-Fe_2O_3 nanostructures were suitable materials in wastewater treatment.

PS2.14
(Student) Photoexcited Carrier Transport Properties of ZnO Nanoparticles-Functionalized Cellulose Nanofiber Films Hiroaki Komatsu, Yurika Kawamoto and Takashi Ikuno; Tokyo University of Science, Japan

Cellulose nanofiber (CNF) films are expected to be applied to flexible substrates for thin-film electronics because of their excellent physical properties such as high visible-light transmittance, mechanical flexibility, high electrical resistance, and low environmental impact [1]. In addition, extra functions have been added to CNF films by compositing different nanomaterials [2,3]. We are aiming to fabricate CNF films with photoconductive properties for optoelectronic applications. However, there have been few systematic studies on the photoconductive properties of the functional CNF films. In this study, we fabricated CNF films with uniformly dispersed ZnO nanoparticles (NPs), and investigated the correlation between ZnO content in the film and photoconductivity of the film.
CNF films containing 0-60wt% ZnO NPs were prepared by the following procedure. First, ZnO NPs (average diameter was 25 nm) were uniformly dispersed in CNF aqueous solution (concentration 1wt%, manufactured by Chuetsu Pulp Industry) using an ultrasonic homogenizer. Next, the solution was sprayed onto a flat substrate heated to 110°C. Then, the CNF film was obtained on the substrate. Finally, the CNF film was peeled off from the substrate using original jig. The microstructure of the film was observed by atomic force microscopy. It was found that the film was composed of ZnO/CNF core/shell nanofibers structure, in which ZnO NPs were coated on the CNF surface. The

photoconductivity of the films was measured as follows. Au thin films were deposited on the CNF films. The *I-V* properties were measured between front and rear surfaces of the film. The time evolution of the photocurrent was measured with irradiating pulsed UV light of 360-370 nm in wavelength while applying a constant voltage. The electrical conduction properties of the CNF film without ZnO NPs showed no photocurrent, while the CNF film with ZnO NPs showed photocurrent, and the photocurrent increased with increasing ZnO concentration. The relationship between the photocurrent and ZnO concentration was investigated, and it was found that the photocurrent increased rapidly when the ZnO concentration was around 45-53wt%. We will discuss the details of the experimental results of the electrical conduction properties of ZnO-functionalized CNF films, along with the results of Monte Carlo simulations based on percolation theory.

[References]
[1] T. Ikuno, *MATERIAL STAGE*, (2020) February Issue.
[2] S. Pirsa *et al.*, *J. Appl. Polym. Sci.*, **135** (2018) 46617.
[3] Y. Kawamoto *et al.*, The 67th Japan Society of Applied Physics, Spring Meeting, March 14, 2020.

PS2.15

(Student) Developments of Hybrid White Organic Light Emitting Diodes with High Efficiency and Colour Quality Exploiting Exciton Allocation Strategy

Malek Mahmoudi[1], Jonas Keruckas[1], Dmytro Volyniuk[1], Jurate Simokaitiene[1], Igor Helzhynskyy[2], Pavlo Stakhira[2] and Juozas Grazulevicius[1]; [1]Kaunas University of Technology, Lithuania; [2]Lviv Polytechnic National University, Ukraine

Global energy consumption may be significantly reduced by broad usage of white organic light-emitting diodes (WOLEDs) with healthy white electroluminescence for solid-state lighting [1]. Due to the commonly accepted characteristics of organic devices such as mechanical flexibility, light weight, or transparency, WOLEDs have great potential for illumination applications [2]. It is a considerable challenge to develop WOLEDs with high-quality white electroluminescence. Two (sky-blue and orange) or three (blue, green and red) emitters producing singlet/triplet excitons usually are utilised in multilayer WOLED structures in which the population of each colour excitons has to be precisely controlled for obtaining high-quality white colour [3]. The spatial exciton allocation strategy was previously proposed for hybrid high-quality WOLEDs based on fluorescent and phosphorescent emitters which showed good efficiency and colour-quality [4]. In this work, we aimed to develop high-efficiency WOLEDs using heavy-metal-free systems based on TADF emitters exploiting the spatial exciton allocation strategy. The systems were based on fluorescence emitting layer in which both singlet and triplet excitons were generated under applied electric field. Then, triplet excitons were transferred to green and red TADF emitters separated from the fluorescent one by a spacer in well optimized system resulting in high-quality white emission. The layers of two new blue emitters containing isomeric *N*-naphthyl-*N*-phenylamines as the donors and benzophenone moiety as the acceptor moiety were used as the spacers in the fabricated hybrid WOLEDs. The derivatives of N-naphthyl-N-phenylamines and benzophenone were selected due to their relatively high triplet energy (ca. 2.5 eV), high thermal stability (5% weight-loss temperatures are above 400°C) and glass-transition temperatures exceeding 100°C. Their solid-state ionization potential values were found to be 5.68 and 5.79 eV. The best hybrid WOLED exhibited maximum external quantum efficiency of 9.5% and stable electroluminescence spectrum with the CIE1931 colour coordinate of (0.36, 0.31), colour rendering index (CRI) of 67 and colour temperature of 3300 K. The device characterized by warm white colour is suitable for indoor lighting.

Acknowledgements
This work was supported by the project of scientific co-operation program between Lithuania and Ukraine “Development of highly efficient white light-emitting diodes utilizing organic emitters with exciplex and thermaly-assisted fluorescence for lighting applications (LUW)” (grant No. S-LU-20-9).

[1] Nat. Mater. 2015, 14, 459
[2] Nat. Photon. 2011, 5, 716
[3] Nat. Mater. 2013, 12, 597
[4] Nature 2009, 459, 234

PS2.16

(Student) Investigation of Dibenzo[A,C]Phenazine Derivatives Substituted by Acridan or Carbazole Moieties as Efficient OLED Hosts or Emitters

Karolis Leitonas, Viktorija Andruleviciene, Dmytro Volyniuk and Juozas Grazulevicius; Kaunas University of Technology, Lithuania

Organic compounds exhibiting thermally activated delayed fluorescence (TADF) in past few years have attracted considerable interest in the field of organic optoelectronics. [1] The organic light emitting diodes (OLEDs) with emissive layer based on TADF capable materials, due to harvesting of triplet excitons through the reverse intersystem crossing (RISC), can reach 100% internal quantum efficiency (IQE). In TADF hosts-based OLEDs, the energy can be transferred to the guest molecules throughout the Förster energy transfer which enables up to 100% of its utilization. [2],[3] In order to have efficient RISC - very tiny singlet–triplet energy gap (ΔEST) is needed, which can be obtained by using molecular design strategy such as spatially separating donor (D) and acceptor (A) units with dihedral angle between D and A fragments approaching the orthogonality. [4],[5] In case of large ΔEST, organic compounds can exhibit triplet-triplet annihilation (TTA) (also co-called triplet-triplet fusion) [6] allowing to reach the theoretical IQE is 62.5%. In this study, we aimed to use advantages of both TADF and TTA in single molecule. Here we report on a pair of carbazole or acridan-substituted dibenzo[a,c]phenazines (named as **CzDbp** or **AcDbp**, respectively [7]) which yellow and orange emissions were characterized by combination of TADF and TTA properties. Both compounds were thoroughly investigated and tested as hosts for red phosphorescent OLED as well as emitters. The device with **CzDbp** host for commercial emitter (piq)2Ir(acac) exhibited excellent parameters of electrophosphorescence allowing to achieve higher maximum external quantum efficiency (EQE) of 15.9% together with low efficiency roll-off in comparison to those of the devices based on the widely used mCP, mCBP, NPB and nBPhen hosts. The maximum EQE of 19.4% and 22.1% for doped yellow and orange devices were achieved when the compounds **CzDbp** and **AcDbp** were used as TADF/TTA emitters, respectively.

Acknowledgement
This work was supported by the project of scientific co-operation program between Latvia, Lithuania and Taiwan “Polymeric Emitters with Controllable Thermally Activated Delayed Fluorescence for Solution-processable OLEDs” (grant No. S-LLT-19-4).

References

[1] Y. Liu, C. Li, Z. Ren, S. Yan, M. R. Bryce, All-organic thermally activated delayed fluorescence materials for organic light-emitting diodes, Nat. Rev. Mater. 18020 (2018) 1-20.
[2] L. Zhang, K.W. Cheah, Thermally activated delayed fluorescence host for high performance organic light-emitting diodes, Sci. Rep. 8832 (2018) 1-6.
[3] X. Ban, F. Chen, Y. Liu, J. Pan, A. Zhu, W. Jiang, Y. Sun, Design of efficient thermally activated delayed fluorescence blue host for high performance solution-processed hybrid white organic light emitting diodes, Chem. Sci. 10 (2019) 3054-3064. https://doi.org/10.1039/C8SC05456H\
[4] M.K. Etherington, J. Gibson, H.F. Higginbotham, T.J. Penfold, A.P. Monkman, Revealing the spin-vibronic coupling mechanism of thermally activated delayed fluorescence, Nat. Commun. 7 (2016) 13680 1-7.
[5] G. Méhes, K. Goushia, W.J. Potscavage Jr. C. Adachi,

Influence of host matrix on thermally-activated delayed fluorescence: Effects on emission lifetime, photoluminescence quantum yield, and device performance, Org. Electron. 15 (2014) 2027-2037.
[6] X. Qiao, D. Ma. Nonlinear optoelectronic processes in organic optoelectronic devices: Triplet-triplet annihilation and singlet fission, Mater. Sci. Eng. R 139 (2020) 100519 1-38.
[7] V. Andruleviciene, K. Leitonas, D. Volyniuk, G. Sini, J. V. Grazulevicius, V. Getautis, TADF versus TTA emission mechanisms in acridan and carbazole-substituted dibenzo[a,c] phenazines: Towards triplet harvesting emitters and hosts, Chem. Eng. J. 127902 (2020).

PS2.17

Single Cell Molecular Profiling on a SERS Based Microfluidic Chip Kamil Reza Khondakar; The University of Queensland, India

Cancer is complex disease and it progresses in multiple ways. Early detection and analysis of cancer biomarkers from liquid biopsies is to reduce mortality rate. Biomarkers have emerged as the indicator for cancer diagnosis, prognosis and therapeutic responses [1]. However, single biomarker is insufficient for complex clinical analysis. Therefore, usage of panel of multiple biomarkers might improve the sensitivity and specificity in clinical diagnosis and expedite the therapeutic process. So, we require innovative assays which can detect multiple biomarkers for better diagnosis. Surface Enhanced Raman spectroscopy (SERS) has emerged as promising versatile technique as it has shown high sensitivity of single molecule detection in complex biological sample with multiplexing capability. Combining SERS with microfluidic assay could be the next generation diagnostic tool for cancer disease management (for better screening, monitoring and diagnosis) as it requires low sample volume, rapid assessment, and spontaneous readout for on-site analysis of the patient samples. We report here a new approach of cellular and molecular biomarker detection which utilizes alternative current electrohydrodynamic (ac-EHD)-induced surface shear forces that provide exquisite control over fluid flow thereby enhancing target-sensor interactions. To realise clinically important multiplexed and highly sensitive detection of Tumor cells and soluble protein biomarkers, this work investigated on the development of a suite of innovative SERS ac-EHD nanodevices for single-cell and single cell receptor distribution analysis [2]. This project provided critical information on disease stages as well as for elucidating the underlying mechanisms of cancer progression.
[1]*Khondakar, K. R.; Dey, S.; Wuethrich, A.; Sina, A. A. I.; Trau, M., Toward Personalized Cancer Treatment: From Diagnostics to Therapy Monitoring in Miniaturized Electrohydrodynamic Systems. Accounts of Chemical Research 2019, 52 (8), 2113-2123.*
[2] Reza, K. K.; Dey, S.; Wuethrich, A.; Sina, A. A. I.; Korbie, D.; Wang, Y.; Trau, M., Parallel profiling of cancer cells and proteins using a graphene oxide functionalized ac-EHD SERS immunoassay. *Nanoscale* 2018**,** *10* (39), 18482-18491.

PS2.18

(Student) Control of Photocurrent Direction by Molecular Dipole Moment in Molecular Heterojunctions with Two-Dimensional Semiconductor Jaeho Shin, Seunghoon Yang, Jung Sun Eo, Chul-Ho Lee and Gunuk Wang; Korea University, Korea (the Republic of)

Until now, a specifically designed functional molecular species has been recognized as an absolute necessity for realizing the diode's behavior in molecular electronic junctions.[1-5] Here, we demonstrate a new type of molecular-scale photodiode implemented by molecular heterostructure composed of standard molecules and 2D semiconductor. Two non-functionalized molecular species that have opposite molecular dipole moment direction (i.e., 1-octanethiol (denoted as C8) and tridecafluoro-1-octanethiol (F6H2)) were used herein. As a 2D semiconductor, a four-layered (4_L)-WSe_2 was used to form a heterojunction with the SAMs. From the changing the molecular dipole moment direction in molecular heterojunction, the band alignment at molecules interfaces can be differently shifted, resulting in change of the photocurrent direction and rectifying direction. Especially, in F6H2/4_L-WSe_2 junction, the current difference between under dark and illumination (λ = 532 nm, 9μW) was higher than 5 orders of magnitude at zero bias. In addition, the constant value of photocurrent over a chopper frequency of 5-1000 Hz was observed. Our work provides a new concept of molecular-scale photodiode and can control the photocurrent direction by changing the molecular dipole moment direction in molecular heterojunction system.
[1] Yasutomi, S. *et al.* A molecular photodiode system that can switch photocurrent direction *Sciecne* **304**, 1944-1947 (2004).
[2] Wieghold, S. *et al.* Photoresponse of supramolecular self-assembled networks on graphene-diamond interfaces *Nat. Commun.* **7**, 10700 (2016).
[3] Najarian, A. M. *et al.* Orbital control of photocurrents in large area all-carbon molecular junctions *J. Am. Chem. Soc.* **140**, 1900-1909 (2018).
[4] Najarian, A. M. & McCreery, R. L. Long-range activationless photostimulated charge transport in symmetric molecular junctions *ACS Nano* **13**, 867-877 (2019).
[5] Shin, J. *et al.* Tunable rectification in a molecular heterojunction with two-dimensional semiconductors *Nat. Commun.* **11**, 1412 (2020).

PS2.19

(Student) Molar Mass Dependence of P3HT on the Molecular Interaction and Performance in a Fullerene-Free Organic Photovoltaic Blend Yang Liu[1], Long Ye[1,2] and Yanhou Geng[1,3]; [1]Tianjin University, China; [2]Organic and Carbon Electronics Laboratories (ORaCEL), North Carolina State University, United States; [3]Joint School of National University of Singapore and Tianjin University, International Campus of Tianjin University, China

Due to the simple structure and excellent scalability, poly-3-hexylthiophene (P3HT) becomes much popular as a low-cost donor polymer partner with the emerging nonfullerene acceptors in recent years. Presently, P3HT used in the high-performance nonfullerene solar cells are all prepared by the traditional Grignard metathesis method, which is not sustainable compared with direct arylation polymerization. The application and the molar mass dependence of direct arylation polymerized P3HT in fullerene-free organic solar cells have not been explored yet. In this work, five batches of P3HT with weight-average molar mass ranging from ~9 kg/mol to ~90 kg/mol were prepared via direct arylation polymerization (**Figure 1**a), with the aim to detail the interaction-performance relationships in the state-of-the-art P3HT:nonfullerene photovoltaic blend, namely P3HT:ZY-4Cl. Our thermodynamic analysis revealed that the amorphous-amorphous interaction parameters strongly depend on the P3HT molar mass and can be varied by a factor of 2.7 (**Figure 1**b). Owing to the best π-π stacking order deduced from grazing incidence X-ray diffraction and the smallest domain size, the blend based on the medium molar mass batch (26 kg/mol) delivered the highest current density, fill factor, and power conversion efficiency up to 9.6% among the five systems (**Figure 1**c). Our established relationships may be applied to screen the best molar mass batch for P3HT-based organic photovoltaics.

PS2.20

(Student) Effect of Dilute Concentration of Bi on the Optoelectronic Properties of InAs for Long Wavelength Infrared Applications—A First Principle Analysis Indranil Mal and Dip P. Samajdar; PDPM Indian Institute of Information Technology Design and Manufacturing, Jabalpur, India, India

Dilute Bismuth (Bi) containing III-V materials offer superior structural and optoelectronic properties suitable for Long

Wavelength Infrared (LWIR) range applications, which fascinates the material researchers since the last few decades. Commonly used LWIR optoelectronic devices undergoes Auger like non-radiative recombination losses owing to the smaller value of spin-orbit coupling splitting energy (Δ_{SO}) compared to the direct bandgap value (Eg), resulting in substantial decrease in quantum efficiency of the device. Bi, being the largest element of the group V, offers a larger spin-orbit coupling splitting energy to achieve the resonant condition (Eg >Δ_{SO}) in Bi-based induced III-V materials. Bi incorporation in InAs leads to the interaction between As-p and Bi-p orbital energy, thereby causing the valence band-edge lift up. Subsequently Δ_{SO} increases and the direct bandgap decreases, which has been studied thoroughly using the full-potential linearized augmented plane wave (FPLAPW) basis sets in the vicinity of the density functional theory (DFT) with the modified Becke-Johnson (mBJ) exchange correlation (XC) potential as implemented in WIEN2k code. Nevertheless, larger atomic sized Bi influences the stoichiometry of the host material adversely and suppresses the advantage of greater Δ_{SO}, thereby requiring dilute Bi concentration, which guided us to focus on Bi concentrations less than 10%. The structural optimization is performed by considering the Perdew-Burke-Ernzerh of generalized gradient approximation (PBEsol) exchange correlation (XC) functional in DFT calculation, which yields an optimized lattice constant of 6.09 Å for InAs. The optimized lattice constant is more close to the experimental value (6.05 Å) compared to the previously reported studies, due to the sharp values of 1.0×10^{-5} Ry and 1.0×10^{-5}e for energy and charge convergence criterion for structural optimization respectively. To study the effect of Bi impurity, we have considered a 2×2×2 super cell containing 128 In atoms and 64 As atoms each and replace the As atom with Bi, where each Bi atom replacement leads to 3.1% of impurity. Considering the individual optimized lattice constant for pristine and Bi incorporated InAs, we have studied the optoelectronic properties of $InAs_{1-x}Bi_x$ as shown in **Figure 1**. It is evident from the figure that, with increasing Bi concentration, the bandgap decreases at a rate of 40 meV/Bi%, thereby causing a redshift in the operating wavelength at a rate of 435nm/ Bi% and the computed results agree well with previously reported experimental literatures. Along with bandgap reduction, Bi impurity also increases at a sharp rate of 18.4meV/Bi% and the resonant condition occurs beyond 3% Bi impurity. Comparatively higher value of Δ_{SO} with respect to the band gap at Γ point will help to suppress the non-radiative recombination losses in optoelectronic devices like LASERs and Photodetectors. A uniform increment in Δ_{SO} and an unswerving redshift in the operating wavelength beyond 3µm region makes $InAs_{1-x}Bi_x$ a promising contender for the atmospheric infrared communication windows at 3-5 and 8-12 µm.

PS2.21
(Student) Reactive Ion Etching of Mg2Si Substrate Using CF4 and SF6 Rikuto Nakamura, Takeru Miyauchi and Haruhiko Udono; Ibaraki University, Japan

The pn- junction photodiode of Mg_2Si is a promising candidate as a novel SWIR sensor suited for mass production because of its high sensitivity and low toxicity[1-5]. The pn junction with mesa-structure is directly formed on n-type Mg_2Si substrate by thermal diffusion of Ag dopant and following wet-etching. However, while wet-etching has a fast etching rate, it is difficult to apply to microfabrication. In this study, we investigated the reactive ion etching of Mg_2Si substrate surface using CF_4 and SF_6 process gases used widely in silicon process. Single crystalline substrates of n-type Mg_2Si were prepared from melt grown Mg_2Si ingot [3,5]. The surface of substates were polished to a mirror face using an anhydrous fumed silica. Line-and-space patterns in the range from 5 µm to 50 µm were fabricated on the surface using a mask-less laser-beam lithography system. Then, reactive ion etching was carried out using two process gases, CF_4 and SF_6, with a gas flow rate of 30 sccm, pressure of 3.0 Pa, and RF power of 50 W, for the etching time of 10, 20 and 30 min. The surface profiles were evaluated using a 3D Laser Microscope and an AFM. Clear line-and-space patterns observed on both surfaces indicate the etching of Mg_2Si was successfully conducted by both CF_4 and SF_6 gases. The average etching depths of CF_4 and SF_6 were 56 nm and 46 nm, respectively for 30 min. The etching depth is proportional to the etching time, and the etching rates of about 1.6 nm/min and 1.9 nm/min were determined for SF_6 and CF_4, respectively. We have investigated the reactive ion etching of n-Mg_2Si substrate using CF_4 and SF_6 process gases and found good etching conditions and etching rates. A part of this study was supported by NIMS Nanofab. Platform in NPP sponsored by MEXT, Japan.
[1] H. Udono et al, J. Phys. Chem. Sol., 74 (2013)311.
[2] M. Takezaki et al., Phys.Stat.Sol (c)10 (2013)1812.
[3] H. Udono et al, Jpn.J.Appl.Phys., 54 (2015)07JB06.
[4] T. Akiyama et al., JJAP Conf. 5(2017) 011102.
[5] H. Udono, Oyo-Buturi 88(2019)797.

PS2.22
(Student) Optical Transmission Measurement of *In Situ* Annealed Mg2Si Crystals Hiroto Tsuchida, Keigo Gousyu and Haruhiko Udono; Ibaraki University, Japan

Narrow bandgap semiconductor of Mg_2Si is attracting much attention as an eco-friendly material for SWIR sensor applications. The pn-junction photodiode with the cut-off wavelength of 2.1µm is fabricated on n-type Mg_2Si substrate by thermal diffusion of Ag dopant [1-3]. Our previous studies on the high purity Mg_2Si single crystals reveal that the electron density, *n,* in Mg_2Si decreases by annealing above 550°C[4]. The dominant native defect of interstitial Mg (I_{Mg}) acting as a donor may decrease its concentration and precipitate by the annealing. In this study, we measured the transmission spectrum of Mg_2Si crystals before and after annealing. High purity Mg_2Si single crystals were grown by the VGF method using Mg(6N) and Si(10N) raw materials and a high purity graphite crucible. After the growth was completed, in-situ annealing was immediately performed in the growth crucible by controlling the temperature distribution of the electric furnace. Three crystals were prepared with annealing conditions of 500°C (#2), 650°C (#3) for 24 hours, and no annealing (#1). From these crystals, samples of about 5 x 5 x 1.2 mm were cut out and polished to a mirror finish. Transmission measurements were carried out using the UV-Vis-NIR spectrophotometer (Hitachi: UH4150) and FTIR spectrophotometer (JASCO: FT/IR-420). The electron concentration, *n*, in #1 - #3 were also evaluated by the Hall effect measurement. Transmittance of #3 was about 3% higher than that of #1 and #2 below the energy gap of 0.6eV, although the *n* in #3 decreased less than a half of #1 and #2. The absorption around 0.4 eV, which is proportional to the electron concentration, is also reduced in #3. This is consistent with the results of the Hall effect measurement, which showed that the electron concentration of the 650°C annealed sample was lower than that of the no annealed and 500°C annealed samples. It has been reported in many crystals that annealing reduces the absorption caused by defects, and the same effect may occur for Mg_2Si
References
[1] D. Tamura et al., Thin Solid Films, 515(2007)8272.
[2] H. Udono et al., Jpn. J. Appl. Phys., 54(2015)07JB06.
[3] H. Udono et al., J. Phys. Chem. Sol., 74(2013)311.
[4] H. Udono：Oyo-Buturi 88(2019)797.

PS2.23
(Student) I-V and C-V Measurements of Metal/n-Mg2Si Junction Makoto Chiba, Takeru Miyauchi, Yudai Ichikawa and Haruhiko Udono; Ibaraki University, Japan

Magnesium half silicide, Mg_2Si, is expected to be a suitable material for short-wavelength infrared (SWIR) sensor that can be widely used in general applications [1-5]. Previously, we reported the formation of Schottky junction on the cleaved surface of

n-Mg_2Si bulk using Au electrode and estimated an electron affinity $\chi = 4.51$ eV [6]. However, it has not been sufficiently verified and analyzed.In this paper, we report the fabrication and electrical properties of metal/n-Mg_2Si Schottky junctions by depositing Au and Ni films on mirror-polished n-Mg_2Si.The mirror polished n-type Mg_2Si substrates were prepared from single crystals grown by the vertical Bridgeman method. After thermal diffusion of Al as an ohmic electrode on the backside of the substrate, Au and Ni were deposited on the surface by a resistive heating evaporation and a RF magnetron sputtering, respectively, to form a metal-semiconductor junction. The electrical characteristics of the junctions were evaluated at room temperature by a source measure unit (Keithley 2450) for I-V characteristics and a LCR meter (Weyne Kerr 6510B) for C-V characteristics.The I-V curves showed clear rectification for both Au and Ni electrode samples, where the diameter of electrode is 0.3 and 0.2 mm for Au and Ni electrode, respectively, confirming the formation of Schottky junction on n-type Mg_2Si.The $1/C^2$-V characteristics of Au/n-Mg_2Si and Ni/n-Mg_2Si show the linear relationship over a wide range, indicating a formation of good M/S interface. The donor densities estimated from the slopes are 1.0×10^{16} cm^{-3} and 2.6×10^{15} cm^{-3} for Au/n-Mg_2Si and Ni/n-Mg_2Si, respectively. These results are close to the electron density of n-Mg_2Si substrates (for Au: 4.3×10^{15} cm^{-3} and Ni: 2.8×10^{15} cm^{-3}) determined by the Hall effect measurements.

[1] H. Udono et al, J. Phys. Chem. Sol., 74 (2013)311.
[2] M. Takezaki et al., Phys.Stat.Sol (c)10 (2013)1812.
[3] H. Udono et al, Jpn.J.Appl.Phys., 54 (2015)07JB06.
[4] T. Akiyama et al., JJAP Conf. 5(2017) 011102.
[5] H. Udono, Oyo-Buturi 88(2019)797.
[6] K. Sekino et al., Phys. Procedia 11(2011)171.

PS2.24

(Student) Electrical Property and Photosensitivity of Mesh-Electrode Type Mg2Si Photodiodes Using Au/Pt P-Side Contact Yudai Ichikawa[1], Takeru Miyauchi[1], Misa Yoshida[2], Daiju Tsuya[2] and Haruhiko Udono[1]; [1]Ibaraki University, Japan; [2]National Institute for Materials Science, Japan

Mg_2Si is an indirect semiconductor with a forbidden band gap (Eg) of 0.61 eV at 300 K. Therefore, it has attracted much attention as an infrared (IR) photodetector that can be used in the near-infrared region below 2.1 μm [1-5]. We have been fabricating pn-junction photodiodes (PDs) with various electrode structures on n-type Mg_2Si substrates by thermal diffusion and following lift-off process [1-5]. In this paper, we report the electrical property and photosensitivity of Au/Pt mesh-electrode PD. A pn-junction was formed by thermal diffusion of p-type impurity Ag at 450 °C for 10 minutes on an n-type Mg_2Si substrate with Au/Al back electrode. After that, a mesa structure was formed by wet-etching using diluted HF and HNO_3 solution, and then a mesh-electrode was formed on the top of the p-type region by a lift-off process. The fabricated PD evaluated by current-voltage(*J-V*) and spectral photo-response measurement. The PD had a fairly good *J-V* characteristic and photosensitivity. The dark current density of Au/Pt electrode PD at -1 V was 0.11 A/cm^2 at 300 K and 1.1×10^{-2} A/cm^2 at 210 K. The value at 210 K is approximately three orders of magnitude higher than that of the circle-electrode type Mg_2Si pn-junction diode (~10^{-5} A/cm^2) [4]. Some current leakage path may be generated by the lift-off process because the current density increases proportionally with the voltage. We also measured the relationship between reverse bias and normalized photosensitivity of Au/Pt Mg_2Si PD at 1400 nm. Clearly, the photosensitivity was increased with the bias voltage and improved more than 4 times at -2 V. The improvement of photosensitivity by applying the reverse bias would indicate the expansion of absorption region.

[1] H. Udono et al, J. Phys. Chem. Sol., 74 (2013)311.
[2] M. Takezaki et al., Phys.Stat.Sol (c)10 (2013)1812.
[3] H. Udono et al, Jpn.J.Appl.Phys., 54 (2015)07JB06.
[4] T. Akiyama et al., JJAP Conf. 5(2017) 011102.
[5] H. Udono, Oyo-Buturi 88(2019)797.

PS2.25

Transport Property and Thermal Stability of the CsH_2PO_4/$NaH_2PO_4.2H_2O$ Composite Electrolytes for Fuel Cells Dharm Veer[1], Pawan Kumar[1], Deshraj Singh[2], Aravind Kumar[3] and Ram S Katiyar[4]; [1]Gurukual Kangri University Haridwar, India; [2]K.G.K. College Moradabad, M.J.P Rohilkhand University, India; [3]Kalindi College, Delhi University, India; [4]University of Puerto Rico, Puerto Rico

Solid acid composite electrolytes CsH_2PO_4(CDP)/$NaH_2PO_4.2H_2O$ ($0 \le x \le 0.35$) were prepared and observed the structural, thermal and transport properties by Fourier scanning electron microscopy (FESEM), Energy dispersive X-Ray analysis (EDX), X-ray diffraction (XRD), Thermogravimetric analysis (TGA), Differential thermal analysis (DTA), Derivative thermogravimetric (DTG), Fourier transform infrared spectroscopy (FTIR) and conductivity measurement. We have investigated superprotonic phase transition from monoclinic to cubic phase at 235°C in CDP, at which the conductivity increased up to 2 to 3 orders of magnitude. The initial dehydration event in CDP occurs at 260°C. The performance of CDP was increased due to the addition of $NaH_2PO_4.2H_2O$ in the form of conductivity and stability. Thermal characterization showed that introducing the additivities, dehydration behavior shifted to the lower at the higher temperature. The conductivity is also increased above the temperature of 250°C up to 1.5 orders of magnitude which were found of the composite electrolytes 6CDP/4SDP.$2H_2O$, 4CDP/6SDP.$2H_2O$. The electrodes were prepared by a vacuum coating unit of silver paste.

PS2.26

(Student) Bicarbazole Derivatives Containing Methoxydiphenylamino or Dimethoxycarbazolyl Substituents as Efficient Hole-Transporting Materials Eduardas Pečiulis[1], Thomas Cadden[2], Jurate Simokaitiene[1], Dmytro Volyniuk[1] and Juozas Grazulevicius[1]; [1]Kaunas University of Technology, Lithuania; [2]University of Strathclyde, United Kingdom

Organic hole-transporting materials (HTMs) are well known for their near-industrial scale usage in perovskite solar cells (PSCs). However, even if HTMs, derived from conductive organic molecules, are being successfully applied, cost-effective HTMs with low ionization potentials are still of great demand. Therefore, it is important to continue the development of HTMs in order to optimize the performance of PSCs and contribute to renewable power sources. Electron rich heterocyclic systems such as carbazoles or di/thiphenylamines were utilized for the synthesis of the materials with potential application as hole-transporting semiconductors in PSCs. To affect ionization potential, electron-donating methoxydiphenylamine- or dimethoxycarbazolyl- groups can be introduced to the molecular structures. In our work we demonstrate synthesis and properties of two new 3,3′-bicarbazolyl-based hole transporting materials, which contain methoxyphenyl and dimethoxycarbazolyl substituents. The compounds were found to be electrochemically and thermally stable and capable of forming molecular glasses with glass transition temperatures higher than 160 °C. The synthesized compounds demonstrated 5% weight loss at temperatures up to of 430 °C. Ionization potentials of bicarbazolyl derivatives estimated by UV photoelectron spectroscopy were in the range of 5,23 – 5,42 eV. Time-of-flight hole-mobilities exceeded 10^{-5} $cm^2/V*s$ at high electric fields.

PS2.27

(Student) Organic Emitters with Photo Induced Conformational Changes for Ratiometric and Colorimetric UV Sensing Matas Guzauskas[1], Edgaras Narbutaitis[1], Dmytro Volyniuk[1], Yu-Chiang Chao[2], Martins Rutkis[3] and Juozas Grazulevicius[1]; [1]Kaunas University of Technology, Lithuania; [2]National Chiao Tung University, Taiwan; [3]University of Latvia, Latvia

Nowadays organic semiconductors get a lot of interest from researchers and manufacturers because of their wide range of applicability in medicine, textile but mostly in electronics [1]. Organic light emitting diodes (OLEDs) are already used in smartphones, tablets and computers displays also for illumination [2]. Another application which gains interest is sensors with organic materials. There are publications about organic semiconductors with room temperature phosphorescence (RTP), which are used as oxygen sensing materials [3]. Still, there are endless applications for these materials, which are created every day. In this work we present novel organic semiconductor with phenothiazine and benzophenone derivatives, EN28, and intensive photophysical investigation of it. Materials EN28 shows thermally activated delayed fluorescence, but EN28 also shows properties of ultra-violet (UV) light enhanced photoluminescence (PL) emission. PL emission of toluene solution of EN28 (emission maxima 413 nm) gets more intensive as it gets illuminated by UV light longer. Also, the PL intensity increases faster as EN28 get illuminated by more intensive UV light. The PL of more polar solutions goes from lower energy wavelength to higher energy wavelength emission (solution in DMF goes from 528 nm to 440 nm) after UV treatment . The increasement of intensity and PL shift to higher energy wavelength range are explained by conformational changes in the molecule induced by UV light photons. This unique property of EN28 can be used for ratiometric and calorimetric UV light sensing.

Acknolegment:
This work was supported by the project of scientific co-operation program between Latvia, Lithuania and Taiwan “Polymeric Emitters with Controllable Thermally Activated Delayed Fluorescence for Solution-processable OLEDs” (grant No. S-LLT-19-4).

References:

[1] “OLED Info | The OLED Experts.” [Online]. Available: https://www.oled-info.com/. [Accessed: 15-May-2019].
[2] Z. Yang *et al.*, “Recent advances in organic thermally activated delayed fluorescence materials,” *Chemical Society Reviews*, vol. 46, no. 3. Royal Society of Chemistry, pp. 915–1016, 07-Feb-2017.
[3] A. Tomkeviciene *et al.*, “Bipolar thianthrene derivatives exhibiting room temperature phosphorescence for oxygen sensing,” *Dye. Pigment.*, vol. 170, Nov. 2019.

PS2.28

(Student) Application of p-NiO/n-ZnO Heterojunction PN Diodes as Transparent Temperature Sensors Junhee Lee and Hongki Kang; Daegu Gyeongbuk Institute of Science and Technology, Korea (the Republic of)

Biological mechanisms are sensitive to temperature changes [1]. Recently, various optical imaging and laser stimulation technologies have been applied to monitor and even modulate the biological mechanisms. However, precise cellular mechanism analysis upon micro-scale temperature change is limited because of a lack of transparent micro-scale temperature sensors.
To overcome this problem, we suggest a transparent active temperature sensing microelectronics device. We developed a 100- μm PN diode tempeature sensor on glass using optically transparent wide bandgap metal oxide semiconductors such as ZnO (E_g=3.26 eV) and NiO (E_g=3.5 eV) [2]. We have demonstrated that the temperature sensors showed transparency of 60 % over a wide range of visible light. In addition, we veified that the 100-μm-sized temperature sensor has thermal sensitivity of 0.866 mV/°C. We deposited zinc oxide and nickel oxide thin films on ITO coated glass substrate using RF sputtering. ITO was used as cathode. Ag/Au ultrathin film anode was deposited by thermal evaporation. The deposition parameters are summarized in Table 1, and the parameters were optimized to obtain PN diode with high transparency and conductivity. As a transparent anode, ultrathin Ag/Au layer was used [3]. 7-nm of Ag was deposited after 1-nm Au seed layer. The multi-layer anode has a similar high transmittance to that of ITO electrode (83 %) and low sheet resistance (32 Ω/sq) while forming ohmic contact to p-type NiO. Therefore, it is suitable for transparent temperature sensing.
Fig. 2(a) shows rectifying I-V characteristics of the diode with a diameter of 100 μm. The I-V curves shows negative shift of the forward bias when the temperature increases. The decrease of the forward voltage was caused by thermal excitation of carriers and enhanced diffusion current. For temperature sensing, we applied 5 nA as constant drive current because the ideality factor of diode was close to 1 at the level of dc current. The forward voltage shift and temperature showed linear relationship as shown in Fig. 2(b). The sensitivity of p-NiO/n-ZnO diode temperature sensor is 0.866 mV/°C at 5 nA. We then attempted to measure continuous temperature changes induced by a wafer-chuck heater (MST-1000B). As shown in Fig. 3, the diode temperature sensor tracks the change of the heater temperature accurately with standard deviation of 0.586 °C despite nearly constant offset from the heater temperature throughout the experiment. The transmittance spectra of the diode (Fig. 4) showed average transmittance of ZnO and NiO as 81 % and 69 % over a range of visible light, respectively. The overall p-NiO/n-ZnO heterojunction diode structure (ITO/ZnO/NiO/Au/Ag) showed 41 % of average transmittance, which is not the highest, but much higher than typical non-transparent temperature sensors. We demonstrated that the metal oxide p-NiO/n-ZnO heterojunction diode with ultrathin metal electrodes is possible to measure microscopic temperature changes while providing higher optical transparency than more common diode temperature sensors made of a single element semiconductor such as Si. It shows a great potential for high resolution temperature sensing on various biochips on glass where optical imaging and modulation are to be applied simultaneously.

References

1) Sonja J. Pyott, The Journal of Physiology**,** 539, **2**, 523–535 (2004).
2) Xiaobo Li et al., IEEE Sensors Journal, **20**, 62–66 (2020).
3) Sylvio Schubert et al., Adv. Energy Mater, **3**, 438-443 (2013).

PS2.29

(Student) Probing the Role of Non-Polar Surfaces of GaN Nanostructures in Efficient and Ultra Stable Photoelectrochemical Water Splitting Yixin Xiao[1], Srinivas Vanka[2,1], Ishtiaque Ahmed Navid[1] and Zetian Mi[1]; [1]University of Michigan–Ann Arbor, United States; [2]The University of British Columbia, Canada

Artificial photosynthesis, which refers to the storage of solar energy as chemical fuels such as hydrogen from solar water splitting, holds tremendous promise for addressing the ongoing challenge of unsustainable levels of CO_2 emission. Gallium nitride (GaN) nanostructures have recently emerged as a new class of materials for artificial photosynthesis, as they have shown outstanding photo(electro)chemical activity and stability. In particular, GaN nanowires, with Pt nanoparticles deposited at the surface as cocatalysts, and grown on Si pn junction via molecular beam epitaxy, have demonstrated stable solar hydrogen evolution in 0.5 M sulfuric acid under one-sun illumination for over 3,000 hours, maintaining an applied bias photon-to-current efficiency of 12%. An understanding of the mechanisms that enable such efficient and stable artificial photosynthesis would provide guidance for future rational designs of photocatalysts. III-nitrides, including GaN, are known for their large polarization field along the wurtzite c-axis along which the inversion symmetry is broken.

At the same time, no such internal electric field exists along axes perpendicular to the c-axis or c-plane. It is known that, in general, the same photoelectrochemical (PEC) or photocatalytic material can exhibit significantly different performance due to a difference in surface crystallographic orientations that can lead to different local electric fields, redox reaction sites, charge carrier mobilities, etc. Theoretical calculations and solid state measurements have shown that the polar c-plane and the non-polar m-plane of GaN possess different electronic properties such as dispersion relation and intra-bandgap defect levels. Here we attempt to elucidate the roles that surface polarity of GaN plays as part of the GaN/Si photocathode in PEC water splitting. We have found that, in the absence of cocatalysts such as Pt, the GaN/Si photocathode not only remained stable, but exhibited self-improvement at least in the first 10 hours of constant PEC hydrogen evolution, in a two-electrode chronoamperometry (CA) configuration, a condition more realistic and harsher than the three-electrode configuration, where the charge carriers at the counter electrode are more readily supplied by the potentiostat. Data from angle-resolved x-ray photoelectron spectroscopy suggest that, during CA, gallium oxynitride formed at the m-plane and served as native hydrogen evolution cocatalysts that are more stable than deposited cocatalysts such as Pt. Consequentially, upward band bending at the m-plane reduced after 10 hours of CA, whereas that at the c-plane did not. The preferential improvement of m-plane's electronic properties for PEC hydrogen evolution during CA led us to investigate the role GaN m-plane plays (in PEC hydrogen evolution). We found that GaN quasi-films, where the sidewalls were largely sealed away and only c-planes were in contact with electrolyte, exhibited no photoactivity. We then subjected the same GaN quasi-films to a photolithographic patterning and etching process to expose the non-polar sidewalls. The patterned GaN samples then exhibited photoactivity similar to GaN nanowires. A series of PEC characterizations further corroborated the finding that GaN m-plane plays a predominant role in PEC hydrogen evolution.

PS2.30

(Student) Temperature Dependence of Thermophotovoltaic Conversion Using InGaAs Air-Bridge Cells Bosun A. Roy-Layinde, Tobias Burger, Dejiu Fan, Andrej Lenert and Stephen R. Forrest; University of Michigan–Ann Arbor, United States

Unlike conversion of solar radiation to electricity using single-junction solar cells, which is limited to efficiencies around 30%, the efficiency of converting thermal radiation to electricity using single-junction thermophotovoltaic (TPV) cells can exceed 50% through a process called photon recycling. Specifically, thermal radiation that is too low in photon energy to excite electronic transitions in the cell is reflected back to the hot emitter, where it has an opportunity to contribute toward emission of higher energy photons that can be converted directly to electricity. To facilitate this process, we recently created a cell architecture that has a thin air layer behind the light-absorbing InGaAs layer. The resulting cell (a so-called air-bridge cell, or ABC) reflects back almost all of the low-energy photons and, in turn, achieves a record-high conversion efficiency of 32% under illumination by ~1450 K SiC emitter [1]. Here we investigate how changing the temperature of the emitter and the cell affects the efficiency of the device with respect to two key factors: spectral management and carrier management.The performance of the InGaAs ABC is remarkably insensitive to temperature changes relative to a cell with a planar back-surface reflector. Furthermore, these experimental data are used to develop a validated model, which allows us to predict the performance of a theoretical InGaAs TPV cell (ABC*) with improved material quality, corresponding to the longest observed lifetimes in InGaAs. Using this model, we predict that efficiencies exceeding 40% can be achieved using the ABC approach under practical operating conditions.

REFERENCE

[1] D. Fan, T. Burger, S. Mcsherry, B. Lee, A. Lenert, and S. R. Forrest, *Near-Perfect Photon Utilization in an Air-Bridge Thermophotovoltaic Cell*, Nature (2020).

PS2.32

Molecular Beam Epitaxy of ScAlN Nanowires—Structural and Optical Properties Ping Wang, Zihao Deng, Boyu Wang, Nguyen Vu, Kai Sun, Ding Wang, Yuanpeng Wu, Yi Sun, John Heron, Emmanouil Kioupakis and Zetian Mi; University of Michigan–Ann Arbor, United States

Alloying AlN with Sc has attracted tremendous attention in recent years, due to the abnormal enhancement of the electromechanical response of ScAlN, providing an additional dimension to engineer the bandgap and polarization. Current studies have been largely focused on ScAlN films/epilayers, which have shown enhanced spontaneous polarization, increased piezoelectric coefficient, and ferroelectric behavior, promising a wide range of applications, including surface acoustic wave (SAW) resonators, high electron mobility transistors (HEMT), micro-electromechanical systems (MEMS), and polarization engineered deep ultraviolet (UV) optoelectronics. To date, however, ScAlN films/epilayers are plagued with the presence of extensive defects and dislocations, severely limiting their practical applications. In this context, we have performed a detailed study of the epitaxy and structural, optical, and ferroelectric characterization of ScAlN nanowires. Due to the significantly reduced strain distribution, nearly dislocation-free wurtzite ScAlN nanowires can be achieved directly on Si wafers over a broad range of Sc compositions.
In this work, we have investigated the epitaxial growth of ScAlN nanowires on Si(111) substrates by using a Veeco GENxplor plasma-assisted MBE system. Spontaneously formed N-polar GaN nanowires are used as a template for the subsequent ScAlN nanowire growth. We show that wurtzite phase ScAlN nanowires with Sc content up to 0.45 can be successfully achieved, which is among the highest Sc content wurtzite ScAlN reported to date by MBE growth. ScAlN nanowires exhibit smooth sidewall for Sc content lower than 0.3, while nanocrystals form on the sidewall when Sc content is beyond 0.4. Meanwhile, nanocrystals with cubic geometry can be observed in ScAlN with higher Sc content (> 0.6), suggesting a cubic phase dominated growth in this regime. The crystal structure has been characterized using a high-resolution transmission electron microscope (HRTEM). For Sc content less than 40%, it is observed that the wurtzite phase of ScAlN is epitaxially aligned with the underlying GaN template, while in-plane rotation, alloy disorder, stacking faults, and phase separation are observed in ScAlN with ScN fraction above 40%. Detailed photoluminescence (PL) and cathodoluminescence (CL) studies further show that the optical emission of ScAlN nanowires is primarily dominated by oxygen-defect related emission, partly due to the limited purity level of Sc source. Furthermore, the ferroelectric properties of these ScAlN nanowires have been studied using a piezoelectric force microscope (PFM). These results provide an insight into the potential applications of ScAlN in nano-optoelectronic/electronic/ferroelectric devices. Work is currently in progress to develop nearly strain and dislocation-free ScAlN epilayers through controlled nanowire coalescence.

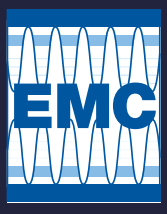

63RD ELECTRONIC MATERIALS CONFERENCE

June 23-25, 2021

THURSDAY ORAL PRESENTATIONS

SESSION O: Water Splitting, Solar Hydrogen and Batteries
Session Chairs: Jung Hyun Kim and Zetian Mi
Thursday Morning, June 24, 2021

11:15 AM O01
(Student) Hot Electron Metal-Free Electrode for Hydrogen Evolution Reaction Hyun Uk Chae, Ragib Ahsan and Rehan Kapadia; University of California, Los Angeles, United States

Recently, carbon-based electrode, especially graphene, has been introduced to replace the noble metals as a low-cost alternative. In this work, we show that the turn on voltage of the electrochemical reaction can be tuned in a semiconductor-insulator-plasma etched graphene (SIEG) device, especially for hydrogen evolution reaction (HER). By using this structured device, the relative energy level can be shifted to modify the onset potential. Besides, O_2 plasma etched graphene was introduced to increase the number of active sites for HER on the surface of the graphene. Figure 1a shows a schematic of the SIEG device. A plasma-etched graphene on an insulator–semiconductor is introduced here. Reactive ion etching (RIE) by oxygen flow method was used to dry etch the graphene to introduce the active reaction sites. Compared to pristine graphene (PG) in Raman Spectroscopy, the I_D/I_G ratio was increased from ~ 0 to 0.58 from PG to EG shown in Figure 1b, suggesting the disruption of the hexagonal configuration by oxygen plasma etching. The result implies the existence of a higher amount of defect sites due to the introduction of plasma-induced edge defects. Figure 2a shows the HER measurement result of SIEG device in both biased and unbiased conditions. It is noteworthy that the onset potential of HER can shift up to ~0.8 V and 90mA/cm^2 current density could be achieved at -0.5V vs RHE at $V_{Gr\text{-}Si}$ = 1.5V. Figure 2b shows the schematic of the mechanism of catalysis due to hot electrons. The high performance of the device comes from the hot electrons possessing high energy which requires a significantly smaller activation energy barrier to overcome compared to the thermal electrons. Figure 3 shows the mechanism of how hot electrons are introduced into the graphene from the silicon. The applied bias between graphene and silicon shifts the conduction band of silicon relative to the reduction potential of H^+/H_2 redox couple, injecting carriers from silicon through graphene, while driving the reaction before any scattering happens in the graphene. To clarify this effect of the applied bias, we analyzed the different current components from the system individually. Here we find out that the silicon current is the major current component for chemical reaction (Redox current) when graphene-silicon voltage is applied as shown in Figure 3b. This result shows that the hot electrons from silicon current directly drive the electrochemical reaction, without affecting the graphene current. Figure 4 shows the overlapping of HER current between SIPG and SIEG device. The result shows that the current density of SIEG device at same experimental condition is ~ 2x higher than that of SIPG device. This indicates that the newly introduced active site for the hydrogen ions breaking through the limiting factor of graphene surface area. Electrochemical surface area (ECSA) achieved by cyclic voltammetry measurement also indicates the enhanced electrochemical area of the plasma etched graphene. In conclusion, we demonstrate that a plasma etched graphene based SIEG device can be a promising electrocatalysts candidate. SIEG device is not confined to this certain structure, we could possibly get better results by replacing each component with other materials. Future experiments could explore other redox reactions for carbon dioxide reduction to useful materials, and other 2-D materials with a high density of active sites that transport electrons more efficiently and adsorb more protons on top of the surface to see if high efficiencies can be achieved at lower voltages.

11:30 AM O02
(Student) Facile and Scalable Ambient Pressure Chemical Vapor Deposition-Assisted Synthesis of Layered Silver Selenide (β-Ag2Se) on Ag Foil as a Possible Oxygen Reduction Catalyst in Alkaline Medium Rajashree Konar[1], Suparna Das[1], Eti Teblum[1], Arindam Modak[2], Ilana Perelshtein[1], Jonathan J. Richter[1], Alex Schechter[2] and Gilbert Daniel Nessim[1]; [1]Bar-Ilan University, Israel; [2]Ariel University, Israel

To alleviate the adverse impacts of utilizing fossil fuel reserves on the environment (global warming, greenhouse emissions), extensive research is being devoted to the development of alternative/renewable energy systems, which include: photovoltaics, fuel cells, batteries, etc. Among them, fuel cells are an excellent solution for energy conversion, where proton exchange membrane (PEM) fuel cells have a wide variety of applications. Some of these applications are portable systems, automotive, etc., where an important reaction occurring at the cathode is the oxygen reduction reaction (ORR). At the current stage in fuel cell technology, platinum (Pt)-based materials are the most practical catalysts1, which, undoubtedly, are the prime choice as the cathode catalyst for the electro-reduction of oxygen, but Pt-based catalysts are expensive. To reduce such costs in commercially viable fuel cells, extensive research is focused on developing alternative catalysts. Silver-based catalysts show a comparatively high thermodynamic stability and excellent catalytic activity over a wide pH range. The TMCs (O, S, Se, and especially Se-based chalcogenides) have attracted significant attention since selenium-based cluster compounds work. Selenium-based metal-rich TMCs catalysts exhibit good electrocatalytic activity, which is mainly attributed to selenium because it improves the electronic structure of the metal by preventing the electrochemical oxidation of metals in most transition metal chalcogenides, as seen for the cases of cobalt selenide and ruthenium selenide. Here, we present a high yield, industrially scalable, and the first-time report on the synthesis of silver selenide from silver foil and selenium powder using a two furnace atmospheric pressure-chemical vapor deposition (AP-CVD) system. We grew low temperature, LT-β-Ag2Se on Ag foil in the AP-CVD system using thermal annealing and leading to a hollow fern-like morphology material and its first-ever reported application as an ORR cathode catalyst. The exfoliated β-Ag2Se is characterized using XRD, EDS, HRTEM, AFM, and HRSEM to determine its stoichiometry and its hollow layered fern-like morphology. Differential scanning calorimetry (DSC) further confirms that the final product is the low-temperature phase β-Ag2Se. Electrochemical oxygen reduction reaction (ORR) of exfoliated β-Ag2Se exhibits sharp oxygen reduction current with an onset potential of 0.88 V/RHE under alkaline conditions, indicating the oxygen reduction property of β-Ag2Se. The large value of limiting current (3 mA cm-2) as well as small Tafel slope (68.5 mV dec-1) corroborates β-Ag2Se as a superior layered transition metal chalcogenide cathode material suitable for such energy-related applications (typically fuel cells and/or metal-air batteries).
References
(1) Ostroverkh, A.; Johánek, V.; Dubau, M.; Kúš, P.; Khalakhan, I.; Šmíd, B.; Fiala, R.; Václavu, M.; Ostroverkh, Y.; Matolín, V. Optimization of Ionomer-Free Ultra-Low Loading Pt Catalyst for Anode/Cathode of PEMFC via Magnetron Sputtering. Int. J. Hydrogen Energy 2019, 44 (35), 19344–19356. https://doi.org/10.1016/j.ijhydene.2018.12.206.

11:45 AM O04
(Student) Molecular Beam Epitaxy, Carrier Dynamics and Photocatalytic Properties of III-Nitride Nanowall Network Ishtiaque Ahmed Navid, Yin M. Goh, Jonathan Schwartz, Ayush Pandey, Peng Zhou, Robert Hovden and Zetian Mi; University of Michigan–Ann Arbor, United States

GaN based nanostructures are increasingly being used for a broad range of device applications, including LEDs, laser diodes,

transistors, and more recently artificial photosynthesis and solar fuel generation. We have performed a detailed investigation of the molecular beam epitaxy and characterization of InGaN nanowall networks with lateral dimensions reaching a new nanometer scale. These nanowall network heterostructures exhibit unusually strong photoluminescence emission in the deep visible, and remarkable photocatalytic activities for solar water splitting and hydrogen fuel generation. In this study, InGaN/GaN nanowall network heterostructures were grown on a thin AlN buffer layer on Si substrate using molecular beam epitaxy (MBE). The nanowall widths vary from as small as a few nanometer to tens of nanometer, while the height is ~0.5 µm depending on the growth duration. The average pore size of ~0.01 square micron in area. Structural properties of InGaN nanowall network is characterized using high-resolution scanning transmission electron microscopy. The selective area electron diffraction (SAED) patterns show that these nanowalls are single crystal and share a common crystallographic axis, in spite of the random nanoscale growth process. We have observed that single-crystallinity is maintained over ~2.5µm of nanowall in cross section with only 0.5° crystal rotation over a distance of 1.75µm. The photoluminescence (PL) spectrum of the nanowall structure shows significantly higher emission intensity compared to that of InGaN nanowires, which is attributed to the robust excitonic emission directly related to the enhanced exciton binding energy in such nanoscale structures. The time dependent photoluminescence (TRPL) measurement shows relatively high carrier lifetime (~3ns-4ns) at room temperature. Such relatively long carrier lifetime is comparable to that of InGaN quantum well structures in spite of the large surface area, suggesting that nonradiative surface recombination plays a negligible role in the carrier recombination. This observation is consistent with the extremely bright photoluminescence emission measured at room temperature and can be well explained by the robust excitonic emission. We have further investigated the photocatalytic properties of such unique nanostructures. It is observed that such InGaN nanowall network structures can drive spontaneous water splitting and hydrogen production with sunlight as the only energy input. Moreover, it is observed that the incorporation of Mg-doping can enhance the photocatalytic activity by nearly one to two orders of magnitude. At an optimum Mg doping level, we measured a solar-to-hydrogen conversion efficiency ~2.6%, which is among the highest values reported for direct solar water splitting. The critical role of Mg doping in significantly enhancing the photocatalytic performance can be explained by the significant impact of Mg doping on the surface band bending and charge carrier extraction. Work is currently in progress to develop InGaN nanowall network artificial photosynthesis devices and systems with both high efficiency and long-term stability.

12:00 PM O05
(Student) Low-Cost, Scalable Fabrication of Stable, High Performance Si-Based Metal-Insulator-Semiconductor Photoelectrodes for Solar-Driven Water Splitting Soonil Lee[1], Li Ji[2] and Edward T. Yu[1]; [1]The University of Texas at Austin, United States; [2]Fudan University, China

Photoelectrochemical (PEC) water splitting is a promising technology for using solar energy to convert water molecules into hydrogen gas. Si's moderate bandgap, high charge mobility and diffusion length, and extensive technology base enable Si-based photoelectrodes to achieve very good PEC performance with the potential for very low cost. However, Si has poor stability in aqueous solutions, limiting long-term stability of Si photoelectrodes for PEC water oxidation or reduction. Metal-insulator-semiconductor (MIS) photoelectrodes have therefore been widely explored for highly efficient and stable PEC water splitting. However, the insulating oxide that protects the semiconductor layer in an MIS photoelectrode typically must be sufficiently thin – a few nm – to enable carrier transport from the semiconductor to the metal catalyst via tunneling, often degrading photoelectrode stability. In this work, we demonstrate a simple, low cost, and highly scalable method to fabricate MIS photoelectrodes with thick SiO_2 insulating layers and localized electrical contacts between the Si absorber and metal catalyst structures. The fabricated photoelectrodes show high efficiency and outstanding stability in aqueous solutions, with photoanode onset potential as low as 0.7 V vs. RHE and saturation current density over 30 mA/cm^2 under AM1.5G illumination. Both MIS photoanode and photocathode structures are being explored. In a 7 day stability test, constant photocurrent density was maintained with no apparent degradation in performance. These results demonstrate a low-cost, highly scalable approach for fabrication of efficient and very stable photoelectrodes that is suitable for large-scale commercial fabrication and readily adaptable to a variety of catalyst, insulator, and semiconductor materials.

12:15 PM BREAK

12:45 PM O06
(Student) Surface-Modified Zero-Strain Spinel-Type Li2Co2-xAlxO4 (where x = 0, 0.3, and 0.60) Cathodes for Lithium-Ion Batteries Chanyeop Yu[1], Jinhyup Han[2], Eungje Lee[2] and Jung-Hyun Kim[1]; [1]The Ohio State University, United States; [2]Argonne National Laboratory, United States

Ever-increasing energy storage demands for vehicle electrification, consumer electronics, and grid energy storage requires further innovations in their performance and safety. To this end, developing new cathode materials has been the major interest in the Li-ion battery community. While cycling, most conventional cathode materials undergo repeated volume changes during Li-ion insertion/extraction (i.e., cycling), which in turn generates stress to the active material particles [1]. As a result of the tensile stress, particles tend to crack and pulverize, leading to a loss of contact and capacity fading. To address the mechanical instability issue from cathode materials, Dr. Lee et al. [2] developed novel spinel-type $Li_2Co_{2-x}Al_xO_4$ (where x = 0 – 1.0) as a "zero-strain" cathode material; it has less than 0.02% of the volume change during charge/discharge processes. This low volume change was explained by a suppression of rock-salt to spinel phase transition due to the presence of Al cations located in 16c site in $[Li_{2-y}Al_y]_{16c}[Co_{2-x}Al_{x-y}Li_y]_{16d}O_4$. Actually, operando synchrotron XRD analysis demonstrates no phase transition during cycling [2]. The zero-strain $Li_2Co_{2-x}Al_xO_4$ cathode can overcome the mechanical instability and offer an extended battery life. On the other hand, electrochemical stability of the $Li_2Co_{2-x}Al_xO_4$ – electrolyte interface is currently unknown. Although the Al-substitution is an effective approach to stabilize the bulk crystal phase, parasitic reactions occurring at cathode – electrolyte interfaces (CEIs) has been a major issue from different types of spinel materials; e.g., transition metal dissolutions from $LiMn_2O_4$ or $LiNi_{0.5}Mn_{1.5}O_4$ [3]. Therefore, it is important to understand the CEI properties of the $Li_2Co_{2-x}Al_xO_4$ and improving the CEI stability further. In this regard, we examined the effect of $LiNbO_3$ coating on the series of $Li_2Co_{2-x}Al_xO_4$ (x = 0 – 0.6). The $LiNbO_3$ coating layer can offer a facile Li-ion conduction while passivating the CEI layers. The results show that the $LiNbO_3$ coating enhances the cycle life and rate capabilities of the $Li_2Co_{2-x}Al_xO_4$ cathodes. Electrochemical impedance spectroscopy (EIS) combined with the distribution of relaxation times (DRT) technique has been studied to identify the improvement mechanisms of the $LiNbO_3$. The aging mechanism of the spinel cathode will be demonstrated by various material characterization and electrochemical analysis. This study will be conducted for conventional Li-ion batteries, but the results will be applicable to all-solid-state batteries via future studies.

Reference:

[1] D.E. Demirocak, B. Bhushan, J. Power Sources, 280 (2015) 256–262.
[2] E. Lee, B.J. Kwon, F. Dogan, Y. Ren, J.R. Croy, M.M. Thackeray, ACS Appl. Mater. Interfaces, 2 (2019) 6170-6175.

[3] J.-H. Kim, N.P.W. Pieczonka, Y. Li, ChemPhysChem, 15 (2014) 1940-1954.

1:00 PM O07
(Student) Multifunctional Composite Binder for High Voltage Lithium-Ion Batteries Lalith Rao, Chanyeop Yu, Adam Schmidt, Cody O'Meara, Jeremy Seidt, Jay R. Sayre and Jung Hyun Kim; The Ohio State University, United States

$LiNi_{0.5}Mn_{1.5}O_4$ is a spinel cathode formulation which is well known for its high operating voltage (~ 4.7 $V_{vs.Li}$) and high specific energy (650 Wh/kg). In addition to this, its Cobalt-free composition makes it a promising candidate for next-generation low-cost batteries. However, with high operating voltage it suffers from severe capacity fading in full-cells (LNMO/Graphite) using traditional polyvinylidene fluoride (PVdF) binder due to unwanted parasitic reactions at the electrode/electrolyte interface. Further, PVdF binder provides weak adhesion between current collector and electrode which results in aggravating the capacity fade from delamination. Studies have shown that advanced binder chemistries can be used to create an effective passivating layer at the cathode-electrolyte interface to prevent such reactions. In addition, aqueous binders can provide positive multifunction while eliminating the use of toxic organic solvents such as NMP. Lithium Polyacrylate (LiPAA) is a water-soluble binder that offsets the loss of Li ions in full cells by providing extra Li and passivates the cathode surface against electrolyte oxidation at high voltages. However, LiPAA induces thermal stresses during the drying process, which results in a brittle cathode especially at higher mass loadings for thick electrodes. To mitigate this problem, Na-alginate is introduced alongside LiPAA to enhance mechanical properties and provide additional passivation.
This study details the effect of different proportions of LiPAA and Na-alginate on the mechanical and electrochemical characteristics of $LiNi_{0.5}Mn_{1.5}O_4$ high-voltage cathodes with higher mass loadings. Mechanical peel tests were performed to measure the adhesion force for various binder composition. Cycle life and impedance spectroscopy tests were carried out to evaluate electrochemical performance. The LiPAA-Na-Alg composite binder showed better mechanical properties than those with simple PVdF, LiPAA or Na-Alg. A strong correlation was observed between mechanical properties vs full-cell capacity retention and impedance spectroscopy results. Finally, the optimum binder composition in terms of electrode quality and cathode performance will be discussed in the context of high-voltage spinel cathodes.

1:15 PM O08
New Long Life/ Safer Lithium Ion Battery with Low Cost/ Li-Corrosion Resistant Ultrananocrystalline Diamond-Coated Components Elida I. de Obaldia[1], Daniel Villarreal[2], Orlando Auciello[2] and Michelle Salgado[1]; [1]Universidad Tecnológica de Panamá, Panama; [2]The University of Texas at Dallas, United States

Novel low cost/electrically conductive/corrosion resistant nitrogen-doped ultrananocrystalline diamond (N-UNCD) coating provides excellent chemically robust encapsulation of commercial natural graphite (NG)/copper (Cu) anodes and new textured Si-based anodes, currently under development for Li-ion batteries (LIB), providing a solution to the problem of LIBs' anode materials degradation due to chemical corrosion induced by Li ions. The N-UNCD encapsulating coating allows for good conductivity of both electrons and Li-ions while exhibiting outstanding chemical and electrochemical inertness to Li ions-induced corrosion, eliminating de Li-induced chemical corrosion of graphite powder in current commercial graphite/copper composite anodes, which result in degradation of the capacity energy after undesirable relatively short numbers of charge/discharge cycles of LIBs. In addition, the electrically conductive N-UNCD coating produce a substantial increase in the mechanical strength of the anode's graphite powder and will also produce the same results for structured Si anodes, resulting in the formation of robust Solid-Electrolyte Interface (SEI) films, which effectively eliminate unceasingly cracking of SEI, observed in graphite/copper anodes, which expose fresh graphite anode surface, thus, repairing of the SEI by electrochemical reduction of the electrolyte and the formation of additional SEI compounds, which increase the impedance for the lithium ion diffusion and causes the electrolyte to be prematurely depleted in anodes without the N-UNCD coating. In addition to the excellent protection to chemical attack of anodes, new preliminary R&D will be presented indicating that electrically conductive N-UNCD coatings can also be used to coat LIB's oxide cathodes to protect them from Li-induced corrosion, as well, and that insulating/corrosion resistant UNCD coating can be used to coat the inner walls of novel metallic aluminum LIB's cases and membranes to protect them from corrosion induced by the Li-based battery environment, and thus enabling to use aluminum as a LIB's case, thus to replace current more expensive partially corrosion resistant metals. The pathway to commercialization of the new UNCD coating technology for LIBs and other LI-based batteries, like thermal Li-sulfur batteries will be discussed.

1:30 PM O10
(Student) Investigation of Lithiated Tin (Sn/Li Alloy) Thin Film as a Low Work Function Termination on Silicon/ Diamond Substrates Sami Ullah, Jude Laverock and Neil Fox; University of Bristol, United Kingdom

Low work function (WF) materials are necessary for energy storage and conversion devices. Scientific literature is full of explorations made in this field with new and emerging technologies applied to different elements with the purpose of creating low work function materials in the bulk and low dimensional regime. Alkali metals and their alloys with tin, cobalt, indium, etc. have been researched very well in batteries and other energy devices. Alkali metals have been shown to effectively aid in reducing the WF of many metals including Pb, Indium, tin, etc. Particular focus has been laid on Sn/Li alloy system where a work function dip up to 1.25 eV has been shown for a stoichiometric ratio of Sn_2Li_5[1][2]. Of course, this has been demonstrated to occur in the bulk alloys. However, with the purpose of achieving a similar goal in low dimensions (thin films), we are demonstrating for the first time the formation of a thin film of low work function Sn/Li alloy, formed using physical vapour deposition technique (E-Beam and Thermal Evaporation) at Ultra High Vacuum (UHV) conditions. The experiment utilises the high-end NanoESCA facility at the University of Bristol, UK, where the in situ deposition and the characterisation using X – Ray photoemission spectroscopy (XPS), Ultra-Voilet photoemission spectroscopy (UPS), spot profile low energy electron diffraction (Spa-LEED) techniques is carried out.[3]. In the initial experiments, a single crystal Si substrate was heated at a temperature of 800 ^oC for the removal of contaminants and Sn was deposited using the E beam deposition while Li was deposited using thermal evaporation method on Si substrate. Si surface was found to be terminated with the oxygen atoms. This should be the reason for the further lowering of WF as oxygen has been found to improve the sticking coefficient between the terminating metal species and the substrate surface. In the beginning, the O terminated Si surface was seen to possess a WF of 4.65 eV and a characteristic 2×1 LEED surface pattern which was then lost due to the disordered Sn and Li layers on the surface. However, Sn 3d peak was seen to shift towards the lower binding energy (B.E.) characteristic of the formation of Sn/Li alloy[4]. The WF was seen to lower to 4.15 eV and the surface was seen to become ordered after going through a series of annealing steps i.e., at 200 ^oC and 300 ^oC for 1 hour each and then 350 ^oC for 2 hours. After the 350 oC anneal, the LEED pattern started emerging. However, the Sn 3d peak was shifted to higher B.E. again which demands further analysis in order to find the optimised stoichiometric ratio between S/Li for ultra-low work

function demonstration.
[1] K. P. Loh, X. N. Xie, S. W. Yang, J. S. Pan, and P. Wu, "A spectroscopic study of the negative electron affinity of cesium oxide-coated diamond (111) and theoretical calculation of the surface density-of-states on oxygenated diamond (111)," *Diam. Relat. Mater.*, vol. 11, no. 7, pp. 1379–1384, Jul. 2002, doi: 10.1016/S0925-9635(02)00014-6.
[2] B. B. Alchagirov, R. K. Arkhestov, and F. F. Dyshekova, "Electron work function in alloys with alkali metals," *Tech. Phys.*, vol. 57, no. 11, pp. 1541–1546, 2012, doi: 10.1134/S1063784212110023.
[3] G. Wan, M. Cattelan, and N. A. Fox, "Electronic structure tunability of diamonds by surface functionalization," *J. Phys. Chem. C*, 2019, doi: 10.1021/acs.jpcc.8b11232.
[4] D.-T. Shieh, J. Yin, K. Yamamoto, M. Wada, S. Tanase, and T. Sakai, "Surface Characterization on Lithium Insertion/Deinsertion Process for Sputter-Deposited AgSn Thin-Film Electrodes by XPS," *J. Electrochem. Soc.*, vol. 153, no. 1, p. A106, Dec. 2006, doi: 10.1149/1.2133711.

SESSION P: Synthesis and Processing of 2D Materials
Session Chairs: Jyoti Katoch and Gilbert Daniel Nessim
Thursday Morning, June 24, 2021

11:00 AM P01
(Student) Higher Ultrasonic Frequency Liquid Phase Exfoliation as a More Efficient Method to Deposit Monolayer to Few-Layer Flakes of 2D Layered Materials Madina Telkhozhayeva[1], Eti Teblum[1], Rajashree Konar[1], Olga Girshevitz[2], Ilana Perelshtein[2] and Gilbert Daniel Nessim[1]; [1]Bar-Ilan University, Israel; [2]Bar-Ilan Institute of Nanotechnology and Advanced Materials, Israel

Dimensionality is the determining critical parameter in any material. Graphene and transition metal chalcogenides are two-dimensional (2D) layered nanomaterials which demonstrate wide array of physical and chemical properties when approaching few-layer thicknesses [1-2]. Large lateral size of these van der Waals nanomaterials with thinner mono- or few-layered flakes possess higher aspect ratios, which makes them suitable for electronic and optoelectronic applications. Among the most reliable techniques for exfoliation, sonication-assisted liquid-phase exfoliation (LPE) is considered to be a simple and cost-effective method for preparing graphene and its 2D inorganic counterparts at reasonable sizes and acceptable levels of defects. Although there were rapid advances in this field, improper sonication may result in unstable dispersions with wide flake sizes and thicknesses distributions, impurities and defects. Previous studies were mainly focused on the effects of solvent selection (predominantly, using high-boiling point solvents or surfactants), sonication time, and power input (usually, high power from probe/tip sonication can cause significant damage to the material). However, the effect of the sonication frequency is poorly understood and often ignored resulting in a low exfoliation efficiency. Here, we demonstrate that simple mild bath sonication at high frequency at relatively low powers contributes to the thickness, size and quality of the final exfoliated products. We show that monolayer graphene flakes can be directly exfoliated from graphite using only ethanol as a solvent at a reasonable sonication time by increasing the frequency of the bath sonicator from 37 kHz (which is usually used) to 80 kHz. The key mechanism involved is the generation of small-sized bubbles resulting from higher frequencies, which can easily penetrate between the interlayer spacing of the 2D materials to facilitate the delamination process with reduced damage to the material [3]. Detailed morphology studies by atomic force microscopy (AFM) indicate that the obtained product is dominated by large lateral size (10-15 μm) monolayer graphene flakes. High resolution TEM (HRTEM) show that the graphene flakes are of high-quality without any significant structural defects, although X-ray photoelectron spectroscopy (XPS) shows evidence of a small oxide population. Additionally, we show that this facile technique can be applied to other inorganic 2D nanomaterials such as digenite (Cu_9S_5) and silver sulfide (Ag_2S). This simple and effective method facilitates graphene and transition metal chalcogenides' processing for a wide range of applications.
References
[1] Coleman et.al, Science, 2011, 331, 568-571.
[2] Novoselov et.al, PNAS, 2005, 102, 10451-10453.
[3] Merouani et.al, Ultrason Sonochem., 2013, 20, 815-819.

11:15 AM P02
(Student) High-Quality MXene Inks for Energy Storage Chuanfang (John) Zhang; Empa–Swiss Federal Laboratories for Materials Science and Technology, Switzerland

Two-dimensional transition metal carbides and nitrides, so-called MXenes, have quickly attracted intensive attention and have found quite promising applications in various fields, such as water desalination, energy storage, catalysis, etc. These cutting-edge applications require the production of high quality MXene nanosheets with a high concentration. However, this has proven to be quite challenging. Here in this talk, I will describe the synthesis of high-quality MXene nanosheets, followed by the oxidation stability mechanism of MXene aqueous solutions, which is quite important for the long shelf life and is the prerequisite for the industrial application of MXenes.[1] Then I will show the importance of the viscous inks in the efficient fabrication of high-performance transparent conductive films/coatings,[2] scalable production of micro-supercapacitors assisted by the additive-manufacturing techniques (Figure 1).[3] The ink viscous nature also allows the MXene nanosheets to perform as a conductive binder for Si nanoparticles, resulting in high mass-loading MXene/Si anodes with an ultrahigh areal capacity (Figure 2), which is 5 times higher than that of commercial anode.[4] In addition, I will show the formulation of organic MXene inks for scalable additive-free printing of energy storage devices, as well as the formulation of composite ink for Lithium-sulfur batteries (Figure 3).[5] We therefore believe the high-quality MXene inks hold a bright future for the next-generation energy storage devices at a low cost.

11:30 AM P03
(Student) MOCVD of 2D-WS2 on Conductive TiN/Si Substrates Annika Grundmann[1], Nils Ackermann[1], Pavel Ondracka[1], Jochen M. Schneider[1], Michael Heuken[1,2], Holger Kalisch[1] and Andrei Vescan[1]; [1]RWTH Aachen University, Germany; [2]Aixtron SE, Germany

Transition metal dichalcogenides (TMDC) are a compelling class of 2D materials with potential in (opto)electronics, flexible electronics, chemical sensing and quantum technologies. So far, most 2D materials are deposited on insulating substrates such as sapphire. Thus, fabrication processes for 2D device structures require one or more transfer processes, which detrimentally affects their quality and optical properties. A direct deposition of 2D/3D heterostructures on conductive substrates, however, could set a benchmark for pure and reproducible 2D structures and interfaces and possibly also enable novel device architectures. This study presents first results on the metalorganic chemical vapor deposition (MOCVD) of WS_2 on conductive TiN-on-Si (TiN/Si) subtrates. The deposition of WS_2 was performed in a commercial AIXTRON multiwafer reactor. Tungsten hexacarbonyl (WCO) and di-tert-butyl sulfide (DTBS) are used as metalorganic precursors and H_2 and N_2 as carrier gases. All samples were characterized using Raman and photoluminescence spectroscopy

(PL), scanning electron microscopy (SEM), atomic force microscopy (AFM) and X-ray photoelectron spectroscopy (XPS). After screening potential substrates, taking into account the requirements of WS_2 MOCVD, we identified TiN/Si as a suitable substrate. For this, 50 nm of TiN were deposited on 2" Si wafers by DC magnetron sputtering in N_2/Ar atmosphere (AFM roughness 0.16 nm). Previous experiments have demonstrated the strong impacts of surface conditioning using H_2 desorption as well as single-precursor exposure. As TiN is exposed to atmosphere before loading into the MOCVD chamber, we expect oxidized species such as TiO_xN_y. It is assumed that both H_2 and DTBS as well as CO formed during the decomposition of WCO could have a reducing effect on such surface oxides. Initially, the influence of the following single-step prebakes on the TiN/Si substrate was investigated (reference: direct growth on as-loaded TiN/Si): H_2 prebake at 1050 °C, 200 hPa for 1 h and H_2, N_2, DTBS and WCO at 825 °C (optimum growth temperature of WS_2) and 30 hPa for 1 h. In addition, two two-step prebakes are analysed: 15 min in H_2 at 825 °C, 200 hPa followed by either 1h DTBS (H_2-DTBS) or WCO (H_2-WCO) at 825°C, 30 hPa. MOCVD of WS_2 on the untreated reference substrate resulted in massive deposition of C compounds, detected by Raman spectroscopy (similar to process on sapphire). After the H_2 prebake at 1050 °C, grain growth of TiN with a size of up to 150 nm occurred, which excessively increases the roughness, and thus the substrate becomes unusable for WS_2 growth. XPS measurements of the TiN substrate before the prebake show that the surface mainly consisted of TiO_2. The H_2, WCO and H_2-WCO prebakes partially depleted the surface of oxygen and the WCO and H_2-WCO prebakes also deposited W. The N_2 prebake does not remove the TiO_2. The DTBS and H_2-DTBS prebakes, on the other hand, completely removed the TiO_2 from the surface and TiS and TiS_2 layers are formed. However, after both DTBS prebakes, sp^2-C was detected, which identifies the S precursor as the origin of C deposition but also shows that a preceding H_2 desorption cannot inhibit it. Analysis of the nucleation of WS_2 on the differently conditioned TiN surfaces showed that WS_2 only weakly binds to TiO_2 and TiO_2-W surfaces present after the N_2, WCO and H_2-WCO prebake. Thus, most of the nuclei stand out vertically rather than being laterally attached to the substrate. The C-TiS_2-TiS surface shows the best suitability for WS_2 deposition having the largest density of lateral nuclei on the surface. Further analysis also showed that the lateral nuclei are dominantly responsible for PL peak of the A exciton of WS_2. Based on these initial experiments, TiN can be identified as a suitable substrate for WS_2, but further process optimization is necessary to deposit a fully coalesced WS_2 monolayer, which could serve as a basis for various devices.

11:45 AM P04
(Student) Scalable Synthesis of Few-Layered 2D Tungsten Diselenide (2H-WSe2) Nanosheets Directly Grown on Tungsten (W) Foil Using Ambient-Pressure Chemical Vapor Deposition for Reversible Li-Ion Storage Rajashree Konar[1], Rosy S[1], Ilana Perelshtein[1], Eti Teblum[1], Madina Telkhozhayeva[1], Maria Tkachev[1], Jonathan J. Richter[1], Elti Cattaruzza[2], Andrea P. Charmet[2], Paolo Stoppa[2], Malachi Noked[1] and Gilbert Daniel Nessim[1]; [1]Bar-Ilan University, Israel; [2]Ca'Foscari University of Venice, Italy

Sustainable energy storage devices demand new materials for energy storage systems, which alleviate their cost and increase longevity. A prominent energy storage technology for modern applications is Lithium-ion batteries. In this regard, two-dimensional (2D) materials attracted substantial and considerable attention due to their unique properties and abundant potential in various applications, including batteries[1]. Controllable synthesis of 2D materials with high quality and better efficiency is essential for their large scale applications, such as their functions as electrode material in batteries. The methods for the synthesis of two-dimensional materials include exfoliation, solvothermal, and chemical vapor deposition (CVD) routes, among which CVD offers better quality, efficiency, and consistency. In this perspective, the family of 2D transition metal di-chalcogenides (TMDCs) gained significant attention for their ability to store metal ions such as Li, Na, and Mg. TMDCs of group 6 transition metals (MX_2 where M = Mo, W, and X = S, Se, Te) have a lamellar structure (space group $P6_3/mmc$) similar to graphite but with larger interlayer spacing. Tungsten di-chalcogenides are significant here because of the larger size of W that provides a further alteration of the 2D structure and has been successfully utilized for various applications such as photodetectors, field-effect transistors (FETs), etc. The typical group 6 TMDC lattice structure show W atoms confined in a trigonal prismatic coordination sphere neighbored to Se atoms. Because of its very high density (~9.32 g cm^{-3}), WSe_2 also has a high volumetric capacity, thereby proving it as a prospective LiB electrode material[2]. Our work focuses on a facile synthesis of 2H-WSe_2 on W foil in the ambient-pressure chemical vapor deposition system using only Argon as carrier gas during the reaction. Extensive characterization of the bulk and exfoliated material confirm that the as-synthesized 2H-WSe_2 is layered (i.e., 2D). XRD (X-Ray Diffraction) confirms the phase. At the same time, HRSEM (High-Resolution Scanning Electron Microscopy), HRTEM (High-Resolution Scanning Electron Microscopy), and AFM (Atomic Force Microscopy) clarify the morphology of the material. FIB-SEM (Focused-Ion Beam Scanning Electron Microscopy) estimates the depth of the 2H-WSe_2 formation on W foil around 5-8 µm and Raman/UV-Vis measurements prove the quality of the exfoliated 2H-WSe_2. The redox processes of Lithium-ion Battery (LiB) studies show an increase in capacity until 500 cycles. On prolonged cycling, the discharge capacity till the 50th cycle at 250 mA/g, the material shows a stable capacity of 550 mAh/g. These observations indicate exfoliated 2H-WSe_2 has promising applications as LiB electrode material.

References

(1) Xia, H.; Xu, Q.; Zhang, J. Recent Progress on Two-Dimensional Nanoflake Ensembles for Energy Storage Applications. Nano-Micro Lett. 2018, 10 (4), 1–30. https://doi.org/10.1007/s40820-018-0219-z.

(2) Share, K.; Lewis, J.; Oakes, L.; Carter, R. E.; Cohn, A. P.; Pint, C. L. Tungsten Diselenide (WSe_2) as a High Capacity, Low Overpotential Conversion Electrode for Sodium-Ion Batteries. RSC Adv. 2015, 5 (123), 101262–101267. https://doi.org/10.1039/C5RA19717A.

12:00 PM P05
(Student) Towards the Rational Design of Printed 2D Materials Zhehao Zhu, Joon-Seok Kim, Michael Moody and Lincoln Lauhon; Northwestern University, United States

The formulation of inks based on 2D materials could enhance the performance of and provide new functional behaviors to printed electronics while retaining scalable manufacturing processes. Recent advances in solution-based exfoliation have demonstrated that the electronic properties of single semiconducting 2D nanosheets can be preserved during ink processing, but there remain several challenges to the production of thin-film transistors based on printed 2D materials. In addition to minimizing inter-sheet resistivity and preserving bulk-like mobilities, the local electronic properties and microstructure of the composite material must be optimized to minimize the resistance of overlapping nanosheets (i.e. junction resistance). To rationally guide the development of 2D inks and related processing, we explored the design principles by integrating device modeling with electrical and scanning probe characterization on transistors consisting of partially overlapping 2D channels (Figure 1a). We examined the limiting factors to the junction resistance by benchmarking a gate-dependent resistor network model with experimentally measured electrical characteristics for model MoS_2/MoS_2 homojunctions and utilized the model to quantify performance trade-offs determined by nanosheet thickness, percent overlap, sheet resistance and inter-sheet resistivity. Kelvin probe force

microscopy (KPFM) was used to measure the surface potential profiles in transistor channels as a function of applied bias conditions and morphological characteristics such as nanosheet thickness. Detailed analysis of the abrupt potential drop measured at the conformal edge provides evidence that the on-state transistor performance of overlapping nanosheets is limited by the local sheet resistance (Figure 1b), which is likely due to weakly screened trapped charges at the edge state. This suggests that passivation and/or functionalization schemes targeting the edges of nanosheets could greatly improve transistor performance. Moreover, we found that screening of the upper portions of overlapping nanosheets produces current crowding at junctions between the edge of one nanosheet and the basal plane of another. Reducing the nanosheet thickness (i.e. the number of layers) increases the carrier concentration of the top nanosheet, thus distributing the current over longer distance and facilitating efficient inter-sheet charge transfer (Figure 2a), which increases the effective mobility and optimum percent overlap (Figure 2b). This provides further motivation to develop exfoliation schemes that preserve intrinsic monolayer properties.

12:15 PM BREAK

12:45 PM P06
(Student) MOCVD Growth of Tungsten Ditelluride Thin Films Thomas V. McKnight, Tanushree H. Choudhury, Anushka Bansal, Ke Wang and Joan M. Redwing; The Pennsylvania State University, United States

Tungsten ditelluride (WTe_2) is a layered, type-II Weyl semimetal transition metal dichalcogenide (TMD) typically observed in a distorted 1T (1T') phase with an orthorhombic crystal structure comprised of planes of distorted triangular lattices of tungsten atoms sandwiched by tellurium atoms. The distortion pushes tungsten atoms closer together in the x-axis than the y or z-axis, generating quasi-one-dimensional chains of these atoms, leading to strongly anisotropic electronic properties throughout the material. It has been shown to have extraordinary physical properties, such as a high magnetoresistance, anisotropic ultra-low thermal conductivity and metal-insulator transition and it also exhibits interesting quantum phenomena such as the quantum spin-Hall effect and pressure-driven superconductivity. These unique properties make WTe_2 an exciting candidate for emerging applications, including phase change memory electrodes, magnetic field sensors, biosensors, microelectromechanical systems, hard disk drives and quantum computing. While bulk crystals of the material have been available for many years, to date, thin films of WTe_2 have only recently been synthesized using techniques such as molecular beam epitaxy and powder source chemical vapor deposition (CVD) that utilize Te powder and W-feedstock. These techniques, however, have a number of challenges including tellurium dimer formation, that can severely hinder growth with high dissociation energies, and the use of salt assisted growth promotors during CVD growth which could contaminate future device fabrication. Metalorganic CVD (MOCVD) growth is of interest as it enables precise delivery of precursors to the substrate at moderate growth pressures (100-700 Torr), while proper precursor selection mitigates the Te dimer formation, but has not yet been studied in detail. In this study, we investigate the use of MOCVD for the growth of WTe_2 on c-plane sapphire substrates. The studies were carried out in a vertical cold wall MOCVD reactor using tungsten hexacarbonyl ($W(CO)_6$) and diethyltelluride (DETe) as precursors for W and Te, respectively, in a H_2 carrier gas. Initial studies, carried out at 100 Torr reactor pressure using a $W(CO)_6$ flow rate of 1.3 $x10^{-4}$ sccm and Te/W ratio of ~8000 : 1, demonstrate the growth of centimeter scale WTe_2 as confirmed by Raman spectroscopy and X-ray photoelectron spectroscopy (XPS). Additional studies to elucidate the growth mechanism and properties of MOCVD grown WTe_2 were then undertook. The growth rate was found to decrease with increasing temperature over the range of 350 - 600°C. Similarly, higher growth rates were observed at lower growth pressures when examined over a range of 50 - 300 Torr. The effect of precursor flow rates was also investigated and demonstrated that the DETe flow rate had little effect on growth rate while changes in $W(CO)_6$ flow rate can be used to directly control growth rate of films. Peaks at ~1340 cm^{-1} and ~1600 cm^{-1} were present in the Raman spectra of some films indicating the presence of carbon in the layers resulting from the DETe source. Higher carbon content was observed at higher growth temperatures and growth pressures. This suggests that our growths are becoming limited by parasitic prereactions of our precursors in the gas phase. When precursors react in the gas phase before reaching the substrate surface, they form carbon containing species which deposit, thus limiting the available reactants to interact on the surface and form WTe_2. X-ray diffraction (XRD) and transmission electron microscopy (TEM) analysis further indicate that films are hexagonal and exhibit the layered 1T' structure. XPS studies over a period of a few weeks reveals that films do not readily oxidize and are quite stable.

1:00 PM *P07
High Yield, Bottom-Up/Top-Down Synthesis of 2D Layered Metal Sulfides, Phosphides and Selenides Using Chemical Vapor Deposition with Applications in Electronics and Electrochemistry Gilbert Daniel Nessim[1,2]; [1]Bar Ilan University, Israel; [2]President Israel Vacuum Society (IVS), Israel

Since the excitement about graphene, a monolayer of graphite, with its 2010 Nobel Prize, there has been extensive research in the synthesis of other non-carbon few/mono-layers exhibiting a variety of bandgaps and semiconducting properties (e.g., n or p type). The main approaches to deposit few/monolayers on a substrate are: (a) bottom-up synthesis from precursors using chemical vapor deposition (CVD) or (b) top-down exfoliation (liquid or mechanical) of bulk layered material. Using a Lego approach of superposing monolayers, we can envisage the fabrication of heterojunctions with original electronic behavior. Here we show a combined bottom-up and top-down approach where (a) we synthesize in one step high yields of bulk layered materials by annealing a metal in the presence of a gas precursor (sulfur, phosphorous, or selenium) using chemical vapor deposition (CVD) and (b) we exfoliate and deposited (dropcast or Langmuir Blodgett) few/mono-layers on a substrate from a sonicated mixture of our material in a specific solvent. It is interesting to note that, besides the structure being 2D layered, the properties of the nanomaterials synthesized slightly differ from the materials with the same stoichiometry synthesized using conventional chemical methods (e.g., solvothermal).
In this talk, we will discuss the chemical synthesis, the very extensive characterizations, and the lessons we learned in making multiple metal sulfides (Cu-S, Ag-S, Ni-S), metal phosphides (Ni-P, Cu-P), and metal selenides (Ag-Se, Cu-Se, W-Se, Mo-Se). We will see how we integrated these new materials into electrochemical devices. We will also explore how to deposit large mono/few layers of these materials using techniques such as dropcasting or Langmuir-Blodgett to build heterojunctions and sensors.

1:15 PM P09
Graphene Interface Mediated Lateral Epitaxy of Monolayer Hexagonal Boron Nitride Ping Wang[1], Perry Corbett[2], Woncheol Lee[1], Nguyen Vu[1], David A. Laleyan[1], Qiannan Wen[1], Jiseok Gim[1], Yuanpeng Wu[1], William H. Koll[2], Boyu Wang[1], Yi Sun[1], Robert Hovden[1], Mackillo Kira[1], John Heron[1], Emmanouil Kioupakis[1], Jay Gupta[2] and Zetian Mi[1]; [1]University of Michigan–Ann Arbor, United States; [2]The Ohio State University, United States

Monolayer hexagonal boron nitride (hBN), the thinnest insulator, has been considered as a fundamental building block for van der Waals (vdW) heterostructures, due to its unique nature of wide

bandgap, high quantum efficiency, high breakdown field, and high thermal conductivity. To date, however, most of the hBN-based vdW heterostructures are fabricated by stacking 2D layers exfoliated from their crystals, leading to limited structural, optical, and electronic properties as well as poor scalability. In addition, rich physics and engineering have been theoretically predicted for in-plane graphene (Gr)-hBN monolayer heterostructures, which are impossible to form by exfoliation approaches. In recent years, intensive efforts have been devoted to the epitaxial growth of hBN on metal, sapphire, SiC, and graphite substrates, and remarkable progress have been achieved by using chemical vapor deposition (CVD), metal-organic chemical vapor deposition (MOCVD), and molecular beam epitaxy (MBE). Due to the similar lattice structure and small lattice mismatch (~1.8%) between hBN and Gr, highly oriented pyrolytic graphite (HOPG) is considered as a promising substrate for the vdW epitaxy (vdWE) of hBN. However, the experimental evidence of theoretical predicted growth kinetics and thermodynamics of Gr-hBN have been rarely reported, and the epitaxy and related properties of hBN on graphite substrates have remained elusive. In this work, we have proposed and further demonstrated a Gr-hBN interface medicated growth model for the controllable synthesis of monolayer hBN on graphite with superior structural, optical, and electrical properties. Morphologic uniform monolayer hBN is achieved on graphite by employing ultrahigh temperature (up to 1600 °C) growth in plasma-assisted MBE. The predicted energetically favorable arm-chair (AC) Gr-hBN interface and energetically stable AC edges for hBN with hexagonal geometry have been confirmed by detailed scanning tunneling microscopy (STM) characterization. The indirect to direct bandgap transition for hBN going from multilayers to monolayer is demonstrated by the deep-ultraviolet (DUV) photoluminescence in the range of 5.7 ~ 6.2 eV. A breakdown field up to12 MV/cm for epitaxial single-layer hBN is confirmed using a conductive atomic force microscope (cAFM), which is in good agreement with theory prediction for pristine hBN. This work provides a framework for controllable epitaxial growth of wafer-scale, monolayer hBN on 2D heteromaterials, which offers promising opportunities for the development of hBN-based electronic, optoelectronic, and quantum devices.

1:30 PM P10
(Student) Impact of Salt and Solvent Identity on the Deposition of a Cobalt Crown Ether Phthalocyanine Monolayer Electrolyte Huiran Wang, Jierui Liang, Shubham Sukumar Awate and Susan Fullerton-Shirey; University of Pittsburgh, United States

We recently demonstrated a non-volatile, two-dimensional (2D) crystal random access memory (RAM) using a monolayer electrolyte[1] consisting of cobalt crown ether phthalocyanine (CoCrPc) and lithium salt. Each CoCrPc molecule includes four crown ethers that each solvate one lithium ion and form an ordered array on 2D crystals including graphene, WSe_2 and MoS_2. The electrolyte is deposited by drop casting from solvent followed by annealing in argon[2]. The key mechanism of the nonvolatile memory is the toggling of lithium ions back and forth through the crown ether cavity by an applied electrical field. The positioning of the ions near the semiconductor surface results in electric double layer (EDL) gating which creates a low resistance (ON) state; when ions are moved away from the semiconductor surface, a high resistance (OFF) state is created[3]. Our published work primarily focused on the combination of 15-crown 5-ether (15C5) CoCrPc and $LiClO_4$ where the salt is deposited by drop-casting in ethanol. However, this salt-solvent combination increased the number of features on the semiconductor surface resembling aggregates of CoCrPc and/or lithium salt. Literature indicates additional combinations of lithium salts (such as LiCl and LiI) and solvents that promote the complexation between 15C5 and Li^+. Therefore, in this study we explore additional salt-solvent pairs to decrease the size and density of the aggregates or eliminate them entirely. The quality of the deposition can be characterized by root mean square roughness (R_q), skewness (R_{sk}), and kurtosis (R_{ku}) using atomic force microscope (AFM) topological scans. In this study, WSe_2 flakes were exfoliated on p-type Si (90 nm SiO_2) and a monolayer of 15C5 CoCrPc was deposited on the flake surfaces. To isolate the impact of anion identity on the monolayer quality, we kept the deposition solvent constant as ethanol while varying the lithium anions: $LiClO_4$, LiCl, and LiI. To isolate the impact of solvent identity, we kept the salt, $LiClO_4$, constant and varied the solvent from ethanol to acetone and acetonitrile (note that acetone and acetonitrile were chosen for their reported tendency to promote ion-(15C5) crown complexation[4].) The monolayer quality is evaluated using AFM in an Argon-filled glovebox with water and oxygen concentration < 0.6 ppm. Among the three salts, LiCl in ethanol gives the most homogenous monolayer with a $R_{q,LiCl} = 0.25 \pm 0.01$ nm. Specifically, with ethanol as the solvent, LiCl gives a monolayer that is 2.4 and 6.2 x less rough than $LiClO_4$ and LiI, respectively. The skewness of LiCl ($R_{sk,LiCl} = 0.15 \pm 0.01$) is close to zero indicating that the surface topology is relatively flat, which is also consistent with the small surface roughness of 2.5 angstrom. Among the three solvents, we observed that acetone gives the best $LiClO_4$ deposition with the lowest R_q (0.42 ± 0.05 nm), which is ~1.5 and 3 x lower than ethanol and acetonitrile, respectively. Also, the skewness ($R_{sk,acetone} = 0.72 \pm 0.24$) and the kurtosis ($R_{ku,acetone} = 5.23 \pm 0.31$) were approximately 1.5 times lower than the other two solvents. These data were taken by averaging over six, 200 x 200 nm locations on each flake.
The data indicate LiCl and acetone as the most promising salt-solvent combination; these results will be reported in the talk. This work is supported by the NSF under Grant # NSF-DMR-EPM CAREER: 1847808.
(1) Liang, et. al., *Nano Lett.* **2019**, *19* (12), 8911–8919. (2) Lu, et. al., *J. Phys. Chem. C* **2015**, *119* (38), 21992–22000. (3) Xu, et. al., *ACS Nano* **2017**, *11* (6), 5453–5464. (4) Izatt, et. al., *Chem. Rev.* **1985**, *85* (4), 271–339.

SESSION Q: Spin Dynamics in Electronic Materials
Session Chairs: Xinyu Liu and Angel Yanguas-Gil
Thursday Morning, June 24, 2021

11:00 AM Q01
Probing the Coherent Spin Dynamics of Divacancies in Silicon Carbide with Low-Field Magnetoresistance Stephen R. McMillan[1] and Michael E. Flatté[1,2]; [1]University of Iowa, United States; [2]Technische Universiteit Eindhoven, Netherlands

Divacancies in silicon carbide have attracted attention in the quantum information community due to remarkably long room-temperature spin coherence times [1] and the potential for integration with the photonics and communications sectors due to energies in the near-infrared regime [2]. Isolated neutral divacancies are realizable and are addressable via optically detected magnetic resonance [3]. The long coherence times of these individual deep centers suggest that they are ideal candidates for single spin sensing and quantum memory applications. Non-equilibrium correlations between the divacancy spin and the orientation of a spin-polarized contact lead to the formation of bottleneck states that limit the flow of current through the defect. We describe an approach we predict will allow exploration of the coherent spin dynamics of these divacancies through low-field magnetoresistance. Calculation of the magnetoresistance focuses on the steady-state current through the defect using a stochastic Liouville formalism similar to that used in previous work exploring the signatures of exchange coupled spin-1/2 centers [4]. Here we link the features in the magnetoresistance to terms in the spin-1 Hamiltonian, which we expect to provide not only a means of electrically probing the dynamics of the spin center itself, but

also sensing local magnetic, electric, and strain fields. We acknowledge support for this work from DOE BES through grant number DE-SC0016379.
[1] A. L. Falk, et al., Nat. Commun. 4:1819 (2013)
[2] N. T. Son, et al. Phys. Rev. Lett. 96, 055501 (2006)
[3] D. J. Christle, et al., Nat. Mater. 14, 160 (2015)
[4] S. R. McMillan, et al., Phys. Rev. Lett. 125, 257203 (2020)

11:15 AM Q02
Ultra-Low Field Frequency-Swept Electrically Detected Magnetic Resonance—Multiple Photon Transitions and Bloch-Siegert Shifts James P. Ashton, Brian R. Manning and Patrick M. Lenahan; The Pennsylvania State University, United States

Electrically detected magnetic resonance (EDMR) measurements are often utilized to elucidate structural information regarding defects in semiconductor and insulator devices.[1,2] EDMR is typically achieved by placing a device within a linearly varying magnetic field B_0 with a perpendicular oscillating microwave or RF field B_1 held at constant frequency. The application of B_0 splits the electron energy levels of paramagnetic defects. When the energy of the B_1 field $E=h\nu$ matches the energy difference between "up" spin and "down" spin, $g\mu_B B_0$, the electron will "flip" spin. Here, h is Planck's constant, ν is the microwave or RF frequency, g is a defect-dependent number, and μ_B is the Bohr magneton. In EDMR, these spin flipping events give rise to a change in recombination rate. The spin dependent recombination (SDR) process can be understood through the theoretical description introduced by Kaplan, Solomon, and Mott.[3] Conduction and defect electrons couple to form triplet and singlet states with $S = 1$ and $S = 0$, respectively. Here, S is the spin angular momentum. Triplet states tend to dissociate since recombination process involving a triplet state does not conserve spin angular momentum. Spin flipping events under electron spin resonance transform triplet states with $S = 1$ into singlet states with $S = 0$. Since spin angular momentum is conserved under singlet recombination, the transformation will cause a spin dependent change in the recombination current that constitutes the EDMR spectrum. Recent EDMR measurements in organic devices illustrate the detection of ultra-strong coupling mechanisms, namely the Spin-Dicke effect,[4] Floquet spin states, and Bloch-Siegert shifts[5] in organic light-emitting diodes. These ultra-strong coupling effects are possible in systems with relatively weak spin-orbit coupling and long lifetimes by the application of a strong driving field B_1, whose magnitude is comparable to the static field B_0. Sub-mT measurements enable the condition $B_1 \approx B_0$ but are difficult because of the existence of a near-zero field magnetoresistance (NZFMR) effect that pervades the sub-mT regime.[6] We have developed an EDMR spectrometer capable of probing ultra-strong coupling effects in the sub-mT regime by effectively eliminating interference caused by the NZFMR effect. Our spectrometer design employs a frequency sweep of the RF field with the static field held constant. We term this new EDMR technique ultra-low field frequency-swept EDMR (FSEDMR). In our FSEDMR measurements, we observe multiple photon transitions in interface SDR measurements on 4H-SiC MOSFETs, which indicate the existence of Floquet spin states arising at interface silicon vacancy variant defects. We also observe the Bloch-Siegert shift of the FSEDMR spectrum. Measurements are performed with static fields $B_0 \approx 0.1\text{-}0.5$ mT and B_1 varying between 0.02-0.1 mT. These measurements are possible because of the relatively long spin-lattice and spin-spin relaxation times, indicating potential utility for quantum engineering applications, such as spin-based quantum computation.
This work at Penn State was supported by the US Army Research Laboratory. This work was also supported by the Air Force Office of Scientific Research under Award No. FA9550-17-1-0242.
[1] T. Umeda, T. Kobayashi, M. Sometani, H. Yano, Y. Matsushita, and S. Harada, Appl. Phys. Lett. **116**, 071604 (2020).
[2] C.J. Cochrane, P.M. Lenahan, and A.J. Lelis, Appl. Phys. Lett. **100**, 023509 (2012).
[3] D. Kaplan, I. Solomon, and N.F. Mott, J. Phys. Lettres **39**, 51 (1978).
[4] D.P. Waters, G. Joshi, M. Kavand, M.E. Limes, H. Malissa, P.L. Burn, J.M. Lupton, and C. Boehme, Nat. Phys. **11**, 910 (2015).
[5] S. Jamali, V. V. Mkhitaryan, H. Malissa, A. Nahlawi, H. Popli, T. Grünbaum, S. Bange, S. Milster, D. Stoltzfus, A.E. Leung, T.A. Darwish, P.L. Burn, J.M. Lupton, and C. Boehme, *Floquet Spin States in OLEDs* (2020).
[6] C.J. Cochrane and P.M. Lenahan, J. Appl. Phys. **112**, 123714 (2012).

11:30 AM Q03
Electrode Materials Influence on Molecular Spintronics Devices Eva Mutunga[1], Bishnu R. Dahal[1], Marzieh Savadkoohi[1], Andrew C. Grizzle[1], Christopher D'Angelo[1], Vincent Lamberti[2] and Pawan Tyagi[1]; [1]University of the District of Columbia, United States; [2]Y-12 National Security Complex, United States

Devices with active molecular components benefit from the fact that molecules are highly tunable nanostructures. Their optical, electrical, and magnetic properties can be customized using synthetic chemistry. Therefore, molecular devices pave the way to a new class of metamaterials [1]. Novel molecular spintronics devices were demonstrated by connecting molecules between two ferromagnetic electrodes [2]. Moreover, intriguing transport and magnetic properties were observed when the molecule possesses a net magnetic spin and interacts with the electrodes' spin state. In this study, we focus on molecular spintronic devices that are created by bridging paramagnetic molecules across the dielectric of a prefabricated tunnel junction device. The molecules covalently bond with the metallic electrodes along the exposed edges resulting in tunnel junction based molecular spintronic devices (TJMSD) [3]. Previously we observed that paramagnetic molecules produced strong exchange coupling between magnetic electrodes. The molecular impact was dependent on the type of TJMSD's electrodes [4]. Experimental research on the effect of metal electrode type can be extremely challenging because each TJMSD fabrication with a new metal electrode type may require significant device optimization. In this paper, we used Monte Carlo simulation to study the effect of a wide range of electrodes on TJMSD properties. We utilized the 3D Ising model to simulate the experimentally studied TJMSD design. We varied the Heisenberg exchange coupling parameter for one TJMSD electrode. This variation simulated a magnetic electrode with low to high Curie temperature for ferromagnetic materials. Our simulation also studied the effect of antiferromagnetic and paramagnetic electrodes in conjunction with the ferromagnetic electrode of TJMSD. We recorded the temporal evolution of TJMSD magnetization and observed the impact of electrode type on the nature of the evolution of equilibrium state. We varied thermal energy to understand the role of electrode types. We have recorded the correlated distribution of the electrodes' magnetic moment with respect to molecular junctions to elucidate the spatial impact range of molecules as a function of electrode type. We recorded the effects of electrode type on magnetic susceptibility and heat capacity. This research may enable designing novel molecular spintronics devices by providing a knowledge base about the impact of a wide range of electrode materials. This research is supported by National Science Foundation-CREST Award (Contract # HRD- 1914751), Department of Energy/ National Nuclear Security Agency (DE-FOA-0003945).
References
1. Bogani, L. and W. Wernsdorfer, *Molecular spintronics using single-molecule magnets.* Nature Materials, 2008. **7**(3): p. 179-186.
2. Rocha, A.R., et al., *Towards molecular spintronics.* Nature Materials, 2005. **4**(4): p. 335-339.
3. Tyagi, P., *Multilayer edge molecular electronics devices: a review.* Journal of Materials Chemistry, 2011. **21**(13): p. 4733-4742.

4. Tyagi, P., C. Baker, and C. D'Angelo, *Paramagnetic molecule induced strong antiferromagnetic exchange coupling on a magnetic tunnel junction based molecular spintronics device.* Nanotechnology, 2015. **26**(30): p. 305602.

11:45 AM Q04
Suppression of the Optical Linewidth and Spin Decoherence of a Quantum Spin Center in a *p–n* Diode Denis R. Candido[1,2] and Michael E. Flatté[1,2]; [1]University of Iowa, United States; [2]The University of Chicago, United States

We present [1] a quantitative theory of the suppression of the optical linewidth due to charge fluctuation noise in a *p–n* diode, recently observed in Ref. 2. We connect the local electric field with the voltage across the diode, allowing for the identification of the defect depth from the experimental threshold voltage. Furthermore, we show that an accurate description of the decoherence of such spin centers requires a complete spin–1 formalism that yields a bi-exponential decoherence process, and predict how reduced charge fluctuation noise suppresses the spin center's decoherence rate. The material is based on work supported by the U.S. Department of Energy, Office of Basic Energy Sciences, under Award Number DE-SC0019250.
[1] Denis R. Candido and Michael E. Flatté, arXiv:2008.13289
[2] C. P. Anderson, A. Bourassa et al., Science **366**, 1225 (2019).

12:00 PM Q05
Controlled Synthesis of Screw Dislocations in Semiconductor Nanomembranes for Spintronic Applications Emma J. Renteria[1,1], Mengistie Debasu[1], Divya J. Prakash[1,1], Shelley Scott[2], Donald Savage[2], Max G. Lagally[2] and Francesca Cavallo[1,1]; [1]The University of New Mexico, United States; [2]University of Wisconsin-Madison, United States

Screw dislocations (SDs) in a single-crystalline semiconductor have been theoretically predicted to exhibit a 1D spin orbit coupling (SOC) along the dislocation core.[1] This 1D SD-SOC is predicted to reside deep in the band gap of semiconductors and to lie in a much narrower range of angles than that resulting from either the Rashba or Dresselhaus effects. Thus SDs hold the promise to produce coherent, highly polarized spin currents that are useful for spintronics devices. Motivated by these recent theoretical findings, we investigated and established approaches to controlled synthesis of SDs in single-crystalline semiconductors.
We use single-crystalline semiconductors in the form of sheets with nanoscale thickness (nanomembranes, NMs), as NMs create a pathway to fabrication of SDs in a variety of semiconductors, including ternary and quaternary alloys. This capability, which strongly depends on the ionicity of the material, is crucial to tailor the 1D SOC along the dislocation core. Additionally, NMs containing SDs may be sandwiched between ferromagnetic contacts to form the basis for novel generation of spintronics devices, including vertical spin valves and vertical spin field-effect transistors that depend on 1D SOC. Our approach to controlled synthesis of SDs relies on overlaying two arrays of pixelated NMs of the same material at a non-zero twist angle to create an array of disregistry at the interface. Subsequent annealing of bonded NMs at a temperature $T \geq 1000$ °C fosters propagation of SDs across the thickness of the NMs. The spatial distribution of SDs in supported and freestanding NM as probed by weak-beam transmission electron microscopy well correlates with twist angle between the two NMs. ACKNOWLEDGEMENT. Work at the University of New Mexico was supported by the U.S. Department of Energy (DOE), Office of Science, Basic Energy Sciences (BES), under Award # DE–SC0020186. Work at the University of Wisconsin-Madison was supported by the U.S. Department of Energy (DOE), Office of Science, Basic Energy Sciences (BES), under Award # DE–FG02–03ER46028. This work was performed, in part, at the Center for Integrated Nanotechnologies, an Office of Science User Facility operated for the U.S. Department of Energy (DOE) Office of Science by Los Alamos National Laboratory (Contract 89233218CNA000001) and Sandia National Laboratories (Contract DE–NA–0003525).
[1] L. Hu, H. Huang, Z. Wang, W. Jiang, X. Ni, Y. Zhou, V. Zielasek, M. G. Lagally, B. Huang and F. Liu, *Phys. Rev. Lett.*, 2018, **121**, 66401.

12:15 PM BREAK

12:45 PM Q06
(Student) Deterministic Switching of a Perpendicularly Polarized Magnet Using Unconventional Spin-Orbit Torques in WTe_2 I-Hsuan Kao[1], Ryan Muzzio[1], Hantao Zhang[2], Menglin Zhu[3], Jacob Gobbo[1,4], Daniel Weber[3,4], Rahul S. Rao[5], Jiahan Li[6], James H. Edgar[6], Joshua Goldberger[3], Jiaqiang Yan[7,8], David Mandrus[7,8], Jinwoo Hwang[3], Ran Cheng[2], Jyoti Katoch[1] and Simranjeet Singh[1]; [1]Carnegie Mellon University, United States; [2]University of California, Riverside, United States; [3]The Ohio State University, United States; [4]Karlsruhe Institute of Technology, Germany; [5]Wright-Patterson Air Force Base, United States; [6]Kansas State University, United States; [7]Oak Ridge National Laboratory, United States; [8]The University of Tennessee, United States

Spin-orbit torque (SOT) driven deterministic control of the magnetization state of a magnet with perpendicular magnetic anisotropy (PMA) is key to next-generation spintronic applications including non-volatile, ultrafast, and energy-efficient data storage devices[1-3]. But field-free deterministic switching of perpendicular magnetization remains a challenge because it requires an out-of-plane anti-damping torque, which is not allowed in conventional spin source materials such as heavy metals (HM)[1-3] and topological insulators[4] due to system symmetry. The exploitation of low-crystal symmetries in emergent quantum materials offers a unique approach to achieve spin-orbit torque with unconventional form[5,6]. Here, we report the first experimental realization of field-free deterministic magnetic switching of a perpendicularly polarized van der Waals (vdW) magnet employing an out-of-plane anti-damping SOT generated in layered WTe_2 which is a low-crystal symmetry quantum material. The numerical simulations confirm that out-of-plane antidamping torque in WTe_2 is responsible for the observed magnetization switching in the perpendicular direction.
1. Miron, I. M. *et al*. Perpendicular switching of a single ferromagnetic layer induced by in-plane current injection. *Nature* **476**, 189-193, (2011).
2. Liu, L. *et al*. Spin-Torque Switching with the Giant Spin Hall Effect of Tantalum. *Science* **336**, 555-558, (2012).
3. Liu, L. *et al*. Current-Induced Switching of Perpendicularly Magnetized Magnetic Layers Using Spin Torque from the Spin Hall Effect. *Physical Review Letters* **109**, 096602, (2012).
4. Mellnik, A. R. *et al*. Spin-transfer torque generated by a topological insulator. *Nature* **511**, 449-451, (2014).
5. MacNeill, D. *et al*. Control of spin-orbit torques through crystal symmetry in WTe_2/ferromagnet bilayers. *Nature Physics* **13**, 300-305, (2017).
6. Xue, F. *et al*. Unconventional spin-orbit torque in transition metal dichalcogenide--ferromagnet bilayers from first-principles calculations. *Physical Review B* **102**, 014401, (2020).

1:00 PM Q07
(Student) Spin-Wave Edge Modes Excitation in a Tapered Thin Film Kwangyul Hu and Michael E. Flatté; University of Iowa, United States

Spin wave edge modes can form at the edge of magnetic materials and provide approaches to guide the propagation of magnetic excitations for data processing through the designed shape of structures. The strong confinement of these edge modes also leads to large amplitudes of the magnetic oscillations, and thus provide helpful approach to maximize coupleing of these travelling magnetic excitations to localized spins such as quantum spin centers. Edge modes can appear at surfaces because of a non-

uniformity of the internal demagnetization field. Such edge modes have been observed in various simple structures such as a rectangular thin film[1-3] and a circular or elliptical cylinder[4-5]. It is also possible to generate edge modes by creating the non-uniform demagnetization field with geometrical irregularities such as tapering of edges. Tapering itself is a common unintended consequences of patterning films, so it is important to understand spin wave modes in such tapered thin films. Here we describe spin wave edge modes in a tapered thin film. Spin wave spectra and mode profiles were obtained by using a micromagnetic simulation program MUMAX3[6]. We considered a micron scale (10 μm×50 μm×1 μm) thin film with a trapezoidal cross section. The tapered thin film was magnetized with an in-plane external static field that corresponds to the Damon-Eshbach geometry. Then, we simulated the excitation of spin waves with an RF magnetic field. For the magnetic parameters of the film we simulated for $V[TCNE]_{x\sim2}$, a low loss semiconducting organic ferrimagnet[7] with saturation magnetization M_s=7560 A/m[8], an exchange stiffness constant of 2.2×10^{-15} J/m[9], and a Gilbert damping constant of $\alpha=4\times10^{-5}$[9]. Changes of the spin wave spectra caused by modifications of the taper angle will also be described. We anticipate that the results will explain spin waves modes in tapered thin films and will describe the potential applications of these edge modes.
We acknowledge funding from NSF Grant No. DMR-1808742.
[1] J. Jorzick et al., *Phys. Rev. Lett.* **88**, 047240 (2002).
[2] B. B. Maranville, R. D. McMichael, S. A. Kim, W. L. Johnson, C. A. Ross and J. Y. Cheng, *J. Appl. Phys.* **99**, 08C703 (2006).
[3] R. C. McMichael and B. B. Maranville, *Phys. Rev. B.* **74**, 024424 (2006).
[4] G. d. Loubens, V. V. Naletov, O. Klein, J. B. Youseff, F. Boust, and N. Vukadinovic, *Phys. Rev. Lett.* **98**, 127601 (2007).
[5] J. Jersch *et al.*, *Appl. Phys. Lett.* **97**, 152502 (2010).
[6] A. Vansteenkiste *et al.*, *AIP Adv. 4*, 107133 (2014).
[7] N. Zhu, X. Zhang, I. H. Froning, M. E. Flatté, E. Johnston-Halperin, and H. X. Tang, *Appl. Phys. Lett.* **109**, 082402 (2016).
[8] H. Yu *et al.*, *Appl. Phys. Lett.* 105 012407 (2014).
[9] A. Franson *et al.*, *Appl. Materials.* 7(12) 121113 (2019).

1:15 PM Q08
(Student) Neutron Diffraction and Transport Properties of Antiferromagnet CaFe2O4 Jonathan E. Valenzuela, Sunil Karna and Doyle Temple; Norfolk State University, United States

The oxide compounds containing iron are widely studied because of many interesting phenomena including charge disproportionation, spin polarization, and the magentoresistive effect. $CaFe_2O_4$ crystallizes in the orthorombic *Pnma* structure which consists of distorted FeO_6 distorted octahedra through edge- and corner-sharing with intercalated Ca atoms. We have recently grown a large single crystal of $CaFe_2O_4$ by the optical floating-zone method. The two transitions T_1~240 K and T_2~200 K are observed in our magnetic susceptibility measurements. Our neutron powder diffraction reveals two competing magnetic phases Γ6 and Γ3 at low temperatures which are distinguished by their *c*-axis stacking of ferromagnetic b-axis stripes. Γ6-type magnetic phase develops below 240 K that starts to reduce with the emergence of Γ3-type magnetic phase below 200 K. The detailed magnetoresistance measurements in different crystal orientations will also be discussed in the presentation.

1:30 PM Q09
First Principles Calculation of the Electronic Structure of $V(TCNE)_2$ Yueguang Shi and Michael E. Flatté; The University of Iowa, United States

Vanadium tetracyanoethylene, $V(TCNE)_2$, is a room temperature ferrimagnetic semiconductorwith a T_c ~ 600 K, which has very low loss ferromagnetic resonance and spin-wave propagation. [1,2,3,4,5] Previous firstprinciples calculations of the electronic structure have indicated an indirect band gap at 0.8 eV, substantiallylarger than the 0.5 eV from experimental inference from the conductivity activation energy. [6,7] The study of Ref.1 used a local-orbital calculation with B3LYP hybrid functional. Here we explore the electronic structure using aplane-wave code VASP and XC functional Heyd-Scuseria-Ernzerhof (HSE06). [8,9,10] We confirm that the structure ofVTCNE has a triclinic unit cell with each V atom surrounded by 6 organic ligands, as found in Ref. 1. However,in contrast to the previous study we find a direct band gap of 0.4 eV, instead of an indirect band gap, located ata different k-point. This band gap better agrees with the experiment. We also studied magnetic anisotropy, theoptical properties, magnetic dynamics, and magnetoelastic properties.
We acknowledge funding from NSF Grant No. DMR-1808742.
[1] H. Yu, M. Harberts, R. Adur, Y. Lu, P. C. Hammel, E. Johnston-Halperin, and A. J. Epstein, Appl. Phys. Lett. 105, 012407 (2014).
[2] N. Zhu, X. Zhang, I. H. Froning, M. E. Flatté, E. Johnston-Halperin, and H. X. Tang, Appl. Phys. Lett. 109, 082402 (2016).
[3] H. Liu, C. Zhang, H. Malissa, M. Groesbeck, M. Kavand, R. McLaughlin, S. Jamali, J. Hao, D. Sun, R. A. Davidson, L. Wojcik, J. S. Miller, C. Boehme, and X. V. Vardeny, Nat. Mater. 17, 308–312 (2018).
[4] A. Franson, N. Zhu, S. Kurfman, M. Chilcote, D. R. Candido, K. S. Buchanan, M. E. Flatté, H. X. Tang, and E. Johnston-Halperin, APL Materials 7, 121113 (2019).
[5] J. M. Manriquez, G. T. Yee, R. S. McLean, A. J. Epstein, and J. S. Miller, Science 252, 1415 (1991).
[6] G. C. De Fusco, L. Pisani, B. Montanari, and N. M. Harrison, Phys. Rev. B 79, 085201 (2009).
[7] V. N. Prigodin, P. R. Nandyala, K. I. Pokhodnya, J. S. Miller, and A. J. Epstein, Adv. Mater. 14, 1230 (2002).
[8] G. Kresse and J. Hafner, Phys. Rev. B 47, 558 (1993); ibid. 49, 14 251 (1994).
[9] G. Kresse and J. Furthmüller, Comput. Mat. Sci. 6, 15 (1996).
[10] G. Kresse and J. Furthmüller, Phys. Rev. B 54, 11 169 (1996).

1:45 PM Q10
Magnetic and Magnetoresistive Properties of Nickel/ Nanoporous-GaN Composites Yonatan Calahorra; Technion–Israel Institute of Technology, United Kingdom

The ability to add functions to semiconductors is attractive in realizing smart materials and semiconductor devices with for a broadened application range. In the case of magnetic materials and semiconductors a wide variety of applications opens up, from magnetic and current sensors, through magnetically controlled devices to spintronics. GaN is an interesting candidate for such coupling due to its dominant role in established and emerging semiconductor applications. GaN is also piezoelectric, providing further electromechanical functionality to it, as well as offering a coupling route to magnetic materials through elasticity. In this talk we describe the realization and magnetic characterization of nickel and nanoporous-GaN composites. Motivated by elastic coupling, the relatively large magnetostriction of nickel is attractive to study this application. The results show tuneable magnetic properties of the composite and an indication of mechanically mediated coupling between the magnetic field and the semiconductor device transport. Conductive layers of n-doped GaN were electrochemically etched to form controlled nanoporous structures. Subsequently two nickel deposition methods were studied: electrodeposition, using the remaining GaN material as a working electrode, and sputtering, directly onto the porous surface. Vibrating sample magnetometry (VSM) of samples electrodeposited for different durations demonstrated magnetization evolution from a relatively isotropic and “hard” response to a layer-like response, even without an over-grown layer that is associated with very long times or very fine pores. Furthermore, shorter deposition times, resulted in asymmetric coercivity, which could indicate exchange bias associated with antiferromagnetic NiO coating the nickel inclusions. Energy

dispersive X-ray spectroscopy (EDX) results provide support for this suggestion, as it exhibited increased oxygen presence in the porous region where there is more nickel as well. Room-temperature, high-field (10 T) magnetoresistance of sputter coated porous GaN was measured using a DynaCool PPMS. The relative magnetoresistance showed markedly different responses from samples with larger and smaller pores (obtained by different electrochemical etch voltage) for both low- and high-field. This was despite negligible differences between their magnetization and zero-field resistance. In particular, the magnetoresistance of the larger-pore sample was negative, while the smaller-pore sample was positive and increasing. Nickel generally has negative magnetoresistance, and this is an indication that the larger-pore sample conductance is dominated be nickel deposited inside the larger pores. The positive magnetoresistance of the smaller-pore sample could indicate elastic coupling between nickel magnetostriction and porous-GaN piezoresistance – which corresponds to the motivation of this work. Overall, the use of nanoporous-GaN as an active and controllable template for deposition of nickel was demonstrated, and the process details were found to significantly influence the magnetic and magnetoresistive properties of the composites. This encourages further investigations both to validate the hypothesis for the observed details, as well as to explore applications based on the coupling of GaN and nanostructured magnetic materials.

SESSION R: Group III-Nitride Materials and Applications
Session Chairs: Fatemeh (Shadi) Shahedipour-Sandvik and Christian Wetzel
Thursday Morning, June 24, 2021

11:00 AM R01
Rhenium-Based Ohmic Contacts to n-GaN Amit P. Shah and Arnab Bhattacharya; Tata Institute of Fundamental Research, India

Low-resistivity electrical contacts are essential for reliable performance of GaN-based optical and electronic devices. A titanium-aluminum based multilayer metallization (Ti/Al/Ni/Au) annealed at a suitable conditions is the most commonly used scheme for ohmic contacts with low specific resistivity on n-GaN. For this, high temperatures of more than 800°C are typically used to form reliable ohmic contacts [1]. However, annealing at high temperatures can result in intermixing of layers in the multi-quantum-well active region and also introduce additional defects. The work function of rhenium (Re) is similar (4.72 eV) to Ti (4.33 eV). There are no reports to the best of our knowledge on ohmic contact formation using Re on GaN. In our study, 1.3 µm thick silicon-doped GaN layers were grown on 1 µm thick un-doped GaN buffer layers on c-plane sapphire substrates by MOVPE using silane (SiH_4) as n-type dopant. Hall measurements were carried out to measure the carrier concentration, N_d, of n-GaN which was ~5 x 10^{18} cm^{-3}. The sheet resistivity of the n-GaN is around 35 Ω/sq. Circular transmission line measurements (C-TLM) [2] were used to measure specific contact resistivity (r_c) and current-voltage (I-V) characteristics were carried out to check for ohmic contact behavior. Circular contact pads of 250 µm diameter with nominal separation of 10, 15, 20, 25, 30, 40, 50, 60 and 75 µm were patterned by photolithography. A multilayer of Re/Al/Ni/Au were deposited by electron beam evaporation and then lift-off in photoresist remover. The samples were individually annealed in nitrogen ambient for 1 minute in the temperature range of 450°C to 800°C in steps of 50°C. I-V characteristics were measured at a fixed separation of 40 µm for samples as-deposited and annealed at 450, 500, 550, 600, 650, 700, 750 and 800°C. The samples as-deposited and annealed up to 450 °C show non-linear behaviour, while the samples annealed above 500°C show linear characteristics showing ohmic contact. We have achieved the lowest specific contact resistance, r_c ~ 1.08 x 10^{-7} Ω-cm^2 at 700 °C, with a wide annealing temperature window (550—800°C) for a specific contact resistivity of less than 5 x 10^{-5} Ω-cm^2. We have observed a reduction of at least 100 °C annealing temperature as compared to Ti-based ohmic contacts. The RMS roughness values measured by AFM are around 26 nm (550°C), and 36 nm (700°C), as compared to Ti-Al based contact which is about 50 nm (800°C). Ohmic contact formation at lower annealing temperature using Re-based metallization can be very useful to improve the performance of III-nitride devices like LEDs and lasers.

References

[1] F. Lucolano, F. Roccaforte,a A. Alberti, C. Bongiorno, S. Di Franco, and V. Raineri, Jour. Appl. Phys. **100**, 123706 (2006).
[2] J.H. Klootwijk, and C.E. Timmering, Proc. IEEE 2004 Int. Conference on Microelectronic Test Structures, **17**, 247 (2004).

11:15 AM R02
(Student) Characterization of AlxIn1-xN Mismatched to GaN for Thin Oxide Applications Elia Palmese[1], Justin Goodrich[1], Syed Ahmed Al Muyeed[1], Haotian Xue[1], Xiongliang Wei[1], Renbo Song[1], Nelson Tansu[2,1] and Jonathan J. Wierer[1]; [1]Lehigh University, United States; [2]The University of Adelaide, Australia

The properties of Aluminum Indium Nitride ($Al_xIn_{1-x}N$) lattice matched to Gallium Nitride (GaN) are well documented [1]. It is an ultra-wide band gap (UWBG) semiconductor with similar power figure of merit as high Al content Aluminum Gallium Nitride (AlGaN) and Gallium Oxide (Ga_2O_3). These semiconductors have higher critical electric fields and temperature stability compared to narrower bandgap semiconductors and are promising candidates for power devices. An additional benefit of AlInN is that it can be oxidized into insulating layers using simple thermal oxidation techniques and can be used as gate oxides for devices such as metal oxide semiconductor (MOS) transistors. The oxidation kinetics and oxidation process for $Al_xIn_{1-x}N$ lattice matched to GaN (x~0.82) has been studied, resulting in an insulating oxide with promise for use in MOS devices [1,2]. Although these oxides are promising, oxides formed from mismatched AlInN layers with different Indium content could provide enhanced properties such as higher breakdown fields and bandgaps. In this work, $Al_xIn_{1-x}N$ layers grown on GaN with varying Indium content are characterized and oxidized for potential use as thin layer gate oxides. The samples are grown on sapphire substrates using MOCVD and consist of an unintentionally doped GaN layer followed by a layer of AlInN which varies in composition. The $Al_xIn_{1-x}N$ layers have Indium content that varies from x~0.13 to ~0.21 and are ~240 nm thick. The Indium content is varied by changing the growth temperature from 790 °C to 750 °C. The refractive index and extinction coefficient for the mismatched $Al_xIn_{1-x}N$ layers are determined using spectroscopic ellipsometry. The spectroscopic ellipsometry data are fit using a Tauc-Lorentz oscillator model using known refractive index, n, and extinction coefficients, k, for the underlying GaN. From these fits the n and k for AlInN are determined. The refractive index at 500 nm decreased from 2.217 to 2.146 as the indium content decreases, consistent with a decreasing bandgap. After characterizing the n and k for the $Al_xIn_{1-x}N$ layers, they are then are oxidized to determine oxidation rates at each indium composition. The samples are oxidized at 830 °C for 2 hours in a dry O_2 environment with a flow of ~13 SCFH in a 3” diameter tube. The oxide thicknesses are then obtained using spectroscopic ellipsometry, and thickness is plotted against indium composition. The initial data shows that the samples with higher indium content oxidize faster than the lower indium content samples. For the highest Indium content (x=0.21), the oxidation rate is ~ 1.6 nm/min while with the lowest indium content AlInN layer (x=0.13) has an oxidation rate of ~0.1 nm/min. This significant difference in oxidation rate could affect the properties of the oxide such as roughness, dielectric constant, and

bandgap. From the spectroscopic ellipsometry data, the preliminary n and k values for the oxide layers are also obtained. Additionally, the effects of indium composition on the oxides roughness and insulating characteristics are investigated to assess which compositions and layer thicknesses are suitable as thin gate oxides for devices.

[1] M. R. Peart, X. Wei, D. Borovac, W. Sun, N. Tansu, and J. J. Wierer, Jr., ACS Appl. Elec. Mat., 1, 1367-1371 (2019).
[2] E. Palmese, M. Peart, D. Borovac, R. Song, J. J. Wierer Jr., and N. Tansu "Oxidation Kinetics of $Al_{0.83}In_{0.17}N$ Films Grown on GaN" submitted (2020).

11:30 AM R03
(Student) Growth and Characterization of Preferential (100) Oriented AlN Thin Films Grown on Mo Coated Si (100) Substrate by Reactive RF Sputtering Amal Das; IIT Madras, India

Aluminum Nitride (AlN) is one of the most promising piezoelectric material for high frequency applications, because of its CMOS fabrication compatibility, wide bandgap (6.2 eV), high thermal conductivity (285 W m^{-1} K^{-1}), high breakdown field strength (5 MV/cm) and high acoustic velocity in both lateral (~11,354 m/s) and transversal (~6000 m/s) modes[1]. Acoustic properties of AlN thin films depend on its growth direction. As compared to c-axis (002) AlN films, a-axis (100) AlN films are more suitable for shear-horizontal acoustic wave applications[2]. In the present work, preferential (100) oriented AlN thin films were grown on Mo coated Si (100) substrate using reactive RF magnetron sputtering. We have chosen Mo as the bottom electrode due to its good lattice match with AlN, etching compatibility, and high acoustic velocity (~ 6,250 m/s). This combination of preferential (100) oriented AlN and Mo hetero-structure will be very useful for high frequency SAW and BAW resonators applications. The optimized sputtering parameters for AlN and Mo deposition are mentioned in Table 1. Fig. 1(a) shows the grazing incidence angle X-ray diffraction (GIXRD) pattern of AlN films deposited on Mo/Si (100) substrate. The XRD peaks at 33.2°, 37.8° and 59° show the polycrystalline nature of AlN thin film with (100), (101) and (110) planes, respectively. The most prominent peak at 33.2° corresponds to (100) plane of polycrystalline hexagonal structure of AlN (ref: JCPDS no: 00-025-1133). The XRD peaks at 40.6° and 74.2° show the polycrystalline nature of Mo thin film with (110) and (211) planes, respectively. It confirms the (100) preferred orientation of AlN thin film on highly (110) oriented Mo coated Si substrate.
The thickness of the AlN and Mo films were nearly 890 and 200 nm as shown in fig. 1(b). Fig. 1(c) shows the surface morphology of AlN thin films. The root mean square (RMS) roughness of the film observed from surface profiler measurement was around ~1.92 nm as shown in fig. 1(d). Figs. 2(a) and 2(b) show the current density (J) and capacitance (C) vs electric field (E) plots for the fabricated Mo-AlN-Mo (MIM) capacitors. The measured resistivity ($\rho = E/J$) was 9×10^9 Ω.cm for the voltage sweep from – 50 to + 50 V. The dielectric constant of the deposited AlN film was found to be ~ 5.4. Results will be presented and discussed in detail.

References:

1. E. Iborra, J. Olivares, M. Clement, L. Vergara, Sens. Actuators, A **115**,501 (2004).
2. S. Wu, R. Ro, Z. X. Lin, and M.-S. Lee, Applied Physics Letters **94**, 092903 (2009).

11:45 AM R04
(Student) AlGaN/GaN HEMT-Based Detection of Reactive Oxygen Species Molecule H2O2 Isra Mahaboob, Roger Reinersten, Benjamin McEwen, Kasey Hogan, Emma Rocco, Vincent E. Meyers, J. A. Melendez, Nathaniel Cady and Fatemeh (Shadi) Shahedipour-Sandvik; SUNY Polytechnic Institute, United States

AlGaN/GaN high electron mobility transistors (HEMTs) have been extensively studied for biochemical sensing applications due to their high sensitivity to surface phenomena, fast response time, aqueous stability, and biocompatibility [1]. In HEMT sensors, the two-dimensional electron gas (2DEG) acts as a highly conductive channel that can be modulated by changes in the surface potential. The detected signal in the gate region is amplified and measured as a change in the 2DEG conductivity, which makes the HEMT a good sensing device. Due to their unique electrical and chemical properties, AlGaN/GaN HEMTs show great potential for the detection of reactive and transient biological components, such as reactive oxygen species (ROS). In this study, we demonstrate the potential of AlGaN/GaN HEMT sensors for the detection of ROS molecules such as hydrogen peroxide (H_2O_2) [2]. A boronate-based fluorescent probe was used with this device to detect the presence of micromolar levels of hydrogen peroxide typically associated with intracellular processes. A non-functionalized, non-metallized open-gate AlGaN/GaN HEMT sensor is employed in this study. The real-time progression of the reaction is monitored by measuring the modulation of the 2DEG current in response to changes in the surface potential caused by the interaction between the semiconductor surface states and the products of the reaction. The electrical response of the HEMT sensor showed a gradual decrease in the 2DEG current as the reaction proceeded over time. A corresponding increase in the emission intensity was measured from the fluorescent probe with the progression of the reaction. The fluorescence from the boronate probe was used as an indicator to confirm the detection of H_2O_2. The response of our HEMT sensor shows its applicability to the detection of micro-molar concentrations of H_2O_2, which is in the range typically present in intracellular processes of living systems [3]. The results from this study demonstrate the possibilities of interfacing biocompatible electronics with existing bioorthogonal probes to expand the capabilities of existing fluorescent probe-based detection techniques.

[1] F. Ren and S.J. Pearton, *Phys. Status Solidi C* 9, 393 (2012).
[2] I. Mahaboob, R. J. Reinersten, B. McEwen, K. Hogan, E. Rocco, J. A. Melendez, N. Cady, and F. Shahedipour-Sandvik. *Exp. Biol. Med*. (2020).
[3] V. S. Lin, B. C. Dickinson, and C. J. Chang. *Methods Enzymol.* 526, 19–43 (2013).

12:00 PM R05
(Student) Analysis of Patterned GaAsSbN Nanowires via Boltzmann Sigmoidal Model Sean Johnson[1], Rabin Pokharel[1], Michael Lowe[1], Hirandeep Kuchoor[1], Surya Nalamati[1], Klinton Davis[2], Hemali Rathnayake[2] and Shanthi Iyer[1]; [1]North Carolina A&T State University, United States; [2]University of North Carolina at Greensboro, United States

The first reports of applying the Boltzmann Sigmoidal model on pitch-dependency in patterned nanowires (NWs) of dilute nitride GaAsSbN on p-Si (111) substrates by self-catalyzed plasma-assisted molecular beam epitaxy are presented in this study. Morphological and structural characterizations of the patterned NWs are accomplished via field emission scanning electron microscope (FESEM) and high-resolution transmission electron microscope (TEM), respectively. Top, middle, and bottom NW segments captured via selected area electron diffraction (SAED) characterization confirmed the single-crystal zincblende structure of the NWs. The absence of satellite spots in the SAED pattern indicates the NWs are free of planar defects. Sizeable bandgap tuning of ~75 meV, as ascertained from 4K photoluminescence

(PL), is demonstrated over a pitch length variation of 200 nm to 1200 nm. Axial and radial growth rates reveal a logistic sigmoidal growth trend with respect to pitch, which differs from those commonly observed in other patterned non-nitride III-V NWs. The Boltzmann sigmoidal model offers additional insight into the shift of the PL spectral arising from differences in Sb and N incorporation from pitch induced variation in secondary fluxes. The extracted inflection points, p_0, of 636 nm and 806 nm, for axial growth rate correlate very well with the homogeneous broad peaks revealed by PL analysis at these pitch lengths. Furthermore, the inflection point indicates the pitch length where the pitch dependent effects on the secondary fluxes play a prominent role in axial and radial growth of patterned NWs. Additionally, the values of the sigmoidal slope, α, correlate well with the range of pitches where Sb and N incorporation are observed with broad PL spectra. Results indicate that the extracted parameters obtained via the sigmoidal model of inflection point, and slope can be used as a rubric for optimal pitch length for patterned array design of homogeneous nitride NWs and can be extended to other highly mismatched alloy compounds. This work is financially supported by National Science Foundation (Award No. 1649517) and through the Title III HGBI Ph.D. Fellowship.

SESSION S: Metasurfaces and Epitaxially-Grown Optical Materials and Devices
Session Chairs: Anthony Hoffman and Jason Valentine
Thursday Afternoon, June 24, 2021

12:45 PM S01
Metasurface Orbital Angular Momentum Holography Stefan Maier and Haoran Ren; LMU Munich, Germany

Recent advances in metasurface technologies have allowed the use of an ultrathin device to manipulate the amplitude, phase, and polarization of light, leading to a versatile platform for digitalising an optical hologram with nanoscale resolution. To increase the bandwidth of a metasurface hologram, essential for high-capacity holographic memory devices, different properties of light including polarisation, wavelength, and incident angles have been exploited for holographic multiplexing, however, the bandwidth of a metasurface hologram has remained too low for any practical use. The OAM space with an unbounded set of orthogonal helical modes holds great promise to increase the bandwidth of a metasurface hologram. For achieving OAM sensitivity, a hologram needs to be designed in momentum (Fourier) space. Even though a Fourier-based metasurface hologram with phase-only modulation has recently been demonstrated for OAM holography, the neglected amplitude information breaks the linear superposition principle for holographic multiplexing and incurs strong crosstalk in holographic multiplexing. Mathematically, a complex-amplitude hologram with complete amplitude and phase control could allow the superposition principle to continue to hold, and preserve an exact convolution of a complex-amplitude image channel and an OAM helical wavefront; hence opening the possibility of eliminating holographic multiplexing crosstalk. We present the design of a complex-amplitude metasurface hologram for ultrahigh-dimensional OAM-multiplexing holography in momentum space. To realise a complex-amplitude Fourier hologram, we have introduced an OAM diffuser array with a random phase function, capable of scaling down the amplitude variation in a typical Fourier image as well as eliminating the coherence of holographic image channels. In addition, we report a novel platform for 3D laser manufacturing of a large-scale complex-amplitude metasurface in a polymer matrix, unleashing the 3D design degrees of freedom of a meta-atom. As a result, incident OAM beams with helical mode indices ranging from -28 to 28 have been used to experimentally address 60 OAM-dependent orthogonal image frames in 3D space. Metasurface OAM holography offers a promising platform for various application areas, including optical and quantum communications, holographic displays and encryption, all-optical machine learning, biological imaging, and astronomical observations.

1:00 PM S02
Hybridization of Multi-Plasmon Modes on Coupled Nanoridge Array Metasurfaces for Super-Resolution Imaging Milan Palei[1], John Haug[1], Anjan Goswami[1], Joshua D. Shrout[1,1], Paul W. Bohn[1,1], Evgenii Narimanov[2] and Anthony Hoffman[1]; [1]University of Notre Dame, United States; [2]Purdue University, United States

Metamaterials and metasurfaces are promising optical materials for many applications in optics and optoelectronics as the optical characteristics can be engineered via sub-wavelength features. Hyperbolic metamaterials and metasurfaces—a particular class of these designer materials—have been widely studied due their uncommon optical characteristics that enable effects such as negative refraction, light beam steering, subdiffraction imaging, spontaneous and thermal emission engineering, and broadband optical absorption. These materials have been demonstrated across much of the optical spectrum using myriad approaches. Recently, negative refraction of optical surface modes was accomplished using a hyperbolic metasurface comprising coupled nanoridge arrays. For applications in super-resolution imaging, hyperbolic metasurfaces are of particular interest because a larger fraction of the electromagnetic field will interact with the object being imaged, rather than residing inside of the bulk of the material. One approach to imaging using metasurfaces is to leverage structured illumination imaging (SIM), a paradigm where an object is illuminated via a sub-diffraction pattern that can be externally controlled, such as by varying the angle of the incident light. In SIM, a super-resolution image is computed from several diffraction-limited images. Exciting and localizing modes with large effective modal indices provide a path towards increasing the resolution beyond conventional SIM approaches, such as localized surface plasmon SIM. However, coupling to these high-index modes is challenging. In this talk, we will demonstrate hyperbolic metasurfaces appropriate for SIM. These metasurfaces utilize finite-length coupled nanoridge arrays. The coupling between nanoridges is used to engineer the effective modal index of the supported optical modes. These optical modes are then confined by introducing small gaps (90 nm) along the nanoridges, resulting in standing waves that can serve as an illumination pattern for SIM. Large arrays of coupled-nanoridge metasurfaces are fabricated using silver on Si via electron beam lithography and standard metal lift-off. The arrays are characterized using angle-, polarization-, and wavelength-dependent reflection spectroscopy. Optical modes corresponding to multipolar plasmon resonances ($n = 2$ and $n = 3$) are identified, including a mode that is identified as a localized hyperbolic mode. The energy and dispersion of all the observed modes agree well with numerical models of the effective modal index. Numerical simulations of the reflection of free-space light also agree well with the measurements. A numerical demonstration of the imaging capabilities for these modes at 458 nm of 9 nm quantum dots, including realistic material losses, predicts a 3.3X improvement in the resolution over diffraction-limited images.

1:15 PM S03
(Student) All-Epitaxial Spectrally Selective Dual-Color Surface Plasmon-Polariton Infrared Detectors Leland J. Nordin[1], Priyanka Petluru[1], Aaron J. Muhowski[1], Eric Shaner[2] and Daniel Wasserman[1]; [1]The University of Texas at Austin, United States; [2]Sandia National Laboratories, United States

The mid-infrared (mid-IR) wavelength range is vital for a range of sensing, security and defense, and fundamental science

applications. While some of these applications, such as infrared imaging, can function with a single value readout, the majority of them, such as chemical spectroscopy, thermography, or ranging, require spectral information. Unfortunately, generating spectral information often necessitates bulky additional optics, such as filters or spectrometers. There is thus a significant need for a high-performance infrared detector, which can provide bias-dependent spectral information in a monolithic form factor. The field of plasmonics leverages the use of metallic materials to manipulate light into sub-diffraction limited volumes and therefore dramatically enhance light-matter interaction. In the MIR, plasmonic layers have been used to signficantly enhance light emission [1,2] and detection [3]. Thin plasmonic materials can host two surface plasmon-polariton (SPP) modes, the lower energy short-range SPP (SRSPP) and the higher energy long-range SPP (LRSPP) [4]. These modes are spectrally separate and therefore are promising candidates for bias-selectable dual-color infrared detection. Additionally, these SPP modes are tightly bound to the plasmonic layer, enabling relatively thin absorbers and consequently lower dark current. We present a dual-color detector structure which selectively couples light into very longwave infrared (VLWIR) and long-wave infrared (LWIR) type-II superlattice (T2SL) nBn detectors. The detector structures are grown by molecular beam epitaxy (MBE). The device is comprised of a thin plasmonic (n^{++}) mid-wave infrared (MWIR) InAs/InAsSb T2SL layer, sandwiched between a LWIR nBn detector above and a VLWIR nBn detector below. Following growth, mesas are delineated using a standard wet etch. After mesa delineation, the top surfaces of the detector mesas are patterned with contact pads and with Au square antennas of period $\Lambda = 2.5$ µm and width of 1.25 µm. Grating dimensions are chosen to maximize coupling into both the LWIR and VLWIR nBn detectors' absorbers. Initial normalized spectral response is presented, showing bias-selectable dual-color operation at 9.6 µm and 11.3 µm. Additionally, a rigorous coupled-wave analysis (RCWA) model of the sample structure is presented where the n^{++} layer is treated as a simple Drude metal and the nBn absorbers are modeled with a $(E-E_g)^{1/2}$ dependence. Our simulations accurately model both the spectral shape and peak response of our experimentally measured bias-selectable dual-color detector. The presented devices demonstrate bias-selectable dual-color selective detection using thin-film SPP modes. Future work will focus on leveraging low-loss LRSPP modes to realize ultra-spectrally selective infrared detectors. The authors acknowledge support from the National Science Foundation (ECCS-1926187), the Laboratory Directed Research and Development (LDRD) program at Sandia National Laboratories, and the use of facilities within the Texas Nanofabrication Facility supported by NSF grant NNCI-1542159. Sandia National Laboratories is a multimission laboratory managed and operated by National Technology & Engineering Solutions of Sandia, LLC, a wholly owned subsidiary of Honeywell International Inc., for the U.S. Department of Energy's National Nuclear Security Administration under Contract No. DE-NA0003525.

[1] L. Nordin et al. ... D. Wasserman. *Appl. Phys. Lett*., **116,** 021102 (2020)
[2] A. Briggs et al. ... S. R. Bank. *Optica*, **7**, 1355 (2020)
[3] L. Nordin et al. ... D. Wasserman. *ACS Photonics*, **7**, 1950 (2020)
[4] P. Berini, *Adv. Opt. Photon*., **1**, 484 (2009)

1:30 PM S04
(Student) Mid-Wave to Near-IR Optoelectronic Properties and Epsilon-Near-Zero Behavior in In-Doped CdO Angela Cleri[1], Joshua R. Nolen[2], Joshua Caldwell[2], Evan Runnerstrom[3] and Jon-Paul Maria[1]; [1]Pennsylvania State University, United States; [2]Vanderbilt University, United States; [3]U.S. Army Research Office—Materials Science Division, United States

Cadmium oxide (CdO) is one of the most promising material systems for low-loss infrared (IR) plasmonics to date. Through reactive co-sputtering using high power impulse magnetron sputtering (HiPIMS) and radio frequency (RF) sputtering, doped CdO demonstrates high mobility films with tunable carrier concentrations across a range corresponding to epsilon-near-zero (ENZ) modal frequencies spanning the mid-IR and reaching into the near-IR. Specifically, indium-doped CdO (In:CdO) yields carrier densities ranging between $2x10^{19}$ cm^{-3} and $5x10^{20}$ cm^{-3} while maintaining mobilities between 300-400 cm^2/Vs across this range, thus allowing for the widest accessibility of the IR spectrum (1650-5325 cm^{-1}) of a single plasmonic material grown by sputtering. Fully accessing the spectrum of plasmonic applications, including surface plasmon oscillations, ENZ modes, and strong coupling phenomena requires that one maintains these appealing transport properties over a film thickness range spanning a few tens to a few thousands of nanometers. Extensive CdO fabrication experiments using high-power impulse magnetron sputtering reveal a strong dependence of carrier density and mobility on film thickness when thickness drops below 100 nm, a particularly significant range for ENZ modes. We attribute this behavior to well-reported surface charge accumulation and depletion layers caused by Fermi level pinning. In this presentation, we demonstrate the reversal between surface charge accumulation and depletion in In:CdO. Further, we show how these surface effects can influence optical properties, and how they can be controlled by understanding and manipulating CdO defect chemistry. Lastly, we will show preliminary results of plasmonic tunability via ferroelectric switching.

1:45 PM S05
(Student) Long-Range Surface Plasmon Polaritons in All-Epitaxial Structures Priyanka Petluru[1], Leland J. Nordin[1], Aaron J. Muhowski[1], Eric Shaner[2] and Daniel Wasserman[1]; [1]The University of Texas at Austin, United States; [2]Sandia National Laboratories, United States

Surface plasmon polaritons (SPPs) are hybrid excitations of collective charge oscillations in an optical metal ($\varepsilon_m < 0$) coupled to electromagnetic waves in a dielectric ($\varepsilon_d > 0$), propagating at the interface between the metal and dielectric. The simplest SPP is the mode propagating at the interface between semi-infinite metal/dielectrics. However, three-layer systems such as metal/dielectric/metal (MDM) or dielectric/metal/dielectric (DMD) structures can also support and guide plasmon polariton modes [1]. While MDM structures can offer strong confinement of such modes, this increased confinement is offset by additional loss [2]. DMD structures support a short-range (anti-symmetric) and long-range (symmetric) surface plasmon polariton mode, where the symmetry refers to the profile of the transverse component of the electric field [3]. The long-range surface plasmon polariton (LRSPP) mode is more weakly bound to the metal, and as a result is lower loss, with important applications including waveguides, modulators, and nano-scale plasmonic sources [4,5,6]. In this work, we present an all-epitaxial structure capable of supporting LRSPP modes at long-wave infrared wavelengths. The sample is comprised of dielectric layers consisting of integrated long-wave infrared (LWIR) and very-long-wave infrared (VLWIR) InAs/InAsSb type-II superlattice (T2SL) emitters above and below a highly doped n^{++} mid-wave infrared (MWIR) InAs/InAsSb T2SL layer, which serves as the plasmonic metal. The top surface of the sample is patterned with a Au grating of period $\Lambda = 2.8$ µm and width of 1.4 µm, in order to provide the requisite momentum for coupling into the LR- and SRSPP modes The DMD structure is characterized by angle- and polarization-dependent infrared reflection and photoluminescence spectroscopy, from which the dispersion of both the symmetric and anti-symmetric SPP modes is extracted. The sample is modeled analytically using a simplified three-layer model, and numerically using rigorous coupled-wave analysis (RCWA). For the latter analysis, the highly doped MWIR T2SL layer is modeled as a Drude metal, while the LWIR and VLWIR T2SLs are simulated as having a constant real permittivity and an imaginary permittivity calculated from a T2SL

absorption coefficient and modeled as having a $\sqrt{(E-E_g)}$ dependence. Our simulations show excellent agreement with experimental results, with coupling to SPP modes observed at wavelengths longer than 8.5 µm, as expected from the modeled dispersion. Based on features identified in the TM-polarized angle-dependent reflection data, it is apparent that the sample structure supports both short-range surface plasmon polariton (SRSPP) and LRSPP modes, in addition to a metal-dielectric-metal mode at longer wavelengths. Furthermore, the integrated T2SL materials also allow luminescent probing of the SPP modes. The presented structure offers a viable approach to all-epitaxial plasmonic-optoelectronic devices and optical systems in the LWIR. The authors acknowledge support from the National Science Foundation (ECCS-1926187), the Laboratory Directed Research and Development (LDRD) program at Sandia National Laboratories, and the use of facilities within the Texas Nanofabrication Facility supported by NSF grant NNCI-1542159. Sandia National Laboratories is a multimission laboratory managed and operated by National Technology & Engineering Solutions of Sandia, LLC, a wholly owned subsidiary of Honeywell International Inc., for the U.S. Department of Energy's National Nuclear Security Administration under Contract No. DE-NA0003525.

[1] E. N. Economou, *Physical Review*, **182** (2), p. 539 (1969).
[2] M. T. Hill et al., *Optics Express,* **17** (13), p. 11107 (2009).
[3] P. Berini, *Adv. Opt. Photon*., **1** (3), p. 484 (2009).
[4] T. Nikolajsen et al., *Appl. Phys. Lett.,* **85** (24), p. 5833 (2004).
[5] K. Leosson et al., *Optics Express,* **14** (1), p. 314 (2006).
[6] P. Berini and I. De Leon, *Nature Photonics,* **6** (1), p. 16 (2011).

SESSION T: High Electron Mobility Transistors (HEMT) & Characterization of 2-Dimensional Electron, Hole Gases
Session Chairs: Brianna Klein and Siddharth Rajan
Thursday Morning, June 24, 2021

11:15 AM T01
(Student) Influence of Buffer Layer Thickness and Type on Laser Lift-Off of AlGaN/GaN HEMTs Epilayers on Sapphire Substrates Md Didarul Alam, Mikhail Gaevski, Mohi Uddin Jewel, Shahab Mollah, Abdullah Mamun, Mohammad K. Hussain, MVS Chandrashekhar and Asif Khan; University of South Carolina, United States

We present results of a study conducted to determine the influence of the buffer layers on the Laser lift-off (LLO) of metal-organic chemical vapor deposition (MOCVD) grown GaN (channel)-AlGaN (barrier) high electron mobility transistor from sapphire substrates. Two different buffer layer types (GaN and AlN) with varying thicknesses were studied. Moreover, our study used a 193nm excimer laser which is different from the other LLO reports. Also, for the first time, we LLO AlGaN/GaN HEMT with a 16 µm thick AlN buffer layer. Such thick buffer layers minimize heat-induced degradation of the overall device performance. The AlGaN/GaN heterostructures used in this study were grown on c-plane double-side polished sapphire substrate by a custom MOCVD. For all samples of this study, 20 nm thick $Al_{0.32}Ga_{0.68}N$ barrier and GaN channel layers were used. For sample A, a 10 nm low-temperature AlN nucleation layer and a 1 µm undoped GaN buffer layer were used. This buffer layer also serves as the channel layer for the device epilayers. For sample B, a 16 µm AlN buffer layer and a 3 µm thick GaN channel layer were used. For samples A and B, gated and ungated transmission line measurement (TLM) patterns were metalized to measure the current-voltage (I-V) characteristics to extract the sheet carrier density (n_s) and the carrier mobility (µ). The field-effect mobility is extracted from g_m vs. V_{GS} plot, and the threshold voltage (V_T) is found from the x-intercept of $V_{GS.}$ These parameters were measured before and after the laser lift-off. For either case, there was no appreciable change in the sheet carrier density (~ 1 x 10^{13} cm^{-2}). For sample A, the carrier mobility decreased from ~2100 to ~1150 cm^2/Vs and the peak currents also decreased by a factor of 4. Whereas, for sample B, the mobility decreased only slightly from ~1765 to ~1660 cm^2/Vs and sheet resistance (400 Ohms/sq) and the peak currents remained nearly the same before and after the LLO. We believe that for sample A, the thin GaN buffer layer (1µm) was not sufficiently thick to prevent heat-induced degradation of the conducting channel. This was confirmed by the change in x-ray diffraction (XRD) full-width at half-maximum (FWHM) values and dispersion in C-V curves which indicates introduction of additional traps from the thermal degradation. Sample B's HEMT's, with the thick AlN buffer for heat dissipation, has their characteristics preserved. In this paper, we will present the details of our LLO process and its influence on the material properties and the transport properties of the fabricated HEMT structures.

11:30 AM T03
(Student) AlGaN/GaN HEMTs on Silicon with High ON Current (> 8 A) and Ultralow Gate Leakage (50 nA/mm at 500 V) Suryansh Upadhyay, Anirudh Venugopalrao, Nayana Remesh, Rijo Baby, Muralidharan R, Srinivasan Raghavan and Digbijoy Nath; Indian Institute of Science, India

While 600V, >30A GaN-on-silicon HEMTs are available commercially, yet, there are few reports in the literature that study wide gate-periphery devices with respect to process challenges, design issues, carrier transport, and physics of various types of leakage currents. In this work, we report breakdown exceeding > 500V and gate current ~ nA/mm (at 500V) in HEMTs with smaller gate widths of 0.1mm; we also demonstrate >8A of ON current and > 100V breakdown in devices with 50mm gate width. The reproducibility and homogeneity of GaN HEMT performance strongly depend on the passivation and surface conditions. Thus, our study also seeks to understand the effect of *insitu* SiN on devices with large gate widths. The MOCVD-grown AlGaN/GaN HEMT stacks consisted of a 2-step AlN nucleation(150nm) on 1mm thick high resistive Si (111) followed by step-graded AlGaN transition layers. A two-step GaN buffer was then grown followed by 25nm AlGaN with 25% Al-content. The standard reference stack has a GaN cap of 3nm whereas the *insitu* variant has 3nm of Si_3N_4 grown at 950°C. Devices with various gate widths of 0.1mm, 2mm, 10mm, 20mm, 30mm, 50mm with self-aligned, gate integrated field-plates were fabricated with standard i-line optical lithography. Bigger devices with 50 mm gate width devices have fifty 1-mm gates. The gate length, gate-source spacing, and gate-drain spacing were 3 µm, 3 µm, and 11 µm respectively. Device fabrication started with optical lithography and metal evaporation (Ti/Al/Ni/Au) for Ohmic stack and annealed(850C). Mesa etching of 300 nm was done by Cl-based reactive ion etching (RIE). Ni/Au (30/150 nm) is deposited as the gate fingers. 10 nm of Al_2O_3 (ALD-deposited, at 250C) was used as the gate dielectric for the reference samples. The fabricated devices had two layers of PECVD deposited SiNx as an inter-layer dielectric for isolating metal lines as they crisscrossed for connecting the source-drain fingers with bigger pads. Finally, a thick Ni/Al (100nm/800nm) metal stack was evaporated for the source and drain inter-connections to the big pads. Gate leakage, transfer characteristics, output characteristics, and 3-Terminal breakdown were measured for the devices with various gate widths. AFM of as-grown samples capped with GaN/*insitu*Si_3N_4 show that the surfaces are extremely smooth with an RMS roughness of 0.8 to 0.9 nm. However, TLM measurements performed on samples indicated a much lower sheet resistance (391ohms/sq) for the samples with *insitu* SiN compared to the reference stack (520 ohms/sq). The reproducibility and homogeneity issues with Al_2O_3 as a gate dielectric for the standard samples also seem to be mitigated for the samples with *insitu* SiN. Devices with 0.1mm gate width for the standard stack had ON

current of ~ 400mA/mm (Vd=10V, Vg=0V, Vth=-7.5) whereas, for the *insitu* SiN sample, it is ~510 mA/mm (Vd=10V, Vg=0V, Vth=-6.5); If linearly extrapolated, 50 mm gate width HEMTs should be capable of exhibiting~ 20A of ON current; however we measure about half that value (~ 9 A) in the standard samples. For smaller devices with 0.1 mm gate width, the ON resistance was estimated to be 13.4 $m\Omega cm^2$and 7.9$m\Omega cm^2$ respectively for references HEMTs and those with *in situ* SiN. The nature of the transfer characteristics and the ON current indicated that series resistance emanating from the metal fingers was a limiting factor. Thus, the thickness of the metal has to be increased further to improve the ON current in 50 mm devices. We observed ultralow Gate leakage (0.1 nA – 20nA) across HEMTs with varying gate widths for both references as well as *in situ* samples. Further, breakdown voltage exceeding 500V (Id@1μA) has been obtained on devices with 0.1 mm gate periphery for HEMTs with Al_2O_3 as the gate dielectric. Large width (50 mm) devices with a similar breakdown and > 9 A ON current will be presented along with the study of comparison of their repeatability, consistency, and challenges involved for both the HEMT stack variants.

11:45 AM T04
Reduced Current Collapse in Forming Gas-Treated AlGaN/GaN HEMT on Silicon with $f_T \times L_G$ of 13 GHz-μm and Breakdown > 100 V Md Arif Khan, Rachana Rao, Aniruddhan Gowrisankar, Muralidharan R and Digbijoy Nath; Indian Institute of Science, India

We report on AlGaN/GaN HEMT on silicon with forming gas annealed SiN passivation layer that exhibits an f_T ~ 19 GHz, collapse < 2 % under 200 ns gate pulsing, 3-terminal breakdown exceeding 100 V for devices with 0.68 μm gate length. This work is expected to be of importance to improve the performance of C-band GaN devices on silicon which could be promising for scalable and cost-effective sub-6 GHz 5G technology. The device was fabricated on the AlGaN/GaN stack comprising of ~3nm GaN cap layer on top of ~20 nm AlGaN barrier on ~200 nm GaN channel which was deposited on ~800 nm Fe doped GaN on top of ~1 μm insulating buffer on Si. The XRD measurement gives ~600 arcsec FWHM in (0002) orientation. The surface roughness of the stack is < 0.5 nm, and sheet resistance (R_s) is 334 Ω/sq. The source and drain Ohmic metallization is formed by Ti/Al/Ni/Au deposition followed by rapid thermal annealing (RTA) at 850° C for 45 s in N_2. A contact resistance of 0.42 Ω-mm was confirmed by TLM. Further, the mesa isolation was defined in RIE by Cl_2/BCl_3 mixed plasma etching. Further, the gates were defined by e-beam lithography using PMMA photoresist and gate stack (Ni 30 nm/Au 100 nm) was deposited to lift-off rectangular-gate structure. Further, a thick (Ni 30 nm/Au 200 nm) pads with a GSG probing layout for RF measurements was developed. Post-GSG, 100 nm thick nitride rich (NH_3/SiH_4 = 35 sccm /2.5 sccm) SiN with 1.82 refractive index was deposited and selectively etched to open up GSG pads for characterization. The developed HEMTs were then characterized pre- and post- annealing in forming gas ambience (FGA) at 300 C for 60s in RTA. The gate length was L_G ~680 nm while the width was (2×100) μm with a source-to-drain distance of ~6.8 μm and gate-to-source distance of ~1.5 μm. The maximum drain current (I_d) in as-developed devices hit compliance current of 500 mA/mm at V_g = 0 V and V_d = 4.9 V, with R_{ON} of 7.2 Ω-mm, whereas post FGA annealing, I_d maximum hits compliance at V_g = 0 V and V_d = 5.4 V, with R_{ON} of 7.7 Ω-mm. The threshold voltage (V_{th}), as extracted by linear extrapolation, and the transconductance (G_m) in the devices, as-developed and post-FGA, was -4.2 V and 175 mS/mm, respectively. The OFF-state current in either case is dominated by the gate-to-drain leakage current (~ 1 μA/mm at -10 V). The small signal analysis provides an f_T and f_{Max} of 15.5 GHz (18.5 GHz) and 11.1 GHz (10.5 GHz), respectively, in the as-developed (post-FGA) devices at V_d = 5 V and V_g = -2.5 V. This puts the $f_T \times L_G$ of the post-FGA devices ~13 GHz-μm. Further, the 3-T leakage current at V_g = -8 V in FGA HEMT is ~35% higher than that of as-developed HEMT (at V_d = 30 V), but merges at Vd = 100 V at ~10 μA/mm, which is significantly lower than the well accepted leakage limit of 1 mA/mm. The 3-T leakage measurement in either case suggests the V_{br} for developed sample with and without annealing remains > 100 V (instrument limit). The most significant improvement imparted by annealing is reduction in the drain current collapse as the current collapse in the as-developed devices at V_d = 6 V and V_g = -1 V is ~17% and it reduces to ~2% for FGA devices at same V_d and V_g. The most probable reason for the observations made in this study regarding reduction in current collapse and increase in f_T while not compromising on the V_{br}, is the marginal leakage increment in the FGA sample, in both gate-drain and 3-terminal leakage configurations, suggesting that the isolating nature of SiN passivation is marginally degraded. Since, non-isolating dielectric improves the current collapse by providing a discharging path to the trapped surface charges [1]. The discharging of trapped states in the gate-drain region, effectively improving the f_T and dispersion values. Power performance with load-pull measurements will be presented at the conference.
Reference:
[1] A. Koudymov, *et al.,* IEEE Electron Dev. Lett., 26 (10), pp. 704-706, 2005.

12:00 PM T05
(Student) A Comparative Study of Slow Current Transients in $Al_{0.4}Ga_{0.6}N$ Channel MOSHFET's with Back Barriers Mohi Uddin Jewel, Shahab Mollah, Mikhail Gaevski, Mohammad K. Hussain, Abdullah Mamun, Grigory Simin, MVS Chandrashekhar and Asif Khan; University of South Carolina, United States

Ultrawide-bandgap (UWBG) Al-rich (x ≥ 0.4) AlGaN metal oxide heterostructure field-effect-transistors (MOSHFETs) are ideal device candidates for solar-blind detection due to their internal transistor gain and inherent solar blind detection (λ ≤ 300nm) ability. We previously reported the deep-trap energies and physical locations responsible for slower transient time in $Al_{0.65}Ga_{0.35}N$/$Al_{0.45}Ga_{0.55}N$ MOSHFETs and suggested using back-barrier (BB) to reduce the trapping effects by screening the channel from the growth interface. We, now, report the optical response and current transient behaviors of $Al_xGa_{1-x}N$ MOSHFETs with a fixed $Al_{0.65}Ga_{0.35}N$ back-barrier and linearly graded $Al_xGa_{1-x}N$ back-barrier. The transfer curves (I_d-V_g) shift towards more negative (~0.63V for fixed BB and ~1.05V for graded BB) under light ($\lambda \sim E_{g,channel}$) in both cases indicates the presence of photoelectrons. The MOSHFETs recovered with light turned off, although a small threshold shift remained ($V_{th,shift}$), by 0.15 and 0.45V (traps ~ 8×10^{11} and 6.5×10^{11} cm^{-2}) in 3 minutes for fixed and graded BB MOSHFETs respectively. Peak responsivities of 3.1×10^5 and 2.3×10^5A/W in the saturation mode for fixed and graded BB MOSHFETs were quenched by one order with strong 365nm UV light used to fill the traps. Consequently, the off-transient time of over 10 minutes reduced to ≤ 12s under 365nm light, while the recovery transient became more symmetric, indicating the presence of deep-traps that were filled in the back-barrier MOSHFETs. These results show that the BB does not have a significant impact on the speed of these devices due to the presence of these deep traps, We will present gate length (L_G) dependent transient measurements with gated-transmission line model (GTLM) MOSHFET devices without BB to isolate transients arising from the access region and from under the channel. Our initial analysis suggests that the transients are similar for both, strongly indicating that the growth interface where the BB was placed is still responsible for slowing down the device. This result is surprising given that the density of those interface traps is ~5×10^{11} cm^{-2}, much smaller compared to the polarization charge introduced by the BB ~$10^{13}cm^{-2}$, suggesting that clustering of point defects near dislocations may play a role as in GaN pn diodes.

12:15 PM BREAK

12:45 PM T06
Polarization-Induced 2D Electron and Hole Gases Homoepitaxially Grown on Single-Crystal AlN Substrates
Jimy Encomendero, Zexuan Zhang, Kevin Lee, Reet Chaudhuri, Debdeep Jena and Huili Grace Xing; Cornell University, United States

Owing to their noncentrosymmetric crystal structure, III-nitride semiconductors exhibit internal polarization fields which can be exploited to dramatically expand the design space of polar heterostructures. Due to their strength (1-10 MV/cm), these built-in electric fields can be harnessed for the realization of novel device functionalities via band-structure engineering and polarization-induced doping. This fundamentally different doping technique completely dispenses with the need of impurity donors or acceptors to generate free carriers, enabling the realization of highly mobile 2D electron and hole gases (2DEGs and 2DHGs) in nitride heterostructures. While polarization-induced doping has been previously engineered in nitride structures grown atop sapphire templates, SiC wafers, and single-crystal GaN substrates; further improvements in device performance are expected when 2DEGs and 2DHGs are grown on high-quality single-crystal AlN substrates. This is possible thanks to the high thermal conductivity and high breakdown electric field of bulk AlN crystals. These outstanding material properties allow not only improved thermal management for high-power devices but also takes advantage of the widest bandgap within the family of nitride semiconductors. This last benefit, however, also prevents efficient generation of free carriers via traditional impurity doping techniques. In this scenario, we leverage the intense built-in spontaneous and piezoelectric polarization fields to generate both types free carriers via polarization engineering. In this presentation, we report, for the first time, the epitaxial growth and transport properties of polarization-induced 2DEGs and 2DHGs in GaN/AlN heterostructures, homoepitaxially grown on single-crystal AlN substrates. The simultaneous demonstration of complementary 2DEG and 2DHG in undoped heterostructures and on a single substrate platform, enables an unmatched level of integration for high-power and high-frequency nitride-based electronics, raising hopes for all-nitride CMOS technology.

1:00 PM T07
Two-Dimensional Hole Gases Induced by Spontaneous and Piezoelectric Polarization in Ga-Face GaN-on-AlGaN Carsten Beckmann, Jens Wieben, Holger Kalisch and Andrei Vescan; Rheinisch-Westfalische Technische Hochschule Aachen, Germany

In analogy to the two-dimensional electron gas (2DEG) in Ga-face AlGaN-on-GaN, the inherent polarization can also be used to generate a two-dimensional hole gas (2DHG) in Ga-face GaN-on-Al(Ga)N. Except for reports on GaN-on-AlN using MBE, all published 2DHG channel transistor structures made by MOVPE also contain a 2DEG, which leads to parallel conduction, RF losses, and device failure especially at high temperatures. In contrast to the common double heterostructures in which the Al(In)GaN barrier is sandwiched between GaN (2DEG below and 2DHG above barrier), we rely on a nearly-relaxed AlGaN buffer and a strained GaN layer on top. The polarization difference between the two layers only induces a 2DHG. The structures were grown in an AIXTRON 200/4 RF-S MOVPE system on 2" sapphire and consist of 300 nm AlN low-/high-temperature nucleation/buffer layer, ~3 µm AlGaN buffer layer, 18 nm unintentionally doped (uid) GaN channel and a 20 nm Mg-doped GaN (p-GaN) ohmic contact layer. Five samples with different Al mole fractions (0.07, 0.14, 0.24, 0.27 and 0.29) in the AlGaN buffer were grown while the AlN nucleation/buffer, the uid-GaN and p-GaN on top were not changed. Additionally, the uid GaN thickness is varied (0, 5, 12, 18, 27, 35 nm), with AlGaN (3 µm, 0.29 Al) and p-GaN (20 nm) constant, to investigate thickness limitations of the strained GaN channel. As a reference, p-GaN was grown on a ~2 µm thick GaN buffer. The thickness and strain of the GaN layers and the strain and alloy composition of the AlGaN buffer layers are analyzed by HRXRD. From reciprocal space maps (RSMs) of the samples with different Al mole fractions, it can be seen that all AlGaN layers are nearly-relaxed (~ 90 %) on AlN, while the GaN layers were grown almost pseudomorphically (≤ 20% relaxation) on the AlGaN buffers. Hall measurements reveal an approximately linear increase in 2D-hole sheet density (2.4×10^{12} to 1.6×10^{13} cm^{-2}) with rising Al mole fraction. The hole mobility shows as expected the opposite trend and decreases from 18.5 to 13.3 cm^2/Vs. The contribution of the p-GaN layer to the Hall measurement results was taken into account by correcting for parallel conductivity determined separately on the reference p-GaN layer (hole density = 1.3×10^{12} cm^{-2} and mobility = 4.5 cm^2/Vs). The polarization-induced sheet charge at the GaN/AlGaN interface is also calculated in dependence of the Al mole fraction according to models in literature. For Al mole fractions ≥ 0.14, the theoretical predictions and the measured values are in good agreement. Further characterization was performed after p-GaN removal by dry etching (depth 24 nm) hereby using the the ohmic contacts as etch mask. The measured hole density for the "etched samples" was lower than the values of the "unetched samples", which indicates etch damage and possibly depletion due to the surface potential. The lower mobilities after etching for all samples also indicate that defects introduced by etching are quite likely. However, these results show that the 2DHG is indeed polarization-induced. Further evidence is given by Hall measurements in the temperature range of 80-350 K, as they show a temperature-independent hole density of ~1×10^{13} cm^{-2} (0.29 Al, p-GaN etched). RSMs of the (105) reflexes of the structures with varying GaN thickness reveal that relaxation is already starting at 25 nm total GaN thickness. As the valence band is shifted upwards with rising GaN thickness, the corresponding hole density still increases up to 32 nm total GaN thickness. Beyond 32 nm GaN layer thickness, relaxation prevails, which reduces carrier density and mobility. In consequence, the uid GaN thickness has to be carefully chosen in dependence of Al content of the AlGaN buffer and p-GaN thickness to avoid relaxation.

1:15 PM T08
(Student) Polarization-Induced 2D Hole Gases in Undoped InGaN/AlN Heterostructures Grown on Single-Crystal AlN Substrates Zexuan Zhang[1], Jimy Encomendero[1], Reet Chaudhuri[1], Kevin Lee[1], Yongjin Cho[1], Masato Toita[2], Debdeep Jena[1,1] and Huili Grace Xing[1,1]; [1]Cornell University, United States; [2]Asahi Kasei Corporation, Japan

A high-conductivity two-dimensional (2D) hole gas is desirable in nitride semiconductors for wide-bandgap p-channel transistors [1, 2]. We report, for the first time, the epitaxial growth, structural characterization, and transport properties of polarization-induced 2D hole gases (2DHGs) at InGaN/AlN interface homoepitaxially grown on high-quality single-crystal AlN substrates without the need of acceptor impurities. Due to the polarization origin of the 2DHG, the density of 2D holes can be tuned by varying the indium composition in InGaN and hence the polarization discontinuity at the heterointerface. A series of three samples with indium composition 0%, 3% and 6% in InGaN were studied. The schematics and atomic force microscopy (AFM) images of these samples are shown in Fig. 1. The smooth surface, along with the presence of clear InGaN atomic steps indicates the step-flow growth mode of these structures and the hetero-interface being atomically smooth. The indium compositions and layer thicknesses of these structures were extracted by fitting X-ray diffraction (XRD) pattern, as shown in Fig. 2. The clearly visible interference fringes in the diffraction pattern suggest smooth hetero-interfaces. The existence of the 2D holes in these structures were confirmed by the Hall effect measurement. The measured hole concentration increases from p = $5.2\text{x}10^{13}$ cm^{-2} to p = $1.1\text{x}10^{14}$ cm^{-2} at room temperature, as the indium composition is increased from 0% to 6%, as seen in Table. 1. This increase in concentration

is consistent with the polarization origin of the 2DHGs as the polarization discontinuity between InGaN and AlN increases when the indium composition becomes higher. Cryogenic Hall effect measurements at 77 K show that hole concentrations are almost independent of temperature, ranging between $p = 2.5x10^{13}$ cm^{-2} and $p = 5.2x10^{13}$ cm^{-2} for indium compositions of 0% and 6%, respectively. These high hole densities, inaccessible by traditional impurity doping at 77 K, further attest to the electrostatic origin of the 2D holes. Our results constitute a pivotal step towards the manufacture of nitride-based p-type field effect transistors (FETs) that can take the advantage of the high thermal conductivity and high breakdown electric fields of single-crystal AlN substrates.
[1]. R. Chaudhuri, *Science* 365, 1454 (2019)
[2]. K. Nomoto, *IEDM* (2020)

1:30 PM T09
(Student) Effect of Acceptor Traps at Positive Polarization Interfaces on the Charge and Mobility of Holes in N-Polar P-Type GaN/(AlN/AlGaN) Superlattices Athith Krishna, Aditya Raj, Nirupam Hatui, Stacia Keller and Umesh Mishra; University of California, Santa Barbara, United States

The use of p-type superlattices (SL) is valuable for III-nitride semiconductor-based LEDs and pFETs (p-type Field effect transistors) because the polarization effects create a periodic oscillation of the energy bands, enhancing the ionization of the deep acceptors (Ex: Mg) [1-3]. Recently, the existence of acceptor traps 0.8eV above the valence band of GaN, located at the positive polarization interfaces in III-nitride systems, was shown [4]. This acceptor trap level was the main source of holes in systems which had insufficient or no Mg doping in them. The present study experimentally demonstrates the effect of these acceptor traps on the charge and mobility of holes in N-polar p-type GaN/(AlN/AlGaN) superlattices. N-polar modulation doped GaN/(AlN/$Al_{0.24}Ga_{0.75}N$) 7-period superlattices were grown using metalorganic chemical vapor deposition (MOCVD). Each superlattice period was 20nm thick composed of 5nm GaN:Mg /5nm unintentionally doped (u.i.d) GaN/ x nm u.i.d. AlN/ (5-x) nm u.i.d AlGaN/ 5nm AlGaN:Mg, where the AlN layer thickness, x, was 0 nm ≤ x ≤ 1.6 nm. In addition to the AlN thickness series, the Mg doping was varied for each AlN thickness with 3.75×10^{18} $cm^{-3} \leq [Mg] \leq 2.5\times10^{19}$ cm^{-3}. The Mg doping in the samples was calibrated using Secondary Ion Mass Spectroscopy, and the SL quality and composition was measured using X-Ray Diffraction. Mg activation was carried out at 800°C and Pd/Au contacts were deposited to prepare the samples for room temperature Hall measurements. The experimental results were compared to those calculated using STR-FETIS. When the band-bending of both GaN and AlN was < 0.8eV, the sheet charge concentration of holes (p_s) measured using Hall matched with the calculated values. For each of the samples where band-bending of either GaN or AlN was ≥ 0.8eV(without accounting for the impact of trap ionization on band-bending), the measured p_s was greater than the amount of Mg dopants put into the sample. This showed that the excess holes came from the acceptor traps at the positive polarization interfaces, here - AlGaN/GaN and AlN/AlGaN interfaces. The acceptor trap ionized when either band-bending was ≥ 0.8eV and the Fermi level was pinned at this trap level leading to the very high measured p_s. A low sheet resistance (~3.4kΩ/■) was observed for N-polar modulation doped GaN/AlN/AlGaN SLs, with $p_s \sim 1.3\times10^{14}$ cm^{-2} and $\mu_p \sim 14$ cm^2/Vs. For the samples in this study, the two-dimensional hole gas (2DHG) exists at the GaN/AlN interface or a GaN/AlGaN interface, if no AlN present. It was observed for each of the AlN thickness series (with various Mg doping levels) the μ_p decreased in samples where the acceptor traps ionized. It was further observed within those set of samples that μ_p decreased to a great extent (>50% decrease) for those samples where AlN band-bending was ≥ 0.8eV – independent of the GaN band-bending in the same sample. The 2DHG is closer to the AlN/AlGaN positive polarization interface (PPI-1) (0 to 1.6nm) compared to the AlGaN/GaN positive polarization interface (PPI-2)(10nm). Therefore, the more dominant source of scattering (and hence the decreased mobility) are the ionized acceptor traps which exist at the AlN/AlGaN positive polarization interface, the closer interface. While the ionized traps at AlGaN/GaN interface also cause scattering, their effect is not as pronounced because they are far away from the 2DHG. This explains the higher mobility observed in in samples where only the GaN band-bending was ≥ 0.8eV, and the AlN band-bending was < 0.8eV leading to the ionization of traps at only the AlGaN/GaN positive polarization interface (PPI-2). Further details of simulations, experiments and methodology will be presented at the conference.
[1] P. Kozodoy, et al., *APL*(1999) [2] A. Raj, et. al., *IEEE-EDL* (2020) [3] C.J. Zollner, et. al., *OME* (2020) [4] A. Krishna, et. al., *APL* (2020)

1:45 PM T10
(Student) Concurrent Quantum Hall Effect and Superconductivity in an Epitaxial Nitride Semiconductor/Superconductor Heterostructure Phillip Dang[1], Guru Khalsa[1], Celesta S. Chang[1,1], D. S. Katzer[2], Neeraj Nepal[2], Brian P. Downey[2], Virginia D. Wheeler[2], Alexey Suslov[3], Andy Xie[4], Edward Beam[4], Yu Cao[4], Cathy Lee[4], David A. Muller[1,1], Huili Grace Xing[1,1,1], David J. Meyer[2] and Debdeep Jena[1,1,1]; [1]Cornell University, United States; [2]U.S. Naval Research Laboratory, United States; [3]National High Magnetic Field Laboratory, United States; [4]Qorvo, Inc., United States

The integer quantum Hall effect (IQHE) is a paragon of topological protection in electronic states, exhibiting exceptional precision in resistance, while superconductivity allows exceptional precision in voltage due to flux quantization. To create seamless heterostructures of these two electronic phases is highly desirable for the discovery of new physics and use in future electronics based on topological quantum computing. However, the two topologically robust electronic phases are typically incompatible due to conflicting magnetic field requirements. To this end, we design an all-epitaxial superconductor/semiconductor nitride heterostructure, based on GaN two-dimensional electron gases (2DEGs) and superconducting NbN, using an industrial device process that is compatible with silicon and nitride semiconductor technology. Through individual magnetotransport measurements of the spatially separated GaN 2DEG and superconducting NbN layers, we demonstrate the existence of a small regime of magnetic fields and temperatures in which the epitaxial layers retain their respective IQHE and superconducting properties. Such a demonstration in an all-epitaxial nitride heterostructure is the first of its kind and paves the way for new quantum technologies. The epitaxial nitride structure consists of a 50 nm NbN layer, a 20 nm AlN nucleation layer, a 1.5 μm GaN buffer layer, and an AlN spacer/AlGaN barrier/GaN cap stack that defines the 2DEG. The NbN layer is grown on a 3-inch diameter semi-insulating Si-face 6H-SiC wafer by plasma-assisted MBE, and the semiconducting and insulating nitride layers were grown on top by MOCVD. Gated Hall bar and HEMT devices were fabricated via Ti/Al/Ni/Au ohmic contact annealing, mesa isolation with a plasma etch, atomic layer deposition of a 15 nm Al_2O_3 gate insulator, and Pt/Au metallization for the gate and probe pads. I-V and C-V measurements were made on the devices to confirm the 2DEG and gauge the device characteristics. TEM was also performed on these devices to observe the high quality, epitaxial structure and confirm the metal polarity of the semiconducting layers. Resistivity and Hall-effect measurements were taken on a gated Hall bar device in a hybrid superconductor/resistive magnet up to 45 T and at temperatures as low as 350 mK. By analyzing the Shubnikov-de Haas oscillations, we extract a gate capacitance of $C_{gs} \sim 149$ nF/cm^2 and 2DEG densities from less than 1.1×10^{12}/cm^2 to 6.7×10^{12}/cm^2 when the gate voltage is varied over $-6.3\ V < V_{gs} < 0$ V. The Hall coefficients indicate electron mobilities ranging from $1200 < \mu < 8500$ cm^2/Vs at 390 mK over the range of 2DEG densities. By varying gate voltage,

the GaN 2DEG was able to enter the IQHE regime in magnetic fields as low as 15 T. We then made electrical contact to the buried NbN layer to conduct magnetotransport measurements and extract the superconducting critical temperature and critical fields. The T_c is 16.5 K with a sharp transition of $\Delta T = 0.16$ K in width, and the maximum out-of-plane H_c is 17.8 T. Therefore, superconductivity and IQHE are concurrent in this structure for $T < 1$ K and 15 T < $B < 17.8$ T. These results indicate that the nitride material system has the potential to become an industrially viable platform for robust quantum devices based on topologically protected transport.

SESSION U: Diamond, Gallium Oxide and Related Materials
Session Chairs: Jung-Hun Seo and Patrick Shea
Thursday Morning, June 24, 2021

11:00 AM *U03
Observation of High Electrical Conductivity and Insulator-to-Metal Transition in *N*-Type Nitrogen Implanted Diamond Thin Films Dhruba Das and M. S. Ramachandra Rao; Indian Institute of Technology Madras, India

Electronic properties of doped-diamond are of great technological interest due to the possibility of diamond-based electronic devices for high power electronics and for the fabrication of QUBITs. With a bandgap of 5.5 eV at room temperature (RT), diamond is a perfect electrical insulator, however when it comes to substitutional incorporation of impurities in its lattice via doping, its conductivity has been seen to change drastically[1,2]. Towards the path of making diamond *n*-type[3,4] for efficient device applications, nitrogen doping has not yet brought much success in terms of electrical conductivity during the past one decade as it fails to form a shallow donor level 1.7 eV below the conduction band because of the dramatic localization of the donor electron on a neighboring carbon atom with a subsequent formation of a lone-pair on the nitrogen atom. Phosphorus, on the other hand, being a large impurity does not relax in an analogous fashion unlike nitrogen, and thus leads to a substantially shallower donor level at 0.6 eV, which is still rather deep for room-temperature ionization[5]. Here, we report on the formation of *n*-type diamond by nitrogen implantation in ultra-nanocrystalline and micro-crystalline diamond films that exhibit high electrical conductivities and insulator-to-metal transition observed at low temperature. Ion implantation by N^+ ions with different energy and fluences resulted in the formation of *n*-type diamond confirmed by Hall measurements. Annealing was performed to make the vacancies and dopants mobile so that the lattice heals from implantation induced damages which can further ensure substitutional doping inside the lattice. Ion-impact induced changes in these implanted films were characterized by Raman spectroscopy both before and post annealing. In case of low dose implantations as observed in x-ray absorption spectra, the long-range ordering in the diamond lattice is completely intact with some disorder being introduced in the system forming point defects and with little to no change in the crystallinity of the films however it gets affected in high dose regime where a signature of formation of tetrahedral amorphous carbon (*ta*-C) opens up the path for percolative type conductivity.
References:
[1] Ekimov, E. A., *et al. Nature* 428.6982 (2004): 542.
[2] Abdel-Hafiez, M., Kumar, D., Thiyagarajan, R., Zhang, Q., Howie, R. T., Sethupathi, K., ... & MSR Rao. (2017). *Physical Review B*, *95*(17), 174519.
[3] Bhattacharyya, S., *et al. Applied Physics Letters* 79.10 (2001): 1441-1443.
[4] P. Zapol, M. Sternberg, L. A. Curtiss, T. Frauenheim, and D. M. Gruen, *Physical Review B* 65, 045403 (2001).
[5] X. Hu, J. Ye, H. Hu, X. Chen, and Y. Shen, *Applied Physics Letters* 99, 131902 (2011).

11:15 AM U01
(Student) Mapping Boron Concentration in HPHT-Diamond Using Continuous and Time-Resolved Cathodoluminescence Spectroscopy Nicolas Tappy[1], Christian Monachon[2] and Anna F. Morral[1]; [1]Ecole Polytechnique Fédérale de Lausanne, EPFL, Switzerland; [2]Attolight SA, Switzerland

Diamond is a wide band-gap semiconductor with high carrier mobility, high breakdown field, and among the best thermal conductors known. For this reason, it is a promising material for power electronics and UV photodetection. However, like most emerging semiconductor materials, the large scale synthesis of perfect-quality material and the control of its electronic properties remain challenging. Diamond can be synthesised both using Chemical Vapor Deposition (CVD) and the High-Pressure-High-Temperature (HPHT) processes. Boron can be incorporated as a p-type dopant during growth. Like in all semiconductors, monitoring the dopant concentration is important for any application, and spectroscopy methods have emerged as fast, non-destructive way to do it. Specifically, low-temperature cathodoluminescence (CL) spectroscopy can be used at moderate concentrations, **$< 10^{18}$ [cm^{-3}]**. In these conditions, the ratio of free and boron-impurity bound excitonic peak intensities depends linearly on the concentration when calibrated against Secondary Ion Mass Spectroscopy (SIMS) measurements. In CVD diamond, a spatially resolved measurement is not necessary as the dopant distribution is intrinsically homogeneous. It is however not the case for HPHT diamond, where local variations can be important. We expect microprobe spectroscopy-based techniques to perform well in those cases, since they can easily be applied at a micron-sized spatial resolution. Nevertheless, to the best of our knowledge, spatially resolved spectral CL maps of diamond have not been published yet. Here, we present how low-temperature spectral CL mapping can measure the doping concentration of B-doped HPHT diamond with a sub-micron spatial resolution. The sample studied shows doping concentration varying over 1 order of magnitude, in the **$10^{16} – 2x10^{17}$ [cm^{-3}]** range. The data obtained are refined to a **±5%** sensitivity, and the absolute accuracy of our measurements is estimated to be a factor 2. This is achieved by measuring the ps-dynamics of the exciton peaks using Time-Resolved CL spectroscopy with the help of a pulsed electron beam. In such measurements, the free exciton lifetime provides an independent, direct way of determining the dopant concentration. In contrary, the lifetime of the Boron-bound exciton is independent of the doping level. We find 175 ± 9 [ps] for the latter, which is shorter than the previously reported value of 270 ± 50 [ps]. Finally, we discuss the impact of growth sector on the incorporation of dopants, as well as the influence of some crystalline defects on the Boron incorporation, through their impact on the CL signal. We show that in some cases, a deficit of boron incorporation can be measured whereas in other cases, the defect doesn't present the slightest dopant concentration variation. A red-shift of the free exciton with increasing boron concentration is also noticed, whereas the boron-bound exciton remains at a fixed energy.

11:30 AM U02
(Student) Making Diamond N-Type with Enhanced Conductivity via Ion Implantation Technique Dhruba Das and M. S. Ramachandra Rao; Indian Institute of Technology Madras, India

Diamond is considered as one of the best next generation wide-bandgap semiconductors due to its exceptional properties but suffers from a drawback. Finding a shallow donor with reduced thermal activation energy is a necessity for its application in high power electronics. Achieving high conductivity in bulk diamond has been challenging and thus diamond films in ultra-

nanocrystalline form (UNCD) with increased grain boundary (GB) fraction have been found to be good electrical conductors which can be easily made p-type or n-type resulting in many orders of magnitude increase in film conductivity that promise applications in high temperature heterojunction electronic devices[1]. Obtaining p-type diamond by boron doping has been quite easier and successful that exhibits metallicity and even superconductivity at lower temperatures[2]. Donors like nitrogen and phosphorus are the suitable candidates for n-type doping, while nitrogen forms a deep donor at 1.7 eV below conduction band (CB) phosphorus is best suited and the most anticipated due to its relatively less activation energy of 0.6 eV[3,4,5]. We report on the formation of *n*-type ultra-nanocrystalline diamond exhibiting high electrical conductivity, $\sigma_{RT} \sim 10^4\ \Omega^{-1}m^{-1}$ by phosphorus ion implantation. Raman study confirms the restoration of crystallinity upon high vacuum and high-temperature annealing post implantation process at 850 °C. Varying the fluence enabled us to obtain reduced thermal activation energy of $E_a \sim 8$ meV with very high carrier concentrations $n_e \sim 10^{21}\ cm^{-3}$. Hall measurements confirm the *n*-type nature in phosphorus implanted diamond at a high fluence of 10^{16} ions/cm^2 and the non-linear Hall effect reveals the signature of two band conduction mechanism, one via impurity band and the other through the conduction band.

References
[1] O. A. Shenderova and D. M. Gruen, Ultrananocrystalline diamond: synthesis, properties and applications (William Andrew, 2012).
[2] D. Kumar, M. Chandran, and M. Ramachandra Rao, *Applied Physics Letters* 110, 191602 (2017).
[3] S. Kajihara, A. Antonelli, J. Bernholc, and R. Car, *Physical review letters* 66, 2010 (1991).
[4] E. Gheeraert, S. Koizumi, T. Teraji, H. Kanda, and M. Nesladek, *physica status solidi (a)* 174, 39 (1999).
[5] X. Hu, J. Ye, H. Hu, X. Chen, and Y. Shen, *Applied Physics Letters* 99, 131902 (2011).

11:45 AM U04
Connections Between Local Structure and Electronic Performance of Intrinsic Diamond Detectors Erik Vyhmeister[1] and Elias Garratt[1,2,1]; [1]Michigan State University, United States; [2]Fraunhofer Center Mid West, United States

Diamond is a highly favorable material for sensing radiation in harsh environments such as the beamlines of high energy particle colliders. Diamond also has a low intrinsic carrier concentration and extraordinarily high carrier mobility, which allows for a high signal-to-noise ratio, fast response times, and operation at room temperature whereas conventional Silicon detectors require cryogenic temperatures. While the degradation of signal due to lattice damage occurring during operation is well-documented, the effect of individual defects and defect structures is not well understood. This work investigates the relationship between local lattice structure and electronic performance – carrier mobility and average lifespan. Understanding which defects more strongly affect performance will inform annealing procedures to increase the operational lifespan of the detector. Previous work on structure-property relationships in diamond has been focused on doped diamond in applications as a semiconductor and does account for the inhomogenous nature of damage by high-energy radiation beams. This study presents spatially resolved imaging of point defects (GR1, NV, TR12, etc.) using Photoluminescence, lattice bonds (sp3 vs sp2 vs hybridization) using Raman spectroscopy, crystal quality from X-ray diffraction and overlays it with local electronic properties so that the effect of specific defects or structures on the electrical properties can be identified. Electronic properties are measured using a known radiation source under forward and reverse bias so that both electron and hole mobility and lifetimes are obtained.

12:00 PM U05
Controllable Crystal Plane Curvature of CVD Single Crystal Diamond and Its Boundary Between Single-Crystalline and the Polycrystalline Within Adjusted Constrained System Shengyuan Bai[1], Ramón Diaz[1], Aj Bensman[1] and Elias Garratt[1,2]; [1]Michigan State University, United States; [2]Fraunhofer Center for Coating and Diamond technology, United States

Great details remain unclear to overcome the challenges in diamond growth using Microwave Plasma Assisted Chemical Vapor Deposition (MPACVD). This research will report the single crystal diamond (SCD) grown in several angled holders designed to achieve better epitaxial lateral outgrowth (ELO) and to maintain an optimized lateral growth rate. Multiple depositions are carried out using angled holders from larger angled pockets to smaller angled pockets. These results in larger size ELO with possible PCD growth, intermediate smooth ELO growth, and inward lateral growth. All as-grown samples are measured with the X-ray rocking curve (XRC) mapping technique to reveal the crystallographic structural properties, and compared to that of the original substrates. Diamond 400 crystal plane curvature/flatness and morphology, XRC FWHM of 400/113/111 diamond peaks are plotted using self-made analytical software to compare the quality revolution before and after the growth. Quantitative birefringence maps are also taken to present the internal crystal structural defects within the CVD diamond. Other than these, the growth behavior within such kinds of adjusted constrained systems will be analyzed to reveal the preference of atomic level diamond growth. Mapping results show that CVD SCD grown using wider angled pocket, though with PCD rims, has better flatness (small curvature) and higher average structural quality (small FWHM); Diamond grown with intermediate pocket, with pure SCD growth, also has not only a good lateral growth behavior, but also intermediate crystal morphology and intermediate structural quality; Those are using smaller pocket results area shrink, but with larger crystal plane curvature, indicating the CVD SCD is compressed due to the smaller size of the pocket.
Cross polarized birefringence and quantitative birefringence images of all samples care taken to understand the internal structure of the CVD SCDs. Thus, an intermediate choice would be the best way for iterative SCD growth to maintain the lateral growth rate and the crystal quality at the same time.

12:15 PM BREAK

12:45 PM U06
(Student) β-Ga2O3 Nanomembrane and Diamond P-N Heterojunction Integrated with Oxide Quantum Tunneling Layer Edward Swinnich, Yixiong Zheng, Md Nazmul Hasan and Jung-Hun Seo; University at Buffalo, The State University of New York, United States

Power electronics is a key component in everyday life for managing and transforming electric power. Semiconductor power switching devices play an important role in enabling such electronics. As future power electronics require improved electrical property, better heat handling capability, and smaller footprint, the development of another class of wide bandgap (WBG) materials and structure are urgently needed to fulfill such needs. As an emerging WBG semiconductor, beta-phase gallium oxide (β-Ga_2O_3) has been intensively researched in recent years due to its large bandgap ($E \sim 4.9$ eV) and high electron mobility, making it a potential WBG semiconductor for next-generation power electronics and optoelectronics. Despite promising material properties of β-Ga O , the well-known deficiency of β-Ga_2O_3, the lack of an efficient p-type dopant, largely prohibits the use of β-Ga_2O_3 toward a wider spectrum of power electronics. In fact, this is the common deficiency in all WBG semiconductors, namely, the lack of one or the other type of efficient dopant. For example, ZnO, SiC, GaN, and β-Ga_2O_3 lack or do not have an efficient p-type dopant. This deficiency reversely happens to

n-type diamond. While p-type doping in diamond is easy and well-known, the effective ntype doping in diamond is known to be challenging, due to the small lattice constant of diamond compared with potential n-type dopants.

In order to overcome aforementioned material challenges, we have developed a new way to heterogeneously integrate two dissimilar single-crystalline semiconductors using an ultra-thin oxide quantum tunneling interface layer. As shown in Figure 1(a) and (b), our new heterogeneous integration method between two dissimilar semiconductors is enabled by employing novel single crystal nanomembrane (NM) and an ultra-thin oxide as a quantum tunneling layer that is formed by atomic layer deposition (ALD), and a reliable micro-transfer printing method. In this work, we have heterogeneously integrated β-Ga O NM with diamond to form an ultra WBG p-n diode (Figure 1(c) and (d)). To understand the band-alignment of the heterostructure, ultraviolet photoelectron spectroscopy (UPS) and X-ray photoelectron spectroscopy (XPS) was performed and determined their conduction band offset and valence band offset (Figure 1(e) and (f)). Furthermore, we have developed an insitu electron affinity tuning method from +2eV to -1eV by the excessive hydrogenation of the diamond surface in the ALD chamber, thus it is possible to adjust band offset of β-Ga_2O_3/diamond heterojunction and perform oxide deposition in a single process step which ensures the stability of the diamond surface chemistry. As shown in Figure 1(d), the fabricated β-Ga_2O_3/diamond p-n heterojunction shows excellent rectifying behavior with extremely low reverse current (below 1pA) and relatively low ideality factor (n ~ 2). The excellent electrical property together with a large tunability of band-offset suggest that our method can offer a customized solution depending on the application as shown in Figure 1(g); namely, we can intentionally increase the band offset (i.e., the built-in potential of the p-n junction), when the device needs low leakage current or high breakdown. We can also reduce it when we want to enhance the recombination or generation of the device. In summary, a seamless ultra WBG heterojunction p-n diode between β-Ga_2O_3 NM/diamond was successfully demonstrated. The capability of tuning the band offset of the heterojunction provides a great degree of freedom to customize the device performance. Our research can be widely applied to any other of the WBG semiconductors which suffer from unbalanced material properties. For example, unique heterostructures such as AlGaN/ Diamond, Boron nitride(BN)/AlN, and β-Ga_2O_3 /GaN are possible which conventional method cannot offer, thus this method will enable us to fully utilize each material's unique property and feature.

1:00 PM U07
MBE Growth and Optical Characterization of Large E_g Rocksalt-Structured Semiconductors Patrick Taylor[1], Arl Garrett[1], George De Coster[1], Masahiko Matsubara[2], Enrico Bellotti[2] and Anand Sampath[1]; [1]U.S. Army Research Laboratory, United States; [2]Boston University, United States

Alkaline-Earth Chalcogenide (O, S, Se, Te) semiconductors have cubic, rocksalt crystallographic symmetry and possess unusually large energy gap. [1, 2] Interestingly, this family of materials also have large lattice constants that ranges from 0.42 nm for MgO to 0.7 nm for BaTe, and are thus suitable for several commercial substrates to facilitate scaling. These materials are similar to the PbTe family of narrow gap materials, and thus, may be much easier to obtain p-type and n-type doping profiles for electro-optical devices. Despite these attributes, this family of semiconductors remains largely unexplored.
In this work, we present new results from the MBE growth and optical characterization, as well as density-functional theory (DFT) calculations of two large-gap alkaline-earth chalcogenides: SrSe and SrTe. High-resolution x-ray diffraction was used to confirm single-crystal epitaxial growth at low-temperature (~600 K), and the lattice constants, 0.62 nm and 0.66 nm respectively, were determined. Ultraviolet photoluminescence and absorbance measurements show relatively bright UV emission at < 350 nm, and UV absorbance beginning strongly at 425 nm. These optical measurements are consistent with DFT calculations of the energy band structure showing both direct and indirect transitions.
[1] D. Partin, IEEE Journ. of Quant. Electr., Vol. 24, No. 8, p. 1716 (1988)
[2] D. Fritsch, H. Schmidt, M. Grundmann, Appl. Phys. Lett. 88, 134104 (2006)

1:15 PM U08
(LATE NEWS, Student) Deep Levels and Self-Trapped Excitons at Iridium/Edge-Fed Grown β-Ga_2O_3 Interfaces Daram N. Ramdin[1], Micah Haseman[1], Kevin Leedy[2], Joel B. Varley[3] and Leonard J. Brillson[1,1]; [1]The Ohio State University, United States; [2]Air Force Research Lab Sensors Directorate, United States; [3]Lawrence Livermore National Laboratory,, United States

β -Ga_2O_3 has attracted considerable technological and scientific interest due to its ultra-wide ~ 4.8 eV band gap and its extremely high projected ~ 8 MV/cm breakdown field, both of which can advance high-power and high-speed electronics. However, to reach the full potential of these applications, an understanding and control of electrically - active native point defects and impurities in β -Ga_2O_3 is needed. Besides their contribution to shallow dopants, deep levels of such extrinsic states can compensate free carriers and have a major impact on their recombination and transport, and possibly their ultimate breakdown voltage strength. Luminescence studies [1-3] have identified commonly observed emissions at 2.5 eV, 2.8 eV, 3.0 eV, 3.5 eV and 3.8 eV, some of whose nature can be related to native defects. The deep level defect nature of extrinsic impurities such as Ir in β -Ga_2O_3 is of interest since high quality single crystal growth techniques such as edge-defined film-fed growth (EFG) make use of iridium dies and crucibles and because large EFG crystals can be grown with quality that is suitable for technological applications. Hence, the impact of Ir in β -Ga_2O_3 is of both scientific and practical concern. We used depth-resolved cathodoluminescence spectroscopy (DRCLS) and surface photovoltage spectroscopy (SPS) to explore the nature of optical transitions at Ir- Tamura Corp. (010) UID EFG interfaces. Low-kV e-beam excitation through 25 nm-thick, e-beam-deposited Ir-Ga_2O_3 diodes provided DRCL spectra with near-nm depth resolution. Near - surface and bulk DRCLS of adjacent bare Ga_2O_3 reveals a prominent ~3.2 eV emission similar to a photoluminescence/cathodoluminescence feature reported previously [4,5], while our SPS identifies a similar transition located 3.15 eV± 0.1 eV below the conduction band. These results are consistent with various theoretical and experimental studies that attribute the ~3.2 eV emission to recombination involving self-trapped holes. Near-nm scale DRCLS at the Ir-Ga_2O_3 interface shows the emergence of 2.1 eV and 2.6 eV features, which is consistent with transitions associated with the complementary $Ir_{Ga(II)}$ (0/+) and $Ir_{Ga(II)}$ (+/0) levels predicted theoretically [6]. The ~3.2 eV emission peak energy maximum also shifts downward towards the Ir-Ga_2O_3 interface, which correlates with the emergence of a sharp ~2.9 eV emission that can possibly be identified with a $Ir_{Ga(I)}$ charge state transition. These measurements provide a distinction as well as possible interplay between deep level emission due to Ir impurities and possible self-trapped polarons that can introduce deep level recombination that affect free carrier transport, density, and dielectric breakdown. These results also suggest that Ir is readily incorporated into the Ga_2O_3 lattice and can produce a major luminescence feature that may produce significant free carrier recombination and compensation. Research efforts are currently underway to perform rapid-thermal annealing on the Ir-deposited sample to determine the activation energy and diffusion coefficient for Ir in Ga_2O_3. DNR, MSH, and LJB gratefully acknowledge AFOSR Grant No. FA9550-18-1-0066 (Ali Sayir).
[1] H. Gao *et al.,* Appl. Phys. Lett. **112**, 242102 (2018).

[2] H. Gao *et al.*, J. Phys. D: Appl. Phys. **53** 465102 (2020).
[3] Y. Wang *et al.,* Sci. Rep. **8**, 18075 (2018).
[4] S. Yamaoka *et al.*, Physical Review B **95**, 094304 (2017).
[5] T. Onuma *et al.,* Appl. Phys. Lett. **103**, 041910 (2013).
[6] J.R. Ritter *et al.,* Appl. Phys. Lett. **113**, 052101 (2018).

1:30 PM U09
(LATE NEWS, Student) Time-Dependant Simulations of Defect Kinetics and Thermodynamics in Gallium Oxide
Nathan P. Yonkee[1], Abdul Shaik[2] and Michael Scarpulla[1];
[1]University of Utah, United States; [2]Arizona State University, United States

β-gallium oxide (Ga_2O_3) is a promising material for applications in power electronics and as a transparent conducting oxide due to its wide bandgap of 4.8 eV and high breakdown electric field of 8 MV/cm. Fundamental properties such as doping, mobility, optical absorption, luminescence, and charge trapping are determined by the device's ensemble of defects. Thermodynamic simulations model the limiting case where the system has reached equilibrium; however, all real systems are limited by both kinetics and thermodynamics during device processing and operation. Here, we present a coupled reaction-diffusion solver used to study time-dependent, one- and zero-dimensional systems, going beyond thermodynamic predictions for defects. By using a detailed reaction mechanism, we can model carrier-defect interactions, such as trapping and emission, resulting in an in-depth description of time-dependent device behavior and accurate device characterization. The solver uses the finite volume method to approximate spatial derivatives and implicit time stepping for time derivatives. This allows us to model surface defect formation and subsequent diffusion into the bulk, as well as bulk defect formation. Using an implicit time stepping scheme enables us to study an extraordinary range of time scales, from femtoseconds to years, unlocking possibilities to simulate device lifetime reliability in addition to device processing.

1:45 PM U10
(LATE NEWS) Rare-Earth Chromites and Rare-Earth Manganites—Structural-Property Relations Jianhang Shi and Menka Jain; University of Connecticut, United States

Rare-earth chromites ($RCrO_3$) have Néel temperature (T_N, above which these become paraelectric) in the range of 100-280 K, which is much higher than the magnetic transitions observed in rare-earth manganites ($RMnO_3$). These family of compounds have been studied for the magnetoelectric-multiferroic (ME-MF) for their potential applications in various devices including magnetic field sensors, energy harvesting devices, and magnetic refrigeration (MR), to name some. In case of ME-MF based devices, it is desirable to have the transitions close to room temperature. In this talk, the structure, dielectric, and magnetic properties of some $RMnO_3$ and $RCrO_3$ based materials will be presented with a focus on their band gap and mutliferroic behavior and the structure-property relations.

SESSION V: Nanoscale Characterization
Session Chairs: Elisabeth Mansfield and Edward Yu
Thursday Afternoon, June 24, 2021

3:00 PM V01
Crystallographic Symmetry and Pseudo-Symmetry Quantifications in Atomic and Molecular Resolution Images
Peter Moeck; Portland State University, United States

This abstract provides basic information (and references) on a set of novel classification methods for the crystallographic symmetries of the "structural signal" in noisy digital images with atomic or molecular resolution from crystals. These methods enable classifications [1,2] into Bravais lattice types, Laue classes, and plane symmetry groups, i.e. space groups in two dimensions. The objectivity of the crystallographic symmetry classifications is ensured by the selection of the best geometric model for the 2D periodic signal in the raw image data on the basis of geometric Akaike Information Criteria [3]. As recently reviewed [4], this particular crystallographic image classification technique is the only one that can be considered to be objective, i.e. researcher and arbitrary thresholds independent. The technique is analytic in nature (rather than based on machine learning [5]). This feature enables it to deal effectively with all types of pseudo-symmetries [1,2,6] and to obtain geometric Akaike weights, which represent the probability of a particular crystallographic symmetry classification. (Machine learning systems have so far ignored pseudo-symmetries in crystallographic image classification studies [5].) The raw input images are considered to consist of the pixel-wise sums of more or less Gaussian distributed noise and an unknown underlying signal that is strictly 2D periodic. Structural defects in the atomic or molecular 2D array, instrumental image recording noise, and small inaccuracies in the algorithmic [6] processing of the image data all contribute to one generalized noise term. Because there are many different sources of noise that contribute to the generalized noise term and none of them is assumed to dominate, the central limit theorem justifies the overarching assumption that the generalized noise is approximately Gaussian distributed. Experimental images from transmission electron microscopes or scanning probe microscopes that are digital and sufficiently well resolved serve as the input of the crystallographic symmetry classifications. (The methods are completely independent of the type of microscope used.) For good processing results and generalized noise suppression, one should record experimental images with a large field of view, containing several tens to about one hundred unit cells of the 2D periodic array. The output of the techniques is the most probable 2D periodic signal distribution from the underlying atomic or molecular array in addition to the most probably plane symmetry group, Laue class, and Bravais lattice type. The generalized noise level is also quantified. The pixel-wise difference between an experimental image and its best symmetrized version, (i.e. the model for the structural information in the data with the least Kullback-Leibler information loss, best generalized noise suppression, and highest geometric Akaike weight), allows for an assessment of the spatial distribution of the generalized noise. This feature of the technique allows in principle for an assessment of strain fields around structural defects in a crystalline array.

[1] P. Moeck, *Symmetry*, vol. **10**, paper 133 (46 pages), 2018, doi: 10.3390/sym10050133.
[2] A. Dempsey and P. Moeck, *arXiv:*2009.08539, September 17, 2020.
[3] P. Moeck, *IEEE Trans. Nanotech.* **18**, 1166–1173 (2019), doi: 10.1109/TNANO.2019.2946597.
[4] K. Kanatani, *IEEE Trans. Pattern Analysis Machine Intelligence* **26**, 1307-1319 (2004), doi:10.1109/TPAMI.2004.93.
[5] R. K. Vasudevan, *private communications*, see also R. K. Vasudevan et al., *npj Computational Materials* **30** (2018) 1–9, https://www.nature.com/articles/s41524-018-0086-7.
[6] P. Moeck and P. DeStefano, *Adv. Struct. Chem. Imaging*, vol. **4**, paper 5 (33 pages), 2018, doi:10.1186/s40679-018-0051-z.

3:15 PM V02
(Student) Controlled Synthesis and Electromechanical Characterization of Europium and Titanium-Containing Nanocrystals—Implications for Energy Storage and Transfer
Benard D. Kavey; Central Michigan University, United States

Novel europium titanate nanorods (EuxTiyOz) and europium-doped barium titanate (Eu-BTO)nanocubes have been synthesized by using a simple solvothermal route at temperatures, as low as 160-180 oC. TEM micrographs of the as-prepared Eu-BTO nanocrystals sample revealed that the nanocubes are highly monodisperse particles with sizes ranging from 14 to 16 nm whereas the nanorods have lengths ranging from 0.3 -1.2 microns. Analysis of the powder X-ray diffraction pattern of the as-prepared nanopowders showed a highly crystalline and single-phase pattern. Scanning probe microscope was used to measure the piezoelectric and magnetic properties of the solution-processed Eu-BTO nanocubes and EuxTiyOz nanorods thin-films. Analysis of the 2D and 3D AFM topography images showed that the nanocrystals can be fabricated into ultra-thin films with thicknesses in the order of 20 nm on a silicon substrate by using a simple drop-cast method with intermittent controlled annealing technique. The piezoelectric displacement in the form of butterfly loops and domain-phase switching dynamics of the piezoelectric EuxTiyOz and Eu-BTO samples were measured by using DART SSPFM. The most important piezoelectric coefficient; the *d33* extracted from the butterfly loops revealed that the *d33* attains a maximum value at the vicinity of the paraelectric to ferroelectric phase transition temperature as expected. Also, the *d33* generally increased with increasing doping concentration and attains a maximum value of 178 pm/V for 3 mol % Eu-BTO thin film at 80 oC. The physical observation of the domain switching mechanism in real time was measured by poling a local region of the thin film sample with a DC bias voltage. The imprinted shapes have been reported in 2D and 3D PFM lithography images and confirms the highly piezoelectric and ferroelectric nature of the thin films. Also, dielectric spectroscopy of the pelletized Eu-BTO sample powders revealed high-k dielectric constant up to e = 4000 at the vicinity of the transition temperature. Magnetic force microscope (MFM) images were obtained by raising a magnetized MFM probe by 80, 30, 20, and 10 nm (delta height) above the sample surface in the tapping/lift mode. Since the probe tip uniformly scans at a height above the sample surface, the topography signal of the sample surface was drastically minimized allowing for the nanoscopic magnetic interactions to be mapped. The widespread nanomagnetic interactions can be visibly seen as a change in contrast (phase shift) in the amplitude and phase images.

3:30 PM V03
Visualizing Oxidation Mechanisms in Few-Layered Black Phosphorus *via In Situ* Transmission Electron Microscopy
Piran Ravichandran Kidambi; Vanderbilt University, United States

Layered two-dimensional (2D) black phosphorus (BP) exhibits novel semiconducting properties including a tunable bandgap and high electron mobility. However, the poor stability of BP in ambient environment severely limits potential for application in future electronic and optoelectronic devices. While passivation or encapsulation of BP using inert materials/polymers has emerged as a plausible solution, a detailed fundamental understanding of BP's reaction with oxygen is imperative to rationally advance its use in applications. Here, we use in situ environmental transmission electron microscopy to elucidate atomistic structural changes in mechanically exfoliated few-layered BP during exposure to varying partial pressures of oxygen. An amorphous

oxide layer is seen on the actively etching BP edges, and the thickness of this layer increases with increasing oxygen partial pressure, indicating that oxidation proceeds via initial formation of amorphous PxOy species which sublime to result in the etching of the BP crystal. We observe that while fewlayered BP is stable under the 80 kV electron beam (e-beam) in vacuum, the lattice oxidizes and degrades at room temperature in the presence of oxygen only in the region under the e-beam. The oxidative etch rate also increases with increasing e-beam dosage, suggesting the presence of an energy barrier for the oxidation reaction. Preferential oxidative etching along the [0 0 1] and [0 0 1] crystallographic directions is observed, in good agreement with density functional theory calculations showing favorable thermodynamic stability of the oxidized BP (0 0 1) planes compared to the (1 0 0) planes. We expect the atomistic insights and fundamental understanding obtained here to aid in the development of novel approaches to integrate BP in future applications. Naclerio et al. ACS Appl. Mater. Interfaces 2020, 12, 13, 15844-15854, DOI:10.1021/acsami.9b21116

3:45 PM V04
Transmission Imaging of 2D Materials in a Conventional Scanning Electron Microscope Elisabeth Mansfield and Jason Holm; National Institute of Standards and Technology, United States

Two dimensional (2D) materials (e.g. graphene, MoS_2) are an emerging class of materials that exhibit desirable properties as atomic-layer thicknesses are approached. As with any new material, understanding structure and inherent defects will help guide manufacturing processes to produce reliable devices. To that end, scanning electron microscopes (SEMs) are ubiquitous in materials characterization facilities and manufacturing process lines, are generally easy to use, and can provide vast amounts of information with diverse detectors. Here, we show how to take advantage of the transmitted electron signal in an SEM to characterize diverse 2D materials (e.g., topological insulators, transition metal dichalcogenides, semiconductors). Two detectors will be described, both of which can be used to implement emerging 4D STEM-in-SEM applications. One detector is more basic and is intended for diffraction imaging, and the other detector incorporates a device that enables on-the-fly user-selectivity for imaging and diffraction. Both detectors are used to demonstrate how one can quantify crystal structure and identify defects in diverse materials.

4:00 PM V05
(Student) Doping Assessment of Ga-Assisted MBE Grown Be-Doped GaAs and Te-Doped GaAsSb Nanowires for Infrared Photodetector Application Priyanka Ramaswamy[1], Rabin Pokharel[1], Mehul Parakh[1], Shisir Devkota[1], Keith Jones[2], Jia Li[1] and Shanthi Iyer[1]; [1]North Carolina A&T State University, United States; [2]Asylum Research, an Oxford Instruments Company, United States

In recent years, III-V semiconductor nanowires (NWs) have significantly attracted researchers due to one-dimensional architecture, quantum confinement effects, and a higher tolerance for stress-strain mismatch that allow greater freedom in engineering combinations of material systems in a variety of various nanowire architectures to meet the demands of next-generation optoelectronic devices. Dopant incorporation in a well-controlled manner is essential to realize advanced devices in NW configuration successfully. Unfortunately, the knowledge obtained on dopant incorporation and carrier concentration from the thin film studies cannot be directly translated to NWs due to the dopant's influence on the growth kinetics and different growth mechanisms along with the axial and radial directions. The commonly used measurement techniques in thin films for the determination of carrier concentration namely, Hall effect, field-effect transistor, and capacitance-voltage require highly sophisticated lithography steps. In the last decade, several characterization methods have evolved for the assessment of dopants in NWs namely, off-axis electron holography for which the sample preparation is complex, and it requires additional information on the NW thickness and homogeneity; secondary ion mass spectrometry and atom probe tomography requires a standard of known dopant concentration and is destructive. Therefore, a combination of conductive-atomic force microscopy (C-AFM), scanning Kelvin probe microscopy (SKPM), X-ray photoelectron spectroscopy (XPS), and ultraviolet photoelectron spectroscopy (UPS), provide a set of excellent characterization techniques for doping assessment, as they do not involve any complex contact fabrications. In this work, we evaluate the carrier concentration and incorporation of Beryllium (Be) dopants in GaAs NWs and Tellurium (Te) dopants in GaAsSb NWs grown using Ga-assisted molecular beam epitaxy (MBE) with variation in Be cell temperatures (T_{Be}) from 750 °C to 950 °C and Te cell temperatures (T_{GaTe}) from 500 °C to 570 °C, respectively. The extensive research interest in GaAs and GaAsSb NWs stems from its narrow bandgap region covering the important optical telecommunication wavelengths of 1.3 µm and 1.55 µm.
The current-voltage measurements using C-AFM of the vertical single NW showed a significant enhancement in current for GaAs NWs doped with T_{Be} at 950 °C and GaAsSb NWs doped with T_{GaTe} at 550 °C. The carrier concentration of Be-doped GaAs and Te-doped GaAsSb NWs are found using COMSOL Multiphysics fitting. From XPS and UPS, the atomic percent, work function, and carrier concentration of Be-doped GaAs NWs and Te-doped GaAsSb NWs are determined. A shift in Fermi level towards the valence band with increasing T_{Be} for GaAs NWs, provided evidence towards higher Be incorporation with T_{Be} - 950 °C doped NWs having a work function of 5.6 eV. Whereas the Fermi level is shifted towards the conduction band in Te–doped GaAsSb NWs. The values of electron density from UPS concur very well with the values of electron density determined from C-AFM. The change in surface potential observed in doped NWs in SKPM characterization also provided strong evidence of Be and Te incorporation. Hence, these surface analytical tools without any contact fabrication are found to be powerful characterization techniques for direct measurement of the dopant levels in NWs, which are critical for bandgap engineering design of optoelectronic devices.
Acknowledgement
This material is based upon research supported by the Air Force Office of Scientific Research (AFOSR) under grant number W911NF1910002.

4:15 PM BREAK

4:45 PM V06
Identification of Ordered Domains in Organic Semiconducting Polymers Using Variable Probe Size 4-Dimensional Scanning Transmission Electron Microscopy Gabriel A. Calderon Ortiz[1], Menglin Zhu[1], Jinwoo Hwang[1] and Letian Dou[2]; [1]The Ohio State University, United States; [2]Purdue University, United States

Organic semiconducting polymers have been widely studied as promising candidates to produce affordable and flexible electronic devices such as solar cells, and transistors. The main challenge so far is the relatively low efficiency of these devices compared to their inorganic counterparts. In order to improve photovoltaic efficiency, a thorough characterization of these materials is required to establish new structure-property relationships and potential ways of improving performance. Here, we demonstrate a novel characterization and quantification of nanoscale ordered domains in organic semiconducting polymers using 4-dimensional scanning transmission electron microscopy (4D-STEM) based on the new generation fast pixelated STEM detector. Our characterization combines high spatial resolution (~ 1 nm) and high dynamic range in signal detection, which allows for quantitative determination of ordering parameters such as type,

size, and volume fraction of the ordered domains with unprecedented precision. We studied Poly(3-hexylthiophene-2,5-diyl) (P3HT) and P3HT: Phenyl-C61-butyric acid methyl ester (PCBM) (P3HT: PCBM). These polymers have been used as a standard organic photovoltaic material, but their structural ordering is complex and hence not fully understood. We first calculated the intensity variance among thousands of diffraction patterns, which was found to be correlated to the expected alkyl and π-π stackings of P3HT. With the addition of the new generation pixelated detector, real space reconstruction of the nanoscale ordered regions can be achieved at different scattering vectors (*k*), which provides further information of the type of ordering and orientation of the polymer. By measuring each ordered domain reconstructed at every acquired k value and annular direction (φ) more detailed information on molecular ordering compared to 1D variance. 2-dimensional histograms were constructed showing the average number of the ordered domains as a function of their size and scattering vector. The histogram shows a very detailed size distribution of the ordered domains and how they are related to the type of the ordering (which is represented by the *k* value). The new detailed information on molecular ordering can be directly compared to theoretical models and variance simulations in order to identify each type of ordered domain reveled in the 2D histogram. Our data indicates a general trend showing that bigger particles possess larger spacing between molecules but are slightly less frequent than smaller particles with smaller spacing between molecules. In summary, our new analysis provides detailed information on type, size, volume fraction, spatial and orientation distribution of the molecular ordering at the nanoscale. By providing such level of detail our technique can potentially help establish better structure-property relationships and improve the overall understanding of not just P3HT:PCBM systems but other materials that are beam sensitive and/or possess medium range ordering.

5:00 PM V07
Rapid and Flexible Few Shot Learning-Based Classification of Scanning Transmission Electron Microscopy Data Sarahl Reehl, Matthew Olszta, Derek Hopkins, Elizabeth Kautz, Bethany Matthews, Le Wang, Yingge Du and Steven Spurgeon; Pacific Northwest National Laboratory, United States

Control of property-defining materials defects for quantum computing and energy storage depends on the ability to precisely probe structure and chemistry at the highest spatial and temporal resolutions. Modern scanning transmission electron microscopy (STEM) is well-suited to this task, having yielded rich insights into defect populations in many systems. However, the dilute nature and complexity of materials defects, coupled with their varied representations in STEM data, makes reliable, accurate, high-throughput statistical defect analysis a significant challenge. Possible analysis approaches include low-level pixel processing, or even the application of machine learning methods for classification and image segmentation. However, the latter requires large sets of labeled training data that are difficult to obtain for many practical materials science studies. Here, we describe the use of an emerging few shot learning capability for rapid and flexible STEM data classification. This approach requires minimal information at the start of the analysis and uses a generally pre-trained encoder network to make inferences on experimental data. Our results show drastic improvements in data annotation costs, reproducibility, and scalability in comparison to neural network training from scratch. We demonstrate how few shot techniques can quickly extract feature maps and global statistics from a variety of STEM data, enabling a new quantitative understanding of defect populations.

5:15 PM V08
(Student) Identifying Defect Origins of Single-Photon Emitters Using Infrared Nano-Optic Probes Ryan Kowalski[1], Joshua R. Nolen[1], Thomas G. Folland[2], Richard F. Haglund[1] and Joshua Caldwell[1]; [1]Vanderbilt University, United States; [2]The University of Iowa, United States

Point defects in wide bandgap semiconductors can provide robust, on-demand single photons that can be used in quantum technologies. Despite the appeal of defect-based single-photon emitters (SPEs), sub-diffractional length-scales of defects make traditional optical characterization techniques insensitive to local variations in the material response. Traditionally, photoluminescence (PL) spectroscopy is used to measure the emission spectrum and even map local intensities, however, spatial resolution is typically restricted to sizes on the order of a micron. However, advances in nano-optic probe technologies such as scattering-type scanning near-field optical microscopy (s-SNOM), can provide optical information about a material with nanoscale spatial resolution (< 20nm)[1]. Here, s-SNOM employs local evanescent fields confined to the apex of a metallized AFM tip following irradiation with a monochromatic laser to probe the material response with this sub-diffractional spatial resolution. While s-SNOM can be performed with a range of frequencies from visible to THz, infrared frequencies are used to exploit the contrast in vibrational resonances between a material and any local defects, thereby creating a two-dimensional spatial map. The tradeoff for high resolution s-SNOM is excessive scan times over large areas (>100μm^2) and imaging at only a single incident frequency, therefore another imaging technique must be used to navigate the sample of interest and to identify spectroscopic resonances of interest. Here, PL and nano-FTIR spectroscopies offer a highly complementary toolset with s-SNOM. Using PL intensity mapping in a scanning confocal microscope, ensembles of nano diamonds (d=134nm) with nitrogen-vacancy (NV) defects can be identified by high-intensity regions (Fig. 1a) and verified from the corresponding collected emission spectrum (Fig. 1b). FTIR spectroscopic measurements of similar diamond samples with very high NV densities have been found to correlate with additional vibrational absorption bands in the 1100-1400cm^{-1} range (Fig. 1c) with two prominent peaks[2], indicative of vibrational modes due to the modified crystal bonds making up the NV defect. By mapping spatial regions featuring nano diamond NVs via s-SNOM, we hypothesize that one can map out the local distribution of the defect vibrational states. This is presented through s-SNOM phase maps recorded within a region of high PL intensity using a probing frequency (1177cm^{-1}) within the absorption band of the NVs (Fig. 1d). Regions of high phase contrast correspond to high local absorption and three regions, circled in white, display magnitudes of high contrast at this frequency. However, the phase contrast is diminished when probing the sample with a different frequency (1450cm^{-1}), outside of the NV absorption band (Fig. 1e). Regions of high phase contrast present in both images (1d,e) are attributed to fabrication residue, polymethyl methacrylate, which absorbs at both probed frequencies. The s-SNOM and PL maps suggest that the highlighted features are nano diamonds containing photoluminescent NVs but is still inconclusive. However, nano-FTIR provides direct measurements of IR reflection and absorption spectra from samples without diffraction limitations[3] using s-SNOM principles. Employing it to measure the spectra of the high contrast regions will enable a direct comparison to its bulk counterpart, conclusively determining the nature of the additional vibrational modes. Correlating PL with s-SNOM imaging has been demonstrated on extended defects, but not so with point defects[4]. Diamond NVs are appropriate for developing this technique because of their high brightness at room temperature[5]. This technique could provide a non-destructive method of investigating defect-based SPEs in materials such as hexagonal boron nitride and gallium nitride, whose defect structures have not been fully characterized but are yet still under intense investigation.

5:30 PM V09
(Student) Measurement of Minority Carrier Diffusion Lengths in Core-Shell GaAs NW p-n Junctions Mingze Yang[1], Ali Darbandi[1,2], Simon Watkins[1] and Karen Kavanagh[1]; [1]Simon Fraser University, Canada; [2]SickKids Hospital, Canada

Core-shell semiconductor nanowires (NWs) are an attractive alternative to planar devices for multiple applications, including field-effect transistors, photovoltaic devices, light-emitting diodes, and lasers. The core-shell radial junction structure enables electron- or photo-induced electron-hole pairs (EHPs) to be collected with shorter diffusion lengths due to the small NW diameter. Furthermore, the collection of the EHPs inside the core is free from surface recombination, potentially improving the energy harvesting efficiency. Electron-induced-beam current (EBIC) measurement is a complementary technique *in situ* in a scanning electron microscope (SEM), collecting excess carriers in a biased diode as a function of beam position and accelerating voltage. In this talk, we will present the analysis of carrier diffusion properties in unprocessed, free standing core-shell GaAs NW diodes. The carrier kinetics in both the n-type core and the p-type shell were determined by analyzing radial EBIC profiles as a function of beam energy. These profiles are highly sensitive to changes in depletion widths and minority carrier diffusion lengths due to geometric effects. Combined with Monte Carlo simulations, they permitted measurement of the n-type core, minority carrier diffusion length, as well as the depletion widths as a function of radial direction. A relatively short minority carrier diffusion length (50 nm) found near {112}B surface facets can be attributed to bulk point defects originating from low-temperature growth (400 °C). Depletion widths were found to be smaller in <112>B directions than in <112>A, likely due to different dopant corporation efficiencies of Te and Zn in the core and the shell, respectively, and to the very thin shell on the {112}B surfaces.

5:45 PM V10
(Student) Understanding Relaxor Ferroelectrics at Atomic Scale Abinash Kumar[1], Jonathon Baker[2], Matthew Cabral[3], Preston Bowes[2], Shujun Zhang[4], Elizabeth Dickey[5], Douglas Irving[2] and James LeBeau[1]; [1]Massachusetts Institute of Technology, United States; [2]North Carolina State University, United States; [3]The University of Sydney, Australia; [4]University of Wollongong, Australia; [5]Carnegie Mellon University, United States

Relaxor ferroelectrics show a slim hysteresis loop, low remnant polarization, high saturation polarization, and exceptional electromechanical coupling coefficient, finding applications in ultrasound imaging and energy storage devices. The presence of nanoscale chemical and structural heterogeneity has been associated with such compelling properties. As relaxors comprise of complex structural features, finding the connection between their structure and properties has been a seemingly intractable problem. In this presentation, I will discuss how we employ aberration-corrected scanning transmission electron microscopy (STEM) to quantify the various contributions of nanoscale heterogeneity to relaxor ferroelectric properties in the prototypical relaxor ferroelectric system, PMN-PT. Specifically, we found three main contributions, chemical ordering, oxygen octahedral tilting and oxygen octahedral distortion that are difficult to otherwise differentiate. Through STEM, the elusive connection between chemical and structural heterogeneity and local polarization variation is revealed. Through these measurements, design principles for next generation relaxor material are elucidated.

SESSION W: Organic and Hybrid Materials and Devices I
Session Chairs: Deidra Hodges and William Wong
Thursday Afternoon, June 24, 2021

3:00 PM W01
Improving Metal-Top-Contact/Organic Interfaces via Monolayers Jacob W. Ciszek; Loyola University Chicago, United States

Organic optoelectronic devices (OLED, OFETs, OSCs) are commonly configured such that a metal contact must be deposited on top of the organic semiconductor. These interfaces often suffer from numerous flaws including poor adhesion, metal penetration, poor surface wetting (discontinuous films), and significant charge injection barriers. We demonstrate that monolayers, placed on top of the organic material, represent a superior method to the adlayer approaches currently utilized for improving interfaces. Here, chemistry is used to install metal binding groups at the surface of the organic semiconductor, while leaving bulk semiconductor properties intact. We find that a single class of monolayers is capable of addressing multiple interfacial issues. Specifically, a thiolated terminus is shown to reduce metal penetration into a surface, increase adhesion of the contact to the organic surface (increasing durability in flexible applications), and increases wetting of the metal (allowing for the generation of continuous metal contacts that are very thin). Device performance confirms the retention of the bulk semiconductor's properties. Time permitting, the talk concludes with preliminary work on monolayers effects on injection barriers.

3:15 PM W02
(Student) Role of the Injection Barrier on the Performance of Vertical Organic Field Effect Transistors Drona Dahal, Raj Kishen Radha Krishnan, Pushpa R. Paudel and Bjorn Lussem; Kent State University, United States

Vertical Organic Field Effect Transistors (VOFETs) reach a high performance and high switching speeds by downscaling the active channel length into the sub micrometer regime [1]. Furthermore, VOFETs can easily be integrated with organic light emitting diodes into a single device, which can create new perspectives for the current display technology [2]. However, despite these prospects, VOFETs suffer from their own limitations as well, in particular from short channel effects. Often, VOFETs only show a weak saturation in the output characteristic and display high off-currents, which can be explained by the strong influence of the drain potential on the injection at the source electrode [3],[4]. Here, we study the influence of the injection barrier at the Source/Drain electrode on the ON/OFF ratio of these transistors. Vertical transistors made of two different semiconductors are compared: C_{60} and DPA (2,6 Diphenylanthracene). DPA is known to result in a high injection barrier at the source/drain interface, in contrast to C_{60}, which forms a small injection barrier. It is shown that C_{60} VOFETs reach high on-currents and a high transconductance, but at the expense of significant leakage currents between source and drain electrodes, resulting in a low ON/OFF ratio of the transistors. In contrast, the larger injection barrier of DPA VOFETs suppresses the off current, albeit reducing the performance in the ON-state. With the help of a drift/diffusion simulation we are able to show that these experimental results can be generalized. We argue that VOFETs face a device-inherent compromise between large on-currents and high transconductances, which requires a low contact resistance, and low off-currents, which can be increased by an increased injection barrier at the drain.
References
[1] Kleemann, H., Krechan, K., Fischer, A., & Leo, K. (2020). A

Review of Vertical Organic Transistors. *Advanced Functional Materials*, *30*(20), 1907113.
[2] McCarthy, M. A., Liu, B., Donoghue, E. P., Kravchenko, I., Kim, D. Y., So, F., & Rinzler, A. G. (2011). Low-voltage, low-power, organic light-emitting transistors for active matrix displays. *Science*, *332*(6029), 570-573.
[3] Liu, S., Tietze, M. L., Al-Shadeedi, A., Kaphle, V., Keum, C., & Lussem, B. (2019). Vertical organic tunnel field-effect transistors. *ACS Applied Electronic Materials*, *1*(8), 1506-1516.
[4] Greenman, M., Sheleg, G., Keum, C. M., Zucker, J., Lussem, B., & Tessler, N. (2017). Reaching saturation in patterned source vertical organic field effect transistors. *Journal of Applied Physics*, *121*(20), 204503.

3:30 PM W03
(Student) Effect of Annealing Printed Electrodes on Gate Dielectric Hydrophobicity and Device Performance in Organic Transistors Paria Naderi and Gerd Grau; York University, Canada

Printed electronics is an inexpensive way of producing electronic devices for every-day applications such as flexible biosensors, affordable RFID price tags and large-area optoelectronics. Transistors are the most fundamental components of many digital and analog circuits. Printed organic thin-film transistors (OTFT) consist of different functional layers deposited from solution. The conductive electrodes are commonly printed using metal nanoparticles that need to be sintered to become conductive. These electrodes are usually printed on other previously solution-processed layers. However, annealing the electrodes will impose another annealing step on the previously deposited layers. Depending on the chemical structure of these layers, their surface or bulk might undergo changes that might affect the final device performance. In bottom-contact bottom-gate organic transistors, the source and drain electrodes are printed onto the gate dielectric layer, which will undergo the electrode post-annealing. In this work, the effect of changing the annealing temperature of silver electrodes in p-type organic transistors is studied. ITO-coated glass is used as the substrate, where the ITO layer works as the gate electrode. A dielectric layer of Teflon AF 1600 (3% in Fluorinert FC-40) then covers the ITO layer through two spin-coating steps. This dielectric layer is subsequently annealed at 150°C for 30 minutes resulting in 450 nm thickness. Since this dielectric layer has low surface energy, it is not possible to form a line of connected ink droplets through printing, therefore the dielectric layer is plasma treated to increase its surface energy. Afterward, for the source and drain electrodes, silver nanoparticle ink is inkjet-printed with a custom-made printer and a 60 µm diameter nozzle. The transistors have varying channel length (20 - 75 µm) and 1.3 mm width. These electrodes are then sintered at different temperatures for 30 minutes (after 5 minutes heating at 60°C to prevent coffee ring effect). This step also acts as a second post-annealing step for the dielectric layer. Finally, the organic semiconductor PDBPyBT is spin-coated in the last step, followed by annealing at 120°C for 10 minutes. The transistors are p-type and are biased at a drain voltage of -120 V in saturation. Silver annealing temperatures of 80°C, 100°C, 120°C, and 200°C are studied. Devices annealed at 120°C show the best performance with the maximum saturation field-effect mobility of 0.13 $cm^2/V.s$ and the maximum saturation Ion/off ratio of $3.41x10^7$. The difference in performance between different electrode sintering temperatures cannot be explained by changes in electrode conductivity because it is much lower than the channel resistance in all studied cases for this ink. The bulk dielectric properties of the Teflon gate dielectric also remain unchanged during the electrode annealing step with a dielectric constant of 2.1. However, the Teflon surface properties are changed. Water contact angle increases monotonically from 85° with no post-annealing to 120° with 200°C post-annealing. With 200°C electrode annealing, this leads to partial dewetting and accumulation of the semiconductor between the more wettable source and drain electrodes. The resulting large thickness of the semiconductor mainly deteriorates device off-state performance reducing the average on-off-ratio from $1.14x10^7$ to $7.25x10^5$. For 80°C, 100°C, and 120°C electrode annealing, the semiconductor thickness remains constant at 100 nm, however, the Teflon surface becomes more hydrophobic. It has been observed before that organic semiconductors perform better on more hydrophobic surfaces, which usually requires a chemical surface modification step. Here, we show that this can be achieved by a simple post-annealing step, which is already part of device fabrication to sinter the source and drain electrodes and should therefore be considered when designing the process flow of the complete device.

3:45 PM W04
(Student) Elucidating the Role of Water-Induced Traps in the Environmental Stability of Polymer Field-Effect Transistors Hamna Haneef[1], Matthew Waldrip[1], Hu Chen[2], Iain McCulloch[2,3] and Oana Jurchescu[1]; [1]Wake Forest Universtiy, United States; [2]King Abdullah University of Science and Technology, Saudi Arabia; [3]University of Oxford, United Kingdom

Prolific developments in the field of organic electronics have steered the design and synthesis of a multitude of high-performance organic semiconductors (OSCs) with charge carrier mobilities exceeding that of thin film amorphous silicon (> 1 $cm^2V^{-1}s^{-1}$). Conjugated polymers are emerging as leading contenders for use in optoelectronic devices such as organic field-effect transistors (OFETs), organic light-emitting diodes, organic photovoltaic cells, and various sensors. Their enticing potential stems from their chemical versatility by molecular design, low cost, ease of processing, and compatibility with flexible substrates and biological systems. Even with nearly amorphous microstructures, these materials have achieved device uniformity over large areas, a basic requirement for applications such as displays. Despite these exciting advancements, conjugated polymers still encounter several challenges on their path towards next–generation devices. Understanding the mechanism of charge transport in these materials, further advancements in device performance and stability, developing new processing techniques to tailor to specific applications, and identifying novel applications to realize the full potential of their unique properties are a few of them. Another major problem that has sparked a flurry of interest recently is the inadvertent diffusion of atmospheric water into polymer films leading to environmental degradation. The most detrimental consequence of water incorporation in polymer films is the occurrence of charge carrier trapping, a widely observed phenomenon in OSCs that impacts the performance and stability of electronic devices. Despite the considerable amount of experimental and theoretical efforts devoted to clarifying the impact of water on device stability, an in-depth understanding of the role of water molecules in the generation of charge carrier traps, and the process by which they affect the device performance is still lacking. Such an understanding is imperative to devise new approaches to suppress the creation of traps and eventually engineer high-performance devices. In this work, we investigate the role of water-induced traps on the long-term environmental stability of OFETs consisting of the donor-acceptor copolymer, indacenodithiophene-co-benzothiadiazole (IDT-BT). We monitor in real time, the device performance as well as the trap density of states (DOS) spectrum during *in situ* exposure of devices to a desiccant in order to uncover important mechanisms occurring during the process of water removal from these devices. An intriguing observation is made, where a peak originating from deep electronic traps at ca. 0.4 eV from the valence band edge is established after 2 hours of exposure to the desiccant. The deep traps are responsible for threshold voltage instabilities and their origin is attributed to surface defects on the SiO_2 dielectric. The trap DOS spectrum provided a solid platform to study the dynamics of trap generation, which allowed us to invent a new surface passivation route that resulted in complete suppression of the deep traps and a corresponding enhancement in device stability and performance. The passivated devices stored for 90

days in ambient conditions indicated nearly constant mobility and a remarkably low threshold voltage shift of -0.3 V.

4:00 PM W05
(Student) Organic Doping at Ultra-Low Concentrations Raj Kishen Radha Krishnan, Shiyi Liu and Bjorn Lussem; Kent State University, United States

Doping is a technique that is widely used in inorganic devices to tune the Fermi Energy, define majority charge carriers, and improve the stability and performance of devices. Doping plays a key role in CMOS technology[1] that has fueled tremendous technological progress. Doping concentrations used are in the range of tens to hundreds of ppm only, which, however, is sufficient to precisely control the electronic properties of the semiconductor. Doping is as well used in organic electronic devices, and some of the most efficient Organic Field-Effect Transistors use doped organic semiconductors to reach the benchmark mobility[2] of 10 $cm^2V^{-1}s^{-1}$, which makes them viable candidates for certain niche applications like RFID tags[2], gas sensors[3], display backplanes[4] etc. However, in contrast to inorganic doping, the doping concentrations commonly used in organic devices are quite high (in the wt.% range). Such high concentrations not only present challenges for the use of doping in organic field-effect transistors[5], but limit the doping process itself resulting in a low doping efficiency. Overall, this underlines the significance of understanding organic doping better and reaching higher doping efficiency. To study the effect of doping at ultra-low doping concentrations, we established co-evaporation of host and dopant material with a rotational shutter to cut the ratio of dopant that is mixed with host. The rotational shutter consists of a rotating metal disc with slits that sits above the evaporative dopant source and cuts the rate at which the dopant is co-deposited with the host. In our lab we have used this to achieve doping of the order of 100ppm. This has enabled us to systematically study the effect of doping in a number of systems- C60:O-MeO-DMBI-I, Pentacene:C60F36, Pentacene: F6TCNNQ and DNTT: F6TCCNQ. The effect of doping is studied in Organic Field-Effect Transistors and MOS devices. The effect of doping on threshold voltage, mobility, hysteresis has been studied in detail in doped C60 MOS devices. With the help of an AC small signal drift-diffusion model, we were able to fit the experimental data, and gain understanding into the effects of traps and doping at the key OSC/dielectric interface. High performing C60 OFETs with charge carrier mobilities of 3-4 $cm^2V^{-1}s^{-1}$, operating below 1 V are realized by doping the channel at ~500-1700 ppm are realized. The presented results allow us to formulate a statistical model that predicts the doping efficiency in dependence of disorder in the films, activation energy of the doping process, and doping concentration. This model is used to formulate general guidelines for choosing material systems and achieving efficient doping in organic devices, which can guide further materials development.
References
1. Jain, A. The Role of Doping Technology in the CMOS Digital Revolution. Proc. Int. Conf. Ion Implant. Technol. 2018-Septe, 19–28 (2018).
2. Lai, S. et al. A plastic electronic circuit based on low voltage, organic thin-film transistors for monitoring the X-Ray checking history of luggage in airports. Org. Electron. 58, 263–269 (2018).
3. Zhang, S. et al. Gas Sensors Based on Nano/Microstructured Organic Field-Effect Transistors. Small 15, 1–16 (2019).
4. Zhou, L. et al. All-organic active matrix flexible display All-organic active matrix flexible display. Appl. Phys. Lett. 88, 1–4 (2009).
5. Xu, Y. et al. Doping : A Key Enabler for Organic Transistors. 1801830, 13–19 (2018).

4:15 PM BREAK

4:45 PM W06
(Student) Tuning Exciplex Luminescence Using the Stark Effect in Organic Semiconductors Nolan Concannon and Russell Holmes; University of Minnesota Twin Cities, United States

The realization of high efficiency in organic light-emitting devices (OLEDs) requires the harvesting of all electrically generated excitons. In conventional fluorescent materials, this is limited by optically dark spin triplet excitons, leaving only spin singlet excitons to undergo radiative recombination. Molecules that exhibit thermally assisted delayed fluorescence (TADF) permit dark triplets to be endothermically excited back to the singlet where they may also undergo fluorescence, maximizing exciton utilization. Intermolecular TADF has also been observed for exciplexes, excited states formed between electron donating and accepting molecules, with recent demonstrations of very high efficiency in OLEDs. These states warrant further study due to the wide range of active materials that can be included in the emissive layer, *i.e.* donors, acceptors, and hosts, as well as the sensitivity of the emission wavelength and efficiency to the surrounding dielectric, enabling wide tunability. Prior work has demonstrated the ability to shift the exciplex emission energy under an external electrical field. This talk will examine this observation more closely and elucidate its origin. We employ biased, non-injection-type devices to show a reversible and linearly field-dependent energy shift of exciplex photoluminescence. Further we relate our findings to the more general phenomenon of the Stark effect observed in electro-absorption and electro-emission across other excitonic material systems. Finally, we note the relationship between our findings in photoluminescence to observations and opportunities for tunable electroluminescence and exciton management in exciplex OLEDs.

5:00 PM W07
Extending Atomic Scale Simulation for OLED Materials—From Discrete Molecules to Disordered Solid State Morphologies Hadi Abroshan, Paul Winget, Casey Brock, Shaun Kwak and Mathew Halls; Schrödinger, Inc., United States

OLED devices are becoming increasingly complex, composed of hybrid architectures with multiple components. Hence, computer aided design has received significant attention as a critical tool for future OLED materials development. Computational approaches are required to accurately describe sub-nanoscale phenomena, in order to reveal the origin of emergent layer and device-scale properties. To date, the majority of computational efforts have treated OLED materials as isolated entities in the gas phase, although they are applied as thin solid films where intermolecular interactions have a significant impact on critical properties impacting overall device performance. Here, we present a multi-tiered computational workflow to accurately and efficiently investigate the electronic properties of the materials in realistic solid state morphologies. We apply a range of robust and validated methods to fill in the length- and time-scale gap between the morphology and optoelectronic properties. The work highlights the significance of static and dynamic disorder associated with electron-vibration interactions and the amorphous nature of the materials, paving the way for improved future studies of smart materials not only in the context of OLEDs, but also in fields such as spintronics, imaging, and quantum information technologies.

5:15 PM W08
(Student) Understanding the Influence of Spontaneous Orientation Polarization on the Efficiency of Organic Light-Emitting Devices (OLEDs) Evgeny Pakhomenko, John Bangsund, Jack Van Sambeek, Nolan Concannon and Russell Holmes; University of Minnesota Twin Cities, United States

Many common electron transport materials used in organic light-emitting devices (OLEDs) show a preferred molecular orientation

in vacuum deposited thin films. If a molecule has a permanent dipole moment, this alignment can result in spontaneous orientation polarization (SOP), which leads to the formation of an interfacial polarization charge. To balance this polarization charge, carriers of opposite sign (typically holes) accumulate at the adjacent layer. It has been demonstrated previously that phosphorescent OLEDs based on a polarized electron transport layer (ETL) of tris-(1-phenyl-1H-benzimidazole) (TPBi) exhibit substantial exciton-polaron quenching prior to device turn-on, reducing peak internal quantum efficiency by ~ 20%. This is in contrast with the prevailing understanding of exciton kinetics in OLEDs, where it is generally assumed that bimolecular quenching is only significant under high injection. This talk will examine the generality of this result in OLEDs using several ETLs with varying degrees of SOP. Of particular interest in order of increasing SOP are bis(8-hydroxy-2-methylquinoline)-(4-phenylphenoxy)aluminum (BAlq), 4,7-diphenyl-1,10-phenanthroline (BPhen), and tri[3-(3-pyridyl)mesityl]borane (3TPYBM), paired with an emissive layer of the archetypical carbazole host 4,4′-bis(N-carbazolyl)-1,1′-biphenyl (CBP) and the red phosphorescent emitter, bis[2-(2-quinolinyl)phenyl](2,2,6,6-tetramethyl-3,5-heptanedionato)iridium (Ir(dpm)PQ_2). Exciton quenching and charge accumulation in the device is quantified using lock-in photoluminescence and displacement current measurements. The presence of significant exciton quenching prior to device turn-on is observed across devices with more than one type of ETL material, supporting the generality of this effect. For most devices, the results suggest this phenomenon is a major limiting factor for the peak internal quantum efficiency, with the degree of quenching related to the magnitude of the polarization charge. These findings contrast the common practice of attributing lower-than-expected peak efficiency to charge balance losses and highlight the impact of SOP on OLED device efficiency.

5:30 PM W09
(Student) Synthesis and Characterisation of Phosphonated PEDOT—An Organic Material for Energy-Efficient Bioelectronics Jonathan A. Hopkins[1], Kristina Fidanovski[1], Lorenzo Travaglini[1], Pawel Wagner[2], Klaudia K. Wagner[2], Antonio Lauto[3], David L. Officer[2] and Damia Mawad[1]; [1]UNSW Sydney, Australia; [2]University of Wollongong, Australia; [3]Western Sydney University, Australia

Conjugated polymers (CPs) have found great success as active materials in organic electrochemical transistors (OECTs), which can be integrated into bioelectronic devices for cell monitoring and stimulation.[1,2] The success of CPs in this application is dependent on their material design: CPs must exhibit electrochemical activity in aqueous environments and support OECT operation in the energy-efficient, accumulation mode. Current materials such as PEDOT:PSS present several challenges, including depletion mode operation in OECTs, which is less energy-efficient; water solubility, which necessitates crosslinking or post-treatment;[3] and high acidity, which can limit their biocompatibility with specific cell lines.[4] Consequently, there is a clear need to develop new CPs for aqueous OECTs which overcome these limitations. To this end, we have synthesised and characterised a new CP, poly(ethylenedioxythiophene) functionalised with isopropyl-protected phosphonate groups (PEDOT-Phos). This material is readily processed in organic solvents, can be proton doped with non-oxidising acids, and exhibits reversible electrochemical activity in aqueous electrolytes. Most importantly, we used PEDOT-Phos as the channel material in aqueous, accumulation mode OECTs which boast low threshold voltages and high volumetric capacitances and transconductances, without requiring additives or post-treatments. Overall, PEDOT-Phos is a promising electronic material for applications in energy-efficient, organic bioelectronics.

References:
(1) Hopkins, J.; Travaglini, L.; Lauto, A.; Cramer, T.; Fraboni, B.; Seidel, J.; Mawad, D. Photoactive Organic Substrates for Cell Stimulation: Progress and Perspectives. *Adv. Mater. Technol.* **2019**, *1800744*, 1800744. https://doi.org/10.1002/admt.201800744.
(2) Fidanovski, K.; Mawad, D. Conjugated Polymers in Bioelectronics: Addressing the Interface Challenge. *Adv. Healthc. Mater.* **2019**, *8* (10), 1–9. https://doi.org/10.1002/adhm.201900053.
(3) Stavrinidou, E.; Leleux, P.; Rajaona, H.; Khodagholy, D.; Rivnay, J.; Lindau, M.; Sanaur, S.; Malliaras, G. G. Direct Measurement of Ion Mobility in a Conducting Polymer. *Adv. Mater.* **2013**, *25* (32), 4488–4493. https://doi.org/10.1002/adma.201301240.
(4) Mantione, D.; del Agua, I.; Sanchez-Sanchez, A.; Mecerreyes, D. Poly(3,4-Ethylenedioxythiophene) (PEDOT) Derivatives: Innovative Conductive Polymers for Bioelectronics. *Polymers (Basel).* **2017**, *9* (12), 354. https://doi.org/10.3390/polym9080354.

SESSION X: 2D Material Devices and Applications
Session Chairs: Kevin Daniels and Soaram Kim
Thursday Afternoon, June 24, 2021

3:00 PM X01
Reporting and Benchmarking Emerging Field-Effect Transistors Curt A. Richter[1], Zhihui Cheng[1,2], Son T. Le[1,3], Steven J. Koester[4], Eric Pop[5,5] and Aaron D. Franklin[6,6]; [1]National Institute of Standards and Technology, United States; [2]Purdue University, United States; [3]Theiss Research, United States; [4]University of Minnesota, United States; [5]Stanford University, United States; [6]Duke University, United States

Harnessing emerging low-dimensional nanomaterials for use in device applications such as field-effect transistors (FETs) has been a research goal for over three decades and continues to be widely pursued today. However, determining and comparing the promise of these emerging materials is challenging. The performance of research FETs depends on many interrelated parameters beyond just the channel materials, and due to the interdisciplinary nature of this research community there is a lack of consistent reporting guidelines. To overcome this hurdle, the research community needs to embrace more complete and consistent practices for reporting and benchmarking FET parameters. We present the results of our effort to develop a consensus between researchers regarding guidelines for reporting and benchmarking important FET parameters and performance metrics. More specifically, we recommend measurement approaches, specific parameters to extract, reporting procedures, and well-defined benchmarking plots for evaluating device performance. We illustrate these recommendations for two-dimensional (2D) MoS_2-based FETs and compare the extracted parameters to those reported for similar devices to illustrate various benchmarking plots. Following are a few selected examples of these recommendations. Current-voltage (I-V) measurements are commonly used to capture FET performance. Drain current (I_D) as a function of gate-source voltage (V_{GS}) is used to measure the subthreshold characteristics (e.g., slope and off-current) as well as the threshold voltage (V_T) and the on-current. Ideally, I_D is presented on both a linear and log scale. The I_D-V_{GS} sweeps should be conducted at both small and high drain-to-source voltages (V_{DS}) to characterize the device operation in both linear and saturation regimes. These curves enable easy extraction of drain induced barrier lowering (DIBL) and related behaviors. Output characteristics (I_D vs V_{DS} for various V_{GS}) should also be obtained and presented. Both transfer and output characteristics should be acquired with forward and backward sweeps to measure any hysteresis effects (due to charge trapping, etc.). The contact resistance, R_C, is critical to represent

device performance. The transfer length method (TLM) is a commonly used method of extracting R_C and the resistivity of the channel material, which requires a series of FETs with different contact spacings. The contact spacings in the TLM should range from "short" (dominated by R_C) to "long" (dominated by channel resistance) in order to extract reliable information. R_C should be evaluated at a variety of V_{GS} (to assess possible contact gating behavior) and V_T should be separately estimated for each channel length. In order to properly benchmark emerging devices, the device performance must be compared under the same or similar conditions. Typically, one performance metric depends on multiple parameters. For example, the saturated drain current (I_{Dsat}) depends on the carrier concentration, *n,* in the channel, and two reported devices might have the same I_{Dsat} at the same *n*. But I_{Dsat} also depends directly on the device geometry (and R_C, etc.). Benchmarking plots (besides benchmarking tables) are suggested to improve device comparisons and highlight the features of newly reported devices. In order to gain a complete view of device performance, multiple parameters must be considered when interpreting benchmarking plots; therefore, it is critical that all key parameters are annotated on a benchmarking plot. For emerging FETs to be reliably compared, the research community needs to adopt more complete and uniform standards for reporting and benchmarking FET parameters. Our consensus guidelines will help promote an improved approach for assessing device performance in emerging FETs, thus aiding the field to progress more appropriately and meaningfully.

3:15 PM X02
Accumulation-Type Ohmic Contacts Between Degenerately Doped and Nearly Intrinsic 2D Semiconductors Kraig Andrews[1], Upendra Rijal[1], Arthur Bowman[1], Michael Koehler[2], Jiaqiang Yan[2,3], David Mandrus[2,3], Pai-Yen Chen[4] and Zhixian Zhou[1]; [1]Wayne State University, United States; [2]The University of Tennessee, Knoxville, United States; [3]Oak Ridge National Laboratory, United States; [4]University of Illinois at Chicago, United States

Two-dimensional (2D) semiconductors such as transition metal dichalcogenides (TMDs) have captivated the attention of the scientific community for about a decade now because they have demonstrated a multitude of desirable properties for flexible electronics and optoelectronics. However, a major materials challenge of 2D semiconductors is that they tend to form a substantial Schottky barrier (SB) with most metals used for making electrical contacts, severely limiting both the fundamental research and electronics/optoelectronics applications of 2D semiconductors. Efforts to eliminate/minimize the SB by selecting contact metals with high (low) work function for holes (electrons) have been hampered by the nearly ubiquitous presence of Fermi-level pinning. Van der Waals (vdW) contacts have recently emerged as a promising contact-engineering strategy to minimize the Fermi-level pinning effect at the metal/2D semiconductor interface. Electrical contacts formed by transferring prefabricated metal electrodes onto 2D semiconductors demonstrated SB heights (SBHs) approaching the Schottky-Mott limit, which was attributed to the minimization of structural and chemical defects at the interface by avoiding direct metal deposition on the 2D semiconductors. However, these contacts are still depletion-type with a notable positive SBH even when the work function of metal is significantly larger than the ionization energy of 2D semiconductors indicating that Fermi-level pinning is still present. To date, accumulation-type ohmic contacts completely free of a SB have not been experimentally demonstrated in 2D semiconductor FET devices to the best of our knowledge.
We report the realization of accumulation-type vdW Ohmic contacts between nearly intrinsic WSe_2 and degenerately *p*-doped MoS_2 (p^+-MoS_2). Dual-gated WSe_2 field-effect transistors (FETs) with p^+-MoS_2 bottom-contacts were fabricated as a test structure to demonstrate true Ohmic contacts free of a Schottky barrier without the need of electrostatically gating the contact regions. Despite that the back-gate electric field is screened by the p^+-MoS_2 bottom-contacts and the nearly intrinsic nature of WSe_2, these devices exhibit ohmic behavior and similarly high performance in the back-gate as well as in the top-gate configuration (with the other gate grounded), including linear output characteristics, a high on/off ratio of 10^8, and two-terminal extrinsic field-effect mobility exceeding 130 $cm^2V^{-1}s^{-1}$ at room temperature, which approaches the intrinsic mobility of few-layer WSe_2 (~ 200 $cm^2V^{-1}s^{-1}$) with further reduction of the series resistance of excess p^+-MoS_2. The observed ohmic behavior persists to low temperatures. Theoretical modeling shows that a p^+-MoS_2/WSe_2 junction effectively acts as an accumulation-type metal/semiconductor ohmic contact, as signified by an extremely thin depletion region of ~ 1nm in the p^+-MoS_2 side of the junction and that a substantial accumulation layer of free holes in the WSe_2 side. The accumulation-type ohmic contacts between p^+-MoS_2 and WSe_2 is further verified by the results of dual-gated measurements. We attribute the accumulation-type ohmic contacts to nearly ideal metal-semiconductor interface of a vdW junction consisting of 2D materials with similar crystalline and electronic structures, where the SBH is dictated by the Schottky-Mott rule. Because the work function of p^+-MoS_2 (acting as a 2D metal) is slightly larger than the ionization energy of WSe_2 as verified by X-ray photoelectron spectroscopy (XPS), a strong hole accumulation region develops in WSe_2 at the vdW interface as predicted by the Schottky-Mott rule. The 2D vdW contacts with negligible Fermi-level pinning can also be used as the baseline to study the mechanism of Fermi-level pinning at the metal/2D-semiconductor interface.
*****This work was partially supported by NSF (DMR-2004445; ECCS-1849578) and the Kaskas Scholarship Funds.

3:30 PM X03
Why Two-Dimensional Semiconductors Generally Have Low Electron Mobility Yuanyue Liu; University of Texas at Austin, United States

Atomically thin (two-dimensional, 2D) semiconductors have shown great potential as the fundamental building blocks for next-generation electronics. However, all the 2D semiconductors that have been experimentally made so far have room-temperature electron mobility lower than that of bulk silicon, which is not understood. Here, by using first-principles calculations and reformulating the transport equations to isolate and quantify contributions of different mobility-determining factors, we show that the universally low mobility of 2D semiconductors originates from the high "density of scatterings," which is intrinsic to the 2D material with a parabolic electron band. The density of scatterings characterizes the density of phonons that can interact with the electrons and can be fully determined from the electron and phonon band structures without knowledge of electron-phonon coupling strength. Our work reveals the underlying physics limiting the electron mobility of 2D semiconductors and offers a descriptor to quickly assess the mobility. **Ref:** Long Cheng, Chenmu Zhang, and Yuanyue Liu, Phys. Rev. Lett. 125, 177701 (2020)

3:45 PM X04
(Student) Transition Metal Dichalcogenides (TMDCs) Heterostructures Field Effect Transistors (FETs) Fabricated by Sequential Chemical Vapor Deposition (CVD) Lun Jin, Rui Ma and Steven J. Koester; University of Minnesota Twin Cities, United States

Transition metal dichalcogenides (TMDCs) are considered promising channel materials in future sub-5nm transistors due to their atomic-scale thickness, dangling bond-free surface and excellent electrical properties. However, the large contact resistance at the source/drain interface is still a critical issue that limits 2D TMDCs device performance. The contact resistance is affected by the Schottky barrier height (SBH) between the TMDC and the metal contact. Various contact engineering approaches

have been explored to lower the SBH, such as optimizing the contact metals, chemical doping, plasma treatments, phase engineering, and others. One of the advantages of TMDCs in this regard is that many can exist in either a metallic or semiconducting phase, which, a property that can be used to. In our previous work, a lateral homojunction of semiconducting 2H-$MoTe_2$ and metallic 1T'-$MoTe_2$ was synthesized *in-situ*. FETs made on these homojunctions demonstrate an improvement of device performance due to substantially decreasing of the contact resistance compared to direct metal/2H contacts. Those results showed that the SBH of the 1T'/2H contact was much lower than the metal/2H interface. However, *in-situ* grown homojunctions lack controllability and scalability which limits its applications in TMDCs based devices. Here, we characterize sequential CVD techniques that can be generalized to any combination of TMDC materials. To date, we characterized sequentially-grown 1T'/2H homojunctions where the 1T' material is $MoTe_2$ and the 2H material is $MoTe_2$, MoS_2 and WS_2. In all of these structures, the 2H material was first synthesized by CVD on a SiO_2/Si substrate, then metallic 1T'-$MoTe_2$ was synthesized by flux-controlled tellurization of molybdenum thin film. The technique shows capability of integration different TMDCs into heterostructures with controllability and compatibility with CMOS fabrication technique which is critical for both technological applications and fundamental sciences. The technique can both be applied to vertical or lateral heterostructures as well. In this paper, we will describe Raman spectra that show two distinct regions of TMDCs which indicates a successful integration of the differing TMDCs materials. We also describe FET made on the sequential-grown $MoTe_2$ homojunctions, which show comparable electrical performance with the previously reported in-situ-grown $MoTe_2$ homojunctions. 2H-MoS_2/1T'-$MoTe_2$ and 2H-WS_2/1T'-$MoTe_2$ heterostructures also show operational devices which indicates the potential to extend the technique to other TMDCs materials.

4:00 PM X05
(Student) Toward Universal 2D Memory—Conductive-Point Resistive Switching in Non-Metallic Atomic Layers Xiaohan Wu[1], Ruijing Ge[1,2], Deji Akinwande[1] and Jack C. Lee[1]; [1]The University of Texas at Austin, United States; [2]Micron Technology, Inc., United States

In the last two decades, two-dimensional (2D) materials have drawn much attention as a promising candidate in the next-generation electron devices, optoelectronics and bioelectronics. Non-volatile resistive switching (NVRS) is a widely available effect in transitional metal oxides, also known as memristors, of broad interest for memory technology and neuromorphic computing. The memristor represents an emerging memory device where the device resistance can be modulated between a high resistance state (HRS) and a low resistance state (LRS) via an electrical field. Recently, this NVRS phenomenon has been observed in various multilayer 2D materials, including graphene oxide, functionalized or partly oxidized TMDs, multi-layer hexagonal boron nitride (h-BN), and degraded black phosphorus (BP). Nevertheless, the monolayer 2D materials were believed not to exhibit the NVRS effect in vertical device structure due to excessive leakage current. In 2018, we reported the first demonstration of NVRS in monolayer MoS_2 sandwiched between two metal electrodes, substantially reducing the interelectrode distance to sub-nanometers, and resulting in the thinnest memory cells with smaller switching voltages (0.5V- 3V) and higher density prospects. In our most recent work, we expanded the collection of 2D atomic sheets showing NVRS to a dozen materials, including transition metal sulfides (MS_2, M=Mo, W, Re, Sn), transition metal selenides (MSe_2, M=Mo, W, Re, Sn, Pt), a transition metal telluride ($MoTe_2$), a TMD heterostructure (WS_2/MoS_2) and an insulator (h-BN), indicating its potential universality in ultra-thin non-metallic 2D materials. These 2D-based NVRS devices exhibit low switching voltage (<1 V), large on/off ratio (>10^6), fast switching speed (<20 ns), and forming-free characteristics. The difference among various 2D materials may be hidden behind device-to-device and cycle-to cycle variations, a long-standing intrinsic challenge of NVRS devices due to the stochastic nature of the switching process. Further advances in 2D materials growth, fabrication optimization and testing protocol are expected to reduce material variability and promote comprehensive performance comparison of the listed materials. Moreover, we proposed the Dissociation-Diffusion-Adsorption (DDA) model to describe the common mechanism behind bipolar NVRS in 2D crystalline monolayers, a model supported by density functional theory (DFT) calculations showing favorable adsorption of metal atom/ion into native defects (e.g. sulfur vacancy in MoS_2). First, with external bias, metal ions/atoms can be dissociated from the electrodes. The metal ion(s) adsorb into intrinsic defect(s) in the 2D film. Electrons will transport through the metallic conductive point at the vacancy site, leading to a lower resistance state. To experimentally support the Dissociation-Diffusion-Adsorption model, STM measurements were performed and showed direct evidence of the metal ion substitution into a sulfur vacancy during the resistive switching process. This conductive-point random access memory (CPRAM) effect, in contrast to conductive-bridge random access memory (CBRAM) in bulk materials, alludes to a unique feature in ultra-thin 2D materials with atomic-level resistance control. Our work elucidates a broad library consisting of various 2D atomic sheets with different electronic, thermal, and mechanical properties for applications including high-density memory, neuromorphic computing, flexible nanoelectronics and radio-frequency (RF) switches.

4:15 PM BREAK

4:45 PM X06
Rapid Detection of COVID-19 via Epitaxial Graphene Based Sensor Soaram Kim[1,2], Heeju Ryu[3], Sheldon Tai[4], Michael Pedowitz[1,2], Donald Milton[4], Rachel Myers-Ward[5] and Kevin Daniels[1,2]; [1]University of Maryland, United States; [2]Institute for Research in Electronics and Applied Physics, United States; [3]Fred Hutchinson Cancer Research Center, United States; [4]University of Maryland School of Public Health, United States; [5]US Naval Research Laboratory, United States

On March 12, 2020, COVID-19 was classified as a pandemic by the World Health Organization (WHO), an emerging human infectious disease that causes respiratory illnesses of varying severity from the common cold to fatal pneumonia in both humans and animals [1]. As of January 24, 2021, more than 98,000,000 cases of COVID-19 have been confirmed around the world, resulting in 2,000,000 deaths, while about 52% of cases have resulted from the United States of America (USA), and the total deaths in the USA are about 1,000,000 [2]. The current primary diagnosis of COVID-19 is real-time reverse transcription-polymerase chain reaction (RT-PCR), which is the fastest and most reliable method, spreading around the world. However, the RT-PCR needs an RNA preparation process, which causes a decrease in accuracy and sensitivity and takes over three hours to complete the diagnosis of COVID-19. Thus, the direct detection of viral antigens from human to environmental conditions without the RNA sample preparation process is required for ultra-fast and highly accurate immunological diagnostic methods in the future. Two-dimensional (2D) materials such as graphene are promising for the next generation of electronics, i.e., biological and chemical sensors in environmental and safety monitoring and medical health care systems [3]. Also, atomically thin 2D graphene has an extremely high surface-to-volume ratio, which is a vital sensing application parameter. Here we have fabricated a heterostructure of SARS-CoV-2 S1 spike antibodies and epitaxial graphene (EG) on 6H silicon carbide (SiC) substrate for COVID-19 detection. We have combined the advantages of high sensitivity and fast response time of graphene with the high selectivity of antibodies to develop a high sensitivity COVID-19 sensor. A schematic diagram of the fabrication procedure is shown in Fig. 1. Bilayer EG on 6H SiC

was synthesized by Si thermal sublimation [4]. After that, reactive ion etching (RIE, CF_4) was used to prepare a simple pattern, and the metal electrode (Ti/Au = 30/120 nm) was deposited using an e-beam evaporator. Then, the crosslinker and SARS-CoV-2 S1 spike antibodies were immobilized on graphene/SiC directly. Samples were investigated by atomic force microscopy (AFM), X-ray photoelectron spectroscopy (XPS), and Raman spectroscopy to confirm EG substrate integrity and its heterostructure bonding on EG. Lastly, the electrical response of the sensor was measured using the Gamry 3000 Source/Measure Unit to investigate the sensor performance with spike proteins and clinical samples. AFM images of the heterostructure on SiC is shown in Fig. 2. The heterostructure was found to immobilize well onto the EG/SiC and withstand repeated cycles of characterization measurements. Figure 3 presents the (a-c) XPS and (d) Raman results of the heterostructure immobilized EG/SiC. These results indicate that the synthesized structures are indeed EG based heterostructure with antibody/crosslinker. The prepared sensors were tested with SARS-CoV-2 S1 spike protein and clinical samples and showed an ultra-fast response at room temperature, as shown in Fig. 4. The biosensor of antibody/crosslinker prepared on EG/SiC demonstrates exceptional performance for COVID-19 diagnostics due to the synergistic combinations of antibody and EG.

References: [1] WHO. Coronavirus Disease 2019 (COVID-19): Situation Report – 52. https://www.who.int/docs/default-source/coronaviruse/situation-reports/20200312-sitrep-52-covid-19.pdf?sfvrsn=e2bfc9c0_4; [2] WHO. COVID-19 Weekly Epidemiological Update. https://www.who.int/publications/m/item/weekly-epidemiological-update---27-january-2021; [3] X. Zhou et. al. *Chem. Rev.* 115, 7944 (2015); [4] B. K. Daas et. al. *J. Appl. Phys.* 110, 113114 (2011);

5:00 PM X07

Quantitative Models of Charge Transport in Chemically Vapor Deposited Graphene on Germanium Mengistie Debasu[1], Arnab Majee[2], Robert M. Jacobberger[3], Debjit Ghoshal[3], Michael S. Arnold[3], Max G. Lagally[3] and Francesca Cavallo[1,1]; [1]The University of New Mexico, United States; [2]University of Massachusetts Amherst, United States; [3]University of Wisconsin-Madison, United States

In the last decade, self-limiting growth of large-area and monolayer graphene sheets has been demonstrated on Ge (110) substrates.[1,2] Despite the numerous reports focusing on synthesis of graphene/Ge and the amply recognized technological relevance of this materials combination to electronics, there is a limited understanding of charge transport in graphene along the graphene/Ge growth interface. A major challenge in characterizing carrier concentration and mobilities in graphene/Ge is that chemical vapor deposition (CVD) of high-quality graphene on Ge is performed at a temperature, T>900 °C. At this temperature, even intrinsic Ge has been shown to become p-type due to a large concentration of vacancies.[3,4] CVD grown graphene on Ge is thus bonded to a relatively high-conductance substrate, a feature that makes it difficult to characterize and understand the influence of graphene-Ge interactions on charge transport in this 2D system. In this work we quantify lateral charge transport in single-layer graphene grown by CVD on intrinsic Ge (110) substrates using magneto-transport measurements and mobility spectrum analysis techniques. We fabricate graphene Hall bars on Ge (110) substrates and we measure longitudinal (R_{xx}) and transverse (R_{xy}) resistance at varying magnetic field between -7 and 7 T. Maximum-entropy spectrum analysis (MESA) is then used to quantify the number of carrier types and related mobilities in graphene/Ge. The extracted carrier concentration from magneto-transport measurements and MESA are then compared to values estimated from Raman spectroscopy of graphene on Ge.

ACKNOWLEDGEMENT. Work at the University of New Mexico was supported by the U.S. Department of Energy (DOE), Office of Science, Basic Energy Sciences (BES), under Award # DE–SC0020186. Work at the University of Wisconsin-Madison was supported by the U.S. Department of Energy (DOE), Office of Science, Basic Energy Sciences (BES), under Award # DE–FG02–03ER46028. This work was performed, in part, at the Center for Integrated Nanotechnologies, an Office of Science User Facility operated for the U.S. Department of Energy (DOE) Office of Science by Los Alamos National Laboratory (Contract 89233218CNA000001) and Sandia National Laboratories (Contract DE-NA-0003525).

[1] R. M. Jacobberger, M. J. Dodd, M. Zamiri, A. J. Way, M. S. Arnold and M. G. Lagally, *ACS Appl. Nano Mater.*, 2019, **2**, 4313–4322.
[2] G. P. Campbell, B. Kiraly, R. M. Jacobberger, A. J. Mannix, M. S. Arnold, M. C. Hersam, N. P. Guisinger and M. J. Bedzyk, *Phys. Rev. Mater.*, 2018, **2**, 44004.
[3] A. Chroneos, B. P. Uberuaga and R. W. Grimes, *J. Appl. Phys.*, 2007, **102**, 83707.
[4] F. Cavallo, R. Rojas Delgado, M. M. Kelly, J. R. Sánchez Pérez, D. P. Schroeder, H. G. Xing, M. A. Eriksson and M. G. Lagally, *ACS Nano*, 2014, **8**, 10237–10245.

5:15 PM X08

(Student) Investigating the Impact of Dielectric Passivation and Metal Contacts on the Phase Change of 2D MoTe2 via Thermal Annealing Rohan Sengupta[1], Saroj Dangi[1], Sergiy Krylyuk[2], Albert Davydov[2] and Spyridon Pavlidis[1]; [1]North Carolina State University, United States; [2]National Institute of Standards and Technology, United States

$MoTe_2$ is a promising material for phase engineering since it is predicted to possess the smallest energy difference (~50 meV) between its semiconducting 2H and semi-metallic 1T' phases, as compared to other transition metal dichalcogenides (TMDs), such as MoS_2. To date, experimental 2H to 1T' phase transitions in $MoTe_2$ have been achieved through prolonged thermal annealing, controlled CVD growth, strain engineering and electrostatic doping. The application of electric fields in vertical structures has also been used to produce a distorted $2H_d$ phase. Attempts to use laser irradiation resulted in thinning down the material and creating Te vacancies. No report has been presented yet on fast, non-destructive heating as a method for phase transition. In this work, we demonstrate that passivated $MoTe_2$ can undergo a 2H to 1T' phase transition upon rapid thermal annealing (RTA) and confirm no material degradation in this approach. We also investigate the impact of different metal contacts on the ability to induce a phase change. Both 2H and 1T' $MoTe_2$ single crystals were fabricated using a Chemical Vapor Transport process. Flakes were exfoliated on 300 nm SiO_2/Si using the Scotch tape technique and passivated by 12 nm of Al_2O_3 via atomic layer deposition (ALD). XRD and Raman spectroscopy were used to confirm the initial 2H and 1T' phases. Heat treatments were applied in an RTA furnace in vacuum (~3×10^{-5} Torr) and N_2 atmosphere (~10 Torr) at temperatures up to 900 °C. The annealing schedule was: ramp up at 10 °C/s, hold at 900 °C for 10 s, passively cool down (<5 minutes). While bare flakes decomposed after annealing, the passivated $MoTe_2$ did not show a change in thickness as confirmed by AFM. Raman spectroscopy was used to monitor phase change in passivated flakes after the RTA process. The 2H to 1T' phase transition occurred at 900 °C both in vacuum and in N_2, showing no effect of ambient conditions on the transition temperature. The characteristic Raman modes of the 2H phase A_{1g} and E_{2g} at 170 cm^{-1} and 232 cm^{-1}, respectively, disappear, as the A_g mode of the 1T' phase appears at 162 cm^{-1}. The temperature required for phase change showed no thickness dependence in the range of 1-8 nm, which may be explained by the uniform heating in the RTA furnace. Back-gated $MoTe_2$ FETs with Ti/Au, Ti/Pt and Ti/W drain/source contacts were fabricated to measure the electrical conductivity (in air) of the samples before and after the heat treatment. As expected, as-exfoliated 1T'-$MoTe_2$ does not show a gate dependence, while 2H-$MoTe_2$ does. After exposing the devices to 900 °C, 2H-$MoTe_2$ flakes with Pt and Au contacts deteriorated, giving no Raman

signal, whereas flakes with W contacts retained their characteristic 232 cm^{-1} peak. The drain source current (I_{ds}) in devices with Pt and Au reduced. In contrast, despite no sign of phase change occurring per the Raman spectrum, the sample with W contacts showed an approximately 10^6 increase in I_{ds}. SEM images of the samples with Pt and Au contacts revealed a roughening of the $MoTe_2$ in proximity to the contact edges, which could be indicative of alloying or metal diffusion. This will be closely studied in future EDS scans. The $MoTe_2$-Ti/W interface, on the other hand, did not exhibit this change, but a slight discoloration could be observed on top of the $MoTe_2$ flake which could be an interfacial MoO_x layer. The increase in I_{ds} could therefore be attributed to one or more of these effects: reduction of contact resistance via annealing, the beginnings of a transition to the 1T' phase, or surface doping via the formation of a MoO_x layer, which has been reported by others. In summary, we report non-destructive phase change of passivated 2H- to 1T'-$MoTe_2$ using RTA, and demonstrate that the choice of metal contacts influences the phase change process. Further study of passivation and contact materials is thus needed to realize the potential of $MoTe_2$ as a phase change material in future applications.

5:30 PM X09
(Student) Controlled Rhenium Doping of MoS_2 Riccardo Torsi, Yu-Chuan Lin, Jacob Diamint and Joshua A. Robinson; The Pennsylvania State University, United States

Doping is fundamental to CMOS technology. While large-scale synthesis of two-dimensional transition metal dichalcogenides (2D TMDCs) is maturing, controllable and scalable doping in 2D TMDCs must be established before integration in next-generation electronic, logic-memory, and magnetic devices. While ion implantation works well for bulk and thin film silicon, it is difficult to achieve in 2D materials due to their ultrathin nature, therefore other doping methods should be explored to satisfy this technological need. Substitutional doping is a promising candidate for scalable, tunable doping of 2D TMDCs. In this work we use metal organic chemical vapor deposition (MOCVD) to synthesize high quality Re-doped MoS_2. Employing $Re_2(CO)_{10}$ as a gas-source dopant precursor within the MOCVD process, we exhibit unprecedented control over Mo-substitutional doping concentration confirmed by a combination of X-ray photoelectron spectroscopy and Time-of-Flight Secondary Ion Mass Spectrometry measurements. By being able to precisely control precursor injection, we elucidate the importance of dopant introduction timing on doping efficiency. We find that when the dopant is introduced during the nucleation stage, Re incorporated into the lattice is enhanced by ~30% compared to when the dopant is introduced exclusively in the lateral growth stage. Having optimized the substitutional doping process, we show that the dopant ionization energy is large in the monolayer limit due to both quantum confinement effects and reduced dielectric screening. The high ionization energy of Re in ML Re-MoS_2 prevents dopant activation and results in deteriorating transport properties with higher doping levels. Finally, we will discuss the impact of layer number on dopant ionization energy and carrier concentration based on scanning tunneling microscopy and spectroscopy and field-effect-transistors transfer characteristics.

5:45 PM X10
(Student) Computational Modeling of Metal Islands for Hybrid Contacts to MoS_2 Nailah Oliver and Suzanne E. Mohney; The Pennsylvania State University, United States

2D transition metal dichalcogenides (TMDs) have become a topic of intense interest due to their fascinating electronic properties at atomic thicknesses. In particular, molybdenum disulfide (MoS_2) sparks interest due to its useful semiconducting behavior for devices such as field effect transistors (FETs). As novel materials are introduced as candidates for 2D FETs, parameters such as the contact resistance must be reduced to develop devices that do not suffer from significant parasitic losses. Hybrid top/edge metal contacts, such that the metal contacts the semiconductor at both the lateral and longitudinal interfaces, are suggested to reduce the overall contact resistance. This idea is inspired by experimental observations indicating that the contact resistivity at the edge is lower than at the top[1], while top contacts contribute more effective area to aid in reducing the overall contact resistance.
This investigation aims to provide a computational model that studies the changes in overall specific contact resistance when hybrid top/edge Au contacts are prepared on MoS_2, similar to a prototype lateral contact recently demonstrated in our lab for field effect transistors[2]. COMSOL Multiphysics is used to create a resistor circuit model of the Au/MoS_2 contact. Au rectangular prisms are used to model embedded Au nano-islands, with identical edge contact resistivities applied to each surface of the prism. Control cases that examine the potential drop for a system with only a top contact or edge contact are constructed, and the numerical solution is compared to known solutions. Solutions for the potential drop and current densities across the hybrid contact are then analyzed and compared to control cases. For a fixed top contact resistivity of 10 $k\Omega*\mu m^2$, for example, edge contact resistivities between 0.01 $k\Omega*\mu m^2$ – 10 $k\Omega*\mu m^2$ were examined. Hybrid contacts with edge contact resistivities between 0.01 $k\Omega*\mu m^2$ – 1 $k\Omega*\mu m^2$ resulted in a lower overall contact resistance. Systems with smaller yet more plentiful islands also result in a lower overall contact resistance compared to systems with larger islands; however, cases where the edge contact resistivity were >1 $k\Omega*\mu m^2$ led to an increase in contact resistance. These specific trends hold for sheet resistances from 2.5 kΩ – 250 kΩ. This model will aid in the design of hybrid contacts to MoS_2 and other very thin layered semiconductors.
References
[1]M. H. D. Guimarães *et al.*, "Atomically Thin Ohmic Edge Contacts between Two-Dimensional Materials," *ACS Nano*, 2016, doi: 10.1021/acsnano.6b02879.
[2]T. N. Walter, N. Oliver, and S. E. Mohney, "Electron beam evaporated Au islands as a nanoscale etch mask on few-layer MoS2 and fabrication of top-edge hybrid contacts for field-effect transistors," *Nanotechnology*, 2021, doi: 10.1088/1361-6528/abbb4a.

SESSION Y: Devices and Materials for Power Electronics
Session Chairs: Andrew Allerman and Jennifer Hite
Thursday Afternoon, June 24, 2021

3:00 PM Y01
Study of Temperature Effect on Performance of Ultrawide Bandgap $Al_{0.4}Ga_{0.6}N$-Channel Depletion and Enhancement Mode MOSHFETs with ZrO_2/Al_2O_3 Gate Insulator Shahab Mollah, Mikhail Gaevski, Mohammad K. Hussain, Abdullah Mamun, MVS Chandrashekhar, Grigory Simin and Asif Khan; University of South Carolina, United States

Ultrawide Bandgap $Al_xGa_{1-x}N$ channel metal oxide semiconductor heterostructure field effect transistors (MOSHFETs) are promising candidates for high-power, high-temperature harsh environment applications. In our recent reports on $Al_{0.4}Ga_{0.6}N$-channel MOSHFETs with high-*k* ZrO_2 and Al_2O_3 gate-dielectrics we found that, these dielectrics introduce negative fixed charges (Q_{ox}) as high as 1-3×10^{13} cm^{-2} depleting 2DEG density of 2×10^{13} cm^{-2} causing a positive shift of threshold voltage (V_{TH}) compared to that for HFET (no gate dielectric). This is an important step toward realizing enhanced (E-) mode MOSHFET. Our data show that, ZrO_2 possesses higher Q_{ox} resulting in stronger positive V_{TH} shift in devices, while devices with Al_2O_3 demonstrate lower gate

leakage. In this work we use stack of ZrO_2/Al_2O_3 to fabricate MOSHFETs. E-mode device was realized using ZrO_2/Al_2O_3 combined with gate recess. To separate effects of dielectric charges and damage from recess process on device performance depletion (D-) mode and E-mode devices were fabricated on the same wafer. Temperature dependent V_{TH} instability of these MOSHFETs were studied and potential mechanism for this V_{TH} instability is discussed. The pseudomorphic device structure was grown using metalorganic chemical vapor deposition on a AlN/ sapphire template. A graded composition ($Al_xGa_{1-x}N$, x=1-0.4) back barrier was grown to reduce internal stress and improve gate control in the devices[i], [ii] while the top 20 nm graded n-$Al_xGa_{1-x}N$ (x from 0.6 to 0.3) was grown to facilitate ohmic contacts. The contact resistance was as low as 1.7 Ω-mm and the 2DEG sheet resistance was ~1900 ohm/sq. Device processing details published elsewhere.[iii] The fixed gate-length $L_G \approx 2.0$ µm, source to drain spacing, L_{SD}=6 µm, were used for regular devices with 15 µm channel width, while for precise C(V,T,f) measurements we use a test structure with gate area 200x80 µm^2 . The combination of gate recessing and ZrO_2/Al_2O_3 stack resulted in V_{TH} shift of +12.2 V from D to E-mode device. The peak DC currents for D and E-mode devices were found to be 1.1 A/mm and 0.48 A/mm respectively at gate voltage +12 V while in the pulse mode it was 1.3 A/mm and 0.53 A/mm. The gate leakage current in both D and E-mode MOSHFETs is suppressed by ~3 orders of magnitude compared to that of MOSHFETs using singe Al_2O_3 or ZrO_2 layer. ON/OFF ratio as high as 3×10^8 was achieved which is higher than ~2 orders of magnitude than that for Al_2O_3 or ZrO_2. Temperature dependent V_{TH} and gate leakage study was performed on the fabricated MOSHFETs. It has been found that, from RT to 150 °C there is V_{TH} shift of + 1.7 V and -2.9 V for D- and E-mode MOSHFETs respectively. The V_{TH} shift for similar device having Schottky gate HFET was found to be significantly smaller, +0.2 V which indicates that the V_{TH} shift in MOSHFETs is mainly due to the charges in dielectric or at dielectric-barrier interface. In the E-mode devices, the effective channel mobility (µ) and V_{TH} was additionally affected by radiative defects introduced during gate-recess. µ in D-mode devices decreases with temperature while it increases for the E-mode devices. Temperature dependent interface state density ($D_{IT}(T)$) and Q_{ox} (T) were estimated using frequency- dependent C-V measurements. Our analysis show that in D-mode device, $Q_{ox}(T)$ dominates over $D_{IT}(T)$. These fixed negative charges (Q_{ox}) deplete the channel giving a total V_{TH} shift of +1.7 V. The extracted SS values of 99 mV/decade (D-mode) and 134 mV/decade (E-mode) indicate an increased density of D_{IT} at the recessed interface in E-mode device. In E-mode, the D_{IT} value is comparable to Q_{ox} thus compensating the temperature effect on Q_{ox} and making the V_{TH} more negative.

[i]) G. Simin et al., Jpn. J. Appl. Phys., **40**, L1142 (2001).
[ii]) C. Ren et al., J. Semicond. **36**, 014008-1 (2015).
[iii]) S. Mollah et al., Appl. Phys. Express. 14, 014003 (2021).

3:15 PM Y02
(Student) Hybrid $BaTiO_3/SiN_x$/AlGaN/GaN Schottky Barrier Diodes with Low Turn-On and High Breakdown Performance
Mohammad Wahidur Rahman, Towhidur Razzak, Hareesh Chandrasekar and Siddharth Rajan; The Ohio State University, United States

IHigh breakdown field of wide bandgap semiconductors such as GaN makes them attractive for high voltage switching applications. Practical realization of such material breakdown field within a device requires p-n junction, and turn-on voltage comparable to the bandgap of GaN. However, the on-state power loss due to PN diode turn-on voltage can be typically larger than series resistance losses at voltage below 3.2 kV. Schottky barrier diode (SBD) provides the advantage of low turn-on voltage, but the maximum field achievable is limited by metal/semiconductor barrier height. Recently, it was shown that high dielectric permittivity heterojunctions reduce field at metal Schottky barrier [1] and make electric fields more uniform in the depletion region, thus enabling higher average fields and breakdown voltage [2]. However, introduction of high permittivity dielectrics can also increase turn-on voltage of SBD. In this work, we show a hybrid SBD where forward characteristics are determined by metal-semiconductor junction, and reverse characteristics and breakdown are determined by metal/dielectric/semiconductor junction. We show that such hybrid SBD can significantly improve breakdown performance with average breakdown field up to 1.89 MV/cm with reduced turn-on of 0.47 V and enable state-of-art power switching figure of merit for GaN lateral SBDs. Two samples of MOCVD grown 20 nm $Al_{0.25}Ga_{0.75}N$/GaN on SiC, were used for this study. Processing of circular SBD structure was started with ICP-RIE mesa isolation. For high permittivity SBD, 10 nm SiN_x was deposited by PECVD, followed by 160 nm $BaTiO_3$ (BTO) deposition by RF sputtering at 670°C. Then BTO and SiN_x were removed from both anode and cathode regions. Cathode (Ti/Al/Ni/Au) metal was deposited using e-beam evaporation on both samples. Then 170 nm SiN_x was deposited by PECVD on low permittivity SBD and subsequently removed from anode region. Finally, anode (Ni/Au) metal was deposited after etching of 25 nm AlGaN/GaN layer. Dielectric constant of deposited BTO film was estimated to be ~70 from the accumulation region of C-V curve. Hall measurements show that sheet carrier concentration, mobility, and sheet resistance are 8.5×10^{12} cm^{-2}, 1810 cm^2/Vs, and 402 Ω/■ for SiN_x SBD and 7.3×10^{12} cm^{-2}, 1780 cm^2/Vs, and 482 Ω/■ for BTO/SiN_x SBD. Forward characteristics show turn-on voltage (V_{on}) of 0.45 V and 0.47 V for SiN_x and BTO/SiN_x SBDs, respectively. To include V_{on}, total resistance (rather than differential resistance) of both sets of diodes were measured at 100 mA/mm of forward current and calculated specific on-resistance of devices with anode to cathode distance (L_{AC}) of 4/5/6 µm devices were measured to be 0.43/0.56/0.71 mΩ.cm^2 for SiN_x SBDs and 0.44/0.57/0.72 mΩ. cm^2 for BTO/SiN_x SBDs. Reverse characteristics were measured to estimate breakdown voltage (V_{BR}) using criterion of 1 mA/mm. Estimated V_{BR} were 290 V (4 µm), 360 V (5 µm), and 430 V (6 µm) for SiN_x SBDs, corresponding to average electric fields (E_{avg}) of 0.71~0.73 MV/cm. V_{BR} was measured to be 756 V (4 µm), 822 V (5 µm), and 892 V (6 µm) for BTO/SiN_x SBDs, corresponding to E_{avg} of 1.89~1.48 MV/cm. This 2.1~2.6 times increment of V_{BR} in BTO/SiN_x SBDs is due to reduction in leakage and peak electric fields due to the dielectric superjunction effect of the high permittivity dielectric. E_{avg} of 1.89 MV/cm in L_{AC} of 4 µm BTO/ SiN_x SBD represents highest breakdown field reported to date for lateral GaN SBDs for such low V_{on} (0.47 V). To benchmark these results, total on-resistance was compared with other reported lateral GaN SBDs. The reported result is among the best to date and shows that field management enabled by high permittivity dielectrics can provide significant performance improvement in lateral high voltage III-Nitride devices.

Acknowledgment: Authors acknowledge funding from Texas Instrument

[1] Z. Xia, et al. Appl. Phys. Lett. 115, 252104 (2019)
[2] Z. Xia, et al. IEEE-TED, 66, 896 (2019)

3:30 PM Y03
(Student) Re-Engineering of Transition Layer to Achieve Record-High Breakdown Field of 2.05 MV/cm for a Buffer Thickness of 1. 65 µm of AlGaN/GaN HEMT on Si
Nayana Remesh, Anirudh Venugopalrao, Srinivasan Raghavan, Muralidharan R and Digbijoy Nath; Indian Institute of Science, India

AlGaN/GaN HEMTs on silicon are finding rapid market penetration for power switching applications due to their superior performance, low cost, and scalability, but the challenges in terms of material quality and device performance namely, current collapse and reduced reliability due to permanent breakdown remain to be addressed. The presence of vertical leakage paths due to extended defects like threading dislocations are another major bottleneck in the electrically insulating nature of the epitaxial stack. Apart from these extended defects, morphological defects

like V-shaped pits originate from the AlN/Si interface and propagate vertically to the active area leading to device degradation resulting in breakdown voltage (higher leakage current) below theoretically achievable limits of GaN.
In the present study, we report the study of step-graded AlGaN transition layers (TL) in MOCVD-grown GaN HEMT-on-silicon towards improving the breakdown field. The transition layers include three AlGaN epi-layers of 75%, 50%, and 25% Al-content, down-graded from bottom to top. The growth temperature and carbon doping are varied independently to assess the role of the transition layer in reducing the vertical as well as lateral leakage current. While the introduction of high temperature (HT) AlGaN layers is found to alleviate the density of V-pits resulting in the reduction of vertical leakage but increases lateral leakage current. Temperature-dependent data indicate that the increased lateral (mesa) leakage current in HT AlGaN layers is due to space charge limited current, the activation energy of which yields the positions of the defect states within the bandgap. The increase in buffer leakage current in HT AlGaN layers is attributed to the formation of point defects such as Oxygen in Nitrogen site (O_N) and V_{Ga}-O_N complexes. The introduction of C-doping in the top AlGaN transition layer with 25% Al-content helps to reduce lateral leakage in both mesa and 3-terminal configurations. The combination of HT AlGaN (75% Al-content) with C-doped AlGaN (25% Al-content) is found to be the optimal TL design that enabled a vertical breakdown field of 2.05 MV/cm defined at 1 A/cm^2 for a buffer thickness of 1.65 µm, which is record high breakdown field for thin buffer.

3:45 PM Y04
(Student) Carrier Dynamics in Dry-Etched-and-Regrown Nonpolar M-Plane GaN p-n Diodes—A Small-Signal RF Analysis Andrew A. Aragon, Arman Rashidi, Farnood Mirkhosravi, Morteza Monavarian and Daniel Feezell; The University of New Mexico, United States

Small-signal RF measurements were conducted to evaluate the effects of dry-etching on regrown *m*-plane (10-10) GaN *p-n* diodes. Rate equations considering carrier diffusion and recombination processes were used to derive an equivalent small-signal circuit model for the GaN *p-n* diodes. The *p-n* diodes were measured with a network analyzer (NA) utilizing a small signal (-20 dBm) superimposed on a range of DC voltages (-10 V to 10 V) for various frequencies (500 kHz – 2 GHz). Expressions for the input impedance response of the circuit were fit to the real and imaginary parts of the measured impedance reflection coefficient (S11). The fitting of the circuit model produces extracted circuit parameters such as series resistance, differential diode resistance, and capacitance, from which the minority carrier lifetimes can be determined. These parameters are compared for etched-and-regrown diodes and continuously grown diodes. For example, from current-density vs. voltage (*J-V)* results, the continuously grown *p-n* diodes show the lowest reverse leakage current density of ~ 1×10^{-6} A/cm^2 at -10 V. In comparison, the etched-and-regrown *p-n* diodes indicate an influence of the dry-etch process on current leakage with a factor of ~ $1x10^8$ larger reverse current density (~ 100 A/cm^2 at -10 V) compared to that of continuously grown *p-n* diodes. Additionally, the etched-and-regrown *p-n* diodes have a higher leakage current density than the continuously grown *p-n* diodes just below turn on (~ 2 A/cm^2 compared to ~1×10^{-6} A/cm^2) at 1.8V. Leakage mechanisms in etched-and-regrown *p-n* diodes were also analyzed from the extracted circuit elements. Series resistance and differential diode resistance values correlate with differential resistances obtained from DC *J-V* curves. Furthermore, the extracted differential resistances are coupled with extracted capacitance values to obtain minority carrier lifetimes, which are not obtained with typical DC methods. Minority carrier lifetimes determined from the capacitance and differential diode resistance in etched-and-regrown *p-n* diodes are substantially lower (~ 4.8×10^{-8} s at 1.8V) than continuously grown *p-n* diodes (~ 1.3×10^{-6} s at 1.8V) below turn-on. Minority carrier lifetimes are also lower in etched-and-regrown *p-n* diodes (~3.8×10^{-9} s) compared to continuously grown *p-n* diodes (~1.6×10^{-6} s at -10V) under reverse bias. The differences in minority carrier lifetimes are attributed to differences in recombination and diffusion currents which contribute to current leakage in the presence of deep-level defects associated with dry-etching. The method and analysis presented are relevant to the understanding of leakage currents and minority carrier lifetimes in etched-and-regrown junctions, which will be components of next generation high-power electronic devices utilizing selective-area regrowth on GaN. The information, data, or work presented herein was funded in part by the Advanced Research Projects Agency—Energy (ARPA-E), U.S. Department of Energy (DOE) under the PNDIODES program directed by Dr. Isik Kizilyalli. Sandia National Laboratories is a multimission laboratory managed and operated by National Technology and Engineering Solutions of Sandia, LLC, a wholly owned subsidiary of Honeywell International, Inc., for the U.S. Department of Energy's National Nuclear Security Administration under Contract No. DE-NA-0003525. The views expressed in the article do not necessarily represent the views of the U.S. Department of Energy (DOE) or the United States Government.

4:00 PM Y05
(Student) Development of III-Nitride Superjunctions Dennis E. Szymanski[1], Dolar Khachariya[1], Andrew J. Klump[1], Ke Wang[1], Yan Guan[1], Pramod Reddy[2], Seiji Mita[2], Ronny Kirste[2], Spyridon Pavlidis[1], Erhard Kohn[1], Ramón Collazo[1] and Zlatko Sitar[1]; [1]North Carolina State University, United States; [2]Adroit Materials, United States

As silicon technology reaches its practical and theoretical limit, III-nitride materials offer a promising alternative to maintain the growing demand for high power electronic devices. Current GaN devices already show promising results, offering higher breakdown voltages and reduced on resistances compared to their silicon predecessors. However, these devices are still limited by the classical Baliga figure of merit (BFOM). In order to surpass the BFOM, novel device geometries have been introduced such as the superjunction (SJ). The concept of the SJ has been demonstrated in silicon, with devices such as CoolMOS which have surpassed the BFOM. To date, there are no demonstrations of III-nitride SJs in the literature. In order to achieve III-nitride SJs, there are several research barriers to address. First, the necessity for alternating, lateral n- and p-type doping regions with zero net charge. The inherent polar doping selectivity of GaN can be used to achieve the doping scheme for a lateral GaN p/n junction. Oxygen, which unintentionally incorporates into N-polar GaN at levels >10^{19} cm^{-3}, acts as the n-type dopant, whereas Ga-polar GaN does not readily incorporate oxygen. Accordingly, lateral polarity junctions (LPJs) with alternating domains of O doped N-polar and Mg doped Ga-polar GaN have been fabricated to realize lateral p/n junctions. Second, the proper doping profiles must be attained in the N- and Ga-polar domains for SJ operation. For drift regions, the n-type doping in the N-polar domain (and p-type doping in Ga-polar domain) must be reduced to ~10^{17} cm^{-3} for micron wide domains. By implementing the chemical potential control (CPC) framework, MOCVD process conditions were designed in order to decrease the oxygen concentration by increasing the growth supersaturation. This led to a reduction in oxygen from >10^{19} cm^{-3} to low 10^{17} cm^{-3}. Third, due to the difficulty of making reliable Schottky contacts to the N-polar surface, the alternating Schottky/ohmic contacts on a typical superjunction are replaced with alternating p^+/n^- junction (N-polar) and p^+/p^- junctions (Ga-polar). In this direction, a N-polar p/n junction with rectifying behavior comparable to a Ga-polar p/n junction was achieved. Finally, the growth of a GaN LPJs must exhibit N-/Ga-polar domains with a smooth surface and equal growth rates. It is understood that supersaturation can be used to control the surface morphology, relative growth rates, and defect incorporation of the domains. However, the high supersaturation required to realize the necessary doping profile for

SJ operation contradicts the intermediate supersaturation conditions required to obtain a smooth surface morphology and equal domain growth rates. It must be noted that high supersaturations result in low O N-polar dominated growth, and low supersaturations in Ga-polar dominated growth. To overcome these anticorrelated requirements, we demonstrate a supersaturation modulated growth (SMG) where the V/III ratio, and thus supersaturation, was modulated between low and high values. A GaN LPJ with a smooth surface and equal domain heights, with the necessary doping profile is hence demonstrated.

4:15 PM BREAK

4:45 PM Y06
(Student) Deep-Level Optical Spectroscopy in Wet-Treated Etched-and-Regrown Nonpolar M-Plane GaN Vertical Schottky Diodes Andrew A. Aragon[1], Morteza Monavarian[1], Greg Pickrell[2], Mary H. Crawford[2], Andrew Allerman[2], Daniel Feezell[1] and Andrew M. Armstrong[2]; [1]The University of New Mexico, United States; [2]Sandia National Laboratories, United States

Deep level defects induced by inductively coupled plasma (ICP) dry etching in wet-treated and untreated etched-and-regrown n-type unipolar Schottky diodes on nonpolar *m*-plane GaN are evaluated using steady-state photocapacitance (SSPC). Lighted capacitance–voltage (LCV) was also used to measure the depth profile of defect concentrations in the diodes. The current density–voltage (J–V) characteristics of the ICP etched-and-regrown Schottky diodes show the highest reverse leakage of (~3×10^{-2} A/cm^2 at −10 V) of all samples studied with ~1000× increase in the reverse leakage compared to a continuously grown Schottky diodes (~$4 \times 10-5$ A/cm^2 at −10 V). Increased defect concentrations are observed for deep levels at Ec – 1.9 eV, Ec – 2.9 eV, and Ec – 3.3 eV, where Ec is the conduction band minimum, of etched-and regrown Schottky diodes compared to continuously grown Schottky diodes. Deep level depth profiling of an etched-and-regrown sample shows that the concentration of the defect-related SSPC features associated with dry etching depend strongly on the distance away from the regrowth interface.
Defect levels associated with regrowth without an etch were also investigated. Current leakage in these devices show an ~100× larger reverse J compared to that of the continuously grown devices (~3×10^{-3} A/cm^2 compared to ~4×10^{-5} A/cm^2 at −10 V). From depth profiling, the defects in the regrown structure (without an etch) are shown to be highly spatially localized to the regrowth interface. A photoelectrochemical etching (PEC) method and a wet AZ400K treatment reduced the etch-induced deep levels. A significant reduction in the density of deep levels is observed in the samples that were treated with AZ400K and PEC etching after dry etching and prior to regrowth. Additional testing of AZ400K wet-treated ICP etched and regrown diodes shows a reduction in the reverse leakage current (~1×10^{-3} A/cm^2 at -10 V) compared to the ICP etched and regrown diodes. Further comparison of the ICP etched and subsequent PEC etched-and-regrown diode shows further reduction of the reverse J (~3×10^{-4} A/cm^2). The wet treatments performed on ICP etched and subsequent-regrown *m*-plane GaN Schottky diodes show reduction of deep level defects and reduced current leakage which is advantageous for applications in selective-area doping for vertical power switching structures with complex geometries. The information, data, or work presented herein was funded in part by the Advanced Research Projects Agency—Energy (ARPA-E), U.S. Department of Energy (DOE) under the PNDIODES program directed by Dr. Isik Kizilyalli. Sandia National Laboratories is a multimission laboratory managed and operated by National Technology and Engineering Solutions of Sandia, LLC, a wholly owned subsidiary of Honeywell International, Inc., for the U.S. Department of Energy's National Nuclear Security Administration under Contract No. DE-NA-0003525. The views expressed in the article do not necessarily represent the views of the U.S. Department of Energy (DOE) or the United States Government.

5:00 PM Y07
(Student) X-Ray Topography Characterization of Selective Area Doping of Gallium Nitride Epitaxial Layers for Power Electronic Devices Development Yafei Liu, Hongyu Peng, Tuerxun Ailihumaer, Qianyu Cheng, Zeyu Chen, Shanshan Hu, Balaji Raghothamachar and Michael Dudley; Stony Brook University, The State University of New York, United States

The development of wide bandgap semiconductor, Gallium Nitride (GaN) for applications in power electronic devices such as inverters and switches is attracting considerable interest. While most GaN power device development is devoted toward lateral architectures, such as HEMTs that are fabricated in thin layers of GaN grown on foreign substrates such as sapphire, the development of vertical architectures on bulk GaN substrates can help realize the advantages of GaN. To realize this, several selective area doping approaches are being developed. These include ion implantation [1], etching and regrowth method [2, 3], diffusion doping and neutron transmutation [4]. However, the influences of these procedures on the microstructures of GaN epitaxial layers is one of the key factors to determine the performance of the devices. To understand the microstructural impact, in this study, GaN epitaxial layers subjected to these doping processes have been characterized at each step of the procedure. Techniques for characterization include by synchrotron monochromatic beam X-ray topography (SMBXT) [5], High-resolution X-ray Diffraction (HRXRD), synchrotron X-ray rocking curve topography [6] and other characterization techniques such as Raman spectroscopy [7]. The change of distribution of threading screw/mixed dislocations (TSDs/TMDs), threading edge dislocations (TEDs) and basal plane dislocations (BPDs) is characterized after each processing step. The comparison of lattice strain of the material from each step is conducted by both HRXRD and synchrotron X-ray rocking curve topography. Results from these studies will be discussed with their implication for development of vertical device architectures.
References:
1. S. O. Kucheyev, J. S. Williams, S. J. Pearton, Ion implantation into GaN, Materials Science and Engineering: R: Reports, 33, (2001).
2. B. Li, M. Nami, S. Wang, J. Han, In situ and selective area etching of GaN by tertiarybutylchloride (TBCl), Appl. Phys. Lett., 115, 162101 (2019).
3. R. J. Shul, L. Zhang, A. G. Baca, C. Willison, J. Han, S. Pearton, F. Ren, Inductively coupled plasma-induced etch damage of GaN pn junctions, Journal of Vacuum Science & Technology A: Vacuum, Surfaces, and Films, 18, 1139 (2000).
4. R. Barber, Q. Nguyen, J. Brockman, J. Gahl, J. Kwon, Thermal neutron transmutation doping of GaN semiconductors, Scientific Reports, 10, (2020).
5. B. Raghothamachar, M. Dudley, G. Dhanaraj, in Springer handbook of crystal growth, ed. by G. Dhanaraj, K. Byrappa, V. Prasad, M. Dudley (Springer, 2010), p. 1425
6. J. Guo, Y. Yang, B. Raghothamachar, M. Dudley, S. Stoupin, Mapping of lattice strain in 4H-SiC crystals by synchrotron double-crystal x-ray topography, J. Electron. Mater., 47, (2018).
7. Y. Han, J. Peng, B. Li, Z. Wang, K. Wei, T. Shen, J. Sun, L. Zhang, C. Yao, N. Gao, Lattice disorder produced in GaN by He-ion implantation, Nuclear Instruments and Methods in Physics Research Section B: Beam Interactions with Materials and Atoms, 406, (2017).

5:15 PM Y08
Ion Implanted Edge Termination Designs for High Current 1.2kV GaN Vertical PiN Diodes Mona Ebrish[1,2], Travis J. Anderson[1], Matthew Porter[3], Alan G. Jacobs[1], James C. Gallagher[1], Marko Tadjer[1], Robert Kaplar[4], Brendan P. Gunning[4] and Karl Hobart[1]; [1]U.S. Naval Research Laboratory, United States; [2]National Academies of Sciences, Engineering, and Medicine, United States; [3]Naval Postgraduate School, United States; [4]Sandia National Laboratories, United States

GaN is a promising material for future power semiconductor devices due to its superior material properties. Edge termination for vertical GaN power devices remains a subject of significant interest. In this work, different edge termination techniques were systematically evaluated and compared by utilizing broadband electroluminescence technique under various reverse bias conditions. Edge termination is a crucial step in power devices fabrication process, and using nitrogen implant has been reported for GaN PiN diode fabrication to neutralize active Mg dopants. In this work, nitrogen ion implantation into Mg-doped layers was used to form junction termination extension (JTE) and Guard Rings (GR). Several 2" wafers were fabricated in a high yield, large area device (1mm2) process to build 10A, 1.2kV class GaN vertical diodes on a non-homogenous freestanding GaN substrate. In silicon power devices, smoothly tapered implanted doping profiles are often achieved through a controlled diffusion of the implanted dopant islands during activation. Activation and diffusion of acceptor dopants via ion implantation is neither well controlled nor well understood in GaN, thus a compensation approach is implemented to selectively reduce the acceptor concentration of active layers formed by in-situ epitaxial doping. In this work, JTE terminations, GR termination and a combination of both were compared. We compared several devices on the same wafer type and same fabrication process but with different edge termination designs; and spatially resolved the emission spectrum, by utilizing the electroluminescence mapping technique to acquire a series of broadband images under high voltage reverse bias. There is a clear difference in the electroluminescence signature. This is the first time we systematically evaluate the design space of edge termination and observe how it impacts the high field point in the device, which will affect the transport path of the leakage current. Stress testing is in-progress to evaluate the impact of these defects on failure mechanisms. The JTE-only design shows a leakage current as a bright ring on the outer perimeter of the device active region closer to trench isolation while a GR-only design brings the leakage current near the anode, which is typically indicative of a more appropriate design to enable avalanche breakdown. A combination of both termination designs results in scattered leakage points on the outer perimeter of the device and higher breakdown voltage. TCAD simulations of the field profiles of the different structures for comparison to the EL profiles are in-progress and will be reported, along with temperature and bias stressing, in order to understand the stability of the implanted termination and its impact on reliability. This study will have an impact on the future of GaN power devices and allowing development of mature processes to compete with SiC technology.

5:30 PM Y09
(Student) Characterization of Traps in High-Growth-Rate MOCVD-Grown GaN Wenbo Li, Yuxuan Zhang, Zhaoying Chen, Hongping Zhao, Steven A. Ringel and Aaron Arehart; The Ohio State University, United States

Gallium nitride is gaining maturity for power device applications due to its wide bandgap, high breakdown field and high electron mobility. To achieve higher breakdown voltages in vertical GaN devices, both a thick drift layer and controllable low n-type doping density in the low 10^{15} cm^{-3} are needed for typical applications. Achieving higher growth rates is desirable for reduced manufacturing costs while low compensation and minimal trap densities are needed for controllable and repeatable doping. Ideally, the trap densities should be much less than the doping density because, in addition to acting as donors or acceptors and changing the doping density, the traps can change occupancy during device operation leading to changes in effective doping density with time, which will be problematic for device stability. For the focus of this study, deep level transient/optical spectroscopy (DLTS/DLOS) are used to characterize traps in metal-organic chemical vapor deposition (MOCVD) films grown with different growth rates. MOCVD samples were grown on 2 in. GaN templates with a highly n-type lateral conduction layer for improved Ohmic contact followed by a lightly doped n-type layer for Schottky contact, to support a large depletion depth, and enhance the DLTS/DLOS minimum detection limit. The samples had target doping concentrations of 5×10^{16} cm^{-3} and 8×10^{16} cm^{-3} in the depletion region for the 5 µm/hr high growth rate (HGR) and 2 µm/hr low growth rate (LGR) samples, respectively. Lower doping is being explored as well but series resistance and other factors need to be understood to characterize traps at the limit of the controlled doping range. From DLTS/DLOS characterization results, the LGR sample has a very low total trap concentration of 1.5 x10^{15} cm^{-3}, which is low compared with previous MOCVD samples [1][2], with traps at E_C – 0.25 eV (V_N-related [3]), E_C – 0.57 eV (Fe-related [4]), E_C – 1.3 eV (C-related [5]), E_C – 2.6 eV (C -related [6]) and E_C – 3.22/3.28 eV (Mg-/C-related [1][7]). The HGR sample shows no new traps, but has above four times higher total trap concentration due to the latter three traps mentioned above, which have all been associated with C. This is consistent with SIMS results as well. Despite the higher C-related defect concentrations, the higher growth rate is promising as methods to further minimize the C incorporation are being tested and will be reported. Additionally, samples using a new approach to further increase the growth rate and reduce C incorporation are being characterized and will be reported.

References

[1] A. Armstrong *et al.*, Appl. Phys. Lett. **84**, 374 (2004).
[2] K. Collins *et al.*, J. Appl. Phys. **122**, 235705 (2017).
[3] A. Arehart *et al.*, Appl. Phys. Lett. **93**, 112101 (2008).
[4] D. Cardwell *et al.*, Appl. Phys. Lett. **102**, 193509 (2013).
[5] A. Wright, J. Appl. Phys. **92**, 2575 (2002).
[6] A. Armstrong *et al.*, Appl. Phys. Lett. **88**, 082114 (2006).
[7] A. Hierro *et al.*, Appl. Phys. Lett. **77**, 1499 (2000).

5:45 PM Y10
(Student) MOCVD GaN Epitaxy with Fast Growth Rates Yuxuan Zhang, Zhaoying Chen, Wenbo Li, Steven A. Ringel, Aaron Arehart and Hongping Zhao; The Ohio State University, United States

Gallium nitride (GaN) has been considered as a promising candidate for power electronic devices due to its wide bandgap (3.4 eV), high critical electric field (3 MV/cm), and high electron mobility (>1000 cm^2/V s). As a key parameter to evaluate the performance of power devices, Baliga's figure of merit (BFOM) of GaN is more than 500X higher than silicon (Si) and 3X higher than silicon carbide (SiC) [1]. Vertical GaN PN diode with 5kV breakdown voltage (V_{BR}) has been demonstrated [2]. Although tremendous progress has been made in the past few years, achieving vertical GaN power devices with V_{BR} of 10-20 kV remains challenging. Epitaxy of high-quality GaN films with a thick drift layer, low controllable doping, and high mobility is required to advance the field. In this work, the effects of increasing GaN growth rate on the impurity incorporation, charge compensation, surface morphology, and transport properties are systematically studied. Under optimized MOCVD GaN growth condition, high-quality GaN films with controllable low net charge concentration (N_d-N_a) at 4×10^{15} cm^{-3} was demonstrated. Secondary ion mass spectroscopy (SIMS) measured [Si] and N_d-N_a as a function of SiH_4 flow rate was investigated. The compensation level at $(4.8\pm1.0)\times10^{15}$ cm^{-3} was extracted from the intercept of N_d-N_a vs. SiH_4 flow rate. Based on the capacitance-

voltage (CV) and SIMS analysis, the background [C] level was at ~ 7×10^{15} cm^{-3} (SIMS detection limit). Deep level transient spectroscopy / deep level optical spectroscopy (DLTS / DLOS) results show total electron trap concentration at ~2.5×10^{15} cm^{-3}, mainly from carbon-related deep level defects. These high-quality GaN films were grown with a typical MOCVD GaN growth rate of 2 µm/hr. MOCVD GaN epitaxy with fast growth rate at 5.2 µm/hr was achieved via increasing TMGa flow rate. With a controllable N_d-N_a at 1.5×10^{16} cm^{-3}, the SIMS measured [C] was at 2×10^{16} cm^{-3}, which is significantly increased as compared to the films grown at lower growth rates. Atomic force microscope (AFM) imaging on GaN surface shows smooth morphology with step-flow growth mode and RMS of 0.647 nm (10x10 µm scan area). The Mn incorporation from the semi-insulating ammonothermal GaN substrate into epilayer was observed from SIMS measurement. Controlled experiments show that Mn incorporation rate into epilayer is highly related to the film growth rate, sharing similar characteristics as Fe impurity. Quantitative SIMS revealed that both Mn and Fe incorporation can be suppressed with faster growth rates. Room temperature Hall measurements of GaN films show that electron mobility decreases from 852 cm^2/Vs to 604 cm^2/Vs (n~1.5×10^{16} cm^{-3}) as the growth rate increases from 2 µm/hr to 5.2 µm/hr. In summary, systematic MOCVD GaN epitaxy and materials characterization were performed to investigate the effects of GaN growth rate on background impurities incorporation, charge compensation and charge transport properties in Si-doped GaN films. The increase of GaN growth rate leads to higher background C incorporation due to the use of higher TMGa precursor flow rate, as well as the reduction of electron mobility. This is identified as the key challenge to achieving high-quality thick GaN films with low controllable doping at low-mid 10^{15} cm^{-3}. As a comparison, we will discuss the GaN film properties grown with CO_2 laser excitation introduced during the MOCVD epitaxy.
Acknowledgment: The authors acknowledge the funding support from Advanced Research Projects Agency-Energy (ARPA-E), U.S. Department of Energy (DE-AR0001036), and U.S. Department of Energy's Office of Energy Efficiency and Renewable Energy (EERE) under the Advanced Manufacturing Office, FY18/FY19 Lab Call.

SESSION Z: Solar Cell Materials and Devices
Session Chairs: Michael Scarpulla and Mark Wistey
Thursday Afternoon, June 24, 2021

3:00 PM Z01
Sulfur Passivation Effect on Low-Angle Grain Boundaries in Single-Crystal-Like GaAs Flexible Thin Film Solar Cells on Metal Tape Sara Pouladi, Sahil Sharma, Nam-In Kim, Mina Moradnia, Venkat Selvamanickam and Jae-Hyun Ryou; University of Houston, United States

We proposed and demonstrated nearly single-crystalline III-V thin films directly grown on inexpensive polycrystalline metal substrates using crystallinity-transformational buffer layers. This high-quality inexpensive III-V platform aims to address the technical and economic challenges of III-V multi-junction compound semiconductor heterostructures which are the best photovoltaic (PV) materials for high conversion efficiencies. This technology combines the efficiency advantages of high-quality III-V materials with a continuous roll-to-roll deposition process of the thin film on a low-cost tape substrate to produce flexible, cost-competitive, and high-efficiency solar cells (SCs) with application versatility. The first demonstration of flexible single-crystal-like GaAs SC delivered a promising photon conversion efficiency of ~7.6% but lower than expected performance for GaAs SC. This initial device efficiency along with the result of a 2-dimensional SC modeling revealed that the presence of low-angle grain boundaries (LA-GBs) in the single-crystal-like GaAs plays a critical role in limiting the SC performance. According to the model, effective passivation of these GBs can boost the photo-conversion efficiency ~3-4 times. Previously, we reported on a significant enhancement of photon conversion efficiency of flexible single-crystal-like GaAs SCs by trioctylphosphine sulfide (TOP:S) treatment with increases of ~24%, 12.8%, 14.5%, and 64% for *Voc*, *Jsc*, *FF*, and overall efficiency, respectively which resulted in final efficiency performance of 13.5% (two times of the previous record, 7.6%) after anti-reflection coating (ARC). In the present work, we conduct more comprehensive material and device characterizations to further understand TOP:S solution treatment effect on both the passivation of LAGBs in the single-crystal-like GaAs and SC device performance. Dark *I-V* characteristics of the flexible GaAs SCs showed that the dark saturation current decreased from J_o ~2e-3 A/cm^2 to ~3.5e-4 A/cm^2 (at V = -500 mV) after TOP:S treatment. Incident photon-to-current efficiency (IPCE) measurements are also being conducted on the passivated flexible GaAs SCs and the results will be integrated into the resulting short circuit current to be compared with the *I-V* characteristics of SC at 1 Sun AM 1.5G. Various material characterizations were conducted on the TOP:S treated single-crystal-like GaAs including photoluminescence (PL), atomic force microscopy (AFM), scanning probe force microscopy (SPFM) for potential differences at GBs which suggest that TOP:S treatment can partially passivate the energy states at GBs resulting in the efficiency performance improvement of flexible GaAs SCs. A significant enhancement of ~125% in the PL peak was observed after the treatment which indicates a significant decrease in the non-radiative recombination of carriers at the GBs. Surface potential maps of as-grown and TOP:S treated films obtained by SPFM showed that TOP:S treatment can passivate the energy states at grain boundaries and lower the potential barrier. A narrow distribution of the surface potentials, i.e., uniform surface potential, is observed from the TOP:S-treated GaAs film. Such similar potentials between the grain surface and GB surface are attributed to the passivation of defect states of dangling bonds at the GBs, resulting in the decrease of energy barrier height (or valley depth) at these regions. In order to obtain more evidence on the GBs passivation, a scanning transmission electron microscope will be employed to conduct energy-dispersive X-ray spectroscopy (STEM/EDX) on the cross-section of the TOP:S treated flexible GaAs SCs. This characterization will provide us with a map of sulfur distribution at the bulk GBs which can help in further understanding of TOP:S passivation mechanism.

3:15 PM Z02
Nanoscale Morphology of Polymer:Fullerene Blends Investigated by Photoemission Electron Microscopy Falk Niefind[1,2], Rishi Shivhare[3], Stefan C. Mannsfeld[4], Bernd Abel[5] and Mike Hambsch[4]; [1]National Institute of Standards and Technology, United States; [2]University of Maryland, United States; [3]Universität Bern, Switzerland; [4]Technische Universität Dresden, Germany; [5]Leibniz-Institut für Oberflächenmodifizierung e. V., Germany

Two of the United Nation's sustainable development goals are for *Providing Affordable & Clean Energy* and *Climate Action*. They call for a global effort to reduce the amount of greenhouse gas emissions as well as an increase in the share of renewable energy in the global energy mix.[1] Utilizing the power of the sun via photovoltaics is a prominent way of producing renewable electricity, on site without local emissions. Solar cells based on organic materials, such as polymers, can provide a pathway to large scale, low cost availability of generating electricity. However, in order to be commercially successful, the power conversion efficiency (PCE) of the complete solar cell module needs to improve.[2] Apart from the mechanical and electrical

design of the solar cell, the active film where the solar radiation is converted into an electric current plays a fundamental role. Usually, the film is composed of an electron donor and an electron acceptor component. In order to facilitate sufficient charge generation, separation and transport, the interface between the donor and acceptor component need to be as large as possible, while the respective donor and acceptor phases need to be large enough to provide an uninterrupted pathway to the electrodes. Thus, these two requirements contradict each other to a certain degree, making the optimization of the nanoscale structure, also called morphology, nontrivial.[3] An efficient, guided device optimization process relies on a fast, high resolution analysis method for the aforementioned morphology. We present a laser based, tabletop experimental set-up that leverages the nanometer scale resolution of a photoemission electron microscope (PEEM) to directly image the surface morphology of the active film in a solar cell.[4–6] We investigated different blends of poly(3-hexylthiophene-2,5diyl) (P3HT) and [6,6]-phenyl-C_{61}-butyric acid methyl ester (PCBM), a benchmark system in the organic photovoltaic (OPV) community. While proving general feasibility of such an experiment at spatial resolutions down to 50 nm, we highlight the advantages as well as the challenges of the current experimental set-up. Our results indicate a future pathway to image both active components in a single measurement set-up without the need for a synchrotron light source, as it would be needed for Scanning Transmission X-ray Microscopy (STXM), an alternative technique.[7] We found that systems composed of a P3HT:PCBM ratio close to the eutectic point exhibit a similar morphology, opposed to those further away from the eutectic point.

Acknowledgement
F.N. thanks the German Federal Environmental Foundation (DBU) for financial support. F.N. thanks Dr. Sujitra Pookpanratana for her support. All authors are indebted to Dr. Andreas Neff.

References:
1 THE 17 GOALS | Sustainable Development, https://sdgs.un.org/goals, (accessed 15 January 2021).
2 Y. Yang, K. Mielczarek, M. Aryal, A. Zakhidov and W. Hu, *ACS Nano*, 2012, **6**, 2877–2892.
3 C. R. McNeill, *Energy Environ. Sci.*, 2012, **5**, 5653.
4 A. Neff, F. Niefind, B. Abel, S. C. B. Mannsfeld and K. R. Siefermann, *Adv. Mater.*, 2017, **29**, 1701012.
5 F. Niefind, A. Neff, S. C. B. Mannsfeld, A. Kahnt and B. Abel, *Phys. Chem. Chem. Phys.*, 2019, **21**, 21464–21472.
6 F. Niefind, S. Karande, F. Frost, B. Abel and A. Kahnt, *Nanoscale Adv*, 2019, **1**, 3883–3886.
7 H. Ade and A. P. Hitchcock, *Polymer*, 2008, **49**, 643–675

3:30 PM Z03
(Student) Impact of Ar Ion Beam Milling on Metal-Halide Perovskite Solar Cells Yu-Lin Hsu[1], Kaden Powell[1], Chongwen Li[2], Yanfa Yan[2] and Heayoung P. Yoon[1,1]; [1]The University of Utah, United States; [2]The University of Toledo, United States

Metal-halide perovskite solar cells (PSCs) are the most promising photovoltaic (PV) technology owing to their cost-effective processing, tunable energy band-gaps, long carrier diffusion lengths, unique defect tolerance, and "self-healing" capabilities. Despite considerable efforts, the physical mechanisms for the inferior stability of PSCs are not well understood. Some researchers propose that structural defects are the main source of deterioration because they serve as a channel for moisture/oxygen stressors. Others claim that grain boundaries are benign, and the degradation is attributed to trapped charges in the perovskite absorber itself. A robust measurement approach that can characterize individual microstructures (e.g., grain, grain boundary, interface) is required. Focused ion beam (FIB) milling is a well-established sample preparation method that can remove the surface roughness of polycrystalline thin-films. An atomically-smooth surface allows local optoelectronic measurements of a microstructured PV with minimum artifacts from its innate rough surface. While extremely useful, high-energy ion beams (< 30 keV) irradiated on a hybrid organic-inorganic PSC may induce structural damage and/or chemical degradation. In this work, we investigate possible beam damage on PSCs prepared by focused argon (Ar) ion-beam at various doses. In addition, we use Monte-Carlo simulations to estimate the thickness of the damage layer. Our PSC devices were fabricated in a multilayer configuration: Au (60 nm) / Spiro-OMeTAD (220 nm) / $MAPbI_3$ (550 nm) / MoO_x (5 nm) / ITO (200 nm). Here, MA is methylammonium, and Spiro-OMeTAD stands for 2,2',7,7'-Tetrakis [N, N-di(4-methoxyphenyl) amino]-9,9'- spirobifluorene. We performed a series of Ar ion milling processes at room temperature (Fischione Model 1060), with the incident beam irradiated at shallow angles of 1° and 3°. The beam voltage was fixed at 4 kV, and the PSCs were milled for 5 min, 10 min, 15 min, and 20 min. At a first glance, we did not observe any notable changes with the samples milled at an incident beam angle of 1°. In contrast, the 3° milled PSCs showed color changes with an increase of milling time. We are currently working on quantitative EDS (Energy Dispersive X-Ray Spectroscopy) analysis to obtain the evolution of I/Pb ratio at different ion beam doses. It has been reported in the literature that the decrease of the I/Pb from 3 to a lower value indicates compositional deterioration (i.e., $MAPbI_3$ is partially converted to PbI_2). To gain a deep understanding into the interaction of the Ar ion beam with PSCs, we performed Monte-Carlo Simulations. In our model, 20,000 Ar ions at 4 keV were irradiated into $MAPbI_3$ layer at a shallow angle of 3° and 30° from the surface. The estimated damage layer was calculated based on the substrate displacement density. Using a constant contour representing 5 % of the peak damage density, we obtained the damage depth of 8 nm and 13 nm for the incident Ar^+ beam angle of and, respectively. The integrated analysis based on the simulations and the EDS measurements are in progress. Our results provide qualitative information of possible beam damage of PSCs that can occur during sample preparation. We will discuss the mitigation strategies to minimize the beam damage while characterizing the microstructural properties of PSCs. This work was supported by the U.S. Department of Energy's Office of Energy Efficiency and Renewable Energy (EERE) under the DE-FOA-0002064 program award number DE-EE0008985. The assistance of Utah Nanofab is also acknowledged.

3:45 PM Z04
Impedance Spectroscopy for Emerging Non-Fullerene Acceptor Based Organic Solar Cells Vinod K. Sangwan, Antonio Facchetti, Tobin Marks and Mark C. Hersam; Northwestern University, United States

Continued advancement in renewable energy science relies on the discovery of new organic photovoltaic materials with high quantum efficiency, stability, and reliability. Recently, non-fullerene acceptors (NFAs) have shown tremendous improvements in power conversion efficiency, ~18 %, that is attributed to wide spectral absorption, efficient exciton dissociation, and strong π-π interactions leading to excellent charge transport and collection. However, there still are significant losses in all steps of photoconversion that need to be understood and minimized. Conventional ultrafast spectroscopy methods have been effective in understanding intrinsic losses involving excited state relaxation and charge transfer in bulk heterojunctions. However, extrinsic losses are known to dominate in bulk heterojunctions due to non-ideal band energetics, disordered morphology and packing, and poor interfaces and contacts. Electric charge-based spectroscopies, such as impedance, transient, and noise spectroscopy, provide a direct probe to these relatively slow processes. Non-invasive in-situ characterization reveals performance-limiting dynamical processes in fully fabricated devices in operational conditions. In this talk, impedance spectroscopy methods will be discussed in the context of NFA-based organic solar cells. Emerging NFA-polymer systems, including perylenediimide-, indacenodithienothiophene-, and Y6-based NFAs, will be used to

demonstrate the effectiveness of impedance spectroscopy methods in this context.[1-5] In particular, the beneficial role of annealing in ITIC- and Y6-based blends will be elucidated through reduced bimolecular recombination that is further correlated with improved morphology and packing motifs. Integration of impedance parameters with intensity-dependent photocurrent enables more realistic device models that can distinguish the competing effects of end-group functionalization in NFA molecules. This method will be shown to reveal different routes of performance improvement via π-extension and fluorination of NFAs. In this manner, the new understanding gained in these systems is likely to pave the way for further optimization of high performance and stable solar cells.

References:
*[1] Journal of the American Chemical Society **142**, 14532 (2020).*
*[2] Adv. Eng. Mater. **10**, 2000635 (2020).*
*[3] ACS Eng. Lett. **5**, 1780 (2020).*
*[4] ACS Appl. Mater. Inter. **11**, 14166 (2019).*
*[5] Adv. Funct. Mater. **27**, 1703805 (2017).*

4:00 PM Z05
Development of Polymers for Scalable Organic Photovoltaics
Alyssa B. Chinen-Mendez, Hualong Pan, Reed Eisenhart and Laura Nielsen; Phillips 66, United States

ShieldPower™ polymers were developed at Phillips 66 for use in the photoactive layer of scalable organic photovoltaics. This talk will highlight their development from lab to pilot scale evaluation, focusing on the key parameters that enable ShieldPower™ polymers to reach high power conversion efficiencies using scalable coating techniques. The polymers combine high conductivity, as determined by time-resolved microwave conductivity experiments, and good solubility to enable photoactive layers with films >200 nm in thickness to be coated from non-halogenated solvents via slot-die coating in ambient air in a pilot fabrication line resulting modules that reach 5.3% power conversion efficiency. Further tuning the polymers' absorption properties and structures allows for blends with a stable non-fullerene electron acceptor to achieve power conversion efficiencies that remain constant over 250+ hours of illumination.

SESSION AA: Heteroepitaxy on Silicon
Session Chairs: Charles Lutz and Kyle McNicholas
Thursday Afternoon, June 24, 2021

4:45 PM AA01
(Student) High-Reliability InAs QD Lasers on Silicon Through Misfit Dislocation Trapping Layers
Eamonn T. Hughes[1], Jennifer Selvidge[1], Justin Norman[2,1], Chen Shang[1], Mario J. Dumont[1], Aidan A. Taylor[1], M.J. Kennedy[1], Andrew M. Netherton[1], Robert Herrick[3], Kunal Mukherjee[4,1] and John Bowers[1,1]; [1]University of California, Santa Barbara, United States; [2]Quintessent, United States; [3]Intel Corporation, United States; [4]Stanford University, United States

Silicon photonics require a reliable integrated light source to be a viable technology. While heterogeneous integration techniques such as wafer bonding III-V on silicon has proven successful, dramatic cost reductions can be achieved through direct growth of III-V on silicon. This presents numerous challenges to material quality due to mismatches in lattice constant, coefficient of thermal expansion, and crystal symmetry. Even so, decades of work developing defect filtering buffers paired with defect-tolerant quantum dot (QD) active regions have yielded lasers with satisfactory reliability at room temperature, however laser lifetimes at elevated temperatures remain insufficient for commercial applications. We have recently uncovered a source for lagging performance in InAs QD lasers on silicon, namely misfit dislocations (MDs) that lie along the upper and lower boundaries of the active region and act as potent non-radiative recombination centers. We have proposed that these MDs form not due to lattice mismatch in the active region, but instead form by an alternative mechanism based on (1) tensile thermal strain that builds in the AlGaAs cladding layers during cooldown after growth and (2) pinning of threading dislocations (TDs) in the InAs QD active region. TDs, which are mobile in the cladding layers above ~300 °C, glide to relieve the thermal tensile strain in these layers. The TD segment passing through the active region would ideally glide with the segment in the cladding, but as QDs act as powerful pinning sites, glide is prohibited under these low stress conditions. It follows then that MDs will form at both the upper and lower boundaries between the cladding and active region if both cladding layers are above critical thickness due to thermal strain. To solve this, we insert strained indium-alloyed "trapping layers" (TLs) to displace formation of these MDs away from the active region. Unlike the active region, these layers do not contain QDs, but they can still pin TDs in the low stress environment encountered during cooldown because natural compositional fluctuations in the indium-alloyed TLs generate sufficiently large in-layer stress fluctuations. In lasers with TLs, MDs are no longer adjacent to the active region, so their supply of minority carriers is sharply reduced, benefiting not only initial laser performance but also laser reliability since this reduces recombination-enhanced dislocation climb, which we have observed to be a significant source of laser degradation. Initial performance improvements over baseline include median threshold current reduced by half, median slope efficiency increased by over 50%, and median output power increased by over 3×. Thermal performance is also greatly improved with the threshold characteristic temperature, T_0, increased from 70 K in baseline lasers to 100 K in TL lasers, indicating their lasing threshold is less sensitive to temperature. Initial laser aging experiments reveal that TLs dramatically enhance the reliability of InAs QD lasers on silicon. After aging for 1200 h at 60 °C at approximately 2× initial 60 °C threshold current, TL lasers have a median threshold current increase of just 3%, far lower than the 56% increase for baseline lasers, lower than the 19% increase of our previous record lifetime InAs QD lasers on silicon under comparable conditions, and even lower than the 11% median threshold increase of QD lasers on GaAs substrates. We suspect that the TL lasers' lower degradation rate compared to lasers on GaAs, despite their much lower TD density, is due to the higher thermal conductivity of the silicon substrate which reduces the active region temperature during operation. Overall, these reliability results provide a clear path forward toward reliable monolithically integrated light sources for silicon photonics.

5:00 PM AA02
(Student) Dislocation tolerance of n-InGaP Grown on Si
Pankul Dhingra[1], Brian Li[1], Yukun Sun[1], Mijung Kim[1], Ryan D. Hool[2] and Minjoo L. Lee[1]; [1]University of Illinois Urbana Champiagn, United States; [2]University of Illinois at Urbana-Champaign, United States

Monolithic integration of III-V optoelectronic devices on Si requires simultaneous efforts towards achieving a low threading dislocation density (TDD) and finding materials with inherent dislocation tolerance. Early studies showed that the influence of TDD on minority carrier lifetime depends on a material's doping type, doping density, and minority carrier mobility.[1] While the impact of TDD on lifetime has been reported extensively for GaAs, far less has been published about 1.9 eV $In_{0.48}Ga_{0.52}P$ (InGaP hereafter), an important material in multi-junction solar cells and red-light emitters. The hole mobility (μ_p) in n-InGaP in ~5-10× lower than in GaAs, and recombination models[2, 3] suggest the possibility of dislocation tolerance due to slow diffusion of excess minority carriers towards traps. Here, we use time-resolved photoluminescence (TRPL) to compare the effect of TDD on the minority carrier lifetime of GaAs and InGaP double

heterostructures (DHs) grown on GaAs and GaAs/Si. We observe a TRPL lifetime (τ_{TRPL}) of 11.7 ns in n-InGaP on GaAs/Si with TDD ~1×10^7 cm^{-2}, which is the longest value for any III-V material on Si to our knowledge and only 20% lower than similar DHs grown on GaAs. We grew relaxed GaAs with varying TDD on GaP/Si templates ($NaAsP_{III/V}$ GmbH) using a Veeco Mod Gen II molecular beam epitaxy system (MBE). The TDD of 1.6 µm GaAs templates on GaP/Si templates was measured to be > 1×10^8 cm^{-2} using electron channeling contrast imaging. The TDD reduced to ~1×10^7 cm^{-2} in a separate set of templates utilizing a combination of $In_{0.1}Ga_{0.9}As$ dislocation filters and thermal cycle annealing. Next, DH samples were co-grown on GaAs and GaAs/Si templates; p-GaAs, n-GaAs and n-InGaP DHs were grown 500 nm thick with a carrier concentration of 1×10^{17} cm^{-3} and surrounded by 100 nm $Al_{0.4}Ga_{0.6}As$ and $Al_{0.51}In_{0.49}P$ barriers for GaAs InGaP, respectively. At a TDD of ~1×10^7 cm^{-2}, n-GaAs DHs on GaAs/Si exhibit a 9× degradation in steady state PL intensity compared to their counterparts on bulk GaAs, while p-GaAs DHs degrade more strongly by 16×. Consistent with the steady state PL observations, τ_{TRPL} of the n-GaAs DH on GaAs/Si reduced by a factor of 5 from 25 ns to 5.3 ns; while p-GaAs DH showed a factor of 8 reduction from 18 ns to 2.0 ns. All of these measurements in GaAs DHs are similar to previous publications[1] and consistent with strong dislocation-mediated non-radiative recombination. In contrast, we observe only minimal reduction in the steady state PL intensity and τ_{TRPL} of n-InGaP DHs grown on GaAs/Si compared to those grown on GaAs. μ_p in n-InGaP is 40-80 cm^2/Vs, ~5-10× lower than n-GaAs, and we observe < 40% degradation in the steady state PL intensity of n-InGaP with a TDD of ~1×10^7 cm^{-2}. Consistent with PL, τ_{TRPL} of n-InGaP DH on GaAs/Si is ~11.7 ns, close to the value of 14.6 ns we obtained on a native GaAs substrate. We find that Donolato's model[3] relating lifetime and TDD to be consistent with the out TRPL measurements over a wide range of TDD. The n-InGaP DH exhibits the longest τ_{TRPL} for any III-V material grown on Si that we are aware of. The long τ_{TRPL} of n-InGaP is promising for the development of high-efficiency, dislocation-tolerant solar cells on Si utilizing an n-type absorber.

1. C. L. Andre, J. J. Boeckl, D. M. Wilt, A. J. Pitera, M. L. Lee, E. A. Fitzgerald, B. M. Keyes and S. A. Ringel, Appl Phys Lett **84** (18), 3447-3449 (2004).
2. M. Yamaguchi, C. Amano and Y. Itoh, J Appl Phys **66** (2), 915-919 (1989).
3. C. Donolato, J Appl Phys **84** (5), 2656-2664 (1998).

5:15 PM AA03
BxGa1-xP/Si Grown via Hybrid Gas/Solid-Source Molecular Beam Epitaxy Zak H. Blumer, Jacob T. Boyer, Ari N. Blumer, Daniel L. Lepkowski and Tyler Grassman; The Ohio State University, United States

The monolithic, epitaxial integration of III-V materials on Si has long been a target for the realization of high-performance, low-cost optoelectronic devices. GaP has the closest lattice constant to Si of any III-V binary compound and is thus a common choice for the first epitaxial layer. Subsequent strain (composition) grading of ternary or quaternary III-V alloys can then enable access to other III-V materials that may be better suited for a given application. However, the non-negligible compressive GaP/Si misfit (-0.36% at room temperature, but even greater than -0.5% at growth temperature) ultimately leads to a critical thickness of ~40 nm, beyond which dislocations form to relieve the strain. For materials with relatively poor dislocation glide velocities, such as n-GaP, it is especially difficult to mitigate dislocation nucleation and maintain the low TDD necessary for optoelectronic device applications. Compositional grading, which provides control over dislocation content by spreading out the overall system strain across multiple, low-misfit interfaces, has long been used to mitigate dislocation nucleation in metamorphic III-V/III-V growth. Similarly, use of $Ga_xN_{1-x}P$ or $B_xGa_{1-x}P$ compositions, which can be made to provide lattice-matching (and even tensile strain) to Si should enable similar control for III-V/Si integration. We have thus undertaken an investigation of $B_xGa_{1-x}P$ grown via solid source MBE. Because B can be a difficult material to evaporate from solid source, we have instead explored a novel hybrid approach using BCl_3 as a gas-source B precursor [1]. To this end, we have established growth conditions that enable control over the cation fraction, with compositions of up to $B_{0.31}Ga_{0.69}P$ (determined via XRD) demonstrated with good crystallinity and useable surface roughness. This nearly Si-matched composition was grown on a thin, pseudomorphic GaP/Si template to a to produce an effectively strain-free $B_xGa_{1-x}P$/GaP/Si virtual substrate with TDD < 3×10^5 cm^{-2} (as measured via ECCI). Further thick GaP overgrowth results in dislocation introduction, and thus strain relaxation, wherein the resultant misfit dislocations and glide occur at the upper GaP/$B_xGa_{1-x}P$ interface, leaving the GaP/Si interface effectively defect-free. Although these initial results have indeed demonstrated both the ability to grow $B_xGa_{1-x}P$ using this hybrid gas/solid-source MBE approach and to achieve lattice-matching to Si, further detailed characterization via STEM and SIMS have recently indicated the presence of interesting features within the $B_xGa_{1-x}P$ films. For one, there appears to be some degree of compositional nonuniformity within the higher B fraction film layers. This is potentially consistent with minor phase separation resulting from the thermodynamic immiscibility, although no such indication is found via XRD. Perhaps more interestingly, SIMS analysis indicates substantially higher B concentrations than XRD (up to ~70% compared to a maximum of ~5% measured by XRD), suggesting the possibility of extremely high amounts of interstitial loading. Detailed characterization work to better understand and quantify these issues, including high-resolution structural and compositional analysis, is still underway, and we will present up-to-date results at the conference.

[1] Z. H. Blumer, J. T. Boyer, A. N. Blumer, D. L. Lepkowski, and T. J. Grassman, "Si-matched BxGa1−xP grown via hybrid solid- and gas-source molecular beam epitaxy," *Appl. Phys. Lett.*, vol. 117, no. 12, p. 122102, Sep. 2020, doi: 10.1063/5.0021493.

5:30 PM AA04
(Student) Growth of Low Dislocation Density GaAs Films on Silicon Using Bonded III-V Template Mario J. Dumont[1], Eamonn T. Hughes[1], Yingtao Hu[2], Kunal Mukherjee[3], Di Liang[2] and John Bowers[1]; [1]University of California, Santa Barbara, United States; [2]Hewlett-Packard Enterprise, United States; [3]Stanford University, United States

The explosive growth of silicon photonics has demonstrated its capability to meet the growing demands of datacenters, however the integration of direct-bandgap semiconductors for light emission is still an area of active research. Two approaches have strived to solve this issue. In heterogeneous integration, III-V is bonded to the silicon, which allows efficient coupling of light emission to the silicon waveguide. In contrast, homogeneous integration uses hetero-epitaxial growth to incorporate III-V on a silicon substrate. The later suffers from the mismatch in polarity, lattice spacing, and coefficient of thermal expansion (CTE), however the use of buffer layers to reduce the threading dislocation density (TDD) and the incorporation of InAs quantum dots in the active region has dramatically increased the performance of lasers on silicon [1]. There is still an underlying limitation with heteroepitaxy, which limits the proximity of the quantum dots to the silicon waveguide. In an effort to leverage the advantages of both techniques, MBE regrowth using a bonded III-V layer on an SOI substrate has been investigated. This technique has been investigated with MOCVD [2], however this is the first demonstration of MBE regrowth on bonded III-V. Initial results demonstrated the efficacy of this technique, however a high TDD was measured. In order to reduce the TDD, the use of thin indium bearing quantum wells referred to as Trapping Layers (TLs) were used to reduce the TDD from 7.5E6/cm^2 to 2.0E5/cm^2. This dramatic reduction shows the effectiveness of TLs and

growth on bonded template as an alternative approach mentioned above. We used a secondary electron imaging process, known as electron-channeling contrast imagery (ECCI) and cross sectional transmission electron microscopy (TEM) to analyze defects and the effectiveness of TLs to reduce them. MBE regrowth on a bonded template begins with the bonding of a GaAs wafer to a 400 nm SOI wafer. The bonded GaAs wafer is selectively etched such that a 200-nm-thick layer of GaAs remains. This bonding template is then used as a pseudo GaAs wafer for MBE regrowth. The TDD in GaAs-only films increases with thickness, with a 1 µm of GaAs giving a TDD of 3.5E5/cm^2, while a 2 µm film produced 7.5E6/cm^2. The insertion of a pair of TLs within the first 200 nm of growth reduced the TDD 7.5x from 7.5E6/cm^2 to 1E6/cm^2. By using one TL near the regrowth interface, and another TL near the top surface, the TDD was reduced 5x to 2E5/cm^2. The ability of TLs to reduce TDD is attributed to two principles; strain inversion between the GaAs and the TL, and alloy hardening from the incorporation of indium in random alloys [4]. During growth, both the bulk GaAs and the TL are compressively strained and no strain inversion exists. Fortunately, the small amount of compressive strain in the GaAs layers is relaxed without generating a large number of dislocations [3]. During cool down, the relaxed film becomes tensilely strained from CTE mismatch, but the TLs remain compressively strained, creating strain inversion. Dislocation half loops nucleating from the bond interface are now blocked by the TL, giving the large reduction in TDD. The top TL further reduces the TDD through blocking half loops from the surface and inhibiting spiral dislocation multiplication processes. Cross-sectional TEM data shows a high number of MDs at both the bond interface and the lower TL, which shows the TL's ability to block dislocations. Using TLs has alleviated the major challenge in regrowth on bonded III-V, showing a promising future for integrating lasers, photodetectors, and modulators.

References
[1] S. Chen et al., Nat Photon **10**, 307 (2016).
[2] C. Zhang et al, ECS Solid State Letters, **2**, Q82 (2013)
[3] Marée, P. M. J., et al., Journal of Applied Physics **62**, 4413 (1987)
[4] Selvidge, Jennifer, et al., Applied Physics Letters **117**, 122101 (2020).

5:45 PM AA05
(Student) Tuning Band-Alignment at a Semiconductor-Crystalline Oxide Heterojunction via Electrostatic Modulation of the Interfacial Dipole
Matthew D. Chrysler[1], Judith Gabel[2], Tien-lin Lee[2], J.R. Paudel[3], R.K. Sah[3], J.D. Grassi[3], Zihua Zhu[4], Aubrey Penn[5], James M. LeBeau[6], Alexander Gray[3], Steven Spurgeon[4], Peter V. Sushko[4], Scott A. Chambers[4] and Joseph Ngai[1]; [1]University of Texas, United States; [2]Diamond Light Source, Ltd., Harwell Science and Innovation Campus, United Kingdom; [3]Temple University, United States; [4]Pacific Northwest National Laboratory, United States; [5]North Carolina State University, United States; [6]Massachusetts Institute of Technology, United States

Charge transfer across semiconductor heterojunctions and the electric fields that arise therefrom underpin the functionality of virtually all device technologies. In this regard, hybrid heterojunctions formed between semiconductors and crystalline complex oxides offer novel functionality due to their mixed covalent and ionic characteristics. Here we explore how the interfacial structure at such heterojunctions can be exploited to tune band-alignment. Inherent to epitaxial semiconductor-crystalline oxide interfaces is a built-in dipole that modifies the band alignment. We demonstrate that the magnitude of this interfacial dipole can be tuned electrostatically via space charge, thereby enabling band-alignment to be modified via doping. 12 nm thick SrTiO3 (STO) films were deposited epitaxially on nominally undoped Czochralski (CZ) and float-zone (FZ) grown Si wafers using oxide molecular beam epitaxy. Hard X-ray photoelectron spectroscopy measurements reveal a type-III (type-II) band alignment in the STO/Si-CZ (STO/Si-FZ) heterojunction. The difference in band alignment arises from the presence of oxygen impurities in the CZ Si, which act as n-type donors that transfer electrons to STO. The resulting space charge due to this charge transfer creates an electric field across the interface that enhances the interfacial dipole and shifts the band alignment from type-II to type-III. The type-III band alignment is sufficiently large as to induce a hole-gas in the Si of the STO/Si-CZ heterojunction, as revealed by electrical transport measurements. We find the band-alignment is highly sensitive to the concentration and profile of n-type dopants in the Si near the interface. The ability to electrostatically tune band-alignment across hybrid heterojunctions opens pathways for novel functional behavior.

SESSION BB: Gallium Oxide Processing, Characterization and Defects
Session Chairs: Rebecca Peterson and Chintalapalle Ramana
Thursday Afternoon, June 24, 2021

3:00 PM BB01
(Student) Fin-Waist Formation in β-Ga2O3 Fin Arrays Defined by ICP-RIE
Yaoyao Long[1], Wenshen Li[1], Mingli Gong[1], Kathleen Smith[1], Kazuki Nomoto[1], David Lishan[2], Debdeep Jena[1,1,1] and Huili Grace Xing[1,1,1]; [1]Cornell University, United States; [2]Plasma-Therm LLC, United States

Background. β-Ga_2O_3 has been actively studied for power electronics, RF devices, etc. Among various device topologies, fin-structures are particularly attractive since they enable the RESURF effect, which is key in designing high-field electronics and enhancement-mode transistor operation[1,2]. Fin-structures have been successfully employed in demonstrating record-setting devices in β-Ga_2O_3[3,4]. However, we also observed in these devices that a "waist" tends to develop in the middle of a fin thus current flow can be severely pinched by "narrowed waist". Here, we report what has been learned to date on fin-waist formation during ICP reactive ion etching (RIE). Experiments. The fin/trench arrays were fabricated on single-crystal β-Ga_2O_3 substrates with 2 orientations: (010) and (001). Hard masks of Pt were patterned by EBL for fin/trench widths less than 1 µm and optical lithography for wider ones. Definitions of dimensional parameters for fin, trench, fin waist and waist narrowing are illustrated in **Fig.1**. The dry etch parameters were fixed at 350 W ICP power, 20 W RIE power, 5 mTorr, 20C with 35 sccm BCl_3 and 5 sccm Ar. Prior to SEM, the etched samples were soaked in HCl and/or HF to remove etch damage/residue. This dry+wet etch condition has rendered consistently rectangular-shaped *single* fins on (001) β-Ga_2O_3 with a fin height/width aspect ratio (AR) up to 9 and used in our reported devices[3]. Fin-waist dependence on the fin orientation and AR of fins/trenches. Arrays of fins were etched on (001) β-Ga_2O_3 with fin orientation varied. The fin width was varied from 0.15 to 8 µm, the trench width was varied from 1 to 8 µm, and the fin/trench depth was varied from 1.1 to 2 µm, which corresponds to a fin AR of 0.2-9 and a trench AR of 0.5-1.3. Upon examining cross-sections of these fins/trenches under SEM (**Figs. 2-4**), we discover following trends: 1) all outermost sidewalls of fin arrays and single fins appear to be vertical, while inner sidewalls all show waist; 2) there is no noticeable dependence on fin orientation; 3) waist narrowing increases from 50±10 nm for a *trench AR* of 0.5 to 200±10 nm for a trench AR up to 1.3, while appears nearly *independent of fin width*; and 4) wet etch worsens waist narrowing. Fin-waist dependence on the substrate orientation. Similar trench etching experiments were applied to (010) substrates, given their popular use in device development.

Example cross-section SEM images are shown in **Fig. 5**. Though the ranges of fin/trench geometric parameters are slightly different from the ones explored on the (001) β-Ga_2O_3, the trends observed are largely consistent across different substrate orientations. Discussions. To advance fin-based device performance, it is essential to increase filling factor of fins with respect to entire area occupied by devices on wafer; the preferred trench AR is >1. Under the present ICP-RIE etch condition, waist narrowing is minimal for a low trench AR; but low trench AR implies a low filling factor of current-carrying fins. Waist narrowing is tolerable for fat fins, but the resultant fins can suffer from severe waist narrowing for large-AR trenches and narrow fins (**Fig.6**) thus detrimental to realizing smooth current flow in devices. Based on our observations, we hypothesize that in trenches with a high AR, a combination of poor sidewall passivation and ion/electron redistribution can result in appreciable lateral etching thus forming waist in fins or bowing of sidewalls. Similar effects were widely observed in other material systems, and improved passivation of sidewalls and neutralization of charges on sidewalls are common tactics to suppress bowing. Ongoing studies are undertaken to curb this undesirable waist narrowing.
1Hu, et al, EDL, 39, 869(2018). 2Li, et al, TED, 67, 3954(2020). 3Li, et al, IEDM, 270(2019). 4Li, et al, EDL, 41, 107(2020).
* This work is in part supported by AFOSR Center of Excellence: ACCESS (FA9550-18-1-0529). CNF uses are partly supported by NSF NNCI-2025233.

3:15 PM BB02
(Student) Quantitative Defect Characterization of MOCVD-Grown β-(Al,Ga)2O3 and Comparison with β-Ga2O3 Evan M. Cornuelle, Hemant J. Ghadi, Joe F. McGlone, A F M Anhar Uddin Bhuiyan, Zixuan Feng, Hongping Zhao, Aaron Arehart and Steven A. Ringel; The Ohio State University, United States

β-Ga_2O_3 is an emerging ultra-wide bandgap (UWBG) semiconductor that holds promise to enable advances in power, RF and opto-electronic devices. With the introduction of β-$(Al,Ga)_2O_3$, UWBG heterostructures are possible that increase the range of viable devices. In fact, two-dimensional electron gases (2DEG) in modulation-doped β-$(Al,Ga)_2O_3$/Ga_2O_3heterojunctions [1, 2] have already been reported. However, while there are numerous studies on defect spectroscopies and electrical properties of β-Ga_2O_3, comparatively little information on electrically active defects and their impact on material properties in β-$(Al,Ga)_2O_3$ is available. An understanding of traps in β-$(Al,Ga)_2O_3$ will be important to identify and mitigate sources for device degradation, as well as to optimize epitaxial growth. Presented here are deep level transient and optical spectroscopy (DLTS/DLOS) results obtained from β-$(Al_{0.1}Ga_{0.9})_2O_3$ epitaxial layers grown by metal organic chemical vapor deposition (MOCVD). These are discussed in the context of our prior β-Ga_2O_3 results, to provide a baseline from which trends and conclusions can be provided. MOCVD was used to grow b-$(Al_{0.1}Ga_{0.9})_2O_3$ layers in an Agnitron Agilis R&D system, using TEGa, TMAl and O_2 precursors on β-Ga_2O_3 (010) Sn-doped EFG-grown substrates with a growth temperature of 880 °C. To enable useful comparisons with our β-Ga_2O_3 results, an Al cation mole fraction of 0.10 was targeted for our initial studies, which should yield a bandgap of approximately 5.0 eV. Ni Schottky diodes were fabricated on the sample using conventional photolithography methods. Capacitance-voltage, current-voltage and internal photoemission measurements (IPE) revealed the Schottky diodes were suitable for defect spectroscopy measurements and characterize the Ni/b-$(Al_{0.1}Ga_{0.9})_2O_3$ Schottky properties themselves. Comparisons are made to previously characterized Schottky diodes fabricated on a β-Ga_2O_3 epitaxial film grown by MOCVD in the same reactor under the same growth conditions [3]. The net doping concentration in the initial layers under study was measured by CV to be 1.8 x 10^{18} cm^{-3}. Good Schottky behavior was observed, even at this high doping value, with strong rectification, ideality factor of ~1.5, and IPE-determined Schottky barrier heights of ~1.4 V. Preliminary deep level defect characterization using admittance spectroscopy (AS) along with DLTS and DLOS revealed the presence of five trap states within the b-$(Al_{0.1}Ga_{0.9})_2O_3$ bandgap. A state with an activation energy of ~E_C-0.2 eV as observed by AS; three trap levels were revealed by DLTS with approximate trap energies of ~E_C-0.3 eV, ~E_C-0.4 eV and E_C-0.8 eV; and two trap levels were observed in the steady-state photo-capacitance (SSPC) spectra having onset energies of ~E_C-2.0 eV and ~E_C-4.6 eV. Overall, a similar energy distribution of trap states is observed compared with MOCVD grown b-Ga_2O_3 is suggestive of similar physical sources of traps between these the two materials, accounting for the small bandgap differences. A notable difference is the E_C-0.8 eV trap, which is absent in the MOCVD b-Ga_2O_3, but matches the signature in b-Ga_2O_3 grown by other techniques suggesting it may be related to Fe [4]. Much more work is needed to confirm the meaning of these observations, which is ongoing. However, total trap concentrations are markedly different, being ~ 100x larger in the b-$(Al_{0.1}Ga_{0.9})_2O_3$ epitaxial films, which is indicative of the very early stage of β-$(Al,Ga)_2O_3$ epitaxial growth development. Complete discussion of the nature of the traps seen in b-$(Al_{0.1}Ga_{0.9})_2O_3$ and an expanded range of alloy compositions and growth conditions will be presented, including further comparisons to prior data obtained from high quality b-Ga_2O_3[3].

[1] N. Kalarickal, et al, J. Appl. Phys. **127**, 215706 (2020)
[2] Y. Zhang, et al, Appl. Phys. Lett. 112, 233503 (2018)
[3] H. Ghadi, et al, Appl. Phys. Lett. 117, 172106 (2020)
[4] J. F. McGlone, et al, Electron Dev. Lett. 39, 1042 (2018)

3:30 PM BB03
(Student) Nanogaps Formation and Recovery Process of Flexible β-Ga2O3 Nanomembranes Under Uniaxial Strain Md Nazmul Hasan, Junyu Lai, Yixiong Zheng, Edward Swinnich and Jung-Hun Seo; University at Buffalo, The State University of New York, United States

Ultra-wide-bandgap semiconductors (UWBG's) are a very promising material for the next-generation power semiconductors devices due to the rapid developments and requirements of highly efficient power electronics. The beta phase of Ga_2O_3 (β-Ga_2O_3) is considered in a family of UWBG semiconductors, which provides a new opportunity in myriad applications in electronics, optoelectronics, and photonics, with a superior performance matrix than conventional WBG materials. It exhibits some remarkable properties such as ultra-wide bandgap (>4.8 eV) at room temperature, thermally and chemically stability, high carrier mobility (>300 cm2/v.s), critical electric breakdown filed (~8 MV/cm), highest electron-Baliga's Figure of Merit (BFoM). All of these properties could lead β-Ga_2O_3, a potential candidate for high-frequency devices, deep-ultraviolet optoelectronics, and high-power applications. However, the monoclinic and anisotropic crystal structure of β-Ga_2O_3 (a= 12.214 Å, b= 3.037 Å, and c=5.798 Å) exhibits larger lattice constant on the a-axis other than b-axes and c-axes. These benefits could open up a new direction of creating a nanoscale freestanding form of sub-micron thick β-Ga2O3 flake (typically known as nanomembranes, NMs), Recently several research groups have demonstrated creating NMs using the "Scotch tape" method. Thus, β-Ga_2O_3 provides a new opportunity to realize the use of UWBG's in flexible devices that have the advantages of high breakdown electric field, transparency and solar blind photodetection while maintaining good mechanical stability. In fact, our group demonstrated the first flexible electronics (Schottky barrier diode and Solar blind photodetector) based on β-Ga_2O_3 NMs. However, structural-property relationship investigation of β-Ga_2O_3 NMs under mechanical strain conditions has not been well studied yet. Here in this presentation, we will first discuss the formation of nanogaps β-Ga_2O_3 NMs under uniaxial strain conditions, and the impact of randomly generated nanogaps on the electrical and optical properties using the β-Ga_2O_3 NMs fabricated on a plastic substrate. The scanning

electron microscope (SEM) and the atomic force microscope (AFM) was used to identify the strain-induced nano-cracks, which also provided direct evidence of layer delamination and fracture in the β-Ga_2O_3 NMs. It was noticed that the electrical properties of β-Ga_2O_3 NM, such as the sheet resistance and capacitance were changed under uniaxial strain conditions. In order to investigate the change in sheet resistance and capacitance, a transmission line measurement (TLM) pattern was used. The results uncovered a significant degradation in the electrical properties and uneven distribution of the charges in the β-Ga_2O_3 NMs. The sheet resistance increased, and the total capacitance decreased due to substantial degradation of β-Ga_2O_3 NM's under bending conditions. The optical properties of flexible β-Ga_2O_3 NMs were also investigated as a solar-blind photodetector. Interestingly, the degraded performance in β-Ga_2O_3 NM was recovered by employing a water vapor treatment. The presence of OH bonds in β-Ga_2O_3 NM confirmed by X-ray photoelectron spectroscopy (XPS) indicated that a water vapor treatment chemically bonds the nano-cracks effectively. Hence it was possible to recover up to 90 % of the original electrical properties. In addition, the water vapor treatment prevented further performance degradation in β-Ga_2O_3 NM from multiple bending cycles, thus providing good reliability. This result provides a viable route in realizing high-performance flexible devices, which is one of the crucial components in the upcoming internet of things era.

3:45 PM BB04
(Student) The Impact of Interfacial Structure on Thermal Transport Characteristics for Wafer Bonded (-201) β-Ga2O3 | (0001) 4H-SiC Michael E. Liao[1], Kenny Huynh[1], Yekan Wang[1], Zhe Cheng[2], Jingjing Shi[3], Fengwen Mu[4], Tiangui You[5], Wenhui Xu[5], Tadatomo Suga[6], Xin Ou[5], Samuel Graham[3,7] and Mark Goorsky[1]; [1]University of California, Los Angeles, United States; [2]University of Illinois at Urbana-Champaign, United States; [3]Georgia Institute of Technology, United States; [4]Institute of Microelectronics of Chinese Academy of Science, China; [5]Shanghai Institute of Microsystem and Information Technology, Chinese Academy of Sciences, China; [6]Meisei University, Japan; [7]School of Materials Science and Engineering, United States

The thermal properties of 140-nm thick film of (2̄01) β-Ga_2O_3 wafer bonded to (0001) 4H-SiC were studied. Prior to bonding these two materials, the (2̄01) β-Ga_2O_3 substrates were implanted with H^+ ions at 35 keV with a dose of 1×10^{17} cm^{-2} at room temperature. 30 nm of Al_2O_3 was then deposited on the implanted β-Ga_2O_3 substrate surfaces via plasma-enhanced atomic layer deposition at 200 °C. The β-Ga_2O_3 substrate and 4H-SiC substrate surfaces were then subjected to an ion sputtering treatment consisting of Ar and Si ions to create dangling bonds. Next, the two surface treated materials were then brought face-to-face and bonded at room temperature. The resulting bonded interface was a 2.9 nm thick amorphous region between the Al_2O_3 and 4H-SiC. The thin amorphous bonded interface is a common occurrence when bonding materials that exhibit covalent bonding using this technique.[1,2] Finally, the bonded sample was heated to 450 °C to create H_2 blisters at the projected range in the β-Ga_2O_3, which led to exfoliation. ω:2θ X-ray diffraction measurements show that strain from the ion implantation was still present in the β-Ga_2O_3 even after the exfoliation. This residual strain was shown to reduce the thermal conductivity of the β-Ga_2O_3 layer from our previous efforts.[3] In this current study, the bonded samples were annealed at 800 °C for 30 minutes, then 1 hour. The thermal conductivity of the β-Ga_2O_3 layer and thermal boundary conductance (TBC) of the bonded interface were measured after each anneal step. The thermal conductivity of the as-bonded β-Ga_2O_3 layer was 2.9 $Wm^{-1}K^{-1}$ and the TBC of the bonded interface was 66 $MWm^{-2}K^{-1}$. After annealing at 800 °C for 30 mins, ω:2θ measurements showed a reduction in strain for the β-Ga_2O_3 layer, and we simultaneously observed an increase in the β-Ga_2O_3 thermal conductivity to 6.0 $Wm^{-1}K^{-1}$ and TBC to 70 $MWm^{-2}K^{-1}$. Upon further annealing an additional 30 mins at 800 °C, the ω:2θ measurements showed further reduction in strain and an increase in TBC to 77 $MWm^{-2}K^{-1}$, while the β-Ga_2O_3 thermal conductivity did not change. Transmission electron microscopy images were compared before and after the 1 hour 800 °C anneal. The bonded interfacial region thickness at the Al_2O_3 | 4H-SiC interface reduced from 2.9 nm to 2.2 nm. Furthermore, after the anneal, recrystallization of 4H-SiC was observed. On the other hand, the structure of the β-Ga_2O_3 | Al_2O_3 interface did not change before and after the anneal, which suggests the TBC was limited by the distorted Al_2O_3 | 4H-SiC interface. It should be noted that the TBC value consists of 3 distinct interfaces: (1) β-Ga_2O_3 | Al_2O_3, (2) Al_2O_3 | amorphous 4H-SiC, and (3) amorphous 4H-SiC | crystalline 4H-SiC. Upon annealing and recrystallization of 4H-SiC, the thickness of the amorphous region is reduced and the TBC increases. It is expected that for longer anneals, complete recrystallization would lead to a further increase in the TBC due to the removal of the two interfaces involving the amorphous 4H-SiC. The analysis of the evolution of strain and interfacial structure is important because these two factors play significant roles in important characteristics such as thermal and electronic transport.

References:
1. K. Huynh, et al., Meet. Abstr. MA2020-02, 1621 (2020).
2. M.E. Liao, et al., ECS Trans., 86(5), 55 (2018).
3. Z. Cheng, et al., ACS Appl. Mater. Interfaces, 12, 44943 (2020).
The authors M.E.L., K.H., Y.W., Z.C., J.S., S.G., and M.S.G. would like to acknowledge the support from the Office of Naval Research through a MURI program, grant No. N00014-18-1-2429.

4:00 PM BB05
(Student) Micro-Photoluminescence Hyperspectral Mapping of Laser-Induced-Defects in β-Ga2O3 Darpan Verma[1], Michael Tripepi[1], Selim Elhadj[2], Enam A. Chowdhury[1,1] and Roberto C. Myers[1,1]; [1]The Ohio State University, United States; [2]Seurat Technologies Inc., United States

β-Ga_2O_3 is an ultra-wide bandgap semiconductor attractive for high power electronic devices and on-chip direct laser acceleration (DLA) due to its large breakdown field (8 MV cm^{-1}), electron saturation velocity, and Baliga figure of merit [1-3]. In such devices, DC breakdown at a high electric field, and laser-induced damage have a direct relationship [4]. The DC breakdown is caused due to the field exceeding the intrinsic breakdown of the material or can occur at a lower field when extrinsic defects provide alternative breakdown pathways leading to a reduced lifetime of power electronic devices [5]. Here we investigate the room temperature PL spectra of β-Ga_2O_3 as they vary spatially across laser-damage spots. Ultrafast 8-fs laser pulses at 760nm center wavelength were used to create laser damage spots over a range of fluences (F = 0.5-2 J/cm^2) on a single crystal β-Ga_2O_3 sample. The number of shots at each spot is also varied. Micro-photoluminescence spectroscopy is carried out to acquire hyperspectral images of the damaged spots. We observe an anisotropic spatial variation of certain β-Ga_2O_3 PL spectral features associated with defects. For example, the low energy tail at 2.48 eV shows enhanced emission at particular locations of the damaged spots. We will discuss measurements of the dependence of these spectral features on laser fluence and dose. Polarization-resolved PL will be examined to explore the anisotropy of the defect-related PL features.

Acknowledgment
The author acknowledges the support from the Air Force Office of Scientific Reports Award # FA9550-20-1-0278 for providing partial support and Azimuth Corporation contract # 238-5404-OSU for the other part of the funding support.

References
[1] Q. He, W. Mu, H. Dong, S. Long, Z. Jia, H. Lv, Q. Liu, M. Tang, X. Tao, M.Liu, Appl. Phys. Lett. **110**, 093503 (2017).
[2] S.J. Pearton, J. Yang, P.H. Cary IV, F. Ren, J. Kim, M.J. Tadjer, M.A. Mastro, Appl. Phys. Rev. **5**, 011301 (2018).

[3] H. Deng, K. J. Leedle, Y. Miao, D. S. Black, K. E. Urbanek, J. Mcneur, M. Kozák, A. Ceballos, P. Hommelhoff, O. Solgaard, R. L. Byer, and J. S. Harris, "Gallium Oxide for High-Power Optical Applications," Adv. Opt. Mater. 8, 1901522 (2020).
[3] D. Arnold, and E. Cartier, Phys. Rev B 46 (23), 15102 (1992).
[4] J-H Yoo, S. Rafique, A. Lange, H. Zhao, S. Elhadj, Apl. Materials 6, 036105 (2018).

SESSION CC: Gallium Oxide Epitaxy I
Session Chairs: Elaheh Ahmadi and Shin Mou
Thursday Afternoon, June 24, 2021

4:45 PM CC01
(Student) Growth and Characterization of *In Situ* MOCVD-Grown Al2O3 Dielectric / (010) β-Ga2O3 Interface Saurav Roy[1], Adrian Chmielewski[2], Arkka Bhattacharyya[1], Praneeth Ranga[1], Rujun Sun[1], Michael Scarpulla[1,3], Nasim Alem[2] and Sriram Krishnamoorthy[1]; [1]University of Utah, United States; [2]The Pennsylvania State University, United States; [3]The University of Utah, United States

We report on the growth and characterization of in-situ Al_2O_3 on (010) β-Ga_2O_3 using metalorganic chemical vapor deposition (MOCVD) as a better alternative to the most commonly used atomic layer deposition (ALD) technique. The in-situ Al_2O_3 deposition provides in-situ passivation to the underlying epitaxial β-Ga_2O_3 layer and protects the semiconductor surface from undesired contaminants. The MOCVD growth of Al_2O_3 also facilitates high-temperature dielectric deposition compared to other conventional techniques, which is known to enhance the bulk and interface quality of the dielectric. To extract trap densities and electrical properties of the in-situ Al_2O_3/ β-Ga_2O_3 interface, three metal oxide semiconductor capacitor (MOSCAP) structures with three different Al_2O_3 thicknesses (T_{ox} = 14, 24, and 55 nm) were fabricated. The growth of β-Ga_2O_3 was performed in an Agnitron MOVPE reactor with far injection showerhead design using Triethylgallium (TEGa) and Oxygen as precursor gas at a growth temperature of 600 ^{0}C, which is followed by the growth of Al_2O_3 layer at the same growth temperature as the β-Ga_2O_3 layer inside the same chamber using Trimethylaluminum (TMAl) and O_2 as precursors without breaking the vacuum. Transmission electron microscopy (TEM) was used to understand the microstructure of the MOCVD-grown Al_2O_3 layer, showing the formation of polycrystalline domains. Energy-dispersive X-ray spectroscopy and chemical mapping show an abrupt interface between β-Ga_2O and Al_2O_3 layer. Using capacitance-voltage (CV) measurements, the dielectric constant of the Al_2O_3 layer was extracted from the accumulation capacitance and determined to be 8.2 to 8.5. The fast and slow near interface traps at the in-situ Al_2O_3/ β-Ga_2O_3 interface were characterized using stressed CV measurements on MOSCAP structures. Fixed charge is calculated from the flat band voltage (V_{FB}) vs the oxide thickness plot and the polarity of the charges was determined from the slope of the V_{FB} vs T_{ox} plot and a stable positive fixed charge of +2 x 10^{12} cm^{-2} is calculated. The sheet density of near interface trap states with fast and slow emission times was also calculated from the linear relationship of the CV hysteresis versus Al_2O_3 thickness plots and found to be 1.2 x 10^{12} cm^{-2} and 3 x 10^{11} cm^{-2} respectively. The density of all the interface states (D_{it}) (initially filled and unfilled) and their energy dependences were characterized using the deep ultra-violet (DUV) assisted CV technique. The density of bulk dielectric traps in Al_2O_3 is distinguished from the interface traps by linear extrapolation of total average trap density vs oxide thickness to T_{ox} = 0. An average interface trap density (D_{it}) of 7.8 x 10^{11} cm^{-2} eV^{-1}, which is significantly lower than the ALD Al_2O_3/ β-Ga_2O_3 interface from literature is determined. Band offset of the in-situ Al_2O_3/ β-Ga_2O_3 heterostructure is also calculated to be 1.7 eV. Furthermore, the breakdown voltage and leakage currents for the in-situ Al_2O_3/β-Ga_2O_3 MOSCAPs were evaluated using forward and reverse current-voltage (IV) characteristics. An average peak breakdown field of approximately 5.6 to 5.8 MV/cm underneath the center of the anode is extracted using TCAD simulations. This approach of in-situ dielectric deposition on β-Ga_2O_3 can pave the way as gate dielectrics for future β-Ga_2O_3 based high-performance MOSFETs due to its promise of the improved interface and bulk quality compared to other conventional dielectric deposition techniques. We acknowledge funding from AFOSR MURI program under Award No. FA9550-18-1-0507 (PM: Dr. Ali Sayir).

5:00 PM CC02
(Student) Orientation-Dependent Band Offsets at MOCVD Grown β-(AlxGa1–x)2O3/β-Ga2O3 Heterointerfaces A F M Anhar Uddin Bhuiyan, Zixuan Feng, Lingyu Meng, Jared Johnson, Hsien-Lien Huang, Jinwoo Hwang and Hongping Zhao; The Ohio State University, United States

Because of its large bandgap (~4.8 eV) and high breakdown field strength (8 MV/cm), β-Ga_2O_3 is considered as one of the most promising ultrawide bandgap semiconductor material systems for next generation energy efficient power and radio frequency electronics. Alloying β-Ga_2O_3 with Al_2O_3 can expand the energy bandgap and provide opportunities for the formation of high mobility two-dimensional electron gas (2DEG) with high sheet charge density in β-$(Al_xGa_{1-x})_2O_3$/β-Ga_2O_3 heterointerfaces with large band offsets. Our recent studies [1-3] show that β-$(Al_xGa_{1-x})_2O_3$ epitaxy on top of β-Ga_2O_3 substrates is highly dependent on the substrate orientation such as (010), (100) and (-201). Recent theoretical calculations based on density functional theory (DFT) revealed a distinct dependence of the band offsets between β-$(Al_xGa_{1-x})_2O_3$ and β-Ga_2O_3 on crystal orientation [4]. However, experimental measurements of the band offsets at β-$(Al_xGa_{1-x})_2O_3$/β-Ga_2O_3 interfaces with different orientations are still limited. In this work, for the first time we experimentally determined the band offsets of MOCVD grown β-$(Al_xGa_{1-x})_2O_3$/β-Ga_2O_3 heterointerfaces grown along (100) and (010) orientations, with different Al compositions. Phase pure β-$(Al_xGa_{1-x})_2O_3$ epitaxial films were grown on (100) and (010) β-Ga_2O_3 substrates via MOCVD. The valence and conduction band offsets at β-$(Al_xGa_{1-x})_2O_3$/β-Ga_2O_3 heterointerfaces along (100) [x= 0.10, 0.33 and 0.52] and (010) [x= 0.16, 0.26 and 0.35] orientations were determined by using x-ray photoelectron spectroscopy (XPS). By examining the onset of the inelastic energy loss in core-level atomic spectra, the bandgaps of β-Ga_2O_3 and β-$(Al_xGa_{1-x})_2O_3$ alloys with different Al compositions were measured from 4.83±0.12 eV (x=0) to 5.85±0.08 eV (x = 0.52). The valence band offsets were determined to be -0.06±0.06 eV (x=0.10), -0.11±0.06 eV (x=0.33) and -0.19±0.06 eV (x=0.52). The conduction band offsets up to 1.21±0.16 eV (x=0.52), were determined from the extracted bandgaps of (100) β-$(Al_xGa_{1-x})_2O_3$ alloys. Similarly, for (010) oriented β-$(Al_xGa_{1-x})_2O_3$/β-Ga_2O_3 heterointerfaces, the valance and the conduction band offsets of -0.13±0.06 eV and 0.57±0.06 eV were extracted for 35% Al composition. The determined band offsets revealed the formation of type-II (staggered gap) heterojunctions for all Al compositions investigated along (100) and (010) orientations. The bowing parameters extracted from the quadratic fitting of the conduction band offsets along (100) and (010) orientations were 1.25 eV and 0.75 eV, respectively. The (100) orientation exhibited larger conduction band offsets as compared to that of the (010) orientation. Both valence and the conduction band offsets were found to increase as the Al composition increases. The experimentally measured band offsets agreed well with the theoretically predicted values [4]. In summary, we investigated the band offsets at MOCVD grown β-$(Al_xGa_{1-x})_2O_3$/β-Ga_2O_3 heterointerfaces grown along (100) and (010) orientations with the variation of Al compositions up to 52%. Results from this study will provide guidance for future device designs and fabrications.
Acknowledgment: The authors acknowledge the funding support from the Air Force Office of Scientific Research No. FA9550-18-1-0479 (AFOSR, Dr. Ali Sayir) and NSF (1810041, 2019753).
References:
1. Bhuiyan et al., APL Mater. 8, 031104 (2020).
2. Bhuiyan et al., Cryst. Growth Des. 20, 6722 (2020).
3. Bhuiyan et al., Appl. Phys. Lett. 117, 142107 (2020).
4. Mu et al., Appl. Phys. Lett. 117, 252104 (2020).

5:15 PM CC03

(Student) Electrical Characterization of MOVPE-Grown Low Sheet Resistance β-$(Al_xGa_{1-x})_2O_3$/β-Ga_2O_3 Heterostructure Channels Praneeth Ranga[1], Arkka Bhattacharyya[1], Adrian Chmielewski[2], Saurav Roy[1], Rujun Sun[1], Michael Scarpulla[1,1], Nasim Alem[2] and Sriram Krishnamoorthy[1]; [1]The University of Utah, United States; [2]The Pennsylvania State University, United States

Devices based on ultrawide bandgap β-Ga_2O_3 material are of considerable interest due to their potential for high power, high-frequency operation and low cost. β-Ga_2O_3 has an estimated bandgap of 4.7 eV and a breakdown field of 6-8 MV/cm leading to a BFOM(Baliga figure of merit) twice as large as gallium nitride. However, the conduction losses in β-Ga_2O_3 are partly limited by the low channel mobility of β-Ga_2O_3 films (< 200 cm^2/V.s). Based on the ab-initio theory, a modulation-doped β-$(Al_xGa_{1-x})_2O_3$/β-Ga_2O_3 channel could have mobility as high as 500 cm^2/V.s, which is beyond the optical phonon limited mobility of uniformly-doped Ga_2O_3. This is attributed to the dynamic screening of LO phonons at the 2DEG (two-dimensional electron gas) channel [1]. The screening effect is significant only at high electron sheet charge densities (n_s >= 5 x 10^{12} cm^{-2}). 2DEG Sheet charge densities between 1 x 10^{12} cm^{-2} and 5 x 10^{12} cm^{-2} have been attained in MBE-grown β-$(Al_xGa_{1-x})_2O_3$/β-Ga_2O_3 channels in literature [2]. To achieve a high-density 2DEG, a high band offset in conjunction with sharp delta doping is necessary. MOVPE growth of β-$(Al_xGa_{1-x})_2O_3$/β-Ga_2O_3 is promising due to its large growth window. Growth of β-$(Al_xGa_{1-x})_2O_3$ films with composition up to 50 % have already been studied using MOVPE [3]. Successful n-type doping has been demonstrated for composition up to 30 %. Based on our recent study, delta-doped β-Ga_2O_3 with CV measured FWHM of 3 nm was achieved by suppressing the surface segregation of silicon atoms at low temperatures [4]. All the above points indicate the promise of realizing high-density MOVPE-grown β-$(Al_xGa_{1-x})_2O_3$/β-Ga_2O_3 2DEG. In this work, we report on the growth and characterization of MOVPE-grown β-$(Al_xGa_{1-x})_2O_3$/β-Ga_2O_3 heterostructure channel [5]. Growth of β-$(Al_xGa_{1-x})_2O_3$/β-Ga_2O_3 is performed using Agnitron Agilis MOVPE reactor with TEGa, TMAl and O_2 as precursors and silane is used as a dopant. The growth is performed at 600 C to minimize the surface segregation of silicon atoms. Two samples A and B are grown with different spacer thickness, delta sheet density and Al composition. The [Al]/([Al]+[Ga]) precursor ratio is set between 18 - 25 %, which was verified using XRD. After patterning the SiO_2 hard mask, MOVPE n+ β-Ga_2O_3 regrowth is performed at 600 C. CV, TLM and Hall measurements are performed by utilizing the Ohmic and Schottky contacts deposited on the processed samples. Room temperature Hall sheet charge density values of 1.1 x 10^{13} cm^{-2} - 6.4 x 10^{12} cm^{-2} and mobility of 111-125 cm^2/V.s have been measured for samples A and B. Low-temperature Hall measurements showed that the sheet charge reduced to ~ 3 x 10^{12} cm^{-2}, which indicates the presence of a large parasitic channel in the β-$(Al_xGa_{1-x})_2O_3$ barrier. FET structures fabricated on sample A showed a peak current of 22 mA/mm and an on/off ratio of 8 x 10^6 In spite of having a large parasitic channel, a low sheet resistance of 5.3 kΩ/square was measured. This is attributed to the relatively higher mobility of the β-$(Al_xGa_{1-x})_2O_3$/β-Ga_2O_3 channel. Based on the literature, it can be seen that a much smaller value of sheet resistance could be realized by reducing the amount of parasitic charge. This first realization of a completely MOVPE-grown β-$(Al_xGa_{1-x})_2O_3$/β-Ga_2O_3 is promising for high-power and high-frequency devices based on β-Ga_2O_3.

References: [1] A. Kumar et.al J. Appl. Phys. 128, 105703 (2020); [2] N. K. Kalarickal et.al J. Appl. Phys. 127, 215706 (2020);[3] A. F. M. A. U. Bhuiyan et.al Cryst. Growth Des. 20, 6722 (2020 [4] P. Ranga et.al Appl. Phys. Lett. 117, 172105 (2020);[5] P. Ranga et al *Appl. Phys. Express* **14** 025501 (2021);

Acknowledgement: This material is based upon work supported by the Air Force Office of Scientific Research under award number FA9550-18-1-0507 monitored by Dr Ali Sayir. We thank Air Force Research Laboratory, Sensors Directorate for discussions.

5:30 PM CC04

Expanding Growth Window for MOCVD β-Ga_2O_3 Zixuan Feng, A F M Anhar Uddin Bhuiyan, Lingyu Meng and Hongping Zhao; The Ohio State University, United States

Metalorganic chemical vapor deposition (MOCVD) of β-Ga_2O_3 thin films have been demonstrated with record-high room temperature and low-temperature mobilities that approach the theoretically predicted limit. [1-3] The extracted low acceptor concentration (N_a < 10^{15} cm^{-3}) is extremely encouraging for its potential application in power electronics. Si impurities were discovered as the primary contributor to the background n-type conductivity in MOCVD β-Ga_2O_3. [2] Si impurities exist at the substrate interface, where it creates parasitic conductive channel in lateral device structures, posing negative impact on device performances. In our study, the interface charge also interfered the transport characterization on thin films with ultra-low charge density. [2] To address this issue, in-situ Mg acceptor doping was established in MOCVD β-Ga_2O_3. [3] However, Mg diffusion was found to be significantly dependent on the growth temperature, where the lower temperature is preferred due to the confined doping profile. In this study, we expanded the growth window of MOCVD β-Ga_2O_3 in terms of lowering growth temperature of β-Ga_2O_3, as well as increasing growth rate for thick drift layers with low charge density, which are critical to future high-performance β-Ga_2O_3 power electronics.

In our early works, [1] the high quality epitaxy was designed within relatively high growth temperature regime ranging 800 ~ 920 °C. Si incorporation was found to be enhanced at elevated growth temperatures. Defects characterizations combining deep level transient/optical spectroscopy and admittance spectroscopy also registered the deviation in trap states, although the concentration of these traps were much lower as compared to β-Ga_2O_3 synthesized by other methods. [5] In our most recent studies, the growth conditions for MOCVD (010) β-Ga_2O_3 was explored with growth temperature set between 650 ~ 800 °C. As the temperature reduced, the growth rate decreased monotonically. With Si doping concentration at ~1×10^{17} cm^{-3}, room temperature Hall mobilities were measured at ~150 cm^2/Vs for samples grown at 700, 750 and 800 °C. For the growth temperature at 650 °C, the Hall mobility was significantly impacted (~60 cm^2/Vs) due to possible defects formation and reduced crystalline quality. Secondary Ion Mass Spectroscopy (SIMS) analysis revealed that as growth temperature reduces, the carbon concentration eventually increases above the detection limit of SIMS, with concentration of 7×10^{17} cm^{-3} corresponding to growth temperature of 700 °C. The slightly increased charge density in films grown at 700 °C may indicate carbon serving as an donor type impurity in β-Ga_2O_3. However, the role of carbon in Ga_2O_3 still requires further investigation. Surface roughness also increased at lower growth temperature, possibly due to the limited surface adatom mobility. In summary, we expanded and established the growth conditions for MOCVD (010) β-Ga_2O_3 in the low temperature regime. The charge transport characterization indicates that high-quality (010) β-Ga_2O_3 could be achieved under growth temperatures as low as 700 °C. The extended growth window to lower temperature regime can allow us to fully utilize the high-quality epitaxial thin films while manage sharp doping profile for high-performance device fabrication. And this expanded growth window was utilized to develop high quality Mg doping in β-Ga_2O_3 with sharp profile and effective charge compensation.

Acknowledgment: The authors acknowledge the funding support from the Air Force Office of Scientific Research No. FA9550-18-1-0479 (AFOSR, Dr. Ali Sayir) and NSF (1810041, 2019753).

References:
[1] Z. Feng et al., Appl. Phys. Lett., 114, 250601 (2019).
[2] Z. Feng et al., Phys. Status Solidi RRL 14, 2000145 (2020).

[3] Z. Feng et al., Appl. Phys. Lett. 117, 222106 (2020).
[4] G. Seryogin, et. al, Appl. Phys. Lett. 117, 262101 (2020).
[5] H. Ghadi et al., Appl. Phys. Lett. 117, 172106 (2020).

5:45 PM CC05
(Student) Surface Reaction Dependence of Molecular Beam Epitaxy Grown Al on Various Orientations of β-Ga2O3 Kenny Huynh[1], Michael E. Liao[1], Xingxu Yan[2], Akhil Mauze[3], Takeki Itoh[3], James Speck[3] and Mark Goorsky[1]; [1]University of California, Los Angeles, United States; [2]University of California, Irvine, United States; [3]University of California, Santa Barbara, United States

Al was grown on (010), (001), and ($\bar{2}$01) β-Ga_2O_3 substrates via molecular beam epitaxy and the structural and chemical characteristics of the interface were studied. The Al was grown with substrate temperature of 100 °C and background pressure of $2*10^{-9}$ Torr. Transmission electron microscopy and energy dispersive X-ray spectroscopy (EDS) were used to assess interface crystallinity, thickness, and chemical composition. At the interface, amorphous aluminum oxide is observed in all three samples with thicknesses of 3.5 nm for (010) β-Ga_2O_3 and 2 nm for (001) β-Ga_2O_3 and ($\bar{2}$01) β-Ga_2O_3. In addition, gallium was found to diffuse through grain boundaries in the Al layer. The formation of interfacial oxides is not surprising and has been reported in other metal on β-Ga_2O_3 studies.[1,2] The dependence of the oxide thickness on the orientation of the β-Ga_2O_3 substrate and the gallium diffusion into the Al are the key aspects of this study. The atomic structure of β-Ga_2O_3 includes two unique Ga^{3+} ion positions, one that occupies on an octahedral site and the other that occupies a tetrahedral site with a 1:1 ratio in the unit cell.[3] In addition, fundamental studies of β-$(Al_xGa_{1-x})_2O_3$ alloy formation show that substitutional diffusion of Al energetically prefers octahedral sites, which mimic the corundum crystal structure.[4] We show that in Al on (010) β-Ga_2O_3, in which we observe the thickest interfacial oxide layer, diffusional pathways with consecutive octahedral Ga sites exist in the out-of-plane direction. In contrast, the (001) β-Ga_2O_3, and ($\bar{2}$01) β-Ga_2O_3 substrates exhibit alternating layers of tetrahedral and octahedral Ga sites, which we speculate that the layers of tetrahedral Ga sites act as increased energy barriers that impede diffusion of Al into β-Ga_2O_3 further into the substrate. In addition, the excess Ga that is observed in the Al film, suggests that Ga is rejected from the oxide layer following Al interdiffusion. Fundamental understanding of structural characteristics of metal - β-Ga_2O_3 interfaces will help explain thermal and electrical properties, which are inherently anisotropic in β-Ga_2O_3. The authors K.H., M.E.L., and M.S.G. would like to acknowledge the support from the Office of Naval Research through a MURI program, grant No. N00014-18-1-2429.

References

H. T. Aller, et al., Nano letters., 19(12), 8533-8538 (2019).
M. H. Lee, et al., APL Materials., 7(2), 022524 (2019).
S. Geller, J. Chem. Phys., 33, 676 (1960).
H. Peelaers, et al., Applied Physics Letters., 112(24), 242101 (2018).

Panel on Careers and Post-Graduate Studies in Materials Science

Moderators: Suzanne Mohney and Kris Bertness
Thursday Evening, June 24, 2021

7:30 PM - 8:30 PM
Established scientists and engineers from academia, industry and government will discuss career opportunities and their own career paths in material science and related fields. The session will be open to all with an interest in science, technology, engineering and mathematics (STEM), including undergraduate students.

Panelist—Adrienne Stiff-Roberts; Duke University, United States

Dr. Adrienne Stiff-Roberts is Jeffrey N. Vinik Professor of Electrical and Computer Engineering at Duke University, where she is also Director of Graduate Studies for the University Program in Materials Science and Engineering. Stiff-Roberts received a BS degree in physics from Spelman College (1999), a BEE degree in electrical engineering from Georgia Institute of Technology (1999), an MSE degree in electrical engineering (2001) and a PhD degree in applied physics (2004) from the University of Michigan. Her current research interests include organic and hybrid thin-film deposition by resonant-infrared matrix-assisted pulsed laser evaporation (RIR-MAPLE); materials characterization of organic and hybrid thin films; and the design, fabrication and characterization of organic and hybrid optoelectronic devices, especially infrared photodetectors, photovoltaic solar cells and multi-functional sensors.

Panelist—Wenbing Hu; Applied Materials, Inc., United States

Dr. Wenbing Hu is a Senior Process Integration Engineer at Applied Materials, Inc., where he contributes to the field of next-generation display technologies with process integration and device innovations. He received his BS degree in microelectronics at Shanghai Jiao Tong University, China (2010) and PhD degree in electrical engineering at the University of Michigan (2016). His research focused on solution-processed oxide electronic materials and devices. After school, Hu worked at LAM Research Corporation from 2016 to 2019 as a process engineer, developing state-of-the-art dry etch processes and hardware for 3D NAND memory chip manufacturing. Later he moved on as Process Integration Engineer at Royole Corporation.

Panelist—Samuel Graham: Georgia Institute of Technology, United States

Dr. Samuel Graham, Jr. is the Eugene C. Gwaltney, Jr. Chair of the Woodruff School of Mechanical Engineering at the Georgia Institute of Technology. His research is focused on the development of advanced electronic devices for future applications in RF communications, power electronics and energy systems. He also holds a courtesy appointment in the School of Materials Science and Engineering at Georgia Tech, a joint appointment with the National Renewable Energy Laboratory, and he is a visiting professor at Nagoya University in Nagoya, Japan. He is also a member of the Emerging Technologies Technical Advisory Committee of the U.S. Department of Commerce.

Panelist—David Estrada: Boise State University, United States

Dr. David Estrada is the Associate Director of the Center for Advanced Energy Studies, the Advanced Manufacturing Deputy Director of Academic Research at the Idaho National Laboratory, and an associate professor at the Micron School of Materials Science and Engineering, Boise State University. He is a veteran of the U.S. Navy, serving onboard the USS Curtis Wilbur as part of the forward deployed 7th Fleet. He earned his PhD degree in electrical engineering from the University of Illinois at Urbana-Champaign (2013) where he was the recipient of the NSF and NDSEG Graduate Fellowships. His work has been recognized with several awards, including the Society of Hispanic Professional Engineers Innovator of the Year, National TRiO Achiever and NSF CAREER awards. His research interests are in the areas of emergent semiconductor nanomaterials and bionanotechnology.

Panelist—Mona Ebrish; U.S. Naval Research Laboratory, United States

Dr. Mona Ebrish is a National Research Council Postdoctoral Fellow at the U. S. Naval Research Lab investigating wide-bandgap semiconductors for high-voltage applications. She is a Fulbright Scholar who received her BS degree in electrical engineering (2007) from the University of Tripoli. She earned her MS degree and PhD degree in electrical engineering from the University of Minnesota (2011, 2015). Ebrish's PhD dissertation is one of the earliest studies on utilizing the quantum capacitance effect in Graphene for sensing applications. Later she spent 4 years at IBM as an Advisory Research Scientist working on Si-CMOS scaling challenges. Her research resulted in a dozen U.S. patents and over 20 papers and abstracts in major journals and conferences.

Panelist—Michael Abraham; Lockheed Martin, United States

Dr. Michael Abraham is a Staff Semiconductor Materials Scientist/Process Engineer at Lockheed Martin, Santa Barbara Focal Plane, where he works on high end infrared cameras. He completed his BS degree and MS degree of engineering at Cornell University, both in materials science and engineering. For one year he worked at the U.S. Naval Research Laboratory and then joined The Pennsylvania State University materials science and engineering department. After completing his PhD degree at Penn State, he started his job at Lockheed Martin in 2017.

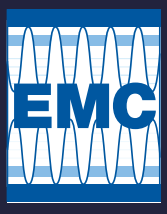

63RD ELECTRONIC MATERIALS CONFERENCE

June 23-25, 2021

FRIDAY ORAL PRESENTATIONS

SESSION DD: Materials for Memory and Logic
Session Chairs: Susan Fullerton-Shirey and Ke Xu
Friday Morning, June 25, 2021

9:15 AM DD01
(Student) Photo Floating-Gate Field-Effect Transistors for Machine Vision Jun Tao, Juan S. Vazquez and Rehan Kapadia; University of Southern California, United States

The prevailing thrive of artificial neural network (ANN) benefits the data-driven industry and academic fields more than any time in the past several decades and increased the demands for more power-efficient hardware to accelerate the computation. To build the ANN and avoid the expensive CMOS area cost, the novel devices, such as memristor-based RRAM, phase change memory, ionic floating-gate memory, Li-ion synaptic transistor, are heavily studied. Here we demonstrate that InP-based photo floating-gate field-effect transistors (PFG-FETs) not only work as synapses in ANN but perform sense and process optical information simultaneously for machine vision. The integration of single-crystalline InP channel based PFG-FETs directly on Si/SiO_2 substrate is enabled by templated liquid phase (TLP) approach and followed by standard metal layer deposition and dielectric stack layer ($Al_2O_3/TiO_2/Al_2O_3$ with 10 nm/2 nm/50 nm thickness) through e-beam evaporation and atomic layer deposition (ALD) respectively. Tin-doped indium oxide (ITO) gate electrode is deposited by sputtering. The transfer characteristic I_{ds}-V_{gs} curve show $>10^3$ on/off ratio and ~5.6V memory window (estimated from V_{th} shift) in the dual sweep. This is enabled by the heterogeneous dielectric structure allowing us to modulate the number of charges being trapped in the floating gate, and perform the short-term or long-term modulation of InP channel conductance to mimic the memory consolidation behavior. Here, the V_{gs} pulse or V_{prog} pulse is interpreted as action potentials from the pre-synaptic neuron, and I_{ds} is interpreted as post-synaptic current (PSC). When the number of V_{prog} pulses (-5V amplitude, 50 μs pulse width, and 100 μs period) increase from 1 to 100, PSCs just after the current potential spike decay in different speed and stabilize at discrete current level. That's because when only one V_{prog} pulse is applied, holes form InP channel tunnel into hold traps in Al_2O_3, adding a net positive charge to the gate dielectric but rapidly decays. However, when 100 V_{prog} pulses are applied, it results in holes being sequentially injected into the Al_2O_3 and then pumped into TiO_2 and lead to PSC modulation in a much longer time scale. A simple model with three exponential decay elements is used to fit the PSCs and quantitatively profile the behavior of our devices. To further boost the computation of ANN in machine vision, the programmable sensor array can take over the job, and directly perform the matrix-vector product operation $\boldsymbol{I}=\mathbf{R}\boldsymbol{P}$, where **R** is the responsivity matrix, $\boldsymbol{P}$ is the patterned power array, $\boldsymbol{I}$ is the output current array. In our PFG-FETs, when the light is illuminated through the highly transparent ITO gate and incorporated with V_{prog} pulses, both pulse amplitude and pulse number attained good responsivity modulation capability from 1 to 20 A/W using 700 nm CW laser. The photovoltaic effect and photogating effect are the two mechanisms that contribute to the photocurrent, but the V_{gs} dependence of photocurrent closely follows the transconductance curve, suggesting photogating effect is the dominant one. Based on this, a simple two-layer classifier for images is constructed and simulated with PFG-FETs ANN array. "U", "S", "C" patterned light power array can directly incident on the device array consist of 48 pieces of PFG-FET, then the output current array is processed by the cross-entropy loss function, and followed by backpropagation training mechanism to perform supervised learning. Clearly, the simulated classifier loss converges quickly, and the accuracy reaches 100% within 40 training epochs. Overall, the InP-based PFG-FET clearly manifests itself as a novel device for emulating complicated synaptic behavior, but more importantly, it can work as the smart sensor for machine vision technology.

9:30 AM DD02
(Student) Deterministic Analogue Resistive Memory for Neuromorphic Computing Based on Transition Metal Oxides Diana S. Kim[1], Elliot J. Fuller[2], Sangmin Yoo[1], Tae Cho[1], Neil P. Dasgupta[1], Wei Lu[1], Albert A. Talin[2] and Yiyang Li[1]; [1]University of Michigan–Ann Arbor, United States; [2]Sandia National Laboratories, United States

The rapid increase in data quantity and processing necessitate novel approaches to computing. Digital computing based on von Neumann architectures may not be optimal for data-intensive operations like machine learning due to the high energy costs of moving data between processor and memory. Neuromorphic computing that combines logic and memory functionality into a single analogue nonvolatile memory element is a promising energy-efficient solution that decreases the energy consumption by orders of magnitude. Filament-based phase-change memory and resistive random access memory are the most well-investigated approaches to neuromorphic computing, but these memories are stochastic due to the unreliability of the nanosized filaments used to store information. In this work, we develop the "bulk" resistive random access memory that stores information using the oxygen vacancy concentration in the 3D bulk. This cell contains a solid electrolyte sandwiched between two mixed ionic and electronic conductors (MIECs). The ion-conducting solid electrolyte blocks electrons and prevents the positive feedback that results in filament formation. Instead, the oxygen vacancy ions are uniformly distributed in the absence of filaments and thermal gradients. To switch the cell, electrochemical voltage pulses (+/-1.5V, 2 μs) shuttle vacancies between the MIECs; the concentration of the vacancies in one MIEC stores the analogue resistive state. This enables exceptionally reliable, linear, and deterministic switching among hundreds of analogue information states, while utilizing CMOS-compatible materials with long endurance and information retention. Atomic force microscopy and physical modeling confirms the absence of filaments. Three types of solid electrolytes are utilized: a thick model single-crystal yttrium-stabilized zirconia (YSZ), a thin-film YSZ grown by sputtering, and ultra-thin-film electrolytes of alumina, hafnia, and zirconia grown by atomic layer deposition. The oxygen vacancy ionic conductivities of these materials play a crucial role in the switching and retention times. The broad classes of oxygen conductors provide significant opportunities for future materials research towards next-generation analogue nonvolatile memory. Reference: "Filament-free bulk resistive memory enables deterministic analogue switching," *Adv Mater*, 32, 2003984 (2020)

9:45 AM DD03
(Student) SiOx Nanorod-Structured Artificial Neuron for Probabilistic Computing Applications Sanghyeon Choi[1], Gwang Su Kim[1,2], Haein Cho[1], Jehyeon Yang[1], Chong-Yun Kang[1,2] and Gunuk Wang[1,1]; [1]Korea University, Korea (the Republic of); [2]Korea Institute of Science and Technology, Korea (the Republic of)

Memristor, which simply consists of a switching layer inserted between two electrodes, is one of the most strong candidates to become a device-platform for imitating the principal characteristics of the biological neural network due to its nonlinear and dynamic electrical characteristics depending on the history of applied electrical programming [1-3]. In this study, we fabricated a nanorod structured SiO_x memristor using E-beam evaporator with glancing angle deposition at the wafer-scale and utilized the device as an artificial neuron for probabilistic computing applications. The device can exhibit a low forming voltage (< 2 V), a high ON-OFF ratio (> 10^5), reliable switching performances, and fast switching time (~40 ns), where the

switching event is attributed to the transition between two Si phases (amorphous Si and Si nanocrystal). Notably, the nanorod structured SiO_x can lead to the considerable reduction of forming voltage and enhancement of stochastic switching characteristics, when compared with the typical SiO_x memristor. Moreover, using voltage pulse trains, the SiO_x nanorod memristor with different glancing angles has successfully mimicked fundamental neuronal dynamics called integrate-and-fire processes and stochastic functionalities for the bayesian network in which each node is probabilistic variables. Then, as a proof of concept, we simulated the probabilistic inference for the correlation between three biological genes. Taken all together, the designed SiO_x memristor neuron could pave the way for stochastic artificial neurons and its based probabilistic computing technology.

References [1] S. Choi, J.-W. Choi, J. C. Kim, H. Y. Jeong, J. Shin, S. Jang, S. Ham, N.-D. Kim, and G. Wang, *Nano Energy*, Under review (2021)
[2] S. Choi, J. Yang, G. Wang, *Adv. Mater.*, 32, 2004659 (2020)
[2] S. Choi, S. Jang, J.-H. Moon, J. C. Kim, H. Y. Jeong, P. Jang, K.-J. Lee, and G. Wang. *NPG Asia Mater.* 10, 1097–1106 (2018)

10:00 AM DD04
(Student) Development of a Single Device-Based Organic Tactile Synapse for Artificial Learning Skin Applications
Seonghoon Jang[1], Kyuho Lee[2], Cheolmin Park[2] and Gunuk Wang[1]; [1]Korea University, Korea (the Republic of); [2]Yonsei University, Korea (the Republic of)

Recently, research on wearable intelligent electronics that detects, remembers, and learns external stimuli in real-time is receiving great interest. And a tactile synaptic device studies have emerged because they have the potential for human-interactive neuromorphic applications capable of large-scale parallel processing. However, the artificial tactile synaptic devices reported so far have complex physical connections between the sensor unit and the memory unit, which are inevitably not suitable for the wearable and patchable device due to the complex and costly manufacturing steps. Here, we demonstrate an artificial organic tactile synaptic device based on the integrated single device that enables the sensing, storing, and learning of a variety of tactile information. The synaptic device is able to be programmed with various tactile input pressures, by using a ferroelectric field-effect transistor structure with a pressure-sensitive ball-shaped top gate electrode. The synaptic device reliably and stably operates with high tactile reception sensitivity of 88 KPa^{-1} under bending conditions. And it was confirmed that synaptic plasticity was stably implemented for 10,000 inputs by various electrical/tactile stimuli, which allows for precise and robust tactile perception learning. Furthermore, we demonstrated that an integrated 4 x 4 tactile synaptic array allows for 2-dimensional tactile learning and proof-of-concept recognition simulations for diverse handwriting patterns with an outstanding error tolerance. As a result, our study proposes the novel platform for a single, integrated tactile neuromorphic system, which can simultaneously sense and learn a variety of external information.

10:15 AM BREAK

10:45 AM DD06
Ferroelectricity of As-Deposited HZO Fabricated by Plasma-Enhanced Atomic Layer Deposition at 300°C by Inserting TiO_2 Interlayers
Yuanshen Qi, Xianbin Xu, Igor Krylov and Moshe Eizenberg; Technion–Israel Institute of Technology, Israel

We report the observation of ferroelectricity in hafnium-zirconium-oxide thin films in the as-deposited state, namely after deposition at a low temperature of 300 °C without post-metallization annealing. The $Hf_{0.5}Zr_{0.5}O_2$ (HZO) thin film was interposed between two TiO_2 interlayers, and all films were produced by plasma enhanced atomic layer deposition and integrated into a TiN-based metal-insulator-metal capacitor. The ferroelectric nature of the as-deposited HZO film was evaluated by a polarization-voltage hysteresis loop and a $2P_r$ value of ~7.4 $\mu C/cm^2$ was achieved. Grazing incidence x-ray diffraction measurements and atomic-resolution scanning transmission electron microscopy characterization revealed the co-existence of fully crystallized polar orthorhombic and monoclinic phases of the dielectric in the as-deposited sample. We concluded that the nucleation and growth of the crystalline polar non-centrosymmetric orthorhombic phases in the 10 nm HZO thin film was prompted by the available energy from the plasma and the tensile lattice mismatch strain provided by the TiO_2 interlayer.

11:00 AM DD07
(Student) Tackling the Total Spin Hall Conductivity—A Multi-Code Approach for Doped and Alloyed Materials
Oliver L. McHugh[1], Martin Gradhand[1,2], Wen F. Goh[3,4] and Derek Stewart[5]; [1]University of Bristol, United Kingdom; [2]Johannes Gutenberg, University Mainz, Germany; [3]University of California, Berkeley, United States; [4]Osceola Consulting, LLC, United States; [5]Western Digital Corporation, United States

Spin Hall materials provide an energy efficient way to flip the orientation of a neighbouring magnetic layer and this ability could form the basis of future low power, high endurance MRAM devices. A wide array of computational techniques has been developed to investigate and optimize the different intrinsic and extrinsic aspects of the spin Hall effect (SHE) in materials. In this study, we use the screened Korringa-Kohn-Rostocker (KKR) methods[1] along with the linearized Boltzmann Transport equation, Quantum Espresso[2] and PAOFLOW[3] to reveal how dilute N or O impurities affect both the intrinsic and extrinsic SHE in bcc and β phase tungsten[4]. Our results, when examined in combination, suggest that the formation of grain boundaries with the doped system plays an important role in amplifying the SHE in β tungsten. Beyond this particular system, further techniques such as the coherent potential approximation enables us to treat not only dilute but concentrated alloys as well. With this expanded tool set, an even wider array of other spintronic materials, such as Pt based alloys will be explored.

[1] L. Peti et al, *Philos. Mag. B* **78**, 449 (1998)
[2] P. Gianozzi et al, *J. Phys.: Condens. Matt.* **21**, 395502 (2009)
[3] M. B. Nardelli et al, *Comp. Mat. Sci.* **143**, 462-472 (2018)
[4] O. L. W. McHugh, M. Gradhand, W. F. Goh and D. A. Stewart, *Phys. Rev. Mat.* **4**, 094404 (2020)

11:15 AM DD08
(Student) Effect of Size and Temperature Variation on Magnetic Tunnel Junction-Based Molecular Spintronic Devices (MTJMSDs)
Marzieh Savadkoohi, Bishnu R. Dahal, Andrew C. Grizzle, Christopher D'Angelo, Joshua Dillard and Pawan Tyagi; University of the District of Columbia, United States

Magnetic Tunnel Junction-based Molecular Spintronic Devices (MTJMSDs) take advantage of molecules' spin to create novel magnetic phenomena and futuristic computer devices. They have potential to create high speed memory and logic devices, reduce power consumption, and increase processing speed significantly. MTJMSD has a multilayer-shaped structure in which magnetic molecules are attached to two layers of ferromagnetic (FM) electrodes. The bridging molecules dictate the magnetic behavior of MTJMSDs by creating spin channels between two FM electrodes. Other attributes such as device dimension, operating temperature, electrodes' type, coupling energy, etc. will play an important role in defining MTJMSD magnetic characteristics. Experimental study of device behavior considering all possible scenarios can be extremely challenging. In our previous work we used Monte Carlo Simulation (MCS) and Metropolis algorithm[1] to investigate the effect of molecule-FM couplings on a cross-junction shaped MTJMSD's behavior. The device dimension used in our simulation is 11*50*50 (H*W*L) where H is the height, W

is the width and L is the length of device. Our result showed that strength and nature of coupling between molecules and left (JmL) and right FM-electrodes (JmR) result in long range ferromagnetic and antiferromagnetic spin orientations. In our previous MCS we studied one device size at fixed temperature. In this study, we are focusing on the effect of thermal energy (kT) variation and device dimensions on MTJMSDs magnetic properties such as magnetic susceptibilities, heat capacity, etc. Our preliminary simulation results suggest that increasing device size (L and W from 150 to 200) does not let FM electrodes and MTJMSD to attain the equilibrium state despite increasing simulation count to 2 billion. However, the transition from low to high magnetic moment occurred for JmR molecular coupling strength ~0.15 while JmL was fixed to 1(strong coupling). It means MTJMSD with increasing length occurred for molecular coupling strength reaching ~15% of Curie temperature. On the other hand, increasing FM-electrodes' thickness (H: up to 51) make noticeable change in required energy to make transitions from ferromagnetic to antiferromagnetic states. The critical point in the latter case shifted to around 0.6 of the Curie temperatures for the thickest device case, I.e. H=51. We also varied the kT range between 0.05 to 1.1 of the Curie temperatures and studied its impact on MTJMSD's magnetic properties. Our MCS study showed that lower temperatures (~0.05-0.1) allow both ferromagnetic and antiferromagnetic couplings between electrodes which result in MTJMSD having zero to maximum total magnetic moment. However, further increase in temperature (starting ~0.3) annihilated the effect of molecular induced magnetic coupling between electrodes and creates dominant noises. Thermal energy induced fluctuations resulted in very low magnetic moment all over MTJMSD device. This comprehensive study may provide insight about optimal conditions needed to experimentally realize and test MTJMSD devices.

11:30 AM DD09
Impact of Anisotropy on the Magnetic Hysteresis of Magnetic Tunnel Junction Based Molecular Spintronics Device (MTJMSD) Properties Bishnu R. Dahal, Marzieh Savadkoohi, Eva Mutunga, Andrew C. Grizzle, Christopher D'Angelo and Pawan Tyagi; University of the District of Columbia, United States

Molecular Spintronics devices (MSD), which possess tunable spin states, are crucial for the advancement of futuristic quantum computing technology [1]. To overcome the dominant issue of reliable mass producibility for existing MSD technology, we have designed a magnetic tunnel junction based molecular spintronics device (MTJMSD). MTJMSD is fabricated by bridging paramagnetic molecules across the edges of the ferromagnetic electrodes to create spin channels. MTJMSD enables the utilization of ferromagnetic electrodes with a wide range of magnetic anisotropies. There is a knowledge gap about the role of magnetic anisotropy on the magnetic swicthing mechanism and equilibrium magnetic prperties of the MTJMSDs. Understanding the role of anisotropy is crucial to apply this technology in futuristic spin valve type memory device applications. In this study we investigated the effect of anisotropy on the nature of the hysteresis curves generated computationally using Monte Carlo Simulations (MCS). We applied the in-plane magnetic anisotropy () along the ferromagnetic electrode of a magnetic tunnel junction. The magnitude of ***A*** varied numerically from 0 to1. ***A=1*** represented strong anisotropy of the order of interatomic Heisenberg exchange on the ferromagnetic electrodes. We also varied the thermal energy of the device from = 0.05 to 1.1. Here, = 0.1 corresponds to the operating temperature ranges from 50^0C to 90^0C with the assumption that the Curie temperature of the device lies between 500^0C to 900^0C. The effect of the anisotropy transformed the regular magnetic hysteresis of MTJMSD into a "wasp-waisted" -like hysteresis curve[2]. The "wasp-waisted" -like hysteresis curve is hypothesized due to the presence of multiple magnetic phases present on the ferromagnetic electrodes caused by strong magnetic anisotropy. Here, the materials possess hard and soft magnetic phases due to the higher and lower values of coercive fields. The "wasp-waisted" -like hysteresis curve was observed relatively at lower magnitudes of anisotropy at low thermal energy. The effect was observed up to = 0.8 with the high magnitude magnetic anisotropy (0.9). As a result, the effect of anisotropy keeps high magnetization of the device close to Curie temperature even when all the coupling effects get nullified due to thermal agitation. This research is supported by National Science Foundation-CREST Award (Contract # HRD- 1914751), Department of Energy/ National Nuclear Security Agency (DE-FOA-0003945).
References
[1] A. R. Rocha, V. M. García-suárez, S. W. Bailey, C. J. Lambert, J. Ferrer, and S. Sanvito, "Towards molecular spintronics," *Nature Materials,* vol. 4, no. 4, pp. 335-339, 2005/04/01 2005, doi: 10.1038/nmat1349.
[2] T. M. de Lima Alves *et al.*, "Wasp-waisted behavior in magnetic hysteresis curves of CoFe 2 O 4 nanopowder at a low temperature: Experimental evidence and theoretical approach," *RSC advances,* vol. 7, no. 36, pp. 22187-22196, 2017.

11:45 AM DD10
(Student) High-Speed Two-Dimensional Solid-State Non-Volatile Memory Based on Electric Double Layer Gating Using a Monolayer Electrolyte Shubham Sukumar Awate[1], Ke Xu[1], Jierui Liang[1], Benjamin Hunt[2] and Susan Fullerton-Shirey[1]; [1]University of Pittsburgh, United States; [2]Carnegie Mellon University, United States

A two-dimensional, solid-state, non-volatile memory has been demonstrated using electric double layer (EDL) gating of two-dimensional (2D) field effect transistors (FETs) with nanosecond scale switching speeds. In EDL gating, oppositely charged ions are accumulated near the 2D semiconductor surface, which induce image charges in the channel. This approach yields large capacitance densities corresponding to sheet carrier densities on the order of 10^{13} -10^{14} cm^{-2}. The monolayer electrolyte random access memory (i.e., MERAM) consists of cobalt crown ether phthalocyanine (CoCrPc) and lithium ions deposited as a monolayer on the surface a 2D semiconductor (WSe_2) by drop casting and annealing. CoCrPc is an electrically insulating (band gap ~ 1.34 eV) material with four crown ethers and it lays flat on the surface of a 2D semiconductor. Each crown solvates a Li^+ ion that can diffuse up or down through the crown ether cavity. In response to an applied electric field, Li^+ ions diffuse through the crown ether cavity and are positioned either near or away from the channel resulting in *on* and *off* states, respectively. We have previously shown switching behavior on 2D FETs using this material with potential application in non-volatile memory. Achieving well-ordered monolayers of CoCrPc and complete solvation of Li^+ into the crown ethers are critical for device operation because the location and orientation of the molecules governs the device mechanism. When the well-ordered electrolyte layer deposited on a WSe_2 FET is capped with h-BN, the off-state is stabilized (as confirmed by density functional theory (DFT)) by providing an energetically favorable state to Li^+ ions. We have demonstrated the bistability using back-gated pulsed voltage testing with pulse width of 1 sec (± 30 V). Switching speeds down to 50 nanoseconds (limit of the instrument) are demonstrated with an on-off current ratio > 10^3. Further, we performed the endurance test on the device and demonstrated the stability of the device for 1000 cycles (max. measured) with 50 ns pulse. The on-off current ratio was maintained (> 10^3) even after 1000 switching cycles. Current work includes quantifying performance metrics for several devices and top-gating these devices to decrease program/ erase voltages.

SESSION EE: Organic and Hybrid Materials and Devices II
Session Chairs: Suprem Das and Gerd Grau
Friday Morning, June 25, 2021

9:00 AM EE01
(Student) Manipulation of Morphological, Mechanical and Photovoltaic Properties of Ternary Organic Photovoltaic Blends for Optimum Operation Zhongxiang Peng[1], Long Ye[1,2] and Yanhou Geng[1,3]; [1]Tianjin University, China; [2]North Carolina State University, United States; [3]International Campus of Tianjin University, China

Organic photovoltaics (OPVs) based on nonfullerene small molecule acceptors have been the subject of renewable energy research in the past five years. Ternary photovoltaic blends comprising a polymer donor, a nonfullerene small molecule acceptor, and a fullerene acceptor have proved to be most efficient active layers for OPV devices. However, the morphological parameters and their relations with mechanical properties and photovoltaic performance of this type of highly efficient polymer:nonfullerene:fullerene OPVs are still unknown to date. To address this question, we characterized the thin-film microstructure and mechanical behavior of the best-performing ternary OPV active layer (PM6:N3:$PC_{71}BM$). Specifically, we alter the relative weight ratio of acceptors and systematically examined the composition dependence of photovoltaic performance, surface/bulk morphology, and mechanical parameters of the ternary blend films. It is shown that the addition of 20 wt% $PC_{71}BM$ to the acceptor component results in the highest power conversion efficiency (PCE) and crack-onset strain (COS) (Figure 1a). Most notably, we discover that it is possible to predict the elastic modulus of the ternary blend films by an extended Halpin-Tsai model (Figure 1b). This work provides simple guidelines for predicting the mechanical properties of many electronic devices based on ternary blends.

9:15 AM EE02
(Student) Structural and Optical Evolution of Mechanochemically Synthesized Zero-Dimensional Cesium Lead Bromide Perovskite Kyeong-Yoon Baek, Woocheol Lee, Jeongjae Lee, Jaeyoung Kim, Hyungbin Lim, Jonghoon Lee, Heebeom Ahn, Junwoo Kim, Keehoon Kang and Takhee Lee; Seoul National University, Korea (the Republic of)

Over the past decade, lead halide perovskites (LHPs) have gained significant interest due to their attractive optoelectronic properties with photoconversion efficiency (PCE) exhibiting *ca.* 22% in perovskite solar-cell (PSC) technologies.[1] Generally, solvent-based synthesis has been utilized as a synthetic method of LHPs. Recently, mechanochemical synthesis (MCS) has emerged as an appealing alternative due to many distinctive advantages such as its solvent-free nature of the process. MCS enables a well-controlled environment where intermediate phases can be analyzed.[2] In this study, we investigated the time-dependent behavior in the synthesis of Cs_4PbBr_6 (referred to as "0D perovskite") by ball milling of stoichiometric precursor mixtures. During the synthesis process, we could identify the coexisting two additional phases: $CsPb_2Br_5$ and $CsPbBr_3$, referred to as 2D and 3D phases, respectively, and derived the weight fraction of each phase from Rietveld refinement and NMR analysis. In addition, the peak photoluminescence (PL) intensity centered at 523 nm was observed to vary depending on the duration time of the synthesis and reached the maximum at around 3 hours of ball milling. The phase fraction analysis of the 0D powders with the maximum PL intensity indicates the presence of a finite amount of 3D phase, which agrees well with previous reports that proposed $CsPbBr_3$ nanocrystals embedded in solution-synthesized Cs_4PbBr_6 microcrystals as the origin of a highly efficient green light with a PLQY of 90%.[3] Our results provide a controllable synthetic methodology for acquiring 0D Cs-based perovskites with an efficient green emission through MCS and paves way for developing high performance perovskite light emitting devices in the future.

References

[1] W. S. Yang, J. H. Noh, N. J. Jeon, Y. C. Kim, S. Ryu, J. Seo, S. I. Seok, *Science*, **2015**, 348, 1234.
[2] F. Palazon, Y. E. Ajjouri, H. J. Bolink, *Adv. Energy Mater.*, **2020**, 10, 1902499.
[3] L. N. Quan, R. Quintero-Bermudez, O. Voznyy, G. Walters, A. Jain, J. Z. Fan, X. Zheng, Z. Yang, E. H. Sargent, *Adv. Mater.*, **2017**, 29, 1605945.

9:30 AM EE03
(Student) Photocurrent Enhancement in Organic Semiconductor/Metal Halide Perovskite Bilayers Colin Tyznik[1], James Lee[1], Jeni Sorli[2], Xiaojie Liu[3], Cynthia S. Day[1], John E. Anthony[4], Yueh-Lin Loo[2], Z. V. Vardeny[3] and Oana Jurchescu[1]; [1]Wake Forest University, United States; [2]Princeton University, United States; [3]The University of Utah, United States; [4]University of Kentucky, United States

Metal halide perovskites (MHPs) have rapidly become a topic of intense interest in both materials physics and device engineering due to their much sought for properties like high charge carrier mobilities, tunable bandgap, and low-cost processability. Various high-performance devices based on MHPs, including photovoltaic cells, light-emitting diodes, transistors and photodetectors have been reported, but a thorough understanding of the mechanism of charge transport and photo-transport in this material is still lacking. Here, we explore the photocurrent properties in bilayers consisting of small molecule organic semiconductors (OSCs) and MHPs. The MHP $CH_3NH_3PbI_{3-x}Cl_x$ was the primary photoactive layer and electron transport layer, while the OSC hole transport layer was 2,8-Difluoro-6,13-Bis(triisopropylsilylethynyl) anthradithiophene (diF-TIPS-ADT). We found that the responsivity of the bilayer optimized device was 28 times greater than neat perovskite film, reaching values as high as 6.4 A/W. Detectivity also improved by a factor of 9, to $1.4*10^{11}$ Jones, in devices with optimum film morphology. We found that the photoresponse can be tuned by altering the microstructure of the organic semiconductor: treatment of the device contacts with (2,3,4,5,6)-Pentafluorothiophenol (PFBT) resulted in grains as large as 155 μm^2 (LG) within the OSC, compared to much smaller grains (SG) seen when the OSC was deposited on the bare Au contacts, which resulted in grains in the order of 10 - 15 μm^2. Additionally, in the heterostructure devices made on a large grain OSC film, hysteresis was eliminated. X-ray diffraction measurements indicate that the crystal structure of both the OSC and MHP is similar in all samples, with diF-TIPS-ADT preferentially oriented with its (001) plane parallel to the substrate, and MHP adopting its tetragonal phase. We concluded that the observed performance improvement does not originate from differences in the interfacial coupling related to molecular orientation or differences in MHP crystal phase. Instead, we conclude that reducing charge trapping at grain boundaries within the OSC layer extends photocarrier lifetime, leading to an improvement in performance.

9:45 AM EE04
(Student) Crystallinity-Dependent Device Characteristics of Polycrystalline 2D Ruddlesden-Popper Perovskite Photodetectors Junwoo Kim, Woocheol Lee, Heebeom Ahn, Jonghoon Lee, Kyeong-Yoon Baek, Jae-Keun Kim, Keehoon Kang and Takhee Lee; Seoul National University, Korea (the Republic of)

Ruddlesden-Popper (RP) perovskites have drawn a lot of attention as an active layer for various optoelectronic devices due to their excellent photophysical properties and environmental stability. Especially, local structural properties of RP perovskites have shown to play important roles in determining the performance of optoelectronic devices [1]. In this presentation, we report the photodetector performance variation depending on the crystallinity of n=4 two-dimensional (2D) RP perovskite polycrystalline films. Through controlling the solvent evaporation rate, phases of 2D RP perovskite films could be distinguished between highly- and randomly-orientated phases [2]. We investigated how different factors related to the film crystallinity are reflected in the variation of photodetector performances by considering grain boundary and low energy edge state effects in n=4 RP perovskites [3]. Better understanding the interplay between these factors that govern the photophysical properties of the devices would be beneficial for designing high-performance RP perovskite-based optoelectronic devices.
References:
[1] Chen Y, Sun Y, Peng J, Tang J, Zheng K and Liang Z, *Adv. Mater.* **30**, 1703487 (2018).
[2] Chen A Z, Shiu M, Deng X, Mahmoud M, Zhang D, Foley B J, Lee S-H, Giri G and Choi J J, *Chem. Mater.* **31**, 1336 (2019).
[3] J. Kim et al., submitted (2020).

10:00 AM EE05
(Student) Controllable Deposition of Organic-Inorganic Halide Perovskite Films with Wafer-Scale Uniformity by Single-Source Flash Evaporation Jonghoon Lee, Woocheol Lee, Heebeom Ahn, Junwoo Kim, Youngrok Kim, Daekyoung Yoo, Keehoon Kang and Takhee Lee; Seoul National University, Korea (the Republic of)

Organic-inorganic halide perovskites (OHPs) are widely studied due to their excellent optoelectronic properties for solar cell and light-emitting diode applications. Conventional solution-processing techniques such as spin-coating method are commonly used in lab-scale device production but it is essential to explore other deposition techniques compatible for large-scale production. To overcome this, single-source flash evaporation technique, in which a single source of materials of interest is rapidly heated to be deposited in a few seconds, is one of the candidate techniques for large-scale thin film deposition of OHPs [1.2]. In this work, we investigated the controllability and reliability of the single-source flash evaporation technique for methylammonium lead iodide ($MAPbI_3$) perovskite [3,4]. In-depth statistical analysis was employed to demonstrate that the $MAPbI_3$ films prepared via the flash evaporation have an ultrasmooth surface and uniform thickness throughout the 4-inch wafer scale. We also show that the thickness and grain size of the $MAPbI_3$ film can be controlled by adjusting the amount of the source and number of deposition steps. In addition, we demonstrate that the reliability of the technique has a direct impact on the device characteristics of the fabricated photodetector devices via statistical analysis.
References
[1] G. Longo, L. Gil-Escrig, M. Degen, M. Sessolo, H. Bolink, Chemical Communications, 51, 7376 (2015).
[2] H. Wei, H. Ma, M. Tai, Y. Wei, D. Li, X. Zhao, H. Lin, S. Fan, K. Jiang, RSC Advances, 7, 34795 (2017).
[3] W. Lee, J. Lee, H.-D. Lee, J. Kim, H. Ahn, Y. Kim, D. Yoo, J. Lee, T.-W. Lee, K. Kang, T. Lee, Sci. Rep. 10, 18781 (2020).
[4] J. Lee et al. submitted (2020)

10:15 AM BREAK

10:45 AM EE06
(Student) Current Noise Analysis on Organo-Metal Halide Perovskite Resistive Switching Memory Heebeom Ahn, Keehoon Kang, Woocheol Lee, Jae-Keun Kim, Junwoo Kim, Jonghoon Lee, Kyeong-Yoon Baek and Takhee Lee; Seoul National University, Korea (the Republic of)

Resistive switching memory devices are being widely studied due to their excellent characteristics such as high scalability, non-volatility, and fast operation speed. Organo-metal halide perovskite (OHP), which is solution-processable and has outstanding optical and electrical properties, is also applied to a resistive memory device. OHP resistive memory has the advantage of being able to operate with a low voltage and large ON/OFF ratio [1]. On the other hand, random distribution in operation voltage remains a challenge in memory application. This stochastic operation characteristic is due to the random formation of conducting filaments that cause resistance changes in the material. Therefore, studies on the structure of the conducting filament are important. However, observing a nano-scale structure is difficult. Moreover, there is insufficient research on how the conducting filaments are formed in OHP materials. In this presentation, the geometric shape of the conducting filaments formed in the perovskite was explored through a current noise analysis. By observing the electrical properties and current noise under different temperature conditions, we investigated how the temperature condition affects the formation of the conductive filaments [2]. Through this, more advanced understanding of the operating mechanism of the perovskite resistive memory device will be possible.
References
[1] K. Kang, H. Ahn et al., *Adv. Mater*. 31, 1804841 (2019).
[2] H. Ahn et al., manuscript in preparation.

11:00 AM EE07
(Student) Molecular-Scale Selector Implemented by a Combination of Different Molecular Dipole Orientation and Two-Dimensional Semiconductors Jung Sun Eo, Jaeho Shin and Gunuk Wang; Korea University, Korea (the Republic of)

Diverse types of molecules such as a donor-s-acceptor molecules and ferrocenyl alkanethiol have been suggested as potential candidates for the electronic component of a molecular rectifier. [1,2] Recently, we demonstrated a novel strategy and design rule for realizing molecular-scale diode features based on the energy band engineering between simple alkanethiol or conjugated molecules and two-dimensional (2D) semiconductors.[3] Here, we firstly suggest a molecular-scale (sub-2nm) selector where is based on a heterojunction structure with a non-functional molecule(1-octanethiol, tridecafluoro-1-octanethiol) and two-dimensional semiconductor(MoS_2, WSe_2), which can be utilized to prevent the crosstalk signal in the crossbar memory array. According to direction of molecular dipole moment, the type of 2D semiconductors (1_L-MoS_2 of n-type), and the metal work function (Au and Pt), we found the nonlinearity at $V_r/2$ scheme can be significantly varied, e.x., 1.2 ± 10^1 for Au/C8/1_L-MoS_2/Au and 3.5 ± 10^2 for Au/F6H2/1_L-MoS_2/Pt. This phenomenon can be understood based on the interfacial energy band adjustment of 2D semiconductor in molecular heterojunction according to the direction of molecular dipole moment. The maximum non-linearity value is found to be 2.7 ± 10^3 for the case of Au/F6H2/1_L-MoS_2/Pt. With this non-linearity, the suggested molecular selector enables to extend the array size up to ~ 9Gbit crossbar array.
[1] Díez-Pérez, I. *et al.* Rectification and stability of a single molecular diode with controlled orientation. *Nat. Chem.* **1**, 635 (2009).
[2] Chen, X. *et al.* Molecular diodes with rectification ratios exceeding 10^5 driven by electrostatic interactions. *Nat. Nanotechnol.* **12**, 797 (2017).

[3] Shin, J. *et al.* Tunable rectification in a molecular heterojunction with two-dimensional semiconductors. *Nat. Commun.* **11,** 1412 (2020).

11:15 AM EE08
(Student) Fiber-Shaped Multi-Synapses Enabling an Electronic-Textile Neural Network for Wearable Neuromorphic Applications Seonggil Ham[1], Minji Kang[2], Seonghoon Jang[1], Jingon Jang[1], Sanghyeon Choi[1], Tae-Wook Kim[2] and Gunuk Wang[1]; [1]Korea University, Korea (the Republic of); [2]Jeonbuk National University, Korea (the Republic of)

A wearable neuromorphic electronic system, that can learn and interpret the non-structural biometric information at extremely low-power, has been brought great attention because of its applicability as the intelligent device that can easily attach onto the human body or any rough surface [1-3]. With this reason, organic-based artificial synaptic devices have been proposed as a potential candidate for wearable neuromorphic applications due to its inherent mechanical flexibility and the material (or device form) variability for the desired functionalities [2,3]. In this study, we designed 1D fiber-shaped multi-synapses comprising ferroelectric organic transistors fabricated on a 100 mm Ag wire and utilized them as multi-synaptic channels in an e-textile neural network for wearable neuromorphic applications. The device mimics diverse synaptic functions, including short- and long-term plasticity with 80 states and spike rate- and timing-dependent plasticity. It exhibited excellent reliability even under 6,000 repeated input stimuli and mechanical bending stress. Various NOR-type textile arrays are formed simply by cross-pointing 1D synapses with Ag wires, where each output from individual synapse can be integrated and propagated without undesired leakage. Notably, the 1D multi-synapses achieved up to ~90% and ~70% recognition accuracy for MNIST and electrocardiogram patterns, respectively, even in a single-layer neural network, and almost maintained regardless of the bending conditions.

References

[1] Park, Y.; Park, M.-J.; Lee, J.-S. Adv. Funct. Mater. **2018**, 1804123
[2] van de Burgt, Y.; Lubberman, E.; J. Fuller, E.; T. Keene, S.; C. Faria, G.; Agarwal, S.; J. Marinella, M.; Talin, A. A.; Salleo A. Nat. Mater. **2017**, 16, 414-418
[3] Jang, S.; Jang, S.; Lee, E.-H.; Kang, M.; Wang, G.; Kim, T.-W. ACS Appl. Mater. Interfaces **2019**, 11, 1071-1080
[4] *S. Ham et al. Sci. Adv. **2020**, 6, eaba1178 [Published]

SESSION FF: Doping and Stoichiometric Effects on Epitaxial Material
Session Chairs: Kurt Eyink and Rachel Goldman
Friday Morning, June 25, 2021

9:00 AM FF01
(Student) Background Carrier Polarity Switching in AlxIn1-xAsySb1-y Digital Alloys Joshua A. McArthur[1], Stephen D. March[1], Dekang Chen[2], Adam A. Dadey[2], Andrew H. Jones[2], Joe C. Campbell[2] and Seth R. Bank[1]; [1]The University of Texas at Austin, United States; [2]University of Virginia, United States

$Al_xIn_{1-x}As_ySb_{1-y}$ (henceforth referred to as AlInAsSb) grown as a lattice-matched digital alloy on GaSb substrates has recently emerged as a promising material system for avalanche photodetectors (APD) operating at near- to mid-IR wavelengths. In particular, AlInAsSb possesses a broadly tunable bandgap over a wide alloy composition range, as well as advantageous band offsets that lead to low-noise avalanche multiplication gain at room- temperature [1]. This makes AlInAsSb a favorable alternative to other bulk APD materials, like Si, which lacks the bandgap flexibility for spectral response at telecom and mid-IR wavelengths, or HgCdTe, which suffers from low manufacturing yield and requires cryogenic operation [2]. The tunability offered by AlInAsSb has enabled the realization of bandgap-engineered devices such as separate absorption, charge multiplier photodetectors [3] and staircase APDs [4]. However, designing these devices is challenging because they are electrostatically-sensitive to both the magnitude and polarity of the unintentional (UID) background carrier concentration. Direct measurements of AlInAsSb carrier concentrations are complicated by the intrinsic conductive nature of GaSb [5] with intrinsic carrier concentrations of ~1017 cm-3 [6]. In order to avoid parallel conductive channels through the substrate, conventional CV measurements are typically used to determine UID carrier concentrations. This method allows for accurate characterization of the magnitude of the UID carrier concentration, but not the polarity. Recently, a double mesa CV method was developed that allows for the measurement of the UID magnitude and polarity for epitaxial films grown on GaSb substrates [7]. Here we present room temperature double mesa CV measurements of nominally-identical AlInAsSb pin diodes grown via molecular beam epitaxy at different points in a growth campaign. Interestingly, the UID polarity appeared to change from p-type to n-type at later times in the campaign. A change in UID polarity dramatically influences device design and performance and is a potentially important feature for the Al-containing antimonide/arsenide superlattice community. In addition, temperature-dependent double mesa CV measurements performed between 80-350K show that the UID polarity remains n-type for samples grown later in a campaign. This is a distinct departure from the temperature-dependent UID of other antimonide/arsenide superlattice systems [8,9]. Further measurements involving deep-level transient spectroscopy as well as secondary ion mass spectrometry are in progress to identify activated energy levels of dopants and possible incorporated impurities. Direct comparisons of devices designed with an assumed p-type background versus an assumed n-type background, as well as more studies that isolate the effect of the aluminum source purity on the UID concentration are in progress and will be presented at the conference. This work was supported by ARO (W911NF-17-1-0065) and DARPA (HR0011-20-9- 0087 and HR0011-20-9-0086).

References:

[1] Maddox, et al. Crystal Growth 2016
[2] Martyniuk, et al. App Phys Rev 2014.
[3] Jones, et al. Nature Photonics 2020
[4] Ren, et al. APL 2016.
[5] Virkkala, et al. Phys Rev B 2012
[6] WaferTech GaSb Wafer Datasheet
[7] Fink, et al. Proc. SPIE 2020.
[8] Cervera, et al. Journ App Phys 2009
[9] Khoshakhlagh, et al. APL 2010

9:15 AM FF02
(Student) Reduction of the Tc and Suppression of the ΔTc of VO2 Epitaxial Films on TiO2 Buffered Sapphire Substrate Binjie Chen, Gowoon Kim, Hai Jun Cho and Hiromichi Ohta; Hokkaido University, Japan

Vanadium dioxide (VO_2) is well-known for its temperature-driven metal-to-insulator transition between the monoclinic (M1) phase and the rutile (R) phase, which is accompanied with abrupt changes in electrical and optical properties. These intriguing changes have attracted great interest and promises a lot of potential applications. However, the phase transition of bulk VO_2 usually occurs around 68 °C with significant thermal hysteresis induced by the latent heat of the first-order transition. The relatively high phase transition temperature T_c and broad hysteresis width ΔT_c are adverse to its practical application. Therefore, the modulation of its phase transition behavior is quite necessary. Accumulating evidence suggests that the strain state plays an important role in the phase transition behavior of VO_2

and it has been confirmed that the specific strain between VO_2 and TiO_2 can significantly reduce T_c[1, 2]. Based on this, in order to finely modulate the phase transition behavior and further investigate its relationship with strain state, we inserted TiO_2 epitaxial film between VO_2 film and the (100) α-Al_2O_3 substrate as the buffer layer. By controlling the thickness of both VO_2 film and TiO_2 buffer layer, the variational strain state can be introduced and further lead to the change of lattice parameters and phase transition behavior of VO_2 film. Specifically speaking, when both VO_2 and TiO_2 layers are thin (~10 nm), these two layers are highly strained to the Al_2O_3 substrate. Due to inconsistent lattice mismatch between [100] and [010] direction, the lattice parameter *a* and *b* of VO_2 will be stretched and compressed respectively, leading to the suppression of phase transition. If increasing the thickness of TiO_2 layer to 200 nm and maintaining the VO_2 thickness of 10 nm, due to the lattice relaxation, TiO_2 will be relaxed to the rutile phase. As the result, the structure of VO_2 layer which is still strained to TiO_2 will change synchronously and exhibit the sharper phase transition with reduced T_c of ~34 °C. This phenomenon is similar to the VO_2 film epitaxially grown on TiO_2 substrate. Lastly, by further increasing the VO_2 thickness from 5.5 to 50 nm, the VO_2 layer will also tend to be relaxed to bulk M1 phase and the T_c can be continuously adjusted in a wide range from 34 to 58 °C. More interestingly, when the VO_2 is thicker than 30 nm, the ΔT_c is extremely narrowed to ~0.4 °C and the lattice parameter *c* exceeds the bulk value correspondingly. We consider the strain-induced lattice parameter change can modify both of the T_c and ΔT_c. And by controlling the strain state, the phase transition behavior of VO_2 can be finely designed. These results may be useful for the design of VO_2-based functional material and device.

[1] Y. Muraoka, Z. Hiroi, *Appl. Phys. Lett*. **80**, 583-585 (2002)
[2] N. B. Aetukuri et al., *Nat. Phys.* **9.10**, 661-666 (2013)

9:30 AM FF03
Electrochemical-Redox-Modulation of the Oxygen Content in Superconducting $YBa_2Cu_3O_{7-\delta}$ Xi Zhang, Gowoon Kim, Qian Yang, Hai Jun Cho and Hiromichi Ohta; Hokkaido University, Japan

The oxygen deficiency, δ plays a decisive role in the superconducting properties of $YBa_2Cu_3O_{7-\delta}$ (YBCO), which is extensively known as the high superconducting transition temperature (T_c). YBCO is metallic when $\delta = 0$, but it becomes a semiconductor when $\delta \approx 1$. The T_c is also strongly dependent on δ and it decreases form ~92 K to ~0 K with the variation of δ from 0 to ~0.6. The traditional method for controlling δ in YBCO is heat treatment in an oxygen atmosphere. However, a high temperature is usually needed, which is very likely to cause detrimental changes in structures by interdiffusion, particularly for thin-film devices. Number of recent researches have demonstrated that by applying an external electric field, oxide ions (O^{2-}) can migrate from the electrode and finally escape from the CuO_x infinite layers, introducing oxygen vacancies in the cuprate superconductor films.[1] This result provides another promising method to tune the oxygen deficiency in YBCO in a mild way. In this study, we proposed an electrochemical strategy to directly add or remove O^{2-} ions in YBCO films using Yttria-Stabilized Zirconia (YSZ) substrate as the solid electrolyte. We fabricated YBCO films (~65 nm) by pulsed laser deposition technique on (100) YSZ substrates with 10%-Gd-doped CeO_2 as the buffer layer.[2] A silver paste was coated on the back side of the YSZ substrate, and the film was then placed on an Au foil for the redox reaction at 300 °C in air. The temperature-dependence resistivity of the YBCO films was measured to evaluated the effect of electrochemical redox on the superconducting properties. The as-grown film showed a T_c of ~46 K and it increased with the oxidation of films. When a negative voltage was applied to the film, the T_c increased to ~76 K, resulting from the intercalation of oxide ions in the film. On the other hand, the positive voltages efficiently removed oxygen from YBCO films and successfully modulated the electrical conductivity of YBCO films from superconductor to insulator. The electrochemical redox reaction induced crystal structural changes were also invested by XRD. Obvious increase of *c*-axis lattice parameters was observed after applying a positive voltage, clarifying the effect of oxygen vacancies on YBCO crystal structure. The thermopower of the YBCO films was measured at room-temperature, according to which, the Jonker plot with a slope of $k/e = -198\ \mu V\ K^{-1}$ based on the plot of the thermopower versus the logarithm of conductivity was obtained. The thermopower changed from positive to negative as the oxygen content increased by applying the negative voltage, indicating that the Fermi energy was successfully modulated. This study provided an efficient approach to manipulate the superconductivity of cuprate in at mild conditions.

References

[1] A. M. Perez-Muñoz *et al.*, *PNAS* **114**, 215 (2017).
[2] Q. Yang, H. Jeen, H. Ohta *et al.*, *Adv. Mater. Interfaces* **6**, 1901260 (2019). <audio controls="controls" style="display: none;"> </audio>

9:45 AM FF04
(Student) Effect of B Distribution on the Band Structure of BGa(In)As Alloys Qian Meng[1], Rasha El-Jaroudi[1], Rachel C. White[1], Tuhin Dey[2], Mohammed S. Reza[2], Seth R. Bank[1] and Mark Wistey[2]; [1]The University of Texas at Austin, United States; [2]Texas State University, United States

The addition of boron into conventional III-V alloys reduces their lattice constants, expanding the materials options for near-infrared photonics on GaAs[1] and offering a path towards direct-bandgap III-V materials lattice-matched to Si.[2] B-III-V active region emitters and detectors on GaAs and Si could have a profound impact on technologies such as telecommunications, laser radar, and photovoltaics. However, the addition of boron into conventional III-Vs forms a highly-mismatched alloy and their material properties alloy are underexplored. Other highly-mismatched constituents in conventional III-V alloys, most notably nitrogen and bismuth, significantly perturb the host band structure, resulting in a technologically-advantageous reduction in the bandgap, while undesirably degrading material properties required for high-performance devices. The addition of B to conventional III-V materials is predicted to degrade material properties less severely than other highly mismatched alloys, since boron is predicted to have a higher solid solubility.[3] This suggests that superior quality material and higher levels of incorporation may be achievable with boron. This work investigates the effects of dilute boron incorporation on the electronic band structure of III-V alloys to determine their ultimate device potential. Dilute-nitrides have been found to suffer a significant reduction in carrier mobility, which was attributed to alloy scattering from large variations in the band edges due to band anticrossing.[4] However, we previously observed a weaker reduction in carrier mobility in the dilute-borides as compared to dilute-nitride alloys and the carrier mobility of p-type doped $B_{0.05}Ga_{0.95}As$ can be at around 180 cm^2/Vs.[2,5] We performed theoretical calculations of the band structure using the density functional theory (DFT) package Vienna Ab initio Simulation Package (VASP) with HSE06 hybrid functionals. We observed a splitting of the conduction band (CB) and a slight perturbation of the lower CB (relative to GaAs) when boron was incorporated substitutionally into (In)GaAs. The perturbed CB showed increased electron effective mass and density of states, which could be leveraged for low-threshold diode lasers with high differential gain, as well as low-noise avalanche photodiodes with suppressed electron-initiated impact ionization. Additionally, we observed similar conduction band perturbation when boron was incorporated as B-B split interstitials into GaAs. Detailed investigation of boron-related defects in BGa(In)As and their effects on the band structure is underway and will be reported. Experimental characterization of the CB splitting in BGa(In)As alloys, grown by solid-source molecular beam epitaxy, will also be reported. This work was performed in part at

the University of Texas Microelectronics Research Center, a member of the National Nanotechnology Coordinated Infrastructure (NNCI), which is supported by the NSF (No. ECCS-1542159). This work was also supported by the National Science Foundation (Award Nos. ECCS-1933836, DMR-1508646, and CBET-1438608). The authors also acknowledge the Learning, Exploration, Analysis, and Processing (LEAP) cluster at Texas State University for computing resources.
1 El-Jaroudi et al. Appl. Phys. Lett. (2012)
[2] McNicholas et al. 60th Electronic Materials Conference (2018)
[3] Hart and Zunger. Phys. Rev. B. (2000)
[4] Fahy and O'Reilly. Appl. Phys. Lett. (2003)
[5] McNicholas et al. Manuscript in preparation

10:00 AM FF05
(LATE NEWS, Student) Growth Optimization of InSbBi Alloys for Wavelength Extension on InSb Rachel C. White, Aaron J. Muhowski, Leland J. Nordin, Daniel Wasserman and Seth R. Bank; The University of Texas at Austin, United States

III-V-bismide alloys have received significant attention over the past few decades due to the extreme bandgap reduction induced by the introduction of small concentrations of bismuth. However, dilute-bismides have struggled to achieve material quality commensurate with other III-V alloys, often attributed to the dramatically different growth temperatures of III-Bi and III-Sb/As materials. $InSb_{1-x}Bi_x$ is a particularly promising candidate for accessing the midwave- to longwave-infrared (MWIR, LWIR respectively) with high-performance optical devices. Surprisingly, while $GaSb_{1-x}Bi_x$ and $InAs_{1-x}Bi_x$ have been widely studied, $InSb_{1-x}Bi_x$ remains comparatively underexplored, with relatively few experimental investigations since the alloy was first synthesized nearly 50 years ago.[1] In particular, growth in the "unity sticking" regime[2] has not been demonstrated and photoluminescence (PL) has not been observed. In this work, we demonstrate high-quality $InSb_{1-x}Bi_x$ films that exhibit a linear dependence of the bismuth concentration on the bismuth flux and, consequently, report the first PL from $InSb_{1-x}Bi_x$ alloys. Epitaxial films, nominally 250 nm thick, were grown by solid-source molecular beam epitaxy on n-type (100) InSb substrates using a growth regime similar to that employed for high-quality $GaSb_{1-x}Bi_x$[3] and $InAs_{1-x}Bi_x$[4] synthesis. Samples were grown at a low substrate temperature of approximately 300°C with V/III flux ratios near stoichiometry. A comparatively fast growth rate of approximately 1 µm/hr was utilized to encourage bismuth incorporation. X-ray diffraction (XRD), PL, and atomic force microscopy (AFM) measurements were performed to characterize the bismuth content, optical quality, and surface roughness. X-ray diffraction measurements of the $InSb_{1-x}Bi_x$ films suggested bismuth concentrations up to ~1.8%, assuming a lattice constant of 6.63 Å for InBi, which is reasonable given Rutherford backscattering spectrometry (RBS) measurements of both $InAs_{1-x}Bi_x$[5] and $InSb_{1-x}Bi_x$.[6] Photoluminescence measurements of the same $InSb_{1-x}Bi_x$ films showed a red shift of PL associated with the InSbBi with increasing bismuth concentration. Specifically, PL measurements suggest a bandgap reduction of ~23 meV/% bismuth, which is comparable to previous reports of bandgap reduction estimated from optical absorption measurements of $InSb_{1-x}Bi_x$ films.[1,6] Temperature-dependent PL measurements of the highest Bi concentration film, containing 1.8% bismuth, showed a decrease in bandgap energy with increasing temperature that is consistent with a direct interband transition. AFM measurements of all films showed relatively smooth surfaces (RMS roughness of approximately 1 nm), however the highest concentration film exhibited large bismuth droplets. We expect droplet formation could be mitigated through optimization of the growth parameters. Thorough studies of the full growth space, particularly substrate temperature, as well as the effects of annealing on optical properties are in progress and will be presented.
This work was supported by Lockheed Martin and NSF (ECCS-1933836). This work was performed in part at the University of Texas Microelectronics Research Center, a member of the National Nanotechnology Coordinated Infrastructure (NNCI), which is supported by the NSF (No. ECCS-1542159). This work was also supported by an NSF Graduate Fellowship (RCW).
*Corresponding Author: coreywhite@utexas.edu, Phone: 1-336-340-8587
[1]A. M. Jean-Louis, B. Ayrault, and J. Vargas *Phys. Status Solidi B* **34** (1969).
[2]S. Spruytte et al., *MRS Internet J. Nitride Semicond. Res.* **5** (2000).
[3]A. J. Ptak et al., *J. Cryst. Growth* **338** (2012).
[4]S. J. Maddox et al., *54th Electronic Materials Conf.* (2012).
[5]S. J. Maddox et al., *55th Electronic Materials Conf.* (2013).
[6]M. K. Rajpalke et al., *Appl. Phys. Lett.* **105** (2014).

SESSION GG: Oxide Semiconductors—Charge Transport and Optical Properties
Session Chairs: Leonard Brillson and Andre Zeumault
Friday Morning, June 25, 2021

10:45 AM GG01
(Student) Defects and Dopants at Ultra-Thin Film Indium Tin Oxide (ITO) Interfaces Jade Cowsky[1], Kevin Leedy[2], David Look[2,3] and Leonard J. Brillson[1,1]; [1]The Ohio State University, United States; [2]Air Force Research Laboratory, United States; [3]Wright State University, United States

We have used depth-resolved cathodoluminescence spectroscopy (DRCLS) to measure defects, defect complexes, and dopant densities localized at nanoscale interfaces of ultrathin indium tin oxide (ITO) on fused silica. Electronic and geometric structural properties of ITO in ultrathin, degenerate thin films strongly affect its transport properties on a nanometer scale. ITO grown by pulsed laser deposition (PLD) is a degenerately doped semiconductor due to Sn cation dopants supplied by Sn alloying into the otherwise In_2O_3 lattice. With its 3.5 eV or higher band gap and high conductivity, ITO is widely used as a transparent conducting oxide (TCO). Degenerate charge densities are achievable even with ultrathin films of 10 – 20 nm thickness and can provide plasmonic coupling with light via a tunable refractive index. Indeed, such nanoscale film thicknesses maximize electric fields in electric double layers used to modulate amplitudes of photons propagating in, *i.e.*, optical waveguides to maximize tunability. Using ITO for electro-optic modulators enables devices to be made smaller and operate at higher frequencies than conventional materials[1], but the minimum electrical or effective thickness of such highly conductive dielectric layers is less than the actual material thickness due to a disordered layer.[2] The nature of such disordered layers in ITO and other TCO semiconductors has not yet been explored at the nm scale of films and can involve a combination of native point defects, lattice disorder, film morphology, and ITO/substrate interface chemical structure. Our DRCLS results for ITO films grown by pulsed laser deposition reveal the presence of new defects localized within 1 -3 nm of the ITO/glass interface that can account for lattice disorder and disordered transport layer. This is in agreement with quantum magnetoconductivity measurements, which find strong disorder at the interface that falls off exponentially toward the surface with a decay constant of about 6 nm. Figure 1 illustrates Monte Carlo rates of electron-hole pair creation inside In_2O_3:10%SnO_2 films on fused silica as a function of incident electron beam energy E_B showing that 0.4 kV to 1.5 kV E_B controls measurement depth on a near-nanometer scale. Figure 2 illustrates significant changes in CL spectrum shape as a function of depth in the 13.1 nm thick ITO film, arising due to variations in defect density and band gap intensity. Defects are labeled with their tentative identifications.

Figure 4 shows the CL emission spectrum at the interface with both ITO and SiO_2 characteristic spectra subtracted out, leaving only features unique to the interface. It reveals a prominent feature at the interface at 3.38 eV and several smaller features at sub-E_G energies. Figure 3 illustrates the subtraction process and Fig. 4 shows the deconvolved spectra used to generate normalized depth profiles. Figure 5 displays emission area as a fraction of total spectrum emission as a function of depth in the 13.1 nm thick ITO film, showing peak intensities in several defect features at or near the interface. Figure 6 depicts one possible band diagram of ITO that could produce luminescence features like those seen in our ITO CL spectra. Other possible explanations for various features include H complexes with native point defects, H interstitials, Sn-related traps, or In interstitials paired with two indium vacancies.[3] Defect and doping densities show significant differences between bulk-like films of several hundred nm versus ultrathin films in the 5 – 40 nm range, suggesting new approaches to minimize disordered layers and optimize interface conductivity.
LJB and JC gratefully acknowledge National Science Foundation Grant no. DMR-18-00130.
1. K. Shi and Z. Lu, J. Nanophotonics **9**, 093793 (2015).
2. D.C. Look and K.D. Leedy, Sci. Repts. **9**, 1290 (2019).
3. J.B. Varley, H. Peelaers, A. Janotti, and C.J. Van de Walle, J. Phys.: Condens. Matter **23**, 334212 (2011).

11:00 AM GG02
(Student) Modulation of Optical and Electronical Properties for Transparent Oxide Semiconductor ASnO3 by the A-Site Ion Substitution Mian Wei, Hai Jun Cho and Hiromichi Ohta; Hokkaido University, Japan

Transparent oxide semiconductors (TOSs) that transmit deep ultraviolet (DUV, 200−300 nm in wavelength) are considered to be preferable as the active material for next generation optoelectronics such as biosensor.[1,2] Among many TOSs, La-doped ASnO$_3$ (A = Ba, Sr and Ca) are considered as a promising candidate f DUV-TOS because of their rather high electrical conductivity and large bandgap (E_g). The optical E_g of electron-doped $BaSnO_3$ and $SrSnO_3$ are ~3.1 eV[3] and ~4.6 eV[4], respectively. Based on this trend, if Ca, an even smaller alkaline element, occupies the A-site, further widening of the E_g value can be expected. However, the effect of A-site substitution on the optical and electrical properties of ASnO$_3$ has not been clarified in detail due to the lack of a systematic study. Here we show that the optical and electrical properties of ASnO$_3$ films can be tuned systematically by changing the average size of A-site ions.[5] We used lattice parameter as a bridge to build the relationship between the A-site substitution and structure factors, and clarified the effect of lattice parameter on the optical and electrical properties. The lattice parameter almost linearly increased from 3.95 to 4.14 Å with increasing A-site ionic radius from 1.34 Å (Ca^{2+}) to 1.61 Å (Ba^{2+}). The optical bandgap ($E_{g\,opt}$) of the resultant films gradually decreases from ~4.6 to ~3.6 eV with increasing lattice parameter with a small positive bowing, while the electrical conductivity gradually increased from ~10^0 to ~10^3 S cm^{-1} due to gradual increases in both the carrier concentration and mobility. These results indicate that larger A-site ion substitutions reduce the $E_{g\,opt}$ and the Fermi energy exceeds the mobility edge (degenerate semiconductor). On the other hand, the carrier generation efficiency increases when the $E_{g\,opt}$ decreases. The carrier relaxation time increases when the mobility edge decreases. Thus, the conductivity increases when larger ion is substituted in the A-site. Meanwhile, La-doped $SrSnO_3$ exhibited a great balance of wide bandgap and high electrical conductivity, which makes it a suitable ASnO$_3$ system for advanced optoelectronic applications. The present results are essentially important for designing ASnO$_3$ based DUV-TFTs.

References

[1] M. Wei *et al*., *Adv. Electron. Mater.* **6**, 2000100 (2020).
[2] M. Wei *et al*., *Appl. Phys. Lett.* **116**, 022103 (2020).
[3] H.J. Kim *et al*., *Phys. Rev. B* **86**, 165205 (2012).
[4] Q. Liu *et al*., *J. Alloys Compd.* **717**, 62 (2017).
[5] M. Wei *et al*., *ACS Appl. Electron. Mater.* **2**, 3971 (2020).

11:15 AM GG03
(Student) Thermal and Bias Stability of InAlZnO-Based Amorphous Thin-Film Transistors Mingyuan Liu[1], Han Wook Song[2] and Sunghwan Lee[1]; [1]Purdue University, United States; [2]Korea Research Institute of Standards and Science (KRISS), Korea (the Republic of)

Amorphous oxide semiconductor (AOS) thin film transistors (TFTs) based on In2O3 have attracted much interest for use as pixel switching elements in next generation active-matrix liquid crystal and active-matrix organic light emitting diode displays. The high field effect mobility of In2O3-based AOS devices (10–25 cm^2/Vsec) offers significant performance improvements over present-day a-Si TFTs (<1 cm^2/Vsec) technology.
There have been considerable efforts to incorporate AOSs into devices, particularly in current-driven active matrix displays such as organic light emitting diode displays as pixel-driving switching elements. Strategies to enhance amorphous phase stability, improve channel/metallization contacts, and suppress channel carrier densities have been studied and successfully applied to the switching TFT application. Third cation elements are often added to binary cation oxide systems to limit the channel carrier generation for TFT channel application. We have recently reported that the addition of Al to InZnO, a typical binary cation material system leads to enhanced amorphous phase stability, carrier suppression capability and higher carrier mobility, up to ~45 cm^2/Vs (Hall Effect mobility) and ~20 cm^2/Vs (field effect mobility)[1]. All of these characteristics are expected to be a key enabler for realizing the next generation ultra-high-definition displays.
Post-process annealing is widely employed in AOS-based TFT fabrication since annealing has been shown to improve field effect mobility[2-3] and channel/metallization contacts[4-5] as well as reduce trap density[6-7]. However, the post-annealing is often accompanied by an increase in channel carrier density that induces an unfavorable increase in the device off-state current and operation voltages[2, 8]. To date, the origin of the increase in channel carrier density has not been fully understood. Furthermore, it has been reported that gate-bias stress (either positive or negative) leads to TFT threshold voltage (V_{Th}) instabilities. In order to achieve reliable device performance by mitigating the V_{Th} shift issues, the understanding of the mechanisms for the V_{Th} instability is to be enhanced. The current study aims to identify the origin of an increase in carrier density after low-temperature annealing conducted in air, particularly for a third-cation AOS system of InAlZnO (IAZO). Through work function investigations and bandgap analysis, the carrier density of IAZO is found to be increased by > 1E4 times compared to that of unannealed IAZO after low temperature annealing at 200 °C in air. Photoelectron spectroscopic studies reveal that the typical intrinsic (vacancy-based native defect) or extrinsic (cation substitution) doping mechanisms are not the primary cause of the channel carrier increase. From high pressure oxidation with much enhanced reactivity of reaction gases, it is identified that the equilibrium carrier density of IAZO is much higher than those used in typical TFT channel application. The low channel carrier density tends to increase and reach the higher equilibrium carrier density in the absence of kinetic constraints. In addition, to investigate the bias stability of IAZO TFTs, the transfer characteristics were measured over bias stress time at a negative gate bias of -30 V and a positive gate bias of 30 V. During the negative bias stress (NBS) tests, no significant changes were observed in transfer characteristics, which is attributed to the depletion of channel free carriers due to the application of negative bias, regardless of stress time. However, clear positive shifts of the TFT transfer characteristics are detected during the positive bias stress (PBS) measurements as shown in the figure above. TFT parameters such as field effect mobility, sub-threshold swing, V_{Th} and interfacial trap density were carefully analyzed during PBS measurements. (Financial support: NSF Award No. ECCS-1931088)

11:30 AM GG04
Charge Transport in Ternary Spinel Oxides Maytal Caspary Toroker; Technion–Israel Institute of Technology, Israel

The small-polaron hopping model has been used for several decades for modeling electronic charge transport in oxides. Despite its significance, the model was developed for binary oxides, and its accuracy has not been rigorously tested for higher-order oxides. To investigate this issue, we chose the $Mn_xFe_{3-x}O_4$ spinel system, which has exciting electrochemical and catalytic properties, and mixed cation oxidation states that enable us to examine the mechanisms of small-polaron transport. Using a combination of experimental results and DFT+*U* calculations, we find that the charge transport occurs only between like-cations (Fe/Fe or Mn/Mn). And due to asymmetric hopping barriers and formation energies, we find that the polaron is energetically preferred to the polaron, resulting in an asymmetric contribution of the Mn/Mn pathways.
Reference:
A. Bhargava, R. Eppstein, J. Sun, M. A. Smeaton, H. Paik, L. F. Kourkoutis, D. G. Scholm, M. Caspary Toroker*, R. D. Robinson*, "Breakdown of the small-polaron hopping model in higher-order spinels", Adv. Mat., 2004490 (2020).

11:45 AM GG05
(Student) Charge Transport and Photoconduction Effects in Quasi Two-Dimensional γ-Al2O3 Grown by Graphene Assisted Atomic Layer Deposition Elaheh Kheirandish, Yuting Lin and Nikolai Kouklin; University of Wisconsin-Milwaukee, United States

Herein we present details of the photoluminescence, photoconduction and polaronic charge transport studies on crystalline quasi-2D γ-alumina synthesized by the two-step graphene assisted Atomic Layer Deposition (ALD) [1]. The Crystallographic and morphology analysis reported prior by us reveals the synthesized 2D nanosheet network to be polycrystalline cubic spinel γ-alumina with a close packed cubic texture in the <111> ALD induced growth direction whereas the morphology of 2D flakes was probed by both SEM and TEM and results point to the nanosheets with nominal thickness in the order of 10nm being sintered together achieving a large thickness for the 2D flakes. Photoluminescence (PL) spectroscopy of crystalline quasi-2D γ-alumina was done by exciting the network with ~320 nm (3.8 eV) light and the samples possess a single emission band centered at ~387 nm (3.2 eV) at the room temperature. The PL-excitation (PLE) measurements confirm presence of three excitation defect bands located within the band gap of 2D γ-Alumina. The PL band at 387 nm (3.2 eV) is assigned to non-interband, intrinsic defect-assisted radiative recombinations involving F, F_2^+ and Al_i^+ defect states. [2] Charge transport mechanism of the 2D-γ-alumina network was investigated by carrying out temperature- and wavelength dependent photoconduction measurements and the charge transport is confirmed to be polaronic with small polarons undergoing a field-induced drift within the polycrystalline network which is in part facilitated by thermally-assisted hopping as well as quantum mechanical tunneling. The polaronic charge transport shows two separate regimes characterized by two activation energies with the polarons bound to deep trap states controlling the charge transport at T>303 K. The RT conductivity of the network exceeds by up to four orders of magnitude that of prior reported by Morell for ~99.5% pure α-alumina.[3] Bandgap energy reduction, presence of transport-active defect centers [4] and texture [5] are likely to play a key role behind enhanced electrical conductivity of 2D-γ-alumina. Intensity dependent photocurrent measurements show that when samples are excited with photons with energy of 4.1 eV (300 nm) the current drops, and the change in the photocurrent depends linearly on the excitation intensity. These results indicate that crystalline, quasi-2D γ-alumina synthesized by the facile graphene assisted ALD synthesis could be a candidate for multiple device applications ranging from photodetectors, photocatalysts to radiation-hard, thermally-stable light emitters, and related nano-optoelectronic devices.
Ref.
[1] E. Kheirandish, M. Schofield, M. Gajdardziska-Josifovska, N. Kouklin, Advanced Material Interfaces, 7, 2000561 (2020)]
[2] E. Kheirandish, N. Kouklin, Journal of Electronic Materials Topical Collections 62nd Electronic Materials Conference (2021)
[3] R. Morell, Handbook properties of Technical Engineering Ceramics, Part 2, Data Reviews, Section I, High Alumina Ceramics, London, p.255, 1987
[4] B. Ealet, M. Elyakhloufi, E. Gillet, M. Ricci, Thin Solid Films, 250, 90-100 (1994)
[5] A.Tan, C.K. Kuo and P.S. Nicholson, Solid State Ionics, 42, 233-241 (1990)

SESSION HH: Group III-Nitride LED I
Session Chairs: Theeradetch Detchprohm and Russell Dupuis
Friday Morning, June 25, 2021

9:00 AM HH01
(Student) Towards Device-Quality Higher Mole Fraction InxGa1-xN Relaxed Templates (0〈x〈15%) Evyn L. Routh[1], Mostafa Abdelhamid[1], Ahmed Shaker[1], Nadia El-Masry[2,1] and Salah Bedair[1]; [1]North Carolina State University, United States; [2]National Science Foundation, United States

InGaN based optical devices have suffered from reduction of external quantum efficiency as the wavelength approaches the green and red region of the visible spectrum. $In_xGa_{1-x}N$ based devices have several challenges arise with the increasing values of *x* needed to reach red emissions. One such issue is as the indium content increases, the lattice mismatch between the GaN substrate and active region grows, creating compressive strain that blue shifts the bandgap [1]. In addition, the strain also induces a piezoelectric field in the c-direction, reducing the recombination probability, leading to decreased efficiency [1]. Therefore, it is of great interest to reduce the strain in the active region of InGaN based devices. In this work, strain-relaxed $In_xGa_{1-x}N$ templates on GaN are grown using the semibulk (SB) approach. We have seen success in device quality templates with x<10% [2], and present our efforts towards 10-15% indium content SB templates grown via metalorganic chemical vapor deposition (MOCVD).
A SB template of 20-30 periods of an $In_xGa_{1-x}N$ layer (15-25 nm) followed by an GaN interlayer (1-4 nm) is used as a growth template for the $In_yGa_{1-y}N$ multiple quantum wells (MQW) (where y>x) [2]. The SB template allows for a gradual relaxation of the lattice parameter, so that the lattice constant of the $In_yGa_{1-y}N$ MQW grown on top is better lattice matched, compared to that of GaN. In addition, the GaN interlayer acts as a mitigating mechanism for the forming *V-pits* as the material is strain relaxed; the GaN interlayer is able to backfill the *V-pits* as the growth progresses. TEM studies have indicated that relaxation was achieved mainly due to *V-pit* formations, rather than generation of misfit dislocations [3]. Our strategy in achieving device quality templates with high In-content is to have a better control of the rate of *V-pit* formation, and their size during relaxation processes. We attempt to avoid the formation of deep *V-pits* during the growth process, as deep *V-pits* can be challenging to overcome. In addition, we attempted to minimize the density of *V-pits*, to avoid the widening, deepening, and coalescence of the pits as the growth progresses. As the SB template gets thicker, more strain energy is stored in the film, thus, we found it is beneficial to slow down the relaxation process by adjust the thickness of the InGaN and GaN layers. Templates are characterized by photoluminescence (PL), atomic force microscopy (AFM), secondary-ion mass

spectrometry (SIMS), and high-resolution x-ray diffraction (HRXRD) to determine the In-content, surface roughness, dislocation density, and percent relaxation. Also, MQW are grown using the SB templates as substrates. Using SIMS, we have seen that the indium incorporation is enhanced in the SB template, as In-content increases as the material relaxes, and have observed an indium increase from 7.4% to 11.8% in the topmost layer of our SB, with an estimation of 90% strain-relaxation. The resulting PL emission of this SB is 420.5 nm. Using AFM, we have measured an RMS roughness of 1.680 nm across a (5 μm)^2 area. Also, HRXRD rocking curves are used to determine the dislocation density of the films, showing preliminary results of mid 10^8 cm^{-2} total dislocation density. By optimizing growth parameters, we are able to achieve templates with In-content of about 13.4% as measured by SIMS, with surface roughness measured via AFM of 3.568 nm, with preliminary dislocation density estimates in the upper 10^8 cm^{-2}. We report on methods to achieve high quality templates with In>15%, as well as the quality of MQWs and performance of LEDs grown on these templates.

[1] S. Saito, R. Hashimoto, J. Hwang, and S. Nunoue, Appl. Phys. Express **6**, 111004 (2013).
[2] E. L. Routh, M. Abdelhamid, N. A. El-Masry, and S. M. Bedair, Appl. Phys. Lett. **117**, 052103 (2020).
[3] T.B. Eldred, M. Abdelhamid, J.G. Reynolds, N.A. El-Masry, J.M. LeBeau, and S.M. Bedair. Appl. Phys. Lett. **116**,102104 (2020).

9:15 AM HH02
(Student) Observation of Interfacial Strain Relaxation in High Indium, AlInN/GaN Heterostructures by Transmission Electron Microscope Keisuke Motoki, Zachary Engel, Christopher M. Matthews, Habib Ahmad and W. Alan Doolittle; Georgia Institute of Technology, United States

AlInN has gathered attention as a candidate material for power electronics and optoelectronics. Historically, there were many challenges in growing AlInN by traditional MBE or MOVCD due to conflicting issues of a) phase separation for high temperature growth, and b) low adatom surface mobility for low temperature growth. Metal Modulated Epitaxy (MME) has proven useful for this challenging material by improving adatom kinetics at low temperature and was shown to improve X-Ray diffraction figures of merit by as much as 11X[1]. However, the source of the film improvement has been unknown up to now. TEM is a useful tool to investigate defect structures but can itself cause damage and induce phase separation if not performed under proper conditions. Of the few TEM reports of AlInN, most focus attention to AlInN around 18% Al and electron-beam induced degradation on AlInN is not investigated. Few reports exist for imaging high In AlInN. The present work focuses on the investigation of MME grown high In AlInN/GaN heterojunctions, explanation of MME's improved quality compared to prior literature and its potential false defect observation because of damage induced by the electron beam in the TEM. Unintentionally doped (UID) MME AlInN films were grown on MME GaN on hydride vapor phase epitaxy (HVPE) GaN templates on c-plane sapphire substrates as described elsewhere[1], using plasma-assisted molecular-beam-epitaxy (PA-MBE) with a target composition of 70% indium. Strain relaxation at a heterojunction of AlInN/GaN in this epitaxial film is investigated by TEM and Scanning TEM (STEM). The cross-section sample is prepared by standard mechanical polishing methods, followed by argon ion milling. Lattice-expansion mapping (or strain mapping) obtained by STEM nano-beam diffractions showed an intermediate lattice constant between AlInN and GaN. This implies that there is a thin intermediate layer where gradual strain relaxation happens from GaN towards AlInN. Moire fringes are detected in the TEM with two-beam condition of g = [1 -1 0 0], indicating full strain relaxation beyond ~10 nanometers via the generation of misfit dislocations at the interface. Moire fringes in MME grown InGaN/GaN resulted from strain exceeding the critical thickness in the first monolayer[2,3]. Thus, like MME grown InGaN which also has high adatom mobility at low temperatures, high In AlInN appears to relax via the same misfit dislocation mechanism resulting in higher film quality above the misfit array. In order to validate the results, it was also necessary to ensure the electron beam did not damage the films under examination. It was found that a low beam dose of 5.7 A/cm^2 was necessary to prevent damage in thicker regions of the AlInN but still appreciably damaged thin sections of the AlInN even for less than 20 seconds exposure. This beam damage threshold is far lower than the ~35 A/cm^2 work on InGaN/GaN[4] suggesting high In AlInN is more sensitive to beam damage than InGaN. In-situ TEM measurements on g = [0 0 0 2] detected decomposition and In clustering in/on the AlInN layer. The beam-induced damage was not observable in the low-resolution strain map obtained by STEM micro-beam diffraction in comparably thicker regions. This extremely low beam damage threshold complicates TEM analysis of high In AlInN and results in less clear images and quicker analysis time requirements. Further work quantifying the degradation from the electron beam as well as varied compositional studies are ongoing.

[1]Engel, et. al., J. Appl. Phys., 127, 125301, 2020
[2]Fischer, *et. al.*, Appl. Phys. Lett., 103, 131101, 2013
[3]Clinton, *et. al,*. Solid-State Electronics, vol.136, pp. 3, 2017
[4]Smeeton, *et. al.*, Appl. Phys. Lett., 83, 5419, 2003

9:30 AM HH03
(Student) Micro-Scale AlGaN-Based Deep Ultraviolet Light-Emitting Diodes Emitting at 265 nm Huabin Yu and Haiding Sun; University of Science and Technology of China, China

The ultraviolet-C (UVC) light with wavelength from 180 nm to 280 nm has been recognized as a preferable avenue to disinfect virus because it can effectively destroy the chemical bonds inside the DNA or RNA of the microorganisms. III-nitride based UVC light-emitting diodes (LEDs) have been recognized as one of the ideal candidates to replace the toxic mercury-based UV-lamps for the application of air/water purification, disinfection/sterilization and biochemical environmental sensing. However, the optical performance of the UVC LEDs is still limited by the poor external quantum efficiency (EQE) [1, 2]. The size and geometry of the active emitting elements are extremely important considerations in optimizing LEDs. As the InGaN-based LED topic, it has been found that the micro-LED approach can offer the potential to improve overall LED efficiency and efficiency droop. However, a systematic investigation on size-dependent AlGaN-based UVC LED on device performance and detailed analysis of the underlying changing mechanisms have not been studied as much as InGaN based visible LEDs, which have longer history.
In this work, the size-dependence of the optical and electrical properties of 265 nm wavelength AlGaN based UVC LED grown on c-plane sapphire is systematically investigated. The LED devices with diameters ranging from 50 μm to 300 μm have been well fabricated. It is shown that the series resistance of the UVC LED increased with the diameter of the device decreased. Moreover, smaller UVC LEDs can deliver higher power densities despite the relatively lower absolute output powers and sustain higher current densities. Our results show that at low injection current densities, the efficiency of smaller LEDs reduces significantly via the non-radiative recombination induced by sidewall defects. At higher injection current densities, the current crowding effect dominates and the efficiency of smaller LEDs becomes higher.
Reference:

[1] H. Yu, Z. Ren, H. Zhang, J. Dai, C. Chen, S. Long, and H. Sun, "Advantages of AlGaN-based deep-ultraviolet light-emitting diodes with an Al-composition graded quantum barrier," Optics express, 27 (20), A1544-A1553, 2019.
[2] Z. Ren, H. Yu, Z. Liu, D. Wang, C. Xing, H. Zhang, C. Huang, S. Long, and H. Sun, "Band engineering of III-nitride-based deep-ultraviolet light-emitting diodes: A review," Journal of Physics D: Applied Physics, 53 (7), 073002, 2019.

9:45 AM HH04
(Student) Demonstration of High Q Aluminum Nitride on Sapphire Microring Resonator at Green and UV Wavelengths
Walter J. Shin[1], Yi Sun[1], Mohammad Soltani[2] and Zetian Mi[1]; [1]University of Michigan, United States; [2]Raytheon, United States

Aluminum nitride (AlN), an ultrawide direct bandgap semiconductor, has emerged as a promising platform for UV-visible photonic integrated circuits (PICs) that are essentially required for a broad range of classical and quantum photonic applications. AlN has optical transparency over a broad spectral range, including UV, visible and infrared, and this platform enables monolithic integration of light sources, modulators, and detectors on the same platform. To date, however, there have been few studies on the demonstration of AlN microring resonators operating from UV to the deep visible. Herein, we have performed a detailed study of the fabrication and characterization of AlN-on-sapphire microring resonators and demonstrated record high intrinsic Q (Q_{int}) factors of 147,000 and 25,500 at green (532nm), and UV (369.5nm), respectively. This work opens a new realm for developing AlN integrated photonics and quantum photonics from UV to the near-infrared. In this study, 1 µm thick c-plane undoped AlN epi-layer grown on sapphire substrate was used. The microring design targets high Q_{int} with critical coupling condition at 532nm wavelength where 60 µm radius and height of 550nm fully etched structure was used. To increase the coupling between ring and bus waveguide, pulley coupling scheme was utilized where 1µm ring waveguide width, 500nm bus waveguide width, 230nm gap and 90° pulley angle show critical coupling condition and satisfy phase matching. Fabrication process can be found in [1]. After AlN microring resonator is defined, 150nm NiCr micro-heater is deposited on top of SiO_2 cladding for thermo tuning. Since there are limited options of tunable lasers in the green and the UV range, we use a thermo-optic (TO) tuning of the resonator and sweeping its resonance across a fixed wavelength laser using NiCr micro heater. The measurement technique was first calibrated by characterizing the resonator spectrum at ~780 nm wavelength using a tunable laser by sweeping the wavelength across the resonance, and at different voltages applied to the microheater. By doing this experiment we can find the resonance shift versus applied voltage square to the heater which shows clear linear relationship. Based on the measured resonance shift at 780nm, and the following equation, $\Delta\lambda_{res}=\lambda_{res}\Delta n_{res}/n_{res}=\lambda_{res}\delta n_{res}\Delta T/(n_g\delta T)\propto V$, the wavelength offset at 532nm can be calibrated where $\Delta\lambda_{res}$ is the resonance shift due to ambient temperature change ΔT. $\delta n_{res}/\delta T$ is the thermo-optic coefficient [2], and n_g and λ_{res} are group index and resonance wavelength, respectively. Here thermal expansion is assumed to be negligible. Group index for each wavelength is simulated with Lumerical MODE Solution. The calibrated transmission characteristic with fixed 532nm laser shows critical coupling condition with extracted Q_{int} of 147,000 and propagation loss of 7.1dB/cm which is the first reported Q_{int} in this wavelength range. The same measurement technique is used at UV wavelength, 369.5nm with a similar structure where Q_{int} was measured to be 25,500 with 59.3dB/cm propagation loss. This study provides a viable path to measure resonance characteristic of microring resonator at wavelengths with limited tunable laser and also offers the opportunity to realize high performance AlN-on-sapphire based integrated photonics in UV/vis range. Work is currently in progress to achieve devices with electro-optic and nonlinear optic functionalities in the visible and UV wavelengths and will be reported.

10:00 AM HH05
(Student) Carrier-Photon Dynamics in InGaN/GaN Quantum-Dots Emitting Green Light Ankit Udai[1], Anthony Aiello[2], Tarni Aggarwal[1], Pratim K. Saha[1], Dipankar Saha[1] and Pallab Bhattacharya[2]; [1]Indian Institute of Technology Bombay, India; [2]Univerity of Michigan, Ann Arbor, United States

Quantum-dots (QDs) are technologically important nanostructures for fabricating high-performance optoelectronic devices. Semiconductor lasers with QDs as an active region have demonstrated low threshold current density, reduced temperature dependence of threshold, high differential gain, and low chirp and linewidth enhancement factor. In particular, InGaN/GaN QDs offer a wide tuneable emission range making them useful for a wide area of applications. The time scale of dominant recombination mechanisms is essential to realize efficient light emitters. An understanding of the carrier-photon dynamics is crucial in determining the modulation bandwidth and turn-on delay for high-speed applications such as optical communication, data storage, and visible silicon photonics. In this study, radiofrequency plasma-assisted molecular beam epitaxy (MBE) is used to grow $In_{0.27}Ga_{0.73}N$/GaN QDs with emission in the green wavelength range. The femtosecond transient differential absorption spectroscopy is used to investigate the dominant electronic and optical processes in these QD nanostructures. The InGaN QDs have a low density of states due to their three-dimensional quantum confinement and low electron effective mass. The GaN barrier region has a comparatively higher density of states. This stark difference in the density of states translates into a gradual filling of carriers in the QD region. It facilitates the sequential absorption of a second photon at later times.
We have successfully studied the carrier and photon dynamics in these QDs. The various carrier transitions and their kinetics are also studied, which gives us significant insight into the hot carrier dynamics in InGaN/GaN QDs. The unique process of sequential two-photon absorption signifies that the electrons occupy the conduction band for a prolonged time. Thus improving radiative efficiency of optoelectronic devices such as lasers, LEDs, and long-wavelength inter-subband sources having InGaN/GaN QDs as the active region.

SESSION II: Group III-Nitride Photodetectors
Session Chairs: Theeradetch Detchprohm and Russell Dupuis
Friday Morning, June 25, 2021

10:45 AM II01
(Student) Low Temperature Geiger-Mode Measurement of Gallium Nitride p-i-n Avalanche Photodiode Hoon Jeong, Eliza A. Gazda, Mi-Hee Ji, Minkyu Cho, Marzieh Bakhtiary-Noodeh, Theeradetch Detchprohm, Shyh-Chiang Shen, Nepomuk A. Otte and Russell Dupuis; Georgia Institute of Technology, United States

III-Nitride (AlInGaN) avalanche photodiodes (APDs) have merits such as high breakdown field, high electron drift velocity, high thermal conductivity, and low dark current. The III-nitride material bandgap is tunable from 0.7 (1772nm) to 6.2eV (200nm), offering good UV sensitivity in both visible blind and solar blind UV regions. The Geiger-mode operation of III-Nitride APDs have numerous applications in UV single-photon detection, such as quantum-key distribution, optical time-domain reflectometry, positron-emission tomography, biomedical research, and UV communications. In this work, we report low-temperature Geiger mode measurements of GaN *p-i-n* APDs by using a thermoelectric cooling system. The GaN *p-i-n* APD structures were grown on *c*-plane hydride-vapor-phase-epitaxy (HVPE) free-standing (FS) GaN or ammonothermal bulk GaN. The epitaxially grown structure consists of a 0.6 mm unintentionally doped GaN, followed by a 2.3mm thick Si-doped GaN *n*-layer with a free-electron concentration of 4×10^{18} cm^{-3}. The *i*-layer of 280nm thickness is grown on top of the *n*-layer, with a background Si doping of 2×10^{16} cm^{-3}, targeting breakdown voltage of 96V. The *p*-layer stack consists of two layers of 100nm Mg-doped GaN and 15nm of highly Mg-doped GaN as the contact layer. The Mg-doped *p*-layer has a free-hole concentration of 1×10^{18} cm^{-3}, and

the highly Mg-doped *p*-layer has Mg concentration of 1×10^{20} cm^{-3}. The fabrication of APD was performed in the following sequence: 1) mesa etching, 2) *n*-type metal deposition, 3) *p*-type metal deposition, 4) passivation and via-hole, and 5) metal interconnect deposition. A gated quenching circuit was used in the Geiger-mode measurement. In detail, a noninverting amplifier with gain of 2 and a transimpedance amplifier are inserted before and after the GaN APD in order to isolate the GaN APD and prevent reflection. An oscilloscope measures and collects the avalanche signals. A computer is utilized to perform signal data processing. For spectral response evaluation, the APD device is illuminated with the UV light from a UV LED with the peak wavelength of 375nm. The UV light is split by a bifurcated fiber: one end is fed to GaN APD, and the other end goes to an attenuator before being fed to a silicon photon counter for reference. For the low-temperature control, the thermoelectric cooler is installed directly under the GaN APD. The thermoelectric cooler is installed in an aluminum cage which serves as water-cooled heat sink. To prevent icing, the aluminum cage is sealed and filled with nitrogen. The Geiger-mode setup is installed in a optically isolated dark box. The method of measurement employed is the Δt method based on Poisson statistics. From the collected avalanche signal, the computer determines time interval between the rising edge of each pulse and its corresponding avalanche signal for 10,000 pulse events, then processes these time interval data into one histogram. Finally, by fitting the exponential function to the histogram, the dark count rate *R* is obtained. With this low-temperature Geiger-mode measurement system, the breakdown voltage was measured at various temperature from -10°C to 10°C with an increment step of 5°C. The breakdown voltage is proportional to the temperature, monotonically varying from 96.9V to 97.25V when the temperature increases from -10°C to 10°C. From this data, we obtained a temperature coefficient of the breakdown voltage of 0.0177±0.0005V/K. Based on the breakdown voltage vs. temperature, the dark count rate of various temperatures at 1V overvoltage above breakdown was measured. The dark count rate decreases as the temperature decreases from 19MHz to 11MHz when temperature decreases from 10°C to -10°C. By fitting Arrhenius equation, the obtained activation energy is . More detailed description will be presented in the conference. *This work is funded by Support from ARO, DoE, NASA, Georgia Tech IEN, and the NSF National Nanotechnology Coordinated Infrastructure (NNCI)*

11:00 AM II02
(Student) Characterization of Ga-Polar and N-Polar III-Nitride (GaN) Diodes Under High-Dose Gamma-Ray Irradiation Farnood Mirkhosravi[1], Kyle Ahn[2], Arman Rashidi[1], Andrew A. Aragon[1], Joshua Gallagher[3], Morteza Monavarian[1], Azaree Lintereur[3], Emily Mace[4], Michael Scarpulla[2] and Daniel Feezell[1]; [1]University of New Mexico, United States; [2]The University of Utah, United States; [3]The Pennsylvania State University, United States; [4]Pacific Northwest National Laboratory, United States

In this research, we investigate the impact of high-dose gamma-ray irradiation on the electrical performance of Ga-polar and N-polar GaN-based *p-n* diodes grown by metalorganic chemical vapor deposition. We compare the current density-voltage (J-V), capacitance-voltage (C-V), and circular transfer length method (CTLM) characteristics of the *p-n* diodes fabricated on Ga-polar and N-polar orientations before and after irradiation. The relative turn-on voltage increases for the Ga-polar diodes with increasing irradiation dose, while it increases initially and then starts to decrease for the N-polar diodes. we propose that the majority of the changes that are apparent in the measurements after gamma-ray irradiation is due to the charge and discharge at the surface states and migration of mobile charges which result in temporary changes in barrier height. The opposite trend in turn-on voltage change was also observed during pre-irradiation J-V characterization due to hysteresis effects in the diodes. The *p*-contact total resistance increases for Ga-polar and decreases for N-polar samples, which we attribute to the formation of point defects and additional Mg activation after irradiation. The J-V characteristics of most of the tested diodes recovered over time, suggesting the changes in the J-V characteristics are temporary and potentially due to metastable occupancy of traps after irradiation. We also study frequency-dependent impedance and forward capacitance measurement to gather more information regarding carrier dynamics and defect properties due to gamma-irradiation. The presence of a higher concentration of surface states on Ga-polar surfaces compared to N-polar was confirmed by calculating the band bending and the corresponding screening effect due to opposite polarization bound charge and ionized acceptors at the surface. The difference in surface stoichiometry and distribution of deep-level defects in these two orientations could be responsible for the different behavior in electrical characteristics after gamma-ray interactions.

11:15 AM II03
(Student) AlGaN-Based Nanowires for Self-Powered Ultraviolet Photodetectors with High Responsivity Danhao Wang and Haiding Sun; University of Science and Technology of China, China

Energy-saving photodetectors have recently attracted intensive research interest to meet the great demands of future photonic systems. Particularly, according to the large photocurrent, high sensitivity, environment-sensitivity, and lithography-free features, self-powered photoelectrochemical-type photodetectors (PEC PDs) have attracted tremendous attention in the optoelectronics community. However, owing to their poor crystal quality and low carrier separation efficiency of chemically synthesized semiconductor materials, PEC PDs based on such materials demonstrate slow response and low responsivity. In our work, we construct PEC PD using defect-free AlGaN nanowires photoelectrode which synthesized through molecular beam epitaxy (MBE)[1][2]. After decorating AlGaN nanowires with noble metal species (Pt or Ru), our PEC PDs feature the combined benefits of effective carrier separation and fast interfacial kinetics, resulting in superior performance compared to previous reported solar-blind PEC PDs (Responsivity of 45 mA/W and response/recovery time of 47/20 ms for Pt decorated p-type AlGaN nanowires; Responsivity of 48.8 mA/W and response/recovery time of 83/19 ms for Ru decorated n-type AlGaN nanowires;). Besides, according to the attractive surrounding sensitivity of PEC PDs, their photoresponse behaviors can be effectively modulated by varying the applied bias potential, light intensity, and the concentration of the electrolyte further promotes its adaptability in different working conditions. Our work suggests that embracement of defect-free wide-bandgap semiconductor nanowires with appropriate surface decoration offers an unprecedented opportunity for designing future energy-efficient and large-scale optoelectronic systems on the silicon platform.
Reference:
[1] D. Wang, X. Liu, S. Fang, C. Huang, Y. Kang, H. Yu, Z. Liu, H. Zhang, R. Long, Y. Xiong, Y. Lin, Y. Yue, B. Ge, T. K. Ng, B. S. Ooi, Z.Mi, J. H. He, and H. Sun "Pt/AlGaN Nanoarchitecture: Toward High Responsivity, Self-Powered Ultraviolet-Sensitive Photodetection," Nano Lett., 2021, 21, 1, 120–129.
[2] D. Wang, C. Huang, X. Liu, H. Zhang, H. Yu, S. Fang, B. S. Ooi, Z. Mi, J. H. He, and H. Sun, "Highly Uniform, Self-Assembled AlGaN Nanowires for Self-Powered Solar-Blind Photodetector with Fast-Response Speed and High Responsivity," Adv. Optical Mater., 2020:202000893.

11:30 AM II04
(Student) UV-Stress Induced Degradation in AlGaN Solar-Blind Schottky and p-i-n Photodetectors Anisha Kalra, Shashwat Rathkanthiwar, Muralidharan R, Srinivasan Raghavan and Digbijoy Nath; Indian Institute of Science, India

In this work, we report on the mechanisms contributing to ultra-

violet (UV) radiation stress induced degradation in self-powered, solar-blind AlGaN photodetectors on c-plane sapphire. Deep-UV p-i-n ($\lambda_{band-edge}$: 289 nm) and Schottky ($\lambda_{band-edge}$: 280 nm) detectors realized over two varying threading dislocation density buffers (TDD_{Total}: 5 x 10^9 cm^{-2} and 5 x 10^{10} cm^{-2}) were stressed under high intensity (10 mW/cm^2) 270 nm monochromatic light up to 10,000 seconds and characterized electrically and optically. $Al_{0.45}Ga_{0.55}N$ Schottky detectors realized over high dislocation density (HDD) AlN buffer were found to degrade severely under front illumination, with a 10,000 s UV exposure resulting in a 40-fold increase in the reverse leakage current (dark current) and a 6-fold decrease in the zero-bias peak spectral response. The peak spectral response for non-zero bias voltages, on the other hand, was found to increase by over 4-times with UV exposure. When tested under back illumination, the variation in device characteristics with UV-stress was found to be < 5%. Similar measurements, when repeated on samples realized over the low dislocation density (LDD) AlN buffer showed no degradation (< 2 %) under forward or back illumination. These observations are suggestive of a dislocation-mediated degradation mechanism operating at the metal/Schottky interface in $Al_{0.45}Ga_{0.55}N$ Schottky detectors. The degradation can be attributed to photo-enhanced chemical reactions which oxidize the Al-rich detector surface near the negatively-biased Schottky contacts. This leads to a large interface trap-state density at the metal/semiconductor interface and consequently, an increased trap-mediated leakage. These trap states can also lead to a higher surface recombination velocity, and consequently a degraded zero-bias carrier collection efficiency and a lower peak response. Finally, enhanced trapping of photo-generated holes can occur at these interface states post the UV exposure, resulting in higher gain-associated photocurrent at finite bias voltages. A reduction in the dislocation density and consequently, the surface terminations of these dislocations is expected to decelerate this reaction, thereby leading to the observed insignificant degradation for the LDD detectors. For the case of p-i-n detectors realized over the HDD buffer, the electrical and optical characteristics were also found to degrade severely with increasing UV-stress. After 10,000 s of UV stress, the reverse leakage current increased by 2-orders of magnitude and the forward current reduced by an order of magnitude, resulting in diodes with poor rectification. The zero-bias responsivity degraded 7-fold post 10,000 s of 270 nm exposure. Interestingly, the increase in series resistance and the decrease in zero-bias responsivity were found to have a linear dependence on square root of the stress time. Like the case of Schottky detectors, the devices realized over the LDD buffer were not found to degrade in the measured time range. The observed degradation in the case of AlGaN p-i-n detectors could be attributed to dislocation-mediated diffusion of impurity atoms towards the active device layers. Vertical architecture photodetectors utilizing wide bandgap semiconducting absorbers such as Aluminium Gallium Nitride (AlGaN) are attractive for a host of applications, with performance stability over large UV exposure times being quintessential. This can be impacted by the device architecture, fabrication process flow, measurement conditions as well as the defect density in the heteroepitaxially-grown active device layers. Investigation of the temporal development of opto-electrical performance parameters under UV exposure, thus becomes important. To our knowledge, this is the first such report for technologically-important AlGaN UV-C detectors and highlights the importance of a low dislocation density buffer for the growth for realization of stable, reliable, high performance detectors.

11:45 AM II05

(Student) Growth and Characterization of p-i-n GaN UV 6 × 6 Avalanche Photodiodes Arrays with Large Detection Area

Marzieh Bakhtiary-Noodeh[1], Minkyu Cho[1], Zhiyu Xu[1], Hoon Jeong[1], Theeradetch Detchprohm[1], Nepomuk A. Otte[1], Ashok K. Sood[2], John W Zeller[2], Parminder Ghuman[3], Sachidananda Babu[3] and Russell Dupuis[1,1]; [1]Georgia Institute of Technology, United States; [2]Magnolia Optical Technologies, Inc., United States; [3]Goddard Space Flight Center, United States

Gallium nitride (GaN) with bandgap energy of 3.4 eV with a high breakdown electric field (~3.3 MV/cm) is useful for ultraviolet (UV) optical detectors. Since GaN avalanche photodiodes (APDs) have a high sensitivity and capability of operation in the visible-blind region with high optical gain with low dark current, UV-APD arrays are considerably well-suited for many applications in UV imaging systems, astronomy, military systems, and bio-aerosol detection to improve the collection efficiency and sensitivity for low-level light detection. Achieving the high crystalline quality of epitaxial layer structures with reduced-defect densities as well as optimizing the fabrication processes will significantly improve GaN APD arrays to achieve a high pixel yield and uniform breakdown voltage with low leakage current. Evaluation of these 6x6 arrays will help to confirm the uniformity of the epitaxial materials and device processing as well.

In this work, visible-blind front-illuminated GaN *p-i-n* APDs were grown by metalorganic chemical vapor deposition (MOCVD) on 25 mm dia. bulk Ammono® *n*-GaN substrates having a low etch pit density (EPD) less than 5 × 10^4 [cm^{-2}] and processed into 6x6 APD arrays. The MOCVD growth was performed in a close-coupled-showerhead AIXTRON 6x2" MOCVD system and employed trimethylgallium and NH_3 as primary precursors and SiH_4, and Cp_2Mg as dopants. X-ray diffraction (XRD) was used for the characterization of the crystallographic quality of the APD structure. The full widths at half maximum of the rocking curve derived from (0.02) and (1.02) diffraction exhibit values of 73 and 41 arc-sec, respectively, primarily determined by the properties of the GaN substrate. Hall-effect characterization was used for the measurement of the electrical properties of the doped layers including the free-carrier concentration, mobility, and resistivity. The epitaxial layers grown on the GaN substrates include a 1.0 µm thick *n*-GaN:Si layer (*n*~7×10^{18} cm^{-3}), 0.2 µm thick *u*-GaN undoped layer, 0.1 µm thick *p*-GaN:Mg layer (*p*~6x10^{17} cm^{-3}) and 0.02 µm thick p^{++}-GaN:Mg layer for a target breakdown voltage of 80 V. The surface morphology of the GaN *p-i-n* UV-APD epitaxial structures were studied by atomic force microscopy (AFM). The corresponding root-mean-square (RMS) values for scanning area of 5×5 μm^2 for GaN/sapphire *u*-GaN template and *n*-GaN substrate are 0.15 nm and 0.07 nm respectively for the typical case. To confirm the doping profile of the layers, secondary ion mass spectrometry (SIMS) measurements were performed. The as-grown wafers were processed using ion-implantation isolation into 6x6 APD arrays having 60 µm-dia. pixels. The reverse-biased J-V characteristics of the GaN APD arrays under dark and 355 nm illumination conditions have been measured at 300K. The dark current density is 10^{-9} A/cm^2 at reverse bias up to -20 V and breakdown voltage of 80 ± 1 V for all 36 devices which confirms a high uniformity of growth and fabrication processes. The maximum avalanche gain reached 3 × 10^5 at the breakdown. The details of growth, characterization, and fabrication processes as well as further device data will be discussed in the presentation.

Work supported in part by US Army Research Office under W911NF-15-1-0489, administered by M. Gerhold, by the US Department of Energy under DESC0019133, and NASA under 80NSSC18C0093. This work was performed in part in the facilities of the Georgia Tech Institute for Electronics and Nanotechnology, a member of the National Nanotechnology Coordinated Infrastructure, which is supported by the National Science Foundation (Grant ECCS-154217). The views and conclusions contained in this document are those of the authors and should not be interpreted as representing the official policies, either express or implied, of DoE, ARO, or the U.S. Government.

SESSION JJ: Printed and Flexible Thin Films
Session Chairs: David Janes and Jae-Hyun Ryou
Friday Morning, June 25, 2021

9:15 AM JJ02
Low Voltage Operation of Flexible Organic Thin-Film Transistors Using Poly(Ionic Liquid) Block Copolymer Based Gating Materials Benoit Lessard; University of Ottawa, Canada

Carbon based electronics, also known as organic electronics are facilitating the development of emerging technologies due to their inherent bendability and potential for low cost manufacturing compared to brittle conventional silicon semiconductors. Furthermore, the chemical toolbox available to us enables the fine-tuning of the materials as a way to design and engineer the desired properties. This talk will focus on our groups recent advances in the development of high performing organic thin film transistors through the self-assembly of well-defined poly(ionic liquids) block copolymer based gating materails for n-type polymer based OTFTs. The use of these block copolymers over conventioanl dielectrics lead to drops in threshold voltages from 35V to under 1V while maininting high swtiching speeds and greater device currents. We aim to build structure property relationships between polymer architecture, thin film processing and device performance.

9:30 AM JJ03
(Student) Inkjet Printed 3D Metal Electrodes on Shape Memory Polymer Towards Improved Electrochemical Bio-Sensing Performance Annatoma Arif, Angela Mendez Contreras and Robert C Roberts; The University of Texas at El Paso, United States

This work presents the design, fabrication, and characterization of 3D thin-film metal electrodes for electrochemical bio-sensing (EBS) applications utilizing inkjet printing (IP) on shape memory polymer (SMP) substrates. Inkjet printing electrodes on SMP allows for 3D electrode formation in a single process step at low temperature and atmospheric pressure. In this study, a thermally contracting SMP has been utilized to print EBS electrode patterns using IP silver nanoparticle ink, extending previous work. The silver nanoparticle ink electrode geometry is sintered and shrunk simultaneously by placing it into an oven for 3 minutes. It is observed that the reduction factor of the processed EBS (sintered and shrunk) achieves up to 60% approximately and creates a complex 3D metal topology which is difficult to obtain using conventional electrode fabrication techniques. SMP is a polymer which remembers its initial shape and returns to that shape when heated above its glass transition temperature. Generally, at room temperature SMP stays at martensite phase and achieves austenite phase after heat application (in this study, 180 C). In order to observe the shrinking characteristics of the SMP film used for this study (MagicShrink), 18 different samples (1 cm by 1 cm) were shrunk at six different temperatures (140 C to 190 C) for 3 minutes. It is observed that, the shrinking mechanism is similar and stable for each sample. The reduction factor of the shrunk film is 0.6 for each sample. In this study, nanoparticle silver ink (ANP DGP-40-LT-15-C) is used to IP EBS pattern using Dimatix Materials Printer (Fujifilm, DMP-2831). This nanoparticle ink becomes conductive by curing it at 120 C ~150 C for 10 minutes. But it is perceived that the desired conductivity can be achieved only within 3 minutes at 140 C to 190 C with SMP (simultaneous curing and shrinking mechanisms). Resistivity measurements of the SMP fabricated electrodes have been performed to characterize the process impact on thin-film performance. Scanning electron microscopy is utilized to further characterize the 3D microstructure and topology created by IP on SMP fabrication process for EBS at different process temperatures. Further, electrochemical characterization of the 3D SMP electrodes are performed and compared to a conventional EBS 2D electrode. Fabricating EBS on SMP with IP technology have shown promising potential to improve electrochemical sensing. The inkjet on SMP process demonstrates significant 3D silver electrode using nanoparticle ink for an increased electrode surface area for EBS, which is difficult to fabricate using conventional techniques, with potential applications for other electrode technologies benefitting from increased device surface area.
References
[1] R. C. Roberts**,** J. Wu, N.Y. Hau, Y.H. Chang, S.P. Feng, D.C. Li, "Facile 3D Metal Electrode Fabrication for Energy Applications via Inkjet Printing and Shape Memory Polymer," *Journal of Physics: Conference Series* 557 (2014) 012006.
[2] R. C. Roberts**,** S. Zeng, and N. C. Tien, "Design and Fabrication of Buckled Metal Strain Gauges using Shape Memory Polymer and inkjet Additive microfabrication," *Technical Digest, The 14th IEEE Conference on Sensors (Sensors 2015)*, Busan, Korea, Nov. 1-4, 2015, pp. 1665-1668.

9:45 AM JJ04
(Student) Skin-Attachable Physical Sensors Using Single-Crystalline III-N Piezoelectric Thin Film for Personal Health and Safety Monitoring Nam-In Kim, Jie Chen, Mina Moradnia, Sara Pouladi and Jae-Hyun Ryou; University of Houston, United States

Wearable electronics are increasingly important in healthcare applications for monitoring of the daily physical condition and diagnosis of an early stage of disorders. In particular, the wearable sensors on human skin can be utilized in real-time continuous monitoring systems because they provide comfortable wearing and consume less power. Pulse detection is one of the options and critical for high-risk groups of cardiovascular diseases such as angina, acute coronary syndrome, and myocardial infarction among the real-time monitoring of several physical parameters. Moreover, the pulse is easily detected from specific points on the human body such as carotid, temporal, fingertip, dorsal, and posterior tibial artery using skin-attachable sensor [Chen, et al. High durable, biocompatible and flexible piezoelectric pulse sensor using III-N thin film, Adv. Funct. Mater. 29, 1903162 (2019)]. Accurate sensing of the eyelid and eyeball movement is another new application. Brain disorders (e.g. Alzheimer's, Parkinson's disease, and stroke) are accompanied by eye-related abnormal motions as early symptoms such as slow movements and the long interval between eye blinking. The diseases can be diagnosed in an early stage from the detection of unusual eye motions before they are seriously progressed. For both applications, the sensors should be light and small to attach on the human body, e.g. temple area. Recently developed thin-film piezoelectric skin-attachable sensor based on lead zirconate titanate (PZT) and ZnO inherently possess weakness for the wearable healthcare sensors. PZT contains lead, which is very harmful to the human body and environment by poisoning. A skin-attachable sensor should be containing toxic-free elements. ZnO sensor shows low sensitivity and resolution from the limitation of material, which demands additional signal processing for amplification of exact signal and minimization of the noise level. The benefit of non-toxicity is canceled by low sensitivity and extra work. As an alternative sensing element, III-N thin films are very promising to detect the physical motion of skin sensing due to their advantages of high sensitivity and durability, rapid response time, non-toxic nature on humans, lightweight, and low power consumption. Especially, single-crystalline gallium nitride (GaN) and aluminum-gallium nitride (AlGaN) piezoelectric thin films have been reported to show excellent output voltage, indicating outstanding sensitivity, rapid response time by a high electromechanical coupling factor, chemical and mechanical long-term stability, high thermal resistance, and excellent biocompatibility [Chen et al. Biocompatible and sustainable power supply for self-powered wearable and implantable

electronics using flexible III-nitride thin-film-based piezoelectric generator, Nano Energy 57, 670 (2019)]. In this study, we developed and demonstrated skin-attachable GaN and AlGaN sensors for the detection of eye-lid motion to monitor the eye blinking and eyeball movements. Flexible III-N thin films were designed by layer transfer method from the rigid silicon substrate. They were analyzed by X-ray diffraction to reveal its single-crystalline quality without second phase or defects. The single sensor was applied to the temple area of the face for sensing of eye blinking and simple eyeball motion. Eye blinking is conducted with three different levels. Then, the multiple sensors were utilized with appropriate distance on the identical region to detect the transverse, longitudinal, diagonal, and rotational eyeball motions, which explain the abnormal eye movements. All the results from each sensor are distinguishable, which indicates that the sensors generated different values of output signals from each position with varied stimulates.

10:00 AM JJ05
(Student) High Performance Strain Sensors Based on Zinc Oxide Nanowire Array/Graphene Nanohybrids Mohan Panth[1], Brent Cook[1], Mohammed Alamri[1], Ashely Tramble[2], Daniel Ewing[2], Amy Wilson[2] and Judy Wu[1]; [1]University of Kansas, United States; [2]National Security Campus, United States

Strain sensors consisting of vertically aligned ZnO nanowires grown on graphene transferred on rigid as well as flexible substrates (Si, quartz, PET) with prefabricated Au/Ti electrodes (ZnO-VANWs/Gr)) have been obtained. The ZnO-VANWs grown using a seedless hydrothermal process are single-crystalline with (0001)-orientation that provides optimal piezoelectric gating on graphene when deformed mechanically. The change of the graphene channel conductance under such a piezoelectric gating through transduction of the mechanical deformation on the ZnO-VANWs/Gr was used to detect the strain induced by the mechanical deformation including compression and bending. High sensitivity up to 3.15×10^{-2} kPa^{-1} was obtained on the ZnO-VANWs/Gr/Si strain sensors at lower pressure of 1.1×10^{-6} – 11 Torr, together with a fast response time of 0.1-0.2 s. The flexible ZnO-VANWs/Gr/PET sensors exhibit high sensitivity to bending of radius of curvature in the range of 0.18 cm^{-1} to 0.45 cm^{-1} with a gauge factor up to ~248 and response times of 0.20 s/0.20 s (rise/fall). Moreover, the response changes polarity when the direction of bending alters between up and down, corresponding to the polarity change of the space charge on the ZnO-VANWs/Gr interface as a consequence of the compressive and tensile strains along the ZnO-VANWs. This result shows that the low-cost and scalable ZnO-VANWs/Gr/Si or PET strain sensors are promising for applications in stress/strain monitoring, wearable electronics, and touch screens, etc.

SESSION KK: MBE—Selective Area Growth and Doping
Session Chairs: Rachel Goldman and Lincoln Lauhon
Friday Morning, June 25, 2021

10:45 AM KK01
(Student) Control of Nucleation Layers for (110) Oriented ZnTe Thin Film Growth on Sapphire r, S-Plane Nano-Facet Substrates Shotaro Kobayashi and Masakazu Kobayashi; Waseda University, Japan

Fabrication of a ZnTe (110) thin film is highly preferable for the application of terahertz wave detection devices utilizing the electro-optical (EO) effect. The preparation of the (110) oriented ZnTe (110) thin film has been tried on a sapphire substrate by molecular beam epitaxy. Sapphire (hetero material) is used as a non EO substrate, and ZnTe is a zincblende structure material and known to exhibit high electro-optical coefficients. However, it is difficult to prepare a ZnTe (110) thin film with high crystallinity. In previous works, the high quality ZnTe layer with the single domain structure of (111) was achieved on the S-plane sapphire substrate. It was also confirmed that high temperature treatments of m-plane sapphire substrates has resulted in nano-facet structures consisting of r- and S-planes. The calculation was performed and revealed that (110) oriented ZnTe layer on the sapphire substrate could be achieved by using a 17.66° off m-plane substrate, and by preferentially nucleating the (111) oriented domain on the S-plane of the nano-facet. The surface coverage of S-plane on the 17.66° off substrate was only about 31 %, which would hinder the preferential nucleation of ZnTe only on the S-plane. In this work, the nucleation process was varied, and the resulting film quality was characterized. The nucleation was initiated by a low temperature deposition of an amorphous layer, and its annealing to form nuclei only on the S-plane of the nano-facet. It was followed by the migration enhanced epitaxy (MEE) of ZnTe to develop the nuclei size. In this work, the MEE sequence was mostly focused, and the substrate temperature along with the MEE cycle were mainly adjusted. It was confirmed from the scanning electron microscopy (SEM) analysis that desorption from r-plane took place at lower temperature and nuclei on the S-plane nano-facet was preferentially remained when the annealing temperature was at around 420°C. When the annealing temperature was 400°C, the selectivity of the nuclei on the nano-facets were disappeared and the nuclei was uniformly observed on the substrate. The MEE was performed at 420°C for 200 cycles and then the substrate temperature was gradually lowered toward 340°C for the film growth. During this temperature lowering process, MEE was also introduced at 400°C with the cycle from 50 to 170. The theta-2theta scan of the film suggested that (110) oriented layer was formed on the substrate surface. Offset for the theta was not required to obtain the 220 diffraction signal. These results suggest that the nucleation of (111) oriented ZnTe preferentially took place on the S-plane of the nano-facet, and the (110) plane was formed parallel to the substrate surface. Although several kinds of additional domains were confirmed from the theta-2theta scan, the dominant domain was (110). When the MEE cycle at 400°C was increased to 170, the 220 X-ray diffraction peak became strong. It is probably associated with the size of nuclei developed during the MEE process. It was developed to much larger size by increasing the MEE cycle at 400 °C, which caused the improvement of the crystallinity. X-ray diffraction pole figure analysis was also performed. The (111) oriented domain formation on the S-plane nano-facet was clearly observed, and four addition domains were observed. Those additional domains were originated from twins formed on {111} planes. Zn molecular beam irradiation was also carried out during the last part of the annealing at 420°C. The pole figure image exhibited pronounced signals originated from the (111) oriented domain on the S-plane nano-facet when the Zn irradiation was employed. The Zn irradiation probably limited desorption of ZnTe from S-plane nano-facets, and increased the density of the nuclei remained on the S-plane nano-facet. This capping of the nuclei has resulted in the improvement of the film quality. This work was supported in part by Waseda University Specific Research Projects.

11:00 AM KK02
(Student) Experimentally-Calibrated Modeling of Molecular Beam Epitaxy Selective Area Regrowth Ashlee Garcia, Alec M. Skipper, Daniel Ironside and Seth R. Bank; The University of Texas at Austin, United States

A molecular beam epitaxy (MBE) approach to selective area epitaxy (SAE) of III-V semiconductors could enable the seamless integration of metals, dielectrics, and high-quality crystalline semiconductors. This technique could advance novel optoelectronic structures, such as high-contrast photonics, site-

controlled quantum emitters, stacked pixel detectors, and photonic integrated circuits. Using patterned dielectrics and metals to define crystal seeding regions, SAE can be performed to embed microstructures into crystalline semiconductors[1]. While SAE by metal organic chemical vapor deposition has been widely successful due to its high material deposition selectivity, a SAE MBE method could enable further advances through its high layer precision and access to non-equilibrium growth conditions[1,2]. SAE is difficult to achieve with conventional (continuous) MBE growth due to III-V polycrystalline nucleation on the mask, even at growth temperatures as high as 700°C. As a result, Allegretti et al. developed periodic supply epitaxy (PSE), a method to inhibit polycrystalline deposition by cycling group III deposition under a constant group V flux[2,3]. SAE with PSE was achieved using high growth temperatures and low growth rates[3-4]. This mitigates nucleation of poly-GaAs through a combination of increased Ga adatom diffusion to seeding windows and desorption of remaining Ga adatoms[3-4], enabling high-quality planar encapsulation of the mask[1]. While an all-MBE approach has been demonstrated to achieve selective growth of features ~2µm in width and ~300nm in height, applications requiring larger features are limited by nucleation of polycrystalline semiconductor on the amorphous surface due to poor deposition selectivity and low adatom surface diffusion[1,3]. We present experimental results of GaAs growth on SiO_2 films that demonstrate decreased poly-GaAs formation at higher temperatures and lower As_4/Ga flux ratios, enabling SAE of larger patterned features. However, this improvement in selectivity has yet to be explained quantitatively. In order to expand the applicability of all-MBE SAE, we developed a PSE model that (1) identifies selective growth regimes to clarify their underlying mechanisms and (2) allows optimized SAE growth conditions to be determined for a given SiO_2 pattern. A numerical 1D model was developed to describe PSE selectivity by fitting adsorption, desorption, and diffusion constants to GaAs growth on SiO_2 films at 600°C with a growth rate of 0.7 Å/s and 65x As_4/Ga ratio[5-8]. Two growth regimes have been identified: desorption- and diffusion-limited. The desorption-limited regime depends only on thermal desorption from the mask surface to achieve selectivity and as a result, is feature-independent. This model has identified the desorption-based selectivity limit to be an 18.7% PSE duty cycle and was demonstrated by observing no polycrystal formation after growth of 100nm GaAs with 10% PSE duty cycle on an SiO_2 film. The remainder of the selective growth space is diffusion-limited and sufficient III adatom diffusion off the mask is required to achieve selectivity. Experiments to fully investigate the influence of growth temperature and V/III ratio on selectivity are underway and will be reported at the conference.

[1] D. J. Ironside et al., *ACS J. Crystal Growth and Design* (2019). [2] A. M. Skipper et al., 2019 MRS Electronic Materials Conf. [3] F. E. Allegretti et al., *Journal of Crystal Growth* (1995). [4] S.C. Lee et al. *Journal of Applied Physics* (2002). [5] S. Shankar. Diffusion in 1D and 2D, MATLAB. Retrieved April 11, 2020. [6] Aseev et al. *Nano. Lett*. (2019). [7] S. C. Lee et al. *Cryst. Growth Des.* 2016. [8] E.M. Gibson et al. *Appl. Phys. Lett.* (1990).

This research was partly done at the Texas Nanofabrication Facility supported by NSF grant NNCI-2025227 and was supported by Lockheed Martin and NSF through the UT CDCM: an NSF MRSEC under Cooperative Agreement No. DMR-1720595, as well as CCF-1838435 and DMR-1839175.

11:15 AM KK03
(Student) Selective Area Doping and Lateral Overgrowth by Solid-Source Molecular Beam Epitaxy Alec M. Skipper, Ashlee Garcia, Daniel Ironside, Daniel Wasserman and Seth R. Bank; University of Texas at Austin, United States

Metals and dielectrics have historically been relegated to the periphery of conventional III-V devices due to the challenges associated with integrating amorphous/polycrystalline material with crystalline semiconductor growth. Epitaxially-embedded patterned metals and dielectrics could be useful in a wide variety of photonic and electronic devices to introduce both passive (e.g. polarizers, mirrors, or waveguides), and active (e.g. buried Ohmic contacts and enhanced optical emission) functionality. Monolithic integration of semiconductors, dielectrics, and metals would allow for 3D integration of optoelectronic devices and photonic integrated circuits. While we have recently reported the molecular beam epitaxy (MBE) overgrowth of patterned dielectrics [1] and metals [2] by III-V semiconductors, all experiments were performed using undoped material. Since dopant incorporation affects the growth kinetics on the surface, the addition of a dopant flux can result in the degradation of material quality. The growth parameters must be carefully tailored to prevent the formation of polycrystalline deposits, voids, and dislocations. We present a method for selective-area doping and epitaxial lateral overgrowth of III-V semiconductors by MBE toward 3D integration of novel embedded structures, mid-IR hyperbolic metamaterials, and self-aligned active devices. Periodic supply epitaxy (PSE), a growth technique that utilizes pauses in the group III flux to increase the desorption and diffusion of adatoms on a dielectric mask, was optimized to allow for the p and n type doping of high-quality GaAs without resulting in the deposition of polycrystals on SiO_2 mesas with a width of at least 300 µm. A growth temperature of 615°C, growth rate of 0.25 µm/hr, As_4/Ga beam equivalent pressure ratio of 65x, and PSE duty cycle of 50% were carefully chosen to (1) ensure smooth crystalline growth in the exposed semiconductor regions and (2) prevent nucleation of polycrystalline GaAs on the dielectric mask. Subsequent lateral overgrowth and planarization steps could allow for the full 3D integration of arbitrary-patterned hyperbolic metamaterials, leveraging the metallic behavior of highly-doped semiconductors in the mid-IR [3] to create photonic structures that can be epitaxially integrated above, below, or in-plane with active devices. Furthermore, selective area doping allows for the implementation of novel active device geometries that minimize parasitics seen in conventional etched and passivated devices [4]. Preliminary device implementation and characterization is currently underway and results will be reported at the conference.

This research was partially supported by Lockheed Martin and the National Science Foundation through the Center for Dynamics and Control of Materials: an NSF MRSEC under Cooperative Agreement No. DMR-1720595, as well as DMR-1839175, CCF-1838435, and ECCS-1926187.

[1] D. Ironside et al., "High-Quality GaAs Planar Coalescence over Embedded Dielectric Microstructures Using an All-MBE Approach," ACS Cryst. Growth Des. (2019)
[2] A. Skipper et al., "Monolithic Integration of Patterned Metal-Dielectric Stacks Overgrown with III-V Semiconductors by Molecular Beam Epitaxy," *62nd Electronic Materials Conf.* (2020)
[3] S. Law et al., "Mid-infrared designer metals," Opt. Express (2012)
[4] U. Singisetti *et al*., "$IN_{0.53}Ga_{0.47}As$ Channel MOSFETs With Self-Aligned InAs Source/Drain Formed by MEE Regrowth," *IEEE Electron Device Letters* (2009)

11:30 AM KK04
(Student) Demonstration of Self-Assembled InGaN/GaN Superlattice on GaN Template Grown by Plasma-Assisted Molecular Beam Epitaxy Kamruzzaman Khan[1], Kai Sun[1,2], Christian Wurm[3] and Elaheh Ahmadi[4]; [1]University of Michigan–Ann Arbor, United States; [2]University of Michigan, Ann Arbor, United States; [3]University of California, Santa Barbara, United States; [4]University of Michigan, United States

The (In,Ga)N material system is attractive for photovoltaic applications as its optical absorption covers the solar spectrum. Thick InGaN films (hundreds of nm thick) with InN mole fraction larger than 10% are required for this purpose. However, the growth of high In-content InGaN films remains challenging due to 10% lattice mismatch between InN and GaN and the large difference between the thermal stability of GaN and InN. While

the optimum growth temperature of GaN by plasma-assisted molecular beam epitaxy (PAMBE) is ~700 °C-730 °C, the growth temperature of InGaN is typically below 600 °C. Therefore, lower growth temperatures are required to grow InGaN films within the miscibility gap. InGaN films can be grown pseudo-morphically on GaN below a critical thickness. As the thickness increases beyond the critical thickness, the InGaN film relaxes. This relaxation may occur through different mechanisms depending on the growth technique and growth conditions (e.g., growth temperature). V-defect formation from threading dislocations is a common way of strain relaxation, especially in InGaN films grown via metal organic chemical vapor deposition, and has been observed in molecular beam epitaxy (MBE) grown InGaN films as well [1]. Pyramidal slip through the Matthews-Blakeslee mechanism and basal plane slip of misfit dislocation are other mechanisms through which strain relaxation occurs in InGaN films. Critical thickness reduces as InN mole fraction in InGaN increases. Bazioti et al [2] studied relaxation mechanism in InGaN films grown by PAMBE. They showed that at lower indium contents, strain relaxation dominantly occurred via formation of V-defects, with concurrent formation of an indium-rich interfacial zone. As indium content increased, this mechanism was replaced by the introduction of a self-formed strained interfacial InGaN layer of lower indium content, as well as multiple intrinsic basal plane stacking faults and threading dislocations in the rest of the film. In this talk, we will present growth of 700 nm-thick InGaN with an average InN mole fraction of ~8% coherently strained to GaN confirmed by XRD reciprocal space map scans. This is several times thicker than the critical thickness of $In_{0.08}Ga_{0.92}N$. Surprisingly, we did not observe generation of new threading dislocations in the InGaN films or misfit dislocations at the interface. Instead, we show that the strain is managed by self-formation of a superlattice structure. The superlattice was confirmed via scanning transmission electron microscopy and atom probe tomography. Photoluminescence (PL) measurements at room temperature revealed peak wavelength of ~450 nm, corresponding to $In_{0.18}Ga_{0.82}N$ with a full width half max (FWHM) of ~36 nm.

Reference:

1. C. Bazioti et al. Structure and strain variation in InGaN interlayers grown by PAMBE at low substrate temperatures Phys. status solidi 252 1155–62 (2015).
2. C. Bazioti et al. Defects, strain relaxation, and composition grading in high indium content InGaN epilayers grown by molecular beam epitaxy J. Appl. Phy. 118,155301 (2015).

11:45 AM KK05

(Student) Investigation of 1µm-Thick InGaN Films Grown on O-face ZnO by Plasma-Assisted Molecular Beam Epitaxy

Kamruzzaman Khan[1], Kanak Datta[1], Kai Sun[1], Mahitosh Biswas[1], Parag B. Deotare[1] and Elaheh Ahmadi[1,2]; [1]University of Michigan–Ann Arbor, United States; [2]University of Michigan, Ann Arbor, United States

The (In,Ga)N alloy system is attractive for optoelectronic applications as it enables direct bandgap tuning within a large range (0.7 eV–3.4 eV). While highly efficient GaN-based blue light emitting diodes (LEDs) have been commercially available for a decade, GaN red LEDs suffer from low efficiency. Red LEDs require high In content InGaN (>35%) QWs. Growth of high In-content InGaN on the GaN substrate is challenging due to high vapor pressure of InN. InN starts decomposing at 500 °C which is well below optimum GaN growth temperature of ~700 °C in molecular beam epitaxy (MBE). There is a large lattice mismatch between InN and GaN (~10%). Therefore, there is a great deal of interest in developing relaxed InGaN buffer as pseudo-substrate for optoelectronics applications. Various techniques have been employed in the past to obtain relaxed InGaN buffer layers including graded InGaN transition film and growth of InGaN on micrometer-size tiles of porousified GaN. Growth on oxide substrates, such as $ScAlMgO_4$ and ZnO have also been explored as an alternative. ZnO has the same crystal structure as (In,Ga)N (wurtzite) and is in-plane lattice-matched with $In_{0.2}Ga_{0.8}N$ [1]. Recently, we demonstrated growth of high-quality ~300 nm-thick (In,Ga)N films with the In content varying from 11% to 23% on ZnO [2]. For this purpose, we developed low-temperature atomically smooth GaN thin films (~2 monolayers (ML)) to suppress the interfacial reaction between nitrides and the ZnO substrate at elevated temperatures using metal-enhanced epitaxy (MEE). In this talk, we will present successful growth of high-quality 1µm-thick InGaN with In content ranging from 19.5% to 30.5% on ZnO substrate by plasma-assisted molecular beam epitaxy. PL analysis showed a relatively uniform InGaN composition on samples grown at 600 °C and 580 °C. Lowering the growth temperature to 560 °C led to clusters with higher In content. The uniformity of low temperature InGaN growth was improved by periodic desorption of In from the surface. Although, STEM image showed a high threading dislocation density generated at the substrate interface, TDD reduced significantly through annihilation of dislocations as InGaN thickness was increased. A self-assembled superlattice structure of the InGaN on ZnO was confirmed by scanning transmission electron microscopy and atom probe tomography. We will show the relaxation of InGaN on ZnO by XRD reciprocal space map measurement.

Reference:

1. A. Kobayashi et al. Pulsed sputtering epitaxial growth on m-plane InGaN lattice matched to ZnO, Sci. Rep. 7 1-6 (2017).
2. K Khan, Growth of high quality (In,Ga)N films on O-face ZnO substrates by plasma-assisted molecular beam epitaxy, AIP Adv. 10 075120 (2020)

SESSION LL: Materials Processing and Integration
Session Chairs: Daniel Ewing and Nate Quitoriano
Friday Morning, June 25, 2021

9:00 AM LL01

Reduced Temperature Preparation of Atomically Clean Si Surfaces to Augment CMOS with Atomic Precision Devices

Evan M. Anderson, Luis Fabian Pena, Esther Frederick, John P. Mudrick, DeAnna M. Campbell, Aaron M. Katzenmeyer, Tzu-Ming Lu, Andrew J. Leenheer, Jeffrey A. Ivie, Scott W. Schmucker, David A. Scrymgeour and Shashank Misra; Sandia National Laboratories, United States

Atomic precision advanced manufacturing (APAM) holds promise for both being able to explore new transistor technologies with atom-by-atom control, and for fundamentally modifying the electronic structure of silicon through doping past the solid solubility limit. These are both enabled by the chemical incorporation of dopant precursors (e.g. phosphine) selectively into pristine parts of the silicon surface, a process that is similar in spirit to area selective deposition. Historically, this process has been masked using atomic resists, like hydrogen, patterned with scanned probe microscopes to make one-off physics demonstration devices. Instead, we focus on the possibility of establishing compatibility with conventional CMOS processing. This opens the door to both using APAM levels of doping to enhance CMOS devices in the future, and to develop APAM inspired transistor technologies rapidly by leveraging existing CMOS device primitives. The primary challenge to producing APAM devices and integrating them with CMOS is thermal – preparing the necessary atomically clean Si surface normally occurs above 850 °C, which would destroy many CMOS elements. Additionally, this method of thermally removing the protective surface oxide enables surface diffusion of dopants – whether from surface contamination or implants – to the detriment of any subsequently fabricated device. This processing has only

been demonstrated in ultra-high vacuum (UHV), which is limited by throughput and scalability. The phosphorous layer itself has a severely restricted thermal budget compared to ion implants, necessitating careful consideration of where to insert APAM processes into a CMOS process flow and unconventional low thermal budget materials and processes after APAM processes. To address the more challenging problem of producing an atomically clean Si surface at reduced temperature, we investigate two different approaches to surface cleaning; chemical etching and mechanical sputtering. Both approaches can be scaled from die-level experiments to wafer-scale processing. We investigate the surface chemical effects of hydrofluoric acid (vapor vs solution phase) on Si(100) using infrared and x-ray photoelectron spectroscopy to achieve a suitable surface termination. Additionally, we demonstrate room temperature surface preparations in both a commercial plasma etcher and a custom installation of a plasma sputter source in a UHV chamber. All reduced temperature surface cleaning methods investigated here result in some degree of surface amorphization. In both chemical and mechanical cases, we demonstrate a suitably clean Si surface for APAM, healed at less than 650 °C, that is compatible with the middle of a CMOS process flow. *This work was supported by the Laboratory Directed Research and Development Program at Sandia National Laboratories and was performed, in part, at the Center for Integrated Nanotechnologies, a U.S. DOE, Office of Basic Energy Sciences user facility. Sandia National Laboratories is a multimission laboratory managed and operated by National Technology & Engineering Solutions of Sandia, LLC, a wholly owned subsidiary of Honeywell International Inc., for the U.S. Department of Energy's National Nuclear Security Administration under contract DE-NA0003525. The views expressed in the article do not necessarily represent the views of the DOE or the U.S. Government.*

9:15 AM LL02
(Student) Kinetics and Mechanism of Metal-Catalyzed Lateral Epitaxy for Growing Lattice-Mismatched Heterostructures via Vapor-Liquid-Solid Galih R. Suwito and Nate Quitoriano; McGill University, Canada

For the last few decades, most of the advancement in electronic and optoelectronic devices have been relying on our ability to integrate dissimilar materials having different lattice constants. By combining multiple different materials to form a heterostructure, we could engineer a particular band structure for a specific purpose. Nowadays the advancement on the integration technology is also motivated by the rapidly-growing field of Si photonics which requires integration of advanced non-Si infrared (IR) devices into the Si platform. However, to grow such devices on Si, one needs to address crystallographic challenges associated with high threading dislocations density caused by lattice mismatch. We have developed a novel materials integration technique, called metal-catalyzed lateral epitaxy, that has showed promising results in the Ge on Si system which has a 4% lattice mismatch. This technique uses a metal catalyst to control the growth location and a PECVD-grown capping layer to ensure growth laterally. The lateral growth is dictated by the vapor-liquid-solid mechanism which has shown a promising potential in suppressing the nucleation of threading dislocations by the extension of misfit dislocations. The main advantages of this technique over others are that it is wafer-scale, grown directly on the Si substrate, and allows direct electrical connection of the grown films to the substrate. In this talk, recent results of our systematic studies on the kinetics and the mechanism of this unique integration technique will be presented based on the heteroepitaxy of Ge-Si and InP-Si systems. Both are crucial heterostructures in Si photonics for high-performance IR photodetector and light source, respectively.

9:30 AM LL03
Carbon Nanotube-Cu Through-Silicon-via Interposer for Microelectronic Packaging Applications Guohai Chen, Rajyashree Sundaram, Atsuko Sekiguchi, Kenji Hata and Don N. Futaba; National Institute of Advanced Industrial Science and Technology, Japan

In microelectronic packaging, through-silicon-via (TSV) interposers using silicon and copper represent a critical element, acting as a bridge between fine pitch inputs/outputs at the integrated circuit chips to the coarser pitch packages at the substrate. As electronic devices continue miniaturization, thermal expansion match between the silicon substrate and copper vias becomes increasingly important to avoid device failure generally caused by delamination or break at the interface due to strain concentration. The demands for interposer materials with high electrical conductivity but low CTE are growing. In this work, we demonstrated the feasibility of the carbon nanotube-Cu (CNT-Cu) composite as a promising via material for TSV interposers which can potentially possess both the high electrical conductivity of Cu and the low coefficient of thermal expansion (CTE) of CNTs. Using a bottom-up, assembly approach, we fabricated a CNT-Cu TSV through combining aspects of the synthesis of lithographically patterned arrays of CNTs [1-4] with Cu deposition [5-6] and with standard processes used in the semiconductor industry. The CNT-Cu TSV showed both Cu-level electrical conductivity (~2.5×10^5 S/cm) and Si-level CTE (~7×10^{-6} /K). The CTE mismatch between CNT-Cu and Si was measured to be less than 1/5 compared with Cu and Si. Further, the functionality of the prepared CNT-Cu TSV interposer was demonstrated for several configurations. These results demonstrate the potential of the CNT-Cu TSV interposer in microelectronic packaging.

References

[1] G.H. Chen *et al*. ACS Appl. Nano Mater., **4**, 869 (2021).
[2] G.H. Chen *et al*. ACS Nano, **7** (11), 10218 (2013).
[3] G.H. Chen *et al*. Nanoscale, **8** (1), 162 (2016).
[4] G.H. Chen *et al*. ACS Biomater. Sci. Eng., **4** (5), 1900 (2018).
[5] C. Subramaniam *et al*. Nat Commun, **4**, 2202 (2013).
[6] R. Sundaram *et al*. J Mater Res Technol, **9** (3), 6944 (2020).

Corresponding: guohai-chen@aist.go.jp (G.H. Chen); Tel: +81-29-861-4416
Web: https://unit.aist.go.jp/cnta/ja/member/Guohai.html

9:45 AM LL04
Autonomous Optimization of Atomic Layer Deposition via Artificially Intelligent Agents Noah Paulson[1], Angel Yanguas-Gil[1], Osama Y. Abuomar[2] and Jeffrey W. Elam[1]; [1]Argonne National Laboratory, United States; [2]Lewis University, United States

Atomic layer deposition (ALD) is a thin film synthesis process capable of conformally coating surfaces with high precision. ALD's process and chemical flexibility makes it well suited to applications in computing, energy, and separations. This flexibility also leads to considerable challenges in identifying processing parameters resulting in optimal film quality with minimal waste and uncontrolled film growth on reactor surfaces. ALD growth per cycle (GPC) can be measured in-situ with a quartz crystal microbalance, but process development still requires time consuming trial and error on the part of the expert. GPC measurement noise adds to this challenge alongside the inherent diversity of responses due to different reactors and surface chemistries. Autonomous approaches that can quickly optimize processing conditions for arbitrary precursor chemistries would significantly accelerate the pace of ALD process development. In this work, we present three different strategies for the optimization of ALD dose and purge timings subject to increasing measurement noise. The first approach is a naïve random optimization strategy that serves as a reasonable baseline. The second is an expert

systems approach which employs logic modeled after human expert strategy and physical intuition. Finally, a Bayesian optimization approach constructs a machine learning surrogate model of the process to guide the optimization. Four ALD systems are studied to evaluate the optimization performance: Al_2O_3 using trimethyl aluminum (TMA) and H_2O at 200°C, Al_2O_3 using TMA and H_2O at 100°C, W using tungsten hexafluoride (WF_6) and disilane (Si_2H_6) at 200°C, and TiO_2 using titanium (IV) isopropoxide (TTIP) and H_2O at 200°C.

10:00 AM LL05
(Student) Nanosphere Coatings for Photonic Light Trapping in Ultra-Thin Film Photoconductive Absorber Layers for THz Generation Rachel Cherry[1] and Robert Coridan[1,2]; [1]University of Arkansas–Fayetteville, United States; [2]University of Arkansas, Fayetteville, United States

Thin film semiconductors are used as photoconductive absorber (PCA) layers in the construction of broadband THZ generation. A femtosecond laser pulse generates a transient increase in the film's conductivity by photoexciting conduction band electrons in the semiconductor, which then thermalize through the emission of THz radiation. This route to the THz generation is not a particularly efficient one, however. Significant losses come from absorption in the substrate beneath the PCA layer. Here, we explore the application of hexagonally close-packed monolayers of chemically synthesized nanospheres as a route to light concentration in ultra-thin films of relevance to THz generation. A layer of nanospheres can induce advantageous scattering texture to increase the effective path length of light transport through the film. The layer can also induce significant absorption enhancements through optical resonances caused by the periodic arrangement of close-packed spheres. To study these effects, we use finite element simulations of absorption in a model GaAs PCA layer. This enables us to map the absorption resonances in the material as a function of PCA layer thickness and sphere diameter. We also construct the equivalent materials to characterize these optical absorption enhancements in real, experimental systems. With these results, we show that a simple light concentration strategy generates a significant enhancement in light absorption, thus improving the light-to-THz power conversion efficiency.

SESSION MM: Gallium Oxide Epitaxy II
Session Chairs: Sriram Krishnamoorthy and Hongping Zhao
Friday Morning, June 25, 2021

10:45 AM MM01
In-Plane Orientation Control of (001) κ-Ga_2O_3 by Epitaxial Lateral Overgrowth Through a Geometrical Natural Selection Mechanism Yuichi Oshima[1], Katsuaki Kawara[2], Takayoshi Oshima[2] and Takashi Shinohe[2]; [1]National Institute for Materials Science, Japan; [2]FLOSFIA, Inc., Japan

Ga_2O_3 can possess various crystal structures such as α-, β-, ε- (κ-), and γ-phase. Each of them is an ultra-wide bandgap semiconductor with a bandgap energy of 4.5 ~ 5.3 eV. Among them, orthorhombic κ-Ga_2O_3 (also referred to as orthorhombic ε-Ga_2O_3), the target material of the present work, exhibits spontaneous polarization owing to the lack of inversion symmetry with respect to the *c*-plane [1]. Therefore, we can expect the formation of 2DEG at a hetero-interface, and high-performance devices utilizing the 2DEG. κ-Ga_2O_3 is a meta-stable phase, but the transient temperature to the β-phase is as high as ~700°C. (001) κ-Ga_2O_3 can be grown on various substrates such as GaN, AlN, SiC, sapphire, although homoepitaxial bulk substrates are not available. However, such κ-Ga_2O_3 films are a mixture of 120° in-plane rotational nano-sized domains [2]. High density of domain walls of such a film should have negative impact on the carrier transport properties, and therefore the in-plane orientation needs to be controlled to solve the problem. In the present work, we demonstrate a solution that utilizes an epitaxial lateral overgrowth technique. κ-Ga_2O_3 was grown by HVPE on a *c*-plane sapphire substrate with a TiO_x buffer layer. Periodic mask pattern was formed on the substrate prior to the growth. When a stripe-patterned mask was parallel to the [11-20] direction of the sapphire, the three in-plane orientations of the κ-Ga_2O_3 domains converged into one whose [010] direction was perpendicular to the stripe through a geometrical natural selection mechanism.
Acknowledgments
Part of this work was supported by Innovative Science and Technology Initiative for Security (JPJ004596), ATLA, Japan.
[1] F. Mezzadri, G. Calestani, F. Boschi, D. Delmonte, M. Bosi, and R. Fornari, Inorg. Chem. **55**, 12079 (2016).
[2] I. Cora, F. Mezzadri, F. Boschi, M. Bosi, M. Čaplovičová, G. Calestani, I. Dódony, B. Pécz, and R. Fornari, CrystEngComm **19**, 1509 (2017).

11:00 AM MM02
(Student) On the Initial Growth Mechanisms of α-Phase Ga2O3 on c-Plane Sapphire by Mist CVD Hitoshi Takane[1], Kentaro Kaneko[1], Yuichi Ota[2] and Shizuo Fujita[1]; [1]Kyoto University, Japan; [2]Tokyo Metropolitan Industrial Technology Research Institute, Japan

Recently, α-Ga_2O_3 have been attracting great attentions as an ultra-wide bandgap semiconductor. However, the reason why meta-stable α-Ga_2O_3, which was originally synthesized at a pressure of 44 kbar and at a temperature of 1000 °C [1], is grown at around 500 °C under atmosphere by mist chemical vapor deposition (CVD) has not been elucidated yet. In this study, in order to analyze the growth mechanisms of mist CVD-grown α-Ga_2O_3, we investigated the growth processes at the initial stage. α-Ga_2O_3 with thickness (*t*) of 2.3, 4.7, 7.8, and 30 nm were grown on (0001) sapphire by the mist CVD method. The four samples were investigated by atomic force micrograph (AFM), transmission electron micrograph (TEM), and X-ray diffraction reciprocal space mapping (XRD RSM). High resolution (HR-) TEM images at the interface viewed along the [11-20] axis indicates that α-Ga_2O_3 is pseudomophically grown on sapphire for *t*=2.3 nm, however, relaxed for *t*=4.7, 7.8, and 30 nm. Therefore, we found that the critical thickness of mist CVD-grown α-Ga_2O_3 on (0001) sapphire is 2.3-4.7 nm. In addition, for *t*=4.7, 7.8, and 30 nm, α-Ga_2O_3 was successfully grown even after the lattice relaxation. In TEM images under two-beam diffraction condition of **g**=10-10 viewed along the [11-20] , dark and bright regions periodically introduced in the film near the interface are seen, but not of **g**=0001, for *t*=4.7, 7.8, and 30 nm. Thus, it is considered that regions strained along in-plane direction or/and misfit dislocations with the Burger's vector parallel to the interface are periodically introduced near the interface after the α-Ga_2O_3 film relaxes. From the electron diffraction patterns and XRD RSM, it is confirmed that the films of *t*=4.7, 7.8, and 30 nm keep α-phase even after the lattice relaxation. XRD RSM also indicates that relaxation ratio gradually increases as the film thickness increases; for *t*=30 nm, the film is almost free standing. We also calculated the critical thickness based on the force-balance model and obtained the value of ~4.2 nm, which is consistent to the prediction (2.3-4.7 nm) derived from the HR-TEM. From the above coincidence, it is considered that the relaxation of mist CVD-grown α-Ga_2O_3 is caused by dislocations. On the other hand, by MBE, PLD, and MOCVD previously reported, the lattice relaxation is caused by phase transition from α to β [2,3], that is, the frustration of taking the α-phase causes the lattice relaxation so that the crystal structure changes from α to β. The lattice relaxation processes by mist CVD are different from those by other growth methods. This may be attributed to the low temperature growth and the association of water in the growth

atmosphere. We will discuss the mechanism in more detail at the conference.
[1] J. P. Remeika *et al*., Appl. Phys. Lett. **8**, 87 (1966).
[2] R. Schewski *et al*., Appl. Phys. Express **8**, 011101 (2015).
[3] Z. Cheng *et al*., Appl. Phys. Lett. **111**, 162104 (2017).

11:15 AM MM03
(Student) Phase Composition and Microstructure of Gallium Oxide Heteroepitaxial Films—Effect of MOCVD Growth Conditions Kunyao Jiang, Jingyu Tang, Anna Park, Liuxin Gu, Robert Davis and Lisa Porter; Carnegie Mellon University, United States

In recent years, the ultra-wide bandgap (4.5-4.9 eV) semiconductor gallium oxide (Ga_2O_3) has been investigated as a next-generation wide bandgap semiconductor because of its high figures of merit for power devices. Ga_2O_3 possesses different polymorphs, i.e., the α-, β-, ε(k)-, and γ-phases. Most reports focus on the β-phase because it is the most stable phase, but its monoclinic structure can present challenges in terms of anisotropic properties and epitaxial growth. Recently, the ferroelectric ε-Ga_2O_3 phase has accrued increased interest; its hexagonal structure presents the potential for better matching with commonly used substrates. In this study, heteroepitaxial Ga_2O_3 films were grown on 0.15° off-axis (toward m-plane), (0001) sapphire substrates using low-pressure metal-organic chemical vapor deposition (MOCVD). We investigated the effects of TEGa flow rate (VI/III ratio), growth temperature, and diluent gas flow rate on the phase(s) of Ga_2O_3 that formed and the microstructure of the resulting films. The films were grown using TEGa and O_2 precursors and N_2 as the carrier and diluent gas. During the growth, the chamber pressure was kept at 20 Torr and the growth temperature was varied from 788K to 843K. The TEGa flow rate was from 0.29 to 1.92 sccm and the diluent gas flow rate ranged from 4 slm to 5.5 slm. XRD 2θ-results indicated that the metastable ε-phase is promoted at lower growth temperature and higher TEGa flow rate (low VI/III ratio), whereas the β-phase forms at higher growth temperature and lower TEGa flow rate (high VI/III ratio), with mixed-phase growth for conditions in between. In addition, the microstructure of the films showed a dependence on the diluent gas flow rate. Hexagonal islands in the ε-Ga_2O_3 films were typically observed in SEM images, in agreement with previous reports of ε-Ga_2O_3 films [1]. However, the islands coalesced to form a continuous, smooth film at a diluent gas flow rate of 5 slm. For the latter growth condition, the XRD 2θ-film peaks also had the highest intensity. XRD phi scans were conducted to characterize the in-plane microstructure of an ε-Ga_2O_3 film. The results suggest that the ε- Ga_2O_3 film has a dominant in-plane orientation with a minor fraction of crystalline domains rotated by 30°. Bandgaps of 4.9 eV and 4.8 eV, respectively, for ε-phase and β-phase films were estimated from Tauc plots and agree with expected values.
[1] Yao, Yao, Serdal Okur, Luke AM Lyle, Gary S. Tompa, Tom Salagaj, Nick Sbrockey, Robert F. Davis, and Lisa M. Porter. "Growth and characterization of α-, β-, and ε-phases of Ga_2O_3 using MOCVD and HVPE techniques." *Materials Research Letters* 6, no. 5 (2018): 268-275.

11:30 AM MM04
Realization of Self-Assisted Growth of Nano-Columnar β-Ga_2O_3 Thin Film on Silicon Substrate Debabrata Das, Nanthakishore Makeswaran, Vishal B. Zade and Chintalapalle Ramana; The University of Texas at El Paso, United States

β-Ga_2O_3 is well known for its multidimensional functionality, such as deep-UV photodetector, high power electronic device, water splitting, CO_2 reduction, gas sensor, etc. Here we are presenting a low cost pulsed laser deposition method to demonstrate nano-columnar β-Ga_2O_3 thin film on silicon substrate with an average crystallite size of ~9 nm. In-situ anisotropic thermal conductivity during the grow process facilitates the unidirectional columnar growth of β-Ga_2O_3 thin film, decorated with nanocrystalline surface morphology. With increasing substrate temperature, it shows blue shifting of band edge absorption with decreasing defect density. Luminescence spectra show drastic improvement in intensity (~30 times), which is beneficial for further optoelectronic application.

11:45 AM MM05
(LATE NEWS, Student) Stabilizing α-Ga_2O_3 and α-$(Al,Ga)_2O_3$ up to 900°C Jonathan McCandless[1], Kazuki Nomoto[1], Celesta S. Chang[1], Joseph Casamento[1], Vladimir Protasenko[1], Patrick Vogt[1], Derek Rowe[1], Katie Gann[1], Shaoting Ho[1], Wenshen Li[1], Riena Jinno[1], Yongjin Cho[1], Andrew Green[2], Chabak Kelson[2], Darrell Schlom[1], Mike Thompson[1], David A. Muller[1], Huili Grace Xing[1] and Debdeep Jena[1]; [1]Cornell University, United States; [2]Air Force Research Laboratory, United States

α-Ga_2O_3 is a polymorph of Ga_2O_3 which has a larger bandgap (~5.3 eV) than the more studied β-phase. Additionally, unlike the β-phase,[1] the α-phase can be readily alloyed with Al over the entire compositional range, facilitating the creation of bandgaps up to 8.8 eV.[2] Moreover, α-phase is of interest because it can be grown on large-area, low-cost single-crystal sapphire substrates. Like low-Al content β-phase films, high-Al content α-phase films are effectively "homoepitaxial" with sapphire. The downside of α-Ga_2O_3, however, is that it is metastable. For example, films grown by mist-chemical vapor deposition (mist-CVD) convert to the β-phase when annealed at 660C.[4] This precludes α-Ga_2O_3 from undergoing processes which involve high temperature anneals. For example, ion implantation is of interest for the creation of ohmic contacts and for the creation of devices where doping profile control in the lateral direction is needed, but ion implantation often requires a high-temperature activation anneal which would result in the conversion of the sample to the β-phase. One approach that has successfully stabilized mist-CVD grown α-phase films, is that of alloying the material with Al.[4] While this has been successful, it is still necessary to develop a method of stabilizing α-Ga_2O_3. In this work we investigate the effects of Mo, SiO_2, and Al_2O_3 capping layers on the stability of α-Ga_2O_3, and we investigate the stability of α-$(Al_{0.47}Ga_{0.53})_2O_3$ (*aka* AlGO), and α-Al_2O_3. All films are epitaxially grown by molecular-beam epitaxy (MBE) on m-sapphire. We perform X-ray diffraction, atomic force microscopy, and absorption spectroscopy to study and quantify the structural evolution of the samples during anneals from 500°C to 900°C. First, we report that the uncapped α-Ga_2O_3 samples behaved in a manner similar to what is reported by mist-CVD grown samples — that is it remained stable only through the 600°C anneal before converting to the β-phase. This was concluded based on the downward shift of the diffraction peak and the reduction in the bandgap. Second, and more importantly, we report that stabilization of α-Ga_2O_3 was achieved up to 900°C anneal when the sample was capped with an amorphous Al_2O_3 layer. The bandgap, diffraction peak location, and direct imagining through transmission electron microscopy (TEM) all confirmed the sample remained in the α-phase and retained its high degree of crystal quality. After performing TEM, it was discovered that the Al_2O_3 cap crystalized during the 900°C anneal. Further, the Al_2O_3 capped sample experienced an improvement in the crystal quality quantified by a reduction in the full-width at half-max rocking curve value, and the sample experienced no substantial rougening. Third, the α-Ga_2O_3 samples capped with Mo and SiO_2 became amorphous upon annealing at 900°C, though the exact mechanism is still under investigation. Fourth, the AlGO and the α-Al_2O_3 samples remained in the α-phase throughout all anneals. The AlGO film became rougher, its rms roughness increasing from 1.37 nm to 1.96 nm after the 900°C annealing. In contrast, the epitaxially grown α-Al_2O_3 experienced a significant reduction in its roughness, decreasing from a rms roughness of 0.44 nm to 0.19 nm after the anneals. In conclusion, we have investigated, for the first time in MBE grown films, structural changes experienced by α-Ga_2O_3, AlGO, and α-Al_2O_3 during anneals from 500°C to

900°C. We have found that Al containing samples experienced no structural changes when grown by MBE, in agreement with what is reported for mist-CVD grown films. We report for the first time a method by which α-Ga_2O_3 films can be stabilized up to 900°C anneal, an important step for facilitating studies of doped samples and the eventual creation of high-performance α-Ga_2O_3 devices.
[1] S. Mu, et al. APL Mater. 8, 091105 (2020), [2] R. Jinno, et al. Sci. Adv. 7,1 (2021), [3] R. Jinno, et al. AIP Adv. 10, 115013 (2020), [4] S.-D. Lee, et al. JJAP 54, 030301 (2015)

SESSION NN: Group III-Nitride Defects
Session Chairs: Andrew Armstrong and Mona Ebrish
Friday Afternoon, June 25, 2021

1:00 PM NN01
(Student) Imaging Photocurrent Distributions from Sub-Bandgap Defects by Polarity Resolved Scanning Photocurrent Microscopy (SPCM) in III-Nitride Devices Fiaz Ahmed, Mohi Uddin Jewel, Shahab Mollah, Joshua Letton, Abdullah Mamun, Mikhail Gaevski, Grigory Simin, Andrew Greytak, MVS Chandrashekhar and Asif Khan; University of South Carolina, United States

High electron mobility transistors (HEMTs) based on tunable wide bandgap AlGaN alloys (360nm-200nm) are promising for true solar blind photodetection devices with potential applications in secure space communications, highly sensitive missile plume detectors, and flame detectors. The wide bandgap provides low dark current, making these devices suitable for compact low-noise detection, while the direct bandgap is ideal for fast photodetection. However, HEMT devices are limited by electrically active sub-bandgap defects on non-native substrates, leading to slow response times >100s and persistent photocurrent (PPC) originating from deep level defects and dislocations. Therefore, the knowledge underlying physical mechanisms of how defects influence device performance is important to understand and predict operational behavior and failure mechanisms of these HEMT devices. Given the geometry of these devices, neither capacitance measurements nor current-based techniques have the spatial resolution to isolate the influence of these defects.
This talk will describe polarity-resolved scanning photocurrent microscopy (SPCM), and its applicability to spatially isolate and image sub-bandgap defect induced photocurrent processes in an AlGaN/GaN HEMT with micron resolution. By using 443nm (2.8eV) blue light, we are able to capture most sub-bandgap defects (typically ~1eV below the conduction band edge) without activating band-to-band transitions at 3.4eV. The SPCM signals on the Drain-Gate (DG) and Gate-Source (GS) junctions are clearly resolved, and are seen to be in opposite directions under certain bias conditions. Our results show clearly that sub-bandgap photoresponse is due to charge collection at the gate-source Schottky junction, while it is due to photoconductive gain in the channel from carriers trapped at the growth interface. Polarity resolved SPCM shows that these two processes give photocurrents in opposite directions, and by modulating the gate voltage, their relative contributions to the overall photocurrent is tuned. By modulating the drain voltage from the linear to saturation regime, the pinch-off of the channel near the drain end leads to increasing photoconductive gain, showing that operating HEMT photodetectors in the linear regime will suppress photoconductive current from the growth interface. Typical transient times for each mechanism is in the 1-10ms range, which is still much slower than the ns recombination times for direct bandgap semiconductors, showing that these are indeed defect states. In summary, by isolating the various sub-bandgap photocurrent mechanisms by polarity resolved SPCM, device designers and crystal growers have additional information to optimize the epitaxial structure, and device geometry depending on the application. In particular, the slow PPC plaguing III-nitride photodetectors arising from sub-bandgap defects can now be diagnosed in greater detail as a function of bias, allowing the full promise of the material to be realized.

1:15 PM NN02
Oxygen Doping Distribution in GaN Lateral Polarity Junction Alexander Chang[1], Dennis E. Szymanski[2], Dolar Khachariya[2], James Tweedie[3], Pramod Reddy[3], Zlatko Sitar[1], Ramón Collazo[2], Spyridon Pavlidis[2] and Lincoln Lauhon[1]; [1]Northwestern University, United States; [2]North Carolina State University, United States; [3]Adroit Materials, United States

Beyond the successful demonstration of lateral AlGaN/GaN Schottky barrier diodes for the next generation power device, vertical p-n devices are promising due to the expected higher breakdown voltages with better scalability and thermal management. For such devices, selective area doping is vital in forming lateral p-n junctions to modulate current flow. Lateral polarity junctions (LPJ) are of increasing interest because one can achieve polarity-dependent doping types using the different impurity incorporation energies of Ga- and N-polar domains. For example, the oxygen adsorption energy is significantly lower on N-polar than Ga-polar GaN surfaces, depending on the relative directions of polarization in Ga-O versus Ga-N bonds.[1]-[2] For Mg (p-type) doped LPJ, Ga-polar GaN is p-type while N-polar GaN is n-type due to the high compensation effect. Although segregation of dilute species to GaN inversion domain boundary has been reported,[3]-[4] the dopant distribution in side-by-side grown GaN LPJ has yet not been reported. Atom probe tomography (APT) characterization was performed on GaN lateral polarity structures. The Ga-polar and N-polar domains were grown simultaneously using metal-organic chemical vapor deposition (Fig. 1). Mg precursor (Cp2Mg) was flown during the growth, and the incorporation of oxygen was controlled via the MOCVD growth conditions. APT specimen tips were prepared each from Ga-polar and N-polar domains and targeting the polarity domain boundary. APT data was collected at various run conditions to investigate the origin of the detected oxygen ions, i.e. oxygen dopants versus surface contamination. Here, we report APT study on the oxygen dopant distribution in the vicinity of GaN LPJ. The distinct field evaporation behaviors of Ga- and N-polar GaN are reflected in the Ga and N hit density maps for the two orientations (Fig. 2). An oxygen peak is observed in the mass spectrum of N-polar GaN, while no O peak is observed in the Ga-polar GaN spectrum. For N-polar GaN, the measured oxygen concentration was relatively insensitive to the evaporation field and laser pulse energy (Fig. 3), suggesting that the oxygen is present as a dopant and not a diffusing surface contaminant. Further work focuses on analyzing the impurity distribution adjacent to the domain boundary, which may provide important insights on charge compensation effects.
[1] R. Collazo, S. Mita, J. Xie, A. Rice, J. Tweedie, R. Dalmau, and Z. Sitar, *Phys. Status Solidi a* (2010) **207**, 45.
[2] T. K. Zywietz, J. Neugebauer, and M. Scheffler, *Appl. Phys. Lett.* (1999) **74**, 1695.
[3] Th. Schmidt, M. Siebert, J. I. Flege, S. Figge, S. Gangopadhyay, A. Pretorius, T. L. Lee, J. Zegenhagen, L. Gregoratti, A. Barinov, A. Rosenauer, D. Hommel, and J. Falta, *Phys. Status Solidi B* (2011) **248**, 1810-1821
[4] Z. Liu, R. Z. Wang, L. M. Liu, H. Yan, and W. M. Laub, *J. Mater. Chem. A* (2014) **2**, 9744-9750

1:30 PM NN03
(Student) Characterization of Prismatic Slip in PVT-Grown AlN Crystals Shanshan Hu[1], Haoyan Fang[1], Yafei Liu[1], Hongyu Peng[1], Tuerxun Ailihumaer[1], Qianyu Cheng[1], Zeyu Chen[1], Rafael Dalmau[2], Jeffrey Britt[2], Raoul Schlesser[2], Balaji Raghothamachar[1] and Michael Dudley[1]; [1]Stony Brook University, The State University of New York, United States; [2]HexaTech Inc., United States

Aluminum nitride (AlN) single crystals are desirable as substrates for nitride based electronic and optoelectronic applications [1]. In order to grow high-quality heteroepitaxial epilayers, a low density of dislocations and other structural defects in bulk AlN substrates is demanded. AlN crystals grown by physical vapor transport (PVT) possess a low density of dislocations and other structural defects [2]. Basal plane slip is the most frequently observed deformation mechanism in AlN crystals grown by PVT. However, prismatic slip takes place as well in such crystals [3, 4].
As the diameter of AlN wafers expands to 50 mm and larger, it becomes critical to manage the thermal gradients in the PVT growth chamber, in order to minimize thermal stresses that cause deformation. Recent synchrotron X-ray topography [5] studies of 50 mm diameter AlN wafers showed that while most wafers contained few to no basal plane dislocations (BPDs), some wafers possessed a 6-fold BPD dislocation pattern [2] which was aligned along the <11-20> directions. This configuration indicated that prismatic slip had likely occurred, such that screw dislocations from the prismatic plane cross slipped onto the basal plane, where they underwent basal plane slip, leading to dislocation multiplication. To investigate the origins of prismatic slip, a radial thermal gradient model was developed showing the resolved shear stress across the entire area of the crystal boule during growth. The results from the model were correlated with experimental observations in order to investigate the role of radial thermal gradients in the nucleation of prismatic slip in AlN during bulk growth. This insight will help guide efforts to reduce structural defects in PVT AlN.

1:45 PM NN04
Microwave-Induced Annealing, Its Impact on Mg Diffusion and Photoluminescence Activity in Implanted and *In Situ* Doped GaN Vincent E. Meyers[1], Emma Rocco[1], Kasey Hogan[1], Benjamin McEwen[1], Michael A. Derenge[2], Kenneth A. Jones[2], Mike Shevelev[3], Vlad Sklyar[3] and Fatemeh (Shadi) Shahedipour-Sandvik[1]; [1]State University of New York Polytechnic Institute, United States; [2]U.S. Army Research Laboratory, United States; [3]Gyrotron Technology, Inc, United States

The next generation of solid-state power electronics will increasingly utilize the $Al_xGa_{1-x}N$ system, benefitting from its large and direct band gap, high switching speed, and high FOM. Formation of selective-area p-type regions is critical for field management and remains a significant challenge for higher-voltage next-generation architectures. Activation of the p-type dopant Mg, especially in the case of ion-implanted $Al_xGa_{1-x}N$, requires temperatures high enough to cause significant diffusion of the dopant, potentially distorting the doped region shape. Microwave annealing has been shown to induce both dopant activation and diffusion, especially for rapid drive-in of B in Si[1] Diffusion dynamics induced by microwave annealing can diverge from those suggested by the bulk thermal condition of the sample. This has been attributed to interaction of the microwave beam with ionized defects and dopants in the material, permitting higher diffusion of electrically charged (ionized) species in the lower-temperature bulk[2]. This makes understanding Mg redistribution in GaN due to microwave annealing in both implanted and in-situ doped material of critical importance to the continued development of selective-area doping. In order to better understand this diffusion and activation behavior, a study was conducted of spatially resolved Mg distribution in in-situ doped and implanted GaN grown by metalorganic chemical vapor deposition (MOCVD) and annealed by gyrotron microwave beam. Annealing conditions between 1160–1410 °C were performed for durations between 30–65 s in total using a quasi-gaussian beam intensity profile and a 2.5 cm beam raster across the sample surface. Low-temperature PL spectra were measured and used as a proxy for acceptor activation before and after annealing of doped GaN. At the locations of PL measurements on samples, depth profiles of [Mg] were taken using dynamic secondary ion mass spectroscopy (D-SIMS). Beyond concentrations of around 10^{16} cm^{-3}, the intensity of PL bands is not linearly related to the density of acceptors in the material[3], however PL spectra have been shown to indicate the presence of conductivity type, provided initial knowledge of the growth condition. The as-implanted [Mg] profile of all samples shows a profile of 1×10^{19} cm^{-3} to a depth of 250 nm with a quasi-Gaussian tail. The in-situ doped as-grown [Mg] of 7×10^{19} cm^{-3} remains constant from the surface to the p-GaN layer depth of ~120 nm before annealing, and the profile does not appreciably change after annealing. After annealing implanted samples above 1350 °C, diffusion of Mg dopant is observed to vary spatially across the sample, correlating approximately with the beam shape and raster. To understand potential correlation of such diffusion with PL bands, measurements on the same location as SIMS measurement was performed. PL measurements show the characteristic near-band edge (NBE) luminescence at 3.47 eV and Mg-acceptor-related UVL at 3.27 eV in all spectra. In the 2.2–2.4 eV range, either the V_N-related GL2 band or the C_N-O_N-related YL band is dominant. Relative intensity of these bands varies across the sample area, however no correlation of PL activity with Mg diffusion is observed. We show that while PL activity reflects the presence of Mg_{Ga} and other optically active defects within the laser excitation depth (~92 nm), (anneal-induced) diffusion has no significant impact on [Mg] within this depth, and therefore that diffused Mg deeper in the sample (200–800 nm) does not necessarily impact PL activity. This may be due in part to the upper limit of PL sensitivity to acceptor concentration[3].
This work was funded by a grant from ARPA-E PNDIODES program, grant #DE-FOA-001691 under the direction of Dr. Isik C. Kizilyalli.
[1] Kohli, P., et al. (2002). *J. of Electron. Mat.*, *31*(3), 214-219.
[2] Booske, J. H., Cooper, R. F., & Dobson, I. (1992). *J. Mat. Research*, *7*(2), 495-501.
[3] Reshchikov, M. A., et al. (2017). S*cientific reports* 7(1), 1-11.

2:00 PM NN05
(LATE NEWS) Point-Defect Management in Homo-Epitaxially Grown Si-Doped GaN by MOCVD for Vertical Power Devices Shashwat Rathkanthiwar[1], Pegah Bagheri[1], Dolar Khachariya[1], Ji Hyun Kim[1], Seiji Mita[2], Pramod Reddy[2], James Tweedie[2], Zlatko Sitar[1] and Ramón Collazo[1]; [1]North Carolina State University, United States; [2]Adroit Materials, United States

The demand for next-generation, kV-class power electronics is on a tremendous increase for applications in electric motor drives, energy storage, power conversion, and energy transportation. The development of highly conducting single-crystal GaN substrates have enabled GaN-based vertical diodes and switches which are poised to enable highly efficient power devices represented by the Baliga's Figure of merit that is several orders of magnitude better than conventionally employed Si. The development of thick n-GaN drift layers with uncompensated doping in the range of low-10^{15} cm^{-3} is the key to the realization of kV-class power devices. However, carbon (C_N) incorporation during MOCVD growth presents a major challenge to achieving reliable doping in the necessary low doping range. In this study, we demonstrate controlled doping in the range of 10^{15} cm^{-3} with mobility >1000 cm^2/Vs in homoepitaxial Si-doped GaN films grown by metalorganic chemical vapor deposition (MOCVD) by point defect management employing chemical potential control (CPC) and defect quasi-Fermi level (dQFL) control. The carbon (C_N^{-1}) related compensation and corresponding electron mobility

collapse [Kaess 2016] were prevented by controlling the electrochemical potential near the growth surface. This was achieved by employing CPC and dQFL control. The CPC approach was used to establish a defect formation energy map of C_N as a function of the growth environment represented by gallium supersaturation at a given growth temperature. [Reddy 2017] The supersaturation was chosen to maximize the formation energy of carbon within practical reactor and growth constraints and thereby, reduce carbon to ~$2x10^{15}$ cm^{-3}. The dQFLC approach was then used to further reduce the fraction of carbon atoms with compensating (acceptor) configuration, i.e., C_N^{-1} to <10^{15} cm^{-3}. The dQFL control approach involves generating excess minority carriers near the growth surface in a steady-state condition by external above-bandgap illumination. This technique induces photo-voltage which performs work against incorporation effectively increasing its formation energy. Theoretical calculations projected that the efficacy of this approach in reducing the C_N^{-1} incorporation is high in the considered doping range of 10^{15}-10^{16} cm^{-3}. To confirm this hypothesis, we grew Si-doped GaN epilayers on sapphire substrate with and without the use of external UV illumination. The dQFLC led to a more than two-fold reduction in [C_N^{-1}] from $1x10^{16}$ cm^{-3} to <$5x10^{15}$ cm^{-3}. With Si doping at $1.5x10^{16}$ cm^{-3}, C_N^{-1} reduction resulted in increased mobility (60 to 620 cm^2/Vs) by mitigating mobility collapse and increased carrier concentration ($3x10^{15}$ to 10^{16} cm^{-3}). Finally, Si-doped GaN grown on semi-insulating GaN substrates with a combination of CPC and dQFLC showed controllable and reliable doping with carrier concentrations in the range of $5x10^{15}$-$2x10^{16}$ cm^{-3} with high mobility > 1000 cm^2/Vs at room temperature owing to [C_N^{-1}] <10^{15} cm^{-3}. The low compensating acceptor C_N^{-1} concentration was confirmed via Temperature-dependent Hall-effect analysis and capacitance-voltage measurements. Maximum mobility of 4000 cm^2/Vs was measured at 120 K.

References:

Reddy et al. Appl. Phys. Lett. **111**, 152101 (2017)
Kaess et al. J. Appl. Phys. **120**, 105701 (2016)

SESSION OO: Novel Materials
Session Chairs: Deidra Hodges
Friday Afternoon, June 25, 2021

1:00 PM OO01

(Student) Experimental Determination of Valence Band Offsets of ZnGeN2 and (ZnGe)0.94Ga0.12N2 with GaN Md Rezaul Karim[1], Brenton A. Noesges[1], Benthara H. Jayatunga[2], Menglin Zhu[1], Jinwoo Hwang[1], Walter R. L. Lambrecht[2], Leonard J. Brillson[1,1], Kathleen Kash[2] and Hongping Zhao[1,1]; [1]The Ohio State University, United States; [2]Case Western Reserve University, United States

Zinc germanium nitride ($ZnGeN_2$) is the II-IV-N_2 analogue of GaN which has a band gap (E_g) very close to that of GaN (~3.4 eV) and a lattice mismatch of <0.1% with GaN [1]. Based on first principles calculations, the predicted valence band offset (VBO) of $ZnGeN_2$ with GaN can be as high as 1.4 eV, [2] which provides great opportunities to design high efficiency InGaN/$ZnGeN_2$ heterostructure quantum wells for visible light emitters [1]. However, there has been no report on the experimentally determined VBO at the $ZnGeN_2$/GaN heterointerface, due to the lack of availability of high quality materials. In this work, we have experimentally determined the VBOs of $ZnGeN_2$ and a 94% $ZnGeN_2$ – 6% GaN alloy ($(ZnGe)_{0.94}Ga_{0.12}N_2$) with GaN using Kraut's method. The VBO between two materials A and B are determined using the core energy levels (E_{CL}) in bulk A, bulk B and at the A/B heterointerface and the position of the valence band maxima (VBM) in bulk A and bulk B. X-ray photoemission spectroscopy (XPS) was used to measure the E_{CL} and VBM values. To determine the VBO between $ZnGeN_2$ and GaN, a GaN/c-sapphire template, a 16-nm-thick $ZnGeN_2$ film and a 2-nm-thick $ZnGeN_2$ layer grown on GaN template were used as the bulk GaN, bulk $ZnGeN_2$ and $ZnGeN_2$/GaN heterostructure, respectively. $ZnGeN_2$ films were grown on GaN/c-sapphire templates via metalorganic chemical vapor deposition (MOCVD) [3,4]. By using the measured Zn 3d (Ge 3d) core levels from $ZnGeN_2$ and the Ga 3d core levels from GaN, the VBO of $ZnGeN_2$ with GaN was extracted to be 1.45±0.15 eV (1.65±0.15 eV). These values are comparable to the values predicted from first-principles calculations using explicit interface calculations [2]. Similarly, the VBO of $(ZnGe)_{0.94}Ga_{0.12}N_2$ with GaN was determined. The samples used include a GaN/c-sapphire template as bulk GaN, a 20-nm-thick $(ZnGe)_{0.94}Ga_{0.12}N_2$ films as bulk $(ZnGe)_{0.94}Ga_{0.12}N_2$ and a 3-nm-thick $(ZnGe)_{0.94}Ga_{0.12}N_2$ film as the $(ZnGe)_{0.94}Ga_{0.12}N_2$/GaN heterostructure. These samples were grown on GaN/c-sapphire templates via MOCVD. The experimentally extracted VBO of $(ZnGe)_{0.94}Ga_{0.12}N_2$ with GaN was 1.29±0.15 eV. Assuming a linear dependence of the VBO with composition x of $(ZnGe)_{1-x}Ga_{2x}N_2$, the predicted VBO of $(ZnGe)_{0.94}Ga_{0.12}N_2$ from the theoretically calculated VBO of $ZnGeN_2$ would be 1.32 eV. Thus, the experimentally measured VBO results agree well with the theoretically predicted values.

The conduction band offsets were derived using the determined VBO values and the energy band gap E_g of the materials. The band gaps of $ZnGeN_2$ and $(ZnGe)_{0.94}Ga_{0.12}N_2$ were estimated from the inelastic energy loss features of N 1s peaks in the XPS spectra of 16-nm-thick $ZnGeN_2$ and 20-nm-thick $(ZnGe)_{0.94}Ga_{0.12}N_2$ samples. The E_g values determined by this method were 3.0±0.2 eV for $ZnGeN_2$ and 3.1±0.2 eV for $(ZnGe)_{0.94}Ga_{0.12}N_2$. The lower values of E_g as compared to the predicted band gap values (~3.4 eV) can be due to the presence of disorder in the cation sublattice.

In conclusion, the valence band offsets of MOCVD-grown $(ZnGe)_{1-x}Ga_{2x}N_2$ with GaN, with x = 0 and 0.06 were determined experimentally using XPS. The measured VBO values are comparable to the predicted values from first-principles calculations. The results from this study will expand device designs based on pure III-nitrides to III-nitrides/II-IV-N_2, which can potentially address key challenges in III-nitride based electronic and optoelectronic device technologies.

This work is supported by the U.S. DOE (DOE SSL: DE-EE0008718) and by the NSF (DMREF: SusCHeM: 1533957).

References

1. L. Han, K. Kash, and H. Zhao, J. Appl. Phys., 120, 103102 (2016).
2. A. P. Jaroenjittichai, S. Lyu, and W. R. L. Lambrecht, Phys. Rev. B., 96, 079907(E) (2017).
3. M. R. Karim, B. H. D. Jayatunga, M. Zhu, R. A Lalk, O. Licata, B. Mazumder, J. Hwang, K. Kash, H. Zhao, AIP Adv. 10, 065302 (2020).
4. B. H. D. Jayatunga, M. R. Karim, R. A. Lalk, O. Ohanaka, W. R. L. Lambrecht, H. Zhao, and K. Kash, Cryst. Growth Des., 20, 189 (2020).

1:15 PM OO02

(Student) Epitaxial Growth of Topological Dirac Semimetal Na3Bi on an Antiferromagnetic Insulator Dana Peirce, Igor Pinchuk, Simranjeet Singh and Jyoti Katoch; Carnegie Mellon University, United States

3D topological dirac semimetals (TDS) such as Na_3Bi and Cd_3As_2 possess Dirac nodes located outside the time-reversal invariant momentum points in the Brillouin zone. Recent theoretical and experimental work show that quantum confinement of 3D TDS can open a tunable bulk gandgap and give rise to thickness-dependent alternate transitions between trivial and quantum spin Hall insulator states. Additionally, we can exploit the magnetic proximity effect (MPE) by layering a 3D TDS with an antiferromagnetic insulator to induce the quantum anomalous Hall (QAH) state. Here we will present our results on ultra-thin growth of Na3Bi films on the antiferromagnet Cr_2O_3 using molecular beam epitaxy (MBE). We will also discuss efforts toward *in-situ* magnetotransport measurements.

1:30 PM OO03
(Student) Hybrid Vapor Phase Epitaxy (HybVPE) of Transition-Metal-Alloyed Single-Crystalline Wide-Bandgap Piezoelectric Semiconductor Films Mina Moradnia[1], Jie Chen[2], Sara Pouladi[1], Nam-In Kim[1] and Jae-Hyun Ryou[1]; [1]University of Houston, United States; [2]Colorado School of Mines, United States

AlN thin film has been one of the primary candidates for various electro-acoustic and high-temperature applications. However, the low piezoelectric response and electrochemical coupling in AlN utilization restrict its performance as a highly functional piezoelectric material for wider applications. As a result, the piezoelectric performance of AlN needs to be improved. Doping with other metals in the AlN structure plays an important role to enhance the piezoelectric coefficient (d_{33}) of AlN. Scandium (Sc) incorporation as a doping element to substitute with aluminum (Al) in wurtzite structure of AlN forms $Al_xSc_{1-x}N$ which could significantly enhance the piezoelectric coefficients of AlN-based materials up to three times. AlScN thin film would have a potential impact on electronic devices e.g. bulk acoustic and surface acoustic wave filter (BAW and SAW), sensors, energy harvesting performance, and ferroelectric nonvolatile memories. Magnetron reactive sputtering system using co-sputtering and compound target sputtering have been the prominent methods for epitaxial growth of AlScN. However, mass production limits, size limitation for high Sc content of compound targets, and difficulty in control of uniform Sc content across the whole area of large substrates cause the necessity of considering hydride vapor phase epitaxy (HVPE) as a more convenient growth method. The HVPE has excellent compatibility between supply control and mass production for the epitaxial growth of AlScN thin film. Therefore, we investigate the thermodynamic calculation of HVPE growth of AlScN for the first time pursuing better control on the composition of aluminum nitride alloy along with an increase of its growth rate. The phase stability of the (Al, Sc)N wurtzite phase is very important in designing highly functional piezoelectric materials. Therefore, a phase separation formation of metastable rock salt cubic ScN structure in above 50% scandium at Al-Sc-N ternary system should be avoided. HVPE method can give a promise to control the Sc content in a more controlled way compared to the sputtering growth method. In this regard, the thermodynamic analysis describes the solid composition of $Al_xSc_{1-x}N$ in terms of the various input partial pressure of an aluminum source gas, a scandium source gas, a nitrogen source gas, and carrier gases. In the present study, we proposed an epitaxial growth using $AlCl_3$, Sc vapor, and NH3, coined here as a hybrid vapor phase epitaxy (HybVPE). We calculate the equilibrium partial pressures and the driving force for AlN and ScN deposition in AlScN based on various temperatures, III/V material input ratios, and carrier gases partial pressures in different source and growth zones. Equilibrium partial pressures of gaseous species over Al metal in the Al source zone at different values of temperature suggest that Al source zone should only be heated up to 750 degree C to avoid any damage to the CVD furnace quartz (SiO_2) tube because of its reaction with AlCl. The preferential reaction in the Al source zone happens at a temperature below 750 degree C which produces $AlCl_3$ as the desired group III input from the Al source zone for AlN deposition in the growth zone. The equilibrium partial pressure of the $AlCl_3$ precursor can be controlled by the amount of input HCl reactant gas in the Al source zone. Moreover, the driving force for the deposition (P^o_{III} - $P_{III} = \Delta P$) resulted from the thermodynamic analysis of the growth zone shows that an Sc doping content of up to 30% can be achieved which is critical for the improvement of piezoelectric properties of AlN alloy by HybVPE method.

1:45 PM OO04
(Student) Progress in MOCVD Growth and Characterization of $ZnGeGa_2N_4$ Films Benthara H. Jayatunga[1], Kathleen Kash[1], Hongping Zhao[2,2], Md Rezaul Karim[2], Jinwoo Hwang[2], Menglin Zhu[2], Okey Ohanaka[1] and Rebecca A. Lalk[1]; [1]Case Western Reserve University, United States; [2]The Ohio State University, United States

$ZnGeN_2$ and GaN are nearly lattice matched and each have band gaps of approximately 3.4 eV. The large band offset of 1.4 eV in the conduction band results in a type II band alignment that has great potential for novel device structures such as high-performance LED structures that emit wavelengths beyond green [1,2]. Recently published work included theoretical predictions revealed a slightly positive mixing energy, indicating a tendency toward phase separation [3], and the lowest energy configuration to be the octet-rule-preserving $Pmn2_1$ phase for $ZnGeGa_2N_4$. Other compositions can be rendered by random stacking of $ZnGeN_2$ and GaN layers along the orthorhombic b axis in octet-rule-preserving (and hence lower energy) phases. [3] MOCVD growth of this alloy on c-, r-, and a-plane sapphire and c-GaN/sapphire substrates showed that films of 50-50 composition exhibit better surface morphologies when grown on r-sapphire substrates. A surprising trend of increasing Zn incorporation with increasing Ga was noted. The optimal growth temperature and pressure were determined to be 670 ^{0}C and 550 torr at which the highest growth rate, 3.46 μm/hr, was obtained for a film grown on r-sapphire. This film also yielded a wurtzite (110) 2θ-ω XRD diffraction peak at $2\Theta = 57.70^0$ with FWHM of 0.76^0 and the lowest RMS surface roughness over an area of 1 μm^2 , ~ 10 nm measured by AFM. [4] The only other experimental work on this alloy reported to date employed a gas reduction nitridation method for synthesis of powders of different compositions, from pure $ZnGeN_2$ to a 50-50 mixture, for photocatalytic applications [5]. Recent progress in growth and characterization is reported here. Atomic-resolution HAADF-STEM images show single-crystal atomic arrangements within 2-3 nm of the substrate interface. The lattice parameters a, b and c measured from these images are 6.429 ± 0.012 Å, 5.585 ± 0.079 Å, and 5.252 ± 0.085 Å, respectively. Introduction of a low-temperature $ZnGeN_2$ buffer layer (480 ^{o}C at 600 torr) improved the surface morphology, resulted in higher Hall mobilities, and gave band edge photoluminescence at approximately 3.5 eV, close to the predicted value for the $Pmn2_1$ phase. [3] Evaluation of several growth experiments with respect to resulting surface morphology and x-ray rocking curve peak line widths show that the optimal growth conditions for $ZnGeGa_2N_4$ with low-temperature $ZnGeN_2$ buffer layers differ significantly from the optimal growth conditions for $ZnGeN_2$ without the low-temperature $ZnGeN_2$ buffer layers. To obtain optimal, nearly stoichiometric $ZnGeGa_2N_4$ films, the precursor DEZn flow rate was reduced by nearly half of that used in the same system for optimal $ZnGeN_2$ growth at the same temperature. This reduction in DEZn flow rate also allows for the achievement of higher growth temperatures for $ZnGeGa_2N_4$ than for $ZnGeN_2$ while avoiding Zn depletion. Growth of a quaternary alloy with composition approximately 25:75% $ZnGeN_2$: GaN also resulted in a continuous film with similar surface morphology, and an rms surface roughness of 10.2 nm over an area of 1 μm^2. This work is supported by the U.S. DOE (DOE SSL: DE-EE0008718) and by the NSF (DMREF: SusCHeM: 1533957).

[1] L. Han, K. Kash, H. Zhao, J Appl Phys **120**, 103102 (2016)
[2] M. R. Karim, H. Zhao, J Appl Phys **124**, 034303 (2018)
[3] B.H.D. Jayatunga, S. Lyu, S. Kumar, K. Kash, W. R. L. Lambrecht, Phys Rev Mat **2** (2018)
[4] B. H. D. Jayatunga, Md R. Karim, R. A. Lalk, O. Ohanaka, W. R. L. Lambrecht, H. Zhao, and K. Kash, Crystal Growth & Design **20**, 189-196 (2020)
[5] T. Suehiro, M. Tansho, T. Shimizu, J Phys Chem **C 121**, 27590 (2017)

2:00 PM OO05
Low-Temperature Epitaxial Growth of Anti-Ferromagnetic MnTe at Bi_2Te_3 Oleg Maksimov[1], Harish Bhandari[1], Bryan Rachmilowitz[2], Zheng Ren[2], Shrinkhala Sharma[2] and Ilija Zeljkovic[2]; [1]Radiation Monitoring Devices, United States; [2]Boston College, United States

There is a significant scientific and technological interest in the epitaxial integration of ferromagnetic or antiferromagnetic materials with the topological insulators (TI). This allows the introduction of the ferromagnetic order into a topological insulator system and may lead to the development of novel spin electronic devices. It is anticipated that these heterostructures can be used as novel magnetoresistive random access memory (MRAM) devices with high charge-to-spin conversion efficiency. This implies that TI-based heterostructures can switch between 0 and 1 memory states much more efficiently, while consuming lower energy than the state-of-the-art magnetic tunneling junction-based heterostructures that use transition metals. The TI-based devices will be less susceptive to weak disorder and perturbations since writing process will occur via conventional writing field while electrical read out process will be topologically protected.
A key requirement for an operational heterojunction is a successful coupling of a TI with the magnetic material, which is facilitated by "atomically-clean" and abrupt junction interface. This should involve low-temperature deposition of the magnetic layer on the TI surface. This eliminates usage of the standard magnetic materials growth techniques, such as molecular beam epitaxy (MBE) and pulsed laser deposition, as they require the substrate temperatures greater than 300-350 ^{0}C, above what TIs can survive. Here, we report on the innovative approach to grow a room-temperature antiferromagnetic semiconductor (MnTe) using atomic layer deposition (ALD) and to epitaxially integrate it with the topological insulator (Bi_2Te_3). MnTe films were deposited at <100> GaAs and <111> InP. While the MnTe at <100> GaAs were polycrystalline, epitaxial growth was achieved at closely lattice-matched <111> InP at temperatures as low as 120 ^{0}C. Bi_2Te_3 was grown by MBE at c-Al_2O_3, *ex-situ* transferred into the ALD system, and used as a template for MnTe growth. High-resolution X-ray diffraction studies demonstrated that epitaxial MnTe growth was achieved at 120 ^{0}C. Transmission electron microscopy showed that the MnTe / Bi_2Te_3 interface was atomically sharp. No amorphous and / or disordered regions were present at the interface within the imaged regions. Magnetotransport properties of the ALD-grown MnTe were also studied and will be reported here. In summary, ALD was successfully used for the low-temperature epitaxial integration of MnTe antiferromagnetic semiconductor with the Bi_2Te_3 topological insulator. This opens the path for the realization of near-room temperature energy-efficient spintronic devices.

SESSION PP: Oxide Thin-Film Transistors
Session Chairs: Gerd Grau and Sarah Swisher
Friday Afternoon, June 25, 2021

1:00 PM PP01
(Student) Control of Transistor Operation Modes for SnO-TFT Yong Zhang, Alex W. Lee, Chi-Hsin Huang and Kenji Nomura; University of California, San Diego, United States

Tin monoxide (SnO) is widely accepted as the promising oxide semiconductor for *p*-channel oxide thin-film transistor (oxide-TFT) to develop oxide-based complementary circuit technology because of the reasonable high hole mobility of 2 cm^2/Vs and low temperature processability less than 300 ^{o}C . Therefore, numerous efforts have been made to develop high-performance *p*-channel oxide-TFT using SnO so far. It is also known that SnO-TFTs exhibit ambipolar behaviors, in which both electrons and holes can concurrently contribute to the field-effect conductions. This makes it also a promising candidate to develop novel logic circuit applications based on SnO ambipolar-TFT. However, these TFT modes are uncontrollable and it is still not clear the origin of two different TFT operation modes in SnO-TFTs. Therefore, it is important to clarify the origin and control the TFT operation modes for SnO-TFTs, in order to develop high-performance *p*-channel oxide-TFT and ambipolar-TFTs for next-generation flexible and ubiquitous electronics. In this paper, we investigated the TFT operation modes of SnO-TFTs based on the back-channel defect analysis and found that the high density back-channel defect controlled the TFT operation modes for SnO-TFTs. Inverted-staggered TFT device was fabricated using 150-nm thermal oxidized SiO_2/heavily doped c-Si substrate and the back-channel defect modification was performed by chemical wet-etching using TMAH and ALD-Al_2O_3 back-channel passivation. The pristine SnO-TFT without any back-channel modification has a strong *p*-type and very weak *n*-type behavior. After excess back-channel defect was introduced by TMAH wet-etching, *n*-type behavior was disappeared and the device turned to operate as *p*-channel oxide-TFT. Back-channel subgap defect analysis revealed that the SnO back channel had high-density donor-like defect near valence band of >10^{14} cm^{-2} eV^{-1}, which acts as a hole trap and leads to *p*-channel operation by Fermi-level pinning. If pristine SnO-TFT back-channel defect was reduced down to ~10^{13} cm^{-2} eV^{-1} by ALD-Al_2O_3 passivation, SnO-TFT exhibited clear ambipolar characteristics with almost symmetric *n*/*p*-channel operations. In this case, Fermi level was unpinned and can be smoothly swept toward to the conduction band by the applied gate bias. Since the origin of back-channel donor-like defect is oxygen vacancy, the appearance of ambipolar behavior after the ALD passivation was considered as the effect of oxygen vacancy defect termination. It is also noticed that for the completely *p*-channel operated SnO-TFT after surface etching, the ambipolarity can still be recovered by eliminating excessive defects with the same ALD surface passivation method. Thus, the SnO-TFT operation modes can be controlled by performing channel surface defect engineering, which exhibited stable and optimized TFT characteristics. The non-passivated SnO-TFT operated with *p*-channel saturation mobility of ~1.4 cm^2/Vs, and on/off current ratio of ~3 × 10^4. After passivation, the ambipolar SnO-TFT exhibited the switching voltage at 0V, *p*-channel mobility of ~1.2 cm^2/Vs and *n*-channel mobility of ~0.03 cm^2/Vs, with on/off current ratio of ~4 × 10^4 and ~3 × 10^3 for *p*-channel and *n*-channel respectively. We also fabricated the complementary-like inverter using two identical ambipolar-TFTs and observed clear inverter action with the voltage gain of 64.1 and 48.8 for the first and third quadrants, respectively.

1:15 PM PP02
(Student) Understanding the Differences Between Hall Mobility and FE Mobility for P-Type Cu2O Thin-Film Transistor Jaesung Jo, Julia D. Lenef, Kishwar Mashooq, Orlando Trejo, Neil P. Dasgupta and Rebecca L. Peterson; University of Michigan, United States

With the successful introduction of n-type oxide semiconductors into commercial display backplane technology, exploring p-type oxide semiconductors is imperative to demonstrate complementary metal oxide semiconductor (CMOS). Development of p-type material would enable oxide semiconductor technology to be introduced in new application areas, which include transparent/flexible electronics and back-end-of-line CMOS thin film transistors (TFTs). Cuprous oxide (Cu_2O) is considered as one of the most promising p-type oxides since it has a high Hall mobility, which originates from its delocalized valence band maximum formed with the Cu 3*d* and O 2*p* orbitals. Although a Hall mobility (μ_{Hall}) of > 50 cm^{2}V^{-1}s^{-1} was demonstrated in previous studies, thin film transistors (TFTs) reported to date have much lower field effect mobility (μ_{FE}), typically < 1 cm^2/V-s. Thus, it is critical to understand the

difference between μ_{Hall} and μ_{FE} to improve p-type Cu_2O TFTs. Here, we prepared Cu_2O films using RF magnetron sputtering and performed material and electrical analyses to investigate the large gap between the two mobility values [1]. First, to understand material properties, films were deposited with different thickness: 10 nm, 20 nm, 40 nm, and 80 nm. After vacuum annealing at 600 °C, each film had different film phase (Cu_2O or Cu_2O+CuO) and surface morphology. The material properties were comprehensively analyzed using X-ray absorption near-edge structure (XANES) analysis, grazing incidence X-ray diffraction (GIXRD), transmission electron microscopy (TEM), scanning electron microscopy (SEM), high-angle annular dark-field scanning TEM (HAADF-STEM), energy dispersive X-ray spectroscopy (EDS), and conductive atomic force microscopy (C-AFM). Second, to understand relationship between material properties and electrical characteristics, devices such as TFTs, capacitor, and Hall sample were fabricated alongside test structures such as transmission line method and sheet resistance pattern. Our study showed that a higher Cu(I) fraction, i.e. formation of Cu_2O, leads to better TFT performance and a measured Hall mobility of 12.1 cm^2/V-s. However, even in films with high Cu(I) fraction, the TFTs still had a much lower μ_{FE} of 0.005 – 0.1 cm^2/V-s. To identify the causes of the comparatively low μ_{FE}, we characterized TFT nonidealities such as interface traps (D_{it}) and contact resistance (R_C). For quantitative analysis, D_{it} was extracted based on the subthreshold slope of TFTs and R_C was confirmed using transmission line method. We found that R_C is ~33% of total resistance in ON state and D_{it} is about ~3×10^{13} $cm^{-2}eV^{-1}$. This work indicates the μ_{FE} of Cu_2O TFTs can be improved by reducing the high R_C and high D_{it}. The authors thank Intel Components Research for helpful discussions and funding. [1] J. Jo, J. D. Lenef, K. Mashooq, O. Trejo, N. P. Dasgupta, and R. L. Peterson, *IEEE Trans. Electron Devices*, vol. 67, no. 12, pp. 5557–5563, Dec. 2020.

1:30 PM PP03
(Student) Temporal Stability of Zinc Tin Oxide TFTs with Active Layers Deposited by Atomic Layer Deposition
Christopher R. Allemang, Tae Cho, Neil P. Dasgupta and Rebecca L. Peterson; University of Michigan–Ann Arbor, United States

The superior electron transport of transparent amorphous oxide semiconductors (TAOS), compared to a-Si and organic semiconductors, has allowed thin-film electronics to be investigated for beyond-display applications as active layers for 3D monolithic integration on top of silicon CMOS ICs.[1] Previously, we showed TFTs with zinc-tin-oxide (ZTO), an earth-abundant TAOS, deposited by atomic layer deposition (ALD) can meet the performance demands (μ_{FE} > 20 $cm^2V^{-1}s^{-1}$) and thermal budget (< 450°C) of 3D monolithic integration.[2] Device stability, essential for both display and beyond-display applications, has only been investigated for ALD ZTO in regard to negative bias instability.[3] Here, we fabricate bottom-gate, top-contact TFTs and study the temporal stability of devices stored in a dark air ambient with and without a passivation layer. Devices without passivation and ZTO annealed at either 400 or 500°C show a negligible increase in field effect mobility, μ_{FE}, of about 2.4% to 12.0 and 12.7 $cm^2V^{-1}s^{-1}$, respectively, and a small decrease in threshold voltage, V_t, of about 1.2 to 0.70 V, respectively. after approximately 100 days. Both of these changes correspond to an increase in free electrons which likely results from an increase in oxygen vacancies. Over the same period, the subthreshold slope, *SS*, remains nearly constant while the hysteresis, ΔV_c, decreases slightly to 1.27 and 0.885 V, respectively, indicating a stable semiconductor/gate insulator interface and reduction of bulk defects with aging. The majority of aging occurs within the first 30 days after which the device performance stabilizes. As the 400 and 500°C annealed devices show similar trends with aging, further studies implementing an Al_2O_3 passivation layer deposited by an O_3-based ALD process[4] were only performed on devices with a 400°C anneal, as those are within the thermal budget of 3D monolithic integration. Passivation immediately results in an apparent decrease in μ_{FE}, V_t, and ΔV_c, and an increase in *SS*. The apparent decrease in μ_{FE} can be attributed to an increase in contact resistance measured using transmission line method. Interface states introduced at the back surface by passivation, as corroborated by Silvaco Atlas Simulations, result in the negative V_t shift and increase in *SS*. The hysteresis of 400°C anneal devices with and without passivation layers is about 2.18 and 1.18 V at 0 days, respectively, and is stable for the device with passivation. Hysteresis for the devices without passivation decreases to about 1.27 V after 100 days of aging, approaching the value of the passivated device. The work presented here demonstrates the excellent temporal stability of ALD ZTO TFTs, which is critical for their adoption in thin-film electronics for beyond-display technologies. This work was supported by the National Science Foundation grant CMMI-1727918. Portions of this work were performed using the Lurie Nanofabrication Facility which is supported by the College of Engineering at the University of Michigan.
[1] Y. Son, B. Frost, Y. Zhao, and R.L. Peterson, Nat Electron **2**, 540 (2019).
[2] C.R. Allemang, T.H. Cho, O. Trejo, S. Ravan, R.E. Rodríguez, N.P. Dasgupta, and R.L. Peterson, Adv. Electron. Mater. **6**, 2000195 (2020).
[3] B.D. Ahn, D. Choi, C. Choi, and J.-S. Park, Appl. Phys. Lett. **105**, 092103 (2014).
[4] C.R. Allemang and R.L. Peterson, IEEE Electron Device Letters **40**, 1120 (2019).

1:45 PM PP04
(Student) Photonic Curing of Solution-Processed Indium Zinc Oxide Thin-Film Transistors
Adam Weidling[1], Vikram S. Turkani[2], Bing Luo[3], Kurt A. Schroder[2] and Sarah L. Swisher[1]; [1]University of Minnesota, United States; [2]NovaCentrix, United States; [3]University of Minnesota Twin Cities, United States

Metal oxide semiconductors such as indium gallium zinc oxide (IGZO) and indium zinc oxide (IZO) have received significant attention over the past few decades due to their desirable electrical and optical properties. Sol-gel techniques are commonly employed to deposit these materials because of the simplicity of the synthesis and the ability to easily tune the film composition. These sol-gel based oxide semiconductors often demonstrate high field-effect mobility even in the amorphous phase, but temperatures of at least 300 C are typically required to decompose the sol-gel and form high-quality semiconductor film. The desire to create high-quality flexible transistors on low-temperature plastic substrates has driven an investigation into alternative thermal processing methods for oxide semiconductors. One such option being explored is pulsed-light processing based on flashlamps, commonly known as photonic curing. Photonic curing offers advantages over conventional thermal processing methods such as ultra-short processing time and compatibility with low-temperature substrates. However, previous work on photonically cured thin-film transistors (TFTs) often results in significant heating of the entire substrate rather than just the thin film at the surface. In this talk, we will discuss our recent work using photonic curing to rapidly and effectively convert metal oxide sol-gels to realize high-quality TFTs. Sol-gel indium zinc oxide (IZO) based TFTs are photonically cured with efficient molybdenum gate absorbers using a xenon flashlamp (NovaCentrix PulseForge 1300) using intense white light delivering radiant energy up to 6 Jcm^{-2}. Simulations indicate that the IZO film reaches a peak temperature of ~590 C while the back of the glass substrate stays near room temperature. This process yields TFTs with a field effect mobility above 20 $cm^2V^{-1}s^{-1}$ and an I_{On}/I_{Off} ratio approaching 10^8, which exceeds the performance of samples annealed at 500 C for 1 hr. We will discuss the requirements and design guidelines for photonic curing metal oxide semiconductors for high-performance TFT applications, focusing on the importance of effective gate absorbers and

optimized pulse designs to efficiently and effectively cure the sol-gel films.

2:00 PM PP05
Designing Printed High-k Modulation-Doping Layers for InO_x Transistors to Break Thermal Processing Barriers William J. Scheideler; Dartmouth College, United States

Metal oxide semiconductors have unmatched properties for driving future thin film electronics, displaying high carrier mobility, high transparency, and the ability to achieve efficient transport in both their amorphous and nanocrystalline state. The ability to solution-process and print metal oxide semiconductors has the potential to deliver new applications in optoelectronic devices for energy, display, and sensing applications. However, these new applications demand precise control of oxides' electronic properties at the nanoscale, particularly in ultrathin oxide semiconductors (< 20 nm) highly sensitive to the back channel interface. This talk will present scalable strategies for surface capping and modulation doping of oxide semiconductors for high-performance thin film transistors manufactured by inkjet printing technology at ultra-low process temperatures (< 200 ºC) compatible with polymer substrates. We develop printed high-k surface capping layers (YO_x, GaO_x, LaO_x) for modulating the electronic properties of InO_x transistors. Solution-processed material design offers incredible flexibility for multi-material integration, including tuning of dopant incorporation and fabrication of layered semiconductors integrating back-channel passivation. In this study, passivation with high-k oxide capping layers is demonstrated to improve both the bias-stress stability and performance of these metal oxide semiconductors. We demonstrate that high- capping layers offer tunable surface passivation for adjusting the carrier concentration by modulation-doping and enhancing mobility via the density of electronic states (DOS) in ultrathin InO_x semiconductors. These effects can be understood by considering the impact of intrinsic hydroxide (OH^-) defects present in low-temperature processed metal oxide semiconductors, which we study with both XPS and XRD techniques. Our high-k capping layers effectively compensate the intrinsic defects in solution-processed metal oxides, breaking the thermal processing barriers limiting flexible metal oxide electronics. We find that these strategies are extensible to other high-mobility binary oxides such as ZnO_x and SnO_x, facilitating applications to various large area optoelectronic devices such as photodetectors and thin film solar cells, which ultimately demand surface passivation and work function control for carrier selective contacts.

SESSION QQ: Group III-Nitride LED II
Session Chairs: Theeradetch Detchprohm and Russell Dupuis
Friday Afternoon, June 25, 2021

1:00 PM QQ01
(Student) Analysis on the Internal Quantum Efficiency of Deep-Ultraviolet Emitting AlGaN Nanowires Jiaying Lu, Yun Zhong and Songrui Zhao; McGill University, Canada

In recent years, AlGaN nanowires grown by molecular beam epitaxy (MBE) have emerged as an appealing platform for semiconductor deep ultraviolet (UV) light-emitting devices [1, 2]. Although the progress, a better understanding of some of the fundamental physical properties of such nanowires is necessary. For example, the internal quantum efficiency (IQE) of AlGaN nanowires is often investigated by the temperature-dependent photoluminescence (PL) technique that assumes a 100% IQE at low temperatures. This assumption is, however, not always valid. This contrasts with the comprehensive understanding of IQE of AlGaN quantum wells and epilayers. Moreover, the efficiency droop of the deep UV emitting AlGaN nanowires is much less studied. In this regard, we analyzed the room-temperature IQE of AlGaN nanowires emitting at ~260 nm, being considered as the most efficient wavelength for disinfection, through a theoretical analysis on the room-temperature excitation dependent PL. A peak IQE of ~55% was derived. Moreover, a carrier delocalization mechanism was pinpointed as a droop mechanism. In this work, the AlGaN nanowires were grown on Si (111) substrates by MBE in the nitrogen-rich condition at a relatively low substrate temperature. Detailed growth conditions can be found in Ref. [3]. The power-dependent PL experiments were performed in a setup consisting of a 213 nm laser and a deep UV spectrometer. We further used a theoretical model that considers the major recombination channels in semiconductors, i.e., An as the Shockley-Read Hall (SRH) nonradiative recombination, Bn^2 as the bimolecular radiative recombination, and Cn^3 as the higher-order nonradiative recombination, where n is the carrier density and A, B, C are the respective recombination coefficients, to analyze the excitation power dependent integrated PL intensity (I_{PL}). In this framework and assuming at steady state, the generation rate G follows $G = An+Bn^2+Cn^3$. Further expressing $I_{PL} = \gamma Bn^2$, where γ is an experimental parameter, one can have, $G = A(I_{PL})^{1/2}/(B\gamma)^{1/2} + I_{PL}/\gamma + C(I_{PL})^{3/2}/(B\gamma)^{3/2}$ (1) Here, G can be experimentally determined by $G = P(1-R_F)\alpha/(A_{spot}h\nu)$, where P is the peak excitation power, R_F is the Fresnel reflection, α is the absorption coefficient, A_{spot} is the laser spot size, and $h\nu$ is the excitation photon energy. The experimentally determined $G - I_{PL}$ dependence can be further fitted to Eq. (1), allowing one to determine the parameter γ; and the IQE is further calculated by IQE = $I_{PL}/\gamma G$. The scattered symbols and the solid line in Fig. 1 show the experimentally determined $G - I_{PL}$ dependence and the fitting curve according to Eq. (1), respectively. It is seen that a good fitting is obtained. The calculated IQE as a function of G is shown in the inset of Fig. 1. It is seen that a peak IQE of ~55% is reached, followed by a droop. To further analyze the droop mechanism, the excitation dependent PL peak energy and full-width-at-half-maximum (FWHM) were analyzed. Shown in Fig. 2, a blueshift of the PL peak energy is observed accompanied by an overall increasing trend of the FWHM, suggesting the role of the carrier delocalization in the efficiency droop. Current studies are on the Al content dependent efficiency droop behavior and will be reported.

References:
[1] S. Zhao *et al.*, "AlGaN Nanowires: Path to Electrically Injected Semiconductor Deep Ultraviolet Lasers," *IEEE Journal of Quantum Electronics* 54, 1 (2018).
[2] S. Zhao *et al.*, "AlGaN Nanowires for Ultraviolet Light-Emitting: Recent Progress, Challenges, and Prospects," *Micromachines* 11, 125 (2020).
[3] Y. Zhong *et al.*, "Molecular beam epitaxial growth and optical characterization of AlGaN nanowires with reduced substrate temperature," *AIP Advances* 10, 025022 (2020).

1:15 PM QQ02
(Student) Deep Ultraviolet Luminescence and Charge-Transfer Excitons in Atomically Thin GaN Quantum Wells Woncheol Lee, Yuanpeng Wu, Zetian Mi, Mackillo Kira and Emmanouil Kioupakis; University of Michigan–Ann Arbor, United States

In this work, we investigate the properties of spatially indirect excitons (IXs) confined in pairs of atomically think GaN wells, separated by polar AlN barriers. Atomically thin GaN is a promising material for realizing strongly bound excitons because of its extreme quantum confinement effect. Also, the spontaneous polarization fields in nitride heterostructures allow IXs to form in atomically thin GaN quantum wells even without external electric fields. We performed first-principles calculations based on density functional theory and many-body perturbation theory to investigate the properties of IXs and DXs in pairs of atomically

thin GaN quantum wells separated by polar AlN layers with varying thickness. Our calculation shows that the overlap of the electron and hole wavefunctions, the degree of electron-hole interaction, and the character (IX or DX) of the lowest-energy exciton can be controlled by changing the thickness and the resulting electrical polarization of the separating AlN barrier. We demonstrate that room-temperature stable IXs with radiative decay rates several orders of magnitude lower than DXs can be realized in these atomically thin polar nitride heterostructures for potential excitonic applications at room temperature based on a commercial semiconductor platform. For realization of IXs in atomically-thin GaN quantum wells, molecular beam epitaxial growth was performed on an n-type Si substrate using a Veeco GEN II system with radio frequency plasma-assisted nitrogen source. The epitaxy includes ~100 nm long GaN nanowires which serves as a template for the subsequent epitaxy of ~150 nm long AlN nanowires. Then, monolayer GaN quantum well/AlN barrier/monolayer GaN quantum well heterostructure was grown on top of AlN nanowires. The thickness of AlN barrier was varied by changing the growth duration. Figure 1 shows the photoluminescence spectra of two samples with 1 ML and 7 MLs thick AlN barriers incorporated, respectively. The emission peak around 5.93 eV can be attributed to the excitonic emission from AlN. DX emission dominates in the spectrum of sample with 7 MLs thick AlN barrier. In comparison, there's a clear shoulder emerging on the lower energy side observed in the sample with 1 ML thick AlN barrier, which can be assigned to indirect exciton (IX) emission. The work is supported by the University of Michigan College of Engineering Blue Sky Research Program. W.L. was partially supported by the Kwanjeong Educational Foundation Scholarship. Computational resources were provided by the DOE NERSC facility.

1:30 PM QQ03
AlGaN UVC Micropixel LEDs with Vertical and Slanted Sidewalls Richard Floyd, Mikhail Gaevski, MVS Chandrashekhar, Grigory Simin and Asif Khan; University of South Carolina, United States

In 2004 our group first reported on interconnected micropixel UVC LED arrays with a pixel size of ~25µm which, compared to equal area square geometry LEDs, exhibited increased light output power (LOP) and decreased series resistance.[1] In 2020, we presented a new modularly interconnected micropixel LED design comprised of parallel-connected sub-arrays of sub-20 µm diameter micropixels with integrated heat-spreaders.[2] Using this design, we showed that a reduction in pixel size down to 5 µm increased the peak LOP 5.25x and reduced the thermal impedance 3.75x of the interconnected arrays compared to a 90 µm diameter reference pixel with equal junction area. Here, we present the first study of the size-dependent light emission and electrical characteristics of individual sub-20 µm diameter micropixel UVC LEDs with slanted and vertical sidewall profiles. For these disk geometry LEDs, we explored the relationship of the light extraction efficiency (LEE) and the mesa perimeter length to area ratio (PL/A) as well as the dependence of the peak DC input power density, before LOP saturation, on the sidewall surface-area to volume ratio (S.S.A/V). Enabled by the largest PL/A and S.S.A/V ratios for our devices, a single 5 µm micropixel with a 48° sidewall profile had a peak measured brightness of 10.2 kW/cm^2 (2 mW) at 50.1 kA/cm^2 (10 mA) when energized with a 0.05% duty-cycle and 500 ns pulses. Using our standard UVC $_{cm}$~275 nm LED epilayers, individual micropixel LEDs were fabricated where the p-ohmic contact size varied from 5 µm to 90 µm in diameter. The n-ohmic contact formed a 20 µm wide picture frame around an individual pixel. athodoluminescence (CL) was then performed on a 90 µm pixel with a sidewall angle of 25° from horizontal prior to metallization. The CL line-scan intensity was fitted with an exponential curve to extract the effective absorption length within the mesa structure, which we estimated to be ~ 15 µm. Next, vertical sidewalled micropixels of each size were measured by focusing the beam in the center of the mesa structure. The peak MQW CL intensity was unchanged with varying pixel size. Hence, we suspect that for slanted sidewall devices, a reduction of the mesa diameter to less than 15 µm will reveal a pixel size dependent LEE enhancement arising from the efficient outcoupling of TM-polarized photons[3]. After the ohmic contact formations and probe-pad deposition, the emitted power from the individual pixels with bare sidewalls was measured under DC and pulsed current injection. Compared to the vertical sidewall devices, those with slanted sidewalls exhibited enhanced LEEs of 1.15x, 1.41x, 1.54x and 1.83x for the 90, 15, 10 and 5 µm pixels, respectively. The vertical sidewall devices had the same LEE, determined from the external quantum efficiency (EQE), regardless of pixel size. This work was supported by an Army Research Office grant W911NF-18-1-0029 that was monitored by Dr. Mike Gerhold.
[1] Adivarahan, V., et al. Applied physics letters 85.10 (2004): 1838-1840.
[2] Floyd, Richard, et al. Applied Physics Express 14.1 (2020): 014002.
[3] Lee, Jong Won, et al. Acs Photonics 3.11 (2016): 2030-2034.

1:45 PM QQ04
(Student) Red-Emitting InGaN/AlGaN/GaN Multiple Quantum Wells with Various Underlayers Haotian Xue[1], Syed Ahmed Al Muyeed[1], Elia Palmese[1], Renbo Song[1], Nelson Tansu[2,1] and Jonathan J. Wierer[1]; [1]Lehigh University, United States; [2]The University of Adelaide, Australia

Displays with inorganic light-emitting diodes (LEDs) have potential advantages over organic LED displays, such as lower power consumption and longer operation lifetimes [1]. These displays require LEDs emitting in at least the three primary colors (blue, green, and red), and this could be achieved with III-nitride LEDs in the blue and green and AlInGaP in the red. However, red AlInGaP LEDs are fabricated with different processes than III-nitrides, and the efficiency drops with decreasing chip size. The alternative is an InGaN-based red-emitting LED, but it is difficult to achieve the required higher indium content in the InGaN quantum well (QW). Challenges include defects formed by lower temperature epitaxy and higher lattice mismatch strain, and phase separation. It has been shown that AlGaN interlayers (ILs) grown on top of the InGaN QW results in higher radiative efficiency for longer wavelength emitters (> 500 nm) [2]. It is also known that indium-containing underlayers grown before the multiple quantum well (MQW) active layers help to reduce the non-radiative defect recombination and enhance radiative efficiency. Here, both interlayers and underlayers are combined simultaneously to achieve high efficiency, red-emitting InGaN/AlGaN/GaN MQWs. In this work, red-emitting MQWs consisting of 5 periods of InGaN/AlGaN/GaN are grown on top of 20 periods of InGaN/GaN underlayers by MOCVD on Si-doped n-GaN templates. The composition, thicknesses, and strain of the structures are determined using X-ray diffraction, reciprocal space mapping, and optical reflectance measurements. The $In_xGa_{1-x}N$ QWs are 3.4 nm thick with x=0.28, the GaN barriers are 9.5 nm thick, and the $Al_yGa_{1-y}N$ ILs are 1.3 nm thick with y varying between 0.43, 0.60, and 0.82. The growth temperatures for InGaN QW and AlGaN QW are 675 °C, and 880 °C for GaN barriers. The optimum Al content was found to be 0.82 by photoluminescence (PL) and used for the MQWs grown on underlayers. The higher Al content IL better retains the In in the QW and controls strain. The Si-doped underlayers consist of 20 periods of $In_zGa_{1-z}N$/GaN with an InGaN thickness of 1.8 nm and GaN with a thickness of 2 nm. The In content, z is varied between 0.015, 0.025, and 0.065. This change in z is achieved by growing the underlayer at 850 °C, 830 °C, and 780 °C, respectively. A fourth sample without an underlayer is grown for comparison. Finally, and full LEDs are grown with a 15 nm thick AlGaN electron blocking layer and 200 nm thick p-type GaN on top of the MQWs.

The MQW samples' radiative efficiencies are determined by measuring photoluminescence at 8 K and room temperature using a 405 nm laser diode. The emitting wavelength of the MQWs are similar and vary from 640 nm to 590 nm, blueshifting with increasing pump power density. The MQW with a z=0.025 underlayer is the most efficient, with a peak radiative efficiency of ≈5.5%. We anticipate this is due to a reduction in the non-radiative recombination rate compared to the other samples and will confirm via differential carrier lifetime analysis [3].

[1] J. J. Wierer, Jr. and N. Tansu, Lasers and Photonics Review, 13, 1900141 (2019).
[2] D. D. Koleske, et al., J. of Crystal Growth 415, 57-64 (2015).
[3] S. A. A. Muyeed, et al., J. Appl. Phys, 540, 125652 (2020).

2:00 PM QQ05
(Student) Exploring Al(X)Ga(1-X)N Nanostructures Fabricated via Top-Down Chemical Wet Etching Barbara A. Kazanowska[1], Keshab R. Sapkota[2], Brendan P. Gunning[2], Kevin S. Jones[1] and George T. Wang[2]; [1]University of Florida, United States; [2]Sandia National Laboratories, United States

$Al_{(X)}Ga_{(1-X)}N$ is a leading candidate for current and future ultra-wide bandgap electronic (e.g. power electronics and sensors) and optoelectronic (e.g. deep-UV light emitting diodes (LEDs) and lasers) applications. However, three-dimensional (3D) etch technologies for $Al_{(X)}Ga_{(1-X)}N$ remain immature compared to silicon, limiting its full potential for novel devices. A more robust study is needed to fully utilize chemical wet etching as a possible processing pathway for future devices. Both KOH and H3PO4 chemistries have been reported to etch GaN into varying nanostructures to be used in novel electronic and optoelectronic setting. Here, we build from the foundation of anisotropic KOH and H_3PO_4 based wet etchants used to fabricate GaN nanostructures and explore $Al_{(X)}Ga_{(1-X)}N$ alloys etched in acids and bases. We investigate the etch reactivity of $Al_{0.14}Ga_{0.86}N$, $Al_{0.65}Ga_{0.35}N$, and AlN in KOH-based chemical etchants in a macroscopic scale, where we perform some of the first non-polar etch rate measurements as a function of Al content. We present the etch evolution of nanostructures as a function of 85% H_3PO_4 and variable temperature which leads to sharp nanowires with tips less than ~10 nm. At extended etch times, we observe interesting surface features made up of short nano-pyramids in both $Al_{0.65}Ga_{0.35}N$ and AlN. Additionally, we pose possible etch mechanisms for the unusual facet evolutions observed. This work is supported by the Center for Integrated Technologies (CINT) User Proposal 2017BC0008, the Sandia Diversity Initiative Partnership, and the Laboratory Directed Research and Development program at Sandia National Laboratories. Sandia National Laboratories is a multi-program laboratory managed and operated by National Technology and Engineering Solutions of Sandia, LLC., a wholly owned subsidiary of Honeywell International, Inc., for the U.S. Department of Energy's National Nuclear Security Administration under contract DE-NA-0003525.

SESSION RR: Late News—Novel Properties, Processing, Modeling and Characterization Methods
Session Chairs: W. Alan Doolittle and Stephanie Law
Friday Afternoon, June 25, 2021

1:00 PM RR01
(LATE NEWS, Student) Kinetic Model of Vertical Indium Segregation During InGaN Epitaxy Christopher M. Matthews and W. Alan Doolittle; Georgia Institute of Technology, United States

One of the most ubiquitous and well-known problems for indium gallium nitride (InGaN) is the tendency for the material to separate into In-rich and In-poor regions during growth – a phenomenon typically referred to as phase separation. This has precluded the effective growth of thick, high-quality, single-crystal InGaN films for many of the applications which have motivated InGaN research since it was first synthesized (e.g., full spectrum or tandem-with-Si solar cells and RGB LEDs). Despite a large volume of research dedicated to this topic over the past three decades, the mechanisms that drive this InGaN composition variability are not fully defined. Metal-rich growth, which can be severely hindered by InGaN phase separation, is often used in MOCVD to drive quantum dot formation and ripening and is the most prevalent surface condition in MBE. In this work, we suggest that bulk diffusion and thus phase separation in the traditional sense, is of lesser concern than surface driven processes. Consequently, we propose that InGaN "phase separation" comes primarily from a combination of at least three distinct phenomena – thermal decomposition, vertical indium segregation (VIS), and lateral indium separation (LIS). A new 1D model describing the vertical segregation mechanism is proposed and evaluated using parameters extracted from state-of-the-art InGaN epitaxy. The thermal and lateral mechanisms will be presented in future revisions of the model. Via RHEED analysis, Moseley et al demonstrated that a critical dose of excess metal exists for metal modulated epitaxy (MME) of InGaN beyond which a diffusion of indium away from the growth surface coupled with an equal gallium diffusion toward the growth surface (VIS) occurs[1]. This phenomenon can be expected to occur for any metal-rich growth of InGaN, although the cyclical nature of MME makes it easier to identify. From this observation, we have built a model for the accumulation and consumption of metal adatoms during MME growth of InGaN based on our current understanding of the surface kinetics. MME is particularly suited to evaluate the model as it occurs at substrate temperatures where decomposition and desorption are inhibited, and lateral diffusion is enhanced leading to uniform adatom mixing. This allows us to evaluate the model in the case where only vertical indium segregation is in effect. Using a system of coupled differential equations, we can model the indium and gallium adatoms as they adsorb onto the surface, grow into the crystal, and transfer between the pseudomorphic, laterally-contracted, and droplet adlayers. We found this model to be self-consistent and in line with our expectations for a realistic growth for all of the following cases: nitrogen-rich InGaN growth, growth up to less than one monolayer of adatom accumulation, growth between one and two monolayers of adatom accumulation, growth into the droplet accumulation regime, and multiple cycles of each metal-rich case (MME). The simplicity of the model should make it easy to expand upon by adding other mechanisms like thermal decomposition and LIS and generalizing to other InGaN epitaxial techniques beyond MME and MBE. Experimental results to validate the model and extract physical parameters are forthcoming, and the model will eventually be made public on an open-source code sharing website allowing widespread use.

[1] M. Moseley, B. Gunning, J. Greenlee, J. Lowder, G. Namkoong, and W. Alan Doolittle, Journal of Applied Physics **112**, 014909 (2012).

1:15 PM RR02
(LATE NEWS) Strong Coupling in Semiconductor Hyperbolic Metamaterials Patrick R. Sohr, Zhengtianye Wang and Stephanie Law; University of Delaware, United States

Hyperbolic metamaterials (HMMs) are highly anisotropic, composite materials comprised of a subwavelength metal and dielectric structure. HMMs have an anisotropic permittivity such that $\varepsilon_{xx}=\varepsilon_{yy}$, $\varepsilon_{\parallel}=\varepsilon_{\perp}<0$. This anisotropy results in an open and hyperbolic isofrequency surface, which enables HMMs to support large wavevector light through cavity modes called volume plasmon polaritons (VPPs). VPPs arise due to the coupling of surface plasmon polaritons at the metal and dielectric interfaces. VPPs provide a mechanism for many interesting and novel light-

matter interactions. One of which is the strong coupling of VPPs to emitters embedded within the HMMs. Strong coupling occurs when the coupling strength for two or more oscillators is greater than their combined decay rates. In this regime, the two oscillators will split and create two hybridized modes. Previous theoretical work has predicted that it is possible to couple the highly confined light in the VPP modes to the intersubband transition (ISBT) of a quantum well (QW) embedded within the dielectric layers of an HMM. In this work, we show evidence of strong coupling between the VPP modes in an Si:InAs/AlSb HMM and the ISBT of an InAs/AlSb QW. A QW with an ISBT of approximately 12.5μm was embedded in each of the dielectric layers of the HMM. Metallic gratings were applied to the surface of the HMMs to couple incident light into the VPP modes. The reflection spectra from the HMM with QWs were measured for multiple gratings to map out the dispersion of the VPP modes and the QW. These results conclusively show avoided level crossing, which is indicative of strong coupling. Additionally, these results were compared to the reflection spectra from an HMM with the same structure but without QWs, which displayed no signed of avoided level crossing. This work provides a starting point for semiconductor devices composed of HMMs and emitters like QWs and quantum dots.

1:30 PM RR03
(LATE NEWS) Preparation by Melt Method and Phase Equilibria in the $CuFeS_{2-\delta}$ – $CuAlS_2$ System Barys Korzun[1], Gert Kloess[2], H.-J. Hoebler[2] and Klaus Bente[2,3]; [1]Borough of Manhattan Community College, The City University of New York, United States; [2]University of Leipzig, Germany; [3]Eberhard Karls University of Tubingen, Germany

The chalcopyrite-type I-III-VI_2 ternary semiconductor compounds (where I - Cu, Ag; III - Al, Ga, In; VI - S, Se, Te) have physical properties, suitable for solar cells and optical filters. $CuAlS_2$ is a semiconductor with a direct-band gap of 3.6 eV at room temperature and belongs to a group of wide band gap chalcogenide materials. These compounds can be used for creation of intermediate band (IB) solar cell, where a band of states inside the fundamental bandgap provides additional optical transitions. In such case it is very important to determine the limits of solubility of the corresponding compounds and construct the phase diagrams. The aim of this paper is to study phase relations in the $CuFeS_2$ - $CuAlS_2$ system. The X-ray studies of alloys were carried out using monochromatic Cu K_α-radiation (1.54018 Å, step size 0.01° or 0.04°, counting time 2 s) using diffractometers DRON-4 and Seifert XRD7. The Rietveld analysis of the X-ray powder diffraction data was done using the FullProf software. SEM-EDX data were obtained using a Hitachi TM 3000 tabletop scanning electron microscope (Hitachi High-Technologies, Clarksburg MD, USA). The EDX data were processed using Quantax70 X-ray microanalysis software (Bruker, Berlin, Germany). Microstructure was studied on freshly-polished samples without additional etching using microscope Keyence VX100. The DTA measurements were performed by means of equipment specially designed and constructed for measurements up to temperatures of 1573 K. The presence of phase transformations and their temperatures were determined with an accuracy of 2 K for the phase transition temperature. Powdered samples (typical mass 1 g) were placed in evacuated silica capsules with Al_2O_3 used as a reference material. DTA was run on samples that were heated at the constant rate of 2-3 K/min. The temperatures of the sample and the reference materials were determined with Pt/90%Pt-10%Rh thermocouples.
The regions of solubility on sides of $CuFeS_2$ and $CuAlS_2$ ternary compounds were determined and T-x phase diagram of the $CuFeS_2$ – $CuAlS_2$ system in the quasibinary approach was constructed. The limited solubility and phase relations in the whole interval of compositions are discussed.

1:45 PM RR04
(LATE NEWS, Student) Nanostructured Semiconductors Prepared Using High Pressure Chemical Vapor Deposition with Mesoporous Templates Briana Laubacker, Ke Wang, Trevor Clark, Haiying Wang and Suzanne Mohney; The Pennsylvania State University, United States

There has been much interest in synthesizing nanostructured semiconductors due to the modified electronic and optical properties these materials possess. However, there are only a few examples of 3D ordered, interconnected structures composed entirely of the same material with features between 2-10 nm. Given their widespread use in devices, silicon and germanium are interesting candidates for exploring new morphologies. A nanoscale framework of silicon or germanium could be advantageous due to novel electronic or optical properties that could arise. Fully infiltrating silicon or germanium within a mesoporous template without the formation of voids or nanoparticles is not feasible using many conventional deposition methods. To overcome these obstacles, high pressure chemical vapor deposition (HPCVD), using mesoporous silicas as templates, is being investigated. This technique uses pressures as high as 35 MPa and a confined reactor geometry to allow substances to be fully infiltrated within nanoscale pores. Using this process, a structure can be obtained that is periodic, with 3-D order and connectivity derived from the original template. Germanium was deposited within the empty pore networks of KIT-5 mesoporous silica using HPCVD. Characterization by small angle x-ray scattering, wide angle x-ray scattering, and transmission electron microscopy confirm that the resulting nanostructured germanium has well-defined ordered features that are 5 nm in size. To date, this is the smallest template material that has been successfully infiltrated with this method.

2:00 PM RR05
(LATE NEWS) Tuning the Magnetic Properties of Two-Dimensional MXenes by Chemical Etching Kemryn Allen-Perry[1], Weston Straka[2], Danielle E. Keith[1], Shubo Han[1], Lewis Reynolds[2], Bhoj Gautam[1] and Daniel E. Autrey[1]; [1]Fayetteville State University, United States; [2]North Carolina State University, United States

Two-dimensional materials based on transition metal carbides have been intensively studied due to their unique properties including metallic conductivity, hydrophilicity, and structural diversity and have shown great potential in several applications. While MXenes based on magnetic transition elements show interesting magnetic properties, not much is known about the magnetic properties of titanium-based MXenes. Here, we measured magnetic properties of $Ti_3C_2T_x$ MXenes synthesized by different chemical etching conditions. Our measurements indicate that there is a paramagnetic–antiferromagnetic (PM-AFM) phase transition, and the transition temperature depends on the synthesis procedure of MXenes. Our observation indicates that the magnetic properties of these MXenes can be tuned by the extent of chemical etching which can be beneficial for the design of MXene-based spintronic devices.

EMC INDEX

This index lists session chairs, presenters and co-authors.

- Session chairs will have the session letter code. (eg: A)
- The plenary speaker will have an *(asterisk) before the session letter code and paper number in bold type. (eg: ***PL01**)
- Presenters will have the session letter code followed by the paper number in bold type. (eg: **A02**)
- Co-authors will have the session letter code followed by the paper number in regular type. (eg: A02)

L

M